



**HAL**  
open science

# Object detection and characterization from faint signals in images : applications in astronomy and microscopy

Olivier Flasseur

► **To cite this version:**

Olivier Flasseur. Object detection and characterization from faint signals in images : applications in astronomy and microscopy. Astrophysics [astro-ph]. Université de Lyon, 2019. English. NNT : 2019LYSES042 . tel-02492795v2

**HAL Id: tel-02492795**

**<https://theses.hal.science/tel-02492795v2>**

Submitted on 17 Jul 2020

**HAL** is a multi-disciplinary open access archive for the deposit and dissemination of scientific research documents, whether they are published or not. The documents may come from teaching and research institutions in France or abroad, or from public or private research centers.

L'archive ouverte pluridisciplinaire **HAL**, est destinée au dépôt et à la diffusion de documents scientifiques de niveau recherche, publiés ou non, émanant des établissements d'enseignement et de recherche français ou étrangers, des laboratoires publics ou privés.





Numéro d'ordre (NNT) : 2019LYSES042

Thèse préparée pour l'obtention du grade de  
**Docteur de l'Université de Lyon**  
opérée au sein de l'**Université Jean Monnet**

Spécialité : **Image, Vision**  
École Doctorale 488, Science Ingénierie Santé

---

# Object Detection and Characterization from Faint Signals in Images: Applications in Astronomy and Microscopy

---

Détection et Caractérisation d'Objets à partir de Signaux Faibles dans des Images :  
Applications en Astronomie et Microscopie

par :

**Olivier Flasseur**

Univ. Lyon, UJM Saint-Etienne, CNRS, Institut d'Optique Graduate School,  
Laboratoire Hubert Curien UMR 5516, F-42023, Saint-Étienne, France

Soutenue publiquement le 19 novembre 2019 devant le jury composé de :

---

Jérôme Idier	Directeur de Recherche CNRS	LS2N	Rapporteur
Antoine Roueff	Maître de Conférences	Institut Fresnel	Rapporteur
Julie Delon	Professeure	Univ. Paris Descartes	Présidente
Anne-Marie Lagrange	Directrice de Recherche CNRS	IPAG	Examinatrice
Michael Muma	Research Fellow	Univ. Darmstadt	Examiner
Laurent Mugnier	Maître de Recherche	ONERA	Examineur
Corinne Fournier	Maître de Conférences	Univ. Jean Monnet	Directrice
Loïc Denis	Maître de Conférences	Univ. Jean Monnet	Co-Directeur
Éric Thiébaud	Astronome	CRAL	Co-Encadrant
Maud Langlois	Directrice de Recherche CNRS	CRAL	Co-Encadrante

---



# Acknowledgements & Remerciements

First, I would like to express my sincere thanks to the Members of the Committee. The opportunity to exchange with them about this work was a real honor for me. I thank Julie Delon for accepting the presidency of the Committee and for the kind insights she brought to my work during the defense. I am very grateful to Jérôme Idier and Antoine Roueff for their careful reading of my manuscript; their numerous remarks, suggestions, and questions have significantly improved the quality of this document. I also thank Anne-Marie Lagrange, Michael Muma, and Laurent Mugnier for examining my work. I particularly appreciated the diversity of their questions and their suggestions for future works.

Parce que ce travail de recherche est très loin d'être un travail solitaire, les remerciements qui suivent sont adressés aux personnes qui y ont contribué, souvent de très près, et à qui je dois bien plus qu'une fière chandelle.

Tout d'abord, mes remerciements se tournent vers Loïc Denis. Que le Lecteur de ce manuscrit en soit averti; je lui dois toute ma reconnaissance car il est à l'origine (et bien plus) de la quasi-totalité des approches méthodologiques développées dans ce présent manuscrit. Je souhaiterais également le remercier pour sa grande implication dans les tâches de rédaction et de relecture des différents articles dont le corps de texte est largement repris dans ce manuscrit. Je mesure réellement la chance que j'ai eu de pouvoir bénéficier de son expertise, de son encadrement particulièrement pédagogue et de son implication au cours de ces trois années. Outre ces aspects, je souhaiterais également le remercier vivement pour son soutien, ses encouragements, sa confiance, sa grande disponibilité et l'enthousiasme sans faille qu'il a témoigné à l'égard de ces travaux; tout cela a aussi largement participé au bon déroulement de ce travail. Quoique l'usage du terme *mentor* dans un contexte scientifique ait parfois pu me faire sourire par le passé, je crois qu'il est tout à fait adapté pour décrire l'admiration que je porte envers ses connaissances et ses qualités d'enseignant et de chercheur!

De manière similaire, je souhaiterais vivement remercier Corinne Fournier qui a dirigé ces travaux et à qui je dois également toute ma reconnaissance pour son implication dans ce travail de recherche. De nombreuses approches sur les aspects microscopie holographique, en particulier celles développées en début de thèse, lui sont en grande partie dues. J'ai également pu bénéficier de son investissement sans faille dans les différentes étapes de la chaîne d'analyse en holographie; depuis la réalisation des acquisitions, en passant par leur traitement et jusqu'à l'interprétation des résultats. Travailler au sein de l'équipe qu'elle coordonne a été pour moi un véritable plaisir. Je souhaiterais également la remercier pour la grande confiance qu'elle m'a témoignée, et cela même avant le commencement officiel de cette thèse alors que j'étais en quête DU sujet et DE l'encadrement qui pourraient me correspondre. Je peux réellement dire que le contrat a été rempli!

Cette thèse, initialement centrée sur le développement de méthodes de traitement pour la microscopie a pu être étendue à l'astronomie grâce à de nombreux échanges avec le

Centre de Recherche Astrophysique de Lyon.

En particulier, j'adresse de profonds remerciements à Éric Thiébaud pour son suivi et son investissement constants tout au long de ces trois années. Je lui dois de très nombreux développements méthodologiques qui ont réellement débloqués ces travaux lorsque les algorithmes se frottaient à la dure réalité des données. Je retiens en particulier nos nombreuses journées d'échanges au CRAL qui ont été de véritables bols d'air frais pour l'avancée de ces travaux. Je souhaiterais également le remercier pour son implication dans les activités de rédaction et de relecture (articles, thèse) ainsi que pour le regard toujours vigilant et bienveillant qu'il y a porté. Je n'ai qu'un seul regret : n'avoir pu explorer, par manque de temps, que le millième des pistes méthodologiques qu'il m'a soufflées !

J'aimerais également adresser de sincères remerciements à Maud Langlois pour l'énergie considérable qu'elle a déployée aux traitements comparatifs des données avec les algorithmes de l'état de l'art. Je souhaiterais également la remercier de m'avoir fait découvrir le domaine de l'imagerie directe qui m'était totalement inconnu. Grâce à son implication, je dois bien reconnaître que j'ai *attrapé le virus* ! Outre ces aspects, j'ai particulièrement apprécié d'avoir été mis au coeur des problématiques applicatives propres à ce sujet. Dans ce sens, son intérêt pour les algorithmes développés ainsi que leur utilisation pour traiter de nouveaux jeux de données sont pour moi de belles reconnaissances envers le travail accompli.

Ce quatuor a été au coeur des développements de cette thèse et j'aimerais, une fois de plus, leur témoigner le véritable plaisir que j'ai eu de travailler à leurs côtés au cours de ces trois années. J'espère sincèrement que nous aurons de nouvelles occasions d'échanger et de travailler ensemble, malgré la fin imminente de cette aventure.

Je n'en oublie pas moins les personnes avec qui j'ai pu travailler de façon plus ponctuelle et qui ont également contribué à ce travail de recherche.

Ainsi, j'adresse mes remerciements aux autres membres présents ou passés de l'équipe *Optical Design and Image Reconstruction* : Thomas Olivier, Fabien Momey, Anthony Berdeu, Frédéric Jolivet, Alexey Brodoline et Dylan Brault. Merci également à Thierry Fournel et à Thierry Lépine pour les échanges ponctuels que nous avons pu avoir.

Je remercie aussi Anthony Cazier pour sa précieuse aide lors du réglage du montage holographique. Je souhaiterais également remercier Nicolas Verrier pour sa très grande réactivité lors de nos échanges à distance sur les approches holographie multi-spectrale qu'il a initiées dans l'équipe juste avant mon arrivée, et dont j'ai largement pu bénéficier. De même, je remercie Loïc Méès pour l'éclairage qu'il m'a apporté en physique de la diffraction. Merci également à Marc Sebban pour sa participation à mes comités de suivi de thèse successifs.

Plus généralement, je souhaiterais remercier les différents membres du Laboratoire Hubert Curien ; chercheurs, personnels techniques et administratifs, post-doctorants, doctorants et stagiaires pour leur accueil et les différents échanges que nous avons pu avoir et l'aide qu'ils m'ont procurée.

Au cours de ces trois années, j'ai également eu l'opportunité de participer aux enseignements de l'école d'ingénieur Télécom Saint-Etienne. Cette expérience a été extrêmement enrichissante pour moi. Je souhaiterais ainsi remercier Olivier Alata, Christophe Ducottet et Corinne Fournier qui m'ont supervisé dans cette initiation. Je les remercie en particulier pour tous les conseils avisés qu'ils m'ont prodigués. Merci également aux étudiants ainsi qu'au personnel administratif de cette école.



# Contents

<b>Acknowledgements &amp; Remerciements</b>	<b>II</b>
<b>Contents</b>	<b>IV</b>
<b>Summary of each chapter (in french)</b>	<b>XVII</b>
<b>Main acronyms and notations</b>	<b>XXII</b>
<b>Scientific context</b>	<b>XXVII</b>
<b>I Introduction</b>	<b>3</b>
<b>1 Signal processing challenges for object detection and characterization in astronomy and microscopy</b>	<b>5</b>
1.1 Introduction . . . . .	5
1.2 Detection and characterization of exoplanets . . . . .	8
1.2.1 Indirect detection methods . . . . .	8
1.2.1.1 Radial velocities . . . . .	8
1.2.1.2 Photometry . . . . .	10
1.2.1.3 Microlensing . . . . .	11
1.2.1.4 Timing . . . . .	12
1.2.1.5 Astrometry . . . . .	12
1.2.2 Direct imaging as a method of choice . . . . .	13
1.2.2.1 General principle and characteristics . . . . .	13
1.2.2.2 Challenges of direct imaging . . . . .	14
1.2.2.2.1 Reaching high angular resolution with adaptive optics . . . . .	15
1.2.2.2.2 Reaching high contrast with coronagraphy . . . . .	16
1.2.2.2.3 Observing strategies . . . . .	16
1.2.2.2.4 Dedicated facilities . . . . .	18
1.2.2.3 Processing pipeline and related signal processing issues . . . . .	21
1.3 Detection and characterization of microscopic objects . . . . .	26
1.3.1 Optical microscopy modalities . . . . .	26

1.3.1.1	Bright field . . . . .	26
1.3.1.2	Dark field . . . . .	28
1.3.1.3	Phase contrast . . . . .	28
1.3.1.4	Polarization . . . . .	28
1.3.1.5	Fluorescence . . . . .	29
1.3.2	In-line holographic microscopy as a method of choice . . . . .	30
1.3.2.1	General principle and characteristics . . . . .	30
1.3.2.2	Challenges of holographic microscopy . . . . .	31
1.3.2.2.1	Extracting relevant information by numerical reconstruction . . . . .	32
1.3.2.2.2	Experimental setups . . . . .	37
1.3.2.3	Processing pipeline and related signal processing issues . . . . .	37
1.4	Methodological angles and thesis organization . . . . .	41
1.4.1	First angle: Background fluctuations modeling . . . . .	41
1.4.2	Second angle: Robustness to outliers . . . . .	42
1.4.3	Third angle: Spectral diversity exploitation . . . . .	44
1.5	Organization of the thesis . . . . .	46

## II Background fluctuations modeling 49

<b>2</b>	<b>Application of background fluctuations modeling in astronomy: detection and characterization of exoplanets</b> . . . . .	<b>51</b>
2.1	Introduction . . . . .	51
2.2	State-of-the-art processing methods for exoplanet detection by direct imaging . . . . .	52
2.2.1	Methods based on image combinations . . . . .	52
2.2.1.1	Classical-ADI algorithms . . . . .	52
2.2.1.2	LOCI type algorithms . . . . .	53
2.2.2	Methods based on mode subtractions . . . . .	54
2.2.3	Methods based on a statistical approach . . . . .	54
2.2.4	Methods based on machine learning techniques . . . . .	55
2.2.5	Comparison and desirable properties . . . . .	56
2.3	PACO: exoplanet detection based on PATCH COvariances . . . . .	58
2.3.1	Statistical model for source detection and characterization . . . . .	59
2.3.2	Statistical learning of the background . . . . .	62
2.3.3	Unbiased estimation of the background statistics . . . . .	69
2.3.4	Estimation of the flux of an exoplanet . . . . .	71
2.3.5	Detection of exoplanets . . . . .	72
2.3.6	Statistical properties . . . . .	73
2.3.6.1	Distribution of the detection criterion . . . . .	73
2.3.6.2	Probabilities of false alarm and of true detection . . . . .	74
2.3.6.3	Astrometric accuracy . . . . .	74
2.4	Implementation details of PACO . . . . .	78
2.4.1	Optimal patch size . . . . .	78
2.4.2	Taking into account missing data . . . . .	79
2.4.3	The PACO algorithm: algorithmic considerations . . . . .	80

---

2.4.4	A fast and approximate version of PACO for large surveys . . . . .	82
2.4.5	Sampling of possible exoplanet locations . . . . .	83
2.4.6	Unsupervised detection and characterization . . . . .	86
2.5	Performance evaluation with on-sky data . . . . .	87
2.5.1	Datasets and algorithms description . . . . .	87
2.5.2	Detection maps . . . . .	89
2.5.2.1	Comparison with state-of-art algorithms . . . . .	89
2.5.2.2	Detection maps with <code>fast PACO</code> . . . . .	95
2.5.2.3	PACO: a general framework . . . . .	96
2.5.3	Contrast curves and detection statistics . . . . .	98
2.5.3.1	Predicted best-achievable-contrast . . . . .	98
2.5.3.2	Actual best-achievable-contrast . . . . .	99
2.5.4	Photometry accuracy . . . . .	102
2.6	Conclusion on PACO's capabilities . . . . .	105
<b>3</b>	<b>Application of background fluctuations modeling in holographic microscopy: detection of diffraction patterns</b>	<b>109</b>
3.1	Introduction . . . . .	109
3.2	Statistical modeling of the background fluctuations . . . . .	110
3.3	EXPACO: detection of EXtended known patterns based on PAtch COvariances . . . . .	114
3.4	Fast computation of detection maps with EXPACO . . . . .	119
3.4.1	Evaluation of the algorithmic complexity . . . . .	119
3.4.2	Fast computation of $b(x_0, y_0)$ for all pixel shifts . . . . .	120
3.4.3	Fast computation of $a(x_0, y_0)$ for all pixel shifts . . . . .	120
3.5	Performance evaluation on holograms . . . . .	122
3.5.1	Accuracy of the EXPACO approximation . . . . .	123
3.5.2	Detection maps . . . . .	126
3.5.2.1	Influence of the number $K$ of pixels in the patches . . . . .	126
3.5.2.2	Influence of the spatial extension $\widetilde{K}$ of the patches . . . . .	130
3.5.3	False alarm rate . . . . .	130
3.6	Conclusion on EXPACO's capabilities . . . . .	134
<b>III</b>	<b>Robust processing</b>	<b>137</b>
<b>4</b>	<b>Robustness to bad frames in direct imaging</b>	<b>139</b>
4.1	The need for robust estimators in direct imaging . . . . .	139
4.2	Local modeling of spatio-temporal fluctuations . . . . .	142
4.2.1	Robust covariance estimation in SAR imaging . . . . .	142
4.2.2	Local modeling of spatio-temporal fluctuations with robust PACO . . . . .	144
4.3	Adaptation of the PACO algorithm . . . . .	146
4.3.1	Estimation of the statistics of the background . . . . .	146
4.3.2	Robust computation of a detection map . . . . .	150
4.3.3	Robust estimation of photometry and astrometry . . . . .	153

---



4.3.4	Sketch of proof of the robustness . . . . .	154
4.4	Characterization of detection, astrometric and photometric performances	156
4.4.1	Improved detection sensitivity . . . . .	156
4.4.2	Assessing the quality of the observations . . . . .	161
4.4.3	Improved astrometric and photometric accuracies . . . . .	162
4.5	Conclusion on robust PACO's capabilities . . . . .	164
<b>5</b>	<b>Robustness to unwanted objects in holographic microscopy</b>	<b>167</b>
5.1	The need for robust estimators in holographic microscopy . . . . .	167
5.2	Improved robustness by weighted least squares . . . . .	170
5.2.1	The least squares solution . . . . .	170
5.2.2	The reweighted least squares solution . . . . .	170
5.3	Distinguishing inliers and outliers . . . . .	176
5.3.1	A bias/variance tradeoff . . . . .	176
5.3.2	Classical approaches . . . . .	176
5.3.3	Proposed criterion for a bias/variance tradeoff . . . . .	177
5.4	Application to lensless microscopy videos . . . . .	180
5.4.1	Holographic video of an object of constant size . . . . .	181
5.4.1.1	Dataset and algorithm description . . . . .	181
5.4.1.2	Results analysis . . . . .	182
5.4.2	Holographic video of evaporating droplets . . . . .	184
5.4.2.1	Dataset and algorithm description . . . . .	184
5.4.2.2	Results analysis . . . . .	184
5.5	Conclusion . . . . .	187
<b>IV</b>	<b>Multi-spectral processing</b>	<b>189</b>
<b>6</b>	<b>Exoplanet detection and characterization with integral field spectrographs</b>	<b>191</b>
6.1	Introduction . . . . .	191
6.2	Statistical modeling of background fluctuations . . . . .	195
6.2.1	Local multivariate Gaussian model . . . . .	195
6.2.2	Local learning of the parameters . . . . .	196
6.3	Detection maps . . . . .	204
6.3.1	Detection at a single wavelength . . . . .	204
6.3.2	Combining multiple detection maps . . . . .	207
6.3.2.1	Combination assuming spectral independence . . . . .	207
6.3.2.2	Accounting for spectral correlations . . . . .	209
6.3.2.3	Improving the detection based on a prior spectrum model	213
6.3.2.4	Robust estimation of the spectral correlations . . . . .	213
6.3.2.5	Optimality of the detection criterion wS/N . . . . .	214
6.3.2.6	Combination of S/N maps with spectral whitening . . . . .	216
6.3.2.7	Comparison between wGLRT and wS/N . . . . .	216
6.4	Source characterization . . . . .	220
6.4.1	Astrometric estimation . . . . .	220
6.4.2	Estimation of the spectral energy distribution . . . . .	221

---

6.4.2.1	Unsupervised setting of the smoothing parameter $\mu$ for SED estimation . . . . .	222
6.5	Implementation details of PACO-ASDI . . . . .	225
6.6	Performance evaluation with on-sky data . . . . .	228
6.6.1	Datasets and algorithms description . . . . .	228
6.6.2	Detection performance . . . . .	234
6.6.2.1	Detection results . . . . .	234
6.6.2.2	Achievable contrast . . . . .	235
6.6.3	SED estimation performance . . . . .	236
6.7	Conclusion on PACO-ASDI's capabilities . . . . .	245
<b>7</b>	<b>Improved characterization of microscopic objects with multi-spectral holography</b> . . . . .	<b>249</b>
7.1	Introduction . . . . .	249
7.2	Calibration issues of holographic color microscopy . . . . .	253
7.2.1	Calibration issues related to the wavelengths of the sources . . . . .	253
7.2.2	Calibration issues related to the CMOS color sensor . . . . .	255
7.2.2.1	Spectral crosstalk . . . . .	255
7.2.2.2	Optical crosstalk . . . . .	257
7.2.2.3	Electronic crosstalk . . . . .	258
7.2.2.4	Summary of crosstalk effects . . . . .	258
7.3	Reconstruction using a parameter-based inverse problem approach . . . . .	259
7.4	Self-calibration of a color microscope . . . . .	262
7.4.1	Estimation of the wavelength of the sources . . . . .	262
7.4.1.1	Wavelength calibration in color holography with a parameter-based inverse approach . . . . .	262
7.4.1.2	Experimental results and discussion . . . . .	263
7.4.1.3	Estimation of the reference wavelength . . . . .	265
7.4.2	Calibration of the crosstalk phenomenon affecting the sensor . . . . .	266
7.4.2.1	Principle of crosstalk estimation using the parameter-based inverse approach . . . . .	266
7.4.2.2	Experimental results and discussion . . . . .	268
7.5	Improving object reconstruction with self-calibration . . . . .	269
7.5.1	Accounting for self-calibration in physics-based models . . . . .	269
7.5.2	Self-calibration applied to the reconstruction of parametric objects . . . . .	270
7.5.2.1	Reconstruction of parametric opaque objects . . . . .	270
7.5.2.2	Theoretical limits of precision . . . . .	272
7.5.3	Self-calibration applied to the reconstruction of images in color holography . . . . .	274
7.5.3.1	Color hologram reconstruction method . . . . .	274
7.5.3.2	Reconstruction of non-parametric opaque objects . . . . .	276
7.6	Conclusion . . . . .	277

---

---

<b>V</b>	<b>Conclusion</b>	<b>279</b>
<b>8</b>	<b>Conclusion, ongoing and future works</b>	<b>281</b>
8.1	Summary of the main contributions . . . . .	281
8.2	Ongoing and future works for astronomy . . . . .	283
8.2.1	On the applicative side . . . . .	283
8.2.1.1	Automatic processing pipeline . . . . .	283
8.2.1.2	Exploitation of PACO for astronomy applications . . . . .	286
8.2.1.2.1	Determination of mass limits . . . . .	286
8.2.1.2.2	Analyzing an IFS sequence around $\beta$ Pictoris . . . . .	288
8.2.2	On the methodological side . . . . .	288
8.2.2.1	Statistical model of the background . . . . .	290
8.2.2.2	Detection and reconstruction of extended objects . . . . .	290
8.2.2.3	Automatic adaptation of the detection threshold . . . . .	295
8.3	Ongoing and future works for microscopy . . . . .	301
8.3.1	On the applicative side . . . . .	301
8.3.2	On the methodological side . . . . .	301
8.3.2.1	Detection of extended patterns with a transform-based approach . . . . .	301
8.3.2.2	Image reconstructions accounting for the correlated background . . . . .	304
	<b>Appendices</b>	<b>306</b>
<b>A</b>	<b>Estimation of covariance matrices by shrinkage</b>	<b>307</b>
A.1	The oracle estimator . . . . .	307
A.2	The Oracle-Approximating Shrinkage (OAS) estimator . . . . .	309
<b>B</b>	<b>Unsupervised regularization of the estimated SEDs</b>	<b>310</b>
B.1	SED regularization with the GML approach . . . . .	310
B.2	SED regularization with the GML, GCV, and SURE approaches: additional numerical results . . . . .	311
<b>C</b>	<b>Modeling background fluctuations of ASDI datasets</b>	<b>320</b>
C.1	Estimation of the means . . . . .	320
C.2	Estimation of the scaling factors . . . . .	321
C.3	Estimation of the covariances . . . . .	322
<b>D</b>	<b>Example of an automatic report generated by PACO</b>	<b>324</b>
	<b>Bibliography</b>	<b>336</b>
	<b>List of publications</b>	<b>367</b>

# Table des matières

<b>Remerciements &amp; Acknowledgements</b>	<b>II</b>
<b>Table des matières</b>	<b>IV</b>
<b>Résumé par chapitre</b>	<b>XVII</b>
<b>Notations et acronymes principaux</b>	<b>XXII</b>
<b>Contexte scientifique</b>	<b>XXVII</b>
<b>I Introduction</b>	<b>3</b>
<b>1 Défis du traitement du signal pour la détection et la caractérisation d'objets en astronomie et en microscopie</b>	<b>5</b>
1.1 Introduction . . . . .	5
1.2 Détection et caractérisation des exoplanètes . . . . .	8
1.2.1 Méthodes de détection indirectes . . . . .	8
1.2.1.1 Vitesses radiales . . . . .	8
1.2.1.2 Photométrie . . . . .	10
1.2.1.3 Microlentille . . . . .	11
1.2.1.4 Chronométrie . . . . .	12
1.2.1.5 Astrométrie . . . . .	12
1.2.2 L'imagerie directe : une méthode de choix . . . . .	13
1.2.2.1 Principe général et caractéristiques . . . . .	13
1.2.2.2 Défis associés à l'imagerie directe . . . . .	14
1.2.2.2.1 Atteindre une haute résolution angulaire avec l'optique adaptative . . . . .	15
1.2.2.2.2 Atteindre un haut-contraste avec la coronographie . . . . .	16
1.2.2.2.3 Stratégies d'observation . . . . .	16
1.2.2.2.4 Instruments dédiés . . . . .	18
1.2.2.3 Chaîne de traitement et problématiques associées . . . . .	21
1.3 Détection et caractérisation d'objets microscopiques . . . . .	26

1.3.1	Modalités de microscopie optique . . . . .	26
1.3.1.1	Microscopie en champ clair . . . . .	26
1.3.1.2	Microscopie en champ sombre . . . . .	28
1.3.1.3	Contraste de phase . . . . .	28
1.3.1.4	Polarisation . . . . .	28
1.3.1.5	Fluorescence . . . . .	29
1.3.2	La microscopie holographique en ligne : une méthode de choix . . . . .	30
1.3.2.1	Principe général et caractéristiques . . . . .	30
1.3.2.2	Défis associés à la microscopie holographique . . . . .	31
1.3.2.2.1	Extraction d'informations d'intérêt par reconstruction numérique . . . . .	32
1.3.2.2.2	Configurations expérimentales . . . . .	37
1.3.2.3	Chaîne de traitement et problématiques associées . . . . .	37
1.4	Angles d'attaque méthodologiques et organisation de la thèse . . . . .	41
1.4.1	Premier angle : Modélisation des fluctuations du fond . . . . .	41
1.4.2	Second angle : Robustesse aux données aberrantes . . . . .	42
1.4.3	Troisième angle : Exploitation de la diversité spectrale . . . . .	44
1.5	Organisation de la thèse . . . . .	46

## II Modélisation des fluctuations du fond 49

### 2 Application de la modélisation des fluctuations du fond en astronomie : détection et caractérisation des exoplanètes 51

2.1	Introduction . . . . .	51
2.2	Méthodes de traitement de l'état de l'art pour la détection d'exoplanètes par imagerie directe . . . . .	52
2.2.1	Méthodes basées sur la combinaison d'images . . . . .	52
2.2.1.1	Algorithmes du type ADI classique . . . . .	52
2.2.1.2	Algorithmes du type LOCI . . . . .	53
2.2.2	Méthodes basées sur la soustraction de modes . . . . .	54
2.2.3	Méthodes basées sur une approche statistique . . . . .	54
2.2.4	Méthodes basées sur les techniques d'apprentissage automatique . . . . .	55
2.2.5	Comparaison et propriétés souhaitées . . . . .	56
2.3	PACO : détection d'exoplanètes basée par les COvariances de PAtchs . . . . .	58
2.3.1	Modèle statistique pour la détection et la caractérisation de sources . . . . .	59
2.3.2	Apprentissage statistique du fond . . . . .	62
2.3.3	Estimation non biaisée des statistiques du fond . . . . .	69
2.3.4	Estimation du flux d'une exoplanète . . . . .	71
2.3.5	Détection des exoplanètes . . . . .	72
2.3.6	Propriétés statistiques . . . . .	73
2.3.6.1	Distribution du critère de détection . . . . .	73
2.3.6.2	Probabilités de fausse alarme et de détection . . . . .	74
2.3.6.3	Précision astrométrique . . . . .	74
2.4	Implémentation détaillée de PACO . . . . .	78
2.4.1	Taille optimale de patch . . . . .	78
2.4.2	Prise en compte des données manquantes . . . . .	79

2.4.3	L'algorithme PACO : considérations algorithmiques . . . . .	80
2.4.4	Une version rapide et approximée de PACO pour le traitement de vastes données . . . . .	82
2.4.5	Échantillonnage spatiale des exoplanètes . . . . .	83
2.4.6	Détection et caractérisation non supervisées . . . . .	86
2.5	Évaluation des performances sur des observations du ciel . . . . .	87
2.5.1	Jeux de données et description des algorithmes . . . . .	87
2.5.2	Cartes de détection . . . . .	89
2.5.2.1	Comparaison avec les algorithmes de l'état de l'art . . . . .	89
2.5.2.2	Cartes de détection avec <b>fast PACO</b> . . . . .	95
2.5.2.3	<b>PACO</b> : un cadre général . . . . .	96
2.5.3	Courbes de contraste et détection statistique . . . . .	98
2.5.3.1	Estimation du meilleur contraste atteignable . . . . .	98
2.5.3.2	Estimation du contraste atteint . . . . .	99
2.5.4	Précision photométrique . . . . .	102
2.6	Conclusion sur les capacités de PACO . . . . .	105
<b>3</b>	<b>Application de la modélisation des fluctuations du fond en microscopie holographique : détection de motifs de diffraction</b>	<b>109</b>
3.1	Introduction . . . . .	109
3.2	Modélisation statistique des fluctuations du fond . . . . .	110
3.3	<b>EXPACO</b> : détection de motifs connus et spatialement étendus basée sur les Covariances de PAtchs . . . . .	114
3.4	Calcul rapide de cartes de détection avec <b>EXPACO</b> . . . . .	119
3.4.1	Évaluation de la complexité algorithmique . . . . .	119
3.4.2	Calcul rapide de $b(x_0, y_0)$ pour tous les décalages pixéliques . . . . .	120
3.4.3	Calcul rapide de $a(x_0, y_0)$ pour tous les décalages pixéliques . . . . .	120
3.5	Évaluation des performances sur des hologrammes . . . . .	122
3.5.1	Précision de l'approximation d' <b>EXPACO</b> . . . . .	123
3.5.2	Cartes de détection . . . . .	126
3.5.2.1	Influence du nombre $K$ de pixels des patches . . . . .	126
3.5.2.2	Influence de l'extension spatiale $\tilde{K}$ des patches . . . . .	130
3.5.3	Taux de fausse alarme . . . . .	130
3.6	Conclusion sur les capacités d' <b>EXPACO</b> . . . . .	134
<b>III</b>	<b>Traitement robuste</b>	<b>137</b>
<b>4</b>	<b>Robustesse aux images aberrantes en imagerie directe</b>	<b>139</b>
4.1	Le besoin d'estimateurs robustes en imagerie directe . . . . .	139
4.2	Modélisation locale des fluctuations spatio-temporelles . . . . .	142
4.2.1	Estimation robuste de covariances en imagerie SAR . . . . .	142
4.2.2	Modélisation locale des fluctuations spatio-temporelles avec <b>robust PACO</b> . . . . .	144
4.3	Adaptation de l'algorithme PACO . . . . .	146
4.3.1	Estimation des statistiques du fond . . . . .	146
4.3.2	Calcul robuste d'une carte de détection . . . . .	150

4.3.3	Estimation robuste de la photométrie et de l'astrométrie . . . . .	153
4.3.4	Éléments de preuve de la robustesse . . . . .	154
4.4	Caractérisation des performances de détection et d'estimation astrométrique & photométrique . . . . .	156
4.4.1	Amélioration de la sensibilité de détection . . . . .	156
4.4.2	Évaluation de la qualité des observations . . . . .	161
4.4.3	Amélioration des précisions astrométrique et photométrique . . . . .	162
4.5	Conclusion sur les capacités de <b>robust PACO</b> . . . . .	164
<b>5</b>	<b>Robustesse aux objets indésirables en microscopie holographique</b>	<b>167</b>
5.1	Le besoin d'estimateurs robustes en microscopie holographique . . . . .	167
5.2	Amélioration de la robustesse par les moindres carrés pondérés . . . . .	170
5.2.1	La solution des moindres carrés . . . . .	170
5.2.2	La solution des moindres carrés pondérés . . . . .	170
5.3	Distinguer les données utiles et les données aberrantes . . . . .	176
5.3.1	Un compromis biais/variance . . . . .	176
5.3.2	Approches classiques . . . . .	176
5.3.3	Critère proposé basé sur un compromis biais/variance . . . . .	177
5.4	Application à des séquences vidéo en microscopie sans lentille . . . . .	180
5.4.1	Vidéo holographique d'un objet de taille constante . . . . .	181
5.4.1.1	Jeu de données et description de l'algorithme . . . . .	181
5.4.1.2	Analyse des résultats . . . . .	182
5.4.2	Vidéo holographique de gouttes évaporantes . . . . .	184
5.4.2.1	Jeu de données et description de l'algorithme . . . . .	184
5.4.2.2	Analyse des résultats . . . . .	184
5.5	Conclusion . . . . .	187
<b>IV</b>	<b>Traitement multi-spectral</b>	<b>189</b>
<b>6</b>	<b>Détection et caractérisation des exoplanètes avec un spectrographe intégral de champ</b>	<b>191</b>
6.1	Introduction . . . . .	191
6.2	Modélisation statistique des fluctuations du fond . . . . .	195
6.2.1	Modèle local multivarié gaussien . . . . .	195
6.2.2	Apprentissage local des paramètres . . . . .	196
6.3	Cartes de détection . . . . .	204
6.3.1	Détection à une seule longueur d'onde . . . . .	204
6.3.2	Combinaison de plusieurs cartes de détection . . . . .	207
6.3.2.1	Combinaison supposant une indépendance spectrale . . . . .	207
6.3.2.2	Prise en compte des corrélations spectrales . . . . .	209
6.3.2.3	Amélioration de la détection basée sur un modèle de spectre a priori . . . . .	213
6.3.2.4	Estimation robuste des corrélations spectrales . . . . .	213
6.3.2.5	Optimalité du critère de détection $wS/N$ . . . . .	214
6.3.2.6	Combinaison de cartes de $S/N$ avec un blanchiment spectral . . . . .	216



6.3.2.7	Comparaison entre les critères wGLRT et wS/N . . . . .	216
6.4	Caractérisation des sources . . . . .	220
6.4.1	Estimation de l'astrométrie . . . . .	220
6.4.2	Estimation de la distribution spectrale d'énergie . . . . .	221
6.4.2.1	Réglage non supervisé du paramètre $\mu$ de lissage des SEDs estimés . . . . .	222
6.5	Implémentation détaillée de PACO-ASDI . . . . .	225
6.6	Évaluation des performances sur des observations du ciel . . . . .	228
6.6.1	Jeux de données et description des algorithmes . . . . .	228
6.6.2	Performances de détection . . . . .	234
6.6.2.1	Résultats de détection . . . . .	234
6.6.2.2	Contraste atteignable . . . . .	235
6.6.3	Performance d'estimation de SEDs . . . . .	236
6.7	Conclusion sur les capacités de PACO-ASDI . . . . .	245
<b>7</b>	<b>Amélioration de la caractérisation d'objets microscopiques par holo- graphie multi-spectrale</b> . . . . .	<b>249</b>
7.1	Introduction . . . . .	249
7.2	Problématiques de calibration en microscopie holographique couleur . . . . .	253
7.2.1	Problématiques d'étalonnage liées aux longueurs d'onde des sources . . . . .	253
7.2.2	Problématique d'étalonnage liées aux capteur couleur CMOS . . . . .	255
7.2.2.1	Diaphonie spectrale . . . . .	255
7.2.2.2	Diaphonie optique . . . . .	257
7.2.2.3	Diaphonie électronique . . . . .	258
7.2.2.4	Résumé des effets de diaphonie . . . . .	258
7.3	Reconstruction par une approche problèmes inverses paramétrique . . . . .	259
7.4	Auto-calibration d'un microscope couleur . . . . .	262
7.4.1	Estimation de la longueur d'onde des sources . . . . .	262
7.4.1.1	Calibration de la longueur d'onde en holographie cou- leur avec une approche problèmes inverses paramétrique . . . . .	262
7.4.1.2	Résultats expérimentaux et discussion . . . . .	263
7.4.1.3	Estimation de la longueur d'onde de référence . . . . .	265
7.4.2	Calibration du phénomène de diaphonie affectant le capteur . . . . .	266
7.4.2.1	Principe de l'estimation de la diaphonie par une ap- proche problèmes inverses paramétrique . . . . .	266
7.4.2.2	Résultats expérimentaux et discussion . . . . .	268
7.5	Amélioration de la reconstruction d'objets par auto-calibration . . . . .	269
7.5.1	Prise en compte de l'auto-calibration dans les modèles physiques . . . . .	269
7.5.2	Auto-calibration appliquée à la reconstruction d'objets paramé- triques . . . . .	270
7.5.2.1	Reconstruction d'objets paramétriques opaques . . . . .	270
7.5.2.2	Limites théoriques de précision . . . . .	272
7.5.3	Auto-calibration appliquée à la reconstruction d'images en holo- graphie couleur . . . . .	274
7.5.3.1	Méthode de reconstruction d'hologrammes couleurs . . . . .	274
7.5.3.2	Reconstruction d'objets opaques non-paramétriques . . . . .	276



7.6	Conclusion . . . . .	277
<b>V</b>	<b>Conclusion</b>	<b>279</b>
<b>8</b>	<b>Conclusion, travaux en cours et perspectives</b>	<b>281</b>
8.1	Résumé des principales contributions . . . . .	281
8.2	Travaux en cours et perspectives pour l’astronomie . . . . .	283
8.2.1	Sur le volet applicatif . . . . .	283
8.2.1.1	Chaîne de traitement automatique . . . . .	283
8.2.1.2	Exploitation de PACO pour des applications en astronomie	286
8.2.1.2.1	Détermination de limites de masse . . . . .	286
8.2.1.2.2	Analyse d’une séquence IFS autour de $\beta$ Pictoris	288
8.2.2	Sur le volet méthodologique . . . . .	288
8.2.2.1	Modèle statistique du fond . . . . .	290
8.2.2.2	Détection et reconstruction d’objets étendus . . . . .	290
8.2.2.3	Adaptation automatique du seuil de détection . . . . .	295
8.3	Travaux en cours et perspectives pour la microscopie . . . . .	301
8.3.1	Sur le volet applicatif . . . . .	301
8.3.2	Sur le volet méthodologique . . . . .	301
8.3.2.1	Détection de motifs étendus avec une approche par trans- formées . . . . .	301
8.3.2.2	Reconstruction d’images avec prise en compte des cor- rélations du fond . . . . .	304
	<b>Annexes</b>	<b>306</b>
<b>A</b>	<b>Estimation de matrices de covariances par <i>shrinkage</i></b>	<b>307</b>
A.1	L’estimateur oracle . . . . .	307
A.2	L’estimateur <i>shrinkage</i> oracle approximé . . . . .	309
<b>B</b>	<b>Régularisation non supervisée des SEDs estimés</b>	<b>310</b>
B.1	Régularisation de SED par une approche GML . . . . .	310
B.2	Régularisation de SED par les approches GML, GCV et SURE : résultats numériques complémentaires . . . . .	311
<b>C</b>	<b>Modélisation des fluctuations du fond des jeux de données ASDI</b>	<b>320</b>
C.1	Estimation des moyennes . . . . .	320
C.2	Estimation des facteurs d’échelle . . . . .	321
C.3	Estimation des covariances . . . . .	322
<b>D</b>	<b>Exemple de rapport automatique généré par PACO</b>	<b>324</b>
	<b>Bibliographie</b>	<b>336</b>
	<b>Liste des publications</b>	<b>367</b>

# Résumé par chapitre

Cette partie est un résumé en langue française des différents chapitres de ce document, incluant l'introduction et la conclusion.

## I. Introduction

### 1. Défis du traitement du signal pour la détection et la caractérisation d'objets en astronomie et en microscopie

L'astronomie et la microscopie sont des domaines d'étude qui nécessitent souvent de détecter et de caractériser des objets à partir de signaux faibles issus d'images. Ces images sont généralement dominées par un fond fort, non-stationnaire et spatialement corrélé.

Dans cette thèse, nous considérons la détection et la caractérisation d'exoplanètes par imagerie directe ainsi que d'objets microscopiques répartis dans un volume par microscopie holographique. Pour ces deux applications, les performances des détecteurs ne dépendent pas seulement de la conception instrumentale, mais également des méthodes de traitement du signal & de l'image utilisées. Cette thèse propose plusieurs algorithmes de traitement dédiés à l'astronomie et à la microscopie, basés sur trois angles méthodologiques principaux :

- une modélisation statistique des fluctuations du fond des images enregistrées à une échelle locale à l'aide d'approches par patches,
- la mise en place de stratégies de pondération afin d'améliorer la robustesse des méthodes face à la présence de données aberrantes,
- une exploitation de la diversité spectrale des données afin d'améliorer la sensibilité de détection et la précision de la caractérisation des objets.

## II. Modélisation des fluctuations du fond

### 2. Application de la modélisation des fluctuations du fond en astronomie : détection et caractérisation des exoplanètes

Malgré le couplage d'un système d'optique adaptative extrême et d'un coronographe, la détection d'exoplanètes par imagerie directe reste difficile en raison du contraste très élevé entre l'étoile hôte et les exoplanètes. Ce chapitre présente une nouvelle méthode,

appelée PACO, dédiée à la détection de points sources à partir de données d'imagerie différentielle angulaire. Nous illustrons le potentiel d'une méthode de traitement qui apprend un modèle statistique du fond directement à partir des données. Contrairement aux approches existantes, la méthode proposée tient compte des corrélations spatiales des données. Ces corrélations et la composante moyenne des tavelures stellaires sont apprises localement et conjointement à l'estimation du flux des exoplanètes (potentielles). De par l'absence de soustractions explicites entre les différentes images, la photométrie est intrinsèquement préservée.

PACO offre des caractéristiques attrayantes : l'algorithme est totalement libre de paramètre et sans biais photométrique significatif. De plus, les performances attendues en termes de capacité de détection, de précision photométrique et d'astrométrie peuvent être directement évaluées sans recours à des simulations systématiques du type Monte-Carlo. Une version rapide et approximée de la méthode est également décrite et peut être utilisée pour traiter de grandes quantités de données provenant, par exemple, de larges campagnes d'acquisitions dédiées à la quête d'exoplanètes.

### **3. Application de la modélisation des fluctuations du fond en microscopie holographique : détection de motifs de diffraction**

La microscopie holographique est un autre domaine applicatif qui nécessite de détecter des signaux faibles superposés sur un fond fort. En raison des fluctuations temporelles des séquences d'images enregistrées, le fond ne peut pas être complètement supprimé par de simples soustractions. La détection du motif d'intérêt nécessite alors une modélisation statistique du fond. En raison des difficultés liées à l'estimation des corrélations spatiales du fond et à l'application d'un détecteur optimal tenant compte de ces corrélations, il est de pratique courante de les négliger.

Dans ce chapitre, les corrélations spatiales sont estimées localement, à l'échelle de patches de quelques dizaines de pixels, à partir de plusieurs images de fond. Ce chapitre présente une nouvelle méthode, appelée EXPACO, dédiée à la détection de motifs connus et spatialement étendus, tels que les motifs de diffraction rencontrés en microscopie holographique. Un algorithme rapide pour le calcul des cartes de détection est également dérivé. L'approche est évaluée sur des images obtenues à partir d'un microscope holographique.

## **III. Traitement robuste**

### **4. Robustesse aux images aberrantes en imagerie directe**

En raison de l'évolution des conditions d'observation et de la correction de l'optique adaptative, la qualité des observations directes peut varier de manière significative au sein d'une même séquence. Il est de pratique courante de rejeter les images de moins bonne qualité, comparativement aux autres.

Plutôt que d'écarter l'intégralité de ces images, nous étudions les fluctuations locales du signal dans chaque image et en tirons des cartes de pondération. Les poids dérivés des variances temporelles peuvent être utilisés dans l'algorithme PACO pour améliorer la robustesse de l'étape de détection ainsi que pour réduire les erreurs d'estimation sur

l'astrométrie et la photométrie des sources détectées. L'impact des images de mauvaise qualité peut être analysé en caractérisant les performances théoriques de détection et d'estimation.

## 5. Robustesse aux objets indésirables en microscopie holographique

La microscopie sans lentille est utilisée dans divers domaines, notamment en microfluidique et en imagerie biomédicale, pour l'estimation quantitative de propriétés physiques caractérisant les objets observés. En particulier, pour l'estimation de la taille et de la localisation 3D d'objets microscopiques à partir d'hogrammes, il a été montré dans la littérature que les méthodes du maximum de vraisemblance surpassaient les approches traditionnelles basées sur la reconstruction d'images 3D suivie d'une analyse du volume reconstruit. Cependant, la présence dans les hologrammes de franges de diffraction dues à des objets autres que les objets d'intérêt peut fausser (biaiser) les estimations issues du maximum de vraisemblance.

À l'aide de vidéos d'hogrammes expérimentaux, nous montrons que la combinaison d'une procédure d'estimation robuste au maximum de vraisemblance réduit ce biais. Nous proposons un critère basé sur l'intersection d'intervalles de confiance pour définir automatiquement le niveau de distinction entre les données d'intérêt et les données aberrantes. Cette méthodologie est générale et peut s'adapter à différents problèmes d'estimation en présence de valeurs aberrantes spatialement non-stationnaires. Nous montrons de manière empirique que ce critère atteint un compromis biais/variance. Nous illustrons également que l'analyse conjointe de différents hologrammes d'une même séquence d'acquisition à l'aide de la procédure robuste proposée améliore davantage encore la précision de l'estimation.

## IV. Traitement multi-spectral

### 6. Détection et caractérisation des exoplanètes avec un spectrographe intégral de champ

L'imagerie différentielle angulaire et spectrale combine des observations enregistrées à différents temps et plusieurs longueurs d'onde afin de faciliter la séparation du signal résiduel de l'étoile hôte du signal d'intérêt issu des exoplanètes. La détection n'est rendue possible qu'avec une modélisation précise de ces deux composantes, en particulier du bruit de fond dû aux fuites stellaires de l'étoile hôte masquée par le coronographe. Au-delà de la détection de sources ponctuelles dans le champ de vue, il est également essentiel de caractériser les sources détectées en termes de signification statistique, d'astrométrie et d'estimer leur distribution spectrale d'énergie.

Nous étendons les algorithmes `PACO` (voir Chapitre 2) et `robust PACO` (voir Chapitre 4) afin de capturer les fluctuations spectrales et temporelles des corrélations spatiales du fond. À partir de cette modélisation statistique, nous construisons un algorithme de détection et une méthode d'estimation de distribution spectrale d'énergie : `PACO-ASDI`. La modélisation des corrélations spectrales s'avère à la fois utile pour réduire les artefacts de détection ainsi que pour obtenir des garanties statistiques précises (seuils de détection et intervalles de confiance sur les distributions spectrales d'énergie estimées).

## 7. Amélioration de la caractérisation d'objets microscopiques par holographie multi-spectrale

Les principaux avantages de la microscopie holographique sont liés à la simplicité, compacité et faible sensibilité du dispositif expérimental aux vibrations, ainsi qu'à la possibilité de caractériser avec précision les objets étudiés. Le coût du dispositif peut davantage encore être réduit en utilisant de simples diodes laser comme sources cohérentes de lumière et des capteurs couleurs du type CMOS équipés de filtres chromatiques de Bayer. Cependant, la longueur d'onde centrale délivrée par ce type de laser n'est généralement connue qu'avec une précision limitée et peut évoluer du fait de sa dépendance à la température et à la tension d'alimentation. En outre, les filtres du type Bayer surmontant les capteurs couleurs conventionnels souffrent d'une faible sélectivité chromatique ce qui entraîne un mélange (spectral) des signaux provenant de chaque source (phénomène de diaphonie). Ignorer ces phénomènes conduit à des erreurs significatives dans les reconstructions holographiques.

Nous proposons une méthode d'estimation au sens du maximum de vraisemblance afin de réaliser une auto-calibration des principales propriétés du dispositif : longueur d'onde centrale des sources laser et mélange spectral dû aux filtres de Bayer. Pour cela, nous proposons d'utiliser des objets sphériques naturellement présents dans le champ de vue ou ajoutés en tant qu'objets étalons. Cette méthode d'étalonnage fournit une estimation des longueurs d'onde des sources et de la diaphonie spectrale, avec une précision comparable à celle d'un spectromètre haute-résolution. Nous montrons sur des hologrammes expérimentaux que l'auto-étalonnage de la configuration conduit à une amélioration des reconstructions holographiques.

## V. Conclusion

### 8. Conclusion, travaux en cours et perspectives

Dans cette thèse, nous avons proposé plusieurs algorithmes dédiés à la détection et à la caractérisation d'objets à partir de signaux faibles issus de série d'images. En particulier, les méthodes développées ont été appliquées dans deux contextes applicatifs différents : (i) la recherche d'exoplanètes par imagerie directe en astronomie et (ii) la métrologie optique par microscopie holographique. Les algorithmes présentés dans cette thèse ont été développés en suivant trois angles méthodologiques afin de répondre à des défis communs du traitement du signal :

- Les séries d'images acquises à la fois en astronomie à haut contraste et en microscopie holographique présentent un fond spatialement texturé qui domine fortement les motifs à détecter. Nous avons proposé de modéliser localement le fond corrélé spatialement non-stationnaire des séries d'images en utilisant des approches statistiques par patches. Le modèle du fond conduit à une méthode de détection par application de la théorie de la détection statistique. Nous avons décrit dans la Partie II deux algorithmes dédiés à la détection de motifs connus dans le régime à faible rapport signal sur bruit. Les deux algorithmes proposés diffèrent par l'étendue spatiale des motifs à détecter.

- Malgré le soin apporté au processus d'acquisition, les séries d'images des deux applications ciblées présentent de nombreuses données aberrantes. Dans cette thèse, nous avons proposé des algorithmes tenant compte de ces valeurs aberrantes. Dans la partie [III](#), nous avons décrit deux algorithmes robustes dédiés à la détection et à la caractérisation de motifs, en présence de valeurs aberrantes.
- En astronomie comme en microscopie, il est possible d'enregistrer des données présentant une diversité multi-spectrale en plus de l'étendue temporelle naturelle des séries d'images considérées. Dans cette thèse, nous avons proposé de prendre en compte les spécificités des données multi-spectrales des deux applications ciblées. La Partie [IV](#) décrit deux algorithmes traitant de la diversité spectrale des jeux de données acquis.

# Main acronyms and notations

## Acronyms

### Instrumentation

ADI	Angular Differential Imaging
SDI	Spectral Differential Imaging
ASDI	Angular and Spectral Differential Imaging
(x)AO	(Extreme) Adaptive Optics
CMOS	Complementary Metal Oxide Semi-conductor
ESO	European Southern Observatory
GPI	Gemini Planet Imager
IFS	Integral Field Spectrograph
IRDIS	InfraRed Dual-band Imager and Spectrograph
NaCo	abbreviation of NAOS-CONICA; Nasmyth Adaptive Optics System with COudé Near Infrared CAmera
SPHERE	Spectro Polarimetric High contrast Exoplanet REsearch
VLT	Very Large Telescope

### Algorithms

PACO	PAch COvariances (exoplanet hunter algorithm for ADI)
PACO-ASDI	adaptation of PACO for ASDI
EXPACO	adaptation of PACO for (holographic) EXtended patterns
PACO characterization	characterization step of PACO
PACO detection	detection step of PACO
PACO oracle	oracle version of PACO
fast PACO	fast version of PACO
fast PACO-ASDI	fast version of PACO-ASDI
robust PACO	robust version of PACO
ANDROMEDA	ANgular DiffeRential OptiMal Exoplanet Detection Algorithm
cADI	classical-ADI
KLIP	Karhunen-Loève Image Projection
LLSG	Local, Low-rank, Sparse, and Gaussian noise decomposition
LOCI	Locally Optimized Combination of Images

PCA	Principal Component Analysis
SVD	Singular Value Decomposition
TLOCI	Template-LOCI

### Other methods and quantities

AU	Astronomical Unit
CRLB	Cramér-Rao Lower Bound
FWHM	Full Width at Half Maximum
FPS	Faint Point Source
GCV	Generalized Cross-Validation
GLRT	Generalized Likelihood Ratio Test
GML	Generalized Maximum Likelihood
GSM	Gaussian Scale Mixtures
ICI	Intersection of Confidence Intervals
IRLS	Iteratively Reweighted Least Squares
MAD	Median Absolute Deviation
ML	Maximum Likelihood
MSE	Mean Squared Error
PD	Probability of Detection
PDF	Probability Density Function
PFA	Probability of False Alarm
PSF	Point Spread Function
RGB	Red, Green, Blue
RMSE	Root Mean Square Error
ROC	Receiver Operating Characteristic
SED	Spectral Energy Distribution
S/N	Signal-to-Noise ratio
$S/N_\ell$	Signal-to-Noise ratio at wavelength $\ell$
SURE	Stein's Unbiased Risk Estimator
TPR	True Positive Rate
wGLRT	<i>whitened</i> Generalized Likelihood Ratio Test
wS/N	<i>whitened</i> Signal-to-Noise ratio



# Notations

## Conventions of notation

$x$	a scalar
$\mathbf{x}$	a vector (including vectorized patch values)
$\mathbf{X}$	a matrix

## Statistics

$\hat{\cdot}$	estimator
$\chi_k^2$	chi-square distribution with $k$ degrees of freedom
$\mathcal{C}(\cdot)$	least squares cost function
$\text{Cov}(\cdot)$	covariance
$\mathbb{E}(\cdot)$	expectation
$\mathcal{H}_0, \mathcal{H}_1$	binary hypotheses
$\mathcal{L}$	likelihood
$p(\cdot)$	probability density function
$P(\cdot)$	probability
$\text{Var}(\cdot)$	variance
$\delta$	Cramér-Rao lower bounds vector
$\hat{\mathbf{m}}$	estimated sample mean vector
$\Sigma$	any covariance matrix
$\hat{\mathbf{C}}$	estimated (shrunk) covariance matrix
$\hat{\mathbf{F}}$	estimated variance matrix
$\hat{\mathbf{S}}$	estimated sample covariance matrix
$\mathbf{I}^F$	Fisher information matrix
$\mathcal{N}(\hat{\mathbf{m}}, \hat{\mathbf{C}})$	probability density function of a multivariate Gaussian of mean $\hat{\mathbf{m}}$ and covariance $\hat{\mathbf{C}}$

## Other mathematical functions and notations

$*$	convolution product
$\star$	correlation product
$\bar{\cdot}$	zero-mean quantity, in general
$(\cdot)_+$ or $(\cdot)^+$	positive part
$\arg \max_x(\cdot)$	values of $x$ such that the max is reached
$\arg \min_x(\cdot)$	values of $x$ such that the min is reached
$\det(\cdot)$	matrix determinant
$J_{1c}(\cdot)$	cardinal Bessel function of first order
$\nabla_x(\cdot)$	gradient with respect to $x$
$\mathcal{O}(\cdot)$	Bachmann–Landau asymptotic notation
$\max(\cdot)$	maximum function
$\min(\cdot)$	minimum function
$\cdot^\top$	transpose operator

---

$\text{Re}(\cdot)$	real part
$\text{tr}(\cdot)$	matrix trace
$\ \cdot\ _1$	$\ell_1$ -norm
$\ \cdot\ _2$	$\ell_2$ -norm
$\ \cdot\ _F$	Frobenius norm
$\mathbf{I}$	identity matrix

### Quantities common to astronomy and microscopy applications

$\alpha$	amplitude of a pattern / source
$a$	denominator of the signal-to-noise expression
$b$	numerator of the signal-to-noise expression
$\lambda$	wavelength value
$\ell$	wavelength index
$\mu$	any regularization parameter
$n$	pixel index
$\sigma$	any standard-deviation
$t$	time value
$t$	time index
$\tau$	detection threshold
$C$	number of columns in an image
$K$	number of pixels in a patch
$L$	number of spectral frames
$N$	number of pixels in an image
$R$	number of rows in an image
$T$	number of temporal frames
$d$	data
$f$	background contribution
$h$	(off-axis) PSF
$r$	measured intensity

### Quantities specific to astronomy applications

$5\hat{\sigma}_\alpha$	5-sigma achievable contrast
arcsec	arcsecond
$\Delta_{\text{par}}$	total amount of parallactic rotation of the field of view
$M_J$	Jovian mass (about 318 times the Earth mass)
$\phi_0$	2-D angular location on a reference frame ( $t_0, \ell_0$ )
$\mathcal{F}_{\ell,t}(\phi_0)$	angular location of a point source (due to apparent field of view motion) at time $t$ and wavelength $\ell$ , given its initial location $\phi_0$ at time $t_0$ and wavelength $\ell_0$
$\phi_{\ell,t}$	2-D angular location at wavelength $\ell$ and time $t$ with $\phi_{\ell,t} = \mathcal{F}_{\ell,t}(\phi_0)$
$[\phi_{\ell,t}]$	closest on-grid location to $\phi_{\ell,t}$

$\tilde{T}$	equivalent number of temporal patches
$\tilde{P}$	equivalent number of temporo-spectral patches
$\beta$	expected $S/N_\ell$ values
$\gamma$	spectral energy distribution of a point source
$\mathbf{h}_{n,\ell}(\phi_{\ell,t})$	zoomed-in off-axis PSF centered at the subpixel location $\phi_{\ell,t}$ of the source at the $\ell$ -th wavelength and $t$ -th frame, and sampled on central pixel $n$
$\mathbf{r}_{n,\ell,t}$	vectorized patch of intensity extracted around pixel $n$ , at wavelength $\ell$ , and time $t$
$\mathbb{L}$	Cholesky's factor such as $\Sigma^{-1} = \mathbb{L}\mathbb{L}^\top$
$\mathbb{S}$	whitened vector of $S/N_\ell$ values

### Quantities specific to microscopy applications

$n_p$	complex refractive index on an object $p$
$q_R^G$	crosstalk contribution produced by a Red source on the Green channel of the sensor
$r_p$	radius of a spherical object $p$
$\{x_p, y_p, z_p\}$	3-D location of an object $p$
$\tilde{K}$	spatial extent of a patch
$\theta$	parameter vector
$\mathbf{m}_\theta$	analytical model parametrized by $\theta$
$\vartheta$	opacity
$\mathbf{Q}$	crosstalk mixing matrix

# Scientific context

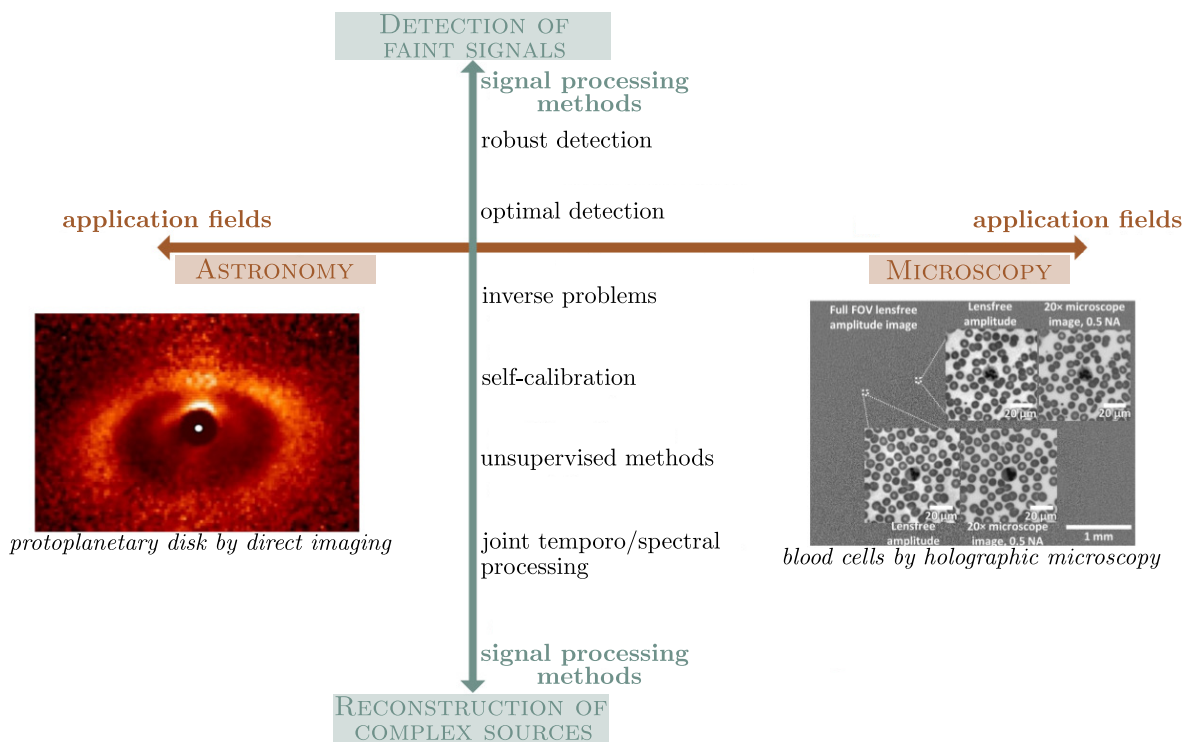


Figure 1 – Visual identity of the project RESSOURCES. The leftmost picture is taken from [Thalmann et al. \(2016\)](#), and the rightmost picture is taken from [Zhang et al. \(2015\)](#). Credit: Loïc Denis.

This thesis has been prepared at the [Hubert Curien Laboratory \(LabHC\)](#), Saint-Etienne, France, and funded by a grant from the [Science, Engineering, Health Doctoral School \(EDSIS\)](#). The LabHC is a joint research unit of the [Jean Monnet University \(UJM\)](#), the [French National Centre for Scientific Research \(CNRS\)](#), and the [Institut d’Optique Graduate School \(IOGS\)](#) with a total staff of about 240, including 130 students. The research activities are split into two departments: *Optics, Photonics and Microwave*, and *Computer Science, Telecom and Image*. In particular, the laboratory research covers the whole imaging process, from light-matter interactions and optical design to high-level understanding and analysis of the images.

I was involved in the *Optical Design and Image Reconstruction* team led by Corinne Fournier, at the interface between optics and signal & image processing. Holographic microscopy has been one of the main research topics of the team since more than 15 years. In parallel, other activities centered on remote sensing and astronomy are conducted under the supervision of Loïc Denis. All these application fields are mainly addressed, from a methodological point of view, within an inverse problem framework. These different themes also benefit from long-term collaborations with other laboratories. Among those, we can cite, for regional cooperations, the [Astrophysics Research Centre of Lyon \(CRAL\)](#), Saint-Genis-Laval, France, and the [Fluid Mechanics and Acoustics Laboratory \(LMFA\)](#), Ecully, France. In particular, there are frequent exchanges on both theoretical and instrumental aspects with [Éric Thiébaud](#), astronomer at the CRAL and expert in signal & image processing, with [Maud Langlois](#), researcher at the CRAL and expert in high contrast instrumentation, and with [Loïc Mées](#), researcher at the LMFA and expert in the physics of light scattering.

Within this context, two research projects supported by the CNRS and led by Loïc Denis were at the heart of this thesis work; [Source Detection for Astronomy and Lensless Microscopy: Optimal Processing and Ultimate Limit in Multi-Variied Imaging \(DETECTION, 2015-2016\)](#), and [Reconstruction of Complex Sources for Astronomy and Microscopy \(RESSOURCES, 2017-2018\)](#). These two projects aimed to build bridges both from an application and methodological point of view between astronomy and microscopy, as illustrated by the visual identity of the project RESSOURCES given in [Figure 1](#). A large part of these two projects are still being supported and investigated with the recent launch of the project [DIAGHOLO \(2019-2024\)](#) funded by the [Region Auvergne Rhône-Alpes \(AURA\)](#), aiming to develop new image reconstruction methods both for microscopy and astronomy. Through these projects, several exchanges with researchers and other students created a very stimulating scientific environment for my thesis work.

In particular, they gave me the opportunity to participate at several conferences and to attend three summer schools covering both application and methodological aspects considered in my thesis:

- First, at the very beginning of my thesis in October 2016, I participated in the [Robust Signal Processing Summer School](#), Rüdesheim am Rhein, Germany, jointly organized by the [IEEE Signal Processing Society \(SPS\)](#) and the [EUROpean Association for Signal Processing \(EURASIP\)](#). During this week, I learned some concepts about robust processing. I was completely novice in this field and this summer school impulsed some ideas for my thesis; two chapters of this manuscript are related to robust processing.
- In 2018, I attended the [Detection and Instrumentation Summer School](#) organized by the [Focal Plane Array for Universe Sensing \(FOCUS\)](#) research group at the [Observatory of Haute-Provence \(OHP\)](#), France. This week alternating both theoretical courses and observations on 1 m class telescopes gave me the opportunity to learn some concepts related to the instrumentation in astronomy, a field in which I was also completely novice. In September 2019, I also took part to a run of observations of the high contrast instrument [SPHERE](#) at the [Very Large Telescope \(VLT, Chile\)](#); a unique chance to discover the observation pipeline of

the type of data that I used throughout my thesis.

- Also in 2018, I attended the Summer School organized by the [French Group of Research for Signal and Image Processing](#) (GRETSI) whose 2018s edition entitled [Data Science, Signal, and Image](#) was dedicated to the processing of large amount of data by machine-learning, deep-learning, and graphs methods. In the same spirit, I recently attended the lectures of the [Deep Learning for Medical Imaging](#) school organized by the [Physics, Radiobiology, Imaging and Simulation](#) (PRIMES) research group. While such methods were not addressed during my thesis, they gave me several ideas for future works.

This thesis work was directed by Corinne Fournier, and I was closely supervised by Loïc Denis. I was also regularly co-supervised by Éric Thiébaud for methodological issues, and Maud Langlois for instrumental and data issues.







**Part I**  
**Introduction**



# Signal processing challenges for object detection and characterization in astronomy and microscopy

---

**Abstract**

*Astronomy and microscopy are fields of study that require the detection and the characterization of faint signals from images dominated by a strong, nonstationary, and spatially correlated background. In particular, we consider the detection and characterization of exoplanets by direct imaging, and the imaging of microscopic objects spread in a volume by holographic microscopy. The performance does not depend solely on the instrumental design but also on the methods applied to process the recorded images. This thesis proposes several algorithms dedicated to astronomy and microscopy that are based on three methodological angles: (i) a statistical modeling of the fluctuations of the background of the recorded images at a local scale using patch-based approaches; (ii) weighting-based strategies to improve the robustness of the methods to the presence of outliers; (iii) exploiting the spectral diversity in the algorithms to improve the detection sensitivity and the estimation accuracy.*

---

## 1.1 Introduction

*Detecting and characterizing* objects in images in the low signal-to-noise ratio (S/N) regime is a critical issue in many areas such as *astronomy* or *microscopy*.

Astronomy is a field of study in which optical progress makes it possible to design new generations of instruments always more efficient and dedicated to specific tasks. In particular, the detection of exoplanets, i.e. planets<sup>1</sup> orbiting a star outside the Solar System, and their characterization by direct imaging from the Earth is a hot research topic. A target star and its close environment (hosting potential exoplanets)

---

1. An object with a mass larger than  $\approx 13 - 17 M_J$  is not strictly considered as a planet since it is above the fusion limit of deuterium. In this case, the standard denomination is *brown dwarf*.

are observed on short temporal exposures and on several spectral channels.

Similarly, recent advances in microscopy in terms of resolution and sensitivity have opened the door to new medical diagnoses. However, this technology remains expensive due to the requirement for high-grade optical and mechanical components. Therefore, holographic microscopy appears to be a cost-effective method of choice for characterizing microscopic objects. Based on the recording of a hologram, it allows a digital focusing in any plane of the imaged 3-D volume.

In these two application fields, the detection and characterization problem is made difficult by the possibly large difference of amplitude between the objects of interest and the strong background of the recorded images.

This thesis attempts to provide answers to the current need for detection and characterization methods both in direct imaging for astronomy and in holographic microscopy. There are several methodological bridges between these two targeted applications. The main focus is put on the use of statistical and/or physical based approaches to detect and to derive reliable estimates characterizing the imaged objects. Another common methodological component is the development of robust detection methods to improve their systematic deployment on data that are sometimes impacted by aberrant values. Finally, information redundancies and complementarities present in the recorded data are also exploited. Among these, temporal and/or multi-spectral redundancies are considered.

This chapter provides an introduction to the principle, characteristics, advantages, and limitations of direct imaging and holographic microscopy and discusses the signal processing challenges that they raise. For clarity, theoretical and/or mathematical considerations, as well as a more complete description of state-of-the-art processing methods, are not given in this chapter, but rather discussed throughout the following more technical chapters.

Section 1.2 of this chapter presents the main issues related to the detection and characterization of exoplanets in astronomy. Following the same structure than Section 1.2, Section 1.3 presents some issues related to the detection and characterization of microscopic objects spread in a volume. Finally, Section 1.4 emphasizes common methodological guidelines exploited in the contributions of this thesis work and presents the organization of this manuscript.

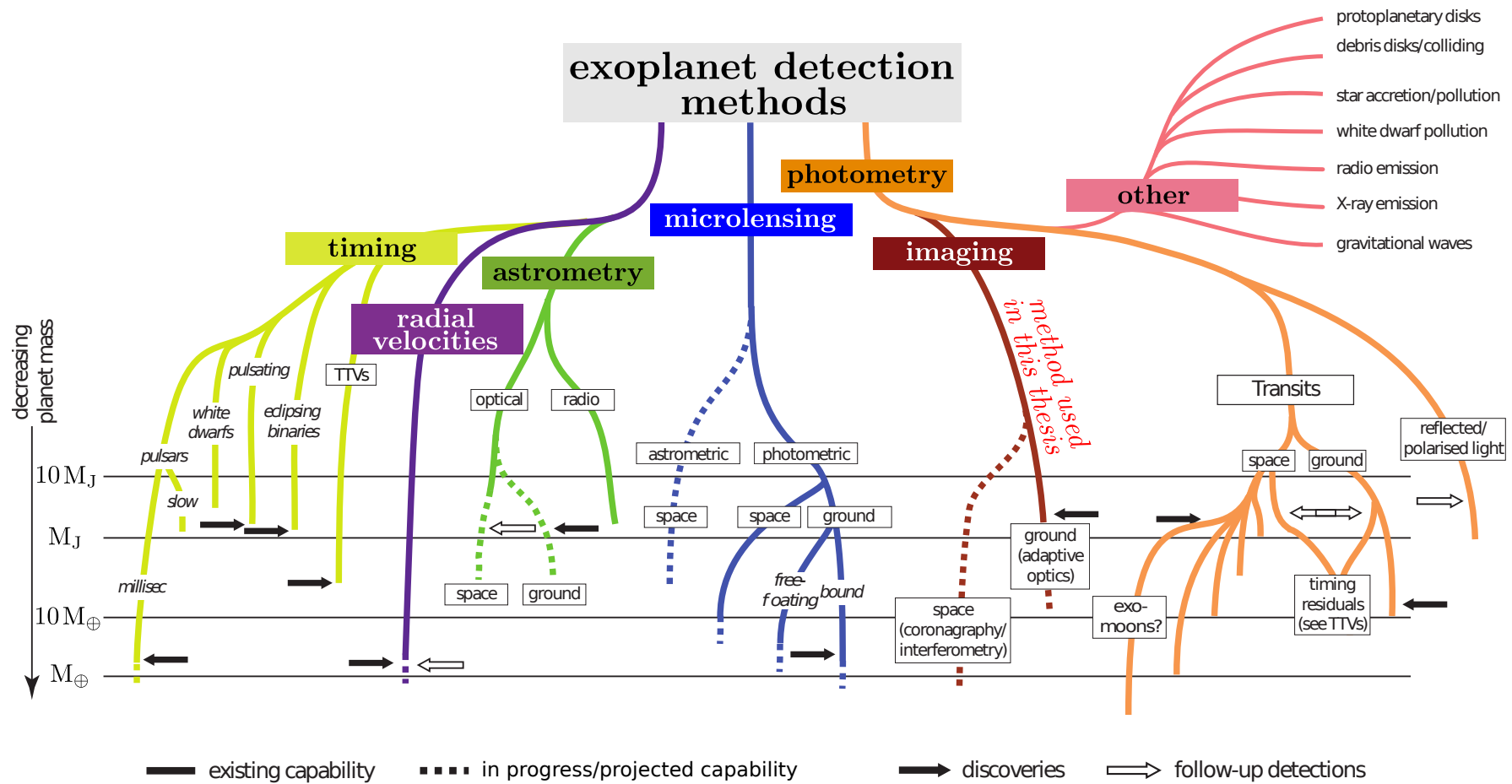


Figure 1.1 – Classification of exoplanet detection methods. The horizontal lines stand for the typical mass of the detected exoplanets.  $M_J$  is the Jovian mass, and  $M_{\oplus}$  is the Earth mass. Adapted from Perryman (2018).

## 1.2 Detection and characterization of exoplanets

In this section, we first briefly discuss the main indirect detection methods, focusing on their general principle, advantages, and drawbacks. Then, we focus on direct imaging, which is the detection technique investigated in this thesis. Only a short introduction to the subject is given in this section. The interested Reader will find a more complete presentation in the *The Exoplanet Handbook* (Perryman, 2018), a recent reference book dedicated to the detection and study of exoplanets, or in other references.

Throughout this section, the Reader can refer to Figure 1.1 giving an overview of the different detection techniques and variants described hereafter, to Figure 1.2 showing their respective principle, to Figure 1.3 presenting over the years the number of discoveries obtained with each method, and to Figure 1.4 giving the mass of the known exoplanets as a function of their semi-major axis. In each of these four figures comparing exoplanet detection techniques, the same color code (one color per method) is used for quicker identification.

### 1.2.1 Indirect detection methods

The *indirect* detection and characterization of exoplanets rely on the study of their influence on the host star. In other words, with these methods, no direct light of the exoplanets is exploited in the science data. We give hereafter the general principle of the main indirect detection methods based on *radial velocities*, *photometry*, *microlensing*, *timing*, and *astrometry* analysis.

#### 1.2.1.1 Radial velocities

Since a two-mass system moves around its center of gravity, the radial velocities method aims to measure the variations of the radial displacement (i.e., *the radial velocities* along the line of sight) of a star due to the gravitational influence of the exoplanets it hosts, see Figure 1.2(a). More precisely, the radial velocities are measured by Doppler spectroscopy through the displacement of the spectral lines of the host star due to Doppler effect. The radial velocities method preferentially detects massive exoplanets orbiting near low-mass stars since the induced displacement of the stellar lines is more important, thus easier to detect. In terms of characterization, this method gives access to a lower bound of the companion mass and almost all its orbital parameters.

We have chosen to present this technique first since it has achieved two significant breakthroughs. (i) The first extrasolar planet was discovered thanks to this technique (Latham et al., 1989). (ii) The first exoplanet orbiting a star of the main sequence<sup>2</sup> was also discovered thanks to this technique a few years later (Mayor and Queloz, 1995), at the Observatory of Haute-Provence. M. Mayor and D. Queloz were awarded the Physics Nobel Prize in 2019 for this breakthrough. Very recently (19-08-2019), a second exoplanet ( $\beta$  Pictoris c) has been discovered (Lagrange et al., 2019b) by radial velocities around  $\beta$  Pictoris, a well known and widely studied star in direct imaging, see

---

2. The life of a star is divided in several periods. A star of the *main sequence*, fuses its hydrogen atoms to form helium atoms in its core, like the Sun.

## 1.2. DETECTION AND CHARACTERIZATION OF EXOPLANETS

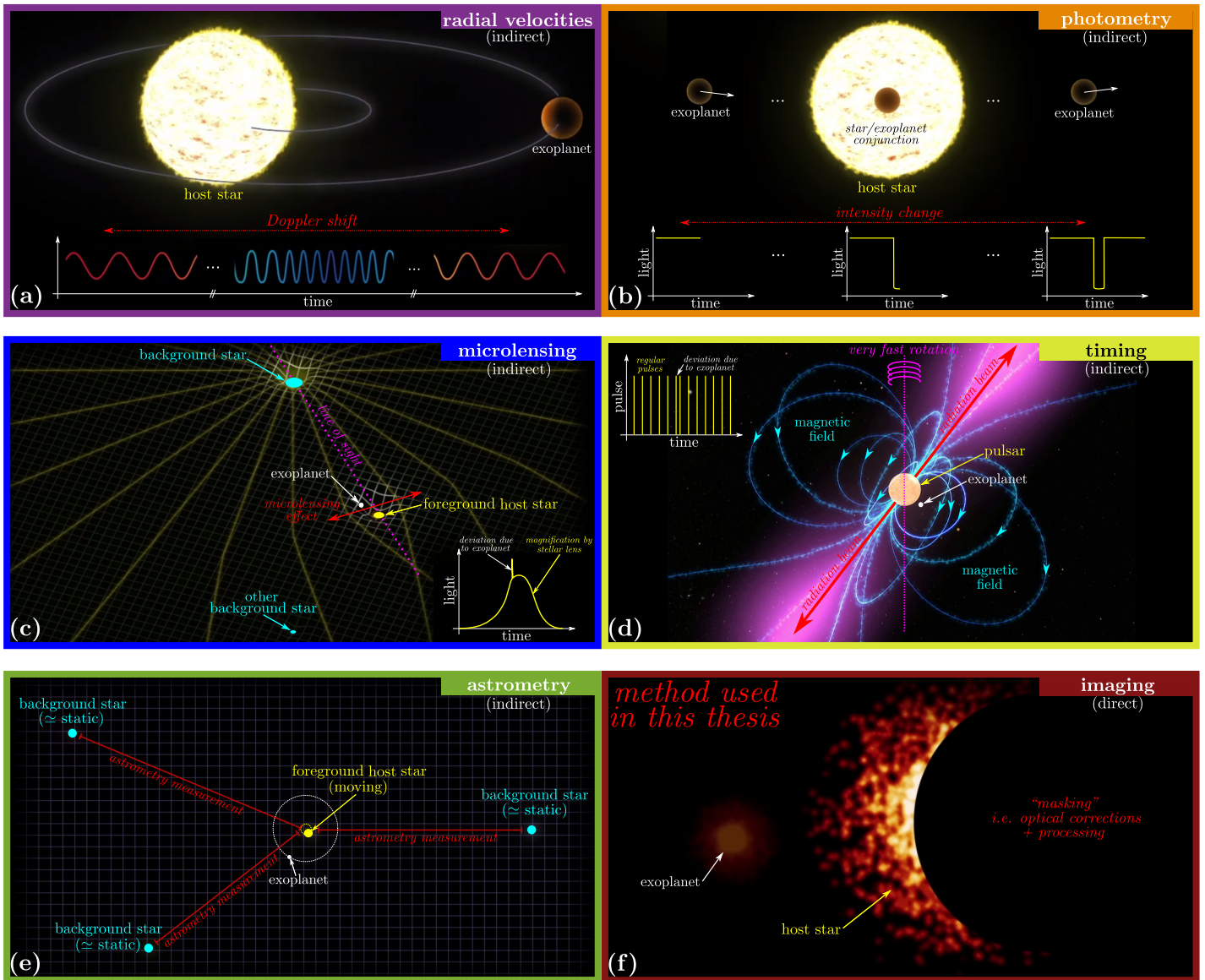


Figure 1.2 – Illustration of the principle of the main exoplanet detection methods: (a) radial velocities; (b) photometry; (c) microlensing; (d) timing; (e) astrometry; (f) imaging. Adapted from [NASA animations](#) (last access: 2019-08-23).

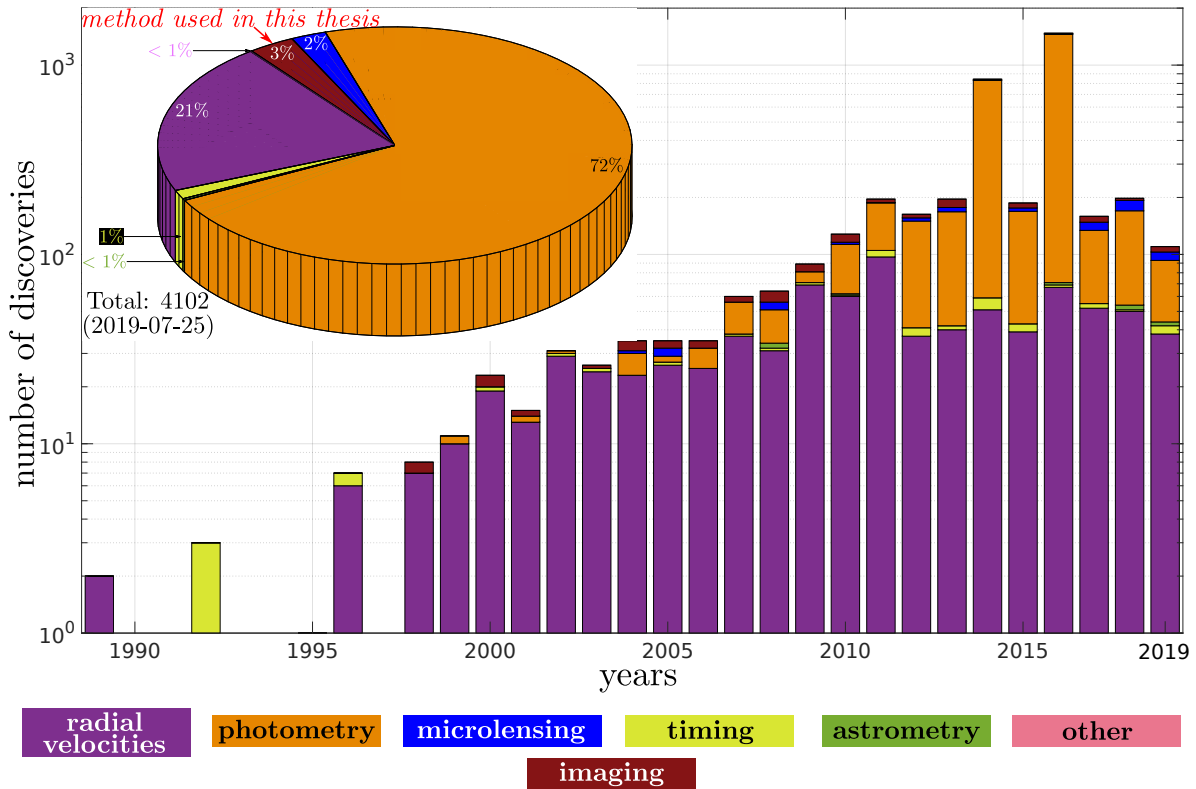


Figure 1.3 – Demography of the discovered exoplanets over years with the main detection techniques. The raw data were extracted the 2019-07-25 from the online [Extrasolar Planets Encyclopaedia](#) (Schneider et al., 2011).

Sections 1.2.2.2.4, 2.5.2.3, 6.6, and 8.2.1.2.2. Radial velocities is also the second best method in terms of number of discoveries: about 21% of the known exoplanets were detected with this method, see Figure 1.3. Several facilities are currently dedicated to the quest of exoplanets using this technique, including the High Accuracy Radial velocity Planet Searcher (HARPS) operating at the La Silla Observatory, or the next generation instrument Echelle SPectrograph for Rocky Exoplanets and Stable Spectroscopic Observations (ESPRESSO) operating since 2018 on an 8.2 m diameter telescope at the VLT.

This method is limited by the star/exoplanet configuration since it requires that the system be close to an edge-on configuration. This technique also produces some false alarms, due to the stellar activity producing a displacement of stellar lines similar to that induced by the exoplanets. Thus, it is often necessary to combine it with a complementary method such as photometry (see Section 1.2.1.2), or direct imaging (see Section 1.2.2) to confirm the presence of a candidate companion and estimate its actual mass.

### 1.2.1.2 Photometry

Photometry methods are based on the analysis of the evolution of starlight intensity over time. Among these techniques, the transit method is the most used. It is based



on the detection of the decrease of a star intensity (so-called *photometry*) when an exoplanet *transits* in front of it, see Figure 1.2(b). A study of the brightness dip (transit depth, duration, ingress and egress duration) gives information about the size of the exoplanet. The transit method is more suitable to detect giant exoplanets orbiting near low-mass stars since the induced brightness dip is greater and thus easier to detect. When it is used jointly with a complementary method such as radial velocities (see Section 1.2.1.1), or imaging (see Section 1.2.2), almost all the companion characteristics (orbital parameters, mass, surface temperature, and atmosphere) can be estimated.

Since the first discovery by Charbonneau et al. (1999), the transit method is of a particular interest since about 72% of the exoplanet discoveries were obtained thanks to this technique, see Figure 1.3. In particular, the space-based telescope Kepler of the American National Aeronautics and Space Administration (NASA) led between 2009 and 2018 to the transit detection of about 2600 exoplanets (over the 4102 known ones) including 8 potential exoEarths. This success is largely explained by the ability of such instruments to image thousands of stellar systems simultaneously. Specific efforts were also put on the processing of the large quantity of data, including the involvement of giant firms of the Internet and the participation of citizen scientists. In spite of the end of the Kepler mission, it is expected that the number of discoveries due to transit analysis will increase even more in the next few years thanks to new missions. Among these, we can cite the Transiting Exoplanet Survey Satellite (TESS) launched in April 2018, the future PLATO (PLANetary Transits and Oscillations of stars, launch scheduled for 2026) space telescope or the future James Webb Space Telescope (JWST, launch scheduled for March 2021) that will embed a 6.5 m diameter telescope, the largest space-based telescope ever built.

This technique is mainly limited by the system configuration that should be close to an edge-on alignment and by its very high false alarm rates, generally reaching about 10% to 40% (Santerne et al., 2012; Morton et al., 2016). As a result, combining the transit method with a complementary method is often mandatory.

### 1.2.1.3 Microlensing

The microlensing method is based on the Shapiro effect stating that light rays are deviated when passing close to a massive object. Thus, a foreground star can induce such a deviation of the light rays from a more distant background star aligned along a common line of sight. In this configuration, the foreground star acts as a *microlens*, deviating and magnifying the light rays from the background star. If an exoplanet orbits the foreground star, the magnification of the light of the background star is disturbed and takes the form of a typical short-lived spike, see Figure 1.2(c). The detection of this spike signs the presence of a potential companion. The microlensing technique preferentially detects small exoplanets at wide orbits around low-mass stars, since the microlensing effect is more important in this configuration. In terms of characterization, only the mass of the companion relative to the star and part of the orbital parameters can be deduced from microlensing observations.

Since the first discovery with this technique (Bond et al., 2004), about 2% of the known exoplanets have been detected by microlensing, see Figure 1.3. One of the most advanced and ambitious projects (partially) dedicated to the detection of exoplanets with this technique is the Wide Field InfraRed Survey Telescope (WFIRST), which

could be launched around 2025.

The main limitation of the microlensing method is its lack of reproducibility. Indeed, the probability of realignment of the foreground star with the same background star is null, and the chance of follow-up alignment with another background star is very unlikely. A second drawback is related to the limited number of characteristics that can be inferred for the detected companions.

#### 1.2.1.4 Timing

There are several sub-methods based on the analysis of *time*-periodic signals from the host star (see Figure 1.1), and one of the most used is pulsar timing. A *pulsar* is a neutron star spinning very fast around its revolution axis at a very regular frequency. During its rotation, it emits time-periodic pulses creating two radio beams from its poles, see Figure 1.2(d). The detection is based on the time-frequency analysis of the pulses whose regularity is slightly disturbed in the presence of exoplanets. The mass and orbital parameters of the detected exoplanets can also be estimated with this technique.

Since the first discovery (Wolszczan and Frail, 1992), less than 1% of the known exoplanets were discovered with this technique, see Figure 1.3.

This method is limited to the detection of exoplanets orbiting pulsars, which are significantly rarer than conventional stars of the main sequence.

#### 1.2.1.5 Astrometry

Finally, the astrometry method is also based on the study of the gravitational effect that an exoplanet has on its host star. While the radial velocities technique aims to detect a star displacement via Doppler spectrometry, the astrometry method detects a star motion via an accurate measurement of its location (so-called *astrometry*) relative to reference background stars, see Figure 1.2(e). As for the radial velocities method, the astrometry technique preferentially detects massive exoplanets orbiting near low-mass stars. This method gives access to some orbital parameters of the detected companions and can help to constrain the mass estimation from other methods such as the radial velocities, see Section 1.2.1.1.

Although it is the oldest method of detection from a theoretical definition point of view, the first detection was obtained only recently (Mutterspaugh et al., 2010). Since then, 9 other exoplanets have been detected with astrometry measurements, see Figure 1.3. This number is expected to increase significantly in the next few years, in particular thanks to the ongoing mission of the satellite Gaia dedicated to astrometric measurements.

The main limitation of the astrometry method is related to the difficulty to derive accurate measurements of the typical small displacement of stars under the gravitational influence of exoplanets. Especially, ground-based accurate astrometry measurements are difficult to obtain due to distortions in the field of view caused by atmospheric turbulence.

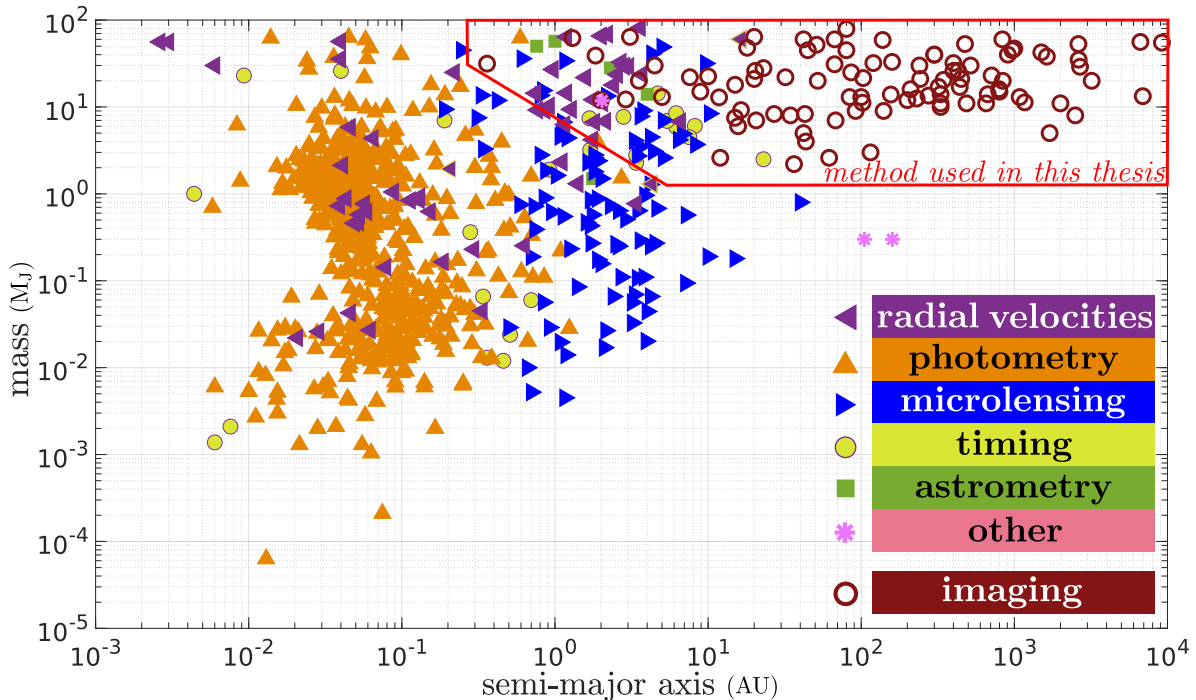


Figure 1.4 – Mass of the known exoplanets and brown dwarfs as a function of their semi-major axis for the different detection methods. All the 4102 known exoplanets are not represented in this graphic since all are not characterized in terms of mass and/or semi-major axis (in particular the ones detected by radial velocities, see Section 1.2.1.1). The raw data were extracted on 2019-07-25 from the online [Extrasolar Planets Encyclopaedia](#) (Schneider et al., 2011).

## 1.2.2 Direct imaging as a method of choice

As a starting point, we consider Figure 1.4 presenting the exoplanet discoveries for each method of detection in the so-called *parameters space*, i.e. a graph showing the estimated mass of the exoplanets as a function of their semi-major axis. It emphasizes that direct imaging is the only method unveiling giant planets orbiting at various distances from their host star. This is one example (among others) showing the complementarity of direct imaging to the indirect methods presented in Section 1.2.1. In this section, we describe its principle, paying particular attention to its specificities in terms of instrumentation, related challenges, and data analysis.

### 1.2.2.1 General principle and characteristics

Direct imaging could be summarized as the taking of a *direct* picture of an exoplanet by *imaging* its host star and its close environment, see Figure 1.2(f).

As illustrated by Figure 1.4, direct imaging preferentially detects high-mass exoplanets, typically between 1  $M_J$  and 100  $M_J$ . While there is also a theoretical preference for wide-orbiting exoplanets (since both the angular resolution and contrast are improved in this configuration), direct imaging proves to be able to detect exoplanets at various

distances<sup>3</sup> from their host stars (with a semi-major axis typically between 10 AU and 10,000 AU). It is also more adapted to detect hot exoplanets (i.e., exoplanets emitting intensively in the infrared band), orbiting relatively young<sup>4</sup> (typically less than 0.5 Gy) and low-mass stars since the contrast is more favorable in this case.

Direct imaging presents several advantages and peculiarities comparatively to the indirect detection methods. First, it is significantly less sensitive to the configuration of the imaged system than indirect methods. Indeed, while face-on-orbit configurations are preferred, direct imaging can also detect exoplanets in edge-on-orbit configurations. Besides, direct observations can be conducted in a relatively short time (typically a few hours), while it is often necessary to combine several months or years of observations with indirect methods, in particular for the photometry and microlensing techniques. Thus, observations can be easily repeated a few months later to possibly rule out the presence of a candidate companion with a physically non-plausible motion. Probably, the main advantage of direct imaging is its ability to derive a large panel of physical properties about the detected candidate companions. The estimated *astrometry* (i.e., the projected distance between the candidate companions and the star) on several observations allows to recover the 6 parameters defining the orbit of the candidate companions. The estimated *photometry* (i.e., the flux of the candidate companions at a single wavelength or their spectral energy distribution (SED) at several wavelengths in a given spectral band) gives access through physics-based models to their age, mass, surface gravity, metallicity, composition, effective temperature, and evolution, see [Claudi et al. \(2019\)](#); [Cheetham et al. \(2019\)](#) for examples of case studies. This information is obtained by fitting orbit models as well as exoplanet formation and evolution models on the estimated astrometry and photometry ([Burrows et al., 1997](#); [Chabrier et al., 2000](#); [Allard et al., 2003](#); [Baraffe et al., 2003](#); [Allard et al., 2007](#); [Saumon and Marley, 2008](#); [Vigan et al., 2010](#); [Baudino et al., 2015](#)). Based on the results of this step, we can conclude on the actual presence of a candidate companion and its status: exoplanet gravitationally bounded to the host star, brown dwarf not necessarily bounded to the host star, or background star imaged in the projected field of view. The accuracy of these estimated quantities can be improved by combining direct imaging with other detection methods such as radial velocities ([Ruffio et al., 2018](#); [Mawet et al., 2019](#)).

### 1.2.2.2 Challenges of direct imaging

Despite the numerous advantages of direct imaging and its promising future, only a dozen exoplanets (see [Figure 1.3](#)) have been successfully detected to date using this technique ([Bonavita et al., 2014](#); [Macintosh et al., 2015](#); [Chauvin et al., 2017](#)). Indeed, the direct detection of exoplanets from the ground is a very challenging task and made possible only in the last decade thanks to the joint progress in optics, instrumental design, and processing methods, see [Pueyo \(2018\)](#) for a review. In particular, two major points must be addressed to make the direct detection of exoplanets possible. First, a *high angular resolution* is mandatory to image such close point-like sources located at several light-years, leading to small angular separations with the host stars (typically between 0.1 and a few arcseconds). The second point is related to the very

---

3. The astronomical unit (AU) is the distance from Earth to the Sun, i.e.,  $1 \text{ AU} \simeq 150 \times 10^6 \text{ km}$ .

4. For comparison, the age of our Solar system is about 4.6 Gy.

*high contrast*, i.e. the very weak ratio between the intensity of the exoplanet and the intensity of the host star (typically less than  $10^{-5}$  in infrared), making the detection very challenging. In the following sections, we briefly discuss experimental solutions included in the exoplanet hunter instruments to handle these two difficulties.

#### 1.2.2.2.1 Reaching high angular resolution with adaptive optics

From a diffraction point of view, the resolution achieved by a telescope is inversely proportional to the diameter of its primary mirror. Increasing its size should then be sufficient to achieve the targeted resolution. In practice, this theoretical resolution is not reached due to atmospheric turbulence resulting from wind changes, pressure, temperature, and humidity inhomogeneities (Aime et al., 2003). Thus, light rays from the star and its potential exoplanets are deviated from their initial trajectories and undergo, at each location of the pupil, a time-varying phase shift. This results in a non-smooth background in the science images, taking the form of spatially correlated blobs (Fitzgerald and Graham, 2006).

To handle the wavefront distortion, one of the most powerful state-of-the-art solutions consists in the use of an (extreme) adaptive optics (x)AO (first concept: Babcock (1953), first on-sky demonstration: Rousset et al. (1990), see also Davies and Kasper (2012); Milli et al. (2016) for reviews). With such a device, the wavefront is dynamically corrected for distortions in a 3 steps procedure:

1. The deformation of the wavefront is analyzed by a wavefront sensor like a Shack-Hartmann (Shack, 1971) device. A Shack-Hartmann wavefront sensor is made of a lenslet matrix focusing the light on a secondary camera. If the wavefront is perfectly plane and orthogonal to the optical axis, each lenslet produces a spot aligned on the optical axis of the lenslet. When the wavefront is distorted, the spot produced by each lenslet is spatially shifted according to the local slope of the wavefront in the pupil of the lenslet.
2. The second step consists in measuring the shift of each spot of light, and reconstructing in real-time the wavefront to compute the correction to apply locally (i.e., a phase delay/advance).
3. The last step consists of applying the correction by sending a command to a deformable mirror. A deformable mirror is split into sub-mirrors ( $41 \times 41$  for SAXO, the xAO of VLT/SPHERE, Beuzit et al. (2019)), each one can independently move a few micrometers with respect to its rest state thanks to numerically controlled actuators.

This procedure is repeated in a closed-loop mode, at a high-frequency rate (1.2 kHz for SAXO, Beuzit et al. (2019)).

On state-of-the-art instruments such as VLT/SPHERE or GEMINI/GPI, the xAO reaches the excellent performance of a Strehl ratio about 0.90 in the H Johnson's band (Beuzit et al., 2019), i.e. 90% of the maximal intensity of the aberration-free on-axis point spread function (PSF) is recovered.



### 1.2.2.2.2 Reaching high contrast with coronagraphy

The second aspect that should be addressed is namely the contrast, i.e. the very large difference between the amount of light received from the star and that received from the exoplanets (Oppenheimer and Hinkley, 2009).

Coronagraphic masks are used to cancel at best the starlight while preserving the signal from the exoplanets. The design of coronagraphic masks is a very active field in optics and several solutions can be adopted (first concept: Lyot (1939), first demonstration for direct imaging: Sivaramakrishnan et al. (2001), see also Guyon et al. (2006); Mawet et al. (2012) for reviews). The simplest one is to place a classical Lyot coronagraph (i.e., a mask in the image focal plane), thus discarding part of the on-axis PSF. It is generally combined with a Lyot stop (i.e., a mask which transmits the light only on an annulus-shaped area) placed in the following pupil plane to attenuate spurious diffraction patterns created by the focal mask whilst most of the light from surrounding sources of interest going up to the camera. State-of-the-art instruments such as VLT/SPHERE are equipped with more advanced devices optimized to reach a high contrast even at small angular separations. Among these devices, the APLC coronagraph (Carillet et al., 2011) combines a pupil plane apodizer, a focal plane mask, and a Lyot coronagraphic stop. Such systems are designed to work in a specific spectral band so that several coronagraphic masks are generally embedded in exoplanet finder instruments. Moreover, coronagraphic systems are coupled with a tip/tilt measurement system to accurately stabilize the star throughput at the center of the coronagraph.

With such devices, it is possible to reach considerably better contrasts between the host star and the exoplanets. Tested on a reference star, the achievable raw contrast (before processing) of VLT/SPHERE is in the range  $[5 \times 10^{-3}; 5 \times 10^{-4}]$  at 0.2 arcsec, and in the range  $[3 \times 10^{-4}; 5 \times 10^{-5}]$  at 1 arcsec, depending on the considered wavelength in the Y-K Johnson's band (Beuzit et al., 2019).

### 1.2.2.2.3 Observing strategies

In order to enhance the achievable contrast, several observation strategies have been developed to exploit (mainly) temporal and/or spectral diversity by recording several frames at different times and/or wavelengths. Hereafter, we present the general principle of the main strategies. More details are given, when needed, throughout the manuscript.

- *Angular differential imaging* (ADI, Marois et al. (2006)) is the most popular observation mode. It consists of tracking the observed target over time following a particular strategy: the telescope derotator is tuned to maintain the telescope pupil stable while the field of view rotates. Consequently, in the resulting 3-D datasets (2-D + time), candidate companions (off-axis sources) follow an apparent motion (due to the rotation of the Earth during the few hours of observation) along a predictable circular trajectory around the host star while the telescope pupil (including the spider arms that maintain the secondary mirror) remains static.
- *Spectral differential imaging* (SDI, Racine et al. (1999); Marois et al. (2000))

consists of recording images simultaneously in several spectral channels using for instance an Integral Field Spectrograph (IFS). It produces, after a pre-reduction step (see Section 1.2.2.3), 3-D datasets (2-D + spectral) in which the stellar speckles due to diffraction are very similar from one wavelength to the other, up to a chromatic scaling (Pueyo and Kasdin, 2007). After compensating for this scaling, speckles are aligned while the candidate companions (originally aligned in the multi-spectral cube) then follow a radial motion from one spectral channel to another (Sparks and Ford, 2002).

- *Angular and spectral differential imaging* (ASDI, Sparks and Ford (2002)) is a natural extension of ADI and SDI consisting of using those two complementary modes of observation simultaneously. This hybrid observation mode produces (after a pre-reduction step, see Section 1.2.2.2.4) 4-D datasets (2-D + time + spectral), combining the separate motion of off-axis objects with respect to the background signal obtained with ADI and SDI. After compensation of the chromatic scaling (as for SDI), the candidate companions describe a circular motion over time and a radial motion along spectral channels. Using ASDI instead of simple ADI brings a spectral diversity. The discrimination between the signal from off-axis sources and the background signal due to stellar leakages is thus improved. Also, ASDI datasets allow both the detection and the spectral characterization of the exoplanets.

Several adaptations of these strategies exist and mainly differ on the way to capture the diversity of information. Among these, the *reference differential imaging* (RDI; Rameau et al. (2012)) consists of recording, in addition to frames from the target star, frames from another star (with no known exoplanet) sharing close astrophysical properties (i.e., age, temperature, brightness). This strategy is mainly used when no pupil tracking mode is available on the planet finder instrument. Besides, this mode of observation can be useful to investigate the area near the star since the processing of the data does not lead to *self-subtraction* of the exoplanet signal (see Section 2.2). The *polarimetric differential imaging* (PDI; Kuhn et al. (2001)) consists of measuring the polarization state of light. This mode is mainly used for the study of extended objects such as stellar disks since it is expected that such objects are polarized in a particular direction (Langlois et al., 2018).

In the datasets produced by these different observation strategies, the (circular and/or radial) apparent motion of the point sources with respect to the background is the key to their detection. Speckles resulting from instrumental aberrations are strongly correlated from one frame to the other. The images can thus be combined to cancel most of the speckles while preserving part of the signal from the off-axis sources. Therefore, the detectability of the exoplanets relies on the combined ability of the instrument and the numerical processing to suppress the light from the host star and extract the signal from the exoplanets from the remaining stellar speckles.

In the next section, we briefly present the most advanced high contrast instruments used to record direct imaging sequences.

#### 1.2.2.2.4 Dedicated facilities

Observations can be performed both from the ground or from the space; each strategy has its own specificities. In this thesis, we focus on ground-based observations which are currently the gold-standard for the detection of faint exoplanets by direct imaging due to the difficulty to embed large telescopes on space-based satellites<sup>5</sup>.

Currently, two ground-based exoplanet finders are optimized with cutting-edge instrumental techniques for direct imaging observations: (i) the Spectro-Polarimetry High-contrast Exoplanet REsearch (SPHERE, [Beuzit et al. \(2008, 2019\)](#)) mounted on one of the four 8.2m diameter telescope of the Very Large Telescope (VLT, Chile) operated by the European Southern Observatory (ESO), (ii) the Gemini Planet Imager (GPI, [Macintosh et al. \(2014\)](#); [Greenbaum et al. \(2018\)](#)) mounted on an 8.1 m diameter telescope of the GEMINI Observatory (Chile) operated by a North and South American countries consortium for astronomy. In particular, these two instruments offer spectroscopic observation capability in the near-infrared. SPHERE saw its first light in the middle 2014, GPI at the end of 2013, both were opened to the scientific community in 2015.

The algorithms dedicated to exoplanet detection and characterization developed during this thesis are tested<sup>6</sup> on datasets from the VLT/SPHERE instrument. Thus, we briefly discuss its main characteristics. SPHERE is made of a common path instrumental unit (CPI) including the adaptive optics and the coronagraphic system, as well as three science instruments, see [Figure 1.5](#):

- The *InfraRed Dual-band Imager and Spectrograph* (IRDIS) is the main imager of SPHERE dedicated to the detection of faint exoplanets. It produces 3-D (2-D + time) datasets for ADI observations (see [Section 1.2.2.2.3](#)). It benefits from a large workable field of view ( $11 \times 11$  arcsec sampled on  $1024 \times 1024$  pixel images at a resolution about 0.01250 arcsec/pixel) and can be used to detect close-by as well as farther away exoplanets (i.e., exoplanets with small or larger angular separation with respect to the host star). It is equipped with a variety of chromatic filters for observations in the Y-J-H-K Johnson's bands (i.e., between  $0.95 \mu\text{m}$  and  $2.35 \mu\text{m}$ ). In its standard mode, IRDIS conducts observations in a *dual-band imaging* (DBI) mode, i.e. it records datasets on two close wavelengths (dual ADI or ASDI at two wavelengths). The wavelengths are selected so that the exoplanet signal be negligible at one of the two wavelengths (so that only the background is captured at that wavelength, which can simplify the detection by image subtraction). In practice, only the spectral channel in which the exoplanet signal is expected to be maximum is considered, generally<sup>7</sup>. Similarly to the DBI

---

5. Direct imaging from the space presents technical drawbacks but offers other advantages like the absence of atmospheric turbulence. Space-based direct imaging facilities include the Hubble Space Telescope (HST), the Spitzer telescope, and the forthcoming James Webb Space Telescope (JWST).

6. It is expected that these algorithms are general and can also work with datasets from different direct imaging instruments. We have for example successfully tested them on datasets from the VLT/NaCo instrument.

7. Joint processing requires to correct for the chromatic factor between the two spectral channels by interpolations. We have observed that signal degradations caused by interpolations generally exceed the gain brought by the consideration of only one additional spectral channel.



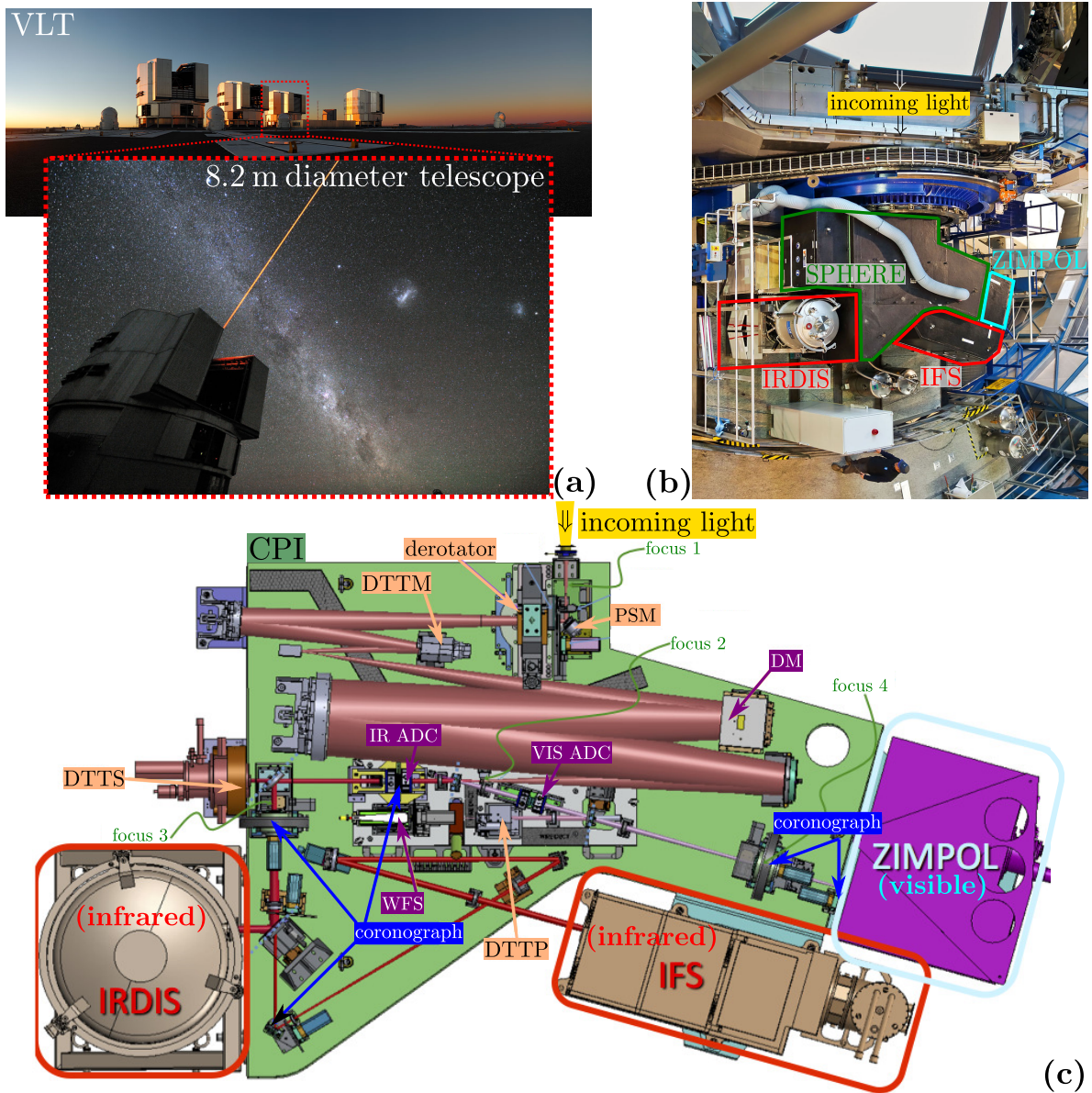


Figure 1.5 – The exoplanet finder VLT/SPHERE. (a) view of an 8.2m diameter unit telescope of the VLT; (b) view of the SPHERE instrument, a man is on the bottom for the scale; (c) schematic representation of the instrument: the infrared (IRDIS and IFS) and the visible (ZIMPOL) imagers around the common path instrument (CPI) unit, adaptive optics elements such as the atmospheric dispersion correctors (IR ADC for the infrared channels, and VIS ADC for the visible channel), wavefront sensor (WFS), and the deformable mirror (DM) are highlighted in purple, coronagraph systems (one per instrument channel) are in dark blue, optical elements such as the derotator, the pupil stabilization mirror (PSM), the differential tip/tilt mirror (DTTM), sensor (DTTS), and plate (DTTP) are in orange, the different focal planes of the instrument are marked in dark green, finally the incoming light from the telescope is marked in yellow. Credits: (a) top part is adapted from [ESO/F. Kamphues](#) picture; (a) bottom part is adapted from [ESO/G. Hüdepohl](#) picture; (b) is adapted from [ESO/J. Girard](#) picture; (c) is adapted from [Beuzit et al. \(2019\)](#).

mode, IRDIS can work in a *dual polarimetry imaging* (DPI) mode, mainly used for morphology studies of stellar disks (Garufi et al., 2017). IRDIS also has a *long-slit spectroscopy* (LSS) mode, mainly used to derive the SED estimations of detected exoplanets having a modest level of contrast (Vigan et al., 2008). Finally, IRDIS can be used in a *classical imaging* (CI) mode (i.e., without coronagraph) for multi-purpose imaging.

- The *Integral Field Spectrograph* (IFS) is the second imager of SPHERE dedicated both to the detection (especially at small angular separations) and characterization of faint exoplanets. It is based on the use of a lenslet array and dispersing elements (forming the integral field unit), placed in a focal plane of the instrument. Light passing through each lenslet is dispersed to form a spectrum on the science camera. This principle allows recording multi-spectral information on a 2-D sensor. A pre-reduction step is then performed by mapping raw observations of the IFS camera into a multi-spectral cube (Pavlov et al., 2008). After such a pre-preprocessing, a 4-D (2-D + time + spectral) dataset is obtained from the ASDI observations (see Section 1.2.2.2.3). The IFS instrument benefits from a smaller workable field of view than IRDIS ( $1.5 \times 1.5$  arcsec sampled on  $290 \times 290$  pixels images with a pixel size of 0.00746 arcsec) but offers a spectral diversity since the resulting ASDI datasets are made of  $L = 39$  spectral channels in the Y-J (i.e., between  $0.96 \mu\text{m}$  and  $1.34 \mu\text{m}$ ) or Y-H (i.e., between  $0.97 \mu\text{m}$  and  $1.66 \mu\text{m}$ ) Johnson's band. This spectral diversity is crucial to characterize the detected candidate companions by analysis of their SED.
- The *Zurich IMaging POLarimeter* (ZIMPOL) is the visible imager of SPHERE. It covers wavelengths between  $0.51 \mu\text{m}$  and  $0.90 \mu\text{m}$  and can work both in ADI, SDI, and ASDI observations strategies within DBI, DPI, and CI modes. It is mainly used for morphology study of both stellar disks (preferentially in DBI and DPI modes, see van Boekel et al. (2017) for a study case example) or other extended objects such as asteroids (preferentially in CI mode, see Fétick et al. (2019) for a study case example).

In this thesis, we deal with both ADI datasets from the SPHERE-IRDIS imager working on a DBI mode for the detection of exoplanets, and ASDI datasets from the SPHERE-IFS imager for the detection and characterization of exoplanets.

There are several secondary facilities dedicated to the detection and characterization of exoplanets by direct imaging. Among these, we can cite the Subaru Coronagraphic Extreme Adaptive Optics (SCEXAO, Jovanovic et al. (2015); Currie et al. (2017)) instrument at the SUBARU telescope (Hawaii) operated by the National Astronomical Observatory of Japan, and the L/M band InfraRed camera (LMIRcam, Leisenring et al. (2012); Rodigas et al. (2012)) system at the Large Binocular Telescope Interferometer (USA) operated by the NASA. Other facilities include the Magellan Adaptive Optics (MagAO, Morzinski et al. (2014); Wagner et al. (2018)) instrument at the Las Campanas Observatory (Chile), the Near Infrared Camera-2 (NIRC2, Howard et al. (2010); Mawet et al. (2019)) instrument at the Keck Observatory (USA), and the Project 1640 (P1640, Oppenheimer et al., 2012; Nilsson et al., 2017)) at Palomar Observatory (USA), all

operated by consortia of North American universities. Finally, the multi-purpose Nasmyth Adaptive Optics System with COudé Near Infrared CAMera (NAOS-CONICA, so-called NaCo, [Lenzen et al. \(2003\)](#); [Currie et al. \(2013\)](#)) was the main exoplanet hunter instrument of the ESO before SPHERE opened to the European community in 2015. NaCo was equipped with the previous generation of adaptive optics systems and was operating on an 8.2 m diameter telescope at the VLT until the end of 2019.

These dedicated instruments lead to several major discoveries, some of which are illustrated in Figure 1.6. Among these, we can cite the discovery in 2004 with the VLT/NaCo instrument of 2M1207 b (estimated mass between  $3 M_J$  and  $10 M_J$ ), the first directly observed exoplanet orbiting a brown dwarf ([Chauvin et al., 2004](#)). A few years later, the first directly imaged planetary system was unveiled: 3 exoplanets (HR 8799 b, c, d) orbiting the HR 8799 star were discovered from observations of the Keck and Gemini Observatories ([Marois et al., 2008](#)). Two years later, a fourth exoplanet (HR8799 e) was detected at a closer angular separation (about 0.37 arcsec) in this stellar system ([Marois et al., 2010](#)).

More recently, we can cite the unprecedented VLT re-detection of the exoplanet  $\beta$  Pictoris b at a very small angular separation (about 0.14 arcsec) on the northeast part of its orbit<sup>8</sup> after its conjunction with its host star, a two years period during which it was no longer detectable ([Lagrange et al., 2019a](#)). We can also cite the first discovery of an exoplanet (PDS 70 b) in formation inside a protoplanetary disk<sup>9</sup> ([Müller et al., 2018](#)). A few weeks ago, a second exoplanet in formation inside the PDS 70 accretion disk has been found at the VLT by a joint analysis of data from the MUSE<sup>10</sup>, SPHERE, and NaCo instruments ([Haffert et al., 2019](#)).

### 1.2.2.3 Processing pipeline and related signal processing issues

In this section, we summarize with Figure 1.7 the typical direct imaging pipeline. It starts with the direct imaging of an *astrophysical scene* (box ①) with a high contrast imager mounted on a telescope conducting *observations* (box ②) of the scene. The *raw datasets* (box ③) produced with ADI and/or ASDI mode(s) should be calibrated. A so-called *cosmetic calibrations* step (box ④) performs several corrections: bad pixels identification and interpolation<sup>11</sup>, thermal background subtraction, flat-field correction, anamorphism correction, true-North alignment, frame centering, compensation for spectral transmission, frame selection, and flux normalization. Such calibrations are done by processing chains dedicated to a specific instrument (e.g., see [Maire et al. \(2016\)](#) for SPHERE). Since ASDI observations are obtained with an IFS (see Sections 1.2.2.2.3 and 1.2.2.2.4) that uses a 2-D sensor to capture a spatial and spectral infor-

---

8.  $\beta$  Pictoris b was initially detected by direct imaging with NaCo ([Lagrange et al., 2009, 2010](#)). Between 2009 and September 2018 it was systematically imaged on the southwestern part of its orbit.

9. A *protoplanetary disk* (or *circumstellar disk*) is a rotating stellar disk made of gas and/or dust surrounding young stars. Exoplanets can form inside these disks by, for example, accretion effect of the matter (in this case, the denomination *accretion disk* is also used).

10. MUSE is a spectroscopic instrument dedicated to the investigation of the deep sky, see Section 1.4.3.

11. In practice, some bad pixels displaying large fluctuations only on a few frames remain after this processing. These can be attributed to either too conservative selection criteria, the temporally evolving behavior of the detector bad pixels or cosmic rays.



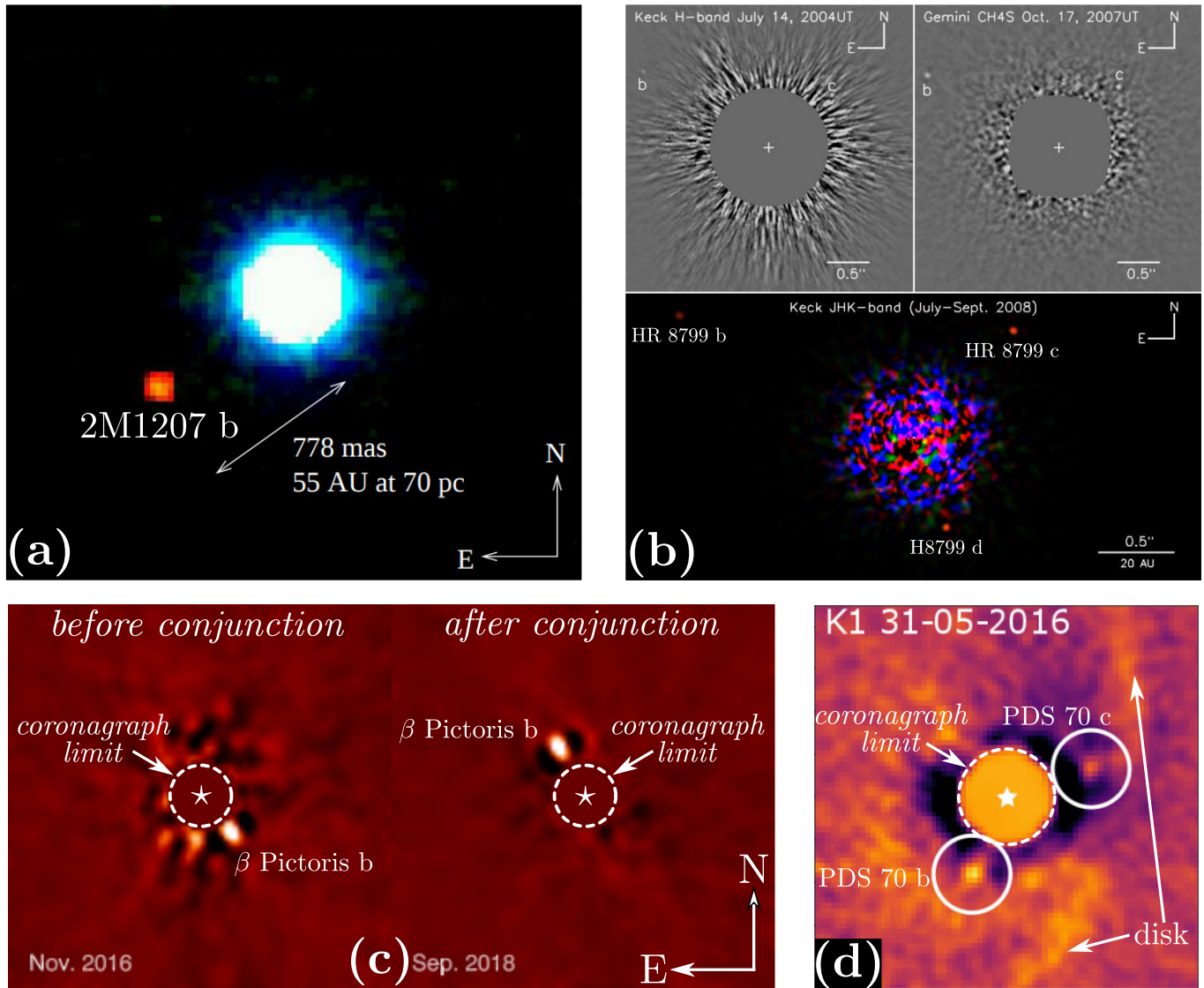


Figure 1.6 – Examples (after processing) of direct imaging discoveries: (a) composite image of the first directly imaged exoplanet 2M1207 b (adapted from Chauvin et al. (2004)); (b) the first directly imaged stellar system HR 8799, the bottom panel is a composite image (adapted from Marois et al. (2008)); (c) the exoplanet  $\beta$  Pictoris b before and after conjunction with its host star (adapted from Lagrange et al. (2019a)); (d) the exoplanets PDS 70 b and c embedded in the accretion disk surrounding their host star (adapted from Haffert et al. (2019)).

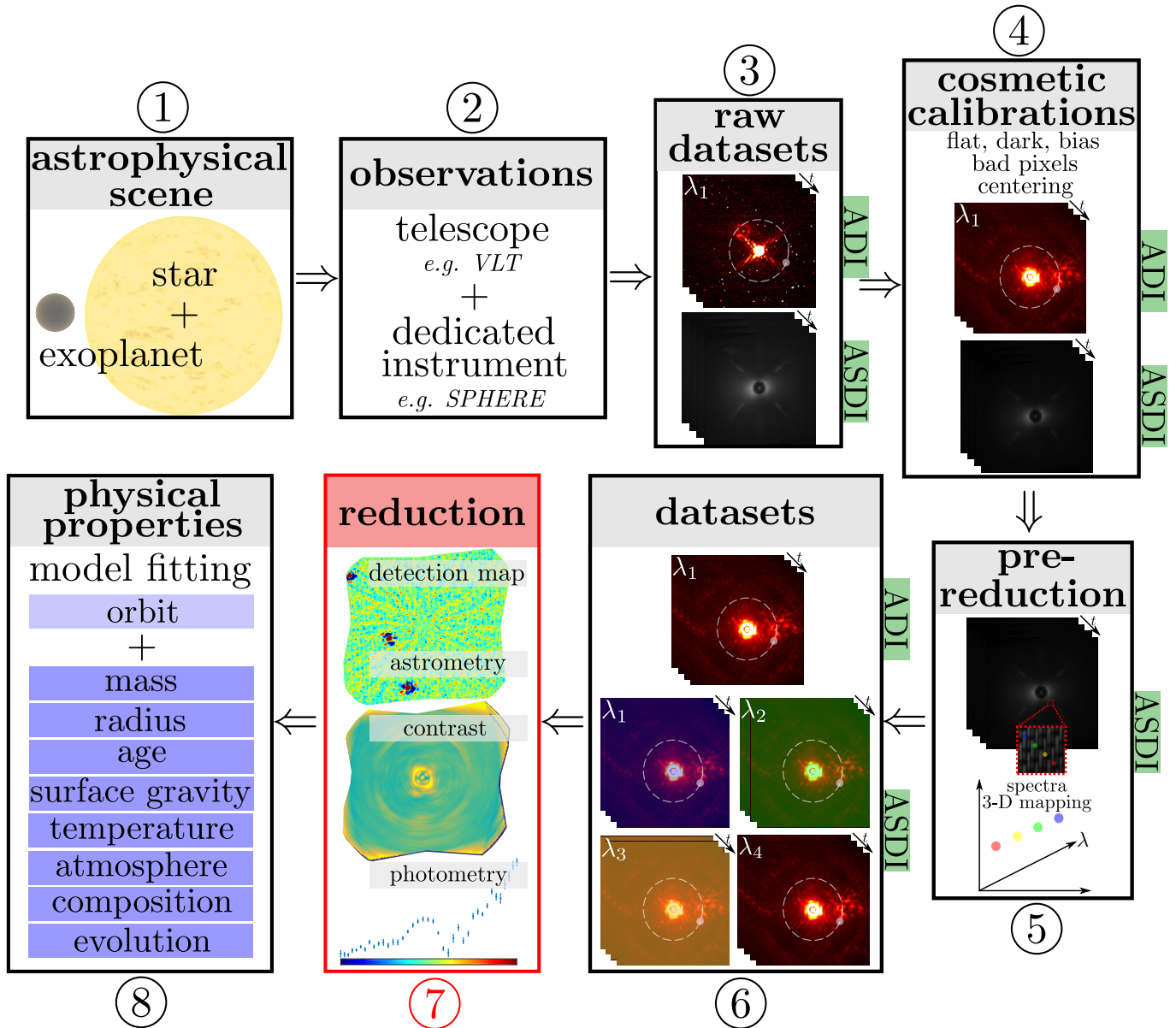


Figure 1.7 – Schematic representation of the typical direct imaging pipeline. The red frame emphasizes the part of the pipeline that is addressed by this thesis.

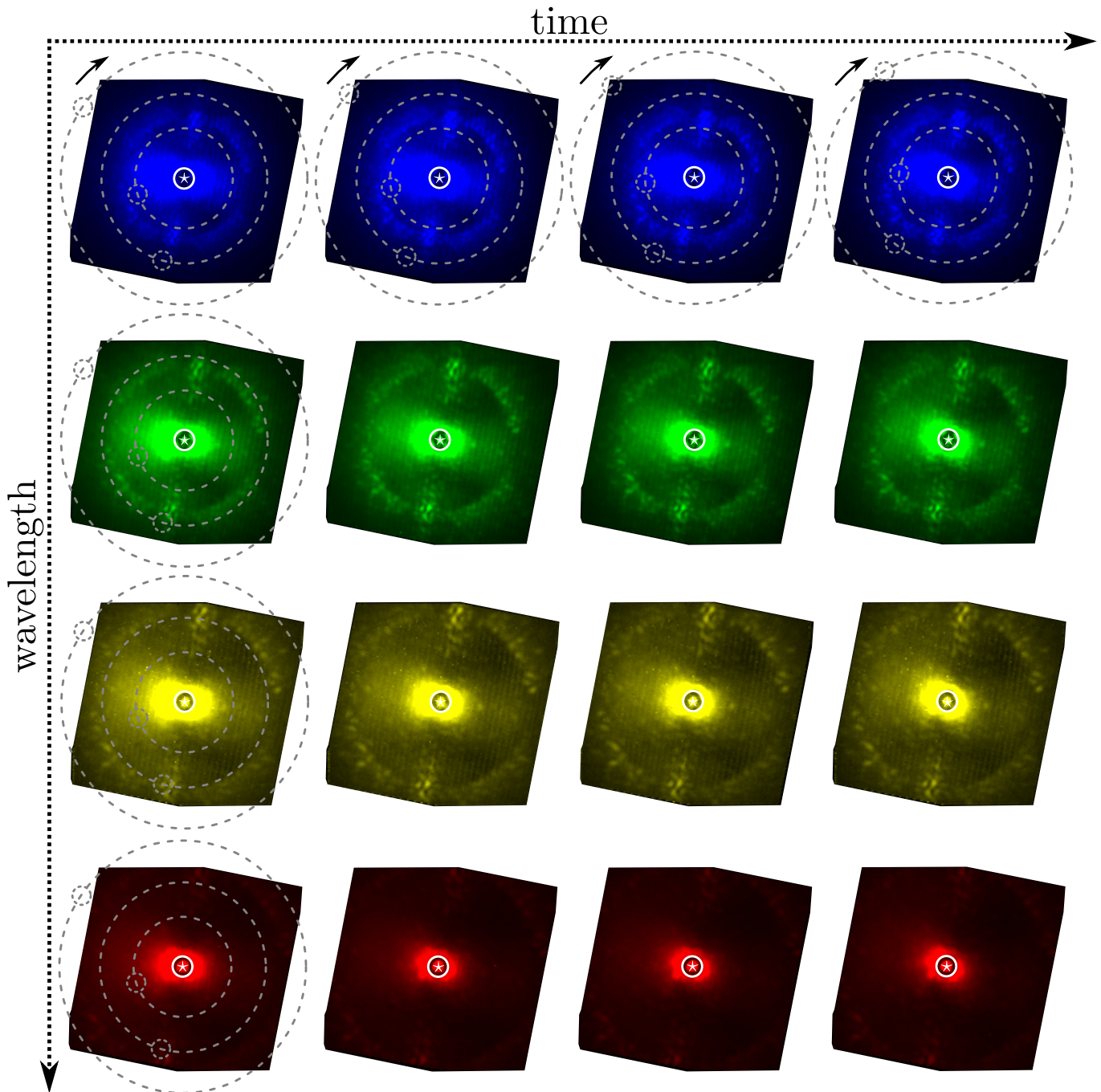


Figure 1.8 – Examples of frames from a calibrated ASDI datasets obtained with the VLT/SPHERE-IFS instrument on the HR 8799 star. The star symbol is for the star center, the solid straight circle close to the image center is for the coronagraphic mask (no source can be detected below this limit), and the gray dashed lines represent the trajectories of three known exoplanets (HR 8799 c, d, e). The data intensity is encoded with false colors for the selected wavelengths.

mation, a *pre-reduction* step (box ⑤) maps raw observations of the IFS camera into multi-spectral cubes. At the end of this step, the datasets (box ⑥) are formed by temporal (or temporo-spectral for ASDI) sequences of calibrated coronagraphic images. In this thesis, we consider both ADI and ASDI calibrated datasets. The following step consists of the *reduction* (red box ⑦), i.e. the processing of these datasets with dedicated algorithms aiming to detect and characterize the potential exoplanets orbiting the imaged star. Four key outputs should be retrieved from the reduction step: a list of detections with the *confidence* associated to each one, the achievable *contrast*; i.e. the minimum flux of an exoplanet to be detected at a given confidence level, the *astrometry* and *photometry*; i.e. the subpixel location and the unbiased flux or spectral energy distribution (SED) for ASDI observations of each detected candidate companions. This thesis is dedicated to the development of such algorithms. Finally, as detailed in Section 1.2.2.1, several *physical properties* (box ⑧) of the detected candidate companions can be estimated. In practice, this process is generally repeated for at least two different observations separated by several months to increase the confidence about the conclusions on the status of the detected source.

Before closing this part, we want to emphasize the processing issues related to the detection and characterization of exoplanets (red box ⑦ of Figure 1.7) from direct imaging datasets. Figure 1.8 gives examples of calibrated ASDI frames (box ⑥ of Figure 1.7) from a dataset obtained with the VLT/SPHERE-IFS instrument on the HR 8799 star (see Table 6.2 for the observation logs). The trajectories of three exoplanets whose detection are reported in the literature (Marois et al., 2008, 2010) are symbolized by gray dashed lines. In spite of the optical corrections of exoplanet-hunter instruments and to the care given in the conduction of the observations, the data remain largely dominated by a strong and spatially correlated and speckled background due to light from the host star (stellar leakages). Thus, the exoplanets are hardly detectable (not visible by visual inspection of the data). This issue is even more acute when the exoplanets are located closer to the host star and/or when the parallactic rotation of the field of view over time is limited. Elaborate processing methods combining multi-temporal and/or multi-spectral data play a central role to reach the ultimate detection limit achievable by direct imaging instruments. This thesis attempts to propose detection and characterization methods for optimal processing of the datasets from exoplanet hunter instruments.

### Direct imaging issues

- The detection and characterization of exoplanets by direct imaging is based on the observation of a star and its close environment by dedicated instruments.
  - In spite of the optical corrections (adaptive optics and coronagraph) and the care taken in the conduction of the observations, the recorded datasets are dominated by a nonstationary and spatially correlated background mainly due to stellar leakages.
- ⇒ The processing of the datasets by dedicated algorithms is mandatory. These algorithms exploit the predictable motion of the (potential) exoplanets in the temporal or temporo-spectral series of images.



## 1.3 Detection and characterization of microscopic objects

In this section, we first briefly discuss the main microscopy methods conventionally used for the observation and study of microscopic objects, focusing on their general principle, advantages, and drawbacks. Then, we give a particular emphasis on the holographic microscopy technique, which is the microscopy modality investigated in this thesis. Like in Section 1.2, only a short introduction to the subject is given in this part. The interested Reader will find a more complete presentation in reference books and reviews such as [Murphy \(2002\)](#); [Stephens and Allan \(2003\)](#); [Black \(2008\)](#), or in other references.

### 1.3.1 Optical microscopy modalities

Since Galileo Galilei's (attributed) claim that he was able to focus his telescope to observe small objects close up, several modalities of microscopy imaging have been invented, motivated in particular by the study of biological samples. Microscopy techniques can be split into three categories: (i) *light-microscopy* that observes samples via the illumination with visible, ultraviolet or infrared light and the collection of reflected, refracted or diffracted light, (ii) *electron-microscopy* that replaces the light beam by an electron beam, and (iii) *scanning-probe microscopy* that scrutinizes the surface of the samples with a mechanical probe. There are plenty of techniques derived from these three general families, and in the following, we focus on light-microscopy techniques. We briefly describe the general principles of the main light-microscopy methods: *bright field*, *dark field*, *phase contrast*, *polarization*, and *fluorescence* microscopy.

#### 1.3.1.1 Bright field

Bright field is the most simple microscopy technique. It consists of illuminating samples by a light (white or in a spectral band in the visible, ultraviolet or infrared range), and to record the optical attenuation of the light passing through the dense parts of samples, see Figure 1.9(a). The resulting image takes the form of dark shapes (corresponding to the image of the samples) on a *bright* background *field* (corresponding to the directly transmitted light). Adjustable optical elements such as a condenser and groups of lenses are incorporated in the setup for beam forming, as well as amplifying, magnifying and focusing the image of the samples on the sensor.

The simplicity of the setup is the main advantage of this technique. However, it offers only a limited contrast (i.e., a low output signal-to-noise ratio between the image of the samples and the background) and resolution due to the out of focus objects located on other planes than the focused objects that blur the image. Besides, transparent or translucent parts of the objects, like the ones encountered in the internal structures of cells, should be stained (e.g., with methylene blue) to be visible, a chemical process that can alter the samples.



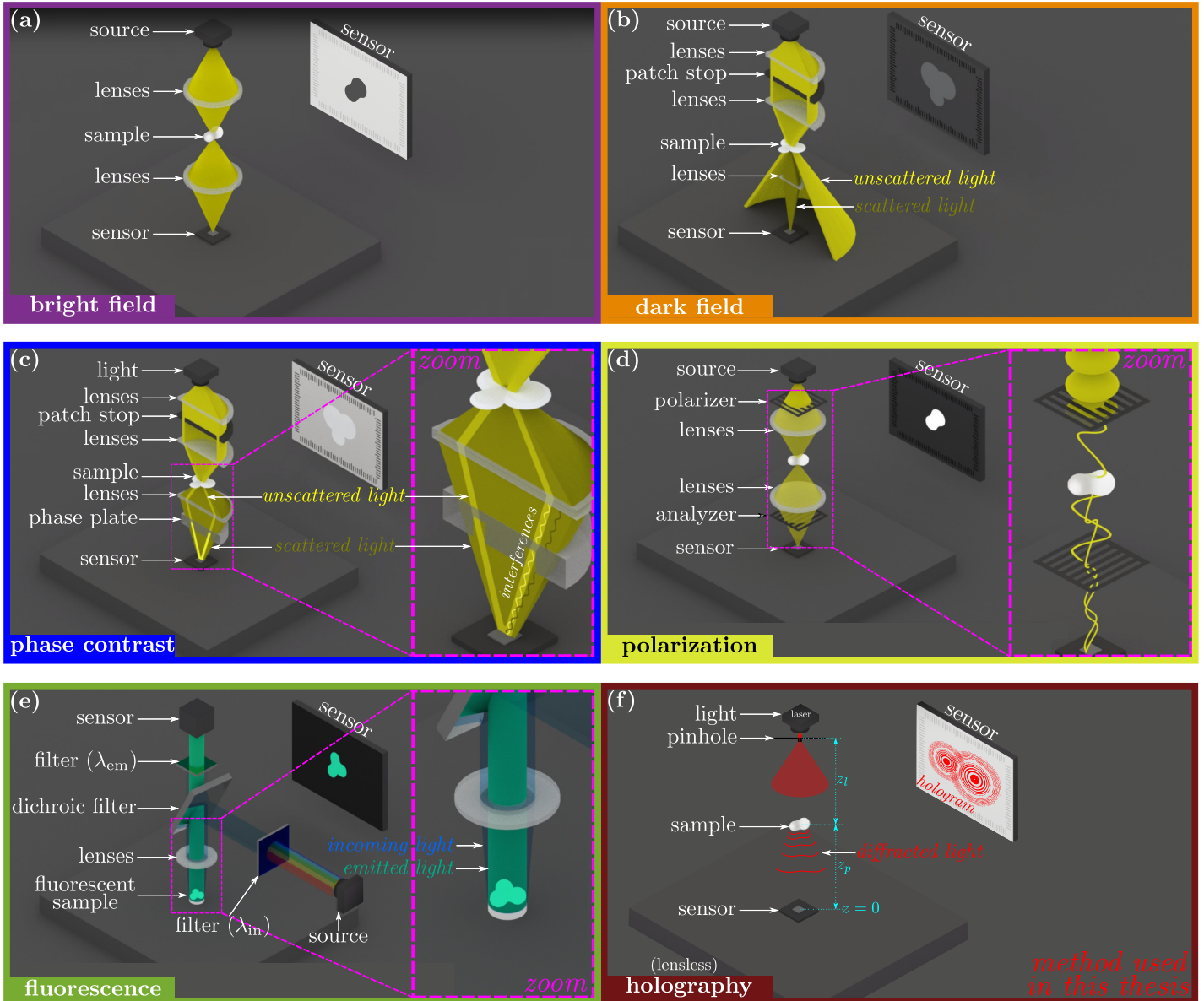


Figure 1.9 – Illustration of the principle of the main optical light microscopy techniques: (a) bright field; (b) dark field; (c) phase contrast; (d) polarization; (e) fluorescence; (f) (lensless) holography. (a)-(e) are adapted from animations supported by the French CNRS (last access: 2019-08-23).

### 1.3.1.2 Dark field

Dark field microscopy is an improvement over the bright field method. It consists of adding a phase ring, namely a *patch stop* following the same spirit than the Lyot stop used in coronagraphy (see Section 1.2.2.2.2), between the light source and the samples to deviate the part of the incoming light that is directly transmitted in bright field microscopy, see Figure 1.9(b). In other words, the unscattered beam is discarded and does not take part in the final image. The resulting image takes the form of bright shapes (corresponding to the light passing through the samples) on a *dark background field* (since directly transmitted light is reduced).

Observations conducted with dark field microscopy benefit from a significantly better contrast than bright field at the cost of more powerful illumination. Besides, transparent or translucent parts of the objects of interest can be visible without staining, allowing the direct study of biological materials. However, this technique does not improve the resolution of bright field microscopy.

### 1.3.1.3 Phase contrast

With phase contrast, a ring-shaped light beam is created by a patch stop, like in dark field microscopy. The light then passes inside optical elements to focus on the samples. Part of the incoming light is scattered by the samples while the majority of the light is transmitted. Phase contrast mainly differs from the dark field microscopy by the addition of a phase plate between the samples and the sensor, see Figure 1.9(c). The scattered light crosses a thicker part of the phase plate than the unscattered background light, thus shifting its phase compared to the directly transmitted light. Due to this phase shift, the two beams (of different amplitudes) interfere constructively and create a brightness change, namely a *phase contrast* on the sensor. This method was invented by F. Zernike for which he was awarded by the Physics Nobel Prize in 1953.

Phase contrast microscopy offers significantly better contrast than dark field microscopy, so that the internal structures of living cells can be studied without staining. However, the resolution remains limited.

### 1.3.1.4 Polarization

Polarization microscopy is based on a similar setup than bright field microscopy. Two additional polarizers are placed respectively between the source and the sample as well as between the sample and the sensor. The first polarizer selects a *polarization*, i.e. a particular orientation among all orientations of the incoming wavefront. This polarized light is then focused on the sample by optical elements. The light scattered by the sample encounters the second polarizer, namely the analyzer, having an orthogonal polarization orientation compared to the first one (i.e., no light passes through the analyzer in the absence of samples). Only scattered light whose polarization has been modified by the samples passes through the analyzer and participates to the image formation on the sensor, see Figure 1.9(d).

Since the recorded intensity depends on the sample orientation, polarization microscopy can be used to derive morphology information (e.g., thickness) about unstained specimens with an improved resolution compared to bright field microscopy. However,

this technique can only be used with birefringent samples, i.e. samples for which the direction of the light inside the samples (directly related to the refractive index) depends on the polarization of the incoming light.

### 1.3.1.5 Fluorescence

Fluorescence microscopy is one of the gold-standard methods for the observation, detection, and characterization of microscopic biological samples. It is based on the recording of *fluorescent* light emitted by the samples of interest. Fluorescence is a physical property of some molecules (so-called fluorophores) capable of emitting light at a specific wavelength  $\lambda_{em}$  when they are excited by an incident light at a different wavelength  $\lambda_{in}$ . This fluorescence can be a natural property of the samples, but the natural presence of fluorophores is generally rare. Thus, fluorescence should be enforced by complex biochemical processes; typically by fixation of fluorescent antibodies on targeted proteins of the samples. Another solution is to induce the fluorescence of a specific part of the (biological) samples by genetic manipulation. The basic fluorescent microscopy setup consists of illuminating the sample by a monochromatic light at  $\lambda_{em}$  (wavelength selection performed with an input filter), and recording the emitted light induced by the fluorescence of the fluorophores, see Figure 1.9(e). A set of optical elements (chromatic output filter and dichroic filter) is used to discard the reflected and directly transmitted beam from the light path before the sensor. In practice, the samples are generally marked with different fluorophores, each one targeting specific components of the samples and reacting/emitting at specific wavelengths. The input/output filters are selected in accordance with the considered fluorophores. By multiplying the recording at different wavelengths (by changing the input/output filters), it is possible to produce, after image concatenation, (false) colored images in which each color signs the presence of a specific type of components inside the samples.

Fluorescence microscopy offers good contrast and one of the best resolution (typically  $\leq 1 \mu\text{m}$ ) achievable with optical lighting microscopy techniques. It is particularly used in biology since it is adapted to the observation and detection of targets at different scales; from multi-cells arrangements to single components of a single cell. The main drawback of this technique is related to the toxicity due to both the biochemical marking and the emitted fluorescence light (generally in the ultraviolet) that degrades the functions of living cells. Thus, they are studied on typically short periods of times, making difficult the observations of their growth or evolution, for example in an incubator.

Several adaptations of this general principle have been considered to handle some of these drawbacks:

- Confocal microscopy consists of adding two pinholes, respectively located after the light and before the sensor (in the focal plane). The first pinhole focuses the light beam on a small sub-part of the samples while the second pinhole selects only the light coming from the imaged sub-part of the samples. The entire 3-D samples are scanned by shifting either the samples or the optical/lighting parts of the setup. After numerical processing, a fluorescence map of the whole samples is obtained. The contrast is generally further improved with this technique since

each sub-part of the samples benefits from the entire lightening power. However, for the same reason, the photo-toxicity increases, also.

- With light-sheet microscopy, the point-by-point scanning is replaced by a line-by-line scanning, perpendicularly to the direction of observation. This modification reduced the photo-damage compared to confocal microscopy, while the contrast and resolution remain almost unchanged.

### 1.3.2 In-line holographic microscopy as a method of choice

A common point of the light microscopy techniques presented in Section 1.3.1 is the recording of in-focus images of the samples to be observed, detected and characterized. The focusing is reached by the use of multiple optical elements such as lenses, as depicted by Figure 1.9(a)-(e). Holographic microscopy differs significantly by recording out of focus images containing information about the phase of the objects, which are not directly interpretable. The detection and characterization of the objects are possible only after a processing step. In this section, we describe the holographic microscopy principle, paying particular attention to its specificities in terms of instrumentation, related challenges, and data analysis.

#### 1.3.2.1 General principle and characteristics

In-line holographic microscopy consists of recording out of focus images of the samples illuminated by a (quasi) coherent and plane<sup>12</sup> wave which is diffracted by the samples, see Figure 1.9(f). The diffracted wave can be seen as the sum of all the spherical waves emitted by all the sub-parts of the samples, with a complex-valued amplitude depending on the local transmission of the samples and the complex-valued amplitude of the incident wave, as classically described by the Huygens-Fresnel principle (Goodman, 2005). After free-space propagation over the distance  $z_p$ , the diffraction pattern produced by the samples is recorded: the *hologram*, see Figure 1.9(f).

This method was invented by D. Gabor (Gabor, 1948) for which he was awarded the Physics Nobel Prize in 1971, 23 years after its initial statement. It can be noted that in 1948, the coherence of available light sources was extremely limited so that holography remained only a theoretical concept. Besides, the holograms were “recorded” or taken on photographic plates. With the development of the laser sources in the 60-70s, the first applications of holography became possible, in particular for velocimetry studies of small droplets spread in a volume (Goodman and Lawrence, 1967; Royer, 1974). In the following, we discuss only methods based on the analysis of *digital holograms*, i.e. holograms recorded by a digital camera.

This so-called *in-line* holographic configuration presents several advantages compared to the other microscopy modalities presented in Section 1.3:

- From a technical point of view, the main advantages are probably the simplicity, compactness, and robustness of the setup. Indeed, no mechanical part (such as accurate microscope stage numerically commanded to focus the image), or

---

12. In practice, the incident wave is not strictly planar but slightly divergent, thus magnifying the samples.

optical part (such as lenses magnifying the samples) are required. The cost-effectiveness of the setup can be further improved by using (quasi)-coherent laser diodes instead of conventional lasers as well as classical complementary metal oxide semi-conductor (CMOS) based sensors widespread in common multimedia devices instead of finer calibrated cameras (Garcia-Sucerquia, 2016; Rawat et al., 2017). Such a design leads to a very affordable and versatile setup, capable of imaging a large variety of samples in different experimental conditions. For example, it proves to be well suited to follow the growth and evolution of unstained cells in an incubator (Dolega et al., 2013; Kesavan et al., 2014), a very tricky task with other microscopy modalities.

- From a signal processing point of view, a single 2-D hologram gives access to information about the whole imaged volume. The 3-D location and the physical properties of the samples of interest are encoded in a modulated signal (i.e., the interferences fringes) spread over the whole field of view. The spatial spread of the information confers intrinsic robustness to this method, e.g. against aberrant local data.

Based on the general holographic principle, several setup configurations have been proposed (Rastogi and Sharma, 2003; Kreis, 2006). They mainly differ in the course of the object and reference waves as well as in the angle between the two incident waves on the sensor. For example, in the so-called *off-axis* configuration (Leith and Upatnieks, 1962), a reference beam and an object beam follow different paths and are recombined before the sensor, like in a Mach-Zehnder type interferometer. The interferences between the reference wave and the wave diffracted by the samples are recorded on the sensor.

This configuration is of particular interest since it gives access, after demodulation of the interferences, to the complex-valued amplitude (i.e., amplitude and phase) of the diffracted wave. This information is of primary interest for two reasons: (i) the interpretation of the recorded hologram is easier (see Section 1.3.2.2.1), (ii) it gives access to the optical thickness of the samples. However, this setup requires careful calibrations of the length of the light paths and is quite sensitive to micro-vibrations that cause large fluctuations of the intensity of the holograms. Also, it is less compact and cost-effective than the in-line setup due to the optical components (e.g., beam splitters and mirrors) that compose it.

In this thesis, we focus on the detection and characterization of small objects for optical metrology applications with cost-effective and robust methods. For these reasons, in the following, we use the in-line holographic configuration exclusively.

### 1.3.2.2 Challenges of holographic microscopy

As discussed in the previous section, the recorded holograms are not directly interpretable images of the samples since they are out-of-focus. The challenge of holographic microscopy lies in the processing, namely the *reconstruction* of the holograms, i.e. the inference of physical properties about the objects from the holograms. In the following, we illustrate from an application point of view the main methodological points that are used in the following of the manuscript. More technical details are given when needed throughout the manuscript.



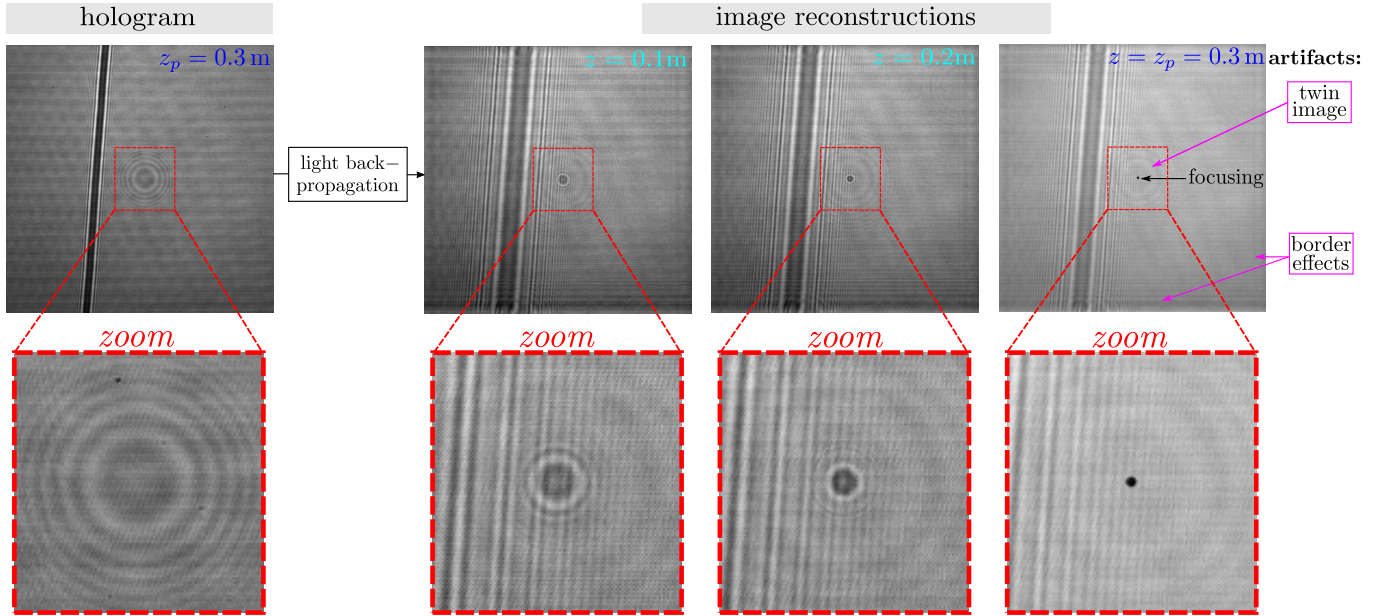


Figure 1.10 – Hologram reconstructions based on light back-propagation. The left-most part is a hologram of a circular deposit of chromium located at  $z_p \simeq 0.3$  m from the sensor plane. The rightmost part gives reconstructions at distances  $z \in \{0.1 \text{ m}, 0.2 \text{ m}, 0.3 \text{ m}\}$  from the sensor. The red frames are zooms around the object of interest.

### 1.3.2.2.1 Extracting relevant information by numerical reconstruction

The conventional approach to reconstruct a hologram is based on simulations of the reverse propagation (so-called *back-propagation*) of the light, starting from the hologram recorded on the sensor plane towards the object plane located at a distance  $z_p$  from the sensor plane (Schnars and Jüptner, 2002; Goodman, 2005). Figure 1.10 gives an example of hologram reconstructions based on the light back-propagation method. It shows that the circular object of interest is progressively focusing when the distance  $z$  in the light back-propagation approaches the distance  $z_p$  of the object plane. Hologram back-propagation is a “numerical focusing” method. It can be used to reconstruct plane by plane the imaged 3-D volume. Then, the 3-D volume can be characterized, i.e. the objects of interest are segmented, located, and sized with conventional image processing methods, like segmentation techniques (Kreis, 2006). While being simple, the accuracy of such an approach is generally limited due to artifacts like spatial distortions close to the image borders and spurious diffraction patterns known as *twin images* impacting the reconstructed holograms (Kreis, 2006), see Figure 1.10. These artifacts are caused by the loss of the phase information during the acquisition<sup>13</sup>. More elaborated processing methods should be used to infer accurate detection and characterization of the imaged objects, in particular for the

13. Digital sensors record only intensity information, not the complex-valued amplitude of the wavefront. Besides, with an in-line configuration, the absence of a reference arm (like the one in an off-axis configuration) prevents the recovery of the complex-valued amplitude by interferences demodulation.

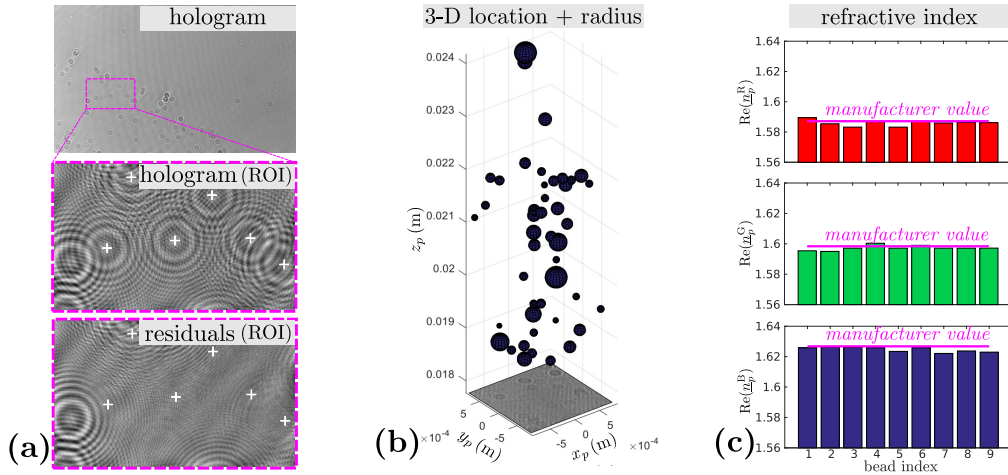


Figure 1.11 – Parameter-based hologram reconstructions of spherical beads. (a) A hologram of calibrated polystyrene beads (THERMO FISHER SCIENTIFIC™,  $5.0 \pm 0.2 \mu\text{m}$  radius) in immersion in oil (CARGILE™, A) between a microscope slide and cover-slip at approximately  $z_p = 0.02 \text{ m}$  from the sensor. The magenta frames are zooms around a selected region of interest (ROI) of the hologram and the residual hologram after subtraction of the fitted image model (only the six beads of maximal intensity in the ROI are modeled here). The white crosses represent the estimated center of the detected beads. (b) View of the reconstructed 3-D volume;  $\{x_p, y_p, z_p\}$  stand for the 3-D coordinates, the size of the blue bubbles is proportional to the estimated radius  $r_p$  of the detected objects. (c) Real part of the estimated complex-valued refractive index of 9 polystyrene beads segmented from oil and/or air bubbles based on the estimated radius. The three graphs correspond to different illuminations, respectively red (THORLABS™, CPS635R,  $\lambda_R^{\text{nom}} = 635 \text{ nm}$ ), green (THORLABS™, CPS532,  $\lambda_G^{\text{nom}} = 532 \text{ nm}$ ), and blue (THORLABS™, CPS405,  $\lambda_B^{\text{nom}} = 405 \text{ nm}$ ). The horizontal magenta lines stand for the ground-truth refractive index values provided by the manufacturer.

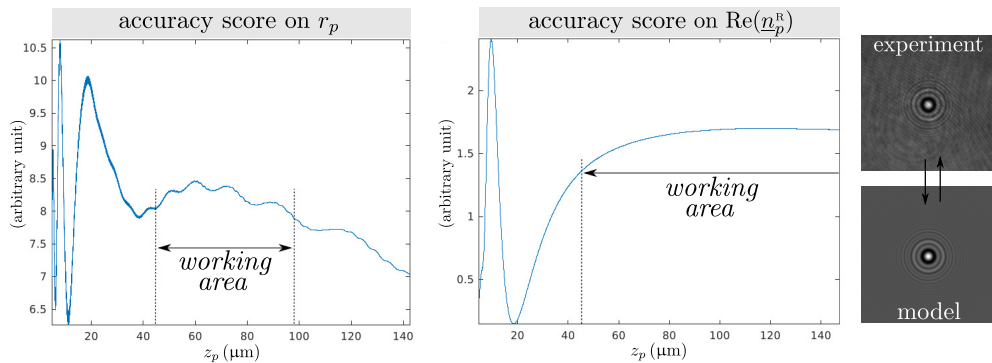


Figure 1.12 – Inferring estimation accuracy with the parameter-based method. Accuracy scores (inversely proportional to the CRLBs) as a function of the distance  $z_p$  between the object plane and the sensor for two parameters of interest of the Lorenz-Mie model: the radius  $r_p$  of the beads and the real part  $\text{Re}(n_p^R)$  of their complex-valued refractive index  $n_p^R$ . Here, the polystyrene beads (THERMO FISHER SCIENTIFIC™) are calibrated at  $4.20 \pm 0.21 \mu\text{m}$  of radius illuminated by a red laser diode (COHERENT™, OBIS 660LX/FP,  $\lambda_R^{\text{nom}} = 661 \text{ nm}$ ). Adapted from Olivier et al. (2018).

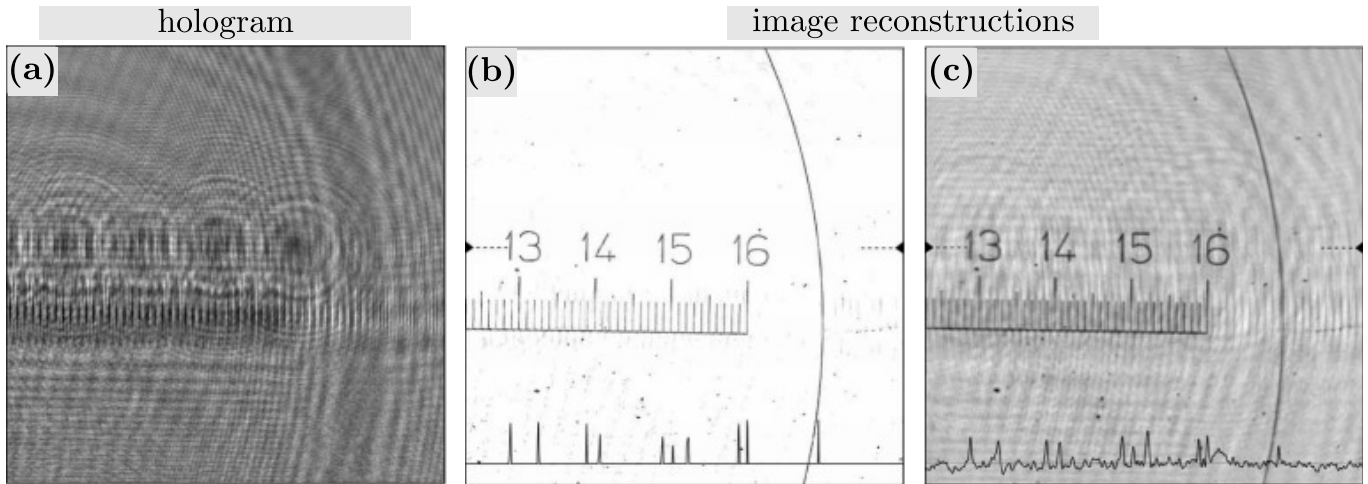


Figure 1.13 – Image-based hologram reconstructions. (a) hologram of a planar target; (b) reconstruction based on inverse-problem; (c) reconstruction based on light back-propagation. Adapted from Denis et al. (2009).

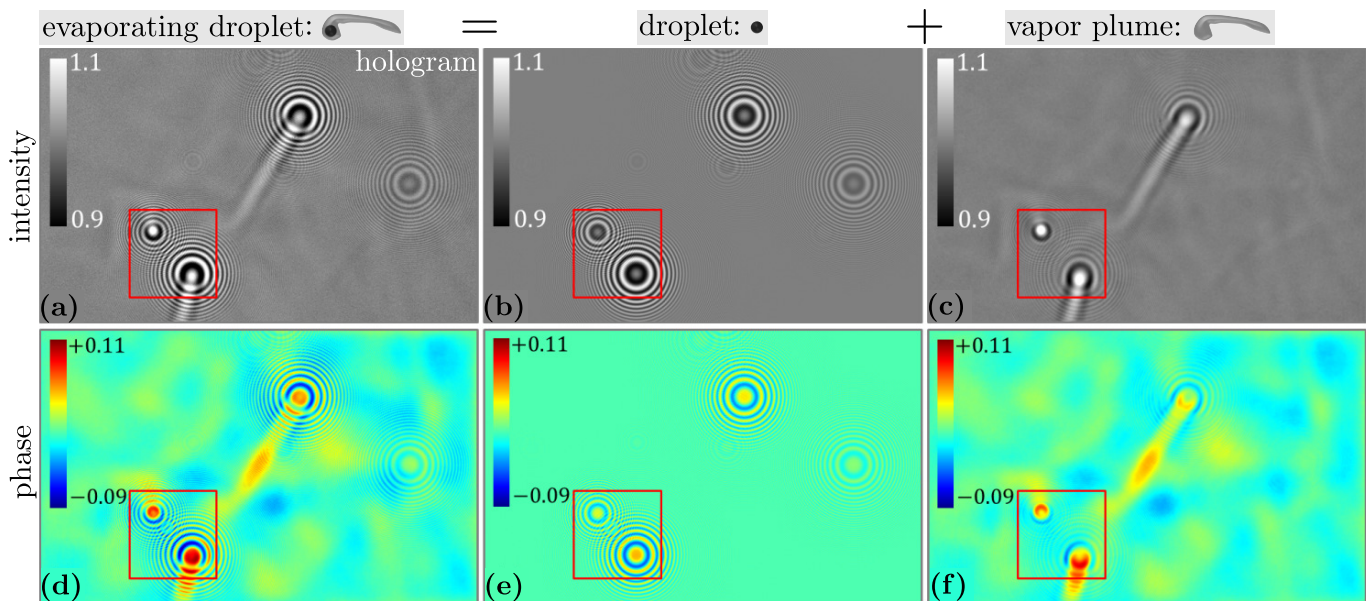


Figure 1.14 – Hybrid parameter-based and image-based reconstructions of evaporating diethyl ether droplets. The intensity on the sensor plane given in (a) is the combination of the contribution of the spherical core of the droplets given in (b) and the contribution of the vapor plumes given in (c). Same decomposition for the phase on the sensor plane in panels (d) to (f). Adapted from Berdeu et al. (2019).



targeted optical metrology applications.

Maximum likelihood methods are very powerful to derive accurate reconstructions of the holograms. They consist of maximizing, with an inverse problem approach, the likelihood of the recorded data (i.e., the hologram) with respect to an image formation model<sup>14</sup>. This general method can be used with different reconstruction frameworks, depending on the nature of the objects and the targeted applications:

- In a *parameter-based* framework, the model is a physics-based model of the diffraction pattern produced by an object of a given shape. In this case, the model depends only on a few *parameters* to be estimated. In particular, models describing the intensity and/or the complex-valued amplitude of a wavefront diffracted by spherical objects are of primary interest since they correspond to a large variety of studied samples like beads and bubbles in fluid flow mechanics or cocci-type cells in biomedical imaging. Among these, we can cite the Thompson model (Tyler and Thompson, 1976) adapted to model the diffraction patterns of opaque<sup>15</sup> spherical objects, or the more general Lorenz-Mie model (Gouesbet and Gréhan, 2011) adapted to opaque, transparent, and absorbent/phase spherical objects. This methodological framework firstly introduced in the holographic community by Soulez et al. (2007a,b) is very accurate to characterize the size and the 3-D locations of beads for fluid-flow applications. The implementation is based on two steps: first, the objects are detected with a discrete *matching-pursuit* procedure; secondly, the parameters characterizing the detected objects are refined in a continuous *local optimization* procedure. Since then, several adaptations and improvements have been considered, such as the optimal processing of multiple detections (Gire, 2009) or acceleration based on a multi-resolution decomposition (Seifi et al., 2012). Such approaches are already used in several fields (see Mudanyali et al. (2010); Greenbaum et al. (2012) for some trends) where the accurate estimation of 3-D location and size over time is crucial, such as in the study of fluid flows (Sentis et al., 2018; Middleton et al., 2019; Go et al., 2019) or biomedical imaging (Rostykus et al., 2018; Allier et al., 2019; Kemper et al., 2019).

Figure 1.11 gives an example of hologram reconstructions<sup>16</sup> following this parameter-based approach. Calibrated polystyrene beads are imaged, detected, and characterized in terms of 3-D location, size, and complex-valued refractive index<sup>17</sup>. In particular, we observe that the estimations of the refractive index of the beads are in good match with the calibrated values delivered by the manufacturer. After subtraction to the hologram of the fitted model, the hologram is

---

14. The optical model can depend on a few parameters (like in an *estimation* framework) or on millions of parameters (like in a *reconstruction* framework).

15. In practice, the Thompson model can also be used to describe diffraction patterns of transparent or absorbent spheres behaving as opaque when sufficiently far from the sensor plane.

16. I realized the experiments and processing of case study examples depicted in Figure 1.11. I took part in the data processing of the experiments shown in Figure 1.12, see Olivier et al. (2018).

17. The optical refractive properties of a medium can be defined by its complex-valued refractive index  $\underline{n}_p$ , where the real part is related to its refractive property, and the imaginary part is related to its absorbance. For dispersive medium (e.g., polystyrene), the index  $\underline{n}_p$  depends on the wavelength of the incident light.

dominated by the residual background structures, which is a qualitative sign of the good match between the estimated model and the data.

Parameter-based methods can also be used to derive the minimal theoretical variance of the estimators of each parameter via the Cramér-Rao lower bounds (CRLBs, Kendall et al. (1948)). For holographic microscopy applications too, the CRLBs are efficient tools to derive lower-bounds of the achievable accuracy (Fournier et al., 2010). Conversely, CLRBS can predict, in a theoretical study preceding the experimentation, the estimation accuracy resulting from a particular configuration of the setup (e.g., distance  $z_p$  of the samples to the camera, choice of the sources). The configuration minimizing the CRLBs is generally chosen. Figure 1.12 gives a case study example consisting of determining, before experimentation, the best axial distance  $z_p$  of the object plane to maximize the accuracy on the estimated radius and refractive index of polystyrene calibrated beads of known size. This study shows that the accuracy on these two parameters is simultaneously maximized when the samples are placed in the range  $[45 \mu\text{m}; 100 \mu\text{m}]$  from the sensor plane, a non-intuitively result.

When the imaged objects are of more complex shape, the recorded interference patterns cannot be easily described by a parameterized model and alternative reconstruction frameworks should be considered.

- In an *image-based* framework, a whole image of the object is reconstructed at a chosen plane by numerical inversion of the hologram formation model in a Bayesian framework (Denis et al., 2009; Brady et al., 2009; Marim et al., 2010). The resulting minimization problem is generally ill-posed and ill-conditioned. Physical priors (e.g., object sparsity, object sharpness, non-emitting object, smooth background) can be added in the form of regularization terms or bound constraints to promote a better solution. Figure 1.13(a) gives an illustration of the reconstructed opacity distribution in the object plane with this type of approach compared to a classical reconstruction based on light back-propagation. The inverse-problem-based reconstruction is of significantly better quality than the reconstruction based on light back-propagation. Methods based on this framework are now intensively used in holographic microscopy, in particular to reconstruct transmittance, and/or phase plane(s) of microscopic biological samples (Hervé et al., 2018; Jolivet et al., 2018; Allier et al., 2019).
- A recent work done at the Hubert Curien Laboratory<sup>18</sup> shows that both the parameter-based and the image-based frameworks can be combined to reconstruct the phase of hybrid-shaped objects such as evaporating diethyl ether droplets. The contribution of the spherical core of the droplets is reconstructed with a parameter-based framework based on the Lorenz-Mie model, while the contribution of the surrounding vapor plumes is reconstructed with a regularized image-based framework, see Figure 1.14.

Finally, new methods based on machine-learning (Bishop, 2006) or deep-learning (LeCun et al., 2015) techniques are regularly emerging to detect and classify micro-

---

<sup>18</sup>. I took part on the acceleration of the parameter-based part of the reconstruction method, see Berdeu et al. (2019).

scopic samples, in particular, cells according to their type or healthy state for new ways of diagnosis (Chen et al., 2016; Hejna et al., 2017; Kim et al., 2018; Liu et al., 2019), or colloidal particles according to their refractive index and/or size for fluid flow study (Grier et al., 2017; Hannel et al., 2018). They are applied to reconstructions of holograms previously obtained, for example, from maximum likelihood methods, or directly to the recorded holograms. In both cases, the generation of the learning base generally requires complex experimentations to cover diverse setup configurations and samples specificities.

In this thesis, we focus on processing methods that improve the sensitivity and accuracy of parameter-based maximum likelihood approaches in the context of optical metrology. We also propose some calibration methods that can be used to improve the accuracy of image-based reconstructions.

#### 1.3.2.2.2 Experimental setups

In this thesis, we mainly consider datasets recorded with a *lensless* in-line holographic setup. This means that no optical devices (such as lenses) are inserted in the light path, as described in Section 1.3.2. Figure 1.15 gives an illustration of the experimental lensless setup built at the Hubert Curien Laboratory before my thesis started, and that we use to produce experimental datasets. It is composed of three laser diodes (red, green and blue) that can be switched on alternatively or simultaneously. When several laser diodes are used simultaneously, their intensities are measured with a portable spectrometer and adjusted before experimentation with density filters. The light produced by each source is combined in a common light path by means of beam splitters before entering a mono-mode light fiber illuminating the object of interest. After free-space propagation of the diffracted wave, the diffraction pattern produced by the object is recorded by a CMOS sensor. Two CMOS sensors (monochromatic and color) can be mounted on the setup so that both monochromatic and color holograms can be recorded with this setup. Besides, the distance between the object and the sensor can be (roughly) adjusted with a manual translation stage. The main advantages of this setup are related to its simplicity and cost-effectiveness: the laser sources are standard laser diodes (about 130€ per laser diode), and the sensor is a basic CMOS sensor (about 30€) not mounted in an optical box. The total cost of the setup, including the arms and supports, is about 800€<sup>19</sup>.

In specific parts of this thesis, we also consider datasets recorded with an in-line holographic setup equipped with a microscope objective. Including a microscope objective significantly improves the resolution and makes it possible to study micron-sized objects. We give more details about this configuration when needed throughout this thesis.

#### 1.3.2.3 Processing pipeline and related signal processing issues

---

19. For comparison, the cost of a commercial bright field numerical microscope equipped with an electronic stage control is generally higher than 10,000€ .

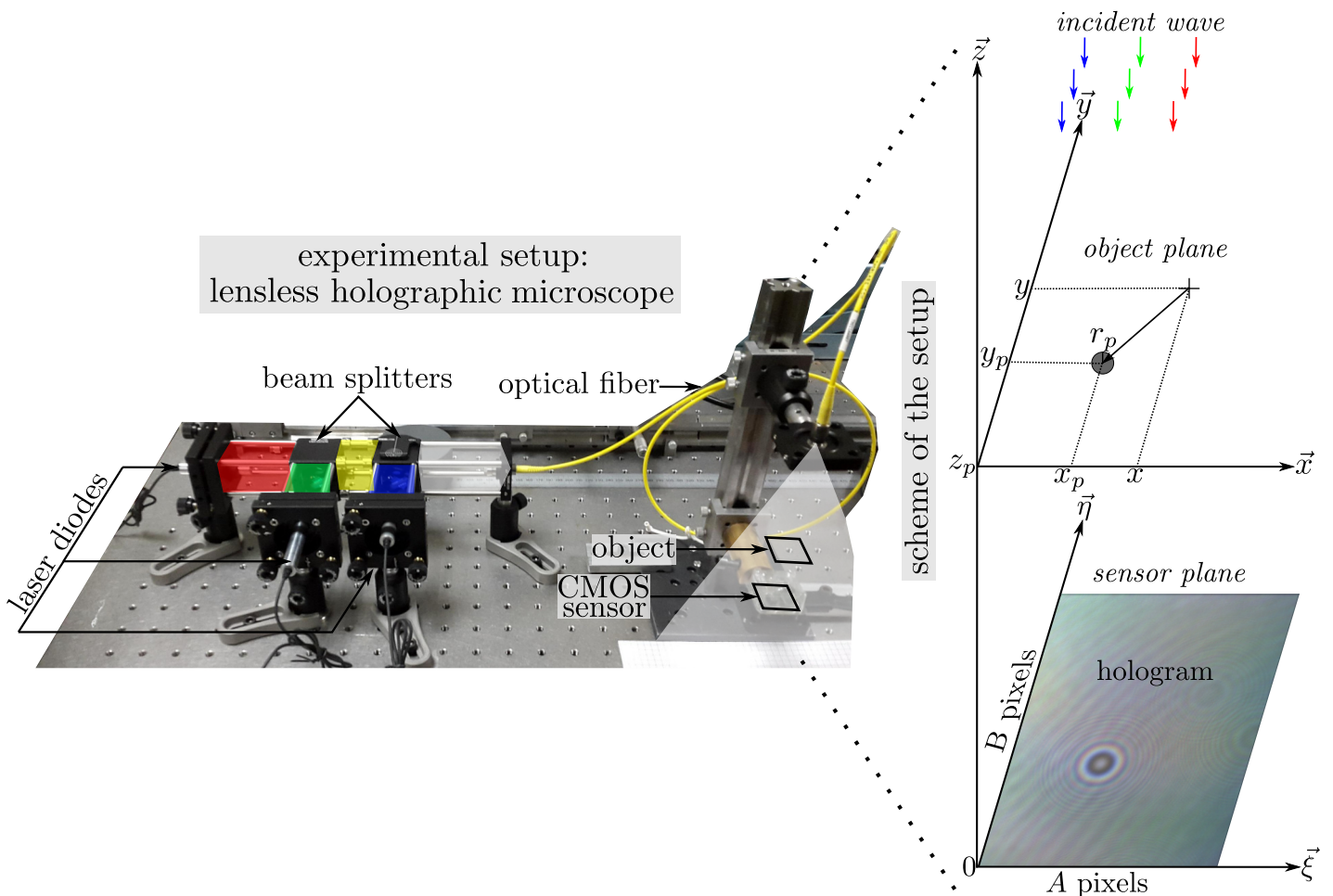


Figure 1.15 – Illustration of the lensless holographic setup used in this thesis. It is made of three laser diodes; one red (THORLABS™, CPS635R, 1.5 mW), one green (THORLABS™, CPS532, 4.5 mW) and one blue (THORLABS™, CPS405, 4.5 mW); and a 12-bit CMOS sensor (BASLER™, daA2500-14um monochromatic sensor, daA2500-14uc color sensor) with  $A \times B = 1944 \times 2592$  pixels with a  $2.2 \mu\text{m}$  pitch. The right part gives a schematic representation of the setup presented in the left part.

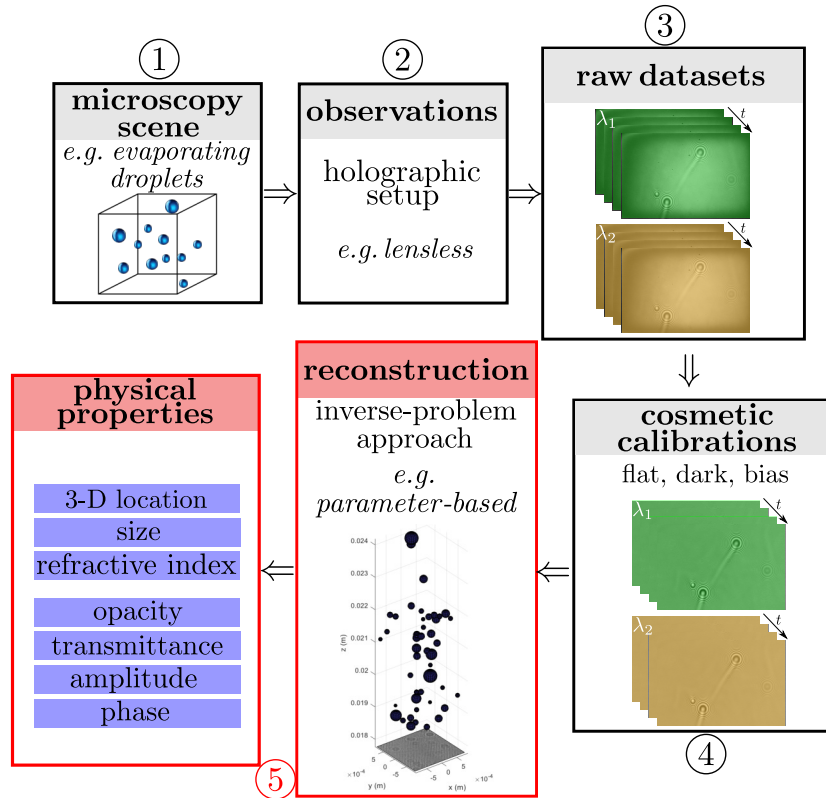


Figure 1.16 – Schematic representation of the typical holographic microscopy pipeline. The red frame emphasizes the part of the pipeline that is addressed by this thesis.

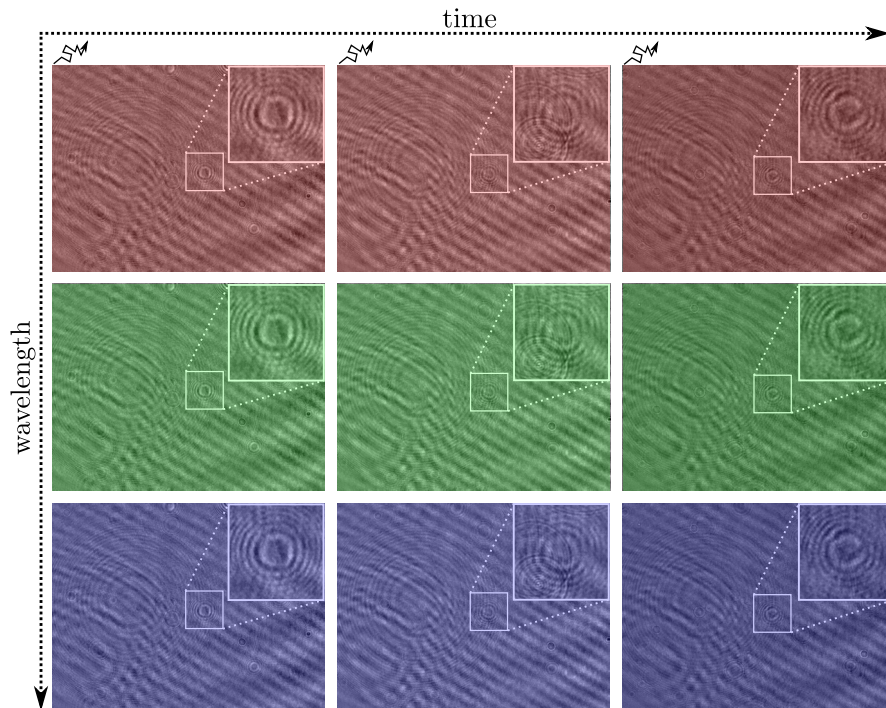



Figure 1.17 – Examples of holographic frames. The object of interest (see inset) is a polystyrene bead in suspension in water, following a Brownian motion over time. False colors (red, green, blue) emphasize that multi-spectral data can be eventually recorded.



In this section, we summarize with Figure 1.16 the typical holographic microscopy pipeline. It starts with the *observation* of a *microscopy scene* (box ①) with a holographic setup (box ②). The *raw datasets* (box ③) can be optionally *calibrated* (box ④) with dark, flat and bias corrections. At the end of this step, the datasets are formed by temporal (or temporo-spectral) sequences of holograms. The following step consists of the *reconstruction* step (red box ⑤), i.e. the processing of the holograms with dedicated algorithms aiming to detect and characterize the imaged samples. Contrary to the direct imaging pipeline presented in Figure 1.7, in holographic microscopy, the estimation of the physical properties of the samples is performed by the reconstruction step itself. In practice, additional information can be retrieved from the estimated quantities. For example, the velocity of beads in a fluid flow is deduced from their estimated 3-D locations over time, giving information about the physical properties of the fluid, like its viscosity. These subsequent interpretations are performed by experts and are out of the scope of this thesis.

Before closing this part, we want to emphasize the processing issues related to the detection and characterization of microscopic objects from holographic microscopy datasets. Figure 1.17 gives examples of holograms of one polystyrene bead (see inset) in suspension in water. It follows a Brownian motion over time in the presence of several unwanted water/air bubbles and dust moving over time. In spite of the care given in the conduction of the experiment, the data remain largely dominated by a strong and spatially correlated background due to laser instability, and by diffraction fringes due to the unwanted objects. Thus, the bead of interest is hardly discernible, and the characterization accuracy could be limited by the unfavorable contrast. Elaborate processing methods combining multi-temporal and/or multi-spectral data play a central role to derive accurate object characterization from holographic data. This thesis proposes detection and characterization methods for optimal processing of holographic data for optical metrology.



**Holographic microscopy issues**

- The detection and characterization of microscopic objects spread in a volume by holographic microscopy is based on the recording of holograms under a coherent illumination.
- The holograms take the form of diffraction patterns that are not directly interpretable but that can be described by an optical model.
- In spite of the care taken in the conduction of the experiments, the recorded datasets of microscopic objects are often dominated by a nonstationary and spatially correlated background.

⇒ The processing of the datasets by dedicated algorithms is mandatory. It can benefit from the temporo-spectral diversity of the data for an improved detection sensitivity and characterization accuracy of the samples.

## 1.4 Methodological angles and thesis organization

This section presents the main methodological angles followed during this thesis work, before diving into a more detailed description in Chapters 2 to 7. In addition to these common methodological guidelines, particular attention is paid to the setting of hyper-parameters throughout this thesis. Indeed, all the developed algorithms are totally unsupervised: weighting and/or regularization parameters are estimated in a data-driven fashion.

### 1.4.1 First angle: Background fluctuations modeling

As illustrated in Sections 1.2.2 and 1.3.2, the image series from the two considered application fields present a spatially textured background that strongly dominates the patterns to be detected.

The detection of a pattern in noisy images is one of the widely studied subjects of the signal processing literature (Kay, 1998a; Van Trees, 2004; Poor, 2013). A large variety of techniques is based on the use of linear or nonlinear correlation filters (Mahalanobis et al., 1987; Réfrégier, 1990; Turon et al., 1994). Among them, the *matched filter* is optimal for maximizing the S/N of detection in the presence of an additive, white, and Gaussian noise (Réfrégier and Goudail, 2013). However, this hypothesis is often a crude assumption to describe real images. More sophisticated image models should be considered. Among them, the SIR (Statistically Independent Regions) approach models the noise as a background component that does not overlap with the target pattern; each component behaving differently from a statistical point of view (Javidi and Wang, 1992; Goudail et al., 1995). Appropriate statistical descriptions of the nature of the background component can be additionally considered. Among the large variety of noise statistics, the exponential family is of particular interest since it covers different types of noise encountered in several image modalities. For example, it encompasses the Poisson statistics adapted to describe noise arising in the low photon regime from astronomical images (Ferguson, 1962), the Gamma distribution can be used to describe the intensity of the speckle field in SAR imaging (Dainty, 2013), and the Rayleigh statistics is adapted to describe the noise of sonar images (Bioucas-Dias and Leitao, 1996). As stated in Réfrégier and Goudail (2013), the challenge of image processors is to choose a noise model able to describe correctly and accurately the observed noise while staying simple enough to be computationally feasible.

In addition, the background and/or target component is not necessarily a white noise but rather a spatially correlated field. A common technique is to use a *whitening process* before applying classical detection methods. The clutter whitening can be performed via filtering in the Fourier's domain the whole image (under a stationarity hypothesis) or on sub-parts of the image (Réfrégier et al., 1999). The Markov fields are also intensively-used methods to model spatial correlations in images (Réfrégier et al., 1996). While they are very efficient in terms of parameter estimation, they infer texture characterizations at a relatively short spatial scale of only a few pixels. More recently, methods based on the analysis of images on small windows encompassing a few tens to a few hundreds of pixels (so-called *patches*<sup>20</sup>) shown to be very efficient

---

20. The patches can be extracted from the images following different strategies: sliding window,

tools for several applications, in particular in image denoising (Buades et al., 2005a,b; Zoran and Weiss, 2011; Lebrun et al., 2013). Since the image series in our two targeted applications present a background with spatial correlations over an area a few tens to a few hundreds of pixels and the correlation structure is nonstationary, we consider patch-based approaches to infer a model of the background structures. We will show that it leads to a good tradeoff between the number of estimated parameters and the range of the correlations that are captured.

In summary, we propose in this thesis to model locally the correlated and nonstationary background of the image series using patch-based approaches. The subsequent estimations of the background fluctuations are accounted for in a statistical detection framework. We describe in Part II two algorithms dedicated to detect the presence of a known pattern in the low S/N regime. The two proposed algorithms differ in the considered spatial extent of the patterns to be detected:

- Chapter 2 presents a totally unsupervised algorithm (PACO) dedicated to the detection and characterization of point sources like exoplanets from ADI series. The underlying statistical model of the background fluctuations, although approximative, achieves a good compromise between the computational burden and the fidelity to the data, leading to an efficient algorithm that demonstrates better detection performance than state-of-the-art exoplanet hunter methods.
- Chapter 3 presents an extension (EXPACO) of the previous algorithm. EXPACO is dedicated to the detection of spatially extended patterns such as the ones encountered in holographic microscopy. Chapter 3 focuses on the necessary adaptation of the PACO algorithm from a methodological point of view. The evaluation of the performance of this approach on image series obtained with a holographic microscope shows an interesting detection capability.

### 1.4.2 Second angle: Robustness to outliers

The image series from the two targeted applications present several aberrant data (so-called *outliers* by opposition of the data of interest called *inliers*) in spite of the care taken during the image acquisition process. These outliers have different natures and causes. In direct imaging, they take mainly the form of large fluctuations due to sudden alteration of the quality of the adaptive optics correction. Moreover, many defective pixels<sup>21</sup> are present in the data due to the high sensitivity of the cooled infrared sensors used. These defective pixels lead to artifacts on a wider scale than one pixel in the science images due to the conventional pre-processing steps, see Section 1.2.2. In holographic microscopy, unwanted objects such as dust or other objects than the object(s) of interest imaged in the field of view produce diffraction fringes acting as outliers since they mix with the diffraction patterns of the objects of interest. This results in a decrease in the accuracy of the characterization of the microscopic objects.

---

similarities between patches, and so on.

21. These defective pixels are cold pixels that remain at low values, hot pixels that are stuck to large values, or aberrant pixels with seemingly random values unrelated to the actual image intensity at that pixel.



In the signal processing literature, several methods deal with the presence of outliers encountered in real-world data.

A first category of approaches is based on a non-Gaussian model of the (large) fluctuations of the clutter. The number of reported works related to this technique is considerable since the chosen statistical model is directly dependent on the considered application. Among these, we can cite the Spherically Invariant Random Vector model (SIRV, [Bausson et al. \(2007\)](#); [Vasile et al. \(2009\)](#)) commonly used in Synthetic Aperture Radar (SAR, [Yamaguchi et al. \(2005\)](#)) imaging. Within this framework, the scattering vector is modeled as the product of a positive random variable accounting for the randomness of the clutter induced by variations in the backscattering power, and of an independent and zero-mean complex Gaussian vector (see [Section 4.2.1](#) for more details). The large fluctuations of the clutter are thus intrinsically captured by the random variable.

A second category of approaches is based on the use of robust estimators (see [Zoubir et al. \(2018\)](#) for a detailed overview) limiting the penalization of large deviations between the data and the image formation model (these large deviations generally correspond to the outliers). Among these methods, M-estimators and other variants ([Yohai, 1987](#); [Hubert et al., 2008](#); [Huber, 2011](#)) consist of replacing the conventional least squares with an objective function that increases more slowly in order to reduce the impact of large deviations. Robust estimators are used in diverse application fields such as array processing in the presence of brief sensor failures ([Muma et al., 2012](#)), fast varying frequency estimation ([Sharif et al., 2013](#)), electrocardiographic monitoring ([Muma and Zoubir, 2016](#)), multi-speaker voice activity detection ([Hamaidi et al., 2017](#)), and others.

Some works combine both an adequate statistical model of the clutter with a robust estimation procedure. For example, this is the case for the detection of anomalies from hyper-spectral data ([Frontera-Pons et al., 2014, 2015](#)). Anomalies ([Chang and Chiang, 2002](#)) are events that differ from the general behavior of the clutter (e.g., a sick tree in a forest) that should be detected without any prior information (e.g., template spectra of sick trees). The elliptical family of distributions is considered to model the impulsive background ([Matteoli et al., 2014](#)) and M-estimators are used to estimate robustly the statistical properties (e.g., mean and covariance) of the non-Gaussian clutter in the presence of strong scatters.

In a nutshell, we propose in this thesis to account for the aberrant data arising in the image series from our two targeted applications. We thus describe in [Part III](#) two robust algorithms dedicated to the detection and characterization of model patterns, in the presence of outliers:

- [Chapter 4](#) presents the **robust PACO** algorithm, which is an extension of the PACO method described in [Chapter 2](#). To improve the robustness of PACO, we modify the statistical model of the background fluctuations by spatially weighting each frame in a data-driven fashion, based on its relative degree of fluctuations. We show that the achievable contrast and the detection performance are particularly improved at small separations, where the stellar residuals dominate.
- [Chapter 5](#) presents an algorithm dedicated to the detection and characterization of microscopic objects in the presence of numerous outliers. It is based on M-

estimators, iterative residuals weighting, and on a new method to set the level automatically to distinguish outliers from inliers. We show on holographic microscopy series that this approach achieves a bias/variance tradeoff improving the overall performance of the conventional least squares method.

### 1.4.3 Third angle: Spectral diversity exploitation

For the two targeted applications, it is possible to record multi-spectral data in addition to the natural time extent of the image series. In direct imaging, 4-D datasets (spatial + time + spectral) are captured by IFS instruments, after a mapping step of the raw observations of the IFS cameras into multi-spectral cubes (Pavlov et al., 2008). As discussed in Section 1.2.2, the spectral diversity is of particular interest both to push back the detection limits, and to characterize the detected point-sources via the analysis of their estimated SEDs (Vigan et al., 2010). In holographic microscopy, two approaches allow recording multi-spectral data: (i) multiple recordings of monochromatic holograms produced sequentially with different coherent light sources, (ii) the joint illumination of the objects of interest with multiple coherent light sources and the recording of a single one hologram with a color camera. While the first approach captures richer information, it requires that the objects of interest remain (quasi) static during the acquisition of the hologram series. For this reason, the second approach is generally preferred. Whatever the chosen approach, the spectral diversity brought by this type of configuration is of primary interest to derive an accurate characterization of the microscopic objects.

Taking advantage of multi-spectral (not contiguous wavelengths) and/or hyper-spectral (contiguous wavelengths) imaging through dedicated processing methods is also a standard strategy encountered in several and diverse application fields. In astronomy, the panoramic integral field spectrograph MUSE (Multi Unit Spectroscopic Explorer) operating at the VLT produces 3-D (spatial + 3600 spectral channels) datasets for spectroscopic investigation of the deep sky (Bacon et al., 2010). Methods based on a Bayesian framework shown to be very efficient to detect the spectral signature of faint galaxies from large volumes of data (Chatelain et al., 2011; Meillier et al., 2015, 2016). Complementary detection methods based on sparse representations can be used to account for the possible hyper-spectral variability of the targets (Bacher et al., 2017). In remote sensing, hyper-spectral imaging is a widely-studied modality (Keshava and Mustard, 2002). It enables material identification and quantification via spectroscopic analysis on a hundred to a thousand spectral channels, possibly covering the visible, near-infrared, and shortwave infrared spectral bands (Bioucas-Dias et al., 2012). The spectral unmixing of the signatures of the various materials within the spatial extent of the field of view is performed by dedicated processing algorithms mainly based on statistical and sparse regression methods (Plaza et al., 2009; Bioucas-Dias et al., 2012). The application fields addressed by this technique are vast, including environment (Adams et al., 1986) or Earth monitoring (Goetz, 2009), military surveillance (Xu and Wang, 2007), but also food (Kim et al., 2001) or drug quality checking (Rodionova et al., 2005), face recognition (Di et al., 2010), and others. In particular, microscopy techniques also benefit from the advantages of hyper-spectral imaging for anatomy, physiology, biochemistry, and pathology analysis of biomedical samples (Schultz et al., 2001; Li et al.,

2013). Closer from our targeted applications, lensless tomography combined with multi-spectral imaging proved to be a successful technique to study the growth of biological materials over time (Berdeu et al. (2018b), see Section 7.1 for further details).

In short, we propose in this thesis to account for the specificities of the multi-spectral data in our two targeted applications. We thus describe in Part IV two algorithms dealing with the spectral diversity of the acquired datasets:

- Chapter 6 presents the PACO-ASDI algorithm dedicated to the detection and characterization (SED estimation) of point-sources (like exoplanets) from ASDI series. Based on the PACO algorithm, PACO-ASDI also presents several methodological adaptations to deal with the specificities of ASDI observations such as the strong spectral correlations of the data. The underlying statistical model of the background fluctuations achieves a good compromise between the model complexity, the difficulty to estimate model parameters, and the relevance of the statistical model with respect to the data. It leads to an efficient algorithm that demonstrates better detection and characterization performance than state-of-the-art exoplanet hunter methods.
- Chapter 7 shows that an inaccurate knowledge of the parameters related to the sources and sensor in color holographic setups leads to an inaccurate characterization of the imaged microscopic objects. This issue is critical since the induced errors can outweigh the theoretical gain of a joint multi-spectral processing. We describe a new method based on an inverse problem approach to perform the self-calibration of the setup, i.e., to estimate automatically the parameters related to the sources and sensor of color holographic microscopes. We show on real holograms that the accuracy of the reconstructions is improved by the proposed approach.

### Methodological angles

In this thesis work, the developed algorithms are based on three methodological angles addressing common issues in the two targeted application fields:

- The background of the images is nonstationary, spatially correlated, and much stronger than the objects of interest.

⇒ The proposed algorithms will model the spatial fluctuations of the background through patch-based approaches.

- The images are impacted by outliers taking the form of unwanted aberrant data and/or large fluctuations.

⇒ The robustness of the proposed algorithms will be improved by weighting-based strategies, decreasing the influence of the outliers.

- It is possible to record multi-spectral data in addition to the natural time extent of the image series.

⇒ The proposed algorithms will be adapted to benefit from the spectral diversity and improve the detection sensitivity and the characterization accuracy.

Besides, all the developed algorithms are totally unsupervised: weighting and/or regularization parameters are estimated in a data-driven fashion.

## 1.5 Organization of the thesis

The main methodological contributions of this thesis are split into six chapters divided into three parts according to the three methodological angles that we listed in Section 1.4. Part II proposes algorithms dedicated to the detection and characterization of faint patterns in nonstationary and correlated background image series. Part III improves the robustness of the processing in the presence of numerous aberrant data in the recorded data. Part IV extends the proposed detection and characterization algorithms to deal with multi-spectral data.

Following this organization, each part is made of two chapters that mirror each other: first a methodological development devoted to astronomy, then an approach for holographic microscopy. Each pair of chapters shares a common guiding thread but also leads to specific developments. Our presentation choice is motivated by giving a coherent methodological presentation. Chapters are not ordered chronologically. The publication dates of the papers related to each chapter indicate, for example, that the last methodological chapter corresponds to the first study considered in the thesis. Figure 1.18 gives a visual overview of the organization of this manuscript emphasizing the methodological bridges (magenta bubbles) between astronomy (red frames) and microscopy (blue frames) applications.

The thesis ends with Part V which summarizes the main contributions of this work, presents additional applications of the proposed algorithms, and indicates some ongoing and future work directions.

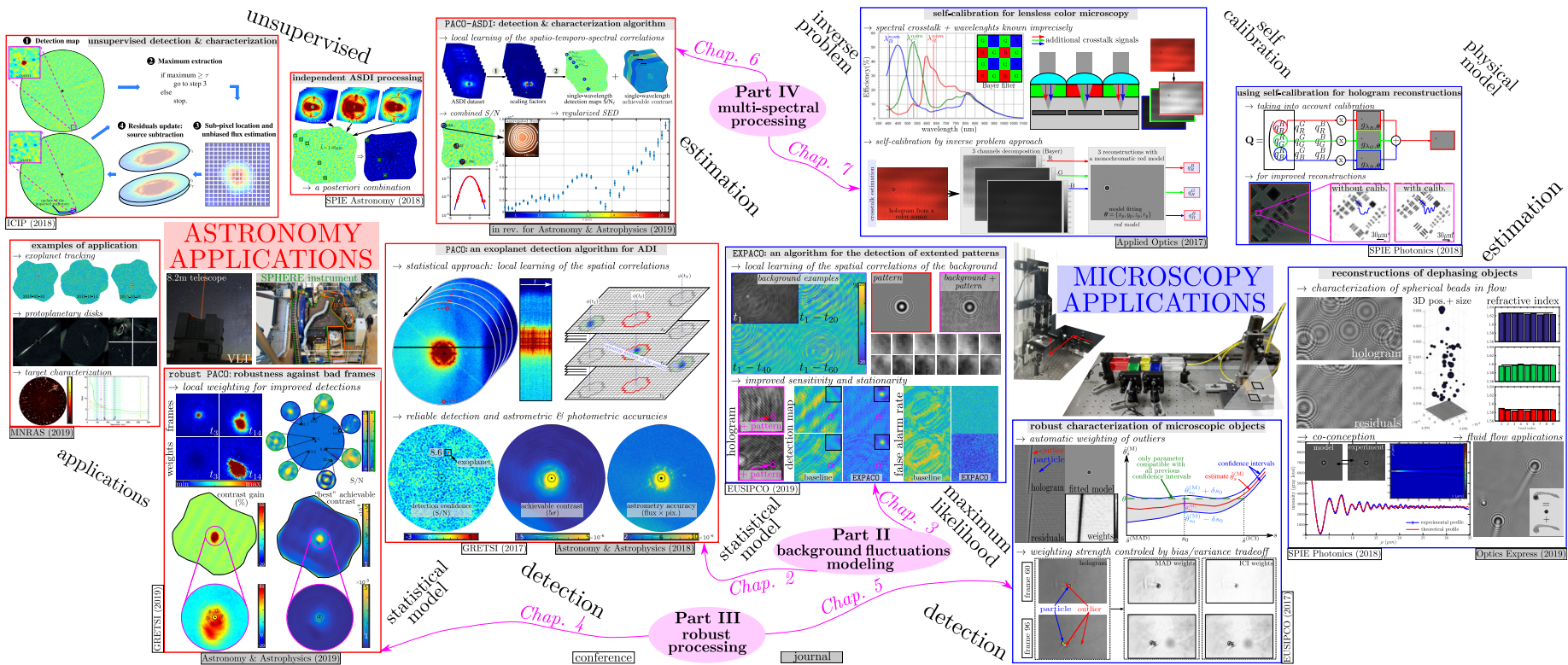


Figure 1.18 – Illustration of the main contributions both for astronomy (red frames) and microscopy applications (blue frames).



## Part II

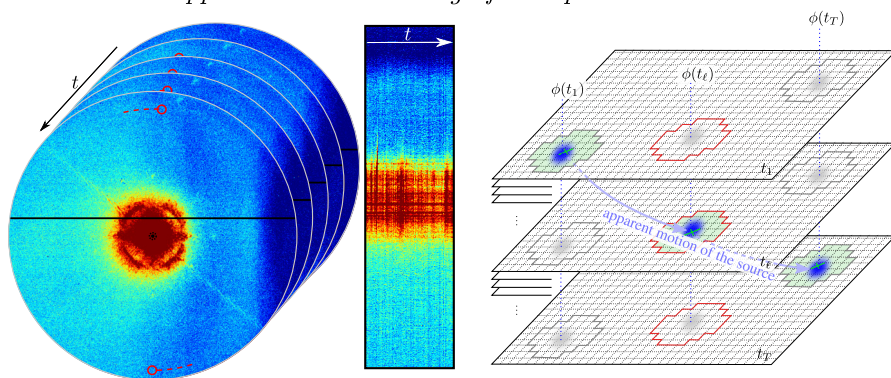
### Background fluctuations modeling

#### ASTRONOMY APPLICATIONS

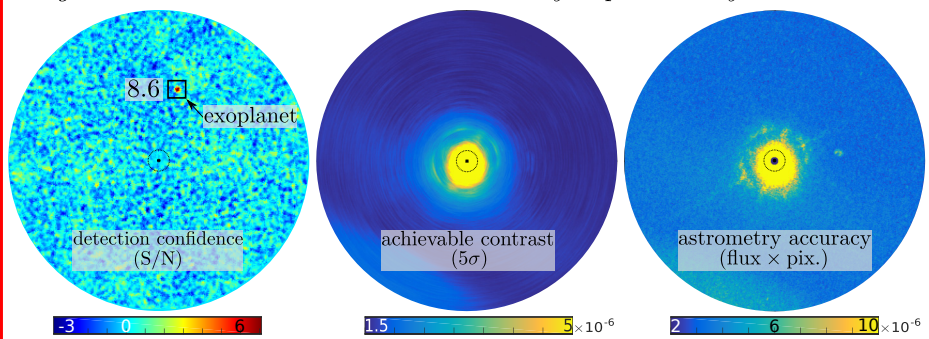
#### Chapter 2

PACO: an exoplanet detection algorithm for ADI

→ statistical approach: local learning of the spatial correlations



→ grounded detection and reliable astrometry & photometry accuracies



GRETSI (2017)

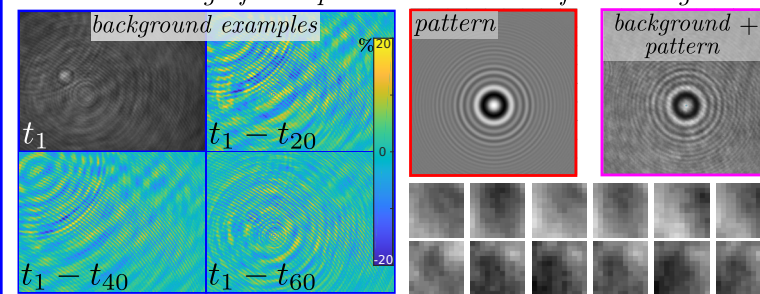
Astronomy & Astrophysics (2018)

#### MICROSCOPY APPLICATIONS

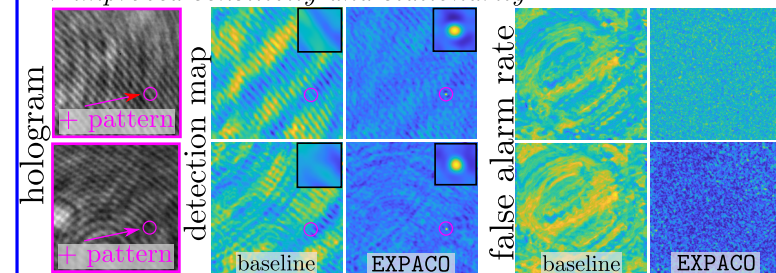
#### Chapter 3

EXPACO: an algorithm for the detection of extended patterns

→ local learning of the spatial correlations of the background



→ improved sensitivity and stationarity



EUSIPCO (2019)

## Part II

# Background fluctuations modeling





# Application of background fluctuations modeling in astronomy: detection and characterization of exoplanets

---

**Abstract**

*Even with the coupling of an extreme adaptive-optics system and a coronagraph, the detection of exoplanets by direct imaging remains challenging due to the very high contrast between the host star and the exoplanets. This chapter introduces a method named PACO, dedicated to source detection from angular differential imaging data. Given the complexity of the fluctuations of the background in the datasets, involving spatially-variant correlations, we show the potential of a processing method that learns a statistical model of the background directly from the data. In contrast to existing approaches, the proposed method accounts for spatial correlations in the data. Those correlations and the average stellar speckles are learned locally and jointly to the estimation of the flux of the (potential) exoplanets. By preventing from subtracting an estimate of the stellar speckles residuals, the photometry is intrinsically preserved. PACO offers appealing characteristics: it is parameter-free and photometrically unbiased. The statistical performance in terms of detection capability, photometric and astrometric accuracies can be straightforwardly assessed. A fast approximate version of the method is also described that can be used to process large amounts of data from exoplanets search surveys.*

---

## 2.1 Introduction

In this chapter, we introduce our exoplanet detection and characterization algorithm based on the local learning of the background fluctuations by means of Patches COvariances (hence the name PACO). We consider ADI series (3-D datasets: spatial + time) in which the potential companions describe an apparent motion along a predictable circular trajectory around their host star while the speckles background remains quasi-static. Starting from pre-reduced and calibrated ADI datasets, we aim to produce statistically-

grounded detections maps as well as reliable astrometry and photometry estimates. Due to the high contrast and slow time evolution of speckles, elaborate processing methods are mandatory to disentangle the exoplanets signal. In Section 2.2, we give a synthetic overview of state-of-the-art detection methods focusing on their main advantages and drawbacks. We present the PACO principle in Section 2.3 and its implementation in Section 2.4. Finally, Section 2.5 illustrates its performance compared to cutting-edge methods. This chapter is based on the journal paper (Flasseur et al., 2018a) and the conference paper (Flasseur et al., 2018b).

## 2.2 State-of-the-art processing methods for exoplanet detection by direct imaging

Recent instrumental progress has spurred the development of dedicated processing methods. New detection algorithms are regularly proposed in the literature. The processing step plays a central role in the direct imaging pipeline. Indeed, the achievable contrast depends both on the instrument design (contrast gain up to 10.000) and the detection algorithm (additional contrast gain higher than 100). Regarding their principle, processing methods can be split into four categories: methods based on *image combinations* or *mode subtractions*, methods following a *statistical approach* or using recent *machine learning* techniques. Hereafter, we discuss the main properties of each one. Throughout the text, the Reader can refer to Figure 2.1 giving a schematic summary of the principle of the main state-of-the-art detection methods.

### 2.2.1 Methods based on image combinations

Several methods have been developed to combine images taken at consecutive times. The key idea is to build a reference stellar PSF image and subtract it from the ADI stack to cancel at best the speckles background.

#### 2.2.1.1 Classical-ADI algorithms

An intuitive solution consists in subtracting the temporal median (“robust mean”) to each frame of the ADI stack. The residual images are then aligned to the true-North (using the parallactic angles) so that the exoplanetary signals are co-aligned in the different images. The aligned residual frames are finally combined following a simple strategy (mean or median). It is the principle of the classical-ADI (cADI) method (Marois et al., 2006) designed to process the first ADI direct observations from giant ground-based telescopes.

Like several other algorithms, this technique is very sensitive to the *self-subtraction* phenomenon. Since the reference PSF is built from observations (containing the potential companions), partial cancellation of the exoplanetary signal is expected simultaneously to speckles attenuation. This problem is more acute at the vicinity of the host star since displacements due to the rotation of the field of view are the smallest there. Marois et al. (2006) and Lagrange et al. (2010) propose some tricks based on frames selection. The so-called smart-ADI (sADI) builds a different reference PSF for each frame of the ADI stack by selecting only images whose rotation is higher than a few

elements of resolution ( $\lambda/D$ ). The radial-ADI (rADI) variant adapts the limit amount of rotation with the angular separation so that small separations benefit from better protection against self-subtraction. [Ren et al. \(2012\)](#) propose to exploit the symmetry of the speckles field by rotating the reference PSF by  $180^\circ$  before subtraction. While this preserves from self-subtraction, the speckles attenuation is generally of poor quality due to the only approximative symmetry of the speckle field (due to optical aberrations, stellar leakages, sensor noise, outliers introduced during the pre-processing step etc.).

### 2.2.1.2 LOCI type algorithms

Direct imaging was significantly boosted by the development of the next generation of processing algorithms based on the Locally Optimized Combination of Images (LOCI) principle ([Lafrenière et al., 2007](#)). The reference stellar PSF to be subtracted to the data is created by a linear combination of images selected in a library of data acquired under experimental conditions similar to those of the observation of interest. The optimization of this combination is performed by minimizing, in the least squares sense, the residual noise inside multiple subareas of the image. To ensure a more efficient suppression of stellar leakages, the reference stellar PSF is generally estimated from data in which the exoplanets are to be detected. While attenuating at best the stellar speckles, severe exoplanet self-subtraction also occurs when the rotation of the field of view is small.

Many variants have been developed to partially alleviate this problem. In the Adaptive-LOCI (ALOCI) algorithm ([Currie et al., 2012a,b](#)), the data are divided into annuli and processed independently, thereby allowing different linear combinations at different angular separations in the definition of the stellar PSF. The Damped-LOCI (DLOCI) algorithm ([Pueyo et al., 2012](#)) solves the LOCI optimization problem under positivity constraint (the reference stellar PSF is obtained by a positive linear combination) and maximizes the estimated flux in a given aperture around the location of a detected source. In other words, candidate exoplanets are first detected using LOCI, and DLOCI is launched locally to refine the contrast estimation. The Matched-LOCI (MLOCI) algorithm ([Wahhaj et al., 2015](#)) injects fake point sources and maximizes their S/N, which also improves the S/N of the sources present in the data. A more elaborate version of LOCI called Template-LOCI (TLOCI) ([Marois et al., 2013, 2014](#)) is currently considered as one of the cutting-edge standards for the detection and characterization of exoplanets by direct imaging. The main variation compared to the standard LOCI algorithm is related to the construction of the reference stellar PSF. Instead of only minimizing the noise (i.e., the norm of the residuals), TLOCI also maximizes the exoplanet S/N in the residuals. In other words, the influence of a specific choice of linear combination on the reduction of the flux of the candidate companion is also considered. The TLOCI algorithm is often calibrated for exoplanet signal self-subtraction by injecting fake faint point sources into the data to determine the algorithm throughput at each position in the field of view after speckles removal. For each injection, the ratio of the point source flux in the resulting image to its initial flux is estimated to produce the 1-D throughput as a function of the angular separation, i.e., a debiasing correction to be applied a posteriori.

### 2.2.2 Methods based on mode subtractions

Several other image subtraction algorithms are based on the Principal Component Analysis (PCA). PCA is a widely used tool in data science and especially in image processing to extract relevant features from multi-dimensional data (Pearson, 1901; Hotelling, 1933; Jolliffe, 2011). One of the most popular applications is face recognition in computer vision. PCA is applied to extract dominant image modes (the so-called *eigenfaces*) from a set of images. Each image is then represented as a linear combination of eigenfaces (Sirovich and Kirby, 1987; Turk and Pentland, 1991). The recognition task is then performed by projecting a test image onto the subspace spanned by the eigenfaces, and classification is then done by distance minimization (Paul and Al Sumam, 2012).

Exoplanet-hunter algorithms based on PCA consider that the fluctuations of the stellar speckles span a small-dimensional subspace. Exoplanets are thus detected on the subspace orthogonal to the one capturing fluctuations of the stellar speckles. This is the principle of the Karhunen-Loève Image Projection (KLIP) algorithm (Soummer et al., 2012) which builds a basis of the subspace capturing the stellar PSF by performing a Karhunen-Loève transform of the images from the reference library. To obtain a model of the stellar PSF, the science data is projected onto a predetermined number of modes. Even if the general principle is close to the LOCI type algorithms, KLIP is much faster thanks to the truncation. The smart-KLIP (sKLIP) (Absil et al., 2013) algorithm partially prevents self-subtraction by building the reference library only from images where the candidate exoplanets underwent a sufficient rotation. More recently, Pueyo (2016) proposes to combine KLIP with a perturbation/propagation-based approach to estimate the self-subtraction amount.

The LLSG algorithm (Gomez Gonzalez et al., 2016) is also related to subspace methods. It locally decomposes a temporal series of images into low-rank, sparse and Gaussian components. It is experimentally shown that the exoplanets signal mostly remains in the sparse term allowing an improved detection. However, it is expected that this method is sensitive to outliers in the data (like bad or hot pixels) that are also recovered in the sparse component together with the candidate exoplanets.

### 2.2.3 Methods based on a statistical approach

After facing the difficulty of canceling speckles background, the evaluation of the confidence of each detection progressively became a critical issue. Then, various statistically-based methods have emerged.

MOODS (MOving Objects Detection optimized for SPHERE) algorithm (Smith et al., 2009) differs significantly from other methods. It estimates the exoplanet contrast jointly to the stellar PSF (considered constant for all observations of a temporal dataset). While it presents very interesting properties, its application on large data surveys remains problematic.

Mawet et al. (2014); Ruane et al. (2017) propose to adjust the detection threshold to the angular separations to balance the increase of the false alarm rate near the host star.

Other methods adopt a statistical framework to perform the detection task on the residual image obtained by a speckle cancellation algorithm (such as LOCI or

PCA types). The ANgular DiffeRential OptiMal Exoplanet Detection Algorithm (ANDROMEDA, Mugnier et al. (2009); Eggenberger et al. (2010); Cornia (2010); Cantalloube et al. (2015)) forms differences of temporal images to suppress stellar speckles and performs the detection of differential off-axis PSFs (i.e., the signature of an exoplanet in the difference images). A generalized likelihood ratio test is then evaluated under a white Gaussian hypothesis. Two output images are produced by the algorithm: (i) a detection map obtained by forming the signal-to-noise ratio, i.e. the ratio between the estimated flux and the standard deviation of the flux, and (ii) a flux map that indicates the estimated flux at each pixel should a source be present at that location. Due to space constraints, only the detection map is represented in Figure 2.1. A matched filter approach can also be used on the KLIP residuals (Ruffio et al., 2017). Since the techniques discussed so far are based on image differences, their performance is directly related to the efficiency of the speckle attenuation.

### 2.2.4 Methods based on machine learning techniques

With the increasing volume of available digital data, machine learning (Bishop, 2006) and deep learning (LeCun et al., 2015) are widely investigated and applied to a large variety of application fields. They infer decisions from the data themselves thanks to a *training step* in which a task-specific model is learned in a supervised or unsupervised fashion. Automatic object detection and recognition task is one of the breakthroughs achieved by these approaches, now reaching excellent results (Zhao et al., 2019).

The application of this methodological framework was also considered in direct imaging to detect weak signals from exoplanets. SODIRF and SODINN methods (Gomez Gonzalez et al., 2018) use respectively a Random Forest (RF) classifier or a Convolutional Neural Network (CNN). The training step is performed by means of numerical injections of fake exoplanets on pre-processed images in which signals from real exoplanets are suppressed as best as possible using a space decomposition. It demonstrates promising results, but the inference of reliable detection confidence measurement is problematic (since such approaches do not model it intrinsically). A recent work (Yip et al., 2019) implements a Generative Adversarial Network (GAN) generating pure background images (no exoplanet in the field of view) used for a CNN-based training step. The performance is evaluated on images from Hubble’s space-based direct observations. It succeeds in detecting synthetic sources at modest levels of contrast (identifiable by visual inspection of the data) from a single image.

The limited number of works related to machine learning techniques applied in direct imaging is directly related to the difficulty of the task, which differs significantly from the object recognition problem encountered in conventional images. The background fluctuations of direct imaging data vary significantly from one observation to the other. A major difficulty for machine learning based approaches is to infer the background structures from a learning dataset that can differ significantly from the testing dataset (template based approaches as TLOCI or KLIP proved to be more effective when estimating the stellar PSF from the current observation rather than different observations). Another difficulty is linked to the nonstationarity of the background which prevents from applying shift-invariant methods like CNNs. Finally, these approaches suffer from the absence of ground-truth (labeled images as *pure background* or *presence*

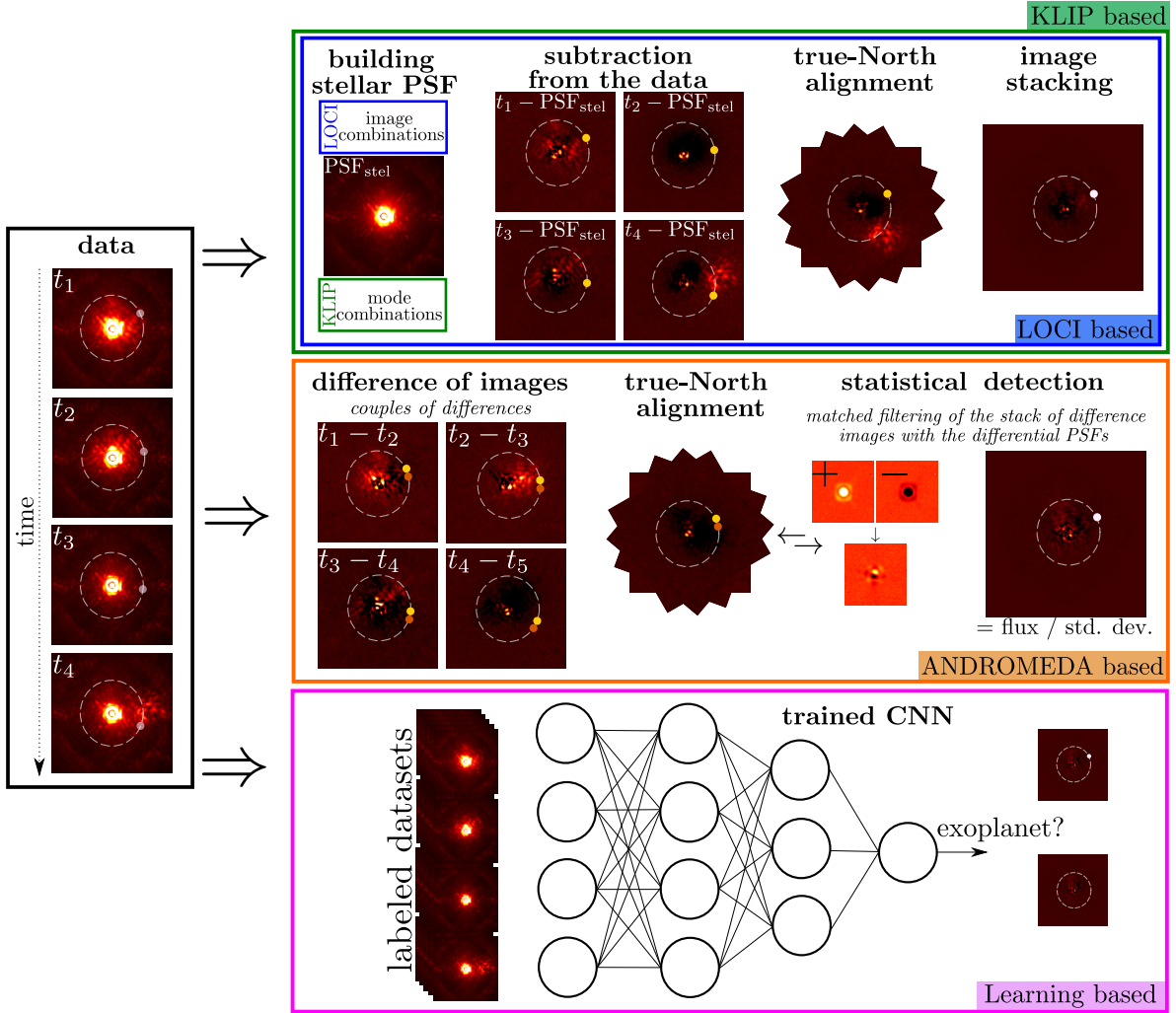


Figure 2.1 – Simplified principle of the main state-of-the-art detection algorithms based on LOCI, KLIP, ANDROMEDA and machine learning.

of an exoplanet). This is a critical point for machine-learning based techniques. Then, the performance is almost upper-bounded by the performance of other state-of-the-art algorithms used to form an exoplanet-free training set before testing.

### 2.2.5 Comparison and desirable properties

The state-of-the-art detection algorithms are subject to different limitations. Most of them are not fully-automatic so that the tuning of several hyper-parameters is often mandatory to reach the best performance of the methods. Such tuning is very time consuming and should ideally be repeated for each dataset since it depends on the dataset properties (considered spectral channel, number of temporal frames, quality of the observations, amount of parallactic rotation, etc.). In addition, many of them are subject to the exoplanet self-subtraction. By combining information (either by image subtraction as in the LOCI type methods, or by mode subtractions as in the PCA type methods) at different times to attenuate the speckles background, the signal of



the exoplanets is also attenuated. Consequently, the photometry is not intrinsically preserved so that resorting to a calibration step via Monte-Carlo injections is mandatory to compensate for the exoplanet self-subtraction (i.e., to correct for this bias a posteriori). Finally, the main limitation of existing approaches is the lack of control of the probability of false alarm on the detection maps. Existing statistical methods generally perform better but also suffer from the lack of reliable detection confidence (since they are applied mainly on speckle-free residual images of other algorithms and do not model the data statistics themselves). It is common for state-of-the-art methods to produce detection maps with many more false alarms than theoretically expected so that the detection is made by visual inspection of the algorithm results, a very time consuming and non-trivial task.

Based on an analysis of the limitations of existing algorithms for ADI data processing and of the needs of astronomers that use planet finder instruments, the following desirable specifications for an exoplanet detection algorithm may be listed:

1. high detection sensitivity,
2. unsupervised source detection,
3. statistical guarantees (i.e., control of the probability of false alarm),
4. characterization of the sources detected: subpixel astrometry and unbiased photometry estimations,
5. robustness and versatility to compensate for evolving aberrations,
6. characterization of the detection sensitivity: computation of a map reporting the contrast required for a source to be detected at a given detection threshold.

Table 2.1 – Qualitative comparison of the main exoplanet-hunter algorithms.

	1.	2.	3.	4.	5.	6.
<b>cADI</b>	⊖⊖	⊖⊖	⊖⊖	⊖	⊖⊖	⊖⊖
<b>LOCI</b>	⊖	⊖	⊖⊖	⊖	⊖⊖	⊖⊖
<b>{A,D,M}LOCI</b>	⊖	⊖	⊖⊖	⊖	⊖⊖	⊖⊖
<b>TLOCI</b>	⊖/⊕	⊖	⊖⊖	⊖	⊖⊖	⊖
<b>(s)KLIP</b>	⊖/⊕	⊖	⊖⊖	⊖	⊖⊖	⊖
<b>LLSG</b>	⊖/⊕	⊖	⊖	⊕	⊖	⊖
<b>ANDROMEDA</b>	⊖/⊕	⊕	⊕	⊕	⊖/⊕	⊕

Based on our strictly personal experience with state-of-the-art algorithms, we compare in Table 2.1 the main exoplanet-hunter algorithms according to the six desirable properties mentioned hereabove. TLOCI and KLIP algorithms reach the highest sensitivity (best achievable contrast), at the cost of a large number of false alarms. They are currently considered as gold-standard methods to process direct observations. They were applied in almost all direct detections reported in the literature (Bonavita et al., 2014; Macintosh et al., 2015; Chauvin et al., 2017) and they are still used intensively to conduct astronomy analysis of new datasets (Lagrange et al., 2019a; Mesa et al.,



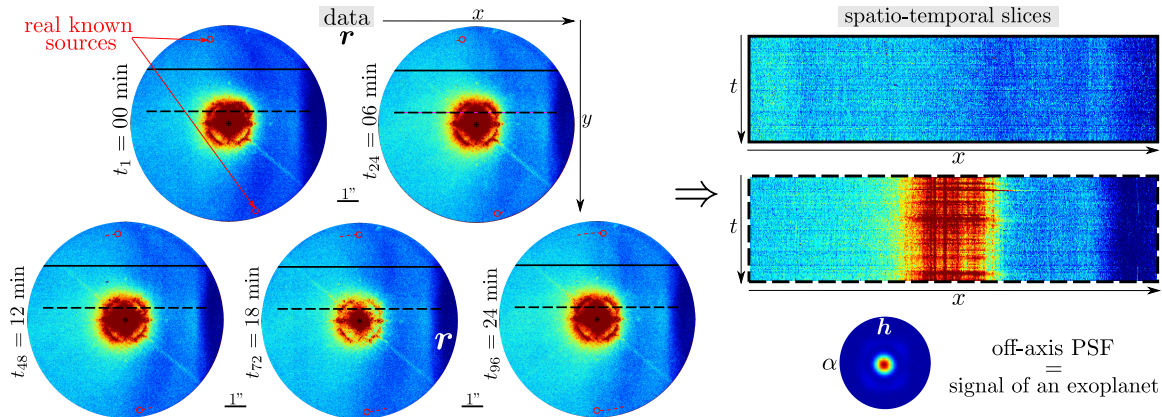


Figure 2.2 – A sample from a VLT/SPHERE-IRDIS dataset (HIP 72192 dataset at  $\lambda_1 = 2.110 \mu\text{m}$ ). Two spatio-temporal slices cut along the solid and dashed lines are displayed on the right of the figure, emphasizing the spatial variations of the structure of the signal. Red circles indicate the location of two point sources. The off-axis PSF  $\mathbf{h}$  is the typical signature of the point-like sources to be detected in the recorded intensity images. For visualization purpose, the scale between the off-axis PSF and the data is not the same.

2019a; Gratton et al., 2019; Gibbs et al., 2019; Maire et al., 2019). For these reasons, in Section 2.5 we compare the PACO performance mainly to these methods. LLSG and ANDROMEDA present very interesting complementary properties, but they are still marginally used by the community. We also confront our results with these methods on some datasets.

In the following, we attempt to address the listed desirable properties by deriving an algorithm from a data-driven statistical modeling of ADI observations. The proposed approach differs significantly from state-of-art methods by its local learning of the speckle background statistics.

## 2.3 PACO: exoplanet detection based on PATCH CO-variances

Figure 2.2 shows an example of science frames derived from VLT/SPHERE-IRDIS data and a view of two spatio-temporal slices extracted at two different locations (along the solid line: far from the host star, along the dashed line: near the host star). Within the central region (angular separations below 1 arcsec at the wavelength  $\lambda_1 = 2.110 \mu\text{m}$ ), the signal is dominated by stellar speckles due to the diffraction in presence of aberrations. At farther angular separations, the noise comes mainly from a combination of photon noise from thermal background flux and detector readout. Observation of the temporal fluctuations in the spatio-temporal cuts reveals spatial variations of the variance of the fluctuations but also an evolution of their spatial correlations. Beyond accounting for the average intensity of stellar speckles, we base our exoplanet detection method on nonstationary modeling of short-range spatial covariances. To ease the sta-

tistical learning of these covariances directly from the data and to obtain a detection method based on local processing, we consider a decomposition of the field of view into small patches whose size covers the core of the off-axis PSF. Our detection method accounts for the spatial covariance of these patches.

### 2.3.1 Statistical model for source detection and characterization

Science images obtained by high-contrast imaging with ADI have two components: (i) the signal of interest, due to the presence of exoplanets or background sources<sup>1</sup> in the field of view, and (ii) a very strong background, produced by the stellar speckles and other sources of noise, that displays temporal fluctuations. The motion of the sources due to the rotation of the field of view is precisely known. An exoplanet at some bi-dimensional angular location  $\phi_0$  at a chosen initial time  $t_0$  is seen at location  $\phi_t = \mathcal{F}_t(\phi_0)$  at time  $t$ , where  $\mathcal{F}_t$  is the geometrical transform (e.g., a rotation) modeling the apparent motion of the field of view between the observation configurations at time  $t_0$  and time  $t$ .

Since very few sources are within the field of view and these sources are faint, we model locally the observed data as the superimposition of a background (stellar speckles and noise) and at most one other source, unresolved and located in the immediate vicinity (no overlapping of several faint sources).

The observed intensity  $r_{n,t}$  at the pixel location  $n$  and time  $t$  can then be decomposed into the two components:

$$r_{n,t} = \alpha h_n(\phi_t) + f_{n,t}, \quad (2.1)$$

with  $\alpha \geq 0$  the flux of the unresolved source to be estimated ( $\alpha = 0$  in the absence of such source),  $h_n(\phi_t)$  the known off-axis PSF, centered on the known location  $\phi_t$  of the source at time  $t$  and sampled at pixel  $n$ , and  $f_{n,t}$  the background at pixel  $n$  and time  $t$  accounting for stellar speckles and noise which must be statistically modeled. Figures 2.2 and 2.3 summarize the notations introduced hereabove.

The major difficulty of the detection of exoplanets lies in the fact that the amplitude of the background  $f_{n,t}$  is much larger than the exoplanet contribution  $\alpha h_n(\phi_t)$  and that it fluctuates from one time  $t$  to another. It is necessary to follow a statistical approach to account for these fluctuations. The collection of all observations  $\{r_{n,t}\}_{n=1:N, t=1:T}$  in the presence of an exoplanet initially located at  $\phi_0$  with a flux  $\alpha$  is then described as a random realization with a distribution given by the probability density function  $p_f$  of the background:

$$p_r(\{r_{n,t}\}_{n=1:N, t=1:T} | \alpha, \phi_t) = p_f(\{r_{n,t} - \alpha h_n(\phi_t)\}_{n=1:N, t=1:T}). \quad (2.2)$$

---

1. Background sources are point objects behaving (from a signal processing point of view) as exoplanets in direct imaging data. Background faint point sources are often brown dwarfs not bounded to the host star (no stable orbit). Differentiating background sources from exoplanets is out of the scope of this thesis. As discussed in Section 1.2.2.3, this specific task is addressed by experts based on the outputs of detection and characterization algorithms. It requires to confront the estimated SEDs (like the ones we extract in Chapter 6) to exoplanet formation models and/or to study the motion of the sources between observations separated by several months. In the following, we do not make a difference between exoplanets and background sources in the methodological explanations.

Based on this model and under the hypothesis that there are few sources within the field of view (so that each source can be considered separately), an unbiased estimation of the flux  $\alpha$ , for a given initial angular location  $\phi_0$  is provided by the maximum likelihood estimator:

$$\hat{\alpha} = \arg \max_{\alpha} p_f(\{r_{n,t} - \alpha h_n(\mathcal{F}_t(\phi_0))\}_{n=1:N, t=1:T}). \quad (2.3)$$

Note that  $\hat{\alpha}$  implicitly depends on the assumed position  $\phi_0$  of the source. The detection of a point source at a given location  $\phi_0$  can be formalized as an hypothesis test:

$$\begin{cases} \mathcal{H}_0 : & \{r_{n,t}\}_{n=1:N, t=1:T} = \{f_{n,t}\}_{n=1:N, t=1:T} \\ \mathcal{H}_1 : & \{r_{n,t}\}_{n=1:N, t=1:T} = \alpha \{h_n(\phi_t)\}_{n=1:N, t=1:T} + \{f_{n,t}\}_{n=1:N, t=1:T}. \end{cases} \quad (2.4)$$

In words, under hypothesis  $\mathcal{H}_0$  the collection of all observations corresponds to pure background (stellar speckles and noise) while under hypothesis  $\mathcal{H}_1$  it is the superimposition of the off-axis PSF with a flux  $\alpha$  and some background.

By replacing  $\alpha$  in  $\mathcal{H}_1$  with the maximum likelihood estimate  $\hat{\alpha}$  obtained from (2.3) for an assumed initial position  $\phi_0$ , the (generalized) likelihood of each hypothesis can be compared to form the generalized likelihood ratio test (GLRT, see for example Kay, 1998a):

$$2 \log \frac{p_f(\{r_{n,t} - \hat{\alpha} h_n(\phi_t)\}_{n=1:N, t=1:T})}{p_f(\{r_{n,t}\}_{n=1:N, t=1:T})} \underset{\mathcal{H}_0}{\overset{\mathcal{H}_1}{\gtrless}} \eta. \quad (2.5)$$

In order to apply Equations (2.3) and (2.5) to the detection and photometric/astrometric estimations, it is necessary to specify the statistical model of the background. In most of the existing methods for exoplanet detection by ADI, some data pre-processing is applied in order to reduce the amplitude of the background term and whiten it (i.e., lessen its spatial correlations). Such pre-processing takes the form of (weighted) temporal differences in ADI, TLOCI and ANDROMEDA, a high-pass filtering, or the projection onto the subspace orthogonal to the dominant modes identified by a PCA in KLIP and its variations. Note that ANDROMEDA is based on a quite similar statistical framework: Equations (2.3) and (2.5) are applied under the assumption of uncorrelated Gaussian noise to detect and characterize sources in residual differential images (see Section 2.2.3). Rather than transforming the data so that a simple statistical model can be assumed (uncorrelated observations), we perform no pre-processing but account for the spatial correlations in our model. Given that more than a few tens of photons are collected at each detector pixel, the Poisson detection statistics can be approximated by a Gaussian distribution. The other contributions for the temporal fluctuations (thermal background noise, evolution of the speckle patterns due to evolving phase aberrations or the decentering of the star on the coronagraph) will be considered, in the absence of a more precise model, to be Gaussian distributed. This Gaussian approximation gives closed-form expressions that have a practical interest for the implementation. The spatial structure of the background is mainly due to that of the speckles (related to the angular resolution) and the interpolation steps in the data reduction pipeline. Most of these correlations are at small scale. Moreover, the off-axis PSF  $h(\phi)$  has a core (also defined by the angular resolution) that is only a few

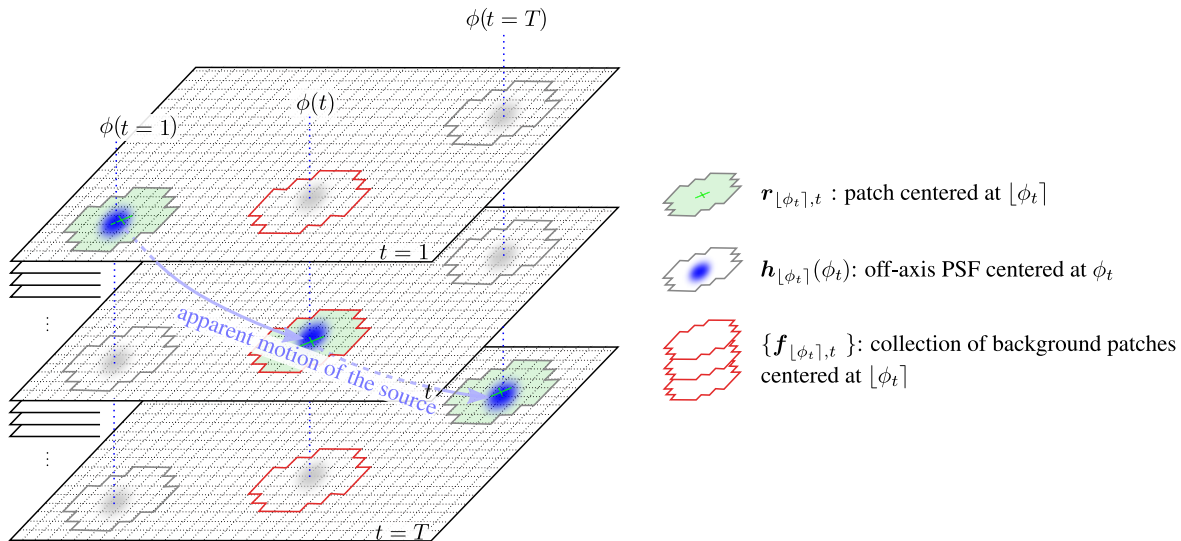


Figure 2.3 – Apparent motion of an exoplanet in an ADI stack of frames. Green patches contain, in each frame, the exoplanet (i.e., the off-axis PSF) superimposed with the background. The statistical model of a background patch is built locally based on observed patches at the same location but at different times (set of red patches).

pixels wide. Hence, in Equations (2.3) and (2.5), only pixels of the dataset such that  $h_n(\phi_t)$  is non negligible have an impact on the estimation or detection. These pixels are represented in green in Figure 2.3.

We denote the set of the  $K$  spatial pixels that form an extended spatial neighborhood centered at pixel  $n$ , at time  $t$ , as the *patch*<sup>2</sup>  $\mathbf{r}_{n,t} \in \mathbb{R}^K$ . In the following, patches are sets of pixels with the shape of a discrete disk. If the radius of this disk is chosen large enough to encompass the core of the off-axis PSF, the collection of all pixel values  $\{\mathbf{r}_{n,t}\}_{n=1:N, t=1:T}$  used in Equations (2.5) and (2.3) to detect or estimate the flux of an exoplanet located at  $\phi_0$  can be reduced to the collection of patches  $\{\mathbf{r}_{[\phi_t],t}\}_{t=1:T}$  that contains the exoplanet (where  $[\phi_t]$  is the closest pixel to the subpixel location  $\phi_t$ ). Only the joint distribution of these observations need be modeled. Since the background is different in each patch (and possibly varies according to time), we use a different model for each patch (local adaptivity of the model), see Figure 2.3.

The reduced number  $T$  of available background patches at a given spatial location (typically, from a few tens to a hundred temporal frames) limits the correlations that can be accounted for. In this chapter, we account only for spatial correlations<sup>3</sup> and use a multivariate Gaussian model to describe the distribution of each background patch. Patches at different times are considered statistically independent. Rather than defining the distribution  $p_f$  of all background pixels, we then model only the distribution of background pixels in the patches of interest. This distribution  $p_f(\{\mathbf{f}_{[\phi_t],t}\}_{t=1:T})$  is modeled as a product of Gaussian distributions defined over each patch that would

2. Bold fonts are used to denote patches while normal fonts are reserved to scalars and angular positions.

3. Taking into account of spatio-temporal (or spatio-temporo-spectral for ASDI datasets) nonstationarities requires specific adaptations which are described in Chapters 4 and 6 respectively.

contain an exoplanet if that exoplanet was initially located at  $\phi_0$ :

$$P_f(\{\mathbf{f}_{[\phi_i],t}\}_{t=1:T}) = \prod_{t=1}^T \mathcal{N}(\mathbf{f}_{[\phi_i],t} \mid \mathbf{m}_{[\phi_i]}, \mathbf{C}_{[\phi_i]}), \quad (2.6)$$

with  $\mathcal{N}(\cdot \mid \mathbf{m}_{[\phi_i]}, \mathbf{C}_{[\phi_i]})$  the probability density function of the multivariate Gaussian (mean  $\mathbf{m}$  and covariance  $\mathbf{C}$ ) that describes background patches centered at pixel  $[\phi_t]$ .

### Patch COvariances modeling

Based on the observation that the background of ADI series present fluctuations involving spatially-variant correlations, we derive the basis of our exoplanet detection and characterization method:

- the observed intensity is modeled as the superimposition of the background contribution and the exoplanet signature,
- a nonstationary multi-variate Gaussian model of the background is learned, capturing together the average speckles and the spatial correlations,
- the decision in favor of the presence or the absence of an exoplanet is performed by a binary hypothesis test.

This methodological approach differs from state-of-the-art algorithms by:

- the absence of explicit image or mode subtractions,
- the learning from the data themselves of the statistics of the background.

## 2.3.2 Statistical learning of the background

In our model, we consider a common mean  $\mathbf{m}_n$  and covariance  $\mathbf{C}_n$  for all  $T$  background patches  $\{\mathbf{f}_{n,t}\}_{t=1:T}$  centered at a given pixel  $n$ . Several estimators of the covariance can be considered to characterize the multivariate Gaussian model of a background patch. A natural solution is to use the sample mean  $\widehat{\mathbf{m}}_n$  and covariance  $\widehat{\mathbf{S}}_n$  estimators which are the maximum likelihood estimators<sup>4</sup>:

$$\widehat{\mathbf{m}}_n = \frac{1}{T} \sum_{t=1}^T \mathbf{r}_{n,t} \quad \text{and} \quad \widehat{\mathbf{S}}_n = \frac{1}{T} \sum_{t=1}^T (\mathbf{r}_{n,t} - \widehat{\mathbf{m}}_n) \cdot (\mathbf{r}_{n,t} - \widehat{\mathbf{m}}_n)^\top. \quad (2.7)$$

However, it should be kept in mind that there are few observations (typically between a few tens and a hundred) compared to the number of parameters to estimate in the covariance matrix ( $K(K+1)/2 \sim 10^3$  parameters, with  $K \sim 50$  the number of pixels in a patch). The limited number  $T$  of temporal frames makes a direct estimation of  $\mathbf{C}_n$

---

4. The unbiased estimator of the covariance leads to the factor  $T-1$  while the maximum likelihood estimator leads to the factor  $T$  in the denominator of  $\widehat{\mathbf{S}}_n$ . However, since the number of observations  $T$  is typically between a few tens and a hundred, the difference between the two formula can be neglected. In the following, we kept the normalization by the factor  $T$  since our formulation of the estimator as a minimizer in Equation (2.38) leads to the  $T$  factor too.



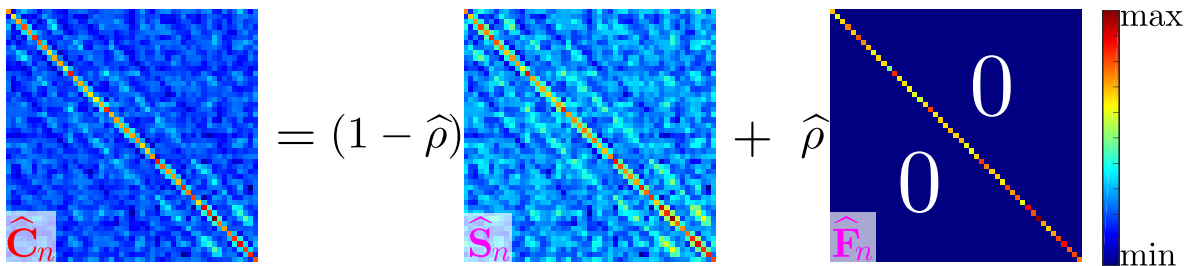


Figure 2.4 – Illustration of the covariance shrinkage approach.

by the sample covariance either rank deficient (if  $T < K$ ) or too noisy. Some form of regularization must thus be enforced. In this section, we discuss and compare several alternatives to address this issue.

The lack of observations on which to base the estimation of the covariance, requires the use of estimators with controlled variance. Indeed, the sample covariance estimator  $\hat{\mathbf{S}}_n$  defined in (2.7) has a variance that is too large. When the number of time frames  $T$  is smaller than the number  $K$  of pixels in a patch,  $\hat{\mathbf{S}}_n$  is moreover rank-deficient and cannot be inverted to compute the detection criterion or to estimate the flux of an exoplanet. This problem can be overcome by introducing a regularization or by combining two estimators.

A classical regularization consists of adding a fraction of identity matrix  $\mathbf{I}$  to ensure that the covariance matrix is invertible:

$$\hat{\mathbf{C}}_n = \hat{\mathbf{S}}_n + \epsilon \mathbf{I}, \quad (2.8)$$

where  $\epsilon$  should be set small enough to introduce a negligible bias.

Another family of estimators is formed by *shrinkage estimators* that combine two (or more) estimators to balance their properties. A typical choice consists of a first estimator that is unbiased but that suffers from a large variance, and a second estimator with much smaller variance but larger bias (reduced degrees of freedom). Following the work of Ledoit and Wolf (2004) and Chen et al. (2010), we consider the combination of the sample covariance matrix  $\hat{\mathbf{S}}_n$  and the diagonal matrix  $\hat{\mathbf{F}}_n$  whose diagonal entries are the empirical variances:

$$[\hat{\mathbf{F}}_n]_{ii} = \frac{1}{T} \sum_{t=1}^T [\mathbf{r}_{n,t} - \hat{\mathbf{m}}_n]_{ii}^2 = [\hat{\mathbf{S}}_n]_{ii} \quad \text{and} \quad [\hat{\mathbf{F}}_n]_{ij} = 0 \quad \text{if } i \neq j. \quad (2.9)$$

The shrinkage estimator is then defined by the convex combination:

$$\hat{\mathbf{C}}_n = (1 - \hat{\rho}) \hat{\mathbf{S}}_n + \hat{\rho} \hat{\mathbf{F}}_n. \quad (2.10)$$

As illustrated by Figure 2.4, diagonal elements of the shrinkage estimator  $\hat{\mathbf{C}}_n$  then correspond to the empirical variance while off-diagonal elements (i.e., covariance terms) are shrunk towards 0 by a factor  $1 - \hat{\rho}$ , hence the name. In the following, we base our study on the work of Chen et al. (2010), and we extend their results giving the closed-form expression of the shrinkage factor  $\hat{\rho}$  to our estimator  $\hat{\mathbf{F}}_n$  with non-constant diagonal values.

If the samples on which the estimators<sup>5</sup>  $\hat{\mathbf{S}}$  and  $\hat{\mathbf{F}}$  are computed are distributed according to a multivariate distribution with covariance  $\mathbf{\Sigma}$ , then the optimal value  $\rho^*$  that minimizes the expected risk  $\mathbb{E}[\|\hat{\mathbf{C}} - \mathbf{\Sigma}\|_{\mathbb{F}}^2]$  is given (see Appendix A for the proof) by:

$$\rho_{\text{O}} = \frac{\mathbb{E}\left(\text{tr}\left(\left(\mathbf{\Sigma} - \hat{\mathbf{S}}\right) \cdot \left(\hat{\mathbf{F}} - \hat{\mathbf{S}}\right)\right)\right)}{\mathbb{E}\left(\|\hat{\mathbf{S}} - \hat{\mathbf{F}}\|_{\mathbb{F}}^2\right)} = \frac{\sum_{i,j} \text{Var}\left([\hat{\mathbf{S}}]_{ij}\right) - \sum_{i,j} \text{Cov}\left([\hat{\mathbf{S}}]_{ij}, [\hat{\mathbf{F}}]_{ij}\right)}{\mathbb{E}\left(\|\hat{\mathbf{S}} - \hat{\mathbf{F}}\|_{\mathbb{F}}^2\right)}, \quad (2.11)$$

where  $\|\cdot\|_{\mathbb{F}}$  is the Frobenius norm and the subscript O in  $\rho_{\text{O}}$  is used to emphasize that this value of  $\rho$  can be computed only provided that an *oracle* has access to the underlying covariance  $\mathbf{\Sigma}$ . The specific form of the estimators  $\hat{\mathbf{S}}$  and  $\hat{\mathbf{F}}$  and the Gaussian assumption lead to the simplified form for  $\rho_{\text{O}}$  (see Appendix A for the proof):

$$\rho_{\text{O}} = \frac{\text{tr}(\mathbf{\Sigma}^2) + \text{tr}^2(\mathbf{\Sigma}) - 2 \sum_{i=1}^K [\mathbf{\Sigma}]_{ii}^2}{(T+1) \text{tr}(\mathbf{\Sigma}^2) + \text{tr}^2(\mathbf{\Sigma}) - (T+2) \sum_{i=1}^K [\mathbf{\Sigma}]_{ii}^2}, \quad (2.12)$$

which is an extension of the result given in Chen et al. (2010) to our estimator  $\hat{\mathbf{F}}$  with non-constant diagonal values. However, this expression cannot be applied in practice. An approximate value  $\hat{\rho}$  is obtained by replacing the unknown covariance matrix  $\mathbf{\Sigma}$  by a previous estimate. This is the principle of the oracle-approximating shrinkage (OAS) estimator of Chen et al. (2010). The following recursion can be applied:

$$\begin{cases} \hat{\rho}_{j+1} = \rho_{\text{O}}(\hat{\mathbf{\Sigma}}_j) = \frac{\text{tr}(\hat{\mathbf{\Sigma}}_j \hat{\mathbf{S}}) + \text{tr}^2(\hat{\mathbf{\Sigma}}_j) - 2 \sum_{i=1}^K [\hat{\mathbf{\Sigma}}_j]_{ii} [\hat{\mathbf{S}}]_{ii}}{(T+1) \text{tr}(\hat{\mathbf{\Sigma}}_j \hat{\mathbf{S}}) + \text{tr}^2(\hat{\mathbf{\Sigma}}_j) - (T+2) \sum_{i=1}^K [\hat{\mathbf{\Sigma}}_j]_{ii} [\hat{\mathbf{S}}]_{ii}} \\ \hat{\mathbf{\Sigma}}_{j+1} = (1 - \hat{\rho}_{j+1}) \hat{\mathbf{S}} + \hat{\rho}_{j+1} \hat{\mathbf{F}} \end{cases} \quad (2.13)$$

This sequence converges to a fixed point that is either  $\hat{\rho} = 1$  or the more useful value (see Appendix A for the proof):

$$\hat{\rho} = \frac{\text{tr}(\hat{\mathbf{S}}^2) + \text{tr}^2(\hat{\mathbf{S}}) - 2 \sum_{i=1}^K [\hat{\mathbf{S}}]_{ii}^2}{(T+1) \text{tr}(\hat{\mathbf{S}}^2) - \sum_{i=1}^K [\hat{\mathbf{S}}]_{ii}^2}, \quad (2.14)$$

which is an extension of the result given in Chen et al. (2010) to our estimator  $\hat{\mathbf{F}}$  with non-constant diagonal values.

Top and middle parts of Figure 2.5 compare signal-to-noise ratio (S/N, see Equation (2.26) for the definition) detection maps computed with PACO considering the two regularization schemes mentioned above. Thirty fake sources are numerically injected in a dataset from the VLT/SPHERE-IRDIS instrument around the HIP 72192 star observed at  $\lambda_1 = 2.110 \mu\text{m}$ . This dataset also contains two real point-sources (see Section 2.5 for more details about the dataset, injection method and results). It shows that the shrinkage estimation of the covariance matrices achieves better performance (since the 30+2 sources are detected with a higher S/N of detection) than a simple regularization by adding a fraction of identity matrix. This may be due to the local and automatic adaptation of the strength of the regularization to the data.

---

5. For compactness purpose, we now drop the pixel index  $n$  for the mean ( $\mathbf{m}_n \rightarrow \mathbf{m}$ ) and covariance ( $\mathbf{C}_n \rightarrow \mathbf{C}$ ) until the end of this section.



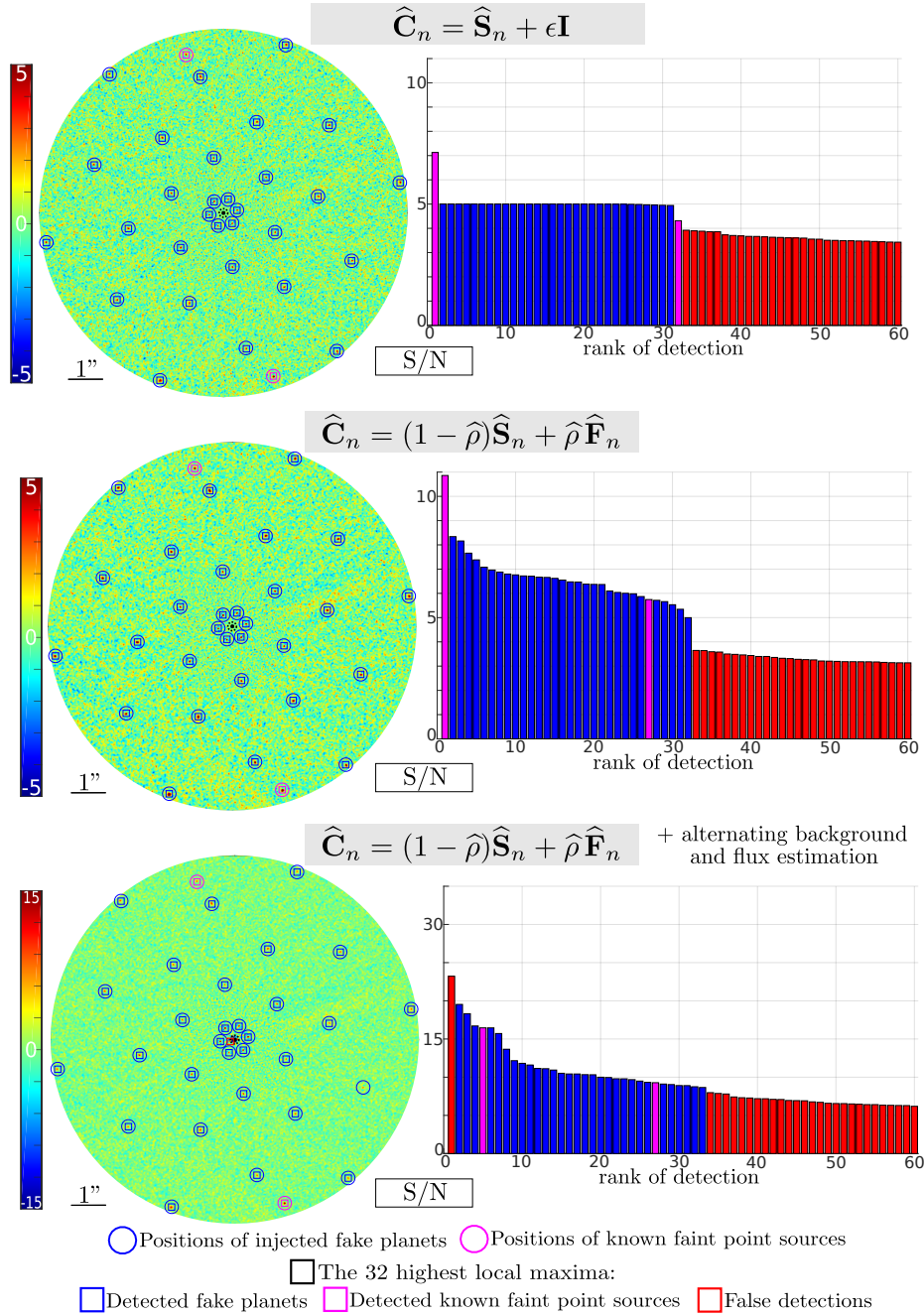


Figure 2.5 – S/N detection maps computed with the PACO algorithm. Top: covariance matrices are regularized by adding the hand-tuned fraction  $\epsilon = 10^{-6}$  of identity matrix (see Equation 2.8). Middle: covariance matrices are estimated using the unsupervised shrinkage technique (see Equations 2.10 and 2.14). Bottom: same than middle but the background statistics are estimated jointly with the source flux (see Equations 2.15). The first 32 detections are marked on the maps using square patterns. The 60 first detections are plotted as bar charts next S/N maps, ordered by decreasing S/N values, with true detections in pink (true background sources) or blue (injected fake sources), and false detections in red. Circles indicate the location of all faint point sources.

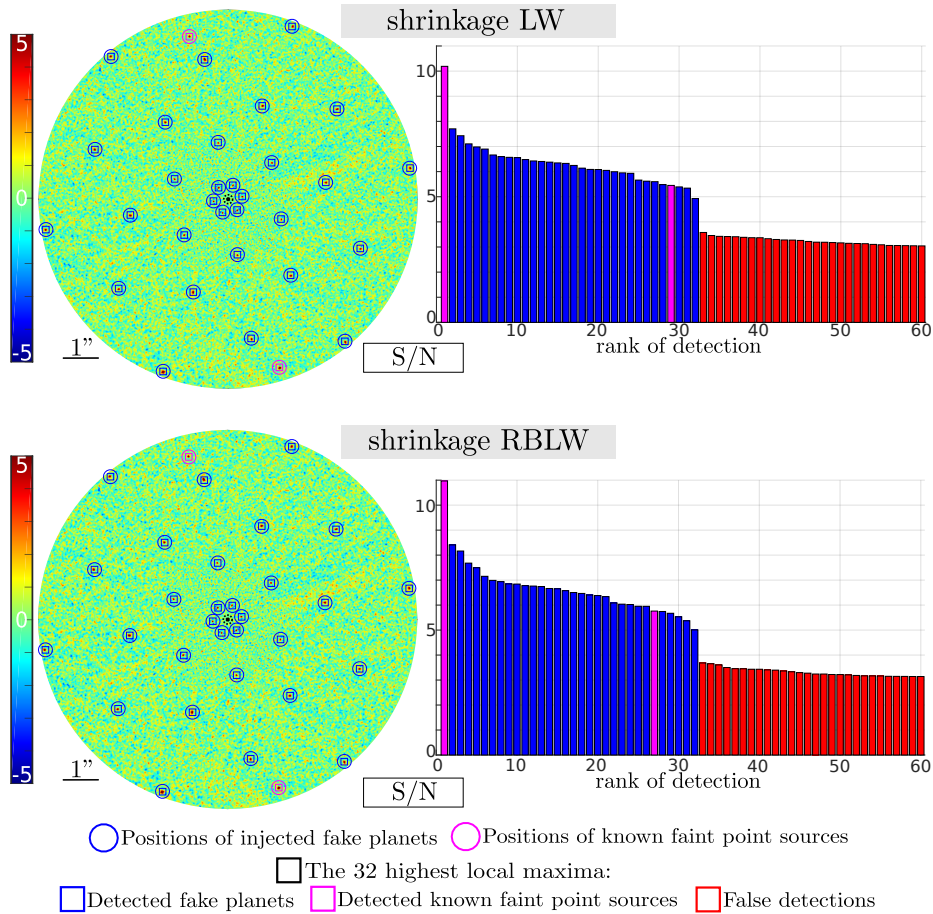


Figure 2.6 – S/N detection maps computed with the PACO algorithm. Top: covariance matrices are estimated using the Ledoit-Wolf shrinkage estimator. Bottom: covariance matrices are estimated using the Rao-Blackwell-Ledoit-Wolf shrinkage estimator. The first 32 detections are marked on the maps using square patterns. The 60 first detections are plotted as bar charts next S/N maps, ordered by decreasing S/N values, with true detections in pink (true background sources) or blue (injected fake sources), and false detections in red. Circles indicate the location of all faint point sources.

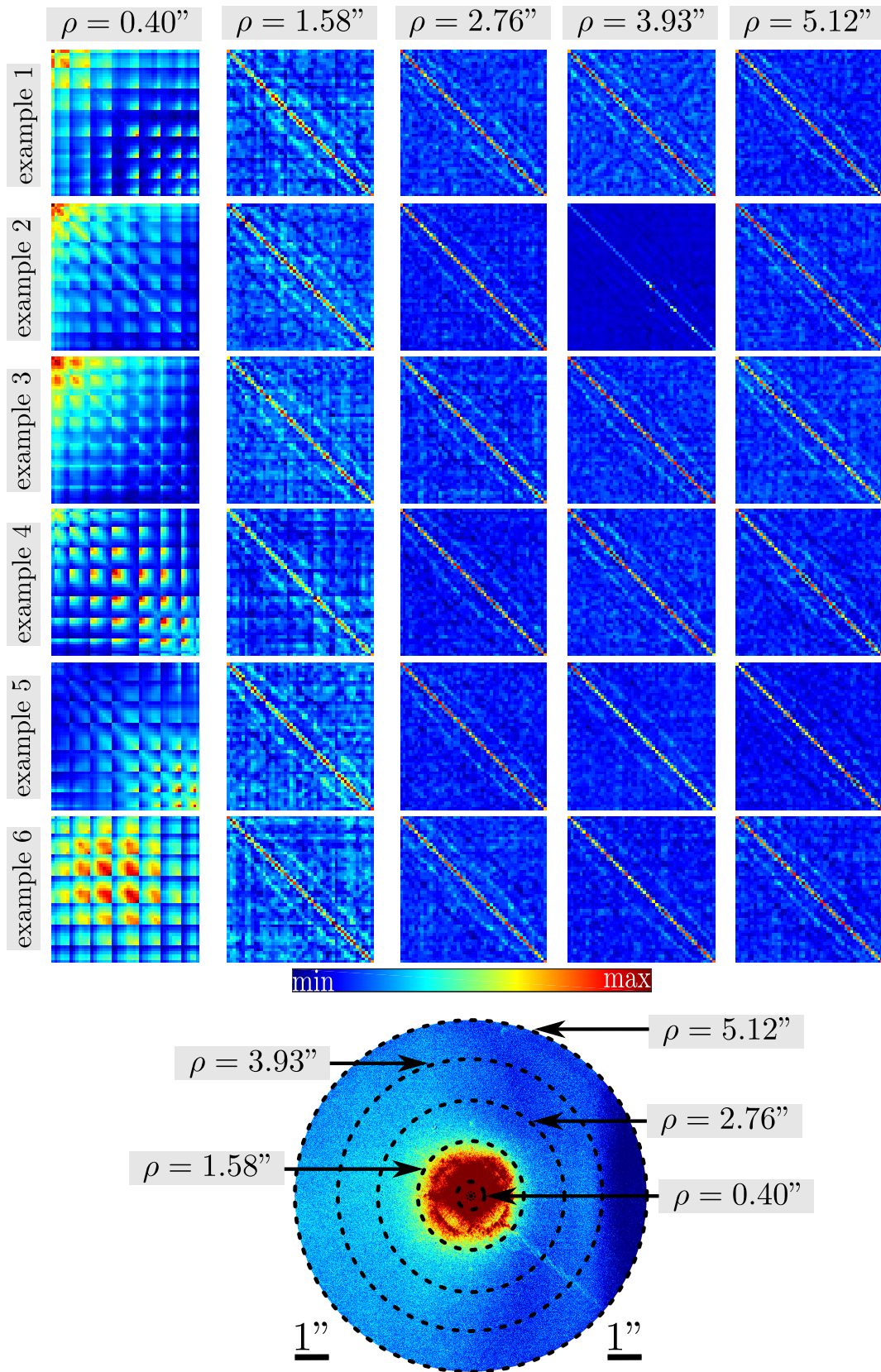


Figure 2.7 – Examples of shrunk covariance matrices  $\hat{C}_n$  estimated at different locations  $n$  of the field of view for different angular separations ( $\rho \in \{0.40; 1.58; 2.76; 3.93; 5.12\}''$ ). The results are obtained on the SPHERE-IRDIS dataset of HIP 72192 at  $\lambda_1 = 2.110\mu\text{m}$ .

Finally, we report that for a fixed patch size at  $K = 50$  pixels, the mean estimated weight  $\hat{\rho}$  is about 0.10 for a dataset containing about  $T = 100$  frames and it reaches up to 0.40 when the number of frames  $T$  is comparable with the number  $K$  of pixels in a patch. This shows that when the number of observations  $T$  is limited, the weight  $\hat{\rho}$  applied to the high bias/low variance matrices  $\hat{\mathbf{F}}$  is large, thereby compensating the expected high variance of the sample covariance matrices  $\hat{\mathbf{S}}$ . Even for non-favorable cases (when  $T \simeq K$ ), the weight given to the sample covariance matrices  $\hat{\mathbf{S}}$  remains predominant, so that  $\hat{\Sigma}$  actually captures the spatial covariances of the data.

Besides, we investigate shrinkage estimators other than OAS. We test the Ledoit-Wolf estimator (LW, obtained by replacing in the rightmost expression of (2.11) the expectation, variance and covariance by sample means, see Ledoit and Wolf (2004); Chen et al. (2010)) and the Rao-Blackwell-Ledoit-Wolf estimator (RBLW, obtained by computing the conditional expectation of the Ledoit-Wolf estimator conditionally to the sufficient statistic  $\hat{\mathbf{S}}$ , see Ledoit and Wolf (2004); Chen et al. (2010)). Figure 2.6 gives the obtained S/N maps on the same dataset than the one used in Figure 2.5. Comparison with middle part of Figure 2.5 shows that the two tested strategies lead to very similar results to that of the OAS estimator.

### Estimation of the background statistics

Each temporal collection of background patches centered at pixel  $n$  is described by a multivariate Gaussian model of mean  $\mathbf{m}_n$  and covariance  $\mathbf{C}_n$ . The mean  $\mathbf{m}_n$  is estimated by the sample mean. Due to the limited number of observations, the sample covariance is noisy or rank-deficient.

⇒ A regularization should be enforced.

- Following the shrinkage approach of Ledoit and Wolf (2004) and Chen et al. (2010), the estimated PACO covariance matrix  $\hat{\mathbf{C}}_n$  is formed by the convex combination between the sample covariance matrix  $\hat{\mathbf{S}}_n$  (low bias/high variance) and the diagonal matrix  $\hat{\mathbf{F}}_n$  (high bias/low variance) whose diagonal entries are the empirical variances:  $\hat{\mathbf{C}}_n = (1 - \hat{\rho})\hat{\mathbf{S}}_n + \hat{\rho}\hat{\mathbf{F}}_n$ .
- The weight  $\hat{\rho}$  balancing locally the bias/variance tradeoff is estimated in a data-driven fashion to minimize the expected risk. We derive its closed-form expression under the specific form of estimators  $\hat{\mathbf{S}}_n$  and  $\hat{\mathbf{F}}_n$  as well as our Gaussian assumption, thus extending the result given in Chen et al. (2010) to our estimator  $\hat{\mathbf{F}}_n$ .
- This approach proves to be adapted to our problem due to its local adaptivity, leading to better detection performance than the other regularization strategies considered.

Based on this study, we retained the unsupervised oracle-approximating shrinkage approach as an unsupervised regularization of the PACO covariances matrices. Figure 2.7 gives some examples of covariance matrices obtained at different locations of the field of view with our shrinkage approach. It emphasizes the presence of strong spatial correlations at moderate angular separations. Far from the host star, the spatial correlations are less important. Still, they remain not negligible, and they account for the

presence of outliers in the data series, like in example 2 at  $\rho = 3.93$ ” given in Figure 2.7.

### 2.3.3 Unbiased estimation of the background statistics

Although we have derived in the previous section estimators robust to the lack of observations, it should be kept in mind that background patches are not directly available. Only observed patches  $\{\mathbf{r}_{n,t}\}_{t=1:T}$  can be used to estimate the mean  $\mathbf{m}_n$  and covariance  $\mathbf{C}_n$ . Should the contribution of the exoplanet not be subtracted prior to computing the statistics of the background, the mean would contain a fraction of the PSF of the exoplanet ( $1/T$ -th of the flux of the exoplanet if the exoplanet is visible only in one of the patches centered on pixel  $n$ ). Then, the mean would be biased by the exoplanet contribution, and the covariance would encode that there are significant variations in the background in the form of an appearing/disappearing PSF. The subsequent estimation of the source flux would be penalized (biased) by these errors on the mean and covariance of the background.

The problem of the superimposition of background and exoplanet signals can be handled by several ways, given that, because of the apparent motion of the field of view, an exoplanet is not visible at the same location throughout the temporal stack:

1. by discarding patches where a hypothetical exoplanet located at  $\phi_0$  would be visible,
2. by discarding patches that are the most correlated with the off-axis PSF (i.e., patches that most likely contain an exoplanet),
3. by using robust estimators (the exoplanet signal being considered as an outlier, as in LLSG (Gomez Gonzalez et al., 2016)),
4. by jointly estimating the flux of the exoplanet and the statistics of the background.

All these methods have been compared and we found the last approach to be the most successful. Approach 1 has a significant drawback: by excluding (during the learning of background statistics) all patches that are later considered in the exoplanet detection test, the test becomes much noisier. Approach 2 is more satisfactory in this respect, but does not completely solve the problem: estimation of the flux of an exoplanet is biased due to the errors in the estimation of parameters  $\widehat{\mathbf{m}}_n$  and  $\widehat{\mathbf{C}}_n$ . Approach 3 can be implemented in several ways. We considered replacing the sample mean by the median and a two-step estimation of the covariance, where, in the second step, patches  $\mathbf{r}_n$  leading to large Mahalanobis distances  $(\mathbf{r}_n - \widehat{\mathbf{m}}_n)^\top \cdot \widehat{\mathbf{C}}_n^{-1} \cdot (\mathbf{r}_n - \widehat{\mathbf{m}}_n)$  were discarded in the computation of the covariance matrix. Only the joint estimation led to truly unbiased estimates of the photometry in our numerical experiments (see Section 2.5 for results about unbiased photometry estimation).

We implement Approach 4 by alternating flux estimation and background statistics estimation, starting from an initial guess of pure background. At the  $q$ -th iteration, after a flux  $\widehat{\alpha}^{(q)}$  has been estimated for the exoplanet assuming background statistics  $\widehat{\mathbf{C}}^{(q)}$



(as explained in Section 2.3.4), the background statistics can be improved by removing the contribution of the exoplanet:

$$\left\{ \begin{array}{l} \widehat{\mathbf{m}}_n^{(q+1)} = \frac{1}{T} \sum_{t=1}^T (\mathbf{r}_{n,t} - \widehat{\alpha}^{(q)} \mathbf{h}_n(\phi_t)) \\ \widehat{\mathbf{S}}_n^{(q+1)} = \frac{1}{T} \sum_{t=1}^T (\mathbf{r}_{n,t} - \widehat{\alpha}^{(q)} \mathbf{h}_n(\phi_t) - \widehat{\mathbf{m}}_n^{(q+1)}) \cdot (\mathbf{r}_{n,t} - \widehat{\alpha}^{(q)} \mathbf{h}_n(\phi_t) - \widehat{\mathbf{m}}_n^{(q+1)})^\top \\ [\widehat{\mathbf{F}}_n^{(q+1)}]_{ii} = [\widehat{\mathbf{S}}_n^{(q+1)}]_{ii} \\ \widehat{\rho}^{(q+1)} = \widehat{\rho}(\widehat{\mathbf{S}}_n^{(q+1)}) \\ \widehat{\mathbf{C}}_n^{(q+1)} = (1 - \widehat{\rho}^{(q+1)}) \widehat{\mathbf{S}}_n^{(q+1)} + \widehat{\rho}^{(q+1)} \widehat{\mathbf{F}}_n^{(q+1)}. \end{array} \right. \quad (2.15)$$

A few iterations of (2.15) and exoplanet flux re-estimations corrects the statistics of the background and prevents from biasing the estimation of the photometry by an erroneous statistical model of the background.

### Unbiased background statistics

- In the presence of an exoplanet, pure background patches are not available to estimate the statistics of the background. The subsequent estimation of the source flux is biased by resulting errors on the mean and covariance of the background.
- We propose to estimate alternatively (i) the background statistics on patches in which the source is subtracted, and (ii) the source flux, to correct the statistics of the background and prevent from biasing the estimation of the photometry.
- While this leads to unbiased photometry characterization, we experimentally show that this approach is not beneficial for detection since it changes the distribution of the detection test in the absence of exoplanet. We thus split our algorithm into two phases:
  1. a *detection step* based on the computation of biased background statistics, leading to a grounded detection test but biased exoplanet photometry,
  2. a *characterization step* is then launched locally around detected sources based on an iterative estimation of the exoplanet flux and background statistics, leading to the unbiased photometry.

The bottom part of Figure 2.5 gives the resulting detection map when the background statistics are estimated jointly with the source flux. This map can be compared to the map in the middle row of the same figure. One can notice that the unbiased estimation of the flux of the exoplanet is not beneficial in the exoplanet detection phase. Indeed, it improves the signal of the exoplanets, but it also changes the distribution of the detection test (see Equation (2.26) for the definition) in the absence of exoplanet, which makes more difficult the setting of a detection threshold. Even a hand-tuned

threshold does not improve the limit detection contrast, the increase of the probability of false alarm exceeding the improvement of the detection probability.

Therefore, we split our exoplanet detection and characterization algorithm into two steps. We start with a *detection step* in which we compute the background statistics  $\widehat{\mathbf{m}}_n$  and  $\widehat{\mathbf{C}}_n$  based on Equations (2.7), (2.9), (2.10) and (2.14) to derive a detection map (see Section 2.3.5). A *characterization step* is then launched by alternating Equations (2.15) with a re-estimation of the flux for the photometric and astrometric estimations only for the detected sources (see Sections 2.3.4 and 2.3.6).

### 2.3.4 Estimation of the flux of an exoplanet

Under our multivariate Gaussian model of the background, the maximum likelihood estimator given in Equation (2.3) for an assumed initial location  $\phi_0$  has a simple expression (see for example Kay, 1998b):

$$\widehat{\alpha} = \frac{\sum_{t=1}^T b_t}{\sum_{t=1}^T a_t}, \quad (2.16)$$

with

$$a_t = \mathbf{h}_{\lfloor \phi_t \rfloor}(\phi_t)^\top \cdot \widehat{\mathbf{C}}_{\lfloor \phi_t \rfloor}^{-1} \cdot \mathbf{h}_{\lfloor \phi_t \rfloor}(\phi_t) \quad (2.17)$$

and

$$b_t = \mathbf{h}_{\lfloor \phi_t \rfloor}(\phi_t)^\top \cdot \widehat{\mathbf{C}}_{\lfloor \phi_t \rfloor}^{-1} \cdot \left( \mathbf{r}_{\lfloor \phi_t \rfloor, t} - \widehat{\mathbf{m}}_{\lfloor \phi_t \rfloor} \right), \quad (2.18)$$

where we recall that  $\mathbf{h}_{\lfloor \phi_t \rfloor}(\phi_t)$  denotes the off-axis PSF for a source at (subpixel) location  $\phi_t$  sampled over a patch of  $K$  pixels and whose center is  $\lfloor \phi_t \rfloor$ , the nearest pixel to  $\phi_t$ . Note that the term  $b_t$  can be interpreted as a correlation between the whitened off-axis PSF and the whitened (zero-mean) measurements while the term  $a_t$  corresponds to the auto-correlation of the whitened off-axis PSF.

The maximum likelihood estimator  $\widehat{\alpha}$  given in Equation (2.16) depends linearly on the data, hence its variance can be easily derived. Noting that  $\widehat{\alpha} = a/b$  with  $a = \sum_{t=1}^T a_t$  and  $b = \sum_{t=1}^T b_t$ , we obtain:

$$\text{Var}\{\widehat{\alpha}\} \approx \text{Var}\{b\}/a^2, \quad (2.19)$$

where the approximation becomes an equality if  $a$  is considered deterministic<sup>6</sup>. The variance of  $b$  is the sum of the variances of the  $b_t$  terms since they are mutually independent (corresponding to different temporal frames). From its expression in Equation (2.18), the variance of  $b_t$  is given by:

$$\text{Var}\{b_t\} \approx \mathbf{h}_{\lfloor \phi_t \rfloor}(\phi_t)^\top \cdot \widehat{\mathbf{C}}_{\lfloor \phi_t \rfloor}^{-1} \cdot \text{Cov}\{\mathbf{r}_{\lfloor \phi_t \rfloor, t} - \widehat{\mathbf{m}}_{\lfloor \phi_t \rfloor}\} \cdot \widehat{\mathbf{C}}_{\lfloor \phi_t \rfloor}^{-1} \cdot \mathbf{h}_{\lfloor \phi_t \rfloor}(\phi_t). \quad (2.20)$$

Our assumptions amount to approximating the distribution of the term  $\mathbf{r}_{\lfloor \phi_t \rfloor, t} - \widehat{\mathbf{m}}_{\lfloor \phi_t \rfloor}$  by a centered Gaussian of covariance  $\widehat{\mathbf{C}}_{\lfloor \phi_t \rfloor}$ . The variance of  $b_t$  therefore simplifies to:

$$\text{Var}\{b_t\} \approx \mathbf{h}_{\lfloor \phi_t \rfloor}(\phi_t)^\top \cdot \widehat{\mathbf{C}}_{\lfloor \phi_t \rfloor}^{-1} \cdot \mathbf{h}_{\lfloor \phi_t \rfloor}(\phi_t) = a_t. \quad (2.21)$$

---

6. The approximation neglects the dependence of the term  $a$  with respect to the estimated quantity  $\widehat{\mathbf{C}}^{-1}$  (which is not deterministic since it depends on the observations). The variance of  $\widehat{\mathbf{C}}^{-1}$  can be neglected in front of the variance of the intensity patches  $\mathbf{r}$  since  $\widehat{\mathbf{C}}$  is estimated from a relatively large number of samples.



Thus an approximate estimator of the variance of  $b = \sum_{t=1}^T b_t$  is  $\sum_{t=1}^T a_t = a$  and the standard deviation of  $\hat{\alpha} = b/a$  can be estimated by:

$$\hat{\sigma}_\alpha \approx 1/\sqrt{a}. \quad (2.22)$$

Obviously, the flux of the source is necessarily positive, we denote by  $\hat{\alpha}^+$  the flux obtained under a positivity constraint<sup>7</sup> (see Thiébaud and Mugnier (2005); Mugnier et al. (2009)):

$$\begin{aligned} \hat{\alpha}^+ &\stackrel{\text{def}}{=} \arg \max_{\alpha \geq 0} p_f(\{r_{n,t} - \alpha h_n(\mathcal{F}_t(\phi_0))\}_{n=1:N, t=1:T}) \\ &= \max(\hat{\alpha}, 0) = \frac{\max(\sum_{t=1}^T b_t, 0)}{\sum_{t=1}^T a_t}. \end{aligned} \quad (2.23)$$

### 2.3.5 Detection of exoplanets

Under our multivariate Gaussian model of the background, the generalized likelihood ratio test (2.5) takes the simplified form:

$$(\text{GLRT}) \quad \frac{\left(\sum_{t=1}^T b_t\right)^2}{\sum_{t=1}^T a_t} \underset{\mathcal{H}_0}{\overset{\mathcal{H}_1}{\gtrless}} \eta, \quad (2.24)$$

with  $a_t$  and  $b_t$  defined according to Equations (2.17) and (2.18).

As discussed in Thiébaud and Mugnier (2005); Smith et al. (2009); Mugnier et al. (2009), it is beneficial to enforce a positivity constraint on the flux  $\alpha$  in the detection test, i.e., to use the estimate  $\hat{\alpha}^+$  to derive the GLRT expression, leading to:

$$(\text{GLRT}^+) \quad \frac{\left(\max(\sum_{t=1}^T b_t, 0)\right)^2}{\sum_{t=1}^T a_t} \underset{\mathcal{H}_0}{\overset{\mathcal{H}_1}{\gtrless}} \eta. \quad (2.25)$$

As noted in Mugnier et al. (2009), the test (2.25) is equivalent to the test:

$$(\text{S/Ntest}) \quad \frac{\sum_{t=1}^T b_t}{\sqrt{\sum_{t=1}^T a_t}} \approx \frac{\hat{\alpha}}{\hat{\sigma}_\alpha} \underset{\mathcal{H}_0}{\overset{\mathcal{H}_1}{\gtrless}} \tau \quad (2.26)$$

when  $\eta \geq 0$ , with  $\tau = \sqrt{\eta}$ . This test can be interpreted as the signal-to-noise ratio (S/N)  $\hat{\alpha}/\hat{\sigma}_\alpha$  of the estimation of the (unconstrained) flux of the source  $\alpha$ . Note that with our definition, the S/N is a signed quantity that is negative whenever  $\hat{\alpha} < 0$ .

The test (S/Ntest) in Equation (2.26) is attractive because the test value  $\hat{\alpha}/\hat{\sigma}_\alpha$  linearly depends on the data. Under our Gaussian model for the data, the S/N  $\hat{\alpha}/\hat{\sigma}_\alpha$  is thus also approximately Gaussian distributed (with unit variance) which simplifies the statistical analysis of the test in terms of false alarm rate or detection probability. This analysis is carried out in the following.

In the hypothesis test (2.4), we considered a hypothetical initial location of the source  $\phi_0$ . To detect all sources within the field of view and locate their positions, the test (S/Ntest) should be evaluated at locations  $\phi_0$  sampled over the whole field of view. By refining the sampling of the field of view, the off-axis PSFs  $\mathbf{h}_{|\phi_t|}(\phi_t)$  better matches the data and the estimate  $\hat{\alpha}$  is more accurate, at the cost of a larger computational effort. Sampling of the field of view is discussed in Section 2.4.5.

---

7. The neg-log-likelihood is a quadratic function of  $\alpha$ , the minimum under positivity constraint is thus obtained by simple thresholding.

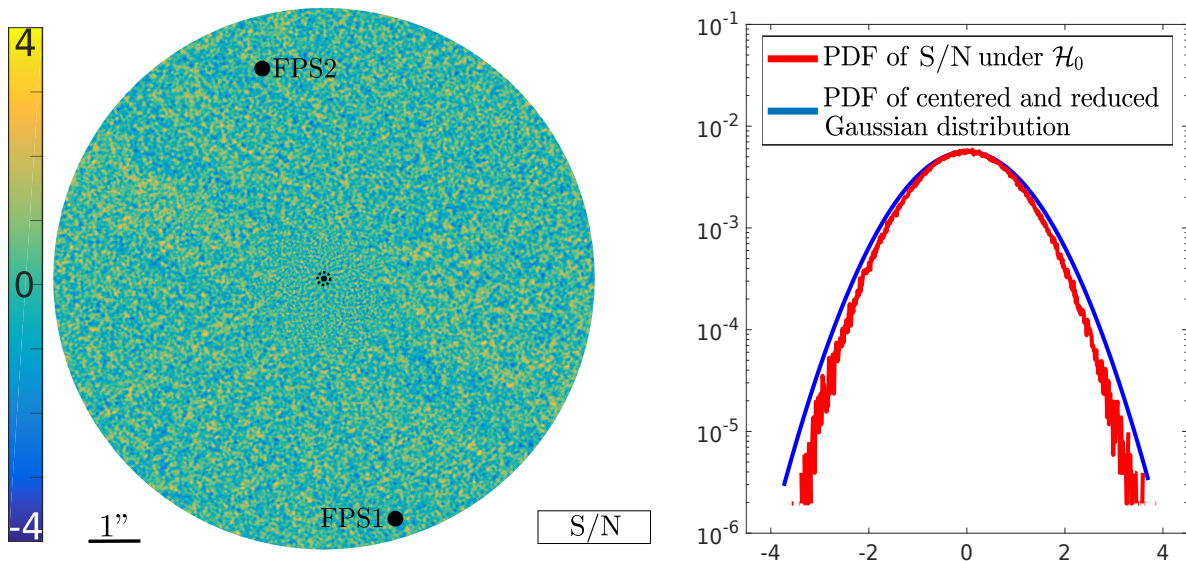


Figure 2.8 – S/N map in absence of object (the two real known faint point sources denoted FPS1 and FPS2 are masked) and its corresponding empirical distribution using the HIP 72192 dataset described in Section 2.5 at  $\lambda_2 = 2.251 \mu\text{m}$ .

## 2.3.6 Statistical properties

### 2.3.6.1 Distribution of the detection criterion

Figure 2.8 illustrates a S/N map  $\hat{\alpha}/\hat{\sigma}_\alpha$  computed using the PACO method on the same VLT/SPHERE-IRDIS dataset around HIP 72192 star as previously at  $\lambda_2 = 2.251 \mu\text{m}$  (more details are given in Section 2.5), with the two real point-sources masked. Visual inspection of the S/N map (left part of Figure 2.8) indicates that the detection criterion is approximately stationary over the field of view<sup>8</sup>, even close to the coronagraphic mask. The empirical distribution of the S/N values (right part of Figure 2.8) shows that the S/N distribution can be considered as a Gaussian that is centered (the empirical mean is 0.01) and approximately reduced (the empirical standard deviation is 0.93). This distribution passes successfully the Lilliefors normality test (Lilliefors, 1967) at the 5% significance level. The relatively good agreement between the empirical distribution of the S/N test and a centered Gaussian distribution of unit variance also supports the assumptions made in Equations (2.19) to (2.26) that neglect the variance of the estimated covariance  $\hat{\mathbf{C}}$ . The small discrepancy with theoretical model may be due to temporal fluctuations that will be better modeled in Chapter 4. The hypothesis that the variance of the S/N under  $\mathcal{H}_0$  is equal to 1 is conservative in the sense that the probability of false alarm is slightly overestimated. Owing to the homogeneous distribution of the S/N criterion across the field of view, this small shift of the detection threshold could be easily fixed by rescaling the S/N by a single factor empirically estimated. No such correction was performed in the following results, though.

Under the hypothesis  $\mathcal{H}_0$ , the S/N follows a centered and reduced Gaussian law

8. The stationarity of the PACO detection maps in the absence of source can be appreciated by comparison with the detection maps presented in Section 2.5.2.1 (in particular in Figures 2.16, 2.17, and 2.22) that are obtained with several state-of-art detection methods.

whatever the angular separation. It is thus possible to apply a unique threshold  $\tau$  to the S/N maps and obtain a consistent detection performance at all angular separations (i.e., a constant false alarm rate). The good fit between the S/N empirical distribution and a Gaussian distribution makes it possible to directly assess the false alarm rate, probability of detection, photometric and astrometric accuracies without post-processing and/or resorting to Monte-Carlo methods (injection of fake exoplanets in the data) in contrast to several state-of-the-art methods, as discussed in Section 2.2.5.

### 2.3.6.2 Probabilities of false alarm and of true detection

The probability of false alarm (PFA) is the probability that the test (2.26) yields  $\mathcal{H}_1$  while  $\mathcal{H}_0$  is actually true, under the assumption that the S/N test (2.26) is Gaussian distributed:

$$\text{PFA}(\tau) = \Pr(\hat{\alpha}/\hat{\sigma}_\alpha > \tau \mid \mathcal{H}_0) = \int_\tau^{+\infty} \frac{1}{\sqrt{2\pi}} \exp\left(-\frac{x^2}{2}\right) dx = 1 - \Phi(\tau), \quad (2.27)$$

where  $\Phi$  is the cumulative distribution function of the standard normal distribution. It is common practice in direct imaging to set the detection threshold  $\tau$  at 5 ( $5\sigma$  detection threshold), thus ensuring a probability of false alarm equal to  $\text{PFA}(5) = 2.87 \times 10^{-7}$ .

The probability of detection (PD) is the probability that the test (2.26) correctly decides for a detection:

$$\begin{aligned} \text{PD}(\tau, \alpha) &= \Pr(\hat{\alpha}/\hat{\sigma}_\alpha > \tau \mid \mathcal{H}_1) = \int_\tau^{+\infty} \frac{1}{\sqrt{2\pi}} \exp\left(\frac{-(x - \alpha/\hat{\sigma}_\alpha)^2}{2}\right) dx \\ &= 1 - \Phi(\tau - \alpha/\hat{\sigma}_\alpha). \end{aligned} \quad (2.28)$$

least equal to some prescribed value PD when the detection threshold  $\tau$  is set according to a given PFA level can be computed by inverting and combining Equations (2.27) and (2.28):

$$\alpha = \left(\Phi^{-1}(1 - \text{PFA}) - \Phi^{-1}(1 - \text{PD})\right) \times \hat{\sigma}_\alpha. \quad (2.29)$$

For example, at  $\tau = 5$ , a probability of detection of 50% is achieved for  $\alpha = 5\hat{\sigma}_\alpha$  and a probability of detection of 80% for  $\alpha = 5.84\hat{\sigma}_\alpha$ . Figure 2.9 illustrates the S/N distribution under the two hypothesis as well as the probabilities of false alarm and of detection.

### 2.3.6.3 Astrometric accuracy

An (asymptotically) unbiased estimator of the position of the source is provided by the maximum likelihood position which is the solution of a non-convex optimization problem. In practice, this problem can be solved by exhaustive search at a finite resolution refined by a local optimization as for example proposed by Soulez et al. (2007a) in digital lensless microscopy for the detection of parametric objects spread in a volume (see Section 1.3.2.2). The astrometric accuracy, i.e. the accuracy on the angular location of the detected objects can be statistically predicted using the Cramér-Rao lower bounds (CRLBs) which represents the minimal variance of any unbiased estimator (Kendall et al., 1948).

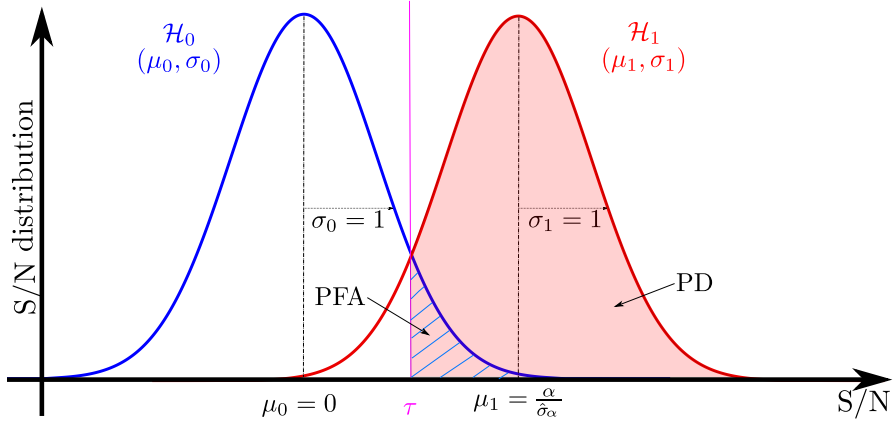


Figure 2.9 – S/N distribution under  $\mathcal{H}_0$  (in blue) and  $\mathcal{H}_1$  (in red). The hatched area is equal to the probability of false alarm (PFA) while the filled area is equal to the probability of detection (PD).

Using a parametric model of the off-axis PSF  $\mathbf{h}$  and noting again that the collection of patches  $\{\mathbf{r}_{n,t}\}_{t=1:T}$  located at the angular position  $n$  is described by a multi-variate Gaussian process  $\mathcal{N}(\cdot | \mathbf{m}_n, \mathbf{C}_n)$ , it is possible to derive the CRLBs from the observed intensity model given in Equation (2.1). In the following,  $\mathbf{\Omega} = \{\alpha, x_0, y_0\}$  (with  $\phi_0 = \{x_0, y_0\}$  the angular position of an exoplanet at time  $t_0$ ) denotes the vector of parameters from which the CRLBs are computed. For a given angular position  $n$ , the Fisher information matrix  $\mathbf{I}_n^F$  can be expressed as (Kendall et al., 1948):

$$[\mathbf{I}_n^F(\mathbf{\Omega})]_{i,j} = \frac{\partial \alpha \mathbf{h}_n(\mathbf{\Omega})^\top}{\partial \Omega_i} \cdot \mathbf{C}_n^{-1} \cdot \frac{\partial \alpha \mathbf{h}_n(\mathbf{\Omega})}{\partial \Omega_j}, \quad (2.30)$$

in which the term  $\alpha \mathbf{h}_n$  represents the off-axis PSF (an isotropic Gaussian can typically be used as a continuous model to compute the derivatives). It follows that the standard deviation  $\boldsymbol{\delta}_n$  on the estimation of the parameter vector  $\mathbf{\Omega}$  is given by:

$$[\boldsymbol{\delta}_n]_i = \sqrt{[\mathbf{I}_n^F(\mathbf{\Omega})^{-1}]_{i,i}} \quad (2.31)$$

A CRLBs map (all the pixels  $n$  of the field of view) for the parameters  $\mathbf{\Omega} = \{\alpha, x_0, y_0\}$ , can be efficiently computed using closed-form expressions of the inverse of Fisher information matrix:

$$\mathbf{I}^F = \begin{bmatrix} I_{\alpha,\alpha}^F & I_{\alpha,x_0}^F & I_{\alpha,y_0}^F \\ I_{x_0,\alpha}^F & I_{x_0,x_0}^F & I_{x_0,y_0}^F \\ I_{y_0,\alpha}^F & I_{y_0,x_0}^F & I_{y_0,y_0}^F \end{bmatrix}. \quad (2.32)$$

This leads, for the estimated vector  $\mathbf{\Omega} = \{\alpha, x_0, y_0\}$ , to the respective CRLBs:

$$\sigma_\alpha^2 = \frac{I_{x_0,x_0}^F I_{y_0,y_0}^F - (I_{x_0,y_0}^F)^2}{D}, \sigma_{x_0}^2 = \frac{I_{\alpha,\alpha}^F I_{y_0,y_0}^F - (I_{\alpha,y_0}^F)^2}{D}, \sigma_{y_0}^2 = \frac{I_{\alpha,\alpha}^F I_{x_0,x_0}^F - (I_{\alpha,x_0}^F)^2}{D}, \quad (2.33)$$

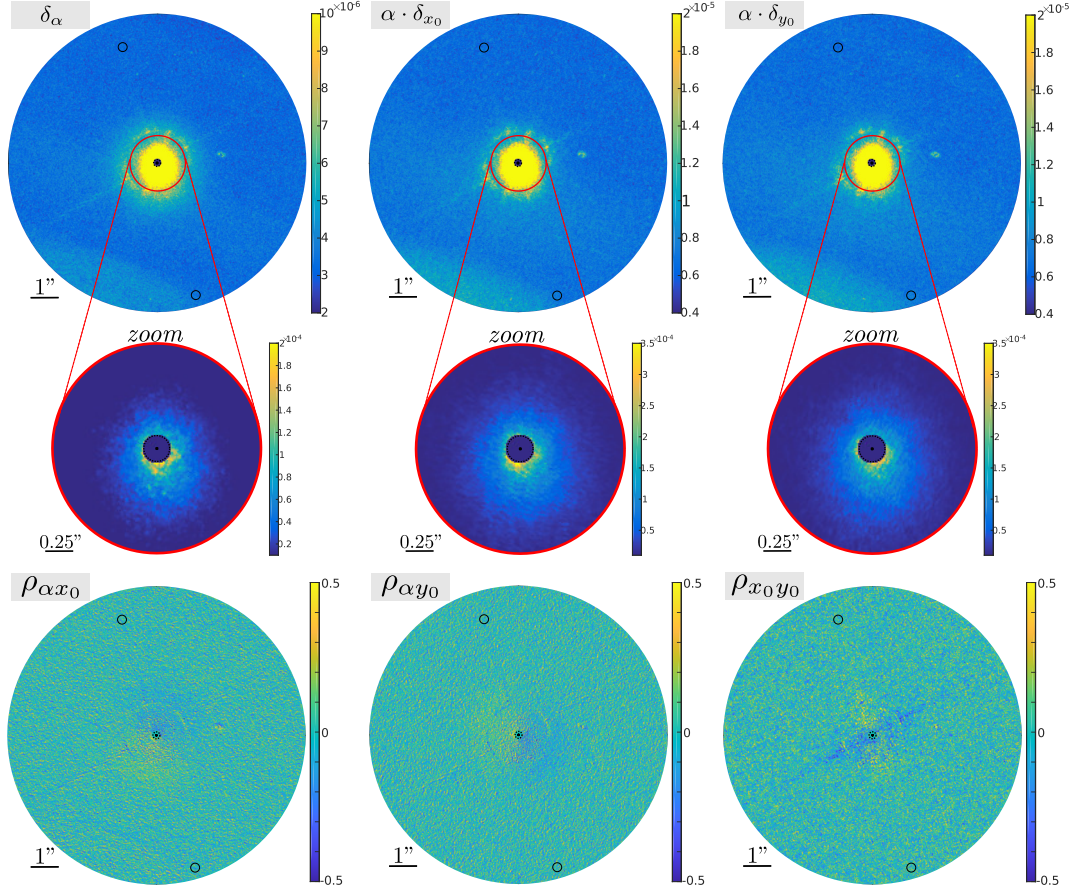


Figure 2.10 – Upper line: Minimal standard deviation (estimated Cramér-Rao lower bounds)  $\delta = \{\delta_\alpha, \delta_{x_0}, \delta_{y_0}\}$  on the estimated parameters  $\Omega = \{\alpha, x_0, y_0\}$ .  $\delta_{x_0}$  and  $\delta_{y_0}$  are multiplied by the flux  $\alpha$  of the exoplanet (expressed in pixels  $\times$  flux). For these two latter quantities, the values should be divided by the flux of the source before being interpreted in terms of confidence intervals on the astrometry. Middle line: Zoom near the host star. Lower line: Coefficients of correlation  $\rho = \{\rho_{\alpha x_0}, \rho_{\alpha y_0}, \rho_{x_0 y_0}\}$  between the estimated parameters  $\Omega = \{\alpha, x_0, y_0\}$ . The computation is performed on the HIP 72192 dataset at  $\lambda_1 = 2.110 \mu\text{m}$ . The positions of the two real faint point sources in the dataset are represented by a circle (not visible otherwise on these maps because the accuracy at their location is similar to the accuracy in the surrounding area).

where

$$D = I_{\alpha, \alpha}^F I_{x_0, x_0}^F I_{y_0, y_0}^F + 2 I_{\alpha, x_0}^F I_{\alpha, y_0}^F I_{x_0, y_0}^F - I_{\alpha, \alpha}^F (I_{x_0, y_0}^F)^2 - I_{y_0, y_0}^F (I_{\alpha, x_0}^F)^2 - I_{x_0, x_0}^F (I_{\alpha, y_0}^F)^2 \quad (2.34)$$

is the determinant of  $\mathbf{I}^F$ .

The minimal standard deviations are given by  $\delta = \{\sigma_\alpha, \sigma_{x_0}, \sigma_{y_0}\}$ . The correlation



coefficients between parameters are obtained by:

$$\rho_{\alpha,x_0} = \frac{I_{\alpha,y_0}^F I_{x_0,y_0}^F - I_{\alpha,x_0}^F I_{y_0,y_0}^F}{\sqrt{\left(I_{x_0,x_0}^F I_{y_0,y_0}^F - \left(I_{x_0,y_0}^F\right)^2\right) \left(I_{\alpha,\alpha}^F I_{y_0,y_0}^F - \left(I_{\alpha,y_0}^F\right)^2\right)}}, \quad (2.35)$$

$$\rho_{\alpha,y_0} = \frac{I_{\alpha,x_0}^F I_{x_0,y_0}^F - I_{\alpha,y_0}^F I_{x_0,x_0}^F}{\sqrt{\left(I_{x_0,x_0}^F I_{y_0,y_0}^F - \left(I_{x_0,y_0}^F\right)^2\right) \left(I_{\alpha,\alpha}^F I_{x_0,x_0}^F - \left(I_{\alpha,x_0}^F\right)^2\right)}}, \quad (2.36)$$

$$\rho_{x_0,y_0} = \frac{I_{\alpha,y_0}^F I_{\alpha,x_0}^F - I_{\alpha,\alpha}^F I_{x_0,y_0}^F}{\sqrt{\left(I_{\alpha,\alpha}^F I_{y_0,y_0}^F - \left(I_{\alpha,y_0}^F\right)^2\right) \left(I_{\alpha,\alpha}^F I_{x_0,x_0}^F - \left(I_{\alpha,x_0}^F\right)^2\right)}}. \quad (2.37)$$

Since  $\{I_{x_0,x_0}, I_{y_0,y_0}\}$  are proportional to  $\alpha^2$ ,  $\{I_{\alpha,x_0}, I_{\alpha,y_0}\}$  to  $\alpha$ , and  $I_{\alpha,\alpha}$  is not dependent on  $\alpha$ ;  $D$  is proportional to  $\alpha^4$ . Hence,  $\delta_\alpha$  is not dependent on  $\alpha$  while  $\{\delta_{x_0}, \delta_{y_0}\}$  are proportional to  $\alpha^{-1}$ .

### Detection test & statistical properties

Based on our multivariate Gaussian model of the background, we derive the maximum likelihood estimator of the exoplanet flux, a detection test, and subsequent statistical properties.

- The detection test can be interpreted as a signal-to-noise ratio and follows in good approximation, and in the absence of exoplanet, a centered and reduced Gaussian distribution. This key component of the PACO algorithm allows to directly interpret detection maps in terms of false alarm rate and probability of detection.
- Astrometric and photometric accuracies are also statistically characterized from the Cramér-Rao lower bounds.

For simplicity, we denote by  $\boldsymbol{\delta} = \{\delta_\alpha, \delta_{x_0}, \delta_{y_0}\}$  the spatial maps representing the accuracy on the parameters  $\boldsymbol{\Omega} = \{\alpha, x_0, y_0\}$ . It can be noted that the CRLB  $\delta_\alpha$  on the source flux differs from the estimator  $\hat{\sigma}_\alpha$  since  $\delta_\alpha$  also accounts for the imprecision on the estimation of the astrometry of the sources. Figure 2.10 gives a view of  $\delta_\alpha$ ,  $\delta_{x_0}$  and  $\delta_{y_0}$  as well as the correlation coefficients  $\rho_{\alpha x_0}$ ,  $\rho_{\alpha y_0}$  and  $\rho_{x_0 y_0}$  between estimated parameters obtained on the HIP 72192 dataset at  $\lambda_1 = 2.110 \mu\text{m}$ . As expected, the estimation error of  $\boldsymbol{\Omega} = \{\alpha, x_0, y_0\}$  increases near the host star. The figure also emphasizes that the Cramér-Rao bounds  $\{\delta_\alpha, \delta_{x_0}, \delta_{y_0}\}$  decrease quickly with the angular separation. Moreover, a small estimation error on one of the three parameters has little impact on the estimation of the other two parameters (low absolute correlation coefficients) except for some localized areas of the field of view. The resulting Cramér-Rao bounds can be usefully considered to evaluate the error on the estimated parameters. For example, for the two real faint point sources located around the HIP 72192 star (their positions are symbolized by a circle in Figure 2.10, the products  $\alpha \cdot \delta_{x_0}$  and  $\alpha \cdot \delta_{y_0}$  are close to  $0.7 \times 10^{-5}$  pixel. This means that at a contrast (i.e., amplitude of the source normalized by the amplitude of the star)  $\alpha = 10^{-5}$ , the sources can be located with an accuracy of about 0.7 pixel.

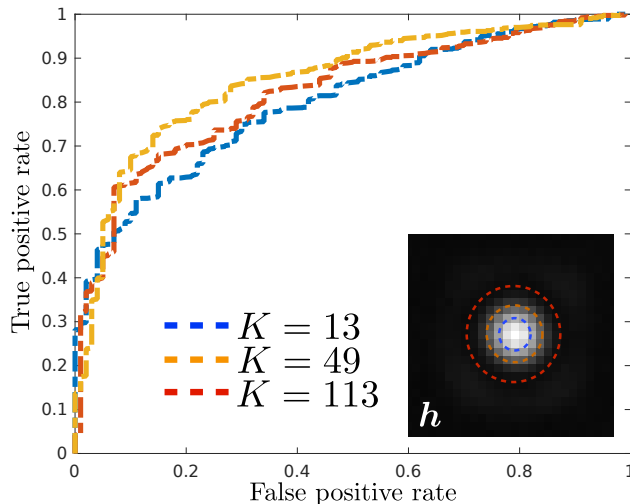


Figure 2.11 – Influence of the patch size: ROC curves for  $K = \{13, 49, 113\}$  pixels in each patch. The ROC curves are obtained by inserting fake exoplanets at a flux  $\alpha \in [10^{-6}; 10^{-5}]$  on the HIP 72192 dataset at  $\lambda_1 = 2.110 \mu\text{m}$ .

## 2.4 Implementation details of PACO

This section is devoted to the description of the implementation of the PACO algorithm presented in Section 2.3. A simplified and faster version for the detection step is also described. This fast version can be useful to conduct pre-analyses in large surveys.

### 2.4.1 Optimal patch size

The patches considered in the PACO algorithm define the area in which the statistics of the background fluctuations are modeled. Since the core of the off-axis PSF is close to circular symmetry, circular patches are used. Their size obeys a tradeoff: on the one hand, the larger the patches, the more energy from the source is contained in the patches which improve the signal-to-noise ratio; on the other hand, learning the covariance of larger patches requires more samples (i.e., more temporal frames).

In practice, since the sources to be detected are faint compared to the level of stellar speckles and their temporal fluctuations, only the core of the off-axis PSF is necessary to perform the detection and a patch size corresponding to twice the off-axis PSF full width at half maximum (FWHM) appears to be a good tradeoff. A more precise (and automatic) determination of the optimal size of the patches with respect to the number of time frames and the structure of the background correlations can be carried out by Monte-Carlo simulations. False exoplanets are randomly injected into the data and receiver operating characteristic (ROC) curves representing the detection probabilities as a function of the false alarm rate are constructed for different patch sizes. The patch size maximizing the area under the ROC curve is then adopted. Figure 2.11 gives ROC curves for three patch sizes and shows that the choice  $K = 49$  pixels per patch, i.e. a patch of 4 pixels of radius, maximizes the area under the curve and is, therefore, the best tradeoff for performing the detection on the HIP 7192 dataset (with 4.5 pixels FWHM) for fake exoplanets injected at a flux  $\alpha$  in the range  $[10^{-6}; 10^{-5}]$ . The number



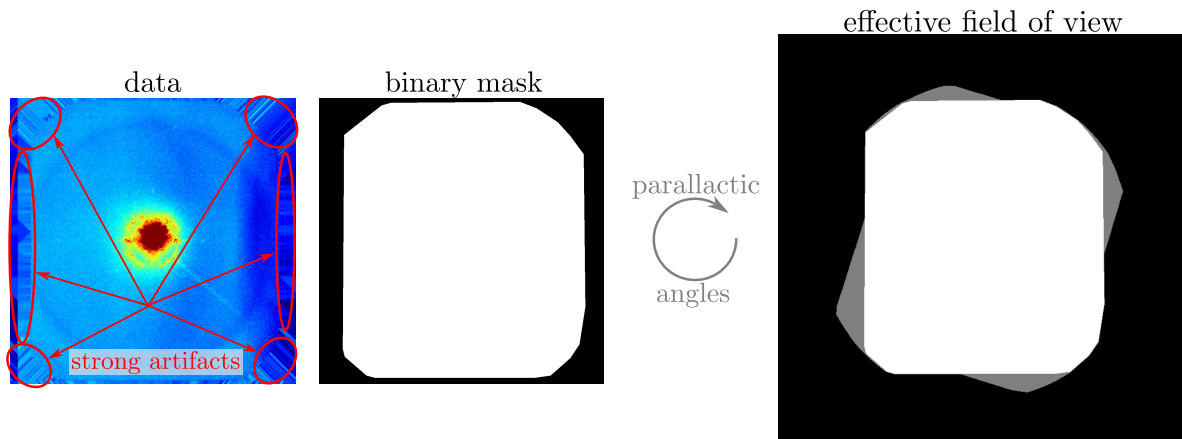


Figure 2.12 – Taking into account missing data: from left to right, a data frame from the VLT/SPHERE-IRDIS instrument, the hand-defined mask discarding aberrant data and the resulting total field of view due to the rotation.

of pixels per patch  $K$  needs to be determined only once for a given instrument since the FWHM of the off-axis PSF varies only marginally from one observation to another.

## 2.4.2 Taking into account missing data

Two aspects are linked to the problem of missing data.

The first one is related to aberrant values occurring on the borders of the field of view of the data. With the VLT/SPHERE-IRDIS instrument, active CCD pixels of the camera do not completely pave the field of view. In addition, the circular aperture of the telescope mask out some other pixels. It results in strong aberrant data on the border of the field of view. Thus, we hand-define a binary mask (only once for a given instrument) to discard these areas.

The second aspect is that, because of the rotation of the field of view, the spatial size of the PACO maps from which the detection is performed can exceed the size of the data frames. Denoting  $R \times C$  the spatial size of the data frames, the PACO maps are of size  $\lfloor \sqrt{2}R \rfloor \times \lfloor \sqrt{2}C \rfloor$ . In words, it is theoretically enough that an exoplanet (with a sufficient level of contrast) lies in the field of view at a single date to be detected. This field of view extension is illustrated in Figure 2.12 on a VLT/SPHERE-IRDIS frame at  $\lambda_1 = 2.110 \mu\text{m}$ . Figure 2.1 also illustrates this effect for state-of-the-art algorithms since the size of the combined maps is larger than the data frames thanks to the true-North alignment step. Consequently, the detection tests (2.24) to (2.26) and other PACO outputs should be adapted by considering in the summation only terms  $t$  for which the expected location  $\phi_t$  of the exoplanet lies in within the mask defining the field of view.

Note that this missing data issue is even more acute for SDI or ASDI processing. Indeed, the recorded images at wavelength  $\lambda$  are scaled by a factor  $\lambda_{\text{ref}}/\lambda$  so that the on-axis PSF and the speckle field are approximately aligned throughout the ASDI stack. Due to the difference between the scaling factors applied respectively to the shortest and the longest wavelengths, only a central area of the field of view is covered by all rescaled images, see Chapter 6.

**Algorithm 2.1: PACO detection**– Computation of the S/N values at initial 2-D angular positions  $\mathcal{G}$  of an unresolved source.

---

**Input:** Set  $\mathcal{G}$  of initial 2-D angular positions.

**Input:** Spatio-temporal dataset  $\{r_{n,t}\}_{n=1:N, t=1:T}$ .

**Output:** S/N map at all initial positions in  $\mathcal{G}$ .

```

forall  $\phi_0 \in \mathcal{G}$  do
     $a \leftarrow 0$ 
     $b \leftarrow 0$ 
    for  $t = 1 : T$  do
         $\triangleright$  Step 1. Extract the relevant patches:
         $\phi_t = \mathcal{F}_t(\phi_0)$ 
         $\mathcal{P}_t \leftarrow \{r_{[\phi_i],t'}\}_{t'=1:T}$ 
         $\triangleright$  Step 2. Learn the background statistics from the patches in  $\mathcal{P}_t$ :
         $\{\widehat{\mathbf{m}}_{[\phi_i]}, \widehat{\mathbf{C}}_{[\phi_i]}\}$  (Equations 2.7, 2.9, 2.10 and 2.14)
         $\triangleright$  Step 3. Update  $a$  and  $b$ :
         $\mathbf{w} \leftarrow \widehat{\mathbf{C}}_{[\phi_i]}^{-1} \cdot \mathbf{h}_{[\phi_i]}(\phi_t)$ 
         $a \leftarrow a + \mathbf{w}^\top \cdot \mathbf{h}_{[\phi_i]}(\phi_t)$  (Equation 2.17)
         $b \leftarrow b + \mathbf{w}^\top \cdot (r_{[\phi_i],t} - \widehat{\mathbf{m}}_{[\phi_i]})$  (Equation 2.18)
     $S/N(\phi_0) \leftarrow b/\sqrt{a}$  (Equation 2.26)

```

---

### 2.4.3 The PACO algorithm: algorithmic considerations

As explained in Section 2.3.3, within the PACO pipeline, the detection and characterization steps are performed by two very similar schemes. First, the detection is performed on the whole field of view using the PACO detection procedure. This step produces a S/N map which is statistically grounded and which can be directly thresholded at a controlled false alarm rate. The estimated flux is however biased by the presence of the exoplanet in the collection of patches used to model the background fluctuations. Thus, a different procedure named PACO characterization is launched in a second step on each detected source in order to refine the flux estimation. This latter procedure provides unbiased flux estimates (i.e., no a posteriori Monte-Carlo based bias correction is necessary).

Algorithm 2.1 summarizes the PACO detection procedure as described more formally in Section 2.3. **Step 1** consists of forming the collection of patches  $\mathcal{P}_t$  on which the statistics of the background must be learned. These patches are all centered at the same position  $\phi_t$  where the source would be at time  $t$ , assuming it was initially at position  $\phi_0$ . In **Step 2**, the background statistics, i.e. the empirical mean  $\widehat{\mathbf{m}}$  and the regularized covariance  $\widehat{\mathbf{C}}$ , are computed based on Equations (2.7), (2.9), (2.10) and (2.14). **Step 3** then forms the numerator and denominator of the test statistics by accumulating values  $a_t$  and  $b_t$  defined by equations (2.17) and (2.18). In Algorithm 2.1, the background statistics are computed assuming no exoplanet is present (i.e., hypothesis  $\mathcal{H}_0$ ) and are thus biased in the presence of a source. This is especially notable when the apparent motion of the exoplanet over time is limited, and the source flux is large.

Once the detection step is performed by Algorithm 2.1, the potential detections

---

**Algorithm 2.2:** PACO characterization– Unbiased estimation of the flux  $\hat{\alpha}^+$  of an unresolved source at initial 2-D angular position  $\phi_0$ .

---

**Input:** 2-D angular position  $\phi_0$  of source at  $t = 0$ .  
**Input:** Spatio-temporal dataset  $\{r_{n,t}\}_{n=1:N, t=1:T}$ .  
**Input:** Optional initial estimate  $\hat{\alpha}^+ \geq 0$ ,  $\hat{\alpha}^+ = 0$  by default.  
**Input:** Relative precision  $\epsilon \in (0, 1)$ .  
**Output:** Estimated flux  $\hat{\alpha}^+$  of the source.

▷ Alternated estimation of  $\hat{\alpha}^+$ ,  $\widehat{\mathbf{m}}(\hat{\alpha}^+)$  and  $\widehat{\mathbf{C}}(\hat{\alpha}^+)$ :  
 $\hat{\alpha}_{\text{old}}^+ \leftarrow +\infty$   
**while**  $|\hat{\alpha}^+ - \hat{\alpha}_{\text{old}}^+| > \epsilon \hat{\alpha}^+$  **do**  
      $a \leftarrow 0$   
      $b \leftarrow 0$   
     **for**  $t = 1 : T$  **do**  
         ▷ **Step 1** Build the collection of patches:  
          $\phi_t = \mathcal{F}_t(\phi_0)$   
          $\mathcal{P} \leftarrow \{\mathbf{r}_{[\phi_t], t'} - \hat{\alpha}^+ \mathbf{p}_{[\phi_t]}(\phi_{t'})\}_{t'=1:T}$   
         ▷ **Step 2** Learn the background statistics:  
          $\{\widehat{\mathbf{m}}_{[\phi_t]}(\hat{\alpha}^+), \widehat{\mathbf{C}}_{[\phi_t]}(\hat{\alpha}^+)\}$  (Equations 2.15)  
         ▷ **Step 3** Update the flux terms  $\hat{\alpha}^+$ :  
          $\mathbf{w} \leftarrow \widehat{\mathbf{C}}_{[\phi_t]}^{-1}(\hat{\alpha}^+) \cdot \mathbf{h}_{[\phi_t]}(\phi_t)$   
          $a \leftarrow a + \mathbf{w}^\top \cdot \mathbf{h}_{[\phi_t]}(\phi_t)$   
          $b \leftarrow b + \mathbf{w}^\top \cdot (\mathbf{r}_{[\phi_t], t} - \widehat{\mathbf{m}}_{[\phi_t]}(\hat{\alpha}^+))$   
      $\hat{\alpha}_{\text{old}}^+ \leftarrow \hat{\alpha}^+$   
      $\hat{\alpha}^+ \leftarrow \max(b, 0)/a$  (Equation 2.16)

---

obtained by thresholding the S/N map at level  $\tau$  should be photometrically characterized using the statistically unbiased PACO characterization procedure summarized in Algorithm 2.2. As discussed in Section 2.3.3, this can be done by alternating between an estimation of the flux of the exoplanet and the statistics of the background. Joint estimation of the flux of the exoplanet and the background statistics could also be performed by hierarchical optimization. The resulting estimate  $\hat{\alpha}$  for a source located at  $\phi_t = \mathcal{F}_t(\phi_0)$  on the frame  $t$  ( $t = 1 : T$ ) corresponds to the minimum of the following cost function:

$$\mathcal{C}(\alpha) = \sum_{t=1}^T \left\{ T \log(\det(\widehat{\mathbf{C}}_{\phi_t}(\alpha))) + \text{tr} \left( \widehat{\mathbf{C}}_{\phi_t}^{-1}(\alpha) \cdot \left( \mathbf{W} \odot \sum_{t'=1}^T \mathbf{u}_{\phi_t, t'}(\alpha) \cdot \mathbf{u}_{\phi_t, t'}^\top(\alpha) \right) \right) \right\}, \quad (2.38)$$

where  $W_{i,j} = 1$  if  $i = j$ ,  $W_{i,j} = 1 - \hat{\rho}$  elsewhere,  $\{i, j\} \in \llbracket 1; K \rrbracket^2$ ,  $\odot$  stands for entrywise multiplication (i.e. Hadamard product), and  $\mathbf{u}_{n,t}(\alpha) = \mathbf{r}_{n,t} - \alpha \cdot \mathbf{h}_{n,t} - \widehat{\mathbf{m}}_n(\alpha)$ . The expression of  $\mathcal{C}(\alpha)$  in Equation (2.38) comes from the neg-log-likelihood under a Gaussian assumption, where matrix  $\mathbf{W}$  is introduced to shrink the covariance estimate towards a diagonal covariance (i.e., to replace the maximum likelihood covariance estimate given

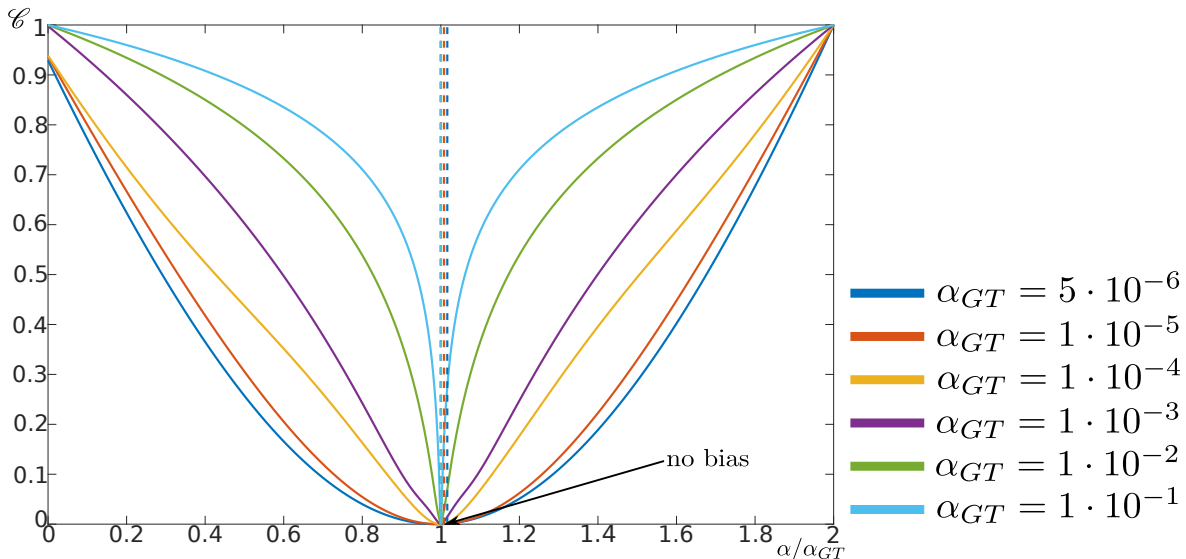


Figure 2.13 – Normalized cost function  $\mathcal{L}$  obtained with Equation (2.38) for fake exoplanets with different fluxes  $\alpha_{GT}$ . The dashed lines indicate the values found by the proposed alternate scheme in Equations (2.15).

by the sample covariance with the shrinkage estimator described in Section 2.3.2).

Figure 2.13 illustrates the cost function  $\mathcal{L}(\alpha)$  that is minimized by our alternating estimation scheme. This cost function is unimodal in the tested range of contrasts (from  $5 \times 10^{-6}$  to  $10^{-1}$ ) indicating that PACO estimation procedure would also correctly characterize exoplanets having a rather high flux. The minimum of the cost function is located near the correct value ( $\hat{\alpha}/\alpha_{GT} = 1$ ) with a discrepancy in agreement with the standard deviation  $\hat{\sigma}_\alpha$ . Minimizing  $\mathcal{L}(\alpha)$  therefore yields an unbiased estimator of the flux. In practice, to minimize  $\mathcal{L}(\alpha)$ , we followed the alternating scheme in Equations (2.15) which is easily implementable and converges within a few iterations (see Section 2.5.4). Our method for unbiased estimation of the flux is summarized in Algorithm 2.2.

#### 2.4.4 A fast and approximate version of PACO for large surveys

Since the data analysis of large surveys is a crucial issue in astronomy, we also propose a simplified and faster version of the PACO detection procedure, which is summarized by Algorithm 2.3. Compared to applying Algorithm 2.1 to a given set of assumed initial source positions to compute a map of the detection criterion, the fast version has a computational burden reduced by a factor at least equal to the number  $T$  of temporal frames.

The acceleration relies on the pre-computation of terms that appear multiple times in the sums of Equations (2.17) and (2.18) when considering all possible source locations. Computations of the background statistics are thus recycled. The S/N map is obtained in a second step by interpolating the precomputed terms denoted by  $c$  and  $d$  in Algorithm 2.3, to align the field of view at all times according to the transform  $\mathcal{F}_t$  which is, in general, a rotation. Such interpolations result in a low-pass filtering

---

**Algorithm 2.3: fast PACO detection**– Fast computation of the S/N values at initial 2-D angular positions  $\mathcal{G}$  of an unresolved source.

---

**Input:** Uniform grid  $\mathcal{G}$  of 2-D angular positions.

**Input:** Spatio-temporal dataset  $\{r_{n,t}\}_{n=1:N, t=1:T}$ .

**Output:** S/N map at all initial positions in  $\mathcal{G}$ .

▷ **Step 1.** Pre-compute terms:

**forall**  $\phi_0 \in \mathcal{G}$  **do**

▷ **Step 1a.** Build the collection of patches centered at  $\phi_0$ :

$$\mathcal{P} \leftarrow \{r_{[\phi_0],t}\}_{t=1:T}$$

▷ **Step 1b.** Learn the corresponding background statistics and pre-compute terms:

$$\{\widehat{\mathbf{m}}_{[\phi_0]}, \widehat{\mathbf{C}}_{[\phi_0]}\} \quad (\text{Equations 2.7, 2.9, 2.10 and 2.14})$$

$$\mathbf{w}_{[\phi_0]} \leftarrow \widehat{\mathbf{C}}_{[\phi_0]}^{-1} \cdot \mathbf{h}_{[\phi_0]}(\phi_0)$$

$$c_{[\phi_0]} \leftarrow \mathbf{w}_{[\phi_0]}^\top \cdot \mathbf{h}_{[\phi_0]}(\phi_0)$$

**for**  $t = 1 : T$  **do**

$$\left[ \begin{array}{l} d_{[\phi_0],t} \leftarrow \mathbf{w}_{[\phi_0]}^\top \cdot (\mathbf{r}_{[\phi_0],t} - \widehat{\mathbf{m}}_{[\phi_0]}) \end{array} \right.$$

▷ **Step 2.** Compute the S/N values:

**forall**  $\phi_0 \in \mathcal{G}$  **do**

$$a \leftarrow 0$$

$$b \leftarrow 0$$

**for**  $t = 1 : T$  **do**

$$\left[ \begin{array}{l} \phi_t = \mathcal{F}_t(\phi_0) \end{array} \right.$$

$$\left[ \begin{array}{l} a \leftarrow a + c_{[\phi_t]}(\phi_t) \end{array} \right. \quad (\text{interpolation of } c)$$

$$\left[ \begin{array}{l} b \leftarrow b + d_{[\phi_t],t}(\phi_t) \end{array} \right. \quad (\text{interpolation of } d)$$

$$\left[ \begin{array}{l} \text{S/N}(\phi_0) \leftarrow b/\sqrt{a} \end{array} \right. \quad (\text{Equation 2.26})$$


---

of the criterion map which slightly degrades the detection performance of PACO (see Section 2.5). The complexity of the fast version given in Algorithm 2.3 is dominated by the pre-calculation step (**Step 1**). Denoting by  $N$  the number of angular positions  $\phi_0$  to process, this step requires  $N \times T$  products of vectors with  $K$  elements as well as the resolution of  $N$  linear systems of size  $K \times K$ . For example, the application of this fast algorithm requires approximately 2 minutes to process a dataset made of 96 temporal frames of size  $1024 \times 1024$  pixels versus approximately 3 hours for the complete algorithm using a basic parallelization done in MATLAB<sup>TM</sup> on 24 cores (processor INTEL<sup>TM</sup> Xeon E5-46170 at 2.90 GHz and  $K = 49$  pixels per patch).

### 2.4.5 Sampling of possible exoplanet locations

The physical position  $\phi$  of an unresolved source may not exactly correspond to a sample of the data, i.e., a pixel  $n$ . To deal with this, we consider patches centered at the nearest pixel  $[\phi_t]$  of the source position  $\phi_t = \mathcal{F}_t(\phi_0)$  in frame  $t$  when it is assumed to be initially at  $\phi_0$ . This means that patches are not exactly centered at the source

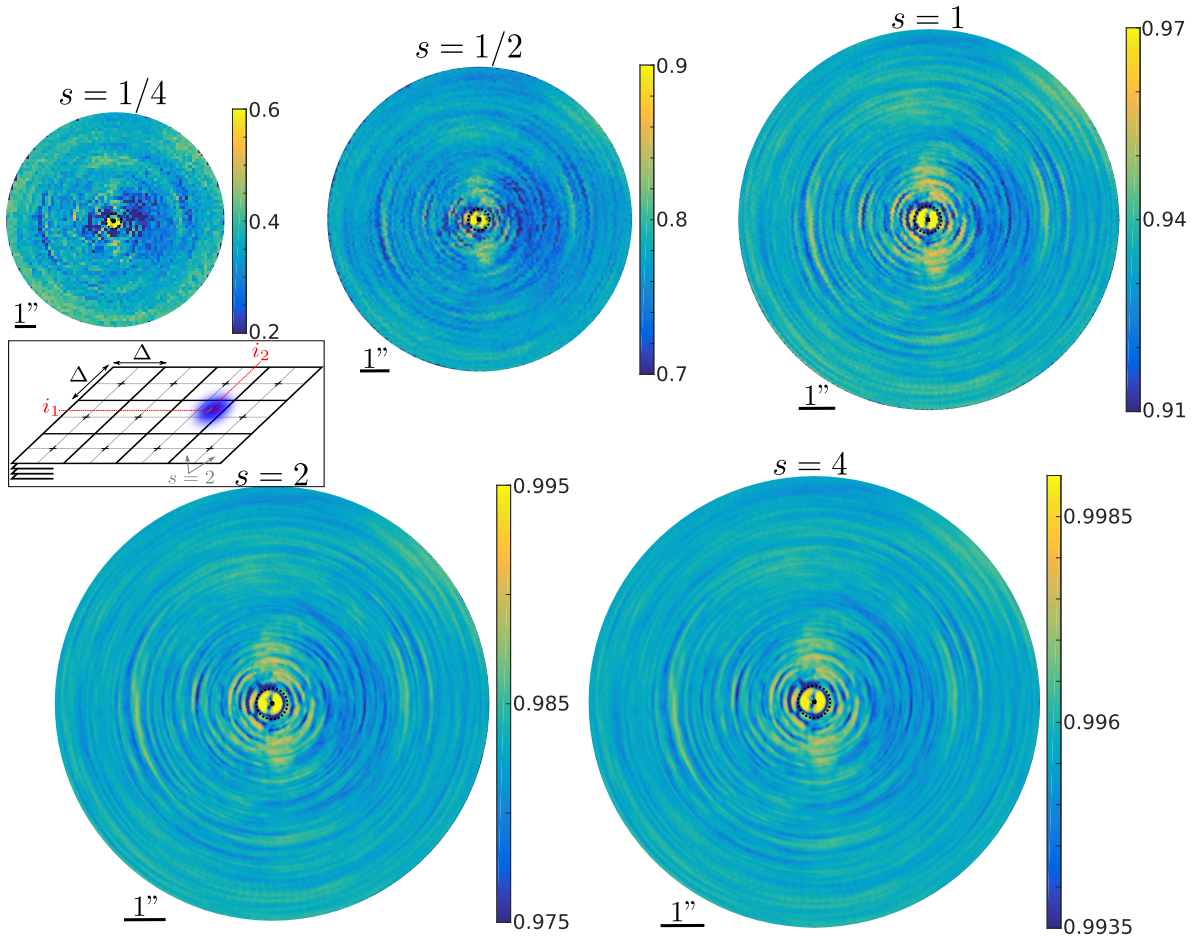


Figure 2.14 – Effect of the sampling grid on S/N: ratio  $\mathbb{E}(S/N(\mathcal{G}_s(\phi_0) | \phi_0)) / \mathbb{E}(S/N(\phi_0 | \phi_0))$  for  $s \in \{1/4, 1/2, 1, 2, 4\}$  computed on the HIP 72192 dataset at  $\lambda_1 = 2.110 \mu\text{m}$ . It informs about the maximum expected reduction in S/N if the exoplanet is not exactly centered on a pixel of the sampling grid.

position  $\phi_t$  with a potential loss of optimality. However, we expect that this loss be small because the pixel size is usually chosen to be much smaller than the diffraction limit (Beuzit et al., 2008, 2019).

There is another issue related to the sampling because the detection is carried out on maps with necessarily a finite resolution for the assumed initial position  $\phi_0$ . One can expect a negative bias for the S/N: the further the detected position in the criterion map to the actual source position, the worse the value of the criterion. The faintest sources may be undetected because of this bias. Fortunately, the direct model in Equation (2.1) assumed by PACO does not impose any finite precision for the source position  $\phi_t$  in each frame, so detection maps can be computed at a resolution small enough to avoid the problem. To limit the computational burden, one would however like to use a somewhat coarse sampling for the detection map. There is a tradeoff to find and, in this section, we attempt to evaluate the S/N loss caused by a given sampling of the detection map. We assumed that the detection map is computed for initial positions on a uniformly



Table 2.2 – Influence of the sampling factor  $s$  on the S/N and on the computation time. The computation time as well as the maximum expected reduction in the S/N are given for values of  $s \in \{1/4, 1/2, 1, 2, 4\}$ . The experiments are conducted on the HIP 72192 dataset at  $\lambda_1 = 2.110 \mu\text{m}$  with the PACO detection Algorithm 2.1. The computation time (last column) is given relatively to the time required to process the considered dataset with the original sampling grid (i.e., for  $s = 1$ ) which, in our experiments, is approximately three hours (see Section 2.4.3).

Sampling factor $s$	Max. S/N reduction	Time
1/4	80 %	1/16
1/2	30 %	1/4
1	9 %	1
2	3 %	4
4	$\leq 1$ %	16

sampled grid  $\mathcal{G}_s$  defined by:

$$\mathcal{G}_s = \left\{ \phi = \frac{\Delta}{s}(i_1, i_2) \mid (i_1, i_2) \in \mathbb{Z}^2, \phi \in \Theta \right\}, \quad (2.39)$$

where  $(i_1, i_2)$  stand for the two components of 2-D angular positions,  $\Delta$  is the pixel size in the data,  $s$  is a chosen sub-sampling factor and  $\Theta$  is the angular area where to perform the detection. The inset of Figure 2.14 summarizes this notation for the case  $s = 2$ .

The ratio  $\mathbb{E}(\text{S/N}(\mathcal{G}_s(\phi_0) \mid \phi_0)) / \mathbb{E}(\text{S/N}(\phi_0 \mid \phi_0))$  informs about the fraction of S/N lost due to the sampling grid  $\mathcal{G}_s$  under consideration, with  $\mathcal{G}_s(\phi_0) = \arg \min_{\phi \in \mathcal{G}_s} \|\phi - \phi_0\|^2$ . The expected value of the S/N under the  $\mathcal{H}_1$  hypothesis at any angular position  $\phi = \mathcal{G}_s(\phi_0)$ , knowing that the exoplanet is initially located at  $\phi_0$ , is:

$$\mathbb{E}(\text{S/N}(\phi \mid \phi_0)) = \alpha \frac{\sum_{t=1}^T \mathbf{h}_{[\phi_t]}(\phi_t)^\top \cdot \widehat{\mathbf{C}}_{[\phi_t]}^{-1} \cdot \mathbf{h}_{[\phi_t]}(\mathcal{F}_t(\phi_0))}{\sqrt{\sum_{t=1}^T \mathbf{h}_{[\phi_t]}(\phi_t)^\top \cdot \widehat{\mathbf{C}}_{[\phi_t]}^{-1} \cdot \mathbf{h}_{[\phi_t]}(\phi_t)}}. \quad (2.40)$$

In practice, this expectation ratio is evaluated in the most unfavorable case for the considered grid, that is to say when the exoplanet is exactly located between two adjacent grid nodes.

Figure 2.14 gives a map of the ratio  $\mathbb{E}(\text{S/N}(\mathcal{G}_s(\phi_0) \mid \phi_0)) / \mathbb{E}(\text{S/N}(\phi_0 \mid \phi_0))$  for a uniform grid with sampling size  $\Delta/s$  for  $s \in \{1/4, 1/2, 1, 2, 4\}$  and  $\Delta$  the pixel size of the data. We note that values of  $s$  smaller than one correspond to a down-sampling of the data pixels, while values greater than one correspond to an up-sampling of the pixels. Figure 2.14 emphasizes that the choice  $s = 1$  (corresponding to a calculation of the detection criteria in each pixel of the data) generates values of the ratio  $\mathbb{E}(\text{S/N}(\mathcal{G}_s(\phi_0) \mid \phi_0)) / \mathbb{E}(\text{S/N}(\phi_0 \mid \phi_0))$  between 0.91 and 0.97. The maximum loss is less than 10% on the S/N values when the exoplanet is exactly located between two pixels. The choice  $s = 4$  ensures a maximum loss on the value of the S/N lower than 0.7% at any point of the field of view at the price of a computational cost of the algorithm multiplied by a factor 16. On the opposite, the choice  $s = 1/2$ , reduces the computational cost of the algorithm by a factor of four at the price of a maximum potential loss

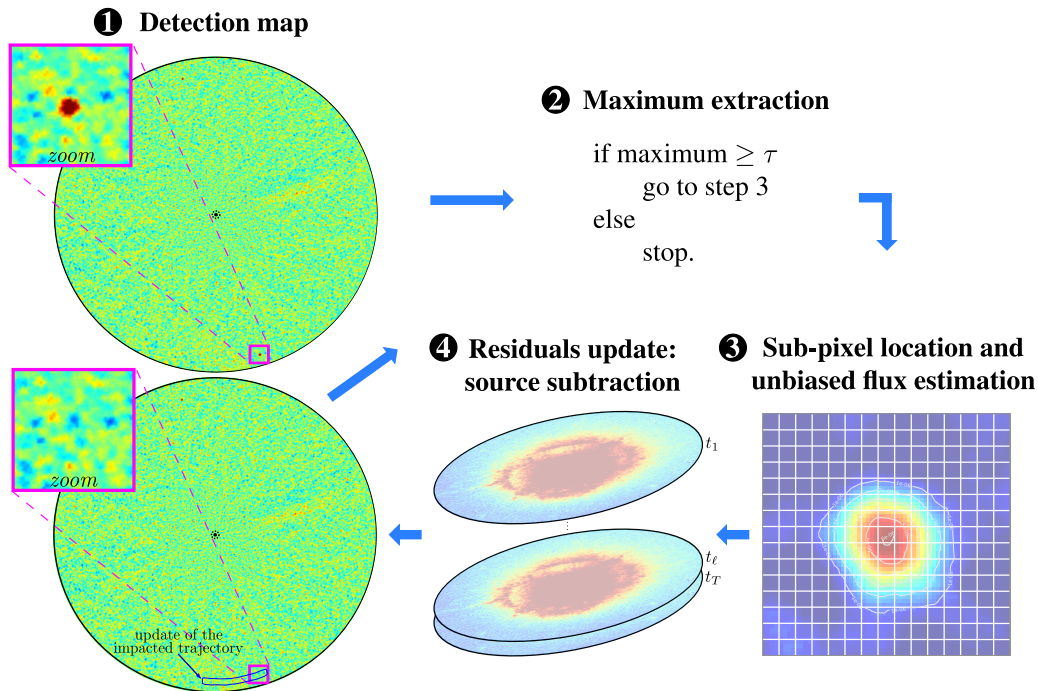


Figure 2.15 – Synopsis of PACO algorithm.

between 10 and 30% (depending on the position in the field of view) on the S/N values if the exoplanet is located exactly between two pixels defined by the sampling grid under consideration. Table 2.2 summarizes the impact of the choice of the sampling factor  $s$  on the maximum expected S/N reduction and the computation time.

## 2.4.6 Unsupervised detection and characterization

Based on these methodological (Section 2.3) and practical (Section 2.4) developments, we derive a processing framework summarized by Figure 2.15. In step 1, the local patch mean and patch covariances are computed. Then, a detection map is obtained by computing the S/N  $\hat{\alpha}/\hat{\sigma}_\alpha$  at each possible location  $\phi_0$  within the field of view. Step 2 checks whether the largest value in the detection map is above the detection threshold. If not, the algorithm stops, otherwise, an exoplanet is detected at the location of the maximum of the detection map. Step 3 then refines the location to subpixel accuracy and improves the estimation of the flux  $\alpha$  of the detected exoplanet by jointly estimating  $\alpha$  and the background means and covariances. If two overlapping sources are detected, their flux is jointly estimated like in a conventional *orthogonal matching pursuit* procedure (Pati et al., 1993). This joint estimation procedure prevents from any signal self-subtraction. The convergence criterion is based on the computed Cramér-Rao lower bounds (see Section 2.3.6.3) on localization and flux accuracies such that the numerical accuracy is better than the estimator standard deviation. Once this local optimization step is finished, step 4 removes the signal of the detected exoplanet from the data as in a conventional *CLEAN* procedure (Högbom, 1974). Step 1 is then repeated on the residual signal, and the subsequent steps, until the condition in step 2 indicates that no more statistically significant detections can be made.

The method is totally unsupervised: no parameter tuning is necessary, the regularization of the covariance matrices is based on automatic shrinkage (see Section 2.3.2); the patch size is set based on a Monte-Carlo study and is constant for a given instrument (see Section 2.4.1); the threshold  $\tau$  is set according to a prescribed false alarm rate. We present in Chapter 8 a short description of the PACO pipeline built with the aim to be totally automatic from the data extraction to the pre-analysis of the results.



### **PACO: algorithmic considerations**

- We propose a fast and approximate version of our exoplanet detection method to conduct efficiently data analysis of large surveys (see Section 2.4.4).
- The detection criterion can be evaluated at any given resolution, thus preventing from a loss of the detection sensitivity due to the grid of the detection map. We also derive a criterion giving the loss due to a given grid (see Section 2.4.5).
- We derive a detection and characterization framework for the PACO algorithm. It is based on a computation of a detection criterion map and to its iterative update following a CLEAN/matching pursuit approach (see Section 2.4.6). This framework is totally unsupervised:
  - the regularization of the covariance matrices is based on automatic shrinkage (see Section 2.3.2),
  - the detection threshold  $\tau$  is set according to a prescribed and controlled false alarm rate (see Section 2.3.6.2),
  - the patch size is set based on a Monte-Carlo study and is constant for a given instrument, (see Section 2.4.1),
  - the astrometric and photometric refinement ends based on the Cramér-Rao lower bounds (see Section 2.3.6.3), such that the residual bias is negligible in front of the minimal variance,
  - the algorithm ends when no source is above the detection confidence threshold  $\tau$  set.

## **2.5 Performance evaluation with on-sky data**

In this section, we assess the performance of PACO on several ADI datasets acquired at the VLT by the SPHERE-IRDIS instrument using the dual-band filters K1 ( $\lambda_1 = 2.110 \mu\text{m}$ ) and K2 ( $\lambda_2 = 2.251 \mu\text{m}$ ).

### **2.5.1 Datasets and algorithms description**

The selected datasets are recorded in various conditions of observation leading to different degrees of difficulty for the detection task. They are obtained around reference

Table 2.3 – Observation logs of the considered ADI datasets.  $\Delta_{\text{par}}$  is for the total amount of rotation of the field of view and the reported conditions of observation are based on seeing value.

Target	ESO ID	Obs. date	$T$	$\Delta_{\text{par}}$	Obs. conditions
HD 131399	095.C-0389	2015-05-12	92	36.7°	average
HD 131399	262.C-5036 (DDT)	2016-05-07	56	39.5°	good
HIP 72192	095.C-0389	2015-06-11	96	17.3°	average

targets hosting well-known faint point sources (exoplanets or background sources such as brown dwarfs). We present additional examples of the astronomical exploitation of PACO results on recent datasets in Chapter 8. Hereafter, we give the main characteristics of each dataset considered in this section.

Two datasets are derived from observations of the HD 131399 system located in the Upper Centaurus Lupus association (De Zeeuw et al., 1999; Rizzuto et al., 2011; Pecauc and Mamajek, 2013). The young center star of A1V-type forms a triple system with two other K- and G-type stars located at a projected distance of about 3 arcsec from the central star (Dommaget and Nys, 2002; Houk and Smith-Moore, 1988). An exoplanet candidate has been recently detected at a projected distance of about 0.83 arcsec from the central star (Wagner et al., 2016). However, more recent observations made it possible to refine the reconstruction of the SED of the candidate companion and its astrometry. This new information proved to be incompatible with the bound-exoplanet hypothesis. It has been discussed to be more likely a background brown dwarf (Nielsen et al., 2017). Both datasets provide observations up to about 5.5 arcsec. To illustrate the performance of the PACO algorithm, we display a region approximately 1.7 arcsec of radius, centered around the star A of the triple system, in order to limit the impact of the other two stars of the system.

To also illustrate the performance of the PACO algorithm on the whole field of view offered by the VLT/SHPERE-IRDIS instrument, we consider a dataset from the observation of the A0-type star HIP 72192 located in the Lupus constellation (De Zeeuw et al., 1999; Schmitt et al., 1993). It hosts two confirmed faint point sources (brown dwarfs).

Table 2.3 summarizes the observations logs of these three datasets.

The performances of the PACO algorithm are compared in terms of detection maps and contrast curves obtained with the two current cutting-edge algorithms TLOCI, and KLIP implemented in the SPHERE/SpeCal reduction tool (Galicher et al., 2018). The SpeCal pipeline also offers the possibility to apply an unsharp filter after the speckle removal algorithm to improve the visual quality of the reduction map, reduce the pollution of the stellar leakages and artificially increase the S/N of the detected point source objects. We note that it is expected that this post-processing partially deteriorates the statistical properties of the resulting detection maps. The performances of PACO are compared to the standard algorithms TLOCI and KLIP both with and without unsharp filtering. With PACO, no post-processing is applied to the data nor on the reduction maps other than the conventional data pre-reduction provided by the SPHERE data center pipeline (Delorme et al., 2017). Comparative results from TLOCI

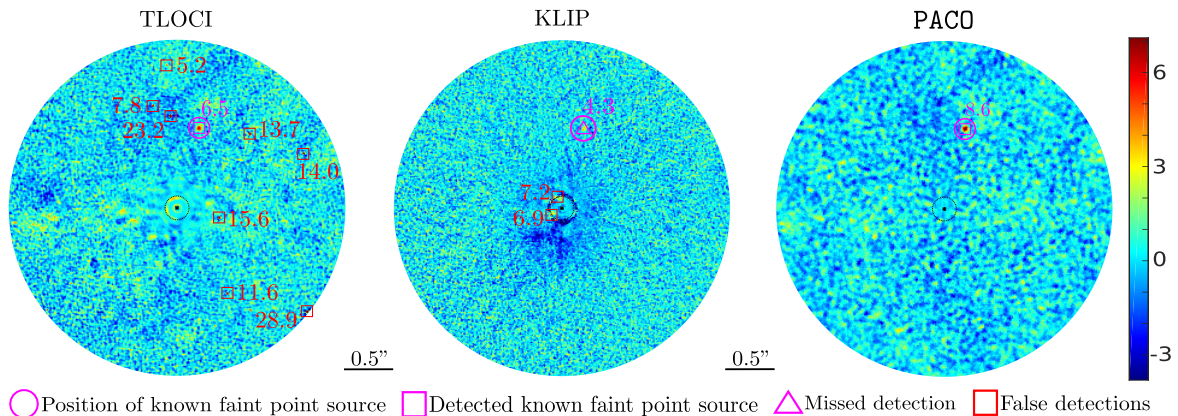


Figure 2.16 – S/N maps computed with the PACO, TLOCI and KLIP algorithms on the HD 131399 (2015) dataset at  $\lambda_1 = 2.110 \mu\text{m}$ . A common threshold at  $S/N = 5$  is applied to defined the detections. A known faint source is present in the field of view. It is identified by a pink circle.

and KLIP algorithms have been obtained by Maud Langlois. The parameters of the different algorithms used are manually tuned to provide the best results.

We also compare PACO in terms of detection capabilities with the recent and emerging algorithms LLSG and ANDROMEDA. The LLSG reductions are performed with the VIP reduction pipeline (Gomez Gonzalez et al., 2017) and the ANDROMEDA results are kindly provided by Faustine Cantalloube (January 2020 version of the ANDROMEDA package).

## 2.5.2 Detection maps

### 2.5.2.1 Comparison with state-of-art algorithms

We start by comparing PACO with the two current cutting-edge methods TLOCI and KLIP. Figure 2.16 shows S/N maps computed with these three algorithms on the HD 131399 (2015) dataset at  $\lambda_1 = 2.110 \mu\text{m}$ . When setting a threshold of  $S/N \geq 5$  on PACO detection map, only one detection is obtained, and this detection corresponds to the faint point source already detected by the other authors. Setting the same threshold on the S/N detection maps produced by TLOCI and KLIP algorithms lead to several false detections. In the case of TLOCI, there are seven S/N values larger than that of the real source, leading to seven false detections. An eighth false detection is obtained due to a local maximum above the threshold  $S/N = 5$ . With the KLIP algorithm, there are two detections corresponding to local maxima above the threshold  $S/N = 5$ , but these are all false detections located close to the coronagraphic mask. The faint point source is not detected with an S/N larger than five and would be detected only by lowering the threshold below  $S/N = 4.3$ . By limiting the amount of signal subtraction, PACO achieves the largest S/N value for the real faint point source ( $S/N = 8.6$ , to compare with TLOCI:  $S/N = 6.5$  and KLIP:  $S/N = 4.3$ ). The second local maxima derived from the PACO S/N is at  $S/N = 3.6$ , which illustrates the ability of PACO to distinguish without ambiguity the faint point source. Moreover, in the absence of sources, the S/N



Table 2.4 – Angular separation and contrast of the injected fake sources on the HIP 72192 dataset for the three considered levels of injection at  $\lambda_1 = 2.110 \mu\text{m}$ . Fluxes have been chosen so that the difficulty of detecting each source be approximately the same at all angular separations.

Separation (")	Mean[ $\alpha$ ]	Min[ $\alpha$ ]	Max[ $\alpha$ ]
<i>Level 1</i>			
0.40	$3.9 \times 10^{-5}$	$2.5 \times 10^{-5}$	$6.1 \times 10^{-5}$
1.58	$2.8 \times 10^{-6}$	$1.8 \times 10^{-6}$	$4.3 \times 10^{-6}$
2.75	$2.7 \times 10^{-6}$	$2.1 \times 10^{-6}$	$4.4 \times 10^{-6}$
3.93	$2.6 \times 10^{-6}$	$1.9 \times 10^{-6}$	$3.7 \times 10^{-6}$
5.12	$2.5 \times 10^{-6}$	$1.6 \times 10^{-6}$	$3.9 \times 10^{-6}$
<i>Level 2</i>			
0.40	$5.8 \times 10^{-5}$	$3.6 \times 10^{-5}$	$8.4 \times 10^{-5}$
1.58	$4.2 \times 10^{-6}$	$3.1 \times 10^{-6}$	$5.8 \times 10^{-6}$
2.75	$3.8 \times 10^{-6}$	$3.0 \times 10^{-6}$	$5.5 \times 10^{-6}$
3.93	$3.5 \times 10^{-6}$	$2.7 \times 10^{-6}$	$4.5 \times 10^{-6}$
5.12	$3.4 \times 10^{-6}$	$2.4 \times 10^{-6}$	$5.1 \times 10^{-6}$
<i>Level 3</i>			
0.40	$8.6 \times 10^{-5}$	$5.2 \times 10^{-5}$	$1.3 \times 10^{-4}$
1.58	$5.6 \times 10^{-6}$	$4.1 \times 10^{-6}$	$7.4 \times 10^{-6}$
2.75	$4.8 \times 10^{-6}$	$4.0 \times 10^{-6}$	$6.7 \times 10^{-6}$
3.93	$4.4 \times 10^{-6}$	$3.6 \times 10^{-6}$	$5.3 \times 10^{-6}$
5.12	$4.3 \times 10^{-6}$	$3.3 \times 10^{-6}$	$6.3 \times 10^{-6}$

map is stationary and false alarms are well controlled: the PFA when the S/N threshold  $\tau$  is set at five is close to the theoretical value of  $2.87 \times 10^{-7}$ : no false alarm is obtained at this threshold in the region of interest. It can be observed that both TLOCI and KLIP have nonstationary detection maps in the absence of source and the probability of false alarms at the S/N threshold of five is much larger than the theoretical value of  $2.87 \times 10^{-7}$ . Hence, the detection threshold must be set manually on these detection maps to prevent false detections, or the numerous false detections must be discarded by analyzing follow-up observations.

To better evaluate the performance of PACO, we also turned to the injection of fake exoplanets on the HIP 72192 dataset at different angular separations. In addition to the two known faint point-sources hosting by the star, we injected 30 fake companions spread on five angular separations at three different levels of contrast, as summarized in Table 2.4. The considered *level 1* of injection approximately corresponds to a detection at mean S/N = 5 using PACO detection Algorithm 2.1 while brighter sources are injected within *levels 2* and *3*. Figure 2.17 shows S/N maps computed with the PACO, TLOCI, KLIP, LLSG, and ANDROMEDA algorithms for the *level 1* of contrast. For TLOCI and KLIP, post-processing by unsharp filtering is also considered. For LLSG, since the resulting S/N depends on the threshold used during the decomposition, the S/N is not statistically grounded. As a result, we have multiplied the signed S/N by a factor 25 to be in a range comparable to the other methods. For this algorithm, we have



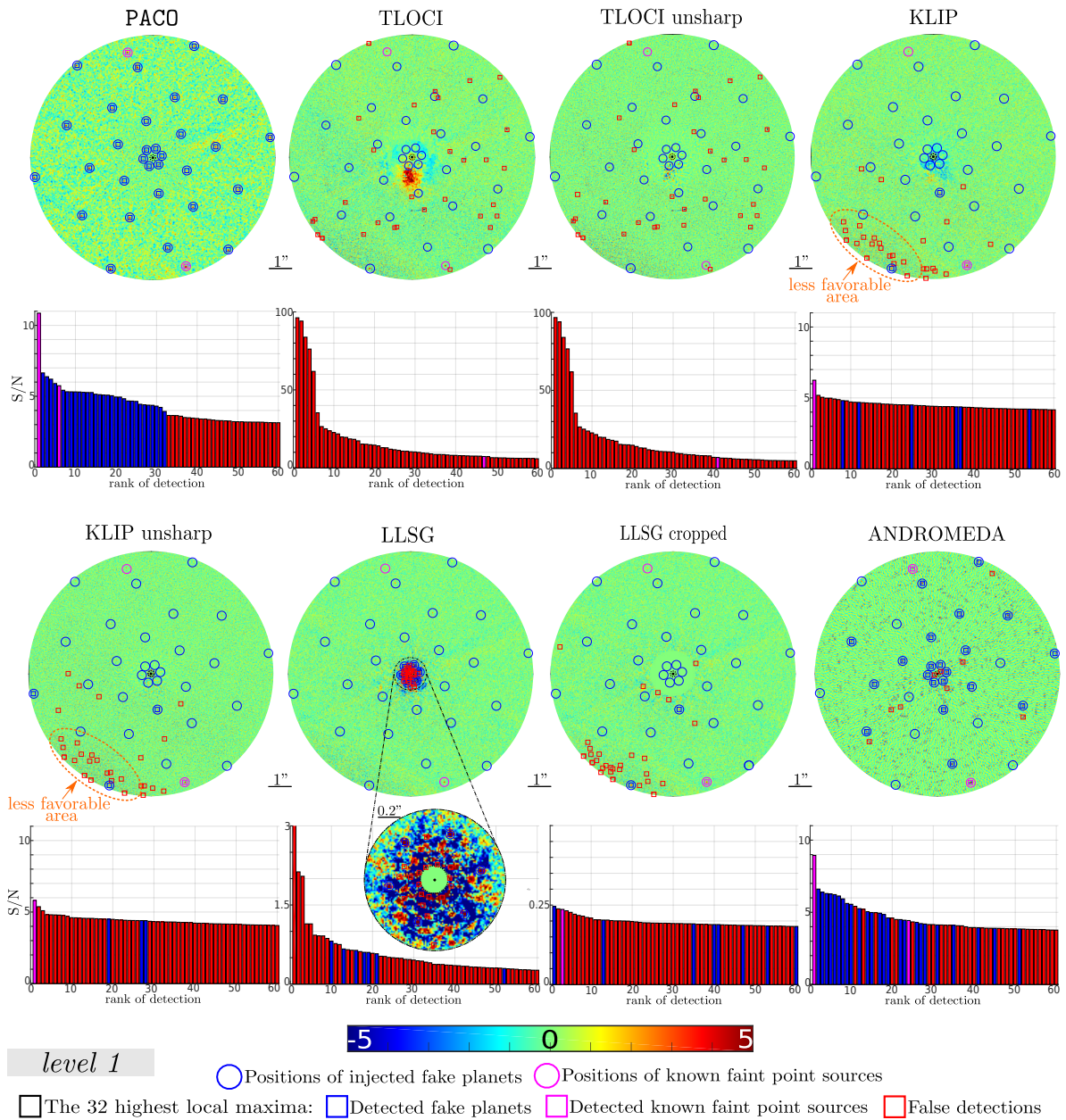


Figure 2.17 – S/N maps computed with the PACO, TLOCI, KLIP, LLSG, and ANDROMEDA algorithms considering the *level 1* of injection. For TLOCI and KLIP, an unsharp filtering applied to S/N maps as post-processing is also considered. For LLSG, the resulting signed S/N is multiplied by a factor of 25 to fall within a comparable range than the other methods. For this latest algorithm, detection is also performed by discarding a central circular area of 1 arcsec in radius. The first 32 detections are marked on each S/N map using square patterns. The 60 first detections are plotted as bar charts below each S/N map, ordered by decreasing S/N values, with true detections in pink (true background sources) or blue (injected fake sources), and false detections in red. Circles indicate the location of the real and injected faint point sources. PACO is the only algorithm capable of detecting correctly all sources without any false detection.

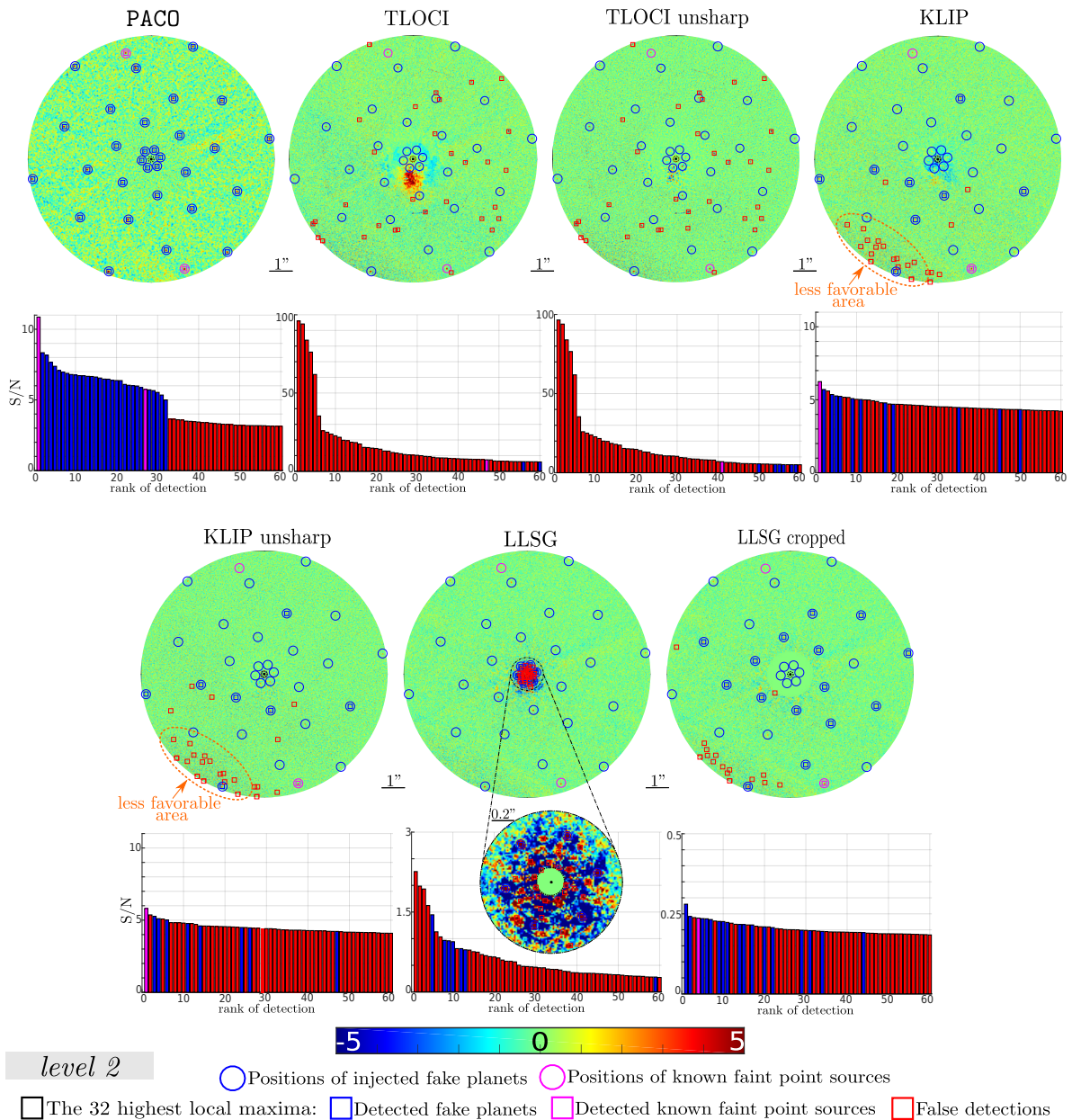


Figure 2.18 – S/N maps computed with the PACO, TLOCI, KLIP, and LLSG algorithms considering the *level 2* of injection. For TLOCI and KLIP, an unsharp filtering applied to S/N maps as post-processing is also considered. For LLSG, the resulting signed S/N is multiplied by a factor of 25 to fall within a comparable range than the other methods. For this latest algorithm, detection is also performed by discarding a central circular area of 1 arcsec in radius. The first 32 detections are marked on each S/N map using square patterns. The 60 first detections are plotted as bar charts below each S/N map, ordered by decreasing S/N values, with true detections in pink (true background sources) or blue (injected fake sources), and false detections in red. Circles indicate the location of the real and injected faint point sources. PACO is the only algorithm capable of detecting correctly all sources without any false detection.



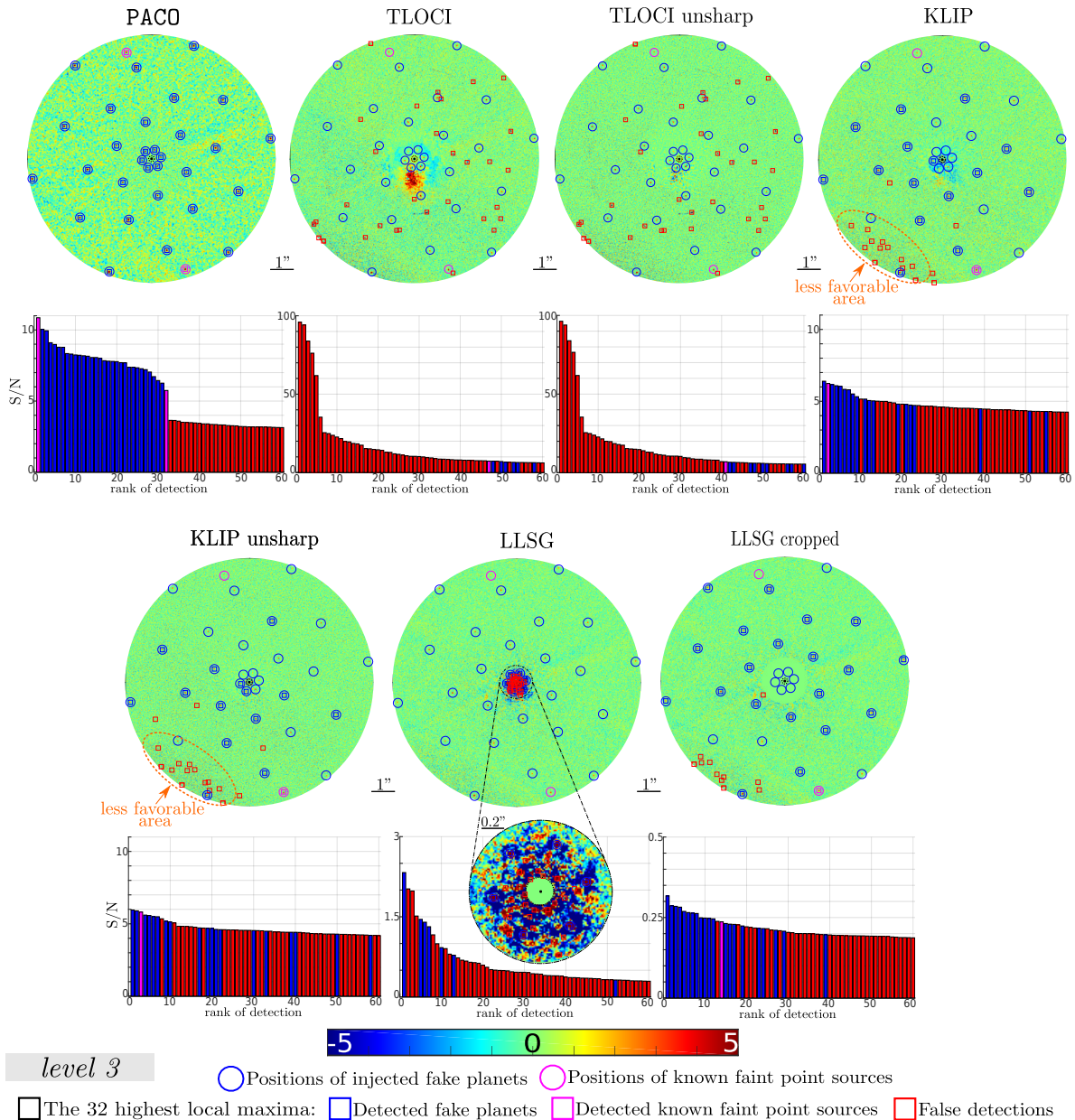


Figure 2.19 – S/N maps computed with the PACO, TLOCI, KLIP, and LLSG algorithms considering the *level 3* of injection. For TLOCI and KLIP, an unsharp filtering applied to S/N maps as post-processing is also considered. For LLSG, the resulting signed S/N is multiplied by a factor of 25 to fall within a comparable range than the other methods. For this latest algorithm, detection is also performed by discarding a central circular area of 1 arcsec in radius. The first 32 detections are marked on each S/N map using square patterns. The 60 first detections are plotted as bar charts below each S/N map, ordered by decreasing S/N values, with true detections in pink (true background sources) or blue (injected fake sources), and false detections in red. Circles indicate the location of the real and injected faint point sources. PACO is the only algorithm capable of detecting correctly all sources without any false detection.

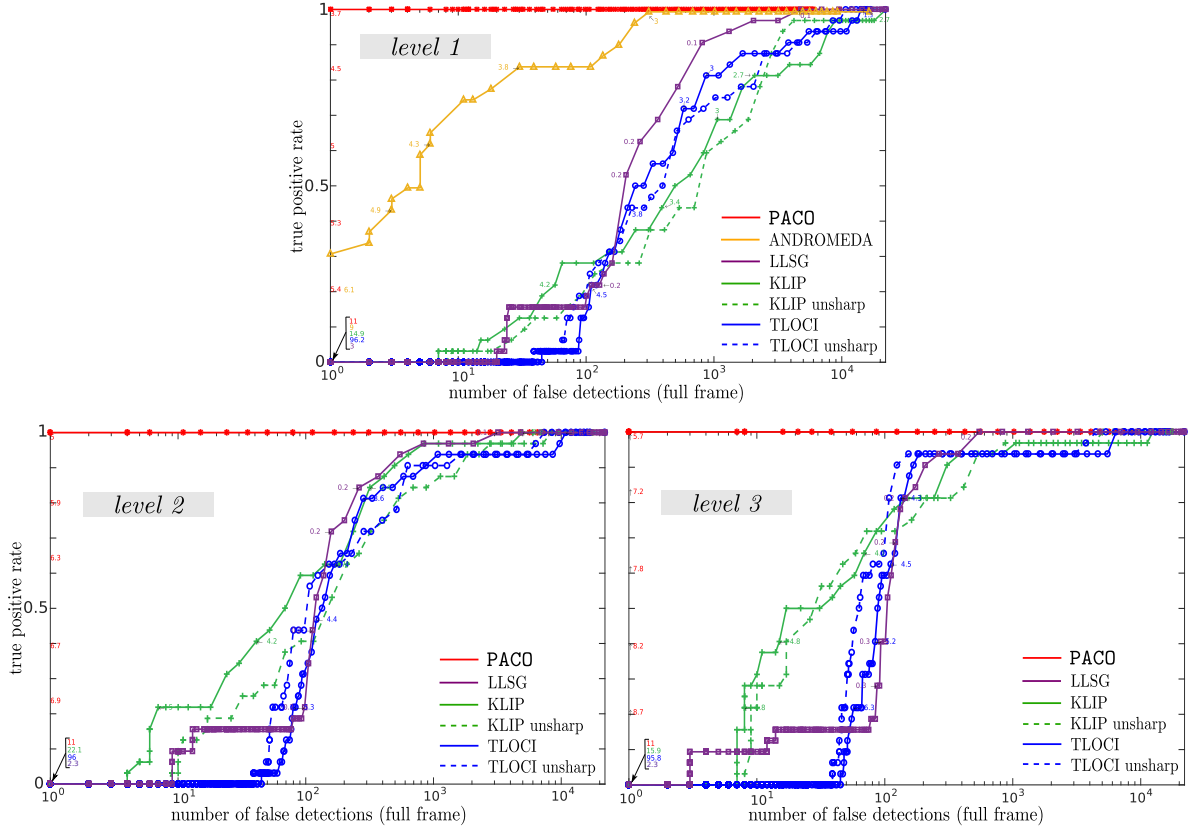


Figure 2.20 – ROC curves showing the true positive rate (fraction of sources correctly detected) as a function of the number of false alarms (i.e., false detections) for the three levels of contrast considered. Values displayed on each curve correspond to the detection threshold used.

also performed the detection by discarding a central circular area of 1 arcsec of radius since the detection seems to be very difficult near the host star. For each reduction map, the S/N of the 60 largest local maxima is given in decreasing order on the same figure. As expected, the S/N maps from PACO are stationary, robust to defective pixels (which have led to aberrant data on a wider scale than one pixel in the science images) and to strong stellar leakages on some frames due to a small decentering of the coronagraph.

The S/N maps derived from PACO are statistically grounded, allowing them to be directly interpreted in terms of PFA without resorting to injections of fake companions via Monte-Carlo simulations. It is clearly not the case for TLOCI which seems very sensitive to defective pixels and large stellar leakages. KLIP performs better than TLOCI, but it also produces nonstationary detection maps, particularly on the southeastern area (see orange dashed area). Interestingly, this area has been identified with PACO as an area where the detection of exoplanets is more difficult (see also the orange dashed area on the contrast map; last row, first column in Figure 2.24). Since PACO locally learns the background fluctuations, the aberrant data or the larger stellar leakages can also be learned locally as typical background fluctuations and are not interpreted in the detection stage as the signature of an exoplanet. The unsharp filtering applied on the detection maps from TLOCI and KLIP improves their visual quality since areas with

large S/N values due to the stellar leakages are largely attenuated, but the detection performance of these algorithms are not significantly improved by this post-processing. LLSG outperforms KLIP far from the host star but the detection maps from LLSG are clearly not statistically grounded since the LLSG decomposition is also coupled with entry-wise thresholding. As a result, the S/N derived from LLSG depends on the choice of the threshold used during the decomposition. A high threshold eliminates a large part of the noise (with the risk of also eliminating faint signals from exoplanets) and artificially increases the S/N of the detected objects. Moreover, the detection of exoplanets near the host star seems to be very difficult based on the LLSG results since the signatures from fake exoplanets are visible but are at the level of false alarms and cannot be easily retrieved by a visual inspection. ANDROMEDA demonstrates appealing characteristics since the S/N map seems almost statistically grounded in the sense that only a few false alarms are detected at  $S/N \geq 5$ . This property is due to the statistical detection step carried out on the residual images after speckles attenuation. However, its detection sensitivity is significantly lower compared to PACO. Indeed, only 12 sources (out of 32) are detected at  $S/N \geq 5$  with ANDROMEDA and it seems to us very difficult to detect the other ones by a visual inspection since the shape of their (potential) detection peaks (blobs spatially correlated on a few pixels) are very similar to the speckles ones. While it performs statistical detection, ANDROMEDA seems to be suffering from its speckles attenuation step (by images subtraction) limiting its detection capability. Finally, only PACO achieves the detection of the 32 sources without any false alarm. In particular, only PACO detects the faintest real point source (pink circle on the top left) at  $S/N \geq 5$ .

Figures 2.18 and 2.19 gives the results obtained where fake exoplanets with a higher flux  $\alpha$  (*levels 2* and *3* of contrast) are injected in the data at the same locations. These complementary results illustrate that, with larger fluxes, all algorithms detect more sources. At these larger fluxes, PACO detects the fake planets with significantly larger S/N values than the other algorithms and the gap between the last true detection and the first false alarm is increased.

Figure 2.20 summarizes the performance of the tested algorithms on the HIP 72192 dataset via receiver operating characteristics (ROC). ROC curves represent the true positive rate (TPR) as a function of the false detection rate. Since the false detection rate cannot be easily assessed, the TPR is represented as a function of the number of false detections (represented in log scale). As discussed in Gomez Gonzalez et al. (2017); Jensen-Clem et al. (2017), this type of representation is very useful to evaluate and compare the performance of exoplanet hunter algorithms. This figure highlights that PACO is the only tested algorithm able to detect both the faintest injected fake exoplanets (*level 1*) and the real faint sources without false alarm, thereby outperforming TLOCI, KLIP, LLSG, and ANDROMEDA algorithms.

### 2.5.2.2 Detection maps with fast PACO

As detailed in Section 2.4.4, detection maps and other related quantities can also be computed by `fast PACO`, our fast implementation of PACO. Figure 2.21 gives the S/N maps computed with `fast PACO` on the HD 131399 (2015) and HIP 72192 datasets at  $\lambda_1 = 2.110 \mu\text{m}$  without injected fake exoplanet. It can be noted that the PACO Algorithm 2.1 and `fast PACO` Algorithm 2.3 lead to very similar detection maps. A low-pass



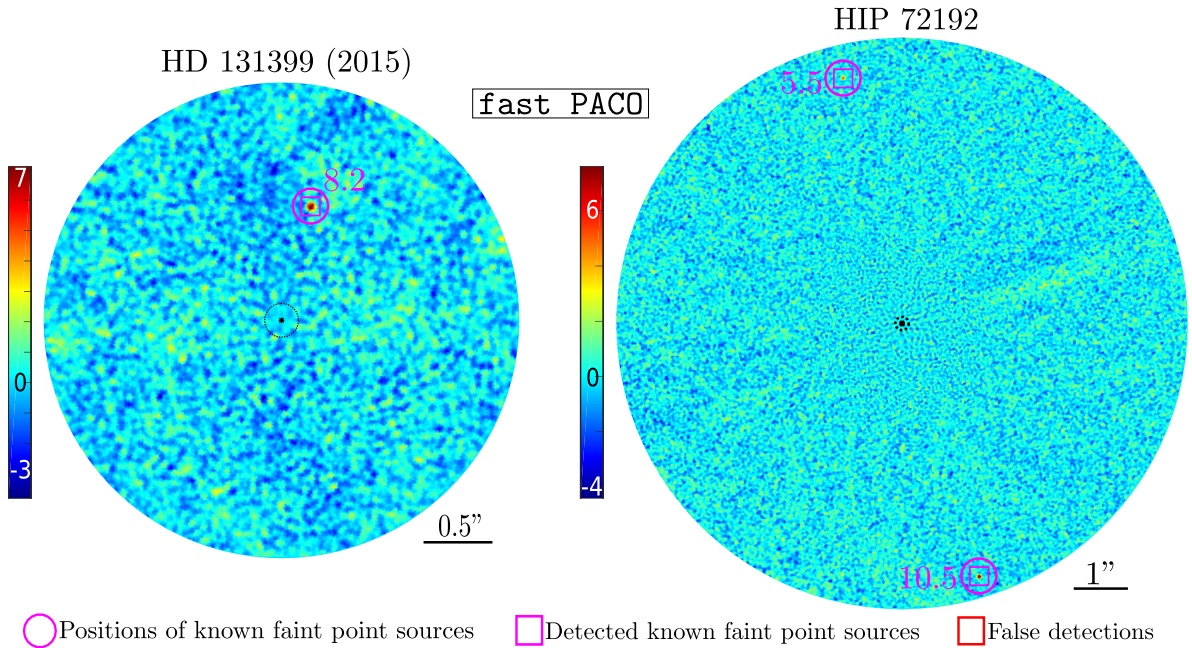


Figure 2.21 – S/N maps computed with `fast PACO` on the HD 131399 (2015) and HIP 72196 dataset at  $\lambda_1 = 2.110 \mu\text{m}$ . Detections over the S/N threshold of five are shown, they correspond to known background faint point sources.

effect is observed on maps derived from `fast PACO` due to the approximations made. Although the real faint point sources present in the data are detected with slightly lower values of S/N (reduction in S/N less than 5%) with the `fast PACO` algorithm, they remain detectable without ambiguity for a conventional detection threshold of  $\tau = 5$ .

This algorithm can be used routinely to process large data surveys. It is currently used to process with state-of-the-art algorithms more than 300 ADI datasets from the SHINE survey (Sphere High-contrast INfrared imaging for Exoplanets, Langlois et al., in prep.). The processing is then refined using `PACO` for the datasets revealing potential faint point sources. These candidate sources are finally characterized (astrometry and photometry), see Chapter 8 for our automated pipeline and application of `PACO` for astronomy purpose on recent datasets.

### 2.5.2.3 `PACO`: a general framework

The `PACO` framework is general and can be applied to ADI datasets from different high contrast instruments. Of course, the gain brought by `PACO` depends on the quality of the dataset and therefore the quality of the optical corrections of the instrument. To illustrate the versatility of `PACO`, we consider an additional dataset recorded by the NaCo instrument equipped with the previous-generation AO system. NaCo is still operating at the VLT. This dataset is delivered as a testing dataset with the VIP processing pipeline (Gomez Gonzalez et al., 2017). It was recorded around the  $\beta$  Pictoris star. This A6V-type star is located in the Pictor constellation and hosts two known exoplanets ( $\beta$  Pictoris b and c).  $\beta$  Pictoris b was discovered (Lagrange et al., 2009) and



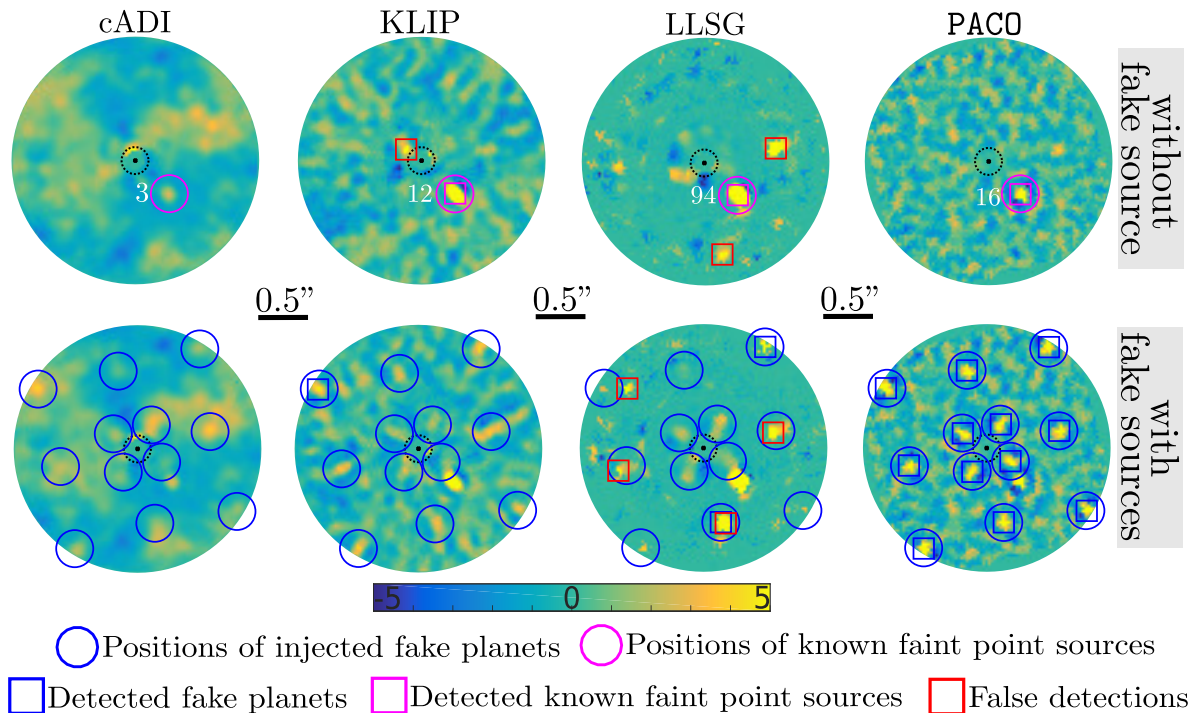


Figure 2.22 – S/N maps computed with PACO, cADI, KLIP, and LLSG algorithms on the  $\beta$  Pictoris dataset at  $\lambda_1 = 3.800 \mu\text{m}$ . Top: without injection of fake faint point source (the location of the exoplanet  $\beta$  Pictoris is identified by a pink circle). Bottom: with injection of fake faint point sources (their locations are identified by blue circles). A common threshold at  $S/N = 5$  is applied to defined the detections.

confirmed (Lagrange et al., 2010) by direct imaging.  $\beta$  Pictoris c was discovered very recently by the radial velocities method (Lagrange et al., 2019b). In the following, we do not consider the presence of  $\beta$  Pictoris c any more<sup>9</sup>. While the achievable contrast with NaCo is generally lower than with SPHERE, the considered dataset benefits from a favorable total amount of rotation of the field of view ( $\Delta_{\text{par}} = 81^\circ$ ,  $T = 61$ ). Moreover,  $\beta$  Pictoris b is expected to be not too close to its host star in this dataset (see Chapter 8 for more challenging conditions of observation).

Figure 2.22 gives the S/N maps obtained with cADI, KLIP, and LLSG algorithms implemented in the VIP package<sup>10</sup>, to be compared with PACO. The results are given without injection of fake faint point sources (only  $\beta$  Pictoris b is expected to be detected) and with the injection of 12 fake faint point sources whose levels of contrast are reported in Table 2.5. The same conclusions can be drawn as those presented in the previous

9.  $\beta$  Pictoris c has a very small angular separation with its host star (0.10-0.15 arcsec at its maximal elongation). For comparison, the limit of the classical coronagraphs of SPHERE-IRDIS masking the host star and its close environment is 0.125 arcsec. Besides,  $\beta$  Pictoris c has a very low flux given its separation (about  $1 \times 10^{-4}$  in the H Johnson’s band). For these two reasons, it could be detected by direct imaging when it is at its maximal elongation only, given the current instrumental and processing capabilities, see Lagrange et al. (2019b).

10. We use here this implementation since the state-of-the-art algorithm’s parameters were already tuned by the VIP’s authors for this dataset.

Table 2.5 – Angular separation and contrast of the injected fake sources on the  $\beta$  Pictoris dataset at  $\lambda_1 = 3.800 \mu\text{m}$ . Fluxes have been chosen so that the difficulty of detecting each source be approximately the same at all angular separations.

Separation (")	Mean[ $\alpha$ ]	Min[ $\alpha$ ]	Max[ $\alpha$ ]
0.27	$9.3 \times 10^{-5}$	$6.2 \times 10^{-5}$	$1.2 \times 10^{-4}$
0.76	$7.6 \times 10^{-6}$	$7.2 \times 10^{-6}$	$8.2 \times 10^{-6}$
1.17	$3.0 \times 10^{-6}$	$2.9 \times 10^{-6}$	$3.2 \times 10^{-6}$

section based on the processing of SPHERE data. LLSG outperforms other state-of-the-art algorithms. However, due to its entry-wise thresholding, its S/N maps are not statistically grounded so that they cannot be interpreted in terms of PFA nor in terms of PD. Only PACO can detect without ambiguity the known exoplanet and the 12 injected fake point sources.

### 2.5.3 Contrast curves and detection statistics

This section is devoted to the quantitative evaluation of the performance of PACO via contrast curves and contrast maps. For a given probability of false alarm PFA (hence, a given detection threshold  $\tau$ ), the contrast represents the minimum flux (normalized to the host star flux) that a source must have to be detected by the algorithm with a probability of detection PD. Throughout this section, we consider a target PFA of  $2.87 \times 10^{-7}$  reached when thresholding the S/N detection maps at  $\tau = 5$ . The resulting contrast is conventionally referred to “contrast at  $5\sigma$ ” in the literature. Since the statistical distribution of the S/N is well controlled with PACO (see discussion in Section 2.3.6.1), the PFA and PD can be predicted at each location  $\phi_0$  based on the local statistics  $\widehat{\mathbf{m}}$  and  $\widehat{\mathbf{C}}$  using Equation (2.29). The resulting contrast is, however, a lower bound since it would only be achievable with exact knowledge of the local statistics  $\widehat{\mathbf{m}}$  and  $\widehat{\mathbf{C}}$ . Given that these local mean and covariance must be estimated in the presence of a source, the actual achievable contrast is higher (i.e., worse). Hence, theoretical curves/maps are referred to as “PACO oracle” (achievable should an *oracle* provide the background statistics  $\widehat{\mathbf{m}}$  and  $\widehat{\mathbf{C}}$ , even in the presence of a source). To assess the actual detection performance of the algorithm, we compute, based on Monte-Carlo simulations, the contrast required to detect sources with PD = 0.5 when applying a threshold at  $\tau = 5$ . These contrasts are referred to simply as “PACO” in the curves displayed in the following figures.

#### 2.5.3.1 Predicted best-achievable-contrast

We first illustrate that the lower bound on the achievable contrast (as reached by PACO oracle) obtained using Equation (2.29) is correct. Figure 2.23 displays the contrast curve as a function of the angular separation on the HD 131399 (2015) dataset at  $\lambda_2 = 2.251 \mu\text{m}$ . The theoretical contrast map for PACO oracle as obtained from Equation (2.29) is radially averaged to obtain a curve of contrast as a function of the angular separation between the source and the host star. Two curves are drawn corresponding to PD = 0.5 and PD = 0.8. Superimposed to these curves, Monte-Carlo

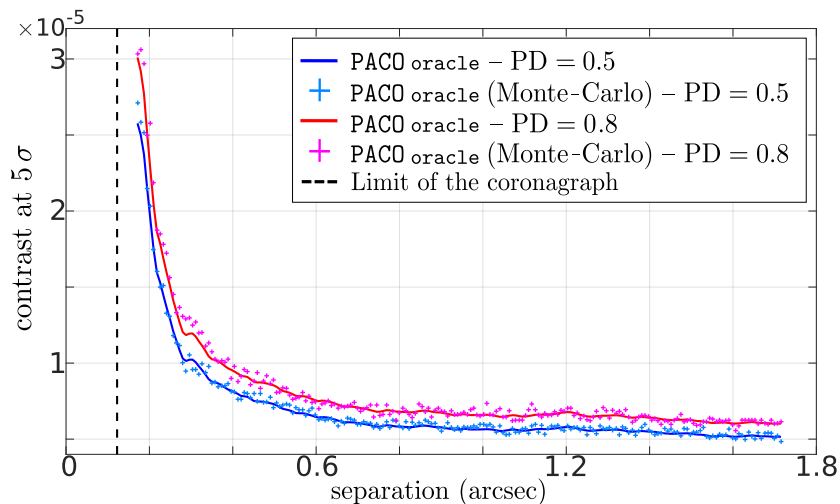


Figure 2.23 – Contrast curves obtained with PACO: comparison between predicted contrast map from PACO derived from Equation (2.29) denoted as “PACO oracle” radially averaged and Monte-Carlo simulations (denoted as “PACO oracle (Monte-Carlo)”) by injection of 20 fake faint point sources at each tested separation on the HD 131399 (2015) dataset at  $\lambda_2 = 2.251 \mu\text{m}$ . The two cases are considered with absence of faint point sources during the learning of the statistics of the background (oracle mode).

simulation results show the contrast necessary to achieve the targeted PD value in oracle mode, that is to say when the statistics of the background are computed on data with no injected source. These contrasts are in good match with the theoretical curves which validate the use of (2.29) to compute this contrast lower-bound.

Figure 2.24 gives the maps of contrast for a probability of detection  $\text{PD} = 0.5$  obtained with PACO oracle on the HD 131399 (2015), HD 131399 (2016) and HIP 72192 datasets, at  $\lambda_1 = 2.110 \mu\text{m}$  and  $\lambda_2 = 2.251 \mu\text{m}$ . As expected, this contrast improves when the angular separation increases since the stellar leakages decrease farther from the star. Interestingly, Figure 2.24 emphasizes that some local areas are less favorable than others for the detection of low-flux exoplanets, because the spatial structures of the background fluctuations may be misinterpreted as low-flux sources. For example, the contrast is locally higher in the southwestern area of the HIP 72192 dataset (see orange dashed area) at  $\lambda_1 = 2.110 \mu\text{m}$ . This can explain the difficulties of state-of-the-art algorithms in this area as emphasized in Section 2.5.2 (see orange dashed areas in Figures 2.17, 2.18, and 2.19). While other algorithms suffer from an increased false detection rate in these areas (due to a lack of local adaptivity of the methods), PACO has a constant false alarm rate. Only the probability of detection is decreased in these more difficult regions, as expected.

### 2.5.3.2 Actual best-achievable-contrast

We now investigate the actual performance of PACO (i.e., without oracle knowledge of the background statistics). The statistics of the background are impacted by the presence of the exoplanet, which decreases the S/N (and hence increases the required contrast to achieve the same probability of detection than in oracle mode).

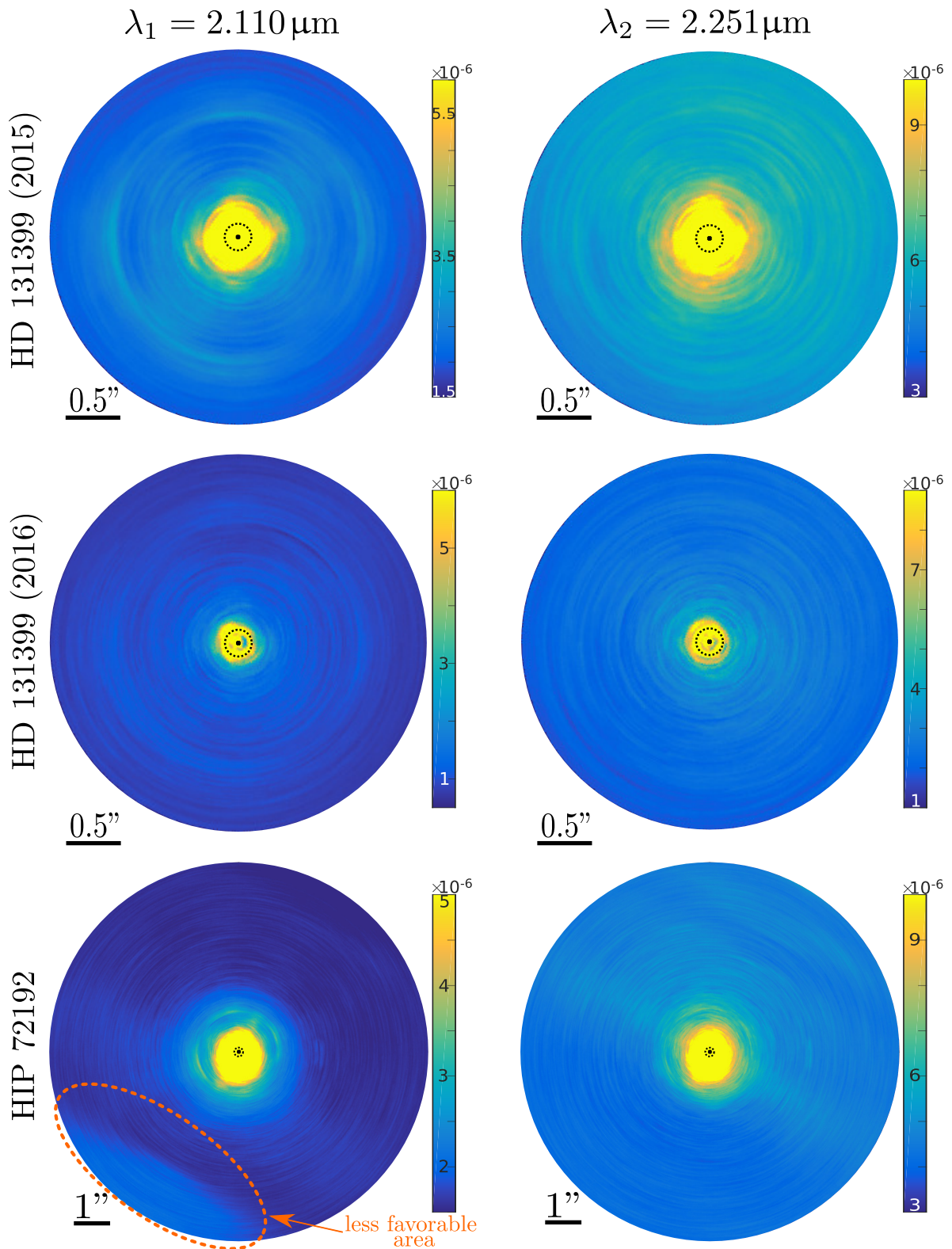


Figure 2.24 – Contrast maps for a probability of detection  $PD = 0.5$  obtained with PACO oracle for HD 131399 (2015), HD 131399 (2016) and HIP 72192 datasets at  $\lambda_1 = 2.110 \mu\text{m}$  and  $\lambda_2 = 2.251 \mu\text{m}$ .



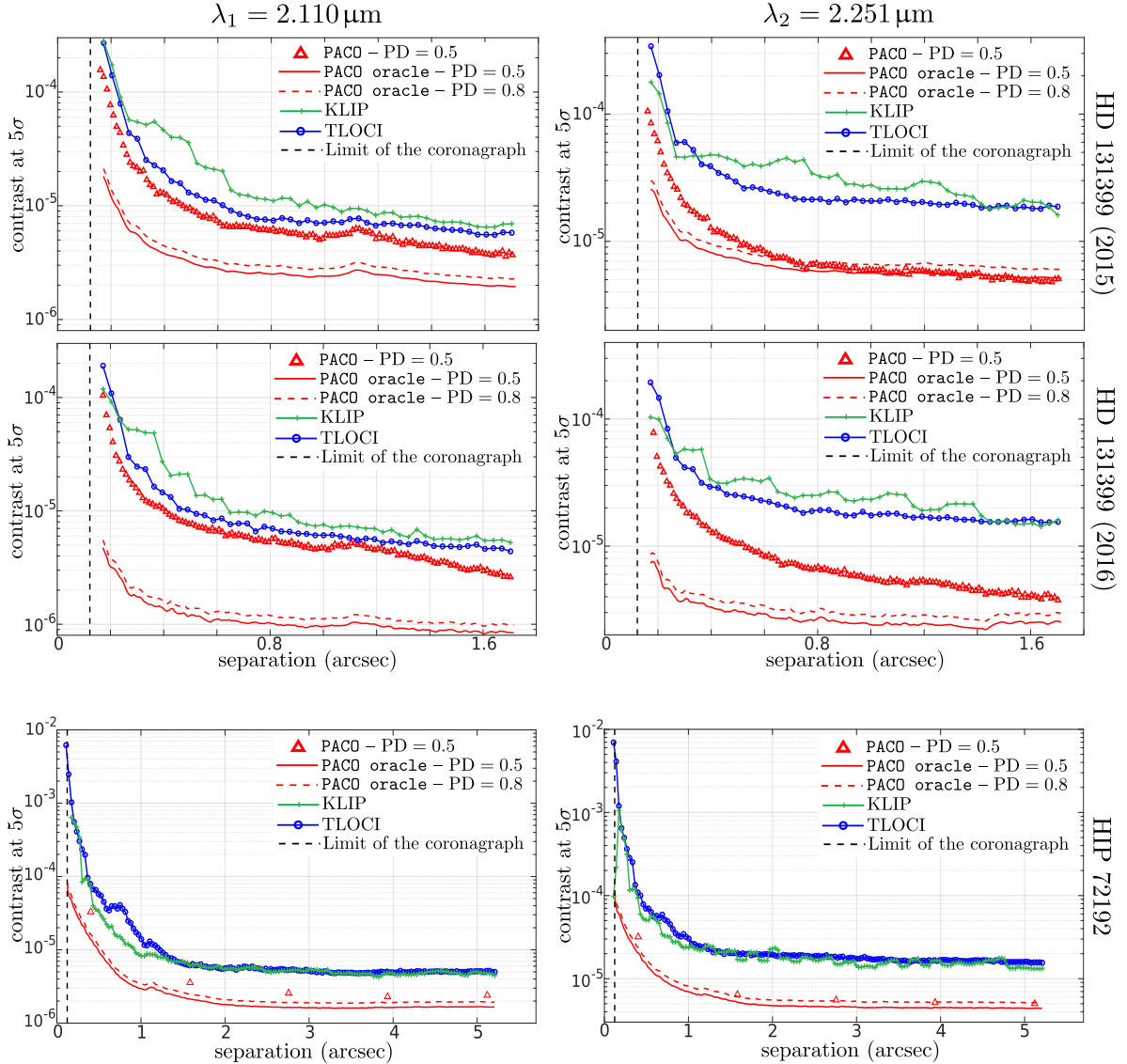


Figure 2.25 – Contrast curves derived from PACO, TLOCI, and KLIP for a probability of detection  $PD \in \{0.5; 0.8\}$  at  $\lambda_1 = 2.110 \mu\text{m}$  and  $\lambda_2 = 2.251 \mu\text{m}$  for the HD 131399 (2015), HD 131399 (2016), and HIP 72192 datasets respectively. Contrast curves as provided by KLIP and TLOCI do not correspond to a  $5\sigma$  false alarm rate contrarily to the contrast curves of PACO. The achievable contrasts are thus significantly over-optimistic for KLIP and TLOCI, see discussion in Section 2.5.3.2.

Figure 2.25 shows contrast curves derived from PACO oracle (i.e., using Equation (2.29)) and PACO (as obtained by Monte-Carlo, i.e., actual contrasts). It emphasizes that PACO oracle gives a reliable approximation of the achievable contrast far from the host star (at angular separations larger than 2 arcsec). At smaller angular separations, PACO oracle over-estimates the achievable contrast because it neglects the impact of the source signal when computing background statistics. At these small angular separations, the motion of the source is limited, which makes background contamination by the source non-negligible. In these cases, resorting to Monte-Carlo simulations is thus

Table 2.6 – Photometric accuracy evaluated by Monte-Carlo simulation with 50 injections of fake sources for each angular separation, on the HIP 72192 dataset at  $\lambda_1 = 2.110 \mu\text{m}$ . Column 2: Mean estimated flux and  $1\sigma$  confidence range. Column 3: Bias. Column 4: Relative error.

Separation (")	$\langle \hat{\alpha} \rangle \pm \sigma$	$ \langle \hat{\alpha} \rangle - \alpha $	$\sigma/\alpha$
<i>Level 1</i>			
0.40	$(3.9 \pm 0.6) \times 10^{-5}$	$0.0 \times 10^{-5}$	15%
1.58	$(2.8 \pm 0.6) \times 10^{-6}$	$0.0 \times 10^{-6}$	21%
2.75	$(2.7 \pm 0.5) \times 10^{-6}$	$0.0 \times 10^{-6}$	18%
3.93	$(2.6 \pm 0.4) \times 10^{-6}$	$0.0 \times 10^{-6}$	15%
5.12	$(2.5 \pm 0.4) \times 10^{-6}$	$0.0 \times 10^{-6}$	16%
<i>Level 2</i>			
0.40	$(5.8 \pm 0.6) \times 10^{-5}$	$0.0 \times 10^{-5}$	10%
1.58	$(4.2 \pm 0.6) \times 10^{-6}$	$0.0 \times 10^{-6}$	14%
2.75	$(3.8 \pm 0.5) \times 10^{-6}$	$0.0 \times 10^{-6}$	13%
3.93	$(3.5 \pm 0.4) \times 10^{-6}$	$0.0 \times 10^{-6}$	11%
5.12	$(3.4 \pm 0.4) \times 10^{-6}$	$0.0 \times 10^{-6}$	12%
<i>Level 3</i>			
0.40	$(8.6 \pm 0.6) \times 10^{-5}$	$0.0 \times 10^{-5}$	7%
1.58	$(5.6 \pm 0.6) \times 10^{-6}$	$0.0 \times 10^{-6}$	11%
2.75	$(4.8 \pm 0.5) \times 10^{-6}$	$0.0 \times 10^{-6}$	10%
3.93	$(4.4 \pm 0.4) \times 10^{-6}$	$0.0 \times 10^{-6}$	9%
5.12	$(4.3 \pm 0.4) \times 10^{-6}$	$0.0 \times 10^{-6}$	9%

necessary to obtain an accurate estimation of the achievable contrast.

Superimposed to these curves, we give the contrast curves provided by TLOCI and KLIP algorithms. These latter curves must, however, be analyzed with care. S/N maps computed on the dataset in which we injected fake sources (Figures 2.17, 2.18, and 2.19) indeed illustrated that thresholding at  $S/N = 5$  the detection maps of TLOCI and KLIP leads to numerous false alarms (many more than expected if the detection maps were distributed according to a standard Gaussian distribution in the absence of source). The contrast curves provided therefore correspond to a much higher probability of false alarm that is not constant in the field of view, and that is very favorable to these algorithms. Therefore, these curves cannot be directly compared to those drawn for PACO. The actual difference between the minimal contrast for source detection with PACO and TLOCI or KLIP would be much larger should the same false alarm rate be considered.

## 2.5.4 Photometry accuracy

This section is devoted to the analysis of the capability of PACO to correctly estimate the flux  $\alpha$  of a detected source. As explained in Sections 2.3.2 and 2.4.3, the PACO characterization scheme is very similar to the PACO detection procedure. The main difference lies in the joint estimation of the flux of the source and the background



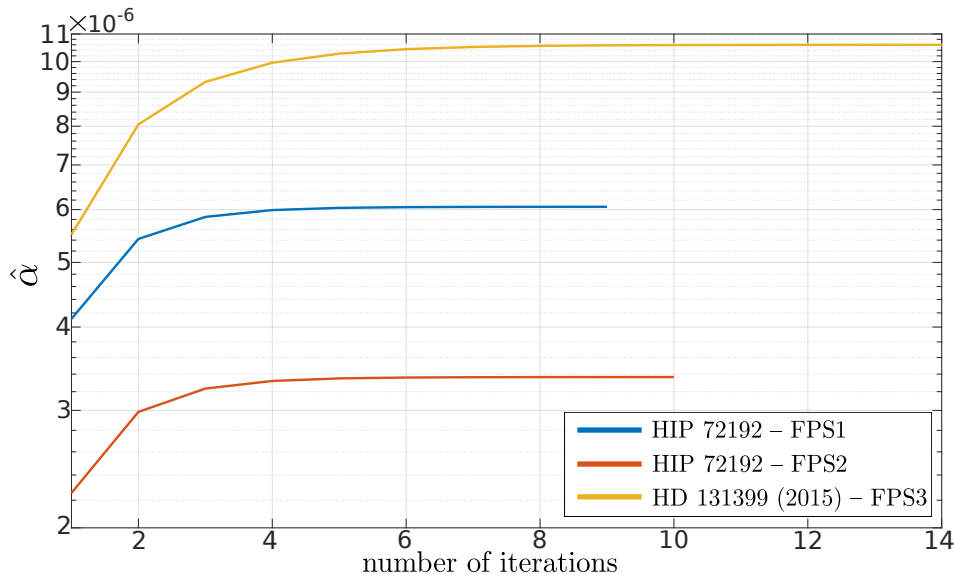


Figure 2.26 – Estimated flux as the function of the number of iterations of PACO characterization Algorithm 2.2 for the three known faint point sources (FPS) of the HIP 72192 and HD 131399 (2015) datasets.

statistics to prevent from under-estimating the flux of the source.

To evaluate the photometric performance of PACO characterization at different angular separations, we performed the following numerical experiment: we injected fake faint point sources with contrast decreasing with the angular separation at the three levels of contrast considered previously (see Table 2.4). For each angular separation, 50 different injections (at different known locations in the field of view) were performed, and each time the flux was estimated at those known locations using PACO characterization Algorithm 2.2. Table 2.6 reports the mean estimated flux  $\langle \hat{\alpha} \rangle$ , the bias, and the photometric standard deviation relative to the source flux. It shows that the bias is negligible compared to the standard deviation, at all angular separations. It also illustrates that the standard deviation depends on the source location (some areas are more favorable than others) but not on the source amplitude, as expected from the theoretical study, see Equation (2.22) which is recalled hereafter:

$$\hat{\sigma}_\alpha \approx 1/\sqrt{a}.$$

. PACO characterization also provides a statistical unbiased photometric estimation even for high levels of flux, i.e., even in cases where the point source contaminates strongly the collection of patches used for the computation of the background statistics. As the standard deviation of the estimated flux does not depend on the flux of the point source, the relative error of the flux improves when the flux of the point source increases.

Figure 2.26 gives the estimated flux  $\hat{\alpha}$  as the function of the number of iterations with the PACO characterization Algorithm 2.2 for the three known point sources close to HD 131399 and HIP 72192 stars. They show that the iterative estimation scheme converges within a few iterations. Figure 2.27 gives the local maps of the estimated flux at  $\lambda_1 = 2.110 \mu\text{m}$  for these three point sources. The estimated flux is compared to the estimated flux obtained without performing an alternate estimation between the

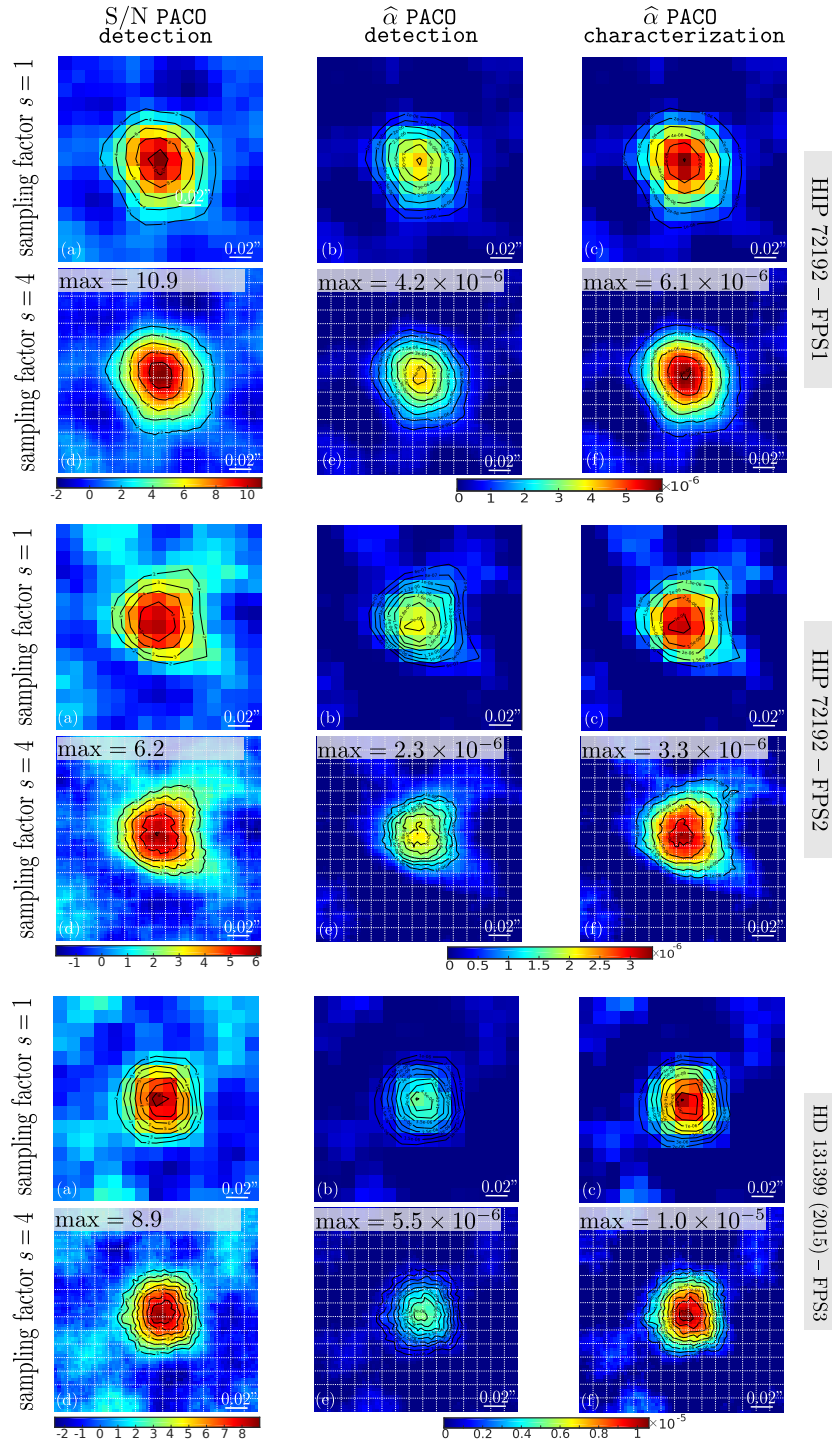


Figure 2.27 – Local S/N maps and estimated flux at  $\lambda_1 = 2.110 \mu\text{m}$  around the known real faint point sources (FPS1 and FPS2) located around the HIP 72192 star and the known real faint point source (FPS3) located around the HD 131399 system. (a): S/N of detection derived from PACO detection Algorithm 2.1. (b): Estimated flux derived from PACO detection Algorithm 2.1. (c): Estimated flux derived from PACO characterization Algorithm 2.2 alternating between the estimation of the flux and the computation of the background statistics. (e-d-f): Respectively correspond to (a-b-c) computed on a subpixel grid with a sampling factor  $s = 4$ . The superimposed white grid represents the original sampling grid (sampling factor  $s = 1$ ).

flux and the statistics of the background. For the two considered cases, the estimation is performed with a sampling corresponding to the data pixel grid (i.e., sampling factor  $s = 1$ ) and with a subpixel sampling (sampling factor  $s = 4$ ). The flux of the objects (and the S/N values) are also significantly under-estimated if the estimation of the flux is not alternated with the estimation of the background statistics. This shows that both (i) the location refinement and (ii) the joint estimation of the source flux and of the background statistics are required to obtain an accurate estimate of fluxes.



### PACO characteristics

Based on the analysis of several ADI datasets, PACO shows several appealing characteristics:

- it produces stationary and statistically grounded detection maps that can be directly interpreted in terms of probability of false alarm and probability of detection,
- it demonstrates significantly better detection sensitivity than other state-of-the-art methods,
- it produces a 2-D contrast map, and the resulting contrast is in good agreement with the actual achievable contrast at a moderate distance from the host star,
- it provides unbiased photometry estimation without resorting to Monte-Carlo methods.

## 2.6 Conclusion on PACO's capabilities

This chapter presents a new method (PACO) dedicated to exoplanet detection in angular differential imaging. PACO differs from the existing methods in its local modeling of the background statistics that captures both the average speckles and the spatial correlations. The decision in favor of the presence or absence of an exoplanet is made by a binary hypothesis test. Since no image subtraction is performed, the photometry is well preserved by the method. PACO is completely parameter-free, from the computation of a detection map to its thresholding to extract meaningful detections and the estimation of fluxes of the detected sources. We believe that this is a significant advantage to obtain consistent performances and deploy the method on large exoplanet surveys.

PACO is statistically grounded so that the false alarm rate, the probability of detection and the contrast can be assessed without necessarily resorting to Monte-Carlo methods. Since the performance of the detection and estimation method is theoretically well understood, it paves the way to the co-design of the next generation of instruments for exoplanet detection, the instrumental design and/or observation planning being easily related to detection performances through the predicted contrast and photometric or astrometric accuracies (see Chapter 4).

We showed using datasets from the VLT/SPHERE-IRDIS instrument that the proposed method achieves significantly better detection performance than current cutting-edge algorithms. The detection maps obtained using PACO also have a stationary behavior even in the vicinity of the host star. Robust processing or joint processing of data from different wavelengths can further improve the detection maps and push down the detection limit. The resulting adaptations of the PACO algorithm are presented in Chapters 4 and 6, respectively.







# Application of background fluctuations modeling in holographic microscopy: detection of diffraction patterns

---

**Abstract**

*Holographic microscopy is another application field which requires the detection of a weak signal superimposed over a background. Because of temporal fluctuations, the background cannot be completely suppressed by subtraction. The detection of the pattern then requires statistical modeling of the background. Due to difficulties related to the estimation of the spatial correlations of the background and the application of an optimal detector that accounts for these correlations, it is common practice to neglect them. In this chapter, spatial correlations at the scale of an image patch are locally estimated based on several background images. This chapter introduces a method named EXPACO, dedicated to the detection of spatially extended known patterns such as diffraction patterns in holographic microscopy. A fast algorithm for the computation of detection maps is derived. The approach is evaluated on images obtained from a holographic microscope.*

---

## 3.1 Introduction

As discussed in Section 1.3.2, the detection and localization of a faint pattern modeled by a few parameters is an essential processing task in holographic microscopy. In particular, small spherical objects such as cocci bacteria, bubbles or droplets can be imaged over time to derive, after detection, physical properties (e.g., size and refractive index) characterizing them (Wang et al., 2016; Philips et al., 2017; Sentis et al., 2018). The resulting holograms are often impacted by a strong *background*, as illustrated by Figure 3.1, due to optical aberrations and the presence of unwanted objects (e.g., dust) in the field of view. Moreover, that background fluctuates over time (see Figure 3.7 and Section 3.5). Fluctuations in the background are due to small variations of the optical path lengths between optical surfaces (because of mechanical vibrations or thermal

inhomogeneities of the air) and are difficult to model fully.

The detection and localization tasks become very difficult when the amplitude of the pattern of interest is small compared to the background fluctuations, and under the presence of nonstationary and correlated background structures. A crude solution is to simply ignore these correlations; the noise is then considered as additive, white, and Gaussian (Verrier et al., 2015; Marié et al., 2017). Several finer strategies can be considered to overcome these difficulties. As in the TLOCI-type algorithms used for exoplanet detection (see Section 2.2), a template image of the background can be formed from a collection of background images. For this purpose, the mean (median) or a linear combination of the backgrounds most correlated to the image of interest can be computed (Krishnatreya et al., 2014; Vandewiele et al., 2017). The resulting template background is then subtracted to the hologram of interest. However, these approaches remain limited when the background fluctuations are large. Another solution, for slowly evolving backgrounds, is to separate the background and the object contributions using a regularized inverse problem approach (Berdeu et al., in prep.). Such a method is based on the use of different holograms recorded at different defocus and different transversal shifts so that the background and the signal of interest can be unmixed. Yet another possibility is to consider the background contribution as *outliers* while the diffraction fringes created by the objects of interest act as *inliers*. In this context, robust approaches based on the iterative re-weighting of the residuals of estimation can be helpful. In Chapter 5, we present such a strategy. In this chapter, we propose an alternative approach: we follow the same statistical framework as in Chapter 2 and we derive an algorithm (EXPACO) dedicated to the detection and localization of spatially EXTended known patterns under a nonstationary and correlated background through the modeling of PATCH COvariances.

This chapter is structured as follows. Section 3.2 describes the statistical modeling of background fluctuations with EXPACO. Section 3.3 presents the statistical framework used for the detection of an extended known pattern based on patch covariances. It gives a particular emphasis on the algorithm complexity and shows that its straightforward implementation leads to a prohibitive computational cost. Section 3.4 derives an efficient algorithm based on fast Fourier transforms to approximate the detection map. Finally, Section 3.6 concludes the chapter with several experiments showing the efficiency of the proposed detection approach. This chapter is based on the conference paper Flasseur et al. (2019).

## 3.2 Statistical modeling of the background fluctuations

As in Chapter 2, we focus on the case where several images of the background are recorded. While it is not possible to learn the background statistics from pure background realizations in direct imaging (an exoplanet, if present, always contributes to the observed signal, see Chapter 2), here we learn the background statistics in the absence of the objects of interest, before performing the detection tasks. From an experimental point of view, the glass slide containing the objects of interest is shifted to an area where only the surrounding medium is present.

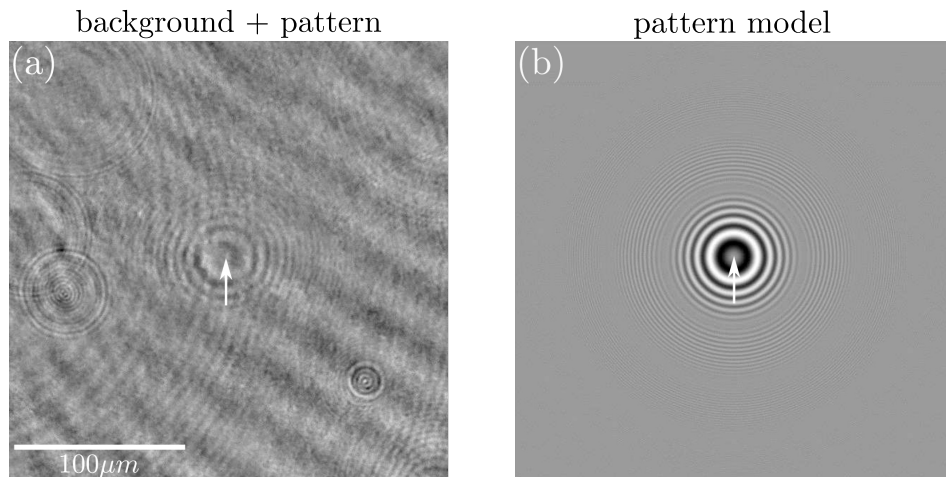


Figure 3.1 – (a) Hologram of a  $0.5\ \mu\text{m}$  radius latex bead in suspension in permuted water. (b) The model of the diffraction pattern of the bead that best fits the data in the least-squares sense (see Section 1.3.2.2.1). Adapted from Verrier et al. (2015).

Because of the temporal fluctuations of the background, subtracting an average background or even a linear combination of the background images is not sufficient to efficiently remove the background from the image: spatially-structured residuals remain and degrade the detection performance (see Section 3.5 and Figure 3.7). To overcome this limitation, a statistical modeling of the background fluctuations can be built to better decide at detection time which part of the signal may be ascribed to the pattern to detect and which part is more likely due to a typical temporal fluctuation of the background.

In holographic microscopy, background fluctuations are generally nonstationary and spatially correlated. Capturing those fluctuations at the scale of an  $N$ -pixels image from only a few tens up to a few hundreds of background images is very difficult: the covariance matrix has  $\mathcal{O}(N^2)$ <sup>1</sup> terms. Either some structure has to be assumed for the covariance matrix or a more local modeling is necessary.

Assuming the spatial stationarity of the covariance matrix constrains the covariance matrix to be Toeplitz-bloc-Toeplitz. Under this hypothesis, the maximum correlation detection method can be adapted by applying a pre-processing step to whiten the observations and the model by shift-invariant linear filtering, see Réfrégier and Goudail (2013). Such an approach is however inapplicable to cases with non-stationary backgrounds like in holographic microscopy. We therefore resort to a local modeling of covariance matrices.

In this section, we follow the same statistical modeling based on Patches Covariances than for exoplanet detection by direct imaging. The PACO algorithm described in Chapter 2 is adapted to detect spatially EXtended known patterns (hence the name EXPACO). Figure 3.2 illustrates the main differences between PACO and EXPACO. First, with PACO, the background statistics are learned in the presence of the (potential) exoplanets to be detected while with EXPACO they are learned in the absence of the objects of interest (by shifting the sample out of the field of view), see column ①. Secondly,

1.  $\mathcal{O}(\cdot)$  corresponds to Bachmann–Landau asymptotic notation.

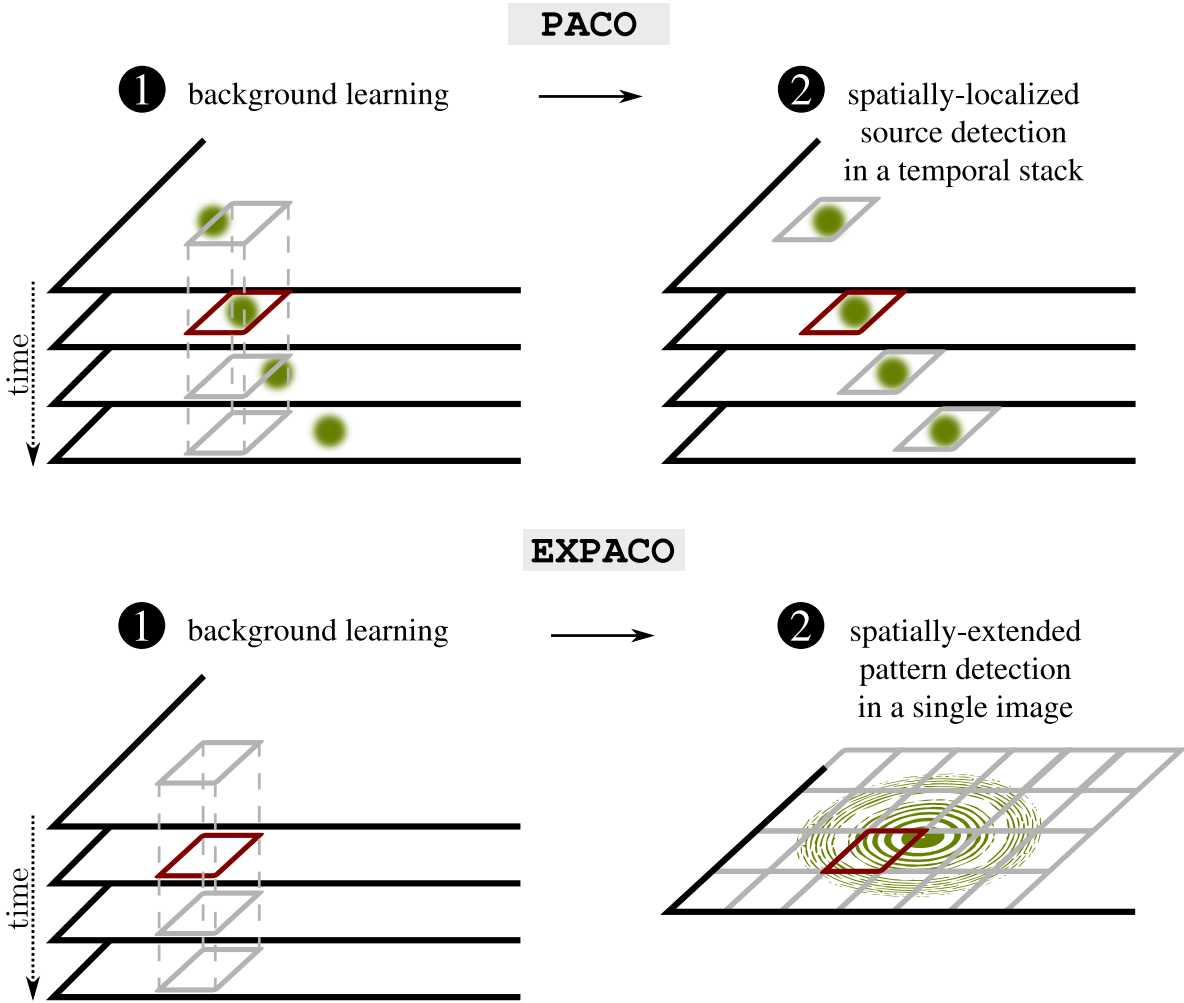


Figure 3.2 – Comparison between the PACO and the EXPACO algorithms.

with PACO, the detection problem is spatially localized (exoplanets behaving as point sources) and multi-temporal (exoplanets having an apparent motion along time) while the problem now consists of detecting a spatially extended pattern (due to the diffraction) at a unique frame (date) with EXPACO, see column ②.

Like in the previous chapter, the background component  $\mathbf{f} \in \mathbb{R}^N$  is decomposed into patches. The patch  $\mathbf{f}_n \in \mathbb{R}^K$  extracted around pixel  $n$  is modeled by a multivariate Gaussian:  $\mathbf{f}_n \sim \mathcal{N}(\mathbf{m}_n, \mathbf{C}_n)$ , where both the mean  $\mathbf{m}_n$  and the covariance matrix  $\mathbf{C}_n$  are estimated locally from the set of background images.

The mean  $\mathbf{m}_n$  is estimated by the sample mean:

$$\widehat{\mathbf{m}}_n = \frac{1}{T} \sum_{t=1}^T \mathbf{f}_{n,t}, \quad (3.1)$$

where the notation  $\mathbf{f}_{n,t}$  indicates the  $K$ -pixels patch centered at pixel  $n$ , in the  $t$ -th background image.

To estimate the covariance matrix of size  $K \times K$  from  $T$  background images, the

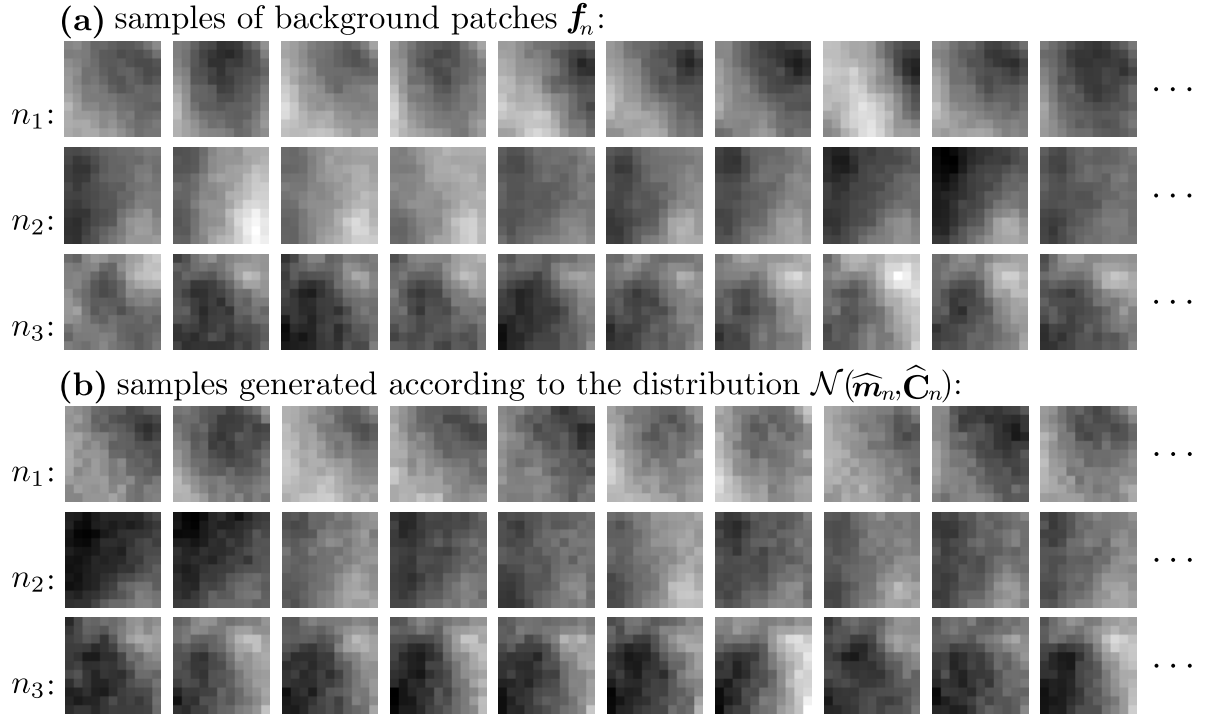


Figure 3.3 – Illustration of the local model for background patches: (a) sample  $11 \times 11$  patches from experimental backgrounds, extracted at three different locations noted  $n_1$ ,  $n_2$ , and  $n_3$ ; (b) patches generated from a multivariate Gaussian model (locally learned from 60 background samples).

sample covariance matrix can be used when  $T \gg K$ :

$$\widehat{\mathbf{S}}_n = \frac{1}{T} \sum_{t=1}^T (\mathbf{f}_{n,t} - \widehat{\mathbf{m}}_n)(\mathbf{f}_{n,t} - \widehat{\mathbf{m}}_n)^\top. \quad (3.2)$$

When  $T \approx K$ ,  $\widehat{\mathbf{S}}_n$  has a large variance and when  $T < K$ ,  $\widehat{\mathbf{S}}_n$  becomes rank-deficient. As discussed in Section 2.3.2, Ledoit and Wolf (2004) and Chen et al. (2010) improve the sample covariance matrix by shrinkage towards a matrix proportional to the identity. In Section 2.3.2, we extended the formula defining the shrinkage estimator as the convex combination of  $\widehat{\mathbf{S}}_n$  and a diagonal covariance matrix  $\widehat{\mathbf{F}}_n$  defined by  $[\widehat{\mathbf{F}}_n]_{a,b} = 0$  if  $a \neq b$ , and  $[\widehat{\mathbf{F}}_n]_{a,b} = [\widehat{\mathbf{S}}_n]_{a,b}$  (see Figure 2.4):

$$\widehat{\mathbf{C}}_n = (1 - \widehat{\rho})\widehat{\mathbf{S}}_n + \widehat{\rho}\widehat{\mathbf{F}}_n, \quad (3.3)$$

where the shrinkage coefficient  $\widehat{\rho}$  is obtained by clipping to the  $[0, 1]$  range the value (see Section 2.3.2 and Appendix A):

$$\widehat{\rho} = \frac{\text{tr}(\widehat{\mathbf{S}}_n^2) + \text{tr}^2(\widehat{\mathbf{S}}_n) - 2 \sum_{k=1}^K [\widehat{\mathbf{S}}_n]_{kk}^2}{(T + 1)(\text{tr}(\widehat{\mathbf{S}}_n^2) - \sum_{k=1}^K [\widehat{\mathbf{S}}_n]_{kk}^2)}. \quad (3.4)$$

Figure 3.3(a) shows some patches extracted at different locations of background images acquired with a holographic microscope (see Section 3.5 and Figure 3.6 for

more details). In Figure 3.3(b), some random realizations drawn according to the local Gaussian model  $\mathcal{N}(\widehat{\mathbf{m}}_n, \widehat{\mathbf{C}}_n)$  learned from 60 background patches are displayed. Patches from three different locations  $n_1$ ,  $n_2$ , and  $n_3$  are shown on two different rows. Fluctuations around the mean background differ according to the location. Generated patches are quite similar to the patches extracted from the background images at the corresponding location.

### 3.3 EXPACO: detection of EXtended known patterns based on Patch COvariances

The joint detection/localization problem of a known pattern  $\mathbf{h}(x_0, y_0)$  centered at the 2-D location  $(x_0, y_0)$  in an observed image  $\mathbf{r}$  corrupted by a background  $\mathbf{f}$  can be formulated as in Chapter 2 by a binary hypothesis test:

$$\begin{cases} \mathcal{H}_0 : \mathbf{r} = \mathbf{f} \\ \text{(background only)} \\ \mathcal{H}_1 : \mathbf{r} = \mathbf{f} + \alpha \mathbf{h}(x_0, y_0), \\ \text{(background+pattern)} \end{cases} \quad (3.5)$$

with  $\alpha > 0$  the amplitude of the pattern.

The estimation of the 2-D location  $(x_0, y_0)$  of the known pattern and its amplitude  $\alpha$  is necessary to decide between the two hypotheses. The neg-log-likelihood of parameters  $\alpha$ ,  $x_0$  and  $y_0$  under  $\mathcal{H}_1$ , with our patch-based modeling and an independence assumption between patches, is:

$$-\log p(\mathbf{r}|\mathcal{H}_1, \alpha, x_0, y_0) = \frac{1}{2} \sum_n \mathbf{g}_n^\top \mathbf{C}_n^{-1} \mathbf{g}_n + c, \quad (3.6)$$

where the residual patch  $\mathbf{g}_n$  is obtained by removing the average background  $\mathbf{m}_n$  and the contribution of the pattern  $\mathbf{h}_n$  to the observed patch  $\mathbf{r}_n$ :  $\mathbf{g}_n = \mathbf{r}_n - \mathbf{m}_n - \alpha \mathbf{h}_n(x_0, y_0)$ , and where  $c$  is a constant that depends only on the sum of the log of the covariance determinants.

At a given location  $(x_0, y_0)$ , the maximum likelihood estimate of the amplitude of the pattern is given by:

$$\widehat{\alpha}(x_0, y_0) = \frac{\max(b(x_0, y_0), 0)}{a(x_0, y_0)} = \frac{[b(x_0, y_0)]_+}{a(x_0, y_0)}, \quad (3.7)$$

with

$$\begin{cases} a(x_0, y_0) = \sum_n \mathbf{h}_n(x_0, y_0)^\top \widehat{\mathbf{C}}_n^{-1} \mathbf{h}_n(x_0, y_0) \\ b(x_0, y_0) = \sum_n (\mathbf{r}_n - \widehat{\mathbf{m}}_n)^\top \widehat{\mathbf{C}}_n^{-1} \mathbf{h}_n(x_0, y_0). \end{cases}$$

Like in the PACO algorithm, the term  $b$  can be interpreted as a correlation between the whitened model and the whitened (and centered) measurements while the term  $a$  corresponds to the auto-correlation of the whitened model, see Section 2.3.4.



To decide in favor of hypothesis  $\mathcal{H}_0$  or  $\mathcal{H}_1$ , for a fixed location  $(x_0, y_0)$ , the generalized likelihood test (GLRT) is:

$$(\text{GLRT}(x_0, y_0)) \quad \log \frac{p(\mathbf{r}|\mathcal{H}_1, \hat{\alpha}, x_0, y_0)}{p(\mathbf{r}|\mathcal{H}_0)} = \frac{[b(x_0, y_0)]_+^2}{a(x_0, y_0)} \underset{\mathcal{H}_0}{\overset{\mathcal{H}_1}{\geq}} \eta,$$

which can be recast for  $\eta \geq 0$  as a test on the signal-to-noise ratio of the pattern  $\mathbf{h}$  (S/Ntest), which follows  $\mathcal{N}(0, 1)$  under  $\mathcal{H}_0$ , see Section 2.3.5:

$$(\text{S/Ntest}(x_0, y_0)) \quad \frac{\hat{\alpha}(x_0, y_0)}{\sigma_{\alpha}(x_0, y_0)} = \frac{b(x_0, y_0)}{\sqrt{a(x_0, y_0)}} \underset{\mathcal{H}_0}{\overset{\mathcal{H}_1}{\geq}} \sqrt{\eta} = \tau. \quad (3.8)$$

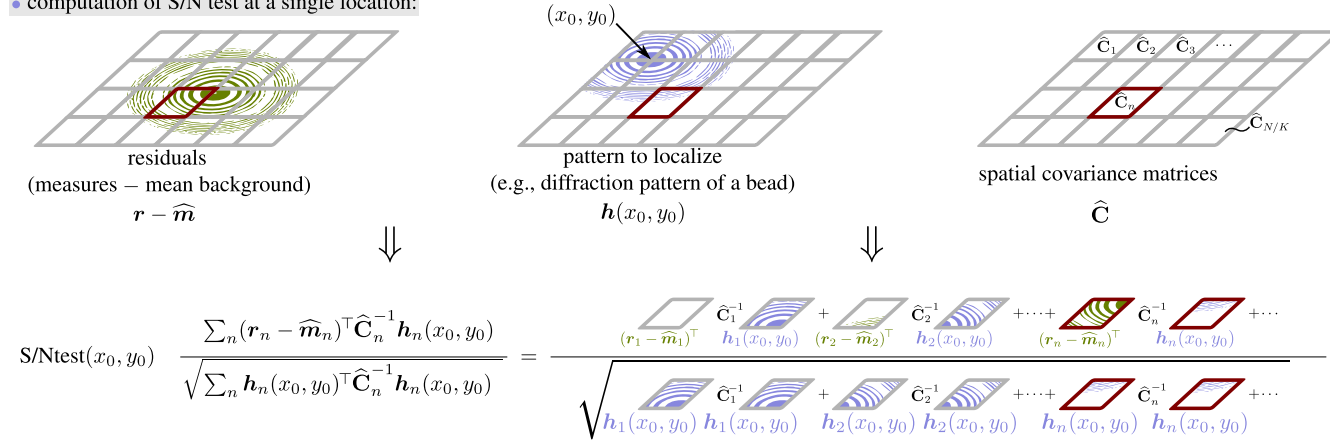
The maximum likelihood location of the pattern is obtained by maximization of the S/Ntest over all possible locations.

Figure 3.4 illustrates the computation of the detection criterion (S/Ntest) with EXPACO at different locations of the field of view. The background statistics are computed only once at each patch location (see leftmost green frames) while the model  $\mathbf{h}$  of the known pattern to detect is shifted at each location  $(x_0, y_0)$  where the detection criterion should be evaluated (see rightmost blue frames). The major difference with PACO comes from the number of patches involved when performing the hypothesis test at a tentative location  $(x_0, y_0)$ : because point-like sources are spatially localized, PACO considered only one patch per frame (a total of  $T$  patches) while EXPACO requires considering all patches of the image (possibly millions of patches).

So far, in our modeling only a single pattern has been considered. If several patterns are superimposed, each centered on a different 2-D location, a greedy approach similar to the matching pursuit can be applied: patterns are detected one at a time by forming the S/Ntest, and after each detection the detected pattern is subtracted from the data so that the next pattern can be detected by applying the S/Ntest on the residuals.

**EXPACO: detection criterion**

- computation of S/N test at a single location:



- computation of S/N test at another location:

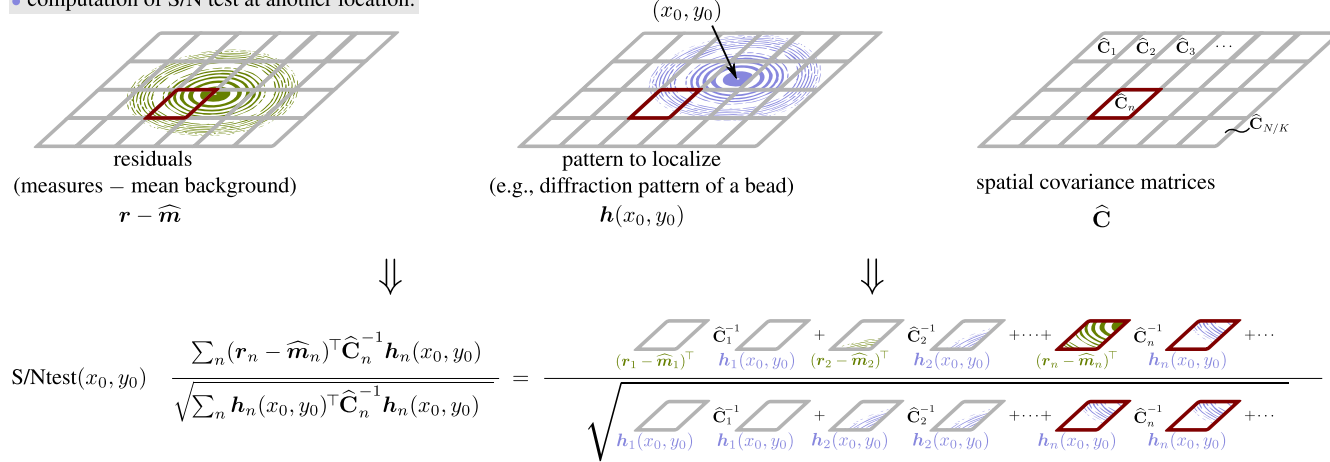


Figure 3.4 – Illustration of the computation of the detection criterion (S/Ntest) with EXPACO.

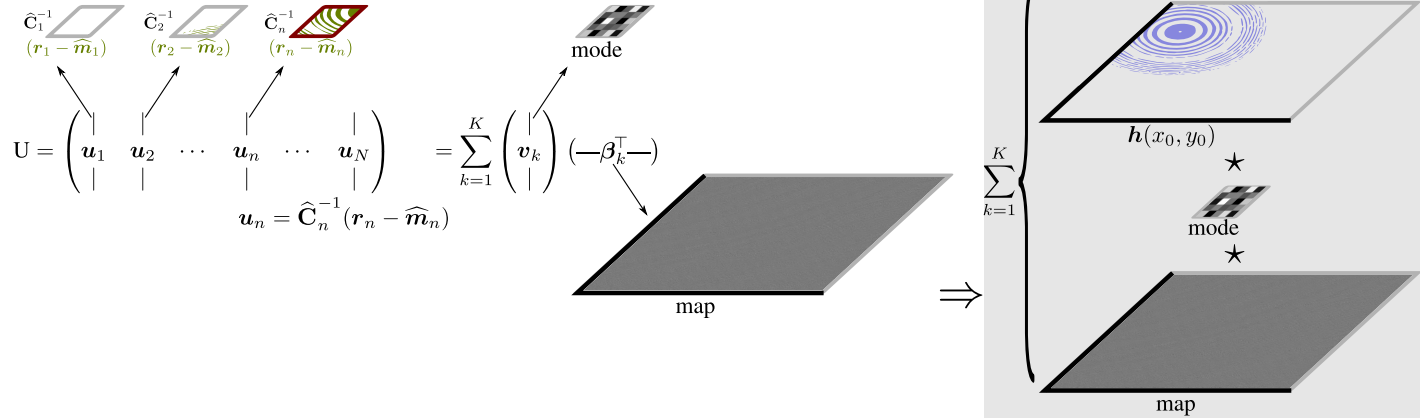


### EXtended PAtch COvariances modeling

- Based on the observation that the background of holographic time series present fluctuations involving spatially-variant correlations, we derive the basis of an algorithm (**EXPACO**) dedicated to the detection of extended known patterns in the presence of a strong and structured background. It uses the same statistical framework than the **PACO** algorithm dedicated to exoplanet detection (see Chapter 2):
  - The observed intensity is modeled as the superimposition of the background contribution and the known pattern signature.
  - A nonstationary multi-variate Gaussian model of the background is learned, capturing together the average fluctuations and the spatial correlations. In particular, the **EXPACO** covariance matrices are estimated following a shrinkage approach based on a data-driven convex combination between a low bias/high variance and a high bias/low variance estimators.
  - The decision in favor of the presence or the absence of a pattern is performed by a binary hypothesis test.
- Since the holographic patterns to be detected are spatially extended, **EXPACO** differs from the **PACO** algorithm by considering many more patches in the detection criterion.
- This methodological approach differs from state-of-the-art approaches by:
  - the absence of explicit background subtraction,
  - the learning from the data themselves of the statistics of the background.

### EXPACO: fast implementation

- fast computation of the numerator:



- fast and approximate computation of the denominator:

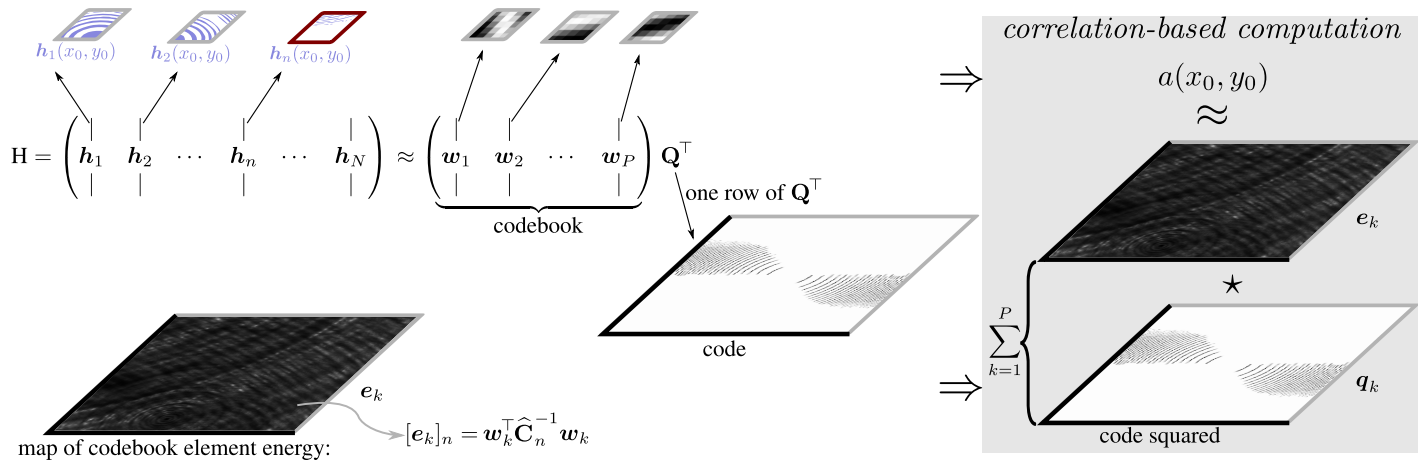


Figure 3.5 – Fast computation of the terms  $b(x_0, y_0)$  and  $a(x_0, y_0)$  for all pixel shifts with EXPACO.

## 3.4 Fast computation of detection maps with EXPACO

### 3.4.1 Evaluation of the algorithmic complexity

Localization of a pattern requires to maximize the S/Ntest. Since the S/Ntest is a non-convex function of the 2-D location  $(x_0, y_0)$ , with many local maxima observed in practice, it is necessary to systematically evaluate the S/Ntest over a grid to identify the global maximum. If the pattern<sup>2</sup>  $\mathbf{h}$  is extended, patches  $\mathbf{h}_n$  extracted from the reference pattern are all non-zero and the sums in Equation (3.8) involve  $N$  terms if patches overlap, or  $N/K$  if patches do not overlap (the pattern is not contained in a single patch but must be decomposed into a tiling of many patches). In the following discussion, we consider that patches overlap, the case of non-overlapping patches is obtained by dividing the complexity by a factor  $K$ .

Evaluating the S/Ntest defined in Equation (3.8) for a given location requires  $\mathcal{O}(NK^2)$  scalar operations if the inverse matrices  $\hat{\mathbf{C}}_i^{-1}$  are precomputed (which requires  $\mathcal{O}(NK^3)$  operations). Therefore, to produce a S/Ntest map, i.e. to compute the S/Ntest for  $N$  locations  $(x_0, y_0)$  spanning the whole pixel grid,  $\mathcal{O}(N^2K^2)$  operations are required. Since the number  $K$  of pixels in a patch is much smaller than the total number  $N$  of pixels in an image, precomputing the inverse of covariance matrices in  $\mathcal{O}(NK^3)$  is negligible compared to producing the map in  $\mathcal{O}(N^2K^2)$  and is a  $K$ -fold improvement compared to inverting linear systems at each location, which would lead to a total complexity of  $\mathcal{O}(N^2K^3)$ . This high computational complexity prevents a direct application of the S/Ntest based on the background modeling described in Section 3.2 with patch covariances.

Several strategies can be considered to overcome this difficulty. Estimating the optimal location  $(\hat{x}_0, \hat{y}_0)$  and the amplitude  $\hat{a}$  of the pattern can be done by iterative minimization based on gradients. Such a strategy requires  $\mathcal{O}(NK^2)$  operations (for a fixed number of iterations of the minimization algorithm). A multi-resolution strategy (Seifi et al., 2012) can be applied: an exhaustive search is performed on a strongly down-sampled version of the image and of the model. Then, a sequence of location estimation is performed by iterative minimization using images with an increasing size (and improved resolution). This can reduce the computational complexity by several orders of magnitude.

In this section, we describe another approach. We derive a fast algorithm to compute S/N detection maps in the case of shift-invariant models  $\mathbf{h}$ . The algorithm is based on a reformulation of Equation (3.8) that involves discrete correlations. These correlations are computed using fast Fourier transforms. We describe in turn how the numerator and the denominator of (3.8) can be efficiently computed. Throughout Sections 3.4.2 and 3.4.3, the Reader can refer to Figure 3.5 summarizing the main steps of the computation of the terms  $b(x_0, y_0)$  and  $a(x_0, y_0)$  for all pixel shifts.

---

2. For compactness, we drop in this paragraph the spatial location  $(x_0, y_0)$  in the notation  $\mathbf{h}(x_0, y_0)$ .

### 3.4.2 Fast computation of $b(x_0, y_0)$ for all pixel shifts

When the model is shifted, restrictions of the model to each patch  $\mathbf{h}_n$  are modified while patches  $\mathbf{u}_n \equiv \widehat{\mathbf{C}}_n^{-1}(\mathbf{r}_n - \widehat{\mathbf{m}}_n)$  remain unchanged. Let  $\mathbf{U} = \begin{pmatrix} | & & | \\ \mathbf{u}_1 & \cdots & \mathbf{u}_N \\ | & & | \end{pmatrix}$  be the  $K \times N$  matrix collecting all transformed patches  $\mathbf{u}_n$ . By application of a singular value decomposition (SVD), matrix  $\mathbf{U}$  can be decomposed into a sum of  $K$  rank-one matrices:

$$\mathbf{U} = \sum_{k=1}^K \begin{pmatrix} | \\ \mathbf{v}_k \\ | \end{pmatrix} (-\beta_k -), \quad (3.9)$$

where  $\{\mathbf{v}_k\}_{k=1..K}$  are the left singular vectors (i.e. modes) and  $[\beta_k]_n$  is the coefficient of each patch  $\mathbf{u}_n$  related to mode  $\mathbf{v}_k$  (obtained as the product of the  $k$ -th singular value and of the  $n$ -th entry of the  $k$ -th right singular vector).

The computation of scalar products  $\mathbf{h}_n^\top \mathbf{v}_k$  for all the patches  $\mathbf{h}_n$  that can be extracted from model  $\mathbf{h}$  is readily obtained by a 2-D correlation<sup>3</sup>:

$$\mathbf{h}_n^\top \mathbf{v}_k = [\mathbf{h} \star \mathbf{v}_k]_n, \quad (3.10)$$

where the notation  $\star$  denotes a 2-D discrete correlation.

Since the transformed patch  $\mathbf{u}_n$  can be expanded as  $\mathbf{u}_n = \sum_{k=1}^K [\beta_k]_n \mathbf{v}_k$ , we obtain:

$$\mathbf{u}_n^\top \mathbf{h}_n = \mathbf{h}_n^\top \sum_{k=1}^K [\beta_k]_n \mathbf{v}_k = \sum_{k=1}^K [\beta_k]_n \mathbf{h}_n^\top \mathbf{v}_k = \sum_{k=1}^K [\beta_k]_n [\mathbf{h} \star \mathbf{v}_k]_n. \quad (3.11)$$

Translating the model  $\mathbf{h}$  leaves the weights  $\beta_k$  unchanged (they depend only on the  $\mathbf{u}_n$ ) but shifts the term  $\mathbf{h} \star \mathbf{v}_k$ . When computing the sum over all positions  $n$  of the product  $[\beta_k]_n [\mathbf{h} \star \mathbf{v}_k]_n$  for all shifts, a correlation is performed:

$$b(x_0, y_0) = \sum_{k=1}^K [\beta_k \star (\mathbf{h}(0, 0) \star \mathbf{v}_k)]_{x_0, y_0}. \quad (3.12)$$

With this formulation, the computational complexity is reduced to that of the computation of the vectors  $\mathbf{u}_n$  ( $\mathcal{O}(NK^2)$  operations if matrix inverses are precomputed), of the SVD of a  $N \times K$  matrix ( $\mathcal{O}(NK^2)$  operations) and of  $2K$  discrete correlations (that can be computed with FFTs in  $\mathcal{O}(N \log N)$  each). The total complexity (including the precomputation of matrix inverses) is then  $\mathcal{O}(NK(K^2 + c \log N))$ , where  $c$  is a constant, which is much better than the original complexity:  $\mathcal{O}(N^2 K^2)$ .

### 3.4.3 Fast computation of $a(x_0, y_0)$ for all pixel shifts

Computation of this term is more challenging because the  $\mathbf{h}_n$  terms are shifted with respect to the location of the covariance matrices  $\widehat{\mathbf{C}}_n$ . It is not possible to derive a

---

3. In the 2-D correlation,  $\mathbf{h}$  has the size of an image while  $\mathbf{v}_k$  has the size of a patch, the resulting correlation at a pixel  $n$  thus involves only the patches  $\mathbf{h}_n$  and  $\mathbf{v}_k$ .



linear expansion and identify discrete correlations. We resort to an approximation in order to compute efficiently this term for all shifts.

Let  $\mathbf{H}$  be the  $K \times N$  matrix that collects all patches extracted from the centered model  $\mathbf{h}(0, 0)$ :

$$\mathbf{H} = \begin{pmatrix} | & & | \\ \mathbf{h}_1(0, 0) & \cdots & \mathbf{h}_N(0, 0) \\ | & & | \end{pmatrix}. \quad (3.13)$$

To reduce the complexity, we approximate each patch  $\mathbf{h}_n$  by a scaled version of an element taken from a  $K \times P$  codebook  $\mathbf{W}$ :

$$\mathbf{H} \approx \underbrace{\begin{pmatrix} | & & | \\ \mathbf{w}_1 & \cdots & \mathbf{w}_P \\ | & & | \end{pmatrix}}_{\text{codebook } \mathbf{W} (K \times P)} \underbrace{\begin{pmatrix} 0 & \vdots & \vdots & \cdots & \vdots & \vdots & \vdots \\ \vdots & \vdots & 0 & \cdots & \vdots & 0 & 0 \\ 0 & \vdots & q(3) & \cdots & \vdots & q(N-1) & q(N) \\ q(1) & 0 & 0 & \cdots & 0 & 0 & 0 \\ 0 & q(2) & \vdots & \cdots & q(N-2) & \vdots & \vdots \\ \vdots & 0 & \vdots & \cdots & 0 & \vdots & \vdots \\ 0 & \vdots & 0 & \cdots & \vdots & 0 & 0 \end{pmatrix}}_{\text{code } \mathbf{Q}^\top (P \times N)} \approx \mathbf{W}\mathbf{Q}^\top, \quad (3.14)$$

where the code  $\mathbf{Q}$  is a  $N \times P$  matrix such that for all row, only a single entry is non-zero. If  $q(n)$  is the value of the non-zero entry of the  $n$ -th row of  $\mathbf{Q}$  and  $p(n)$  is the column number corresponding to that entry, then the patch  $\mathbf{h}_n$  is approximated by  $q(n)\mathbf{w}_{p(n)}$ .

Construction of the codebook can be performed using a modified version of the  $k$ -means clustering algorithm where distances to cluster centers are evaluated by normalized correlation and the update of a cluster center corresponds to a truncated SVD where only the left and right singular vectors corresponding to the largest singular value are kept. This corresponds to a particular case of K-SVD sparse coding algorithm (Elad and Aharon, 2006) where the sparsity is equal to 1. Note that the approximation can be made exact by setting  $P = N$ , but in practice  $P$  will be chosen to be several orders of magnitude smaller than  $N$ .


Next, we build  $P$  maps  $\mathbf{e}_1$  to  $\mathbf{e}_P$  such that  $[\mathbf{e}_k]_n = \mathbf{w}_k^\top \hat{\mathbf{C}}_n^{-1} \mathbf{w}_k$ . The  $k$ -th column  $\mathbf{q}_k$  of the code  $\mathbf{Q}$  indicates which vectors  $\mathbf{h}_n$  are best represented by  $\mathbf{w}_k$ . If we replace each vector  $\mathbf{h}_n$  in the sum  $\sum_n \mathbf{h}_n^\top \hat{\mathbf{C}}_n^{-1} \mathbf{h}_n$  by its closest vector in the codebook, we obtain the approximation:

$$\sum_{n=1}^N \mathbf{h}_n^\top \hat{\mathbf{C}}_n^{-1} \mathbf{h}_n \approx \sum_{k=1}^P (\mathbf{q}_k^2)^\top \mathbf{e}_k, \quad (3.15)$$

where the square is applied element-wise on the vector  $\mathbf{q}_k$ . When the model  $\mathbf{h}$  is shifted, the maps  $\mathbf{q}_k$  indicating the location of patches  $\mathbf{h}_n$  best represented by  $\mathbf{w}_k$  are shifted accordingly. Values of the denominator of the S/Ntest for any pixel shift of the model can then be obtained by discrete correlations:

$$a(x_0, y_0) \approx \left[ \sum_{k=1}^P \mathbf{q}_k^2 \star \mathbf{e}_k \right]_{x_0, y_0}. \quad (3.16)$$

The complexity of the procedure is the following: application of the  $k$ -means algorithm for a fixed number of iterations is performed in  $\mathcal{O}(PN)$ , computation of the maps  $\{\mathbf{e}_k\}_{k=1..P}$  requires  $\mathcal{O}(PNK^2)$  operations, computation of the  $P$  correlations is performed in  $\mathcal{O}(PN \log N)$  with FFTs. The total complexity is thus  $\mathcal{O}(PN(c \log N + K^2))$ , where  $c$  is a constant. This corresponds to a strong improvement compared to the original complexity (in  $\mathcal{O}(N^2K^2)$ ) if we choose a codebook size  $P \ll N$ . Once the (approximate) location of the pattern has been identified, a local optimization based on the exact evaluation of (3.8) can be performed (i.e., no bias is incurred, only the location of the pattern may be missed if the approximation is too coarse and the local optimization then leads to the wrong local optimum).

 **Fast computation of a detection map**

- With the EXPACO framework, the localization of a known pattern requires to maximize a S/Ntest.
- However, if the spatial extent of the known pattern is large, the computational complexity of the algorithm is too high for using a straightforward implementation.

⇒ A fast method should be used to evaluate efficiently the detection criterion.

- We derive a fast (and approximate) algorithm to compute the S/N detection map in the case of a shift-invariant pattern model.
- The algorithm is based on a reformulation of the detection criterion that involves discrete correlations, which are computed efficiently using fast Fourier transforms.
- The proposed strategy leads to a significantly reduced algorithm complexity.

### 3.5 Performance evaluation on holograms

In this section, we assess both the accuracy and the detection performance of EXPACO. For this purpose, we use experimental background images recorded with the holographic microscope presented in Figure 3.6. It results from the adaptation of the original in-line Gabor configuration (presented in Section 1.15 and used in Chapters 5 & 7) to a traditional microscope. While lensless configurations lead to simple and effective setups, including a microscope objective significantly improves the resolution and makes it possible to study micron-sized objects.

Four background images (recorded in absence of object by shifting the glass slide in an area where only the surrounding medium is present) out of the 61 that we collected are shown in Figure 3.7(a)-(b). Fluctuations in the background are due to small variations of the optical path lengths between optical surfaces (because of mechanical vibrations or thermal inhomogeneities of the air) and are difficult to fully model. The diffraction pattern created by a spherical bead is displayed in Figure 3.7(c-d). The bead size and the refractive index contrast between the bead and the surrounding medium

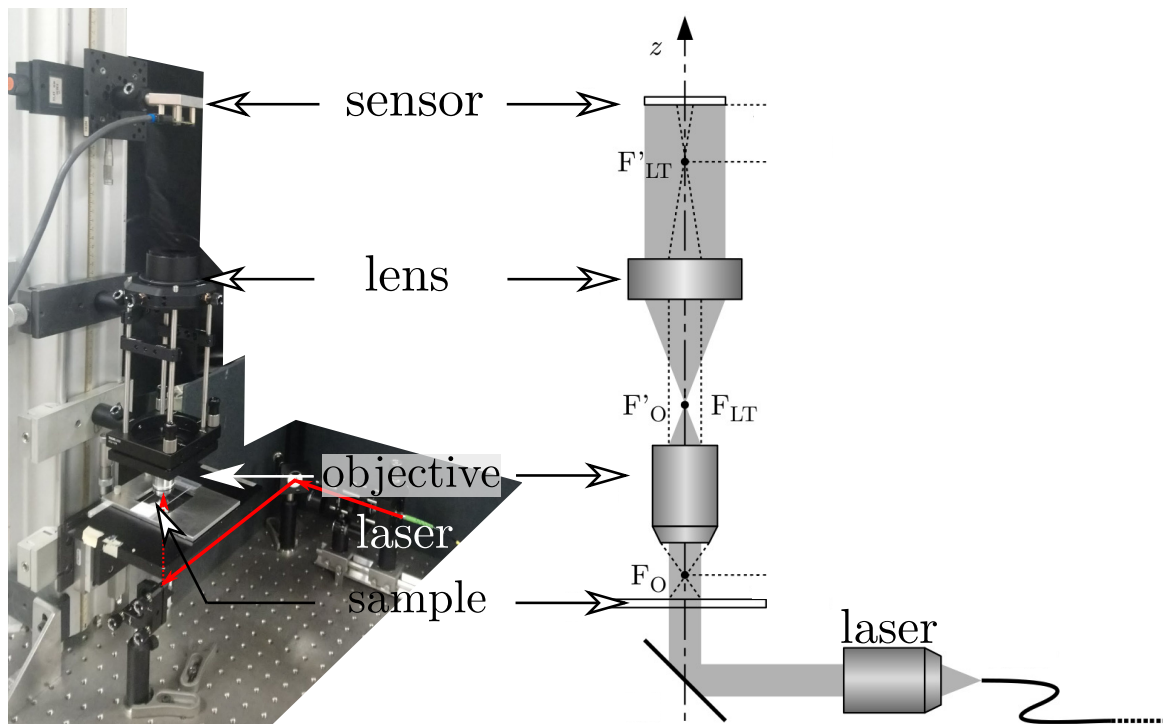


Figure 3.6 – The holographic microscope used in our experiments: picture of the setup (left) and its optical scheme (right).  $F_O$ ,  $F'_O$ ,  $F_{LT}$ ,  $F'_{LT}$  are respectively the front and rear focal points of the microscope objective. The right part of the figure is adapted from [Olivier et al. \(2018\)](#).

(approximately 0.08 here) is sufficient to obtain quite contrasted diffraction fringes. Identification of the diffraction pattern becomes critical when this index contrast or the object size drops, as illustrated by Figure 3.1 where the bead is four times smaller and the fringes are thus less contrasted.

To evaluate the performance of EXPACO, we performed numerical experiments in which we added the simulated diffraction pattern of a microscopic bead to some experimental background images, the other background images were kept to estimate the background statistics  $\widehat{\mathbf{m}}_n$  and  $\widehat{\mathbf{C}}_n$ .

### 3.5.1 Accuracy of the EXPACO approximation

Figure 3.8 evaluates the accuracy of the approximation presented in Section 3.4 to compute efficiently S/N maps. Square patches of size  $7 \times 7$  pixels are used. Since the evaluation of the S/N by direct application of Equation (3.8) has a prohibitive complexity, we compare values of the S/N on only 2000 different locations  $(x_0, y_0)$ . Application of (3.8) takes 12 hours to compute these 2000 locations on 20 CPU cores (processing done with MATLAB<sup>TM</sup>, processor INTEL<sup>TM</sup> Xeon E5-46170 at 2.90 GHz), while our fast approximation produces the S/N map for one million different locations in about 2 minutes (computation of the codebook which must be done only once for a given pattern  $\mathbf{h}$  takes another 2 minutes). As expected, Figure 3.8(a) shows a reduction

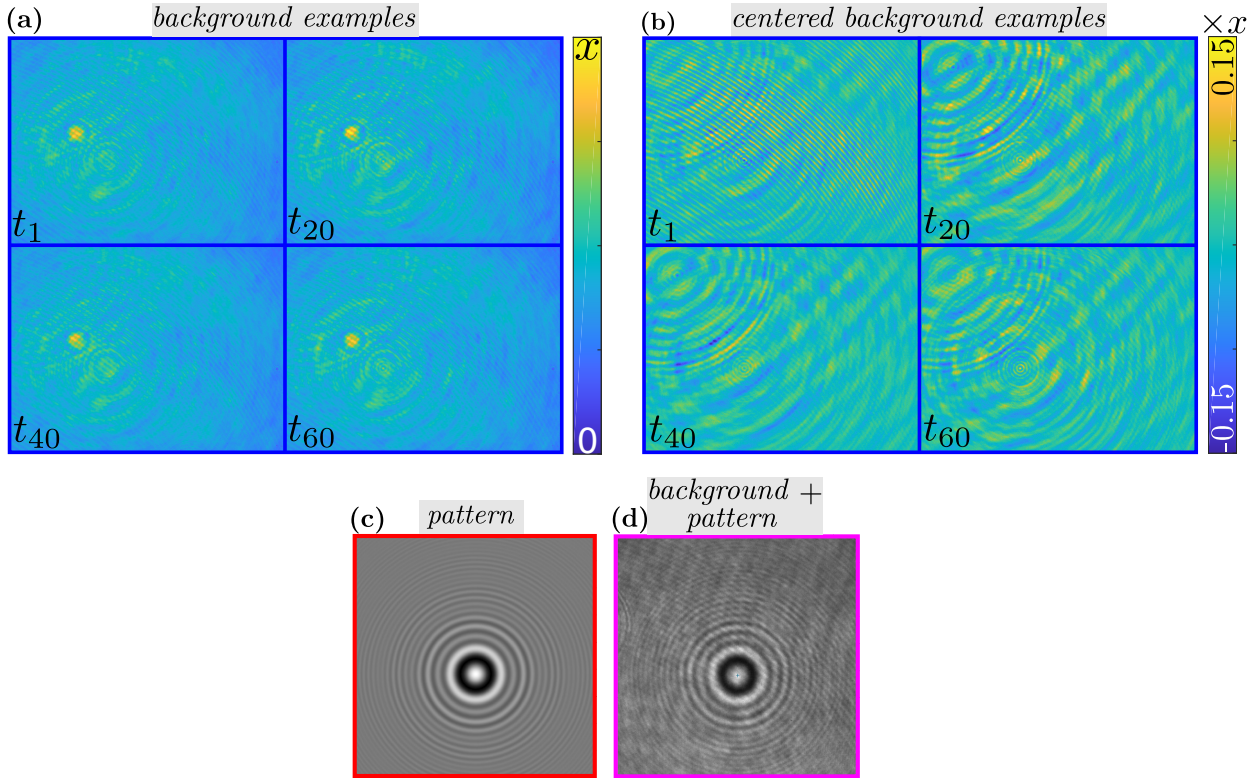


Figure 3.7 – Examples of data recorded by our holographic microscope: (a) some of background images in the absence of object of interest; (b) same than (a) after subtraction of the temporal mean; (c) example of a diffraction pattern (generated with the Thompson model, see Sections 1.3.2.2.1 and 5.4) to be detected in the images; (d) a hologram of a polystyrene microscopic bead of  $2.1\ \mu\text{m}$  radius.

of the approximation error of the S/N when the size of the codebook  $P$  increases. With  $P \approx 200$  elements, the codebook  $\mathbf{W}$  is large enough to capture most of the geometrical structures (see Figure 3.8(c)) of the pattern and to obtain an approximation error below 5%. Since this approximation error depends only on the covariance  $\hat{\mathbf{C}}$  when the number of background images and the number of codebook atoms are fixed, we did not evaluate it systematically for all the different patch configurations that we investigate in the following sections.

The impact of the number of background images in the estimation of the background statistics ( $\hat{\mathbf{m}}_n$  and  $\hat{\mathbf{C}}_n$ ) is assessed by comparing values of the S/N obtained when  $\hat{\mathbf{m}}_n$  and  $\hat{\mathbf{C}}_n$  are estimated from an increasing number of backgrounds (the reference S/N is obtained when 60 backgrounds are used). With  $7 \times 7$  patches, covariance matrices are  $49 \times 49$ . With less than 50 background samples, the obtained S/N map differs significantly from the S/N map obtained with all backgrounds, see Figure 3.8(b).

In the following experiments, we set  $T = 60$ ,  $P = 1024$ , and add a pattern with a very low amplitude on the remaining 61st background image.

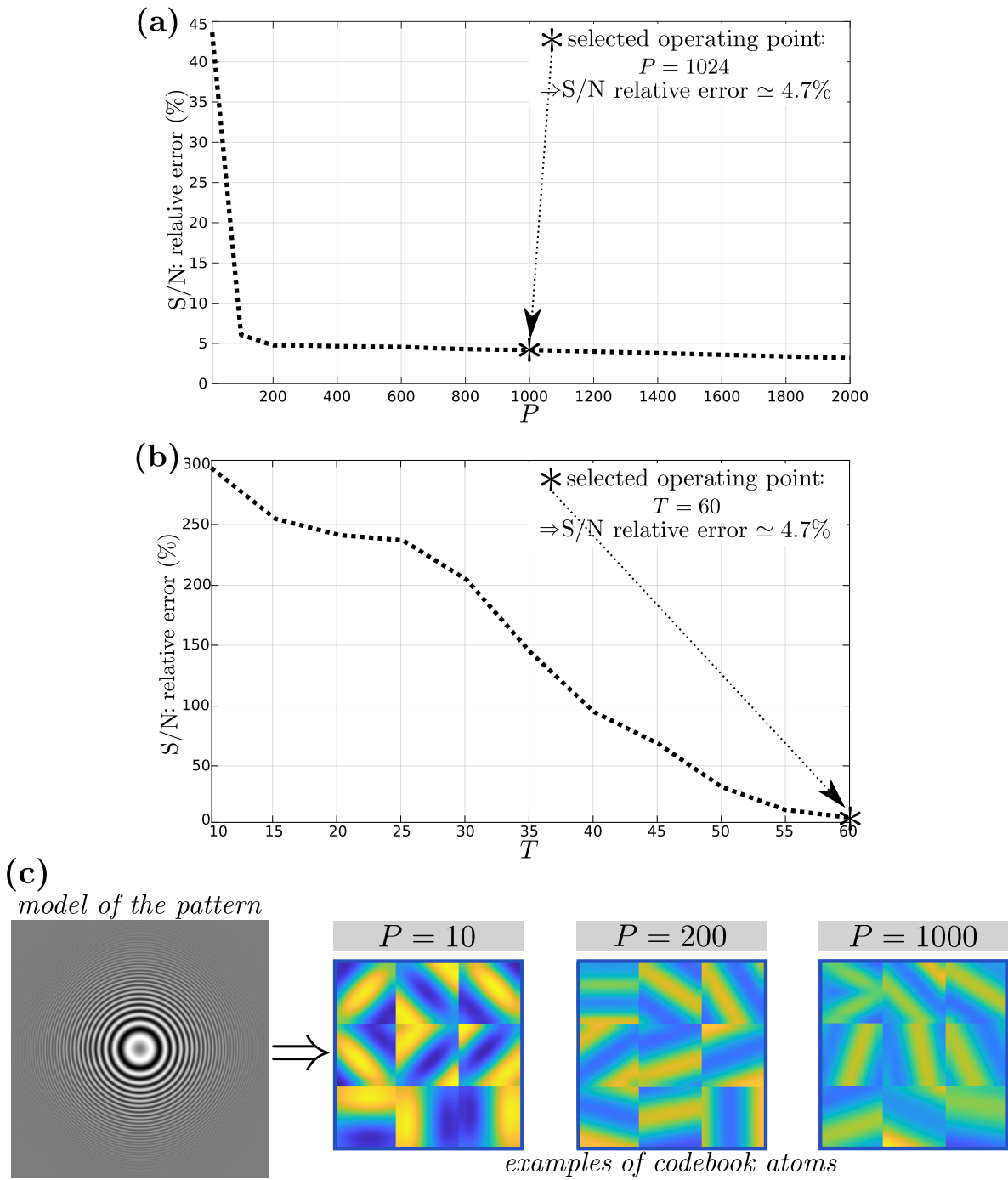


Figure 3.8 – Accuracy evaluation of the EXPACO approximation: (a)-(b) evolution of the relative error induced by the fast approximation as a function of the number  $P$  of atoms in the codebook  $\mathbf{W}$ , and of the number  $T$  of background images available to estimate  $\{\hat{\mathbf{m}}_n\}_{n=1..N}$  and  $\{\hat{\mathbf{C}}_n\}_{n=1..N}$ ; (c) examples of codebook atoms for different sizes  $P$  of the codebook  $\mathbf{W}$ .



### 3.5.2 Detection maps

In the following two parts, we investigate the influence of the patch shape used to compute the statistics of the background. In particular, we focus on the number  $K$  of pixels encompassed in patches as well as the spatial extension of the patches, respectively. To compare the EXPACO results, we consider a background model with a *diagonal covariance* matrix as a baseline. This corresponds to setting  $\hat{\rho} = 1$  for all pixels  $n$  in Equation (3.4). Only the structures that are in the mean background  $\mathbf{m}$  and a per-pixel variance are taken into account in this baseline method: the mean background is subtracted and regions with larger fluctuations have smaller weights in the computation of the detection criterion. No spatial correlations are accounted for, though.

#### 3.5.2.1 Influence of the number $K$ of pixels in the patches

Figures 3.9(c) and 3.10(c) give S/N maps obtained on two regions of interest of  $1,000 \times 1,000$  pixels (see boxes (a)) extracted from the background series shown in Figure 3.7. For EXPACO, the results are given (along columns of the two figures) for different numbers of pixels in a patch ( $K \in \{9, 17, 25, 33, 41, 49, 57\}$ , see boxes (b)). The active pixels of patches are arranged in order to capture spatial correlations in different directions of the field of view. For each case, we test two schemes differing on the paving of the field of view; we consider both *overlapping* and *non-overlapping* patches. In the case of non-overlapping patches, Equations (3.12) and (3.16) are adapted by taking into account only pixel locations that do not overlap (by enforcing a null weight to the  $\beta_k$  and  $\mathbf{e}_k$  terms at the other locations). S/N maps obtained with the considered baseline (diagonal covariance) are also given for the two regions of interest. In each S/N map, a single peak is expected at the location circled in pink, corresponding to the position  $(x_0, y_0)$  of the pattern that has been added to the background image. The contrast between the background and the pattern is about 140. This peak is not visible with the baseline but only with EXPACO. Moreover, with more pixels in a patch, the S/N displays much fewer undesirable fluctuations: typical background structures are better modeled and are thus less likely to be mistaken for the pattern. A visual analysis of the S/N maps also shows that the choice of the paving (overlap or no overlap) of the field of view have a limited influence on the peak in the detection map. Based on the results of this analysis and on the fact that the computation time of the EXPACO procedure remains acceptable when patches overlap, we chose to conduct experiments with overlapping patches in the following sections. The effect of the choice of overlapping or non-overlapping patches, in particular on the distribution of the detection criterion in the absence of object of interest, is left for future works.

Figures 3.9(d) and 3.10(d) give the maps of shrinkage factor  $\hat{\rho}$  for the different patches tested. These maps show that patches with more pixels lead to covariance matrices of larger size, which requires a stronger shrinkage of off-diagonal terms. Still, even for a relatively large number of pixels in a patch ( $K = 57$ , i.e. same order of magnitude than the number of samples:  $T = 60$ ), the shrinkage weight  $\hat{\rho}$  only reaches the value 0.2. In other words, the sample covariance matrix  $\hat{\mathbf{S}}_n$  remains predominant compared to the diagonal matrix  $\hat{\mathbf{F}}_n$ . As a result, the shrunk covariance matrix  $\hat{\mathbf{C}}_n$  effectively accounts for the spatial covariances of the background (i.e., it does not only



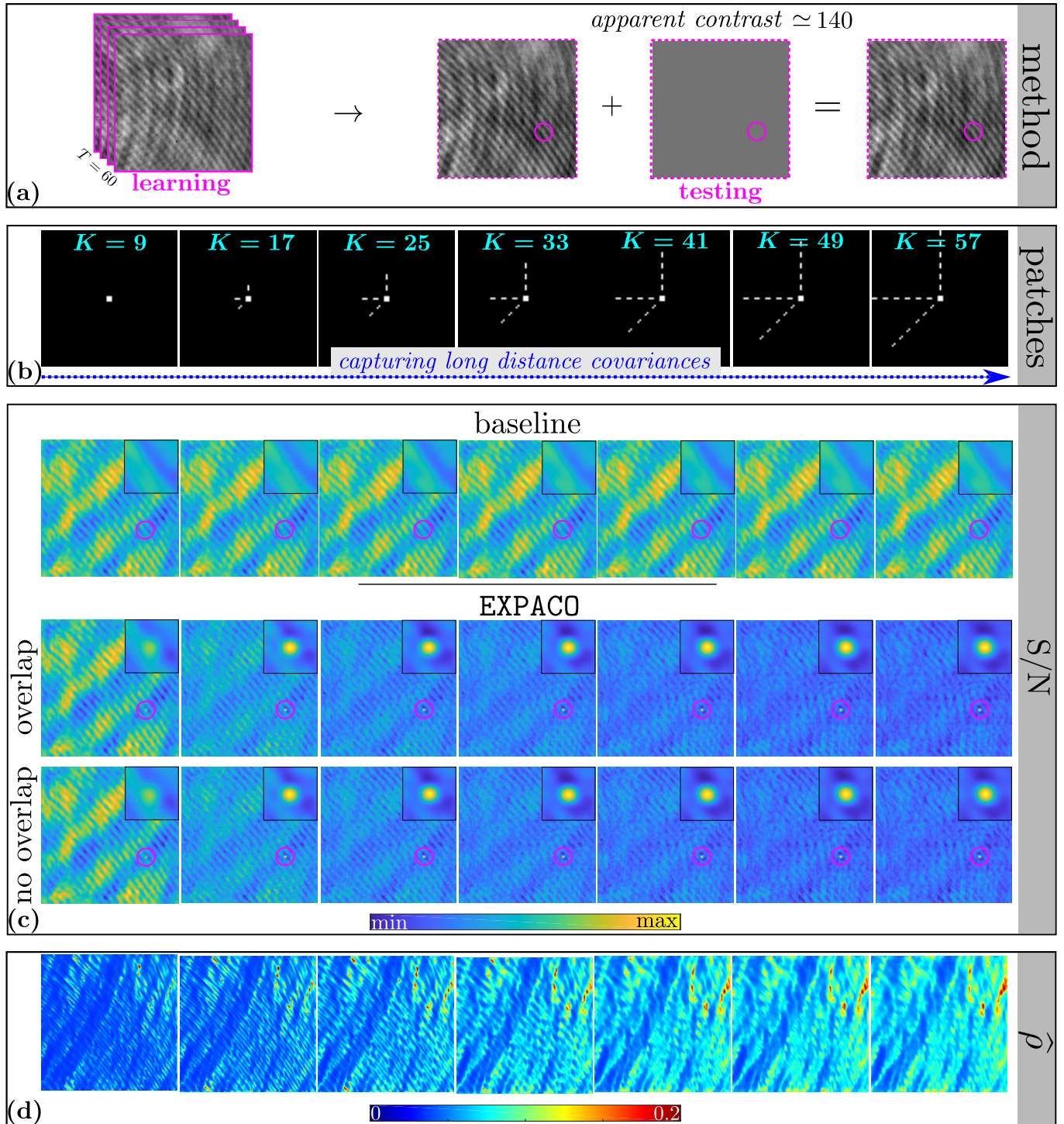


Figure 3.9 – Detection of a pattern in a structured background for different patch shapes. (a) considered region of interest; (b) considered patches; (c) S/N maps from EXPACO (with overlapping and non-overlapping patches) compared to the baseline (diagonal covariance); (d) maps of the estimated amount  $\hat{\rho}$  of covariance shrinkage. The detection map obtained with the baseline does not depend on the considered patch sizes and is thus replicated throughout the columns for easier side-by-side comparison with EXPACO results.

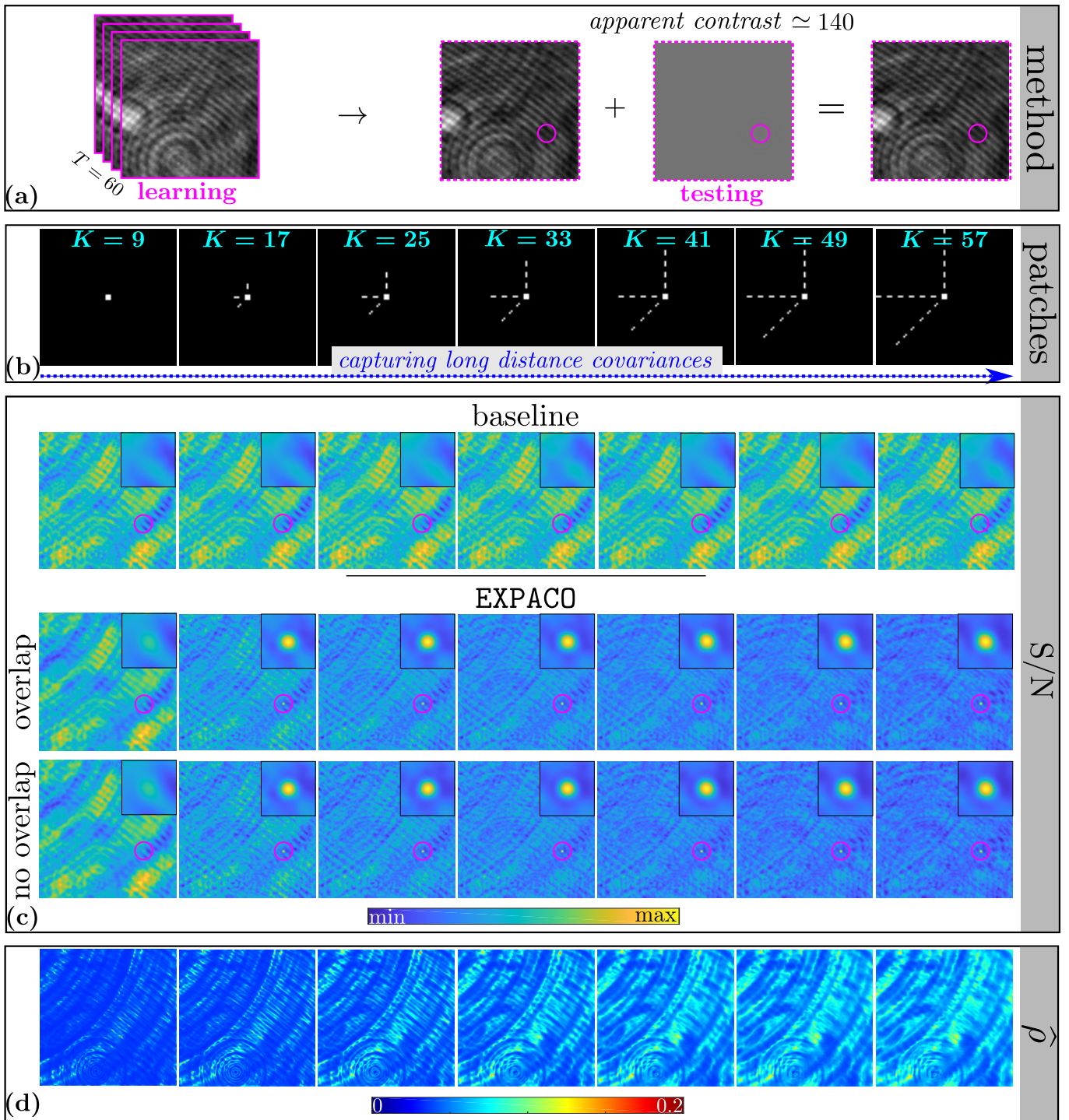


Figure 3.10 – Same illustration than Figure 3.9, for a different region of interest.

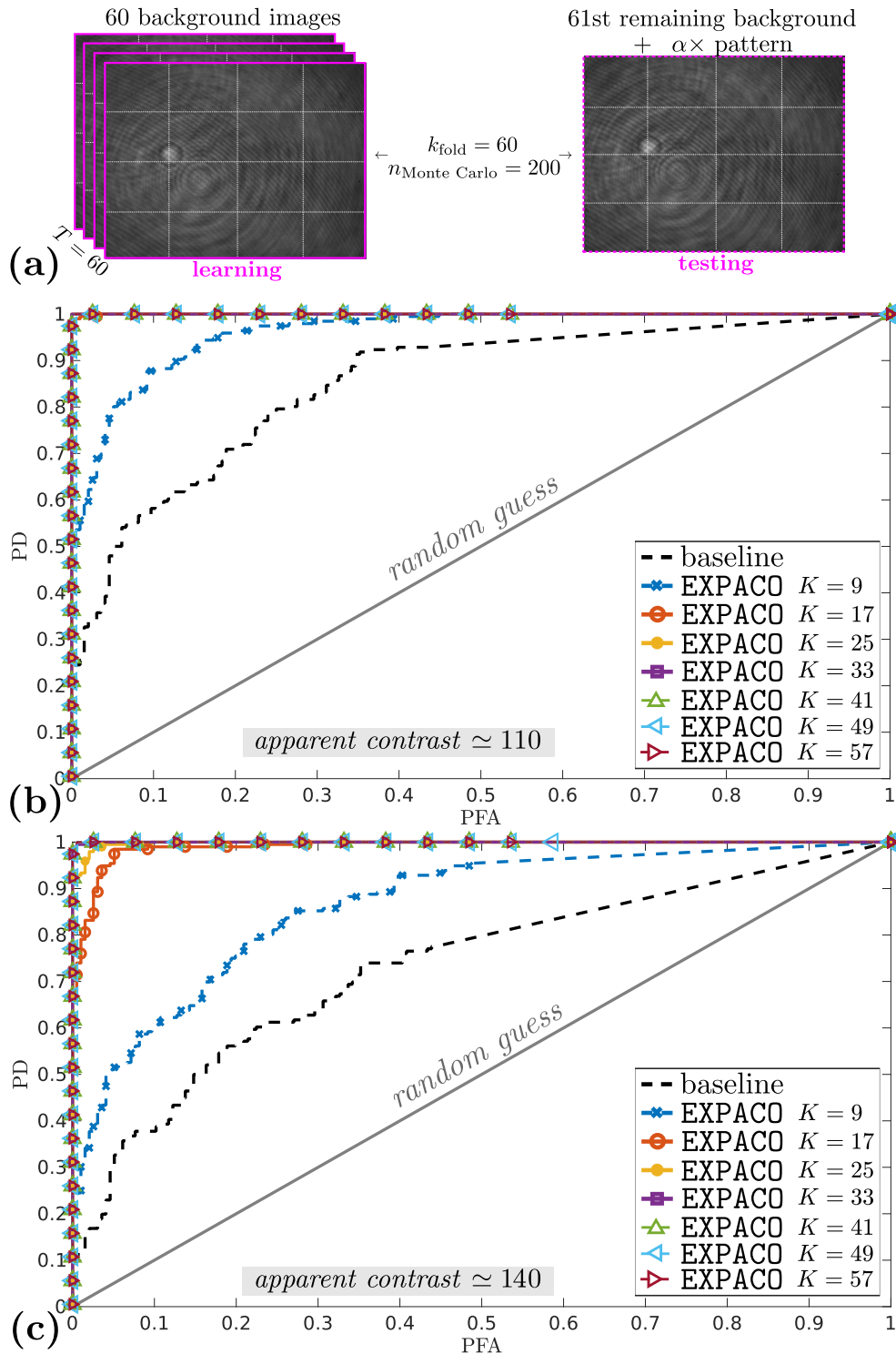


Figure 3.11 – ROC curves of the baseline detector (diagonal covariance) and of EXPACO for various patch shapes. (a) illustration of the considered background images; (b-c) ROC curves for contrasts between the background and the pattern of 110 and 140, respectively.



account for the variances).

The influence of the number of pixels within a patch can be more systematically studied through receiver operating curves (ROC). Patterns are injected one at a time at different locations and on various backgrounds, as illustrated by Figure 3.11(a). Figure 3.11(b-c) reports the evolution of the ROC curves with the number of pixels  $K$  in the patch, for two levels of contrast between the background and the pattern (contrasts 110 and 140). The tested patches are represented in Figures 3.9(b) and 3.10(b). A clear improvement is observed with respect to a detector based on a diagonal covariance assumption. In these simulations, using  $K \geq 17$  pixels when the pattern is 110 times fainter than the background, and  $K \geq 33$  pixels when the pattern is 140 times fainter than the background leads to the detection of 100% of the patterns without false alarms. In contrast, the considered baseline detector reaches only 25% and 15% of detections without false alarms, respectively.

### 3.5.2.2 Influence of the spatial extension $\widetilde{K}$ of the patches

To better analyze the influence of the spatial extension and the number of pixels of patches, in this section, we compare patches with different spatial extension but with a constant number of pixels. In Figure 3.12, we compare S/N maps obtained with the baseline and with EXPACO for the four different patch shapes shown at the top of the figure and for three numbers of pixels  $K \in \{9, 25, 49\}$  inside the patches. For example, when  $K = 25$ , each of the four considered patches has 25 pixels: the first patch is a  $5 \times 5$  full patch, the remaining three patches are patches with holes: a  $19 \times 19$  patch, a  $29 \times 29$  patch and a  $39 \times 39$  patch. The rationale in increasing the size of the patch while keeping the same number of pixels is to capture longer-range correlations without increasing the size of the covariance matrices  $\widehat{\mathbf{C}}_n$ . In each S/N map, a single peak is expected at the location circled in pink, corresponding to the position  $(x_0, y_0)$  of the pattern that has been added to the background image. The contrast between the background and the pattern is about 140. Figure 3.13 completes this study by reporting the evolution of the ROC curve with the number of pixels  $K$  in the patch and with the spatial extent  $\widetilde{K}$  of the patch. Based on the results of this study and of Section 3.5.2.2, we observe that the detection performance of EXPACO improves when larger patches and more pixels are taken into account, since this allows to capture longer-range correlations.

However, the number of pixels  $K$  and the spatial extension  $\widetilde{K}$  should not be too large: a large  $K$  leads to a large covariance matrix which can not be accurately estimated from a limited number of background images (the shrinkage step strongly bias the covariance towards a diagonal covariance matrix if  $K \gg T$ ); if  $\widetilde{K}$  is too large, shorter-range correlations are lost, and the model is less local (hence less adapted to highly nonstationary backgrounds). We found in our experiments that the choices  $K \geq 110$  (pixels)  $\simeq 2T$  and  $\widetilde{K} \geq 50$  (patch width in pixels) both lead to a degradation of EXPACO performance.

### 3.5.3 False alarm rate

A desirable property for detectors is to lead to a constant false alarm rate. In the case of nonstationary backgrounds, this requires robustness to the differences in the structures found in the background. Figure 3.14 shows maps of the false alarm

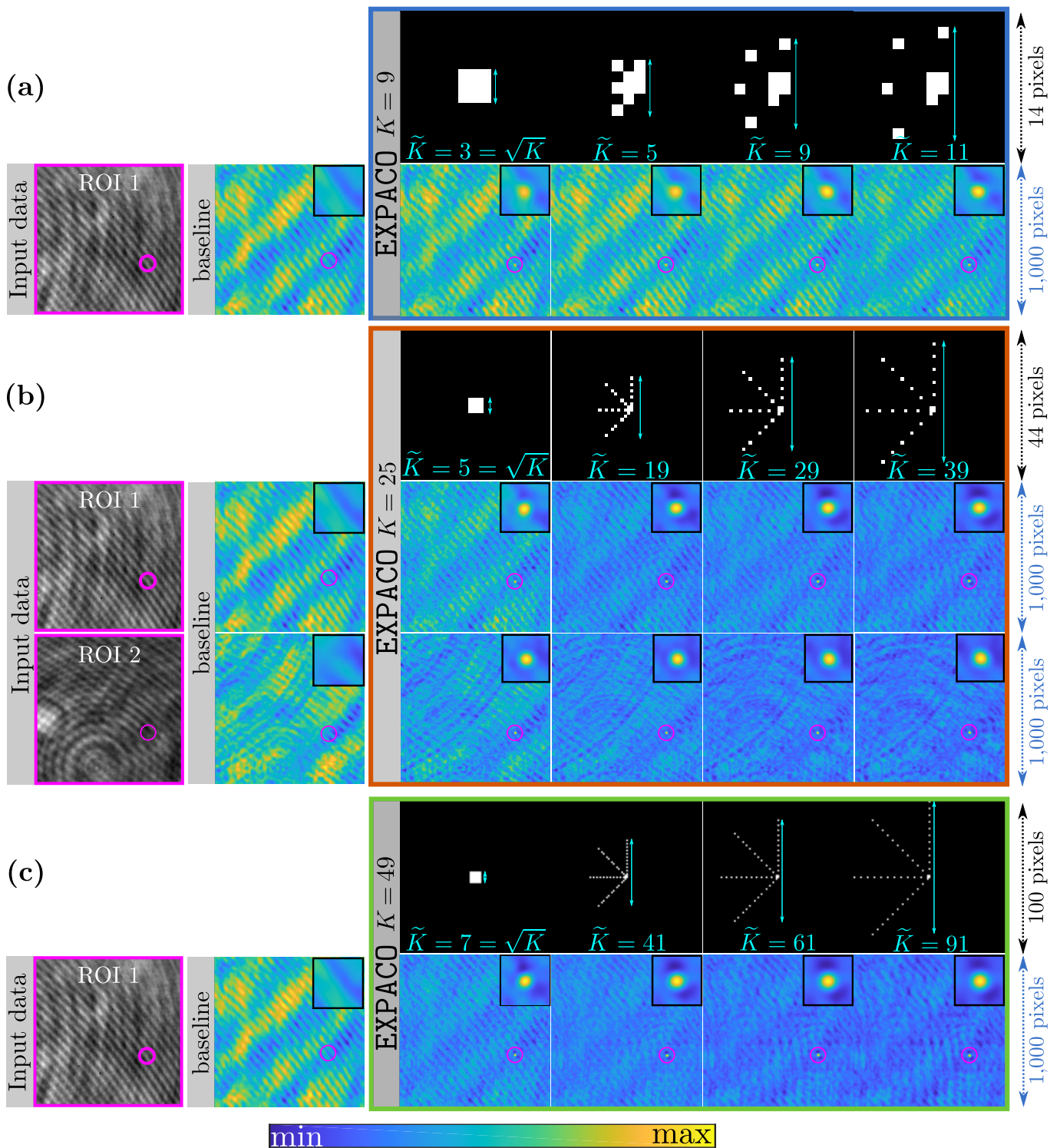


Figure 3.12 – Detection of a pattern in a structured background for different patch shapes at fixed number of pixels in patches: (a)  $K = 9$ ; (b)  $K = 25$ ; (c)  $K = 49$ . S/N maps from EXPACO are compared to the baseline (diagonal covariance) results.

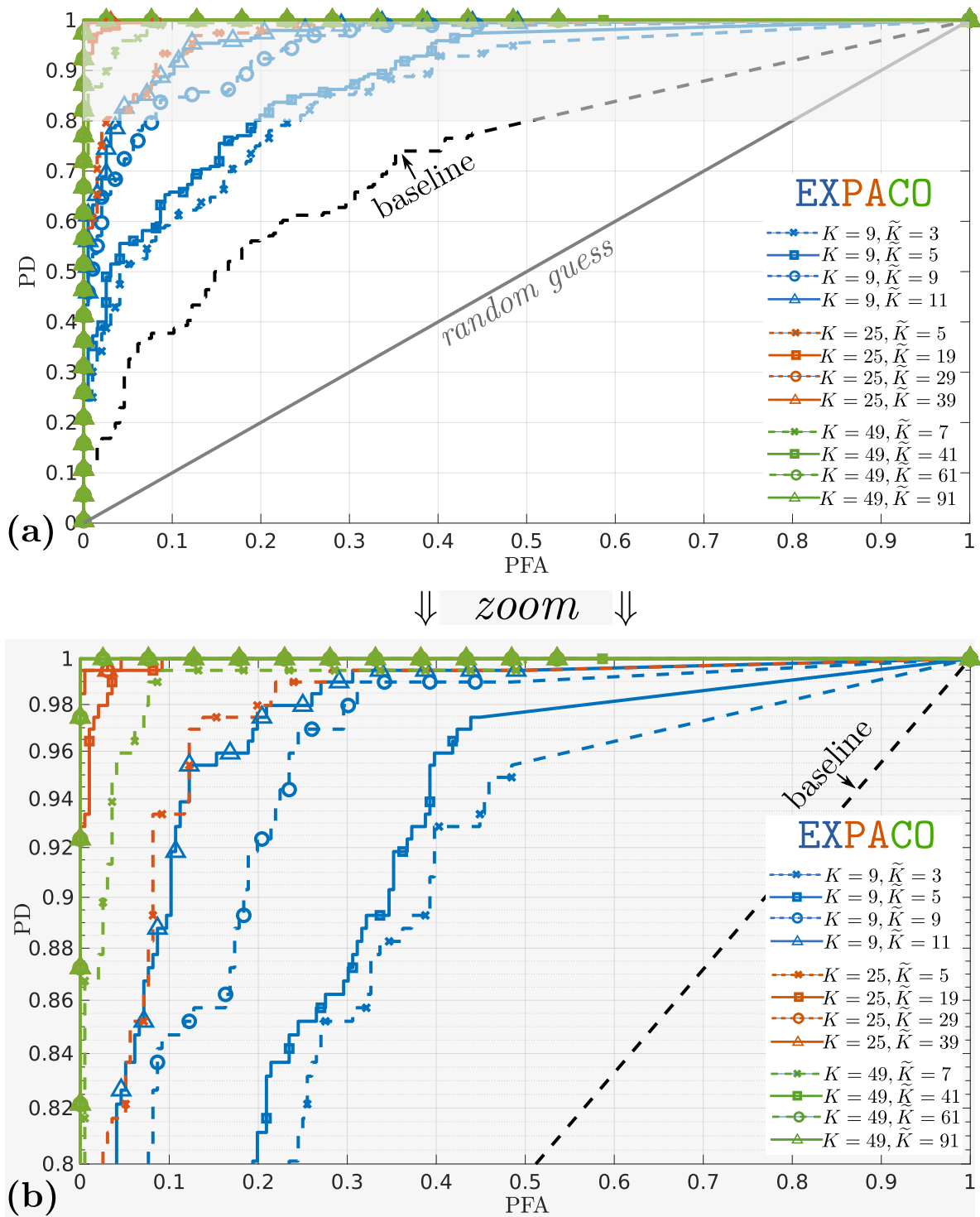


Figure 3.13 – ROC curves of the baseline detector (diagonal covariance) and of EXPACO for different spatial extents  $\tilde{K}$  of patches and a fixed number  $K$  of pixels inside each patch. Part (b) is a close-up view of (a) for  $PD \in [0.8; 1.0]$ .



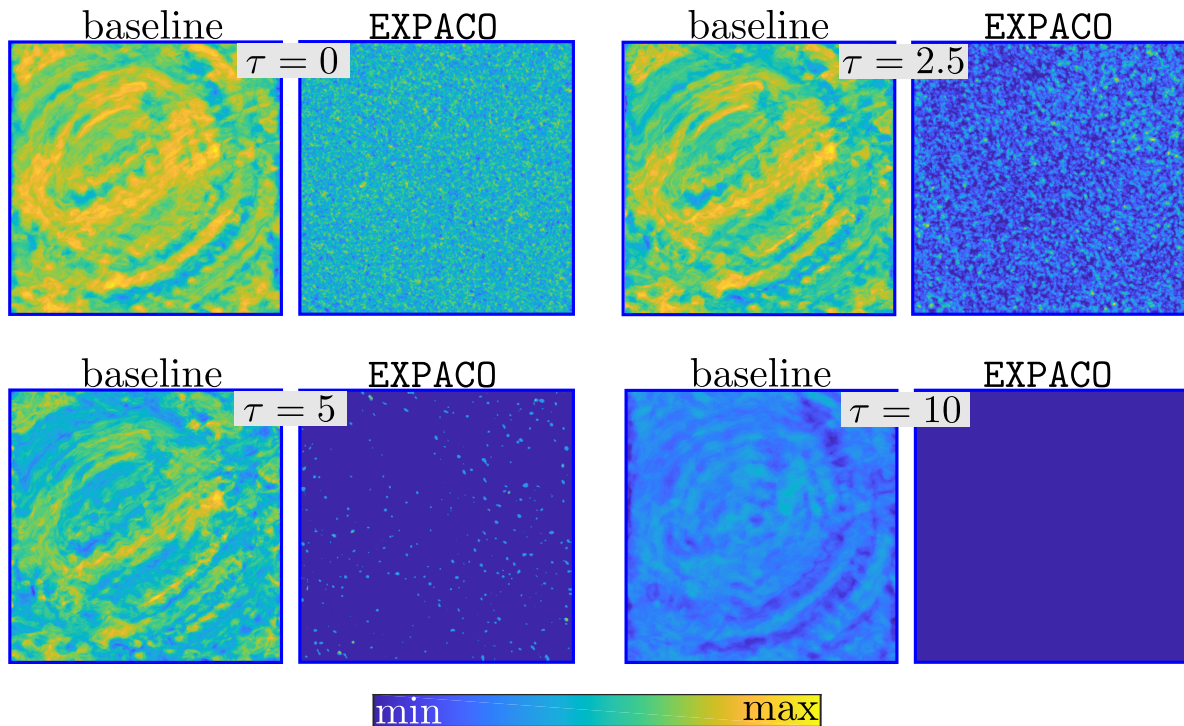


Figure 3.14 – False alarm rates of the baseline detector (diagonal covariance) and of EXPACO for 4 different thresholds  $\tau$ .

rate reached by the considered baseline (diagonal covariance) estimator and by EXPACO. These maps are built by reporting the fraction of positive  $S/N_{\text{test}}$  in the absence of patterns (i.e., under  $\mathcal{H}_0$  hypothesis), for different background images (1 background is selected and the 60 remaining are used to estimate the  $\hat{\mathbf{m}}_n$  and  $\hat{\mathbf{C}}_n$ , in a leave-one-out rotation). Contrary to the diagonal covariance detector, the false alarm rate of EXPACO is almost stationary.

#### EXPACO characteristics

In our numerical simulations, EXPACO showed several appealing characteristics:

- Detection maps are produced in a reasonable computation time ( $\leq 5$  min) on million-pixels images, with a controlled error ( $\leq 5\%$ ) required by the EXPACO detection criterion approximation.
- Significantly better detection sensitivity is obtained compared to a baseline method that considers diagonal covariance matrices, i.e. that accounts only for the average background and for the per-pixel variances to discard large variance areas.
- A constant false rate is achieved in the whole field of view.

### 3.6 Conclusion on EXPACO's capabilities

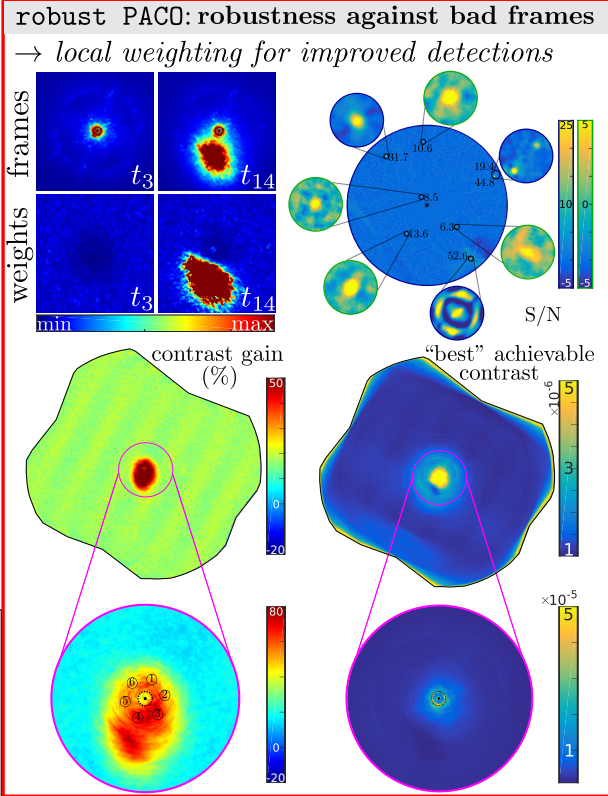
In this chapter, we introduced EXPACO, a fast algorithm dedicated to the detection of extended patterns in nonstationary and correlated backgrounds. This is an adaptation of the PACO algorithm presented in Chapter 2 and dedicated to the detection of point-like sources. As in PACO, a local model of the spatial correlations is learned from a few tens of background images. By accounting for these correlations, the detection performance is improved compared to a standard detector. Patches with holes are shown to lead to a good tradeoff between the size of the covariance matrices to estimate and the range of the correlations that are captured. As for PACO, EXPACO is not strictly dedicated to a particular application field and can be used in other areas where the detection/localization of faint known patterns embedded in strong and nonstationary backgrounds is encountered. In the following two parts (Chapters {4, 5} and Chapters {6, 7}), we show how the detection can be further improved by accounting for the numerous outliers present in the data, and then by combining information from different spectral channels.



Part III  
Robust processing

ASTRONOMY APPLICATIONS

Chapter 4

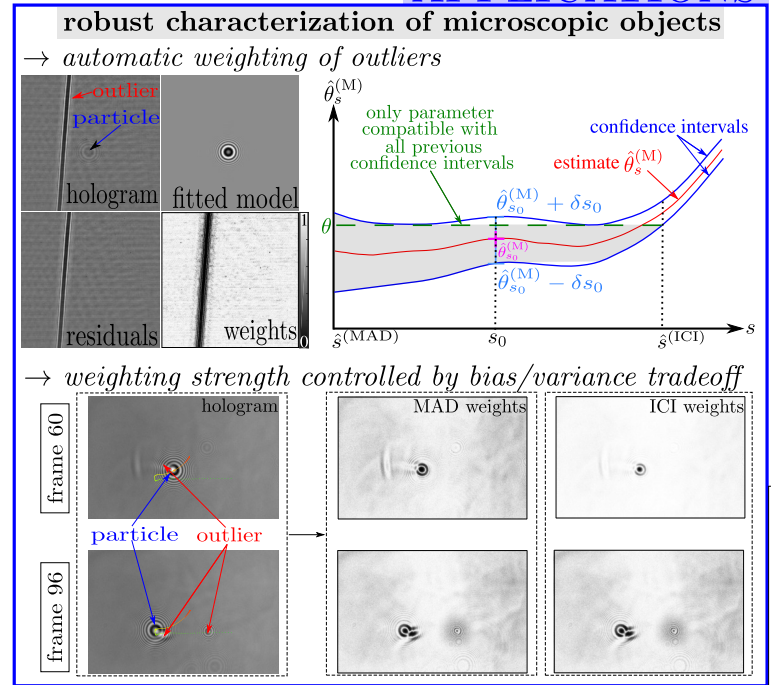


GRETSI (2019)

in rev. for Astronomy & Astrophysics (2019)

MICROSCOPY APPLICATIONS

Chapter 5



EUSIPCO (2017)

**Part III**

**Robust processing**





# Robustness to bad frames in direct imaging

---

**Abstract**

*Due to the evolution of the observation conditions and the AO correction, the quality of direct observations may vary significantly during an observing sequence. It is common practice to reject images with comparatively worse quality. Rather than discarding a full image, we study the local fluctuations of the signal at each frame and derive weighting maps for each frame. The weights derived from the temporal variances can be used in the PACO algorithm to improve the robustness of the detection step and to reduce estimation errors of both the astrometry and photometry. The impact of bad frames can be analyzed by characterizing the theoretical detection and estimation performances.*

---

## 4.1 The need for robust estimators in direct imaging

As discussed in Chapters 1 and 2, direct imaging from the Earth is a method of choice for the detection and characterization of exoplanets (Traub and Oppenheimer, 2010). Confronting numerical models of the estimated astrometry and photometry parameters (Vigan et al., 2010), gives access to quantitative physical properties on the detected sources such as age, mass, and effective temperature (Chabrier et al., 2000; Allard et al., 2003, 2007).

As in Chapter 2, we consider ADI observations obtained by tracking the observation target over time (the telescope pupil remaining stable while the whole field of view rotates). We recall that the companions describe a predictable motion in time while the speckle background remains quasi-static in the time sequences. The recorded ADI images are then combined in a post-processing step to disentangle the signature of the exoplanets from the speckles by dedicated algorithms (see Chapter 2). The statistical modeling of the data plays a central role in these processing algorithms to control the probability of false alarm and prevent spurious detections (Mawet et al., 2014).

The main constraint of direct imaging is due to the very high contrast between the target star and the exoplanets ( $\geq 10^5$  in infrared). In addition, the detection perfor-

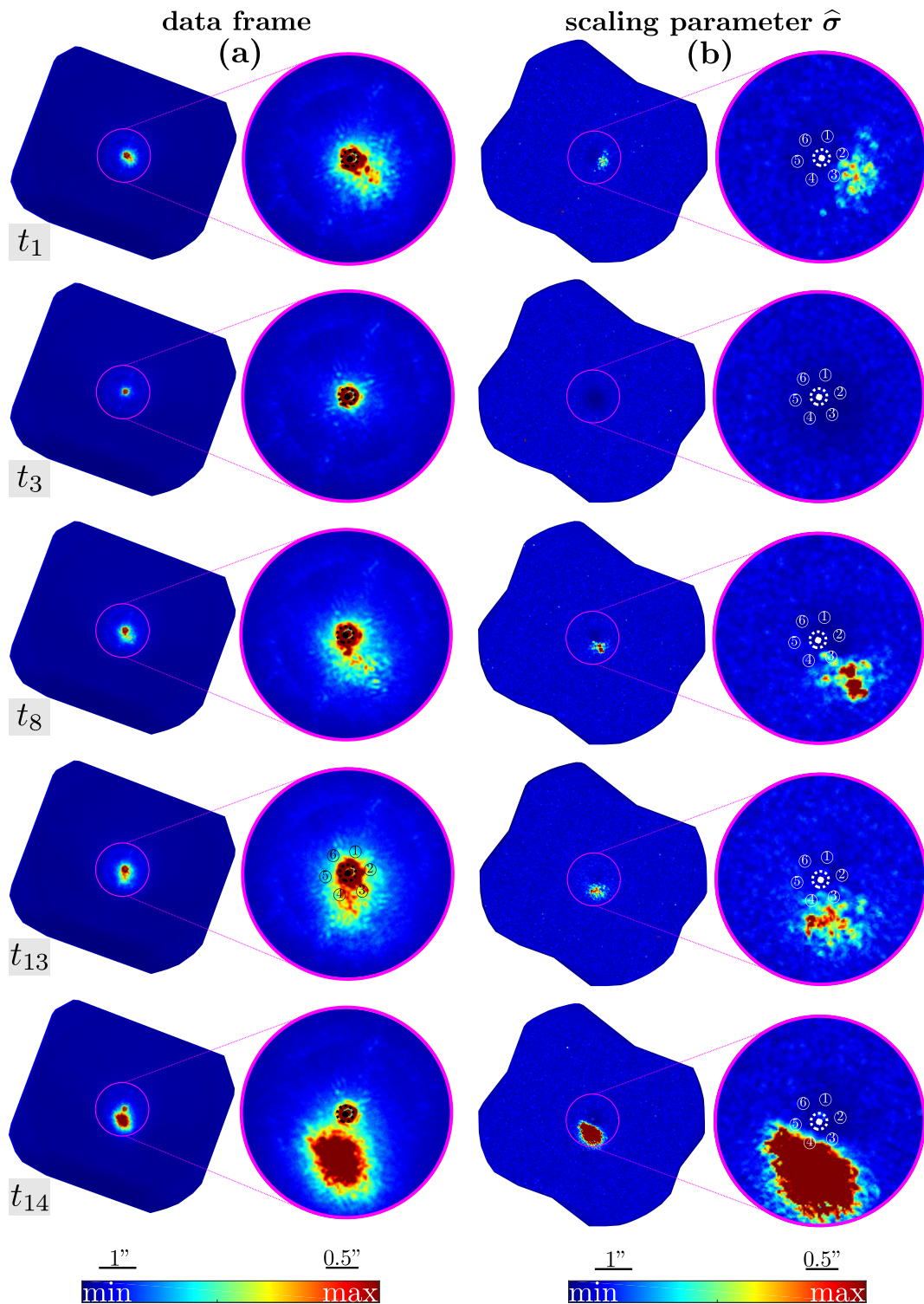


Figure 4.1 – Illustration of the strong temporal fluctuation in the central region of SPHERE-IRDIS images of HIP 72192: (a) measured intensity for 5 selected frames showing the strong temporal fluctuations; (b) map of the estimated temporal scaling parameters  $\hat{\sigma}_{n,t}$  for the matching frames:  $t_1$ ,  $t_3$ ,  $t_8$ ,  $t_{13}$ , and  $t_{14}$ .

mance and the achievable contrast are strongly dependent on both the total parallactic rotation of the field of view and the quality of the observations. Even in the absence of sources in the field of view (other than the star masked out by the coronagraph), there are fluctuations in images from an ADI sequence. There are several factors that induce these fluctuations, in particular: (i) evolution of the PSF due to alterations of the quality of the adaptive optics correction; (ii) photon and thermal noise on the camera as well as the erratic response of some uncorrected bad pixels; (iii) partial decentering of the coronagraph; (iv) evolving non-common-path aberrations (uncorrected by the AO). These artifacts can be spatially localized (e.g., in case of defective pixels) or can impact a larger fraction of the field of view in the form of large fluctuations when a decentering of the coronagraph or a sudden degradation of the AO correction occurs (e.g., a low-wind effect, [Sauvage et al. \(2015\)](#); [Milli et al. \(2018\)](#)). The latter two effects are especially problematic since exoplanets generally have a small angular separation to their host star: they must be detected in the area close to the center of the field of view that is most affected by this type of fluctuations.

In Figure 4.1(a), we illustrate the temporal evolution of the intensity measured with SPHERE-IRDIS instrument around HIP 72192 (the considered dataset is also studied in Section 2.5, see Table 2.3 for the observation logs). We select some frames (out of  $T = 96$ ) that display particularly strong fluctuations due to difficult observing conditions. Since these fluctuations are mostly located around the coronagraph, we also show a zoom on the central region of the images corresponding to a field with a radius of 1.4 arcsec. The fluctuations are spatially structured and their magnitude varies from one image to the other in the ADI sequence.

To the best of our knowledge, there is no particular strategy implemented in the state-of-the-art post-processing algorithms to deal with the evolution of the local quality of the acquired frames. Images presenting large fluctuations compared to the others are simply flagged as “bad frames” and discarded from the ADI stack, even if some areas of these images contain useful information.

In this chapter, we introduce an extension of our exoplanet detection and characterization method that accounts for the patch covariances of the background (PACO algorithm, see Chapter 2). The improvement is based on the modeling of the temporal variations of the amplitude of the background fluctuations jointly to the spatial covariances. To improve the robustness of the method, we spatially weight each temporal frame in a data-driven fashion, based on its relative degree of fluctuations.

Section 4.2 describes our local modeling of the spatio-temporal fluctuations and Section 4.3 details the extension of the PACO algorithm. In Section 4.4, we illustrate on VLT/SPHERE-IRDIS datasets the performance of the proposed method in terms of detection capability, achievable contrast and astrometry accuracy comparatively to two state-of-the-art algorithms routinely used on ADI datasets: TLOCI and KLIP (see Section 2.2 for their general principle). We show that, by preventing the suppression of bad frames, the automatic local weighting of the images improves the achievable contrast on the whole field of view. Finally, Section 4.5 concludes the chapter. This chapter is based on the submitted journal paper [Flasseur et al. \(2020b\)](#), currently under revision.

### Robustness issues in direct imaging

- ADI datasets are impacted by several types of artifacts, including large fluctuations due to a partial decentering of the coronagraph or a sudden degradation of the AO correction,
  - these artifacts limit the achievable contrast in the contaminated areas and impacts detection algorithms.
- ⇒ A robust approach able to deal with the diversity of the quality of the observations should be used.

## 4.2 Local modeling of spatio-temporal fluctuations

In Chapter 2, we modeled the statistical distribution of the patch  $\mathbf{r}_{n,t}$ : the small window made of a few tens of pixels, centered at pixel  $n$ , in the  $t$ -th frame. This patch with  $K$  pixels is described as the possible superimposition of the signal of a point-source (if present) and a background patch  $\mathbf{f}_{n,t}$ , considered as a random realization of a multivariate Gaussian  $\mathcal{N}(\mathbf{m}_n, \mathbf{C}_n)$ , with spatially-variant mean  $\mathbf{m}_n \in \mathbb{R}^K$  and covariance  $\mathbf{C}_n \in \mathbb{R}^{K \times K}$ . At any given pixel  $n$ , the background fluctuations captured through the covariance matrix  $\mathbf{C}_n$  are considered stationary (i.e., not evolving with time). We now improve the modeling by accounting for the nonstationary temporal variance that was observed, for example, in Figure 4.1(a).

### 4.2.1 Robust covariance estimation in SAR imaging

The problem of designing a covariance estimator that is robust to the presence of large deviations has been studied in other domains, particularly in Synthetic Aperture Radar (SAR) imaging (Yamaguchi et al., 2005). Polarimetric SAR (PolSAR) systems give access to the power back-scattered from an imaged scene along different polarization modes. More formally, after synthesis of the PolSAR image, each pixel is formed by a complex-valued scattering vector  $\mathbf{k} \in \mathbb{C}^3$ . The covariance matrix of the scattering vectors<sup>1</sup>  $\mathbb{E}[\mathbf{k}\mathbf{k}^H]$  characterizes the scattering mechanisms (surface scattering, double/triple bounces, volume scattering). Because of speckle phenomenon, estimating this covariance matrix requires averaging several tens of scattering vectors.

Figure 4.2(b) illustrates the presence of spikes in SAR images, i.e., the frequent presence of very strong echos from man-made structures (e.g., poles, cars, fences) in otherwise homogeneous areas. This large difference in backscattering power makes it difficult to reliably estimate polarimetric covariance matrices by analyzing a small window around each pixel. Assuming that scattering vectors  $\mathbf{k}$  follow the circular complex Gaussian model of fully-developed speckle (Goodman, 1976) is not correct in the presence of strong scatterers: these spikes act as outliers that strongly disturb the estimation, see Figure 4.2(c) where the scattering vector of the spike dominates the polarimetric estimator on the whole window (point-like scatterers are spread and become  $7 \times 7$  squares).

1. In this paragraph, the notation  $^H$  stands for the complex conjugate transpose.



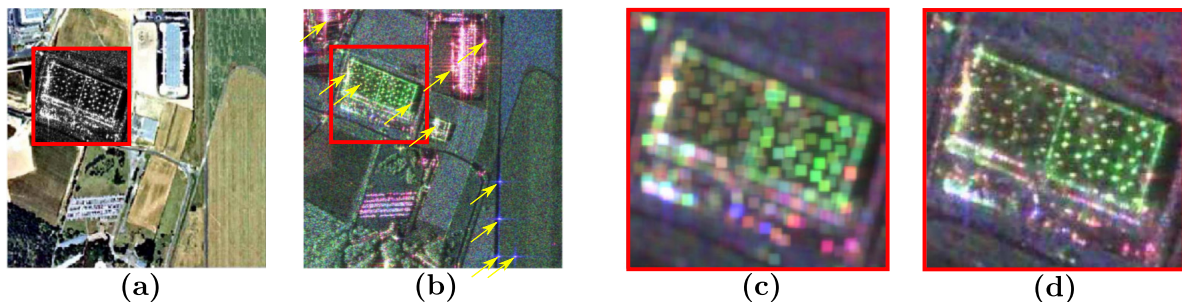


Figure 4.2 – Illustration of the problem of covariance matrix estimation in polarimetric SAR imagery: (a) optical image (area near Brétigny, France); (b) polarimetric SAR image obtained by the RAMSES airborne system of the French Aerospace Laboratory (ONERA): the components of the scattering vector  $\mathbf{k}$  are encoded in false colors at each pixel, the yellow arrows indicate point-like scatterers (*spikes*); (c)-(d) false-color representation of the diagonal of the polarimetric coherence matrix, estimated at each pixel. Images (c) and (d) are a close-up view of the region of interest drawn in red in (a) and (b). The polarimetric coherence matrices in (c)-(d) are computed on  $7 \times 7$  square windows, assuming either (c) a Gaussian clutter, or (d) a spherically invariant random vector (SIRV) model. In the SIRV model, the backscattering power is not supposed constant within the window. Adapted from Vasile et al. (2009).

To circumvent this problem, several works suggest a better statistical model for the scattering vectors: the Spherically Invariant Random Vector model (SIRV), see Bausson et al. (2007); Vasile et al. (2009). The scattering vector  $\mathbf{k}$  is modeled as the product of a positive random variable  $\sqrt{\tau}$  (representing the so-called *texture*, i.e. randomness of the clutter induced by variations in the radar backscattering power) and of an independent and zero-mean complex Gaussian vector  $\mathbf{x} \in \mathbb{C}^3$  (whose covariance matrix defines the polarimetric behavior):  $\mathbf{k} = \sqrt{\tau}\mathbf{x}$ , where  $\mathbf{C} = \mathbb{E}[\mathbf{k}\mathbf{k}^H]$  is the so-called *coherency matrix*. Within a small window, the coherence  $\mathbf{C}$  is supposed constant while the texture  $\tau$  can vary ( $\tau$  is very large at the location of spikes). Several algorithms have been studied to estimate jointly  $\tau$  and  $\mathbf{C}$  in PolSAR imaging (Gini and Greco, 2002; Wang et al., 2006; Pascal et al., 2008).

Beyond SAR imaging, product models in the form “texture parameter” $\times$ “Gaussian random variable” have been studied in image processing, under the name Gaussian scale mixture (GSM, Wainwright and Simoncelli (2000)) or compound-Gaussian model (Conte et al., 1995). GSMs cover a wide range of distributions, in particular, heavy-tailed distributions like gamma distribution, Student’s distribution or the generalized Laplacian. They can account for the presence of outliers in the data, i.e. large deviations. They have in particular been introduced in image denoising to model the distribution of wavelet coefficients (Portilla et al., 2003). In the following section, we describe how this model can be used to account for temporal nonstationarities in direct imaging.

## 4.2.2 Local modeling of spatio-temporal fluctuations with robust PACO

To account for the presence of “bad” frames with stronger background fluctuations than the other frames, we also consider that the background patch  $\mathbf{f}_{n,t}$  is a random realization of a GSM:

$$\mathbf{f}_{n,t} = \mathbf{m}_n + \sigma_{n,t} \mathbf{u}_{n,t}, \quad (4.1)$$

where  $\sigma_{n,t} > 0$  is a scalar (random or deterministic) variable that acts as a scaling parameter and the vectors  $\mathbf{u}_{n,t} \sim \mathcal{N}(\mathbf{0}, \mathbf{C}_n)$  are independent centered Gaussian random vectors.

Rather than directly handling the GSM distribution, we will estimate the scale parameter  $\sigma_{n,t}$  for the patch centered on the pixel  $n$  that is extracted from frame  $t$ , and consider that  $\mathbf{f}_{n,t}$  is distributed according to  $\mathcal{N}(\mathbf{m}_n, \sigma_{n,t}^2 \mathbf{C}_n)$ . This corresponds to considering parameter  $\sigma_{n,t}$  as a deterministic nuisance parameter, see [Pascal et al. \(2008\)](#).

Figure 4.1(b) displays maps of the estimated scaling factors  $\hat{\sigma}_{n,t}$  for the 5 frames shown in 4.1(a). In these maps, large values of the scaling factors match the areas in which the intensities are much larger than the average. The variations observed within the field of view indicate that temporal fluctuations are spatially nonstationary: larger than usual fluctuations occur only in some areas and cannot be compensated for by a factor common to the whole image. By closer visual inspection, it can be noticed that the scaling factors vary over very small distances. This indicates why methods based on linear combinations of template on-axis PSFs (TLOCI) or modes (KLIP) fail to capture such small scale variations, even when a local fitting based on annuli or angular sectors is performed.

An analysis of the empirical distribution of intensities in a patch, in absence of source, is carried out in Figure 4.3. Three cases are compared: (i) patches extracted at a pixel  $n$  close to the coronagraph, selected in order to highlight temporal fluctuations (first two rows of the figure); (ii) patches extracted at a pixel  $n$  farther from the coronagraph, showing only moderate temporal fluctuations (following two rows); (iii) patches extracted all over the field of view (last row). The temporal collection of patches  $\{\mathbf{r}_{n,t}\}_{t=1:T}$  is considered in each case. The empirical distribution of the intensities of the centered patches  $\{\mathbf{r}_{n,t} - \widehat{\mathbf{m}}_n\}_{t=1:T}$  is displayed on the left column. Then, based on a local estimate  $\widehat{\mathbf{C}}_n$  of the spatial covariance matrix, the distribution of spatially whitened and centered patches is displayed on the central column. The Cholesky factor<sup>2</sup>  $\widehat{\mathbb{L}}_n$  (i.e., the lower-triangular matrix such that  $\widehat{\mathbb{L}}_n \widehat{\mathbb{L}}_n^\top = \widehat{\mathbf{C}}_n^{-1}$ ) is used to obtain the collection of spatially whitened patches  $\{\widehat{\mathbb{L}}_n^\top (\mathbf{r}_{n,t} - \widehat{\mathbf{m}}_n)\}_{t=1:T}$ . The empirical distribution of that collection is plotted. The right column displays the distribution of patch intensities when both a spatial whitening and a time-specific scaling is performed. The empirical distribution of the collection  $\{\frac{1}{\hat{\sigma}_{n,t}} \widehat{\mathbb{L}}_n^\top (\mathbf{r}_{n,t} - \widehat{\mathbf{m}}_n)\}_{t=1:T}$  is plotted in that latter case.

Simply removing the temporal mean does not lead to independent and identically distributed normal residuals, as can be observed in the left column of Figure 4.3. The variance of the residuals is much larger near the coronagraph than farther away, a behavior that is generally addressed by introducing a radial scaling of the residuals ([Mawet](#)

2. Note that, in practice, it is more efficient first to compute a Cholesky factorization and then to invert the Cholesky factor using a dedicated routine for triangular matrix inversion, if available.



## 4.2. LOCAL MODELING OF SPATIO-TEMPORAL FLUCTUATIONS

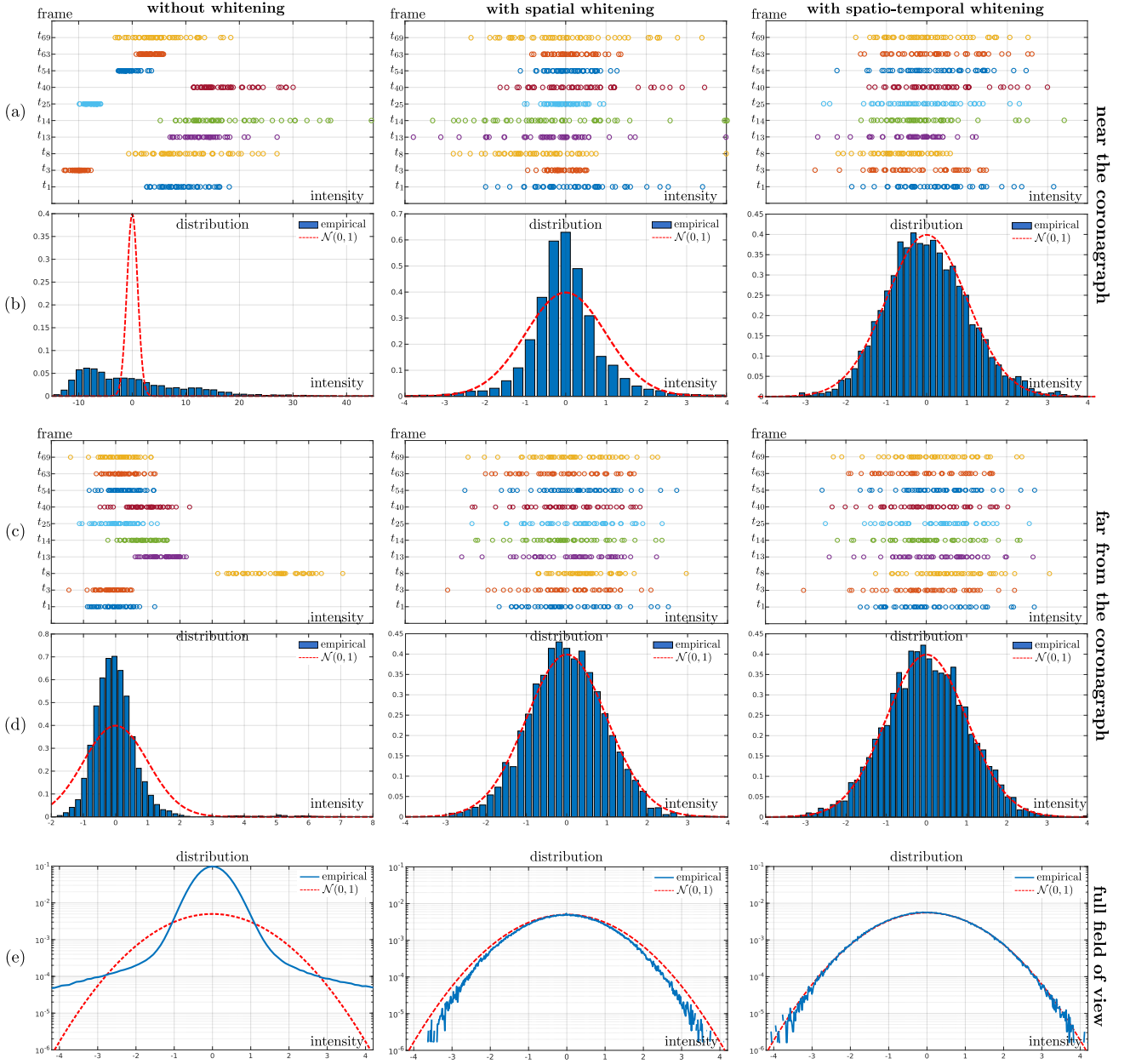


Figure 4.3 – Temporal evolution and empirical distribution of the intensities within a patch: (a)-(b) in patches extracted at a pixel  $n$  close to the coronagraph; (c)-(d) in patches extracted at a pixel  $n$  farther from the coronagraph; (e) in all the patches from the field of view. Rows (a) and (c) give the values within the patches for 10 specific frames:  $t_1, t_3, t_8, t_{13}, t_{14}, t_{25}, t_{40}, t_{54}, t_{63}$  and  $t_{69}$ . Rows (b), (d) and (e) display the empirical histograms computed over all frames  $t_1$  to  $t_{69}$  and, in dashed line, a standard Gaussian. The first column corresponds to centered patches  $\{\mathbf{r}_{n,t} - \widehat{\mathbf{m}}_n\}_{t=1:T}$ . The second column corresponds to centered patches, after whitening the spatial correlations. The last column corresponds to centered patches that have been both whitened for the spatial correlations and equalized with the temporal scaling factors.

et al., 2014). Locally modeling the spatial correlations provides a good approximation of the distribution of the patches in most pixels  $n$ , but fails in regions with large temporal heterogeneity: the distribution in that case is then better described by a GSM, see Figure 4.3(b), central column. The presence of frames with larger fluctuations leads to an over-estimation of the variances in  $\hat{\mathbf{C}}_n$ , which in turn leads to whitened samples with a variance that is less than one (Figure 4.3(e)). When both a local modeling of the spatial covariance and a time-specific local scaling factor are considered, the empirical distributions are well modeled: after whitening, they match very well a standard Gaussian in all cases (near the coronagraph, farther from the coronagraph, and on average over the whole field of view).

The modeling introduced in this chapter and the local patch-whitening transform that derives can be seen as an extension of the radial-scaling strategy that is refined in several ways: (i) locality (vs identical processing of an annulus), (ii) modeling of spatial correlations (vs uncorrelated noise assumption), (iii) modeling of time fluctuations (vs constant correction).



### Modeling of spatio-temporal fluctuations

- Inspired by the robust covariance estimators used in SAR imaging, we propose to weight each ADI patch to account for the temporal nonstationarities of the background.
- The collection of background patches at a given location is modeled by a Gaussian scale mixture, accounting for the mean background, the spatial correlations (as in PACO, see Chapter 2), and the temporal inhomogeneities.
- Within this statistical framework, the empirical intensity distributions of background patches are well modeled: after whitening, they match very well a standard Gaussian at every point of the field of view.

## 4.3 Adaptation of the PACO algorithm

### 4.3.1 Estimation of the statistics of the background

Estimating, at each spatial location, the mean background  $\mathbf{m}$ , the spatial covariance  $\mathbf{C}$  and the scale parameters  $\sigma_1$  to  $\sigma_T$  is very close to the problem of covariance structure estimation in radar under a compound-Gaussian clutter model (Pascal et al., 2008). There are two differences: (i) in radar the signal and covariance matrices are complex-valued, and (ii) the mean value is zero.

In the following, we derive the expression of the maximum likelihood estimators  $\hat{\mathbf{m}}_n$ ,  $\hat{\sigma}_{n,t}^2$  and  $\hat{\mathbf{S}}_n$  of the mean  $\mathbf{m}_n$ , the time-specific scaling  $\sigma_{n,t}^2$  and spatial covariance  $\mathbf{C}_n$ , respectively.

Let  $\{\mathbf{r}_{n,t}\}_{t=1:T}$  be a collection of 2-D patches centered at pixel  $n$ . Under our model, the  $t$ -th patch of the collection is distributed under  $\mathcal{H}_0$  according to a normal distribution with mean  $\mathbf{m}_n$  and spatial covariance  $\mathbf{C}_{n,t} = \sigma_{n,t}^2 \mathbf{C}_n$ . The notation  $\hat{\mathbf{C}}_n$  is kept to

denote the shrinkage estimator obtained by reducing the value of off-diagonal elements of the maximum likelihood estimator  $\widehat{\mathbf{S}}_n$ .

Under the assumption that each patch is an independent realization of our model of the background, the neg-log-likelihood  $\mathcal{L}$  of the collection is given by:

$$\begin{aligned} \mathcal{L} &= -\log p\left(\{\mathbf{r}_{n,t}\}_{t=1:T} \mid \mathbf{m}_n, \{\sigma_{n,t}^2\}_{t=1:T}, \mathbf{C}_n\right) \\ &\propto \sum_{t=1}^T \log \det\left(\sigma_{n,t}^2 \mathbf{C}_n\right) + \sum_{t=1}^T \frac{1}{\sigma_{n,t}^2} \bar{\mathbf{r}}_{n,t}^\top \mathbf{C}_n^{-1} \bar{\mathbf{r}}_{n,t} + \text{const} \end{aligned} \quad (4.2)$$

with  $\bar{\mathbf{r}}_{n,t} = \mathbf{r}_{n,t} - \mathbf{m}_n$ . The maximum likelihood estimators correspond to the location of the minimum of (4.2), where the gradient of the neg-log-likelihood equals zero.

- From the condition  $\left. \frac{\partial \mathcal{L}}{\partial \sigma_{n,t}^2} \right|_{\sigma_{n,t}^2 = \hat{\sigma}_{n,t}^2} = 0$ , it comes:

$$\frac{K}{\hat{\sigma}_{n,t}^2} - \frac{1}{\hat{\sigma}_{n,t}^4} \bar{\mathbf{r}}_{n,t}^\top \mathbf{C}_n^{-1} \bar{\mathbf{r}}_{n,t} = 0,$$

which leads to:

$$\hat{\sigma}_{n,t}^2 = \frac{1}{K} \bar{\mathbf{r}}_{n,t}^\top \mathbf{C}_n^{-1} \bar{\mathbf{r}}_{n,t}. \quad (4.3)$$

The variance at time  $t$  around pixel  $k$  is thus estimated by computing the sample variance of a spatially whitened version of the  $t$ -th patch.

- From the condition  $\nabla_{\mathbf{m}_n} \mathcal{L} \big|_{\mathbf{m}_n = \widehat{\mathbf{m}}_n} = \mathbf{0}$ , we get:

$$-2 \sum_{t=1}^T \frac{1}{\sigma_{n,t}^2} \mathbf{C}_n^{-1} (\mathbf{r}_{n,t} - \widehat{\mathbf{m}}_n) = \mathbf{0}.$$

Since  $\mathbf{C}_n^{-1}$  is not singular, we obtain:

$$\widehat{\mathbf{m}}_n = \frac{\sum_{t=1}^T \frac{1}{\sigma_{n,t}^2} \mathbf{r}_{n,t}}{\sum_{t=1}^T \frac{1}{\sigma_{n,t}^2}}. \quad (4.4)$$

The mean background in patches around the  $n$ -th pixel corresponds to a weighted average where a patch at time  $t$  with large variance is given a small weight.

- From the condition  $\nabla_{\mathbf{C}_n} \mathcal{L} \big|_{\mathbf{C}_n = \widehat{\mathbf{S}}_n} = \mathbf{0}$ , we derive:

$$T \cdot \widehat{\mathbf{S}}_n^{-1} - \widehat{\mathbf{S}}_n^{-1} \left( \sum_{t=1}^T \frac{1}{\sigma_{n,t}^2} \bar{\mathbf{r}}_{n,t} \bar{\mathbf{r}}_{n,t}^\top \right) \widehat{\mathbf{S}}_n^{-1} = \mathbf{0},$$

which gives:

$$\widehat{\mathbf{S}}_n = \frac{1}{T} \sum_{t=1}^T \frac{1}{\sigma_{n,t}^2} \bar{\mathbf{r}}_{n,t} \bar{\mathbf{r}}_{n,t}^\top. \quad (4.5)$$

The spatial covariance estimator corresponds to the sample covariance upon a proper rescaling by a factor  $1/\sigma_{n,t}$  of residual patches  $\bar{\mathbf{r}}_{n,t}$ .

---

<b>Algorithm 4.1:</b> Local background statistics estimation	
<b>Input:</b> $\{\mathbf{r}_1, \dots, \mathbf{r}_T\}$	(stack of $T$ spatial patches, each patch has $K$ pixels)
<b>Output:</b> $\widehat{\mathbf{m}}$	(mean patch)
<b>Output:</b> $\widehat{\mathbf{C}}$	( $K \times K$ spatial covariance)
<b>Output:</b> $\{\widehat{\sigma}_1, \dots, \widehat{\sigma}_T\}$	(scale parameters)
$\widehat{\mathbf{C}} \leftarrow \mathbf{I}$	(initialize at identity matrix)
<b>for</b> $t \leftarrow 1$ <b>to</b> $T$ <b>do</b>	
$\widehat{w}_t \leftarrow 1/T$	(initialize with uniform weights)
$\widehat{\mathbf{m}} \leftarrow \sum_{t=1}^T \widehat{w}_t \cdot \mathbf{r}_t$	(sample mean)
<b>do</b>	
$\triangleright$ <b>Step 1:</b> Estimate scale parameters	
$\{\widehat{\sigma}_1, \dots, \widehat{\sigma}_T\} \leftarrow \text{Algorithm 4.2}(\{\mathbf{r}_1, \dots, \mathbf{r}_T\}, \widehat{\mathbf{m}}, \widehat{\mathbf{C}})$	
$\triangleright$ <b>Step 2:</b> Update temporal weights	
<b>for</b> $t \leftarrow 1$ <b>to</b> $T$ <b>do</b>	
$\widehat{w}_t^{(\text{old})} \leftarrow \widehat{w}_t$	
$\widehat{w}_t \leftarrow \frac{1/\widehat{\sigma}_t^2}{\sum_{t'=1}^T 1/\widehat{\sigma}_{t'}^2}$	
$\triangleright$ <b>Step 3:</b> Update the mean patch	
$\widehat{\mathbf{m}} \leftarrow \sum_{t=1}^T \widehat{w}_t \cdot \mathbf{r}_t$	(weighted mean)
$\triangleright$ <b>Step 4:</b> Update the covariance	
$\widehat{\mathbf{S}} \leftarrow \frac{1}{T} \sum_{t=1}^T \frac{1}{\widehat{\sigma}_t^2} (\mathbf{r}_t - \widehat{\mathbf{m}})(\mathbf{r}_t - \widehat{\mathbf{m}})^\top$	(sample cov.)
$\widetilde{T} \leftarrow 1 / \sum_{t=1}^T \widehat{w}_t^2$	(effective number of frames)
$\widehat{\mathbf{C}} \leftarrow \text{Algorithm 4.3}(\widehat{\mathbf{S}}, \widetilde{T})$	(shrinkage covariance estimator)
<b>while</b> $\max_t  \widehat{w}_t - \widehat{w}_t^{(\text{old})}  \geq \epsilon$ ;	

---

The expression of each estimator depends on the others so that a fixed point is sought to obtain the joint estimator of the local background statistics. Based on the alternating application of formulas (4.3), (4.4) and (4.5), an iterative algorithm is obtained. The algorithm is detailed in boxes 4.1 and 4.2.

It can be noted that, up to the centering to account for the non-zero mean, the obtained fixed-point algorithm matches the estimator derived in Conte et al. (2002) in the context of clutter with a deterministic texture, and also the approximate maximum likelihood estimator derived in Gini and Greco (2002) under a stochastic model of texture. The convergence of the fixed-point algorithm has been established in Pascal et al. (2008) in the real-valued case as well as in the complex-valued case.

Since our estimates are computed in the regime of small sample sizes, we include a shrinkage procedure similar to that described in Section 2.3.2. To account for the weighting of the samples, we compute an effective number of frames

---

**Algorithm 4.2:** Estimate scale parameters
 

---

<b>Input:</b> $\{\mathbf{r}_1, \dots, \mathbf{r}_T\}$	(stack of $T$ spatial patches)
<b>Input:</b> $\hat{\mathbf{m}}$	(estimated mean patch)
<b>Input:</b> $\hat{\mathbf{C}}$	( $K \times K$ estimated spatial covariance)
<b>Output:</b> $\{\hat{\sigma}_1, \dots, \hat{\sigma}_T\}$	(scale parameters)

---

$\hat{\mathbf{L}} \leftarrow \text{chol}(\hat{\mathbf{C}}^{-1})$	(Cholesky factorization)
<b>for</b> $t \leftarrow 1$ <b>to</b> $T$ <b>do</b>	
$\check{\mathbf{r}}_t \leftarrow \hat{\mathbf{L}}^\top (\mathbf{r}_t - \hat{\mathbf{m}})$	(whitened patch)
$\hat{\mu} \leftarrow \frac{1}{K} \sum_{i=1}^K [\check{\mathbf{r}}_t]_i$	(mean value)
$\hat{\sigma}_t^2 \leftarrow \frac{1}{K} \sum_{i=1}^K ([\check{\mathbf{r}}_t]_i - \hat{\mu})^2$	(scale parameter)

---



---

**Algorithm 4.3:** Shrinkage covariance estimator
 

---

<b>Input:</b> $\hat{\mathbf{S}}$	( $K \times K$ sample covariance matrix)
<b>Input:</b> $\tilde{T}$	(effective number of frames)
<b>Output:</b> $\hat{\mathbf{C}}$	(covariance matrix estimate)

---

$\hat{\rho} \leftarrow \frac{\text{tr}(\hat{\mathbf{S}}^2) + \text{tr}^2(\hat{\mathbf{S}}) - 2 \sum_{i=1}^K [\hat{\mathbf{S}}]_{ii}^2}{(\tilde{T}+1) \left( \text{tr}(\hat{\mathbf{S}}^2) - \sum_{i=1}^K [\hat{\mathbf{S}}]_{ii}^2 \right)}$	(shrinkage factor)
<b>for</b> $i \leftarrow 1$ <b>to</b> $K$ <b>do</b>	
$[\hat{\mathbf{C}}]_{i,i} \leftarrow [\hat{\mathbf{S}}]_{i,i}$	(copy diagonal)
<b>for</b> $j \leftarrow i + 1$ <b>to</b> $K$ <b>do</b>	
$[\hat{\mathbf{C}}]_{i,j} \leftarrow (1 - \hat{\rho}) [\hat{\mathbf{S}}]_{i,j}$	(shrink off-diagonal)
$[\hat{\mathbf{C}}]_{j,i} \leftarrow (1 - \hat{\rho}) [\hat{\mathbf{S}}]_{j,i}$	(shrink off-diagonal)

---

$\tilde{T} = (\sum_t 1/\hat{\sigma}_t^2)^2 / (\sum_t 1/\hat{\sigma}_t^4)$  that corresponds<sup>3</sup> to the variance reduction reached when performing a weighted mean with the weights  $1/\hat{\sigma}_t^2$ . This effective number of frames is used to compute the shrinkage factor in Algorithm 4.3. This shrinkage operation can either be applied at each iteration (during step 4 of Algorithm 4.1) or after the alternating updates converged. We tested both approaches and found that they converged to solutions leading to similar detection performances. Applying the shrinkage at each iteration ensures that matrix  $\hat{\mathbf{C}}$  never becomes singular or ill-conditioned.

Figure 4.4 illustrates the fast convergence of the alternating scheme. Each plot corresponds to a different pixel  $n$  in the field of view, depicted by a red dot. From

---

3. The effective number of frames  $\tilde{T}$  corresponds to the number of samples if all weights are equal and is smaller when some weights differ. Let us assume that  $\{r_t\}_{t=1..T}$  is a collection of  $T$  independent and identically distributed random variables. The weighted mean  $\hat{m} = \sum_{t=1}^T w_t r_t$ , where  $w_t \geq 0$  are normalized weights ( $w_t = (1/\sigma_t^2) / (\sum_{t=1}^T 1/\sigma_t^2)$ ), is an unbiased estimator of  $\mathbb{E}[r]$  with a variance  $\text{Var}[\hat{m}] = \sum_{t=1}^T \text{Var}[w_t r_t]$  (by independence of the  $r_t$ ), which leads to  $\text{Var}[\hat{m}] = \text{Var}[r] / \tilde{T}$ , with  $\tilde{T} = 1 / \sum_{t=1}^T w_t^2 = (\sum_{t=1}^T 1/\sigma_t^2)^2 / (\sum_{t=1}^T 1/\sigma_t^4)$  the effective number of samples. If all weights are equal,  $\tilde{T} = T$ : the effective number of samples is equal to the total number of samples. If all weights but one are zero,  $\tilde{T} = 1$ . In practice, the samples  $\{r_t\}_{t=1..T}$  are not identically distributed (their variances differ), but  $\tilde{T}$  still indicates if the mean is reliable.

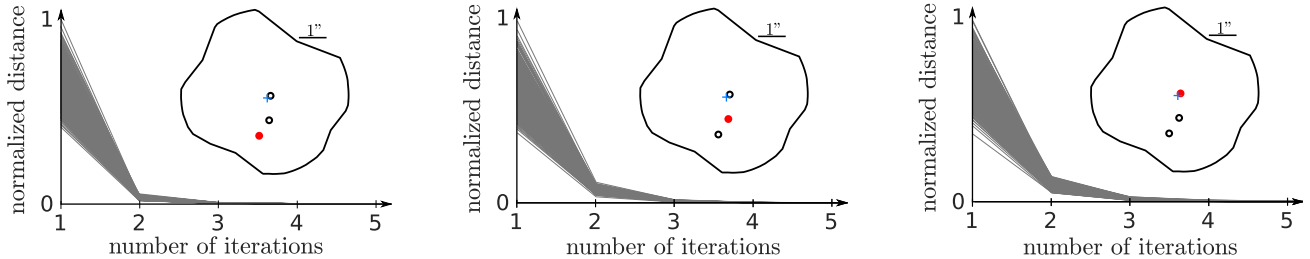


Figure 4.4 – Illustration of the convergence of Algorithm 3: 1,000 random initializations of the weights  $\{\hat{w}_t\}_{t=1:T}$  converge to the same solution as that obtained by initializing with constant weights. Convergence at 3 pixel locations  $n$  depicted on the field of view is shown, covering 3 different cases: small dispersion of the value of scaling parameters (left), medium dispersion (center) and large dispersion close to the coronagraph (right). The blue cross represents the star center.

left to right, they correspond respectively to a region with good temporal stationarity, medium temporal stationarity, and low temporal stationarity (close to the coronagraph). The convergence of Algorithm 4.1 is assessed based on 1,000 random initializations of the weights  $\hat{w}_t$  (following, before normalization, a uniform distribution on  $[0, 1]$ ). The vector of weights at convergence when starting from a constant vector of weights ( $\forall t, \hat{w}_t = 1/T$ ) is used as a reference. At each iteration, the Euclidean distance to the reference vector of weights is reported, with normalization by the largest distance of all the random draws. Very fast convergence is observed to a unique solution, in all random trials. This empirical evidence indicates that the algorithm also converges when the shrinkage step is included at each iteration.

### 4.3.2 Robust computation of a detection map

We recall that the PACO algorithm, introduced in Chapter 2, produces a detection map based on a hypothesis test evaluated at each pixel of the field of view. The ADI sequence of images is processed at the scale of image patches. The size of the patches is selected to capture the core of the off-axis point spread function (PSF), e.g. a disk of  $K = 49$  pixels for SPHERE-IRDIS in K1-K2 observing mode, see Section 2.4.1. If a point source object is located at angular position  $\phi_0$  in some reference frame, then its angular location  $\phi_t$  in the image at time  $t$  can be deduced from the telescope pointing information, by accounting for the rotation of the whole field of view during ADI acquisitions. Source detection is based on the analysis of the collection  $\{\mathbf{r}_{[\phi_t],t}\}_{t=1:T}$  of the  $T$  patches formed by tracking the source through its apparent motion: each patch is extracted at the expected location, rounded to the closest pixel  $[\phi_t]$ , of the point source with reference coordinate  $\phi_0$ , see Figure 2.3.

As in Chapter 2, during the detection step, we assume that the observations are dominated by the background signal due to stellar leakages and by the noise so that background statistics can be computed directly from the data (off-axis point sources are considered negligible at that step). The local statistics of the background (including the spatio-temporal modeling of its fluctuations) are then computed with Algorithm 4.1, for each location  $[\phi_t]$ , based on the collections  $\{\mathbf{r}_{[\phi_t],t}\}_{t=1:T}$  of observed patches all centered



at that same location  $[\phi_t]$ . Once the mean  $\widehat{\mathbf{m}}_{[\phi_t]}$ , spatial covariance  $\widehat{\mathbf{C}}_{[\phi_t]}$  and scaling factor<sup>4</sup>  $\widehat{\sigma}_{[\phi_t],t}$  are estimated for all locations  $[\phi_t]$  corresponding to the trajectory of a hypothetical point source with reference location  $\phi_0$ , the likelihood of two hypotheses can be compared as in Equation (2.4):

$$\begin{cases} \mathcal{H}_0 : & \{\mathbf{r}_{[\phi_t],t}\}_{t=1:T} = \{\mathbf{f}_{[\phi_t],t}\}_{t=1:T} \quad (\text{background only}) \\ \mathcal{H}_1 : & \{\mathbf{r}_{[\phi_t],t}\}_{t=1:T} = \alpha \{\mathbf{h}_{[\phi_t]}(\phi_t)\}_{t=1:T} + \{\mathbf{f}_{[\phi_t],t}\}_{t=1:T} \quad (\text{background + source}), \end{cases} \quad (4.6)$$

where  $\alpha$  is the flux of the point source and  $\mathbf{h}_{[\phi_t]}(\phi_t)$  is a patch of the off-axis PSF extracted around the integer location  $[\phi_t]$ , for a point source located at the subpixel location  $\phi_t$ .

Under the assumption that each of the  $T$  background patches of the collection  $\{\mathbf{f}_{[\phi_t],t}\}_{t=1:T}$  is an independent realization, each distributed according to its local GSM model, the neg-log-likelihood of the data under hypothesis  $\mathcal{H}_0$  is

$$\begin{aligned} -\log p(\{\mathbf{r}_{[\phi_t],t}\}_{t=1:T} | \mathcal{H}_0) &= \frac{TK}{2} \log 2\pi + \sum_{t=1}^T \frac{1}{2} \log \det(\widehat{\sigma}_{[\phi_t],t}^2 \widehat{\mathbf{C}}_{[\phi_t]}) \\ &\quad + \sum_{t=1}^T \frac{1}{2} (\mathbf{r}_{[\phi_t],t} - \widehat{\mathbf{m}}_{[\phi_t]})^\top (\widehat{\sigma}_{[\phi_t],t}^2 \widehat{\mathbf{C}}_{[\phi_t]})^{-1} (\mathbf{r}_{[\phi_t],t} - \widehat{\mathbf{m}}_{[\phi_t]}). \end{aligned} \quad (4.7)$$

The neg-log-likelihood of the data under hypothesis  $\mathcal{H}_1$  cannot be directly evaluated since the flux  $\alpha$  of the point source is not known beforehand. It can, however, be estimated in the maximum likelihood sense, as in Equation (2.16):

$$\widehat{\alpha} = \arg \min_{\alpha} -\log p(\{\mathbf{r}_{[\phi_t],t}\}_{t=1:T} | \mathcal{H}_1, \alpha) = \frac{\sum_{t=1}^T b_t}{\sum_{t=1}^T a_t}, \quad (4.8)$$

with

$$a_t = \frac{1}{\widehat{\sigma}_{[\phi_t],t}^2} \mathbf{h}_{[\phi_t]}(\phi_t)^\top \cdot \widehat{\mathbf{C}}_{[\phi_t]}^{-1} \cdot \mathbf{h}_{[\phi_t]}(\phi_t) \quad (4.9)$$

and

$$b_t = \frac{1}{\widehat{\sigma}_{[\phi_t],t}^2} \mathbf{h}_{[\phi_t]}(\phi_t)^\top \cdot \widehat{\mathbf{C}}_{[\phi_t]}^{-1} \cdot (\mathbf{r}_{[\phi_t],t} - \widehat{\mathbf{m}}_{[\phi_t]}). \quad (4.10)$$

Note that these formulas are very similar to Equations (2.16), (2.17) and (2.18); the differing terms accounting for the temporal fluctuations are highlighted in blue.

The neg-log-likelihood of the data under hypothesis  $\mathcal{H}_1$ , for a source flux  $\widehat{\alpha}$ , is then:

$$\begin{aligned} \log p(\{\mathbf{r}_{[\phi_t],t}\}_{t=1:T} | \mathcal{H}_1, \widehat{\alpha}) &= \frac{TK}{2} \log 2\pi + \sum_{t=1}^T \frac{1}{2} \log \det(\widehat{\sigma}_{[\phi_t],t}^2 \widehat{\mathbf{C}}_{[\phi_t]}) \\ &\quad + \sum_{t=1}^T \frac{1}{2} \mathbf{u}_{[\phi_t],t}^\top (\widehat{\sigma}_{[\phi_t],t}^2 \widehat{\mathbf{C}}_{[\phi_t]})^{-1} \mathbf{u}_{[\phi_t],t}, \end{aligned} \quad (4.11)$$

---

4. Only the scaling factor at time  $t$  is necessary for the detection.

with  $\mathbf{u}_{[\phi_t],\ell} = \mathbf{r}_{[\phi_t],t} - \hat{\alpha}\mathbf{h}_{[\phi_t]}(\phi_t) - \hat{\mathbf{m}}_{[\phi_t]}$ .

As in Section 2.3.4, the generalized likelihood ratio test (GLRT) is (see Equation (2.24)):

$$2 \log \frac{\text{p}(\{\mathbf{r}_{[\phi_t],t}\}_{t=1:T} | \mathcal{H}_1, \hat{\alpha})}{\text{p}(\{\mathbf{r}_{[\phi_t],t}\}_{t=1:T} | \mathcal{H}_0)} = \frac{\left(\sum_{t=1}^T b_t\right)^2}{\sum_{t=1}^T a_t} \underset{\mathcal{H}_0}{\overset{\mathcal{H}_1}{\gtrless}} \eta. \quad (4.12)$$

Only a positive flux  $\alpha$  makes sense for a source. The estimate  $\hat{\alpha}$  should then be replaced by the estimate  $\hat{\alpha}^+ = \max(\hat{\alpha}, 0)$  obtained under a positivity constraint. As in Section 2.3.5 (see Equation (2.26)), the GLRT can then be recast, for  $\eta \geq 0$ , into the form:

$$\text{S/N test: } \frac{\sum_{t=1}^T b_t}{\sqrt{\sum_{t=1}^T a_t}} = \frac{\hat{\alpha}}{\hat{\sigma}_\alpha} \underset{\mathcal{H}_0}{\overset{\mathcal{H}_1}{\gtrless}} \tau, \quad (4.13)$$

with  $\tau = \sqrt{\eta}$ , which corresponds to comparing the signal-to-noise ratio (S/N) of the flux estimate to a threshold.

Under our GSM model, and thanks to the normalization by the scaling factors  $\hat{\sigma}_{[\phi_t],t}$ , the ratio  $\hat{\alpha}/\hat{\sigma}_\alpha$  is thus distributed according to a standard normal distribution. This simplifies the setting of a detection threshold  $\tau$ :  $\tau = 5$  leads to a probability of false alarm equal to  $2.87 \times 10^{-7}$ , i.e., the probability that a Gaussian random variable be greater than 5 standard deviations.

Figure 4.5 illustrates that the ratio  $\hat{\alpha}/\hat{\sigma}_\alpha$  is indeed distributed like a standard normal distribution. Two detection maps are shown for the star HIP 72192. The left part of the figure corresponds to the results of PACO algorithm, as presented in Chapter 2 (see Figure 2.8). The corresponding detection map is approximatively stationary. When representing the empirical distribution of signal-to-noise ratio values in the field of view (after excluding the two areas corresponding to two sources), a relatively good match with a Gaussian distribution is obtained, albeit with a standard deviation slightly below 1. The right part of the figure gives the detection map produced by the extension of PACO accounting for the spatio-temporal fluctuations of the background (denoted **robust PACO** in the following). While both maps are quite similar, it can be noted that time-dependent scaling factors lead to a slightly improved spatial stationarity<sup>5</sup> of the detection map, in the sense that the standard deviation of its distribution is closer to 1 in all the areas of the field of view. An improved match to the standard Gaussian distribution is thus observed. The impact of producing maps with a variance less than one in the absence of source, with the standard PACO algorithm, is to be overly conservative: some detections may be missed at a given false alarm rate while they would be correctly detected with **robust PACO**. We illustrate such behavior in Section 4.4.

The detection map is produced by computing the signal-to-noise ratio for each reference location  $\phi_0$  on a grid. The computational complexity can be significantly reduced by pre-computing terms that can then be shared to evaluate the signal-to-noise ratio at several locations. Such an approach, referred as **fast PACO** in Section 2.4.4, can also

5. The stationarity of the PACO detection maps in the absence of source should be appreciated by comparison with the detection maps presented in Section 2.5.2.1 and 4.4.1 (in particular in Figures 2.16, 2.17, 2.22, and 4.9) that are obtained with several state-of-art detection methods.

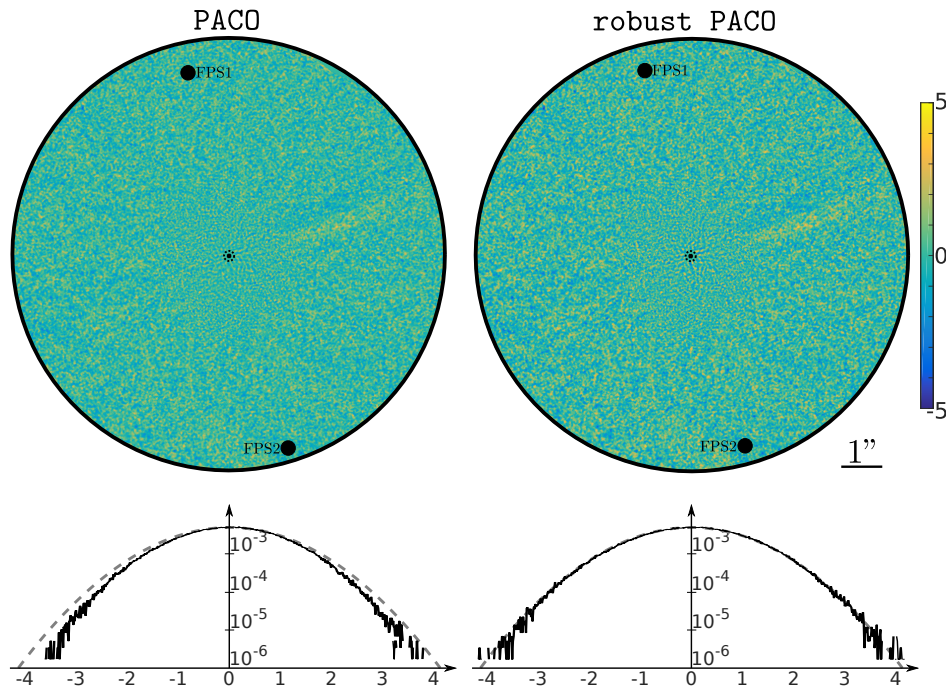


Figure 4.5 – Detection map computed on a SPHERE-IRDIS ADI dataset of HIP 72192. The two faint point sources in the field of view, FPS1 and FPS2 are marked by black dots. There are no other detectable sources in the field of view. The left column corresponds to the standard PACO algorithm, the right column to **robust PACO**. The bottom row gives in solid line the empirical distribution of the signal-to-noise values of the detection maps, excluding areas FPS1 and FPS2. The dashed line corresponds to a standard normal distribution.

be adapted to our GSM model, provided that the background statistics are computed using the algorithm outlined in Section 4.3.1 and that the formulas are updated to include the scaling factors  $\hat{\sigma}_{k,\ell}$ , according to equations (4.9), (4.10) and (4.13). Compared to the original **fast PACO** algorithm, these changes lead to an increase of the computation time by an order of magnitude, corresponding to the typical number of iterations to reach a fixed point in the step that estimates the local background statistics (about 10 iterations).

### 4.3.3 Robust estimation of photometry and astrometry

Similarly to the approach described in Section 2.3.3, when characterizing a source (found above the detection threshold in the detection map), the source flux is to be re-estimated jointly with the background statistics in order to prevent any self-subtraction that would bias the estimation. In practice, this joint estimation is performed by alternating (i) a re-estimation of the local background statistics using the residuals  $\{\mathbf{r}_{[\phi_i],t} - \hat{\alpha}\mathbf{h}_{[\phi_i]}(\phi_t)\}_{t=1:T}$ , where  $\hat{\alpha}$  is the current flux estimate, and (ii) a re-estimation of the source flux with the updated background statistics by applying Equation (4.8).

The accurate astrometric estimation of the source is obtained by evaluating the signal-to-noise ratio, with the unbiased flux estimate, over a refined subpixel grid around the detected location.

Once a source has been characterized both in terms of astrometry and photometry, its contribution to the data can be subtracted and the detection map updated accordingly, similarly to source extraction with the CLEAN algorithm, as described in Section 2.4.6.

### 4.3.4 Sketch of proof of the robustness

In this section, we show that our estimators are robust in the sense that, should the patch  $\mathbf{r}_{n,t^*}$  be replaced by a scaled version  $\mathbf{r}'_{n,t^*} = \eta \cdot \mathbf{r}_{n,t^*}$  with an arbitrarily large factor  $\eta$ , at a given frame  $t^*$ , the estimators of the background statistics  $\widehat{\mathbf{m}}'_n$  and  $\widehat{\mathbf{S}}'_n$  as well as the flux estimator  $\widehat{\alpha}'$  computed on the collection with the scaled patch remain bounded<sup>6</sup>. In fact, when  $\eta$  grows to infinity, we show that the patch  $\mathbf{r}'_{n,t^*}$  gets completely discarded in the estimation of the flux. This contrasts with other data processing methods in ADI that generally lead to incorrect detection confidence and flux estimates if bad frames with large values are present in the dataset<sup>7</sup>.

Since the estimators  $\widehat{\mathbf{m}}_n$ ,  $\widehat{\mathbf{C}}_n$  and  $\widehat{\sigma}_{n,t}^2$  are defined implicitly through a fixed-point procedure, directly proving the robustness is difficult. Instead, we show that when  $\eta$  approaches infinity, the following estimates correspond to a fixed point:

$$\begin{cases} \widehat{\sigma}_{n,t}^{2'} = \widehat{\sigma}_{n,t}^2 & \text{when } t \neq t^* \\ \widehat{\sigma}_{n,t^*}^{2'} \rightarrow \infty \\ \widehat{\mathbf{m}}'_n = \widetilde{\mathbf{m}}_n \\ \widehat{\mathbf{S}}'_n = \frac{T-1}{T} \widetilde{\mathbf{S}}_n + \frac{K}{T} \frac{\mathbf{r}_{n,t^*} \mathbf{r}_{n,t^*}^\top}{\mathbf{r}_{n,t^*}^\top (\widehat{\mathbf{S}}'_n)^{-1} \mathbf{r}_{n,t^*}}, \end{cases} \quad (4.14)$$

where  $\widetilde{\sigma}_{n,t}^2$ ,  $\widetilde{\mathbf{m}}_n$  and  $\widetilde{\mathbf{S}}_n$  correspond to the estimators computed on the collection  $\{\mathbf{r}_{n,t}\}_{t \neq t^*}$  of the patches with the  $t^*$ -th frame removed.

Starting with the initial values given in (4.14), the application of Equation (4.3) leaves the estimated variances  $\widehat{\sigma}_{n,t}^{2'}$  unchanged for all  $t$  different from  $t^*$ . For  $t^*$ ,  $\widehat{\sigma}_{n,t^*}^{2'} \sim \eta^2 \widehat{\sigma}_{n,t}^2$  which tends to infinity when  $\eta$  approaches infinity.

From Equation (4.4), we see that the patch  $\mathbf{r}'_{n,t^*}$  with associated infinite variance  $\widehat{\sigma}_{n,t^*}^{2'}$  has negligible contribution in the weighted mean:  $\frac{1}{\widehat{\sigma}_{n,t^*}^{2'}} \mathbf{r}'_{n,t^*} \underset{\eta \rightarrow \infty}{\sim} \frac{1}{\eta \widehat{\sigma}_{n,t}^2} \mathbf{r}_{n,t^*}$ , so that  $\lim_{\eta \rightarrow \infty} \frac{1}{\widehat{\sigma}_{n,t^*}^{2'}} \mathbf{r}'_{n,t^*} = 0$ . The mean patch then corresponds to that obtained on the collection of patches with the  $t^*$ -th patch excluded.

The approximations  $\widehat{\sigma}_{n,t^*}^{2'} \underset{\eta \rightarrow \infty}{\sim} \frac{\eta^2}{K} \mathbf{r}_{n,t^*}^\top (\widehat{\mathbf{S}}'_n)^{-1} \mathbf{r}_{n,t^*}$  and  $\bar{\mathbf{r}}'_{n,t^*} \underset{\eta \rightarrow \infty}{\sim} \eta \mathbf{r}_{n,t^*}$  together with the update of the sample covariance estimate (4.5) lead to  $\widehat{\mathbf{S}}'_n = \frac{T-1}{T} \widetilde{\mathbf{S}}_n + \frac{K}{T} \frac{\mathbf{r}_{n,t^*} \mathbf{r}_{n,t^*}^\top}{\mathbf{r}_{n,t^*}^\top (\widehat{\mathbf{S}}'_n)^{-1} \mathbf{r}_{n,t^*}}$ .

In conclusion, the set of parameters defined in (4.14) is a fixed-point. Moreover, neither the mean background patch  $\widehat{\mathbf{m}}'_n$  nor the spatial covariance  $\widehat{\mathbf{S}}'_n$  depend on  $\eta$  (i.e., they

6. Note that multiplying the patch by  $\eta$  differs from our modeling since this changes both the mean and covariance while we assumed that only the covariance may be scaled.

7. TLOCI computes medians rather than averages at some steps to improve the robustness. However, such a strategy is generally not sufficient to overcome the presence of large fluctuations on several time frames since some steps include a linear processing of the data.

both remain bounded when  $\eta \rightarrow \infty$ ). It remains to show the robustness of the flux estimator  $\hat{\alpha}$  of a source.

If the scaled patch is not in the collection of all patches that contain the PSF of the source, then its influence is limited since we have just shown that the background statistics are robustly estimated. In the case of the superimposition of a scaled background and of the source of interest (as is the case when a poor correction of the AO leads to large stellar leakages at some locations of the field of view), the estimated flux becomes:

$$\hat{\alpha}(\phi_t) = \frac{\sum_{t=1}^T \frac{1}{\hat{\sigma}_{n,t}^2} \mathbf{h}_{[\phi_t]}(\phi_t)^\top \cdot \hat{\mathbf{C}}_{[\phi_t]}^{-1} \cdot (\mathbf{r}'_{[\phi_t],t} - \hat{\mathbf{m}}_{[\phi_t]})}{\sum_{t=1}^T \frac{1}{\hat{\sigma}_{n,t}^2} \mathbf{h}_{[\phi_t]}(\phi_t)^\top \cdot \hat{\mathbf{C}}_{[\phi_t]}^{-1} \cdot \mathbf{h}_{[\phi_t]}(\phi_t)}. \quad (4.15)$$

Therefore, when  $\eta$  becomes large, the term  $(\mathbf{r}'_{[\phi_{t^*}],t^*} - \hat{\mathbf{m}}_{[\phi_{t^*}]}) / \hat{\sigma}_{n,t^*}^2$  tends to zero and we obtain:

$$\hat{\alpha}(\phi_t) \approx \frac{\sum_{t \neq t^*} \frac{1}{\hat{\sigma}_{n,t}^2} \mathbf{h}_{[\phi_t]}(\phi_t)^\top \cdot \hat{\mathbf{C}}_{[\phi_t]}^{-1} \cdot (\mathbf{r}'_{[\phi_t],t} - \hat{\mathbf{m}}_{[\phi_t]})}{\sum_{t \neq t^*} \frac{1}{\hat{\sigma}_{n,t}^2} \mathbf{h}_{[\phi_t]}(\phi_t)^\top \cdot \hat{\mathbf{C}}_{[\phi_t]}^{-1} \cdot \mathbf{h}_{[\phi_t]}(\phi_t)} \quad (4.16)$$

$$\approx \frac{\sum_{t \neq t^*} \frac{1}{\hat{\sigma}_{n,t}^2} \mathbf{h}_{[\phi_t]}(\phi_t)^\top \cdot \hat{\mathbf{C}}_{[\phi_t]}^{-1} \cdot (\mathbf{r}_{[\phi_t],t} - \hat{\mathbf{m}}_{[\phi_t]})}{\sum_{t \neq t^*} \frac{1}{\hat{\sigma}_{n,t}^2} \mathbf{h}_{[\phi_t]}(\phi_t)^\top \cdot \hat{\mathbf{C}}_{[\phi_t]}^{-1} \cdot \mathbf{h}_{[\phi_t]}(\phi_t)}, \quad (4.17)$$

which indicates that the scaled frame  $\mathbf{r}'_{[\phi_{t^*}],t^*}$  tends to be completely discarded when the scaling factor  $\eta$  is large. Estimation of the photometry and of the astrometry is therefore robust to the presence of a frame with an arbitrarily large background.

#### Estimators accounting for the temporal fluctuations

- Under our Gaussian scale mixture model, the estimator of the background statistics and the estimator of the source flux are both very similar to the ones derived in Chapter 2 under a multivariate Gaussian model of the background fluctuations.
- They differ only by weighting factors related to the estimated temporal scaling factors (inversely proportional to the variance at each time).
- They are robust since they remain bounded in the presence of a frame with arbitrarily large magnitude. The impact of bad frames is limited and becomes negligible for the largest deviations.
- We illustrated on SPHERE/IRDIS data that the time-dependent scaling factors lead to detection maps that are slightly more spatially stationary, in the sense that the standard deviation of their distribution is closer to 1 in all the areas of the field of view. An improved match to the standard Gaussian distribution is thus observed.

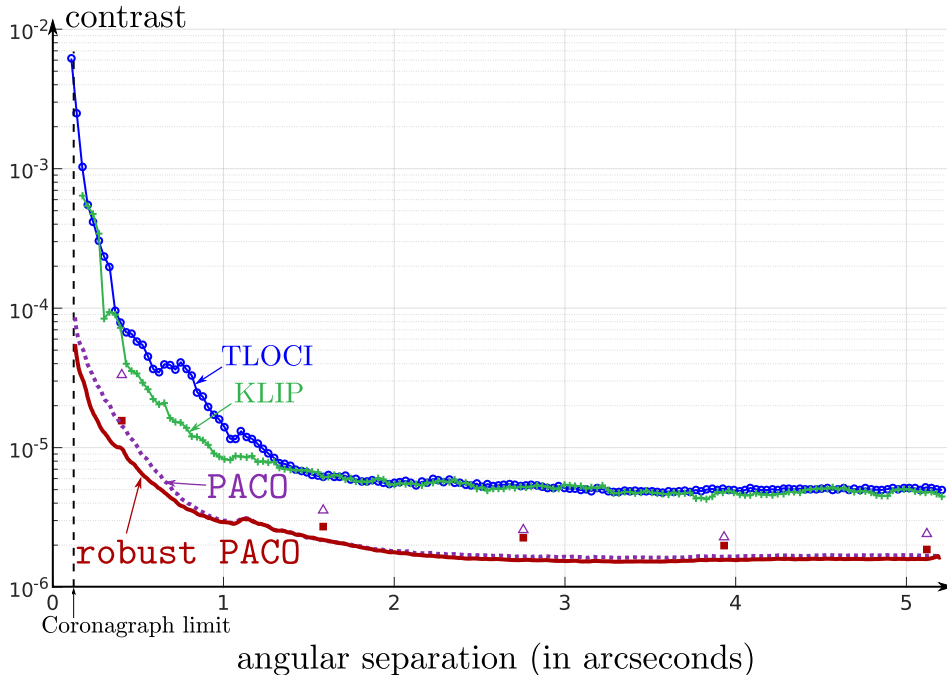


Figure 4.6 – Contrast curves at  $5\sigma$  for TLOCI, KLIP, PACO and robust PACO, around HIP 72192 (SPHERE-IRDIS,  $\lambda_1 = 2.110 \mu\text{m}$ ). The 5 triangles and 5 squares correspond to Monte-Carlo injections.

## 4.4 Characterization of detection, astrometric and photometric performances

### 4.4.1 Improved detection sensitivity

The maximum achievable contrast between the host star and an off-axis point source is an important information to characterize the overall performance of the instrument, including the data processing. We showed in Section 2.5.3.2 that contrast curves produced by reference algorithms like TLOCI and KLIP were over-optimistic due to a coarse statistical model of the residues. Contrast curves predicted with PACO are closer to the actual performance assessed by Monte-Carlo. However, based on the analysis of Figure 2.25, we pointed out that the predicted contrast only provides a lower bound that is not reached in practice. The reason for this discrepancy is that the statistics of the background are learned, in the detection step, on patches that contain both the background and the source(s).

In Figure 4.6, we give contrast curves computed on a SPHERE-IRDIS ADI dataset at  $\lambda_1 = 2.110 \mu\text{m}$  of HIP 72192 (same dataset than the one used in Chapter 2). Four contrast curves are reported, corresponding to TLOCI, KLIP, PACO and robust PACO. As stated in Section 2.5.3.1, contrast curves of TLOCI and KLIP should be analyzed with caution because they were computed based on a threshold at  $5\sigma$  that does not correspond to a probability of false alarm of  $2.87 \times 10^{-7}$  since the residuals are not Gaussian distributed. A modeling of the heavy tail of the distribution of the residuals would be necessary in order to compute a more adequate threshold (providing the residuals



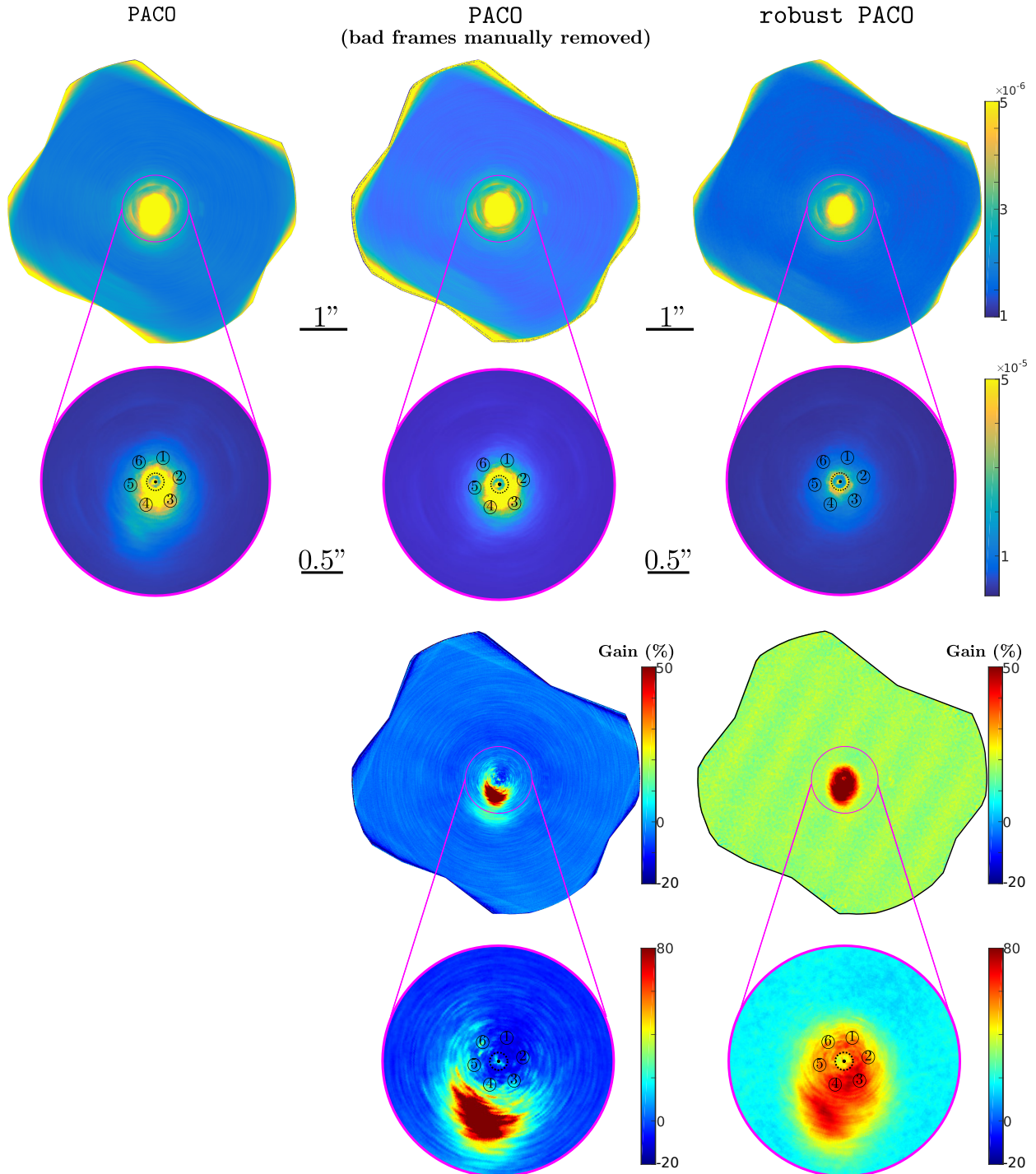


Figure 4.7 – Comparison of contrast maps for HIP 72192 (SPHERE-IRDIS) at  $\lambda_1 = 2.110 \mu\text{m}$ . The top row indicates the largest contrast between the host star and a point source that would lead, theoretically, to a probability of detection greater or equal to 0.5 at the detection threshold  $\tau = 5$ . Three methods are compared: the standard PACO algorithm applied on the whole ADI stack (left), PACO applied to the subset of the ADI stack obtained by removing the 8 frames with the largest fluctuations (center), and the **robust** PACO applied on the whole stack (right). The bottom row gives the gain in contrast with respect to PACO algorithm.

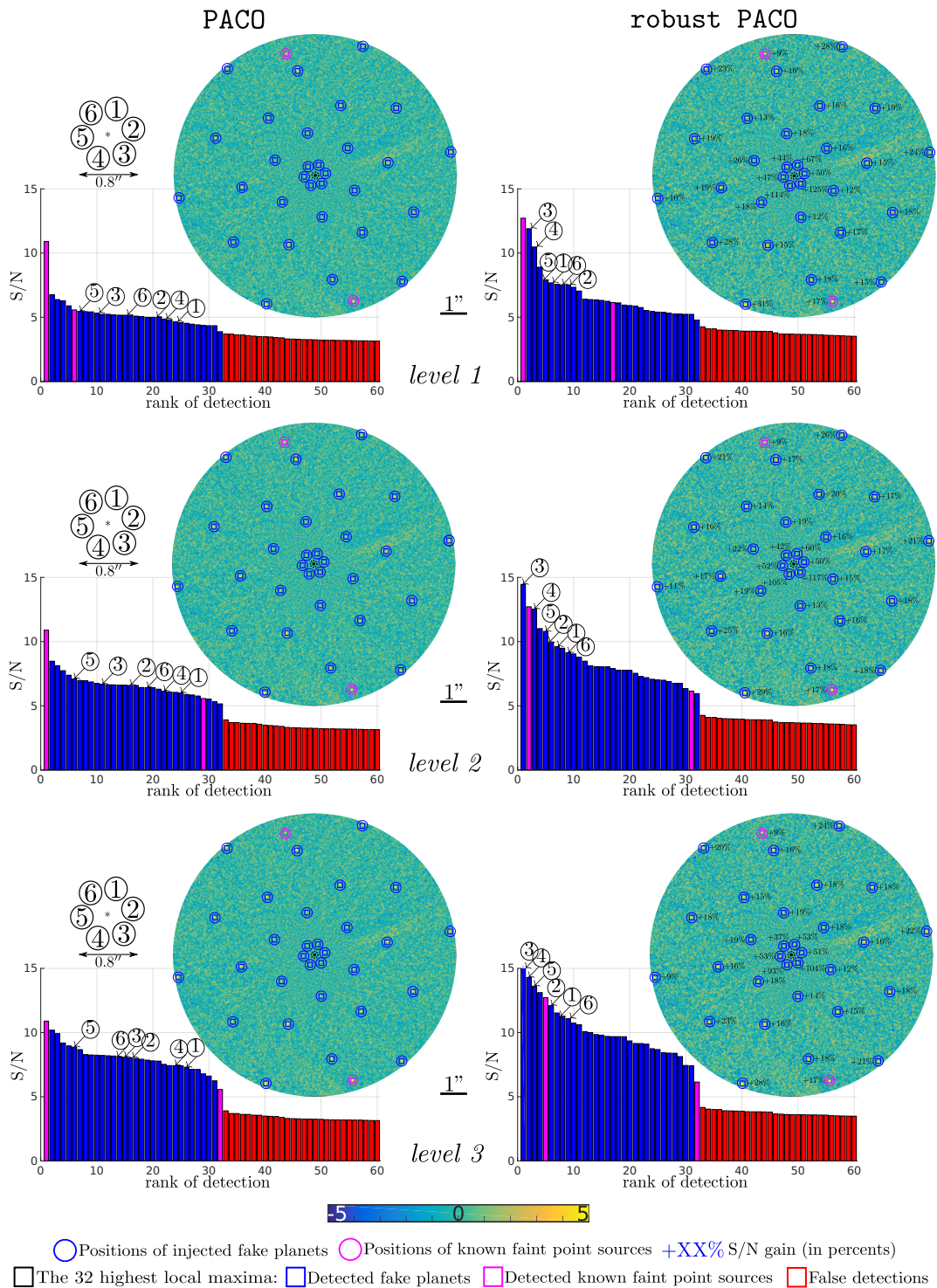


Figure 4.8 – Comparison of PACO (left) and the **robust PACO** on a SPHERE-IRDIS ADI dataset around HIP 72192 (at  $\lambda_1 = 2.110 \mu\text{m}$ ) with 30 fake point sources injected in addition to the 2 known faint point sources (same level of contrast as presented in Table 2.4). The detection maps are given together with the signal-to-noise ratio values of the 60 first detections. The 6 fake sources closest to the host star are denoted by digits ① to ⑥. The two real sources are indicated in pink. The increase in signal-to-noise ratio brought by the robust approach is given in percentage on the detection map.

have stationary distribution). That threshold would be significantly larger than the  $5\sigma$  value, which would shift the contrast curves up to worse contrasts. For **PACO** and **robust PACO**, we give both the theoretical contrast curve and the results of Monte-Carlo simulations computed for 5 different angular separations (triangles for **PACO**, squares for **robust PACO**). The theoretical contrast curves, corresponding to fluxes  $\alpha$  such that  $P(\hat{\alpha}/\hat{\sigma}_\alpha \geq 5) = 0.5$ , are obtained by computing  $5\hat{\sigma}_\alpha$ , i.e.,  $5/\sqrt{\sum_t a_t}$ , at each point of the field of view, with intensities expressed relatively to the intensity of the host star.

**PACO** and **robust PACO** achieve better contrasts than TLOCI and KLIP. The discrepancy between the theoretical contrast and the Monte-Carlo simulations is reduced with **robust PACO** compared to **PACO**. This is because the influence of the source is reduced when robustly estimating the statistics of the background. Moreover, the contrast is clearly improved at small separations.

Figure 4.7 gives the 2-D contrast maps for 3 detection methods, on the same ADI dataset as that studied in Figure 4.6. From left to right are displayed contrast maps of the standard **PACO** algorithm, **PACO** algorithm after manually removing the 8 frames that display the largest fluctuations of the series, and **robust PACO** (without manual removal of frames). The gains in contrast obtained with respect to standard **PACO** are given on the bottom row of the figure. Manually removing the bad frames has two effects: (i) an improvement of the contrast in the area impacted by the large fluctuations of the bad frames, and (ii) a slight degradation of the contrast in the rest of the field of view due to the reduction of the size of the ADI dataset. By locally estimating the scaling factors, **robust PACO** improves the contrast everywhere. Even in regions that are not affected by strong temporal heterogeneity, it is beneficial to account for fluctuations of the scaling factors. As expected, the gain is the largest in the area affected by the strongest fluctuations. There, the gain in contrast reaches 80%.

Standard **PACO** and **robust PACO** are also compared on this SPHERE-IRDIS dataset through injections of faint point sources at the same three levels of contrast than in Chapter 2 (see Table 2.4 for the corresponding levels of contrast). The 30 fake point sources were injected in addition to the 2 known faint point sources, at contrasts such that they could all be detected without a false alarm. Figure 4.8 gives the detection maps produced by **PACO** and **robust PACO**. The corresponding detection maps obtained by TLOCI and KLIP are given in Figures 2.17, 2.18 and 2.19. By including time-specific scaling factors, **PACO** improves the S/N of all sources. The largest increase occurs close to the host star where the S/N is improved by more than 100% for two point sources (sources ③ and ④). These observations can be related to the weighting maps shown in Figure 4.1; sources ③ and ④ are the most impacted by strong temporal fluctuations of the speckles (due to stellar leakages). Then, almost null weights  $1/\hat{\sigma}^2$  are assigned to the patches of this area at the corresponding defective poses, thus attenuating the influence of these outliers in the modeling of the background.

Figure 4.9 compares TLOCI, KLIP, standard **PACO** and **robust PACO** algorithms on an ADI stack of HD 95086 ( $T = 52$  temporal frames acquired under the 2015-05-05 – 095.C-0298(A) ESO program with a total apparent rotation of the field of view  $\Delta_{\text{par}} = 18.2^\circ$ ). The HD 95086 hosts a 5-Jovian mass exoplanet (HD 95086 b) discovered (Rameau et al., 2013a) and confirmed (Rameau et al., 2013b) by direct imaging with the SPHERE instrument. In addition, 6 known background point sources are in the field of view. Figure 4.9 shows that both the **PACO** and the **robust PACO** methods achieve



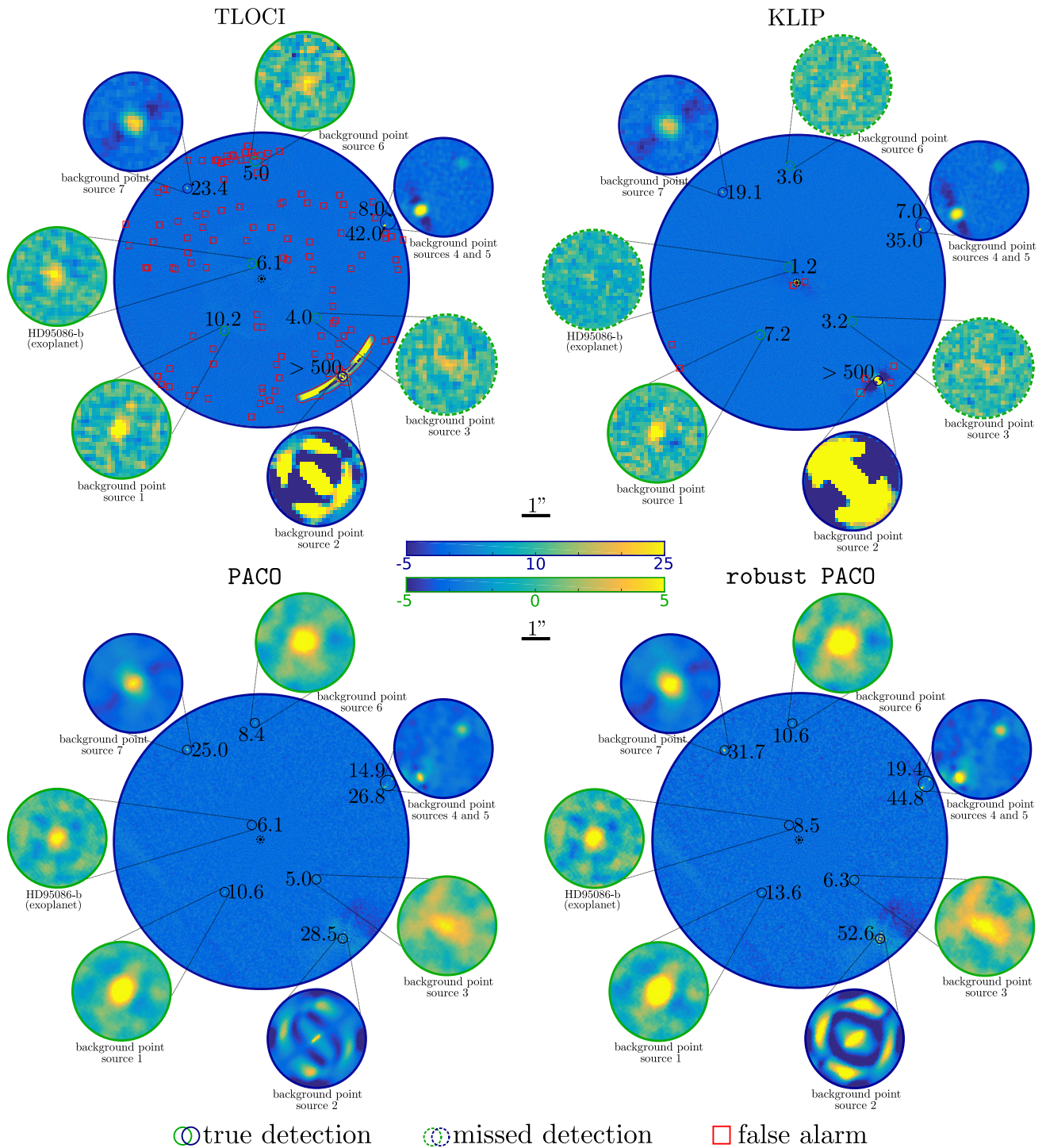


Figure 4.9 – S/N maps from TLOCI, KLIP, PACO and robust PACO on an ADI dataset of HD 95086. 7 circular insets show a zoom of the S/N maps around the known point sources. The S/N maps of these insets are evaluated on a subpixel grid (4 nodes per pixel) for PACO and robust PACO. True detections are marked by straight circles, the missed detections (S/N < 5) are marked by dashed circles and false alarms are identified by red squares.

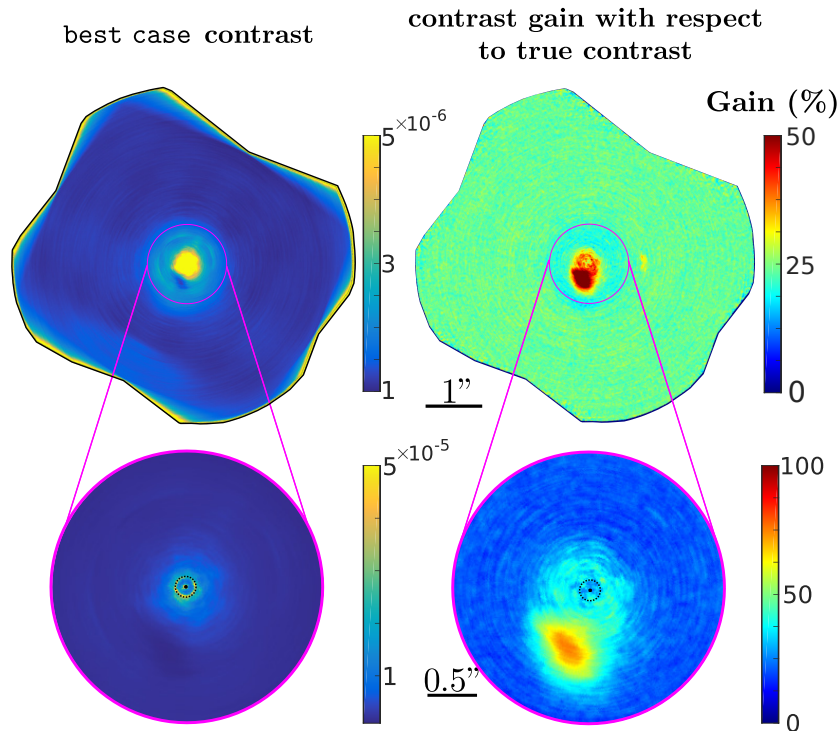


Figure 4.10 – Left: contrast that would be obtained for HIP 72192 under ideal observation conditions (i.e., as good as that of the best image, during the entire ADI acquisition). Right: gain in contrast compared to the actual contrast, computed by accounting for temporal fluctuations of the scale of the residuals.

better detection performance than reference algorithms. In particular, the S/N values of the sources is larger for all sources (except for the background star 2 which poses no detection problem in itself: it is so bright that it is visible directly in a single image of the ADI dataset). With PACO and **robust PACO**, it is possible to detect without any false alarm the 7 known sources by thresholding the S/N maps at  $\tau = 5$ . In comparison, S/N maps from TLOCI and KLIP present several artifacts due to the presence of outliers in the datasets, preventing an automatic analysis of these maps. **robust PACO** increases the detection confidence of all sources present in the field of view, especially for the ones with the smallest angular separations such as the exoplanet HD 95086 b (S/N = 6.1 with PACO vs. 8.5 with **robust PACO**).

#### 4.4.2 Assessing the quality of the observations

The presence of frames of worse quality in an ADI stack degrades the detection performance with respect to an ADI stack of constant quality. It may be useful to the astronomers who planned the observations to compare the contrast achieved given the actual conditions of observation to the contrast that would have been reached should the conditions have been as good as that of the best frames. Such a difference in contrast can be assessed by computing a **best case** contrast where  $\hat{\sigma}_{[\phi_t],t}^2$  in the computation of  $a_t$  in Equation (4.9) is replaced by  $\min_{t'} \hat{\sigma}_{[\phi_t],t'}^2$  (i.e., the smallest scaling factor at that location  $[\phi_t]$ ). Figure 4.10 shows the **best case** contrast for HIP 72192. Compared

to the actual contrast predicted based on the estimated time-specific scaling factors, the **best case** contrast is about 25% better in most of the field of view, and close to 70%-80% in the region most impacted by large temporal fluctuations. If the aim of the observations was to characterize a faint point source that falls in that area, it might be worth considering re-observing in the hope of experiencing better conditions and getting closer to the **best case** contrast.

### 4.4.3 Improved astrometric and photometric accuracies

As in Section 2.3.6.3, the astrometric and photometric accuracies can be characterized over the whole field of view by computing the Cramér-Rao lower bounds (CRLBs). By keeping the notation,  $\boldsymbol{\Omega} = \{\alpha, x_0, y_0\}$  denoting the vector of parameters from which the CRLBs are computed, for a given angular position  $n$ , the Fisher information matrix  $\mathbf{I}_n^F$  accounting for the temporal fluctuations can be expressed as (Kendall et al., 1948):

$$\left[\mathbf{I}_n^F(\boldsymbol{\Omega})\right]_{i,j} = \sum_{t=1}^T \frac{1}{\sigma_{n,t}^2} \frac{\partial \alpha \mathbf{h}_n(\boldsymbol{\Omega})^\top}{\partial \Omega_i} \cdot \mathbf{C}_n^{-1} \cdot \frac{\partial \alpha \mathbf{h}_n(\boldsymbol{\Omega})}{\partial \Omega_j}. \quad (4.18)$$

Figures 4.11 and 4.12 give the astrometric Cramér-Rao lower bounds on the whole field of view obtained with PACO and **robust PACO**. They show that the patch weighting included in **robust PACO** improves the estimation accuracies on the whole field of view, especially in the presence of high stellar leakages (more than 50% improvement near the coronagraph). In practice, the PACO CRLBs are too pessimistic since the covariances are over-estimated due to the presence of outliers in the data; thus **robust PACO** improves the fidelity of the CRLBs.

#### **robust PACO's capabilities**

- **robust PACO** achieves better contrast levels than TLOCI, KLIP and the PACO algorithm described in Chapter 2.
  - The contrast and the detection performance are particularly improved at small separations, where the stellar residuals dominate.
  - The **robust PACO** algorithm also outperforms PACO in every point of the field of view (even if no significant fluctuations can be identified in the data).
- Compared to PACO, with **robust PACO** the predicted contrast more closely matches the actual contrast computed by Monte-Carlo simulation.
- To better analyze the observations conditions, **robust PACO** can also estimate the contrast that would have been reached if the AO correction had been as good as the best correction in the ADI time series.



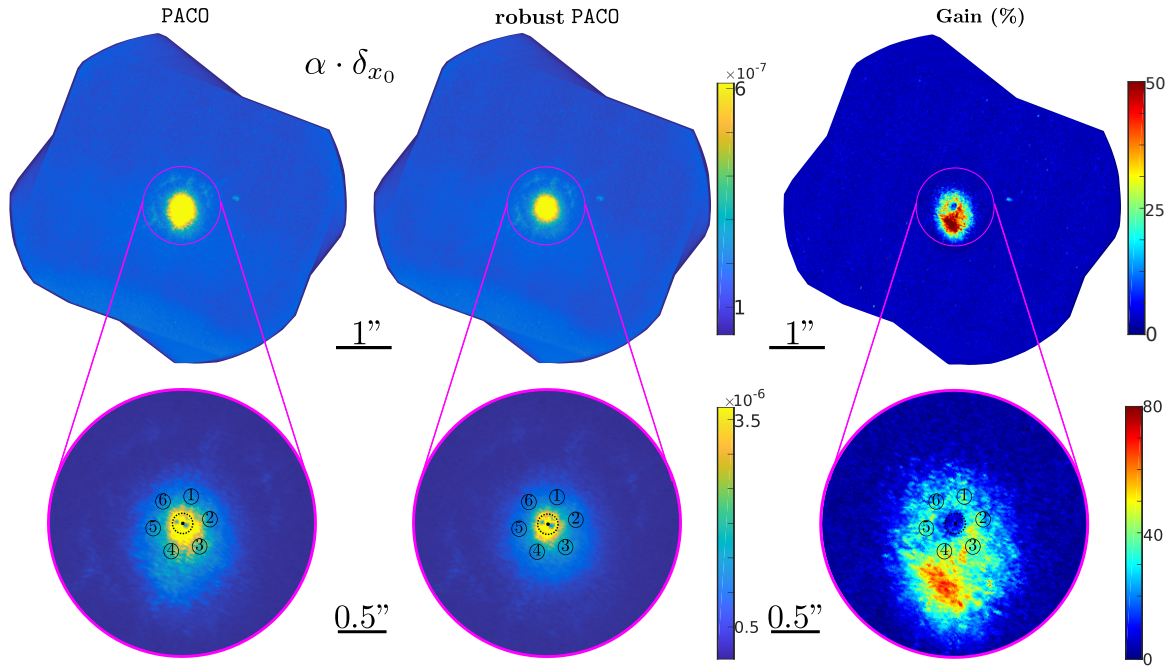


Figure 4.11 – Theoretical accuracy (minimal standard deviation given by the Cramér-Rao lower bounds)  $\delta_{x_0}$  on the estimated astrometric location  $x_0$  from PACO and **robust PACO** around the HIP 72192 star.  $\delta_{x_0}$  maps are multiplied by the flux  $\alpha$  of the exoplanet (expressed in arcsec  $\times$  flux). The gain (in percents) brought by **robust PACO** compared to PACO is given on the right. The 6 fake sources closest to the host star are denoted by digits  $\textcircled{1}$  to  $\textcircled{6}$ .

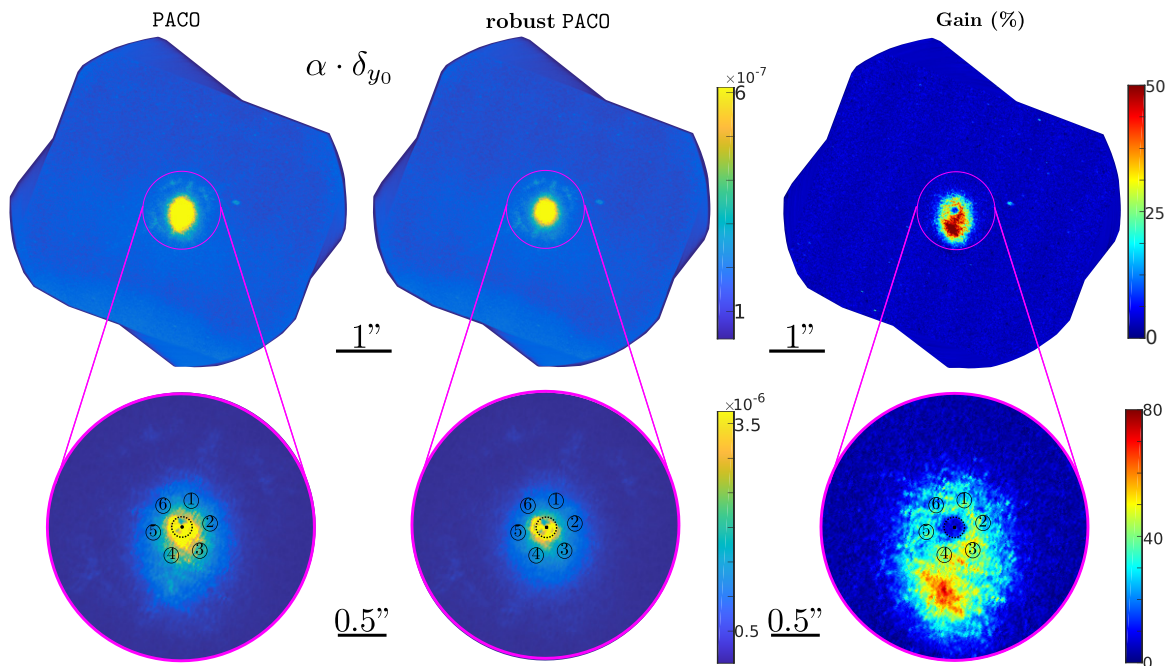


Figure 4.12 – Same illustration than Figure 4.11 for the parameter  $y_0$  instead of  $x_0$ .

## 4.5 Conclusion on robust PACO’s capabilities

Most data processing techniques for point source detection and characterization in ADI datasets are not robust: the presence of images with poor AO correction can considerably degrade their performance. It is, therefore, necessary to detect and eliminate these frames in a preprocessing step.

The approach described in this chapter (**robust PACO**) completes that of Chapter 2 (**PACO**) by modeling the temporal nonstationarities of the amplitude of the background fluctuations jointly to the spatial correlations with a Gaussian scale mixture model. When these fluctuations are accounted for, the estimations are robust to large fluctuations. Rather than discarding full frames, we use a local modeling in order to spatially adapt the processing and give a very small statistical weight only to the areas subject to large fluctuations. That way, **robust PACO** makes the most of the available data.

The **robust PACO** algorithm leads to improved detection performances (in particular at close separations where the stellar residuals dominate). Interestingly, it is also possible to estimate the achievable contrast not only by taking into account the actual image quality of the ADI dataset, but also the contrast that would have been reached if the AO correction had been as good as the best correction in the ADI time series. This information can be highly valuable in order to plan subsequent re-observations.

Coronagraphic observations obtained with integral field spectrographs could also benefit from a modeling of the spatial and temporal fluctuations. We investigate this point in Chapter 6 to include a modeling of the spectral correlations for these instruments.

In the following chapter, we also consider weighting based approaches to improve the robustness of the detection and characterization of samples by holographic microscopy.





# Robustness to unwanted objects in holographic microscopy

---

**Abstract**

*Lensless microscopy is used in various fields, including microfluidics and biomedical imaging to derive quantitative information characterizing the observed objects. In particular, to estimate the size and 3-D location of microscopic objects from holograms, maximum likelihood methods have been shown to outperform traditional approaches based on 3-D image reconstruction followed by 3-D image analysis. However, the presence in the hologram of fringes due to objects other than the object of interest may bias maximum likelihood estimates. Using experimental videos of holograms, we show that replacing the maximum likelihood with a robust estimation procedure reduces this bias. We propose a criterion based on the intersection of confidence intervals to set the level that distinguishes between inliers and outliers automatically. This methodology is general and can address different estimation problems in presence of nonstationary outliers. We show that this criterion achieves a bias/variance tradeoff. We also show that joint analysis of a sequence of holograms using the robust procedure further improves the estimation accuracy.*

---

## 5.1 The need for robust estimators in holographic microscopy

As discussed in Section 1.3.2, thanks to the massive development of low-cost imaging sensors and the simultaneous increase in computational capabilities, holographic microscopy is emerging as a method of choice for time-resolved analysis of microscopic objects. It is already used in several fields (see [Mudanyali et al. \(2010\)](#); [Greenbaum et al. \(2012\)](#) for some trends) where the accurate estimation of 3-D location and size over time is crucial, such as in the study of fluid flows ([Sentis et al., 2018](#); [Middleton et al., 2019](#); [Go et al., 2019](#)) or biomedical imaging ([Rostykus et al., 2018](#); [Allier et al., 2019](#); [Kemper et al., 2019](#)).

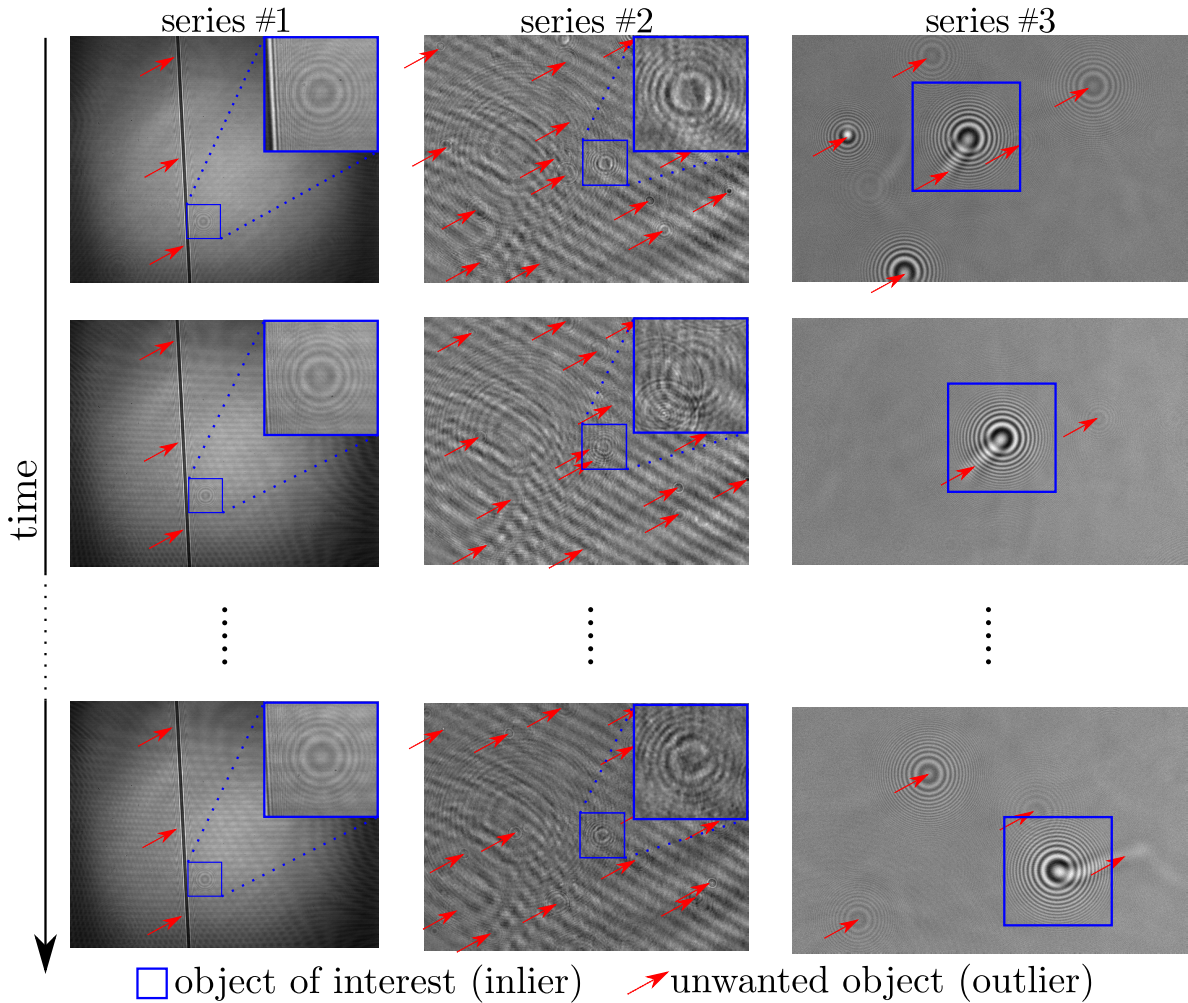


Figure 5.1 – Illustration of holograms corrupted by spurious fringes in holographic microscopy videos. Series #1: a circular chromium deposit (inlier) is shifted over time near a human hair (outlier). Series #2: a polystyrene bead (inlier) in suspension follows a Brownian motion over time in the presence of several moving dust (outliers) and background fringes due to spurious reflections on optical surfaces of the setup. Series #3: an evaporating diethyl ether droplet (inlier) is injected into a turbulent flow in the presence of moving dust (outliers). The vapor plume resulting from the evaporation of the droplet of interest and other evaporating droplets located at a different depths also act as outliers. Series #1 and #2 were recorded by Nicolas Verrier and Corinne Fournier at the Hubert Curien Laboratory, Saint-Etienne, France. Series #3 was recorded by Nathalie Grosjean and Loïc Mées at the Fluid Mechanics and Acoustics Laboratory, Ecully, France.

Analysis of digital holograms is traditionally performed by first reconstructing the 3-D volume by light back-propagation, then analyzing this 3-D volume to segment, locate, and size objects (Kreis, 2006). However, this approach suffers from artifacts due to the imperfect reconstruction step, in particular to spatial distortions close to the image borders and spurious diffraction patterns known as *twin images* in holography (Kreis,



2006). As presented in Section 1.3.2.2, location and size estimates can be significantly improved by using a maximum likelihood estimator, i.e., by fitting a model of the diffraction pattern generated by the object of interest directly on the hologram rather than by reconstructing the image volume (Gire et al., 2008). This method is very successful for the study of isolated objects in optical metrology (Verrier et al., 2015; Wang et al., 2016; Philips et al., 2017).

However, an estimation bias appears when the hologram is corrupted by interference fringes due to other objects or components of the setup. These objects may have complex or unknown shapes, and their influence on the hologram may be difficult to explicitly model and account for. Figure 5.1 illustrates some hologram corruptions typically encountered in holographic microscopy. Among these, we can focus on the time series #3 given in Figure 5.1: a diethyl ether droplet is injected into a nearly isotropic turbulence generated by a set of loudspeakers. The recorded holographic video shows the diffraction pattern produced by the droplet of interest (*inliers*) mixed with other unwanted fringes (*outliers*) such as the vapor plume resulting from the evaporation of the droplet over time, or the diffraction patterns of dust particles. The objects acting as outliers that are very similar to the objects of interest can be identified by putting bound constraints, for example on the estimated size or depth, during the detection and characterization steps. However, their signal still bias the characterization of the objects of interest.

### Robustness issues in holographic microscopy

- Holographic microscopy is a 3-D imaging technique widely used for the characterization of microscopic objects.
- Hologram analysis by a maximum likelihood approach leads to accurate estimations of the object's physical properties that are useful for metrological applications.
- However, a bias of estimation can arise when unwanted fringes alter the hologram.

In this chapter, we aim to address this robustness issue. Like elsewhere in this thesis, we pay a particular attention to the automatic setting of tuning parameters. We suggest replacing the maximum likelihood estimator with a robust estimator so that any notable discrepancy between the model of the pattern of interest and the data due to unwanted fringes has little influence on the final estimate. Section 5.2 describes the proposed robust estimation procedure to characterize microscopic objects. Section 5.3 introduces a new method to set automatically the level to distinguish between inliers and outliers. Section 5.4 illustrates the performance of the proposed method on holographic videos. Finally, Section 5.5 concludes this chapter. This chapter is based on the conference paper Flasseur et al. (2017a).

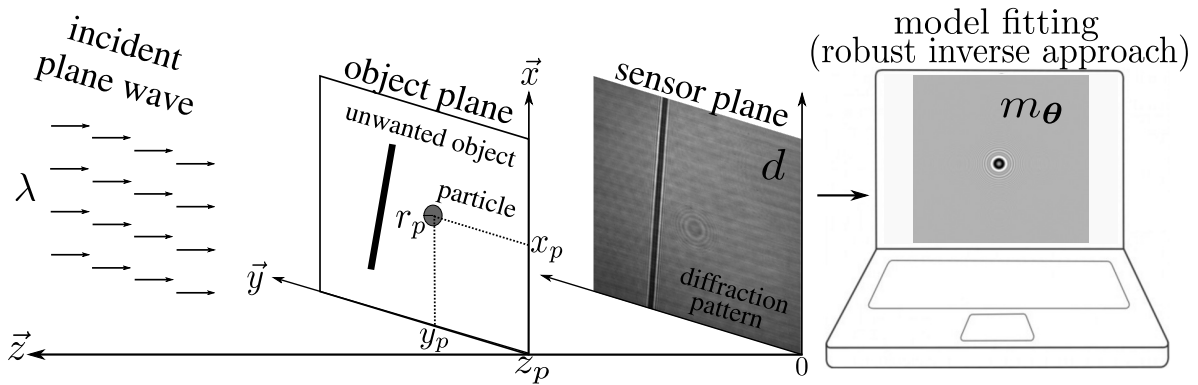


Figure 5.2 – Holographic microscopy setup and object fitting in presence of outliers.

## 5.2 Improved robustness by weighted least squares

### 5.2.1 The least squares solution

We recall the basic configuration used in digital holography to study a spherical object  $p$ . A coherent illumination is used: the incident wave is monochromatic (with wavelength  $\lambda$ ) and plane. After free-space propagation over distance  $z_p$ , a hologram  $d$  is recorded by a monochromatic image sensor, see Figure 5.2. Based on diffraction theory, it is possible to model the diffraction pattern  $m_\theta$  created on the hologram plane by the object of interest. The spherical particle is fully characterized by the vector of parameters  $\theta$  (3-D location, size, and eventually optical index).

Maximum likelihood (ML) estimation of the parameters  $\theta$ , under the hypothesis of additive white Gaussian noise, amounts to solving a nonlinear least squares problem (Soulez et al., 2007a,b):

$$\hat{\theta}^{(\text{ML})} = \arg \min_{\theta} \sum_{a=1}^A \sum_{b=1}^B w(a,b) \cdot [m_\theta(a,b) - d(a,b)]^2, \quad (5.1)$$

where  $d(a,b)$  is the recorded data at pixel location  $(a,b)$ ,  $w(a,b) \propto 1/\epsilon(a,b)^2$  is a weight that is set to zero for defective pixels and that can account for a nonstationary noise variance<sup>1</sup>  $\epsilon(a,b)^2$ , and  $A$  and  $B$  are the height and width of the sensor, in pixels. In this formulation, large deviations between the model and the data (i.e. the outliers) are highly penalized, which can have a large impact on the estimated vector of parameters  $\theta$ .

### 5.2.2 The reweighted least squares solution

To reduce the impact of outliers on the estimation, Huber introduced the so-called *M-estimators* (Huber, 2011) by replacing the least squares by another objective function  $\rho$ . By adequately choosing function  $\rho$ , the penalization of the large deviations between

1. Chapter 3 presents a method accounting for the nonstationarity of the noise arising in holographic microscopy series of images (see Figure 5.1) within a microscopic object detection and characterization framework.

Table 5.1 – Examples of robust objective, score and weight functions classify according to their properties (hard-, soft- or monotone-descenders. The constants  $A, B, T, C, W, L, F$ , and  $H$  appearing in each of them are tabulated values to guaranty a controlled efficiency level of the estimator (typically 95% with the values reported in Table 5.2 under an additive white Gaussian noise).

	Objective $\rho(\mathbf{r})$	Score $\psi(\mathbf{r}) = \frac{\partial \rho(\mathbf{r})}{\partial \mathbf{r}}$	Weight $w(\mathbf{r}) = \frac{\psi(\mathbf{r})}{\mathbf{r}}$	Cond.
<i>Hard-descenders</i>				
<b>Andrews</b>	$\begin{cases} A^2 \left[1 - \cos\left(\frac{\mathbf{r}}{A}\right)\right] \\ 2A^2 \end{cases}$	$\begin{cases} A \sin\left(\frac{\mathbf{r}}{A}\right) \\ 0 \end{cases}$	$\begin{cases} \frac{A}{\mathbf{r}} \sin\left(\frac{\mathbf{r}}{A}\right) \\ 0 \end{cases}$	$\begin{cases}  \mathbf{r}  \leq A\pi \\  \mathbf{r}  > A\pi \end{cases}$
<b>Beaton</b>	$\begin{cases} \frac{B^2}{2} \left[1 - \left(\frac{\mathbf{r}}{B}\right)^2\right]^3 \\ \frac{B^2}{2} \end{cases}$	$\begin{cases} \mathbf{r} \left[1 - \left(\frac{\mathbf{r}}{B}\right)^2\right]^2 \\ 0 \end{cases}$	$\begin{cases} \left[1 - \left(\frac{\mathbf{r}}{B}\right)^2\right]^2 \\ 0 \end{cases}$	$\begin{cases}  \mathbf{r}  \leq B \\  \mathbf{r}  > B \end{cases}$
<b>Talwar</b>	$\begin{cases} \frac{\mathbf{r}^2}{2} \\ \frac{T^2}{2} \end{cases}$	$\begin{cases} \mathbf{r} \\ 0 \end{cases}$	$\begin{cases} 1 \\ 0 \end{cases}$	$\begin{cases}  \mathbf{r}  \leq T \\  \mathbf{r}  > T \end{cases}$
<i>Soft-descenders</i>				
<b>Cauchy</b>	$\frac{C^2}{2} \log\left(1 + \left(\frac{\mathbf{r}}{C}\right)^2\right)$	$\frac{\mathbf{r}}{1 + \left(\frac{\mathbf{r}}{C}\right)^2}$	$\frac{1}{1 + \left(\frac{\mathbf{r}}{C}\right)^2}$	–
<b>Welsch</b>	$\frac{W^2}{2} \left[1 - \exp\left(-\left(\frac{\mathbf{r}}{W}\right)^2\right)\right]$	$\mathbf{r} \exp\left(-\left(\frac{\mathbf{r}}{W}\right)^2\right)$	$\exp\left(-\left(\frac{\mathbf{r}}{W}\right)^2\right)$	–
<b>Fair</b>	$F^2 \left(\frac{ \mathbf{r} }{F} - \log\left(1 + \frac{ \mathbf{r} }{F}\right)\right)$	$\frac{\mathbf{r}}{1 + \frac{ \mathbf{r} }{F}}$	$\frac{1}{1 + \frac{ \mathbf{r} }{F}}$	–
<b>Logistic</b>	$L^2 \log\left(\cosh\left(\frac{\mathbf{r}}{L}\right)\right)$	$L \tanh\left(\frac{\mathbf{r}}{L}\right)$	$\frac{L}{\mathbf{r}} \tanh\left(\frac{\mathbf{r}}{L}\right)$	–
<i>Monotone-descenders</i>				
<b>Huber</b>	$\begin{cases} \frac{\mathbf{r}^2}{2} \\ H  \mathbf{r}  - \frac{H^2}{2} \end{cases}$	$\begin{cases} \mathbf{r} \\ \text{sign}(\mathbf{r})H \end{cases}$	$\begin{cases} 1 \\ \frac{H}{\mathbf{r}} \end{cases}$	$\begin{cases}  \mathbf{r}  \leq H \\  \mathbf{r}  > H \end{cases}$

Table 5.2 – Constant values appearing in the definitions of the robust objective, score, and weight functions to guaranty 95% efficiency of the estimators under an additive white Gaussian noise.

$A$	$B$	$T$	$C$	$W$	$H$	$F$	$L$
1.339	4.685	2.795	2.385	2.985	1.345	1.205	1.400

the model and the data (i.e., their influence) can be reduced. Minimization problem (5.1) is then replaced by:

$$\hat{\boldsymbol{\theta}}^{(M)} = \arg \min_{\boldsymbol{\theta}} \underbrace{\sum_{a=1}^A \sum_{b=1}^B w(a, b) \cdot \rho\left(\frac{m_{\boldsymbol{\theta}}(a, b) - d(a, b)}{s}\right)}_{\mathcal{L}(\boldsymbol{\theta})}, \quad (5.2)$$

where  $\rho$  is a non-negative, continuous and symmetric function with a minimum equal to 0 at 0, and  $s$  is a parameter that scales the residuals by setting the level that distinguishes between inliers and outliers (more details are given in Section 5.3).

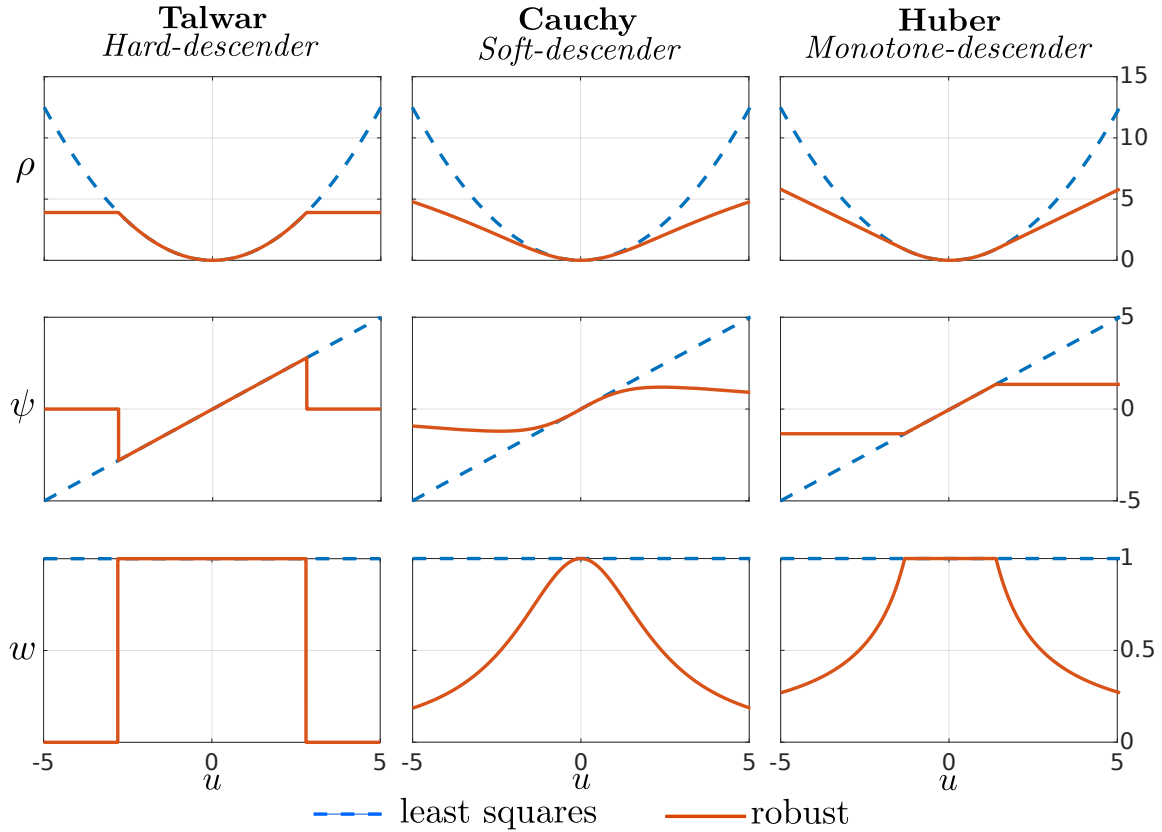


Figure 5.3 – Three examples of robust objective ( $\rho$ ), score ( $\psi$ ), and weight ( $w$ ) functions: Talwar’s (hard-descender), Cauchy’s (soft-descender), and Hueber’s (hard-descender) functions.

Depending on the choice of the function  $\rho$ , the minimization problem (5.2) can be difficult to solve. A simple algorithmic strategy leading to a local minimizer consists in solving a sequence of least squares problems of the form (5.1): the Iteratively Reweighted Least Squares (IRLS, Holland and Welsch (1977); Hill and Holland (1977), see also Sigl (2016) for a recent review). In this scheme, the estimate  $\hat{\boldsymbol{\theta}}_{k+1}$  at iteration  $k + 1$  is obtained by reweighting the squares with weights  $w_k(a, b)$  derived from the residuals of iteration  $k$ :

$$\hat{\boldsymbol{\theta}}_{k+1} := \arg \min_{\boldsymbol{\theta}} \sum_{a=1}^A \sum_{b=1}^B w_k(a, b) \cdot [m_{\boldsymbol{\theta}}(a, b) - d(a, b)]^2, \quad (5.3)$$

where the weights  $w_k(a, b)$  are computed from the residuals at iteration  $k$ ,  $r_k(a, b) = m_{\boldsymbol{\theta}_k}(a, b) - d(a, b)$ , according to an update rule that depends on the objective function  $\rho$ :

$$w_k(a, b) = w(a, b) \cdot \frac{s}{r_k(a, b)} \cdot \underbrace{\frac{\partial \rho(u)}{\partial u}}_{\psi(u)} \bigg|_{u=r_k(a, b)/s}. \quad (5.4)$$

In holographic microscopy, the image formation model  $m_{\boldsymbol{\theta}}$  is often nonlinear with respect to the parameters  $\boldsymbol{\theta}$ . As a result, the minimization problem (5.1) and each IRLS

iteration in (5.3) is solved using a few iterations of Levenberg-Marquardt algorithm (Levenberg, 1944; Marquardt, 1963).

A variety of objective functions  $\rho$ , score function  $\psi$  and resulting IRLS weights  $w$  have been proposed and widely studied in the literature (see Fox and Weisberg (2018) for a review) to perform robust estimations. Table 5.1 gives examples of the most used (Beaton and Tukey, 1974; Bickel, 1975; Dennis Jr and Welsch, 1978; Dutter and Huber, 1981; Wolke and Schwetlick, 1988; Mbamalu and El-Hawary, 1993; Pires et al., 1999).

Interestingly, robust estimation can be compared with joint estimation of the object parameters  $\boldsymbol{\theta}$  and outliers contribution  $\mathbf{e}$  under sparsity constraint. The minimization problem:

$$\{\hat{\boldsymbol{\theta}}, \hat{\mathbf{e}}\} = \arg \min_{\boldsymbol{\theta}, \mathbf{e}} \underbrace{\sum_{a=1}^A \sum_{b=1}^B [m_{\boldsymbol{\theta}}(a, b) - d(a, b) - e(a, b)]^2 + \mu |e(a, b)|}_{\mathcal{C}_{\text{sparse}}(\boldsymbol{\theta}, \mathbf{e})}, \quad (5.5)$$

where  $\mu$  is a regularization parameter, can be solved by alternating between the estimation of  $\boldsymbol{\theta}$  and  $\mathbf{e}$ . At fixed estimate  $\hat{\mathbf{e}} = \arg \min_{\mathbf{e}} \mathcal{C}_{\text{sparse}}(\boldsymbol{\theta}, \mathbf{e})$ , the minimization problem (5.5) corresponds to the robust minimization problem (5.2) where the descender  $\rho$  is the Huber function (Fuchs, 1999; Kekatos and Giannakis, 2011).

The robust functions can be classified in three categories according to their properties:

- *hard-descenders* are functions  $\rho$  that are constant above a given threshold, thereby leading to zero weights for data points that display a misfit larger than the chosen threshold.
- *soft-descenders* are functions  $\rho$  whose limit at infinity is finite, thus asymptotically producing zero weights for large residual values.
- *monotone-descenders* are specific cases of *soft-descenders* functions for which the score function (derivative of the objective function  $\rho$ ) is constant above a given threshold, thereby leading to a constant increase of the penalization of outliers by the  $\rho$  function.

Figure 5.3 gives an example of objective ( $\rho$ ), score ( $\psi$ ) and weight ( $w$ ) functions for each of the categories mentioned above.

Robust estimation has been widely used in the literature and is still studied to address issues such as the detection of outliers data in biomedical for cardiac and brain monitoring (Schäck et al., 2017) as well as in astronomy for direct imaging (Berdeu et al., 2020). To the best of our knowledge, the use of robust estimation for objects characterization in holographic microscopy videos is not referenced in the literature. We thus suggest that it could also benefit for holographic microscopy applications as illustrated in Figure 5.4 on a toy example. In this numerical experiment, we consider a static spherical opaque bead of radius  $r_p = 10 \mu\text{m}$  located at  $z_p = 0.02 \text{ m}$  from the sensor plane and centered on the object plane (i.e.  $x_p = 0 \text{ m}$  and  $y_p = 0 \text{ m}$ , see Figure 5.2 for the notation). We consider another spherical opaque bead with the same radius but located  $0.01 \text{ m}$  closer than the previous bead from the sensor plane. This second bead is moving along the time series and crosses the length of the field of view. The resulting holograms

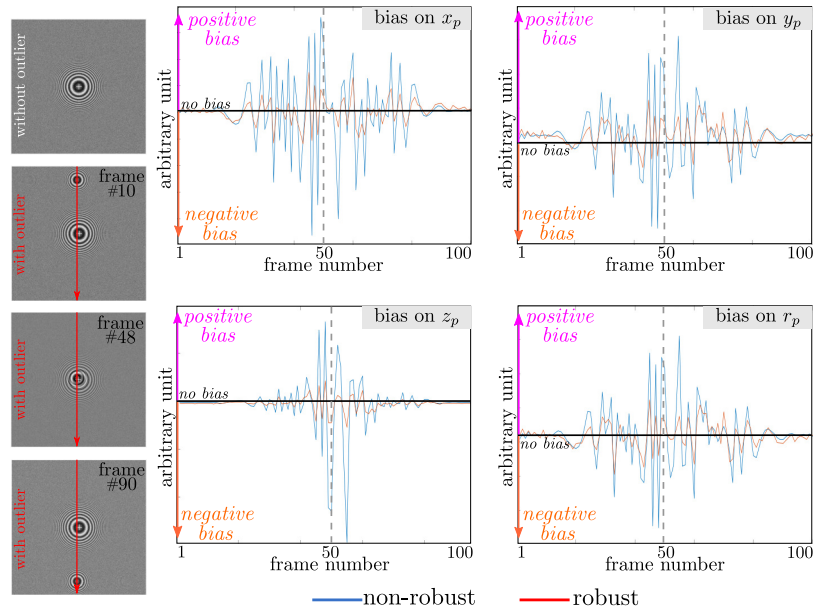


Figure 5.4 – Illustration of the benefit of a robust approach for the characterization of spherical objects with holograms altered by outliers. Left: the trajectory of a moving opaque sphere crosses another opaque sphere at the center of the field of view. Right: estimation bias along the sequence on the 3-D location  $\{x_p, y_p, z_p\}$  and radius  $r_p$  of the static sphere.

are simulated with the Thompson model (see Sections 1.3.2.2.1 and 5.4) considering a monochromatic source at  $\lambda = 532 \mu\text{m}$  and a pixel pitch of  $\Delta_{\text{pix}} = 2.2 \mu\text{m}$ . A white and Gaussian noise ( $S/N = 10$ ) is also added. The second bead acts as an outlier since its diffraction pattern mixes with the diffraction pattern of the bead of interest (see Figure 5.4, left). The estimation bias is reported (Figure 5.4, right) for the four estimated parameters of the static bead (its 3-D location  $\{x_p, y_p, z_p\}$  and its radius  $r_p$ ) for the standard least squares (5.1) and the robust approach (5.2) using a Cauchy descender. For the robust approach, the value of  $s$  appearing in Equation (5.2) is estimated with the conventional MAD estimator, see Section 5.3.2 and Equation (5.6). It shows that a robust least squares estimation reduces the estimation bias by a factor about 2, and more when the outlier bead is close to the bead of interest.

### Bias reduction

The estimation bias due to the interference fringes created by a spurious object close to the object of interest can be reduced using a robust estimation scheme. This implies:

- replacing least squares by another objective function limiting the penalization of the largest deviations between the model and the data.
- solving the resulting (possibly non-convex) minimization problem with an Iteratively Reweighted Least Squares (IRLS) sequence leading to a local minimizer.



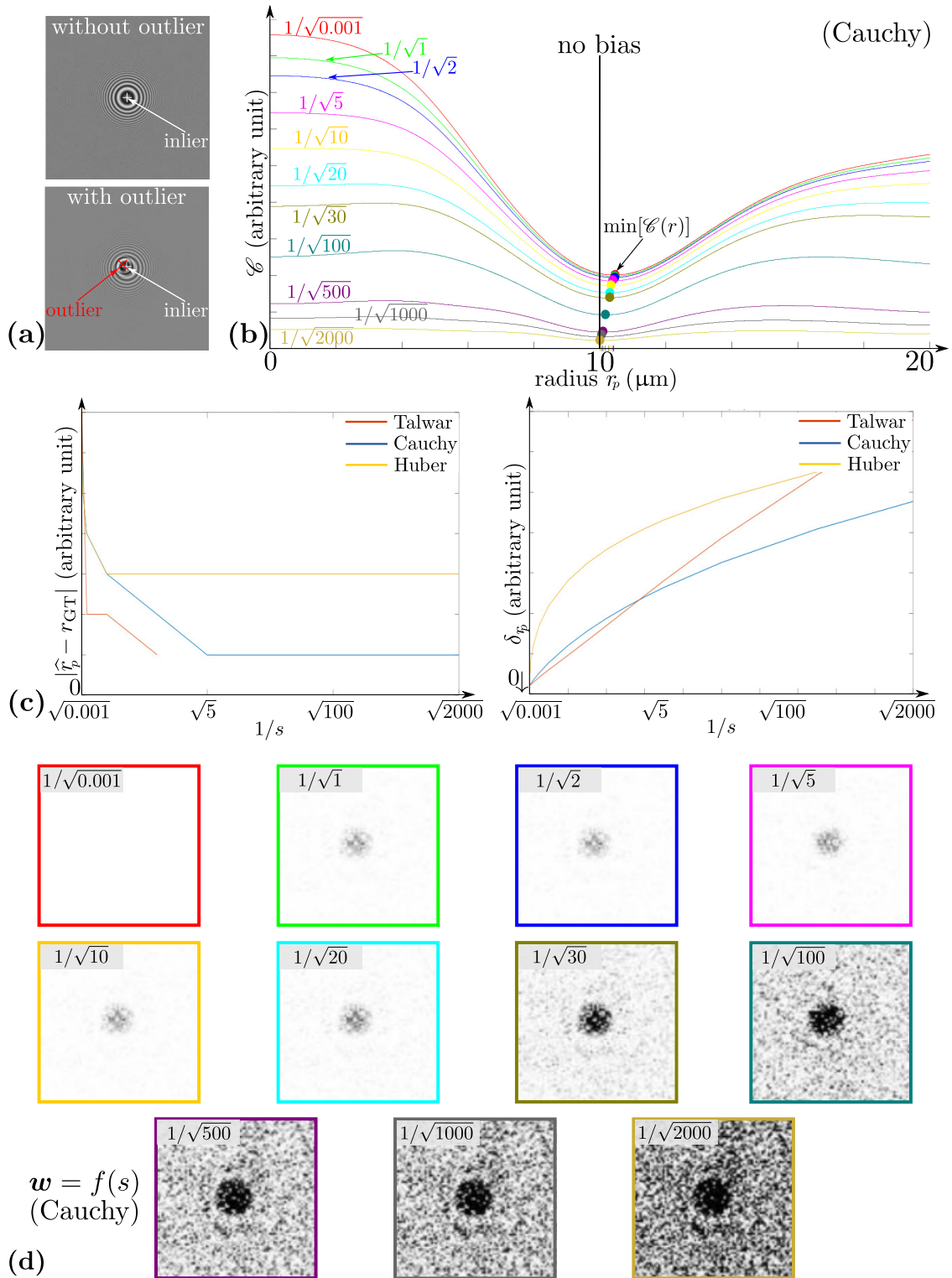


Figure 5.5 – Illustration of the bias/variance tradeoff arising with robust estimation. (a) the considered hologram is formed by a spherical bead (inlier) near another deeper particle (outlier); (b) cost functions  $\mathcal{L} = f(r_p)$  for different values of the hyper-parameter  $s$ . (c) evolution of the bias and the predicted standard deviation (CRLB) as a function of the hyper-parameter  $s$ ; (d): robust weight maps for different values of the tuning parameter  $s$ .

## 5.3 Distinguishing inliers and outliers

### 5.3.1 A bias/variance tradeoff

The tuning parameter  $s$  appearing in Equations (5.2) to (5.4) plays a central role in robust estimation and should be estimated with care (Rousseeuw and Leroy, 2005).

On the one hand, if  $s$  is too low, most residuals  $r_k(a, b)$  will be (much) larger than  $s$  and the weight of the corresponding data points will be small in the subsequent iterations, thereby discarding most of the signal of interest. In this case, this will result in an increase of the variance of estimation. On the other hand, if  $s$  is too large (much larger than the typical discrepancy of outliers), the M-estimator tends to the least squares estimator and loses its robustness properties. In this case, reduction in the bias caused by outliers is no longer obtained. In summary, the hyper-parameter  $s$  controls a *bias/variance tradeoff*.

Figure 5.5 illustrates this bias/variance tradeoff on the frame #48 presented in Figure 5.4, in which an outlier bead is located near a bead of interest. We consider the parameters  $\{x_p, y_p, z_p\}$  known, and Figure 5.5(b) presents the evolution of the cost function  $\mathcal{C}$  as a function of the single parameter  $r_p$ , for different values of the tuning parameter  $s$ . In each case, the bias and the predicted standard deviation (derived from the Cramér-Rao lower bounds, see Section 5.3.3) are reported in Figure 5.5(c). The curves show that the estimation bias on the parameter  $r_p$  can be reduced by decreasing the value of  $s$ , i.e., by decreasing the weight  $w$  given to outliers in the estimation (see Figure 5.5(d)). However, some inliers are also discarded when  $s$  decreases. This results in an increase of the variance of estimation (see Figure 5.5(c)), reflecting the reduction of the curvature of the cost functions plotted in Figure 5.5(a). Finally, examples of robust weighting maps  $\mathbf{w}$  are shown in Figure 5.5(d). They illustrate that weights are close to a segmentation of the pixels impacted by the unwanted object such that diffraction rings characterizing the bead of interest are well preserved when  $s$  achieves a bias/variance tradeoff (i.e. medium values of  $s$ ).

Moreover, based on the analysis of Figure 5.5(c), soft-descenders such as the Cauchy function, seem to be the most adapted penalization for our application since it achieves a good compromise between bias reduction and loss of efficiency of the estimator. We have compared in more details the different robust functions listed in 5.1 (the comparisons between each function are not reported here since they led to close results) and decided to use in the following the Cauchy descender.

### 5.3.2 Classical approaches

A common method to estimate the scale parameter  $s$  in the case of independent and identically distributed noise is based on the median absolute deviation (MAD) estimator, which provides a robust estimate of the residuals standard deviation (Huber, 2011):

$$\hat{s}^{(\text{MAD})} = 1.48 \cdot \text{median} [ |\mathbf{r} - \text{median}(\mathbf{r})| ], \quad (5.6)$$

where  $\mathbf{r}$  denotes the collection of all residuals values  $r(a, b)$  for  $a \in [1, A]$  and  $b \in [1, B]$ .

*MM-estimators* have been proposed to achieve high robustness to the presence of outliers while conserving high efficiency in the absence of outliers (Yohai, 1987). These

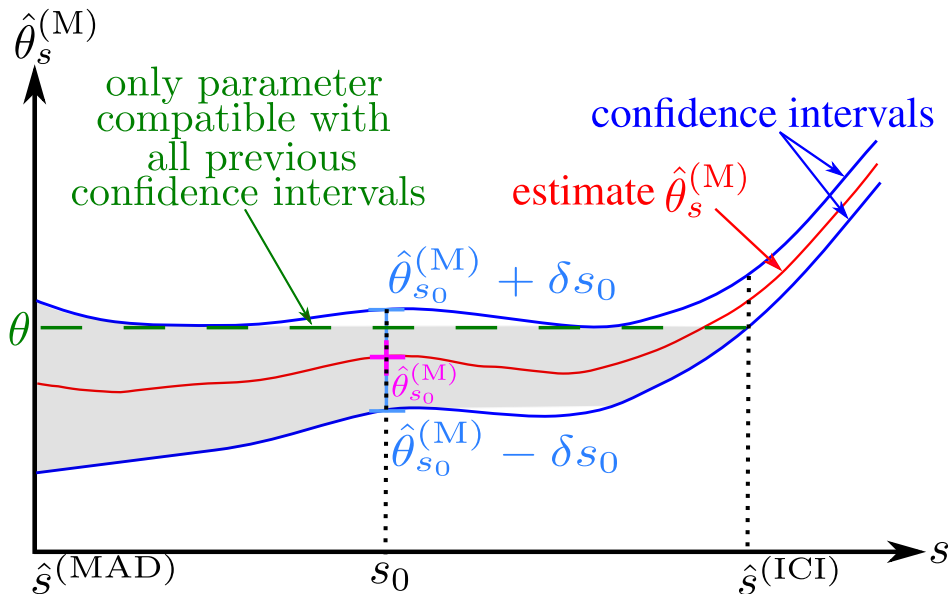


Figure 5.6 – Proposed principle for estimating the hyper-parameter  $s$  based on ICI rule.

estimators consist of two steps: (i) an estimation of the scale of the residuals  $s$  using an M-estimator defined by a descender  $\rho_1$ ; and (ii) the actual estimation of the parameters of interest  $\theta$  with a more efficient penalty function  $\rho_2$ .

One drawback of MAD and MM-estimators for setting parameter  $s$  is that they do not account for the actual impact of the outliers on the estimation. When considering unwanted objects within the field of view, the location of the objects with respect to the object of interest may or may not lead to biases. In other words, while  $\hat{s}^{(\text{MAD})}$  is suitable in cases where the outliers are uniformly distributed in the measured signal, a more appropriate choice of  $s$  could be made in cases of non-uniform distributions of outliers such as fringes located in a particular area of the sensor.

### 5.3.3 Proposed criterion for a bias/variance tradeoff

We propose to estimate parameter  $s$  using a data-driven method that accounts for the actual impact of the outliers on the estimation. Starting from the value  $\hat{s}^{(\text{MAD})}$ , which may be over-conservative, we apply the intersection of confidence intervals (ICI) rule to decide up to what point parameter  $s$  can be increased for variance reduction before being subject to bias due to outliers. The ICI rule has been successfully applied in image denoising to locally select the largest neighborhoods on which to perform denoising by a local polynomial approximation (Katkovnik et al., 2002). Its application only requires knowledge of the estimate and its standard deviation.

The vector of parameters  $\theta$  is estimated using the robust IRLS estimation scheme (5.3) by progressively increasing parameter  $s$  until the new estimate  $\hat{\theta}_s^{(\text{M})}$  obtained with parameter  $s$  leads to a confidence interval  $[\hat{\theta}_s^{(\text{M})} - \delta_s, \hat{\theta}_s^{(\text{M})} + \delta_s]$  with an empty

intersection with the preceding confidence intervals:

$$\hat{s}^{(\text{ICI})} = \max \left\{ s \in \left[ \hat{s}^{(\text{MAD})}, \infty \right) \mid \exists \boldsymbol{\theta}, \forall s_0 \in \left[ \hat{s}^{(\text{MAD})}, s \right], \boldsymbol{\theta} \in \left[ \hat{\boldsymbol{\theta}}_{s_0}^{(\text{M})} - \boldsymbol{\delta}_{s_0}, \hat{\boldsymbol{\theta}}_{s_0}^{(\text{M})} + \boldsymbol{\delta}_{s_0} \right] \right\}. \quad (5.7)$$

This principle is illustrated in Figure 5.6 considering a single parameter  $\theta$ .

To build the confidence intervals, we used the Cramér-Rao Lower Bounds (CRLBs, Kendall et al. (1948)). As stated in Section 1.3.2.2, the CRLB  $\delta(i)$  represents the minimum standard deviation for any unbiased estimator of the parameter  $\theta(i)$ . Under additive white Gaussian noise, the least squares estimator (5.1) asymptotically reaches the CRLB given by:

$$[\boldsymbol{\delta}]_i = \sqrt{\left[ \mathbf{I}^{\text{F}}(\boldsymbol{\theta})^{-1} \right]_{i,i}}, \quad (5.8)$$

where Fisher information matrix  $\mathbf{I}^{\text{F}}$  is defined by:

$$\left[ \mathbf{I}^{\text{F}}(\boldsymbol{\theta}) \right]_{i,j} = \sum_{a=1}^A \sum_{b=1}^B w(a,b) \frac{\partial m_{\boldsymbol{\theta}}(a,b)}{\partial \theta(i)} \frac{\partial m_{\boldsymbol{\theta}}(a,b)}{\partial \theta(j)}. \quad (5.9)$$

In the presence of outliers, we approximate the confidence intervals by computing the CRLB with the weights obtained by the IRLS procedure.

To reduce the computational cost of estimating parameter  $s$  according to the ICI rule (5.7), we consider a non-uniform discretization of the set  $\left[ \hat{s}^{(\text{MAD})}, \infty \right)$  such that two successive  $s$  values lead to a given decrease in the CRLBs. In practice, each  $s$  value is obtained by bisection to achieve the prescribed CRLBs reduction.

We now illustrate the proposed tuning of parameter  $s$  based on the ICI rule (5.7) on a simple 1-D problem: estimating the  $x_p$  location of a Gaussian-shaped pattern  $m$ . We simulate 100 noisy realizations  $d$  by adding to the model a Gaussian white noise (with a peak S/N of 10) and a constant outlier formed by a rectangular function with 3 samples in width (with a peak S/N of 1), see Figure 5.7(a).

The ICI rule leads to values of  $s$  that are about 5 times larger than  $\hat{s}^{(\text{MAD})}$  when the outlier is too far to introduce a significant bias (see Figure 5.7(a)), and to values of  $s$  close to that of  $\hat{s}^{(\text{MAD})}$  when the outlier affects the estimation (see Figure 5.7(b-c)). When  $\hat{s}^{(\text{ICI})}$  is higher than  $\hat{s}^{(\text{MAD})}$  (resulting in a weaker penalization of the residuals), the mean square error (MSE) on the location of the pattern is reduced by a factor between 2 and 4. In practice, the empirical standard deviation reaches the CLRb when the outlier has little impact on the estimate. A difference of a few tens of percent is observed when the constant outlier has an impact on the estimate since the estimator is no longer asymptotically unbiased. Determination of  $s$  with an ICI rule based on CRLBs is still possible. Another solution could be to compute an empirical estimation of the confidence intervals instead of a theoretical estimation using bootstrap methods, see e.g. Davison and Hinkley (1997) for a review. In conclusion, choosing the parameter  $s$  with the ICI rule improves the mean square error compared to a MAD estimator.

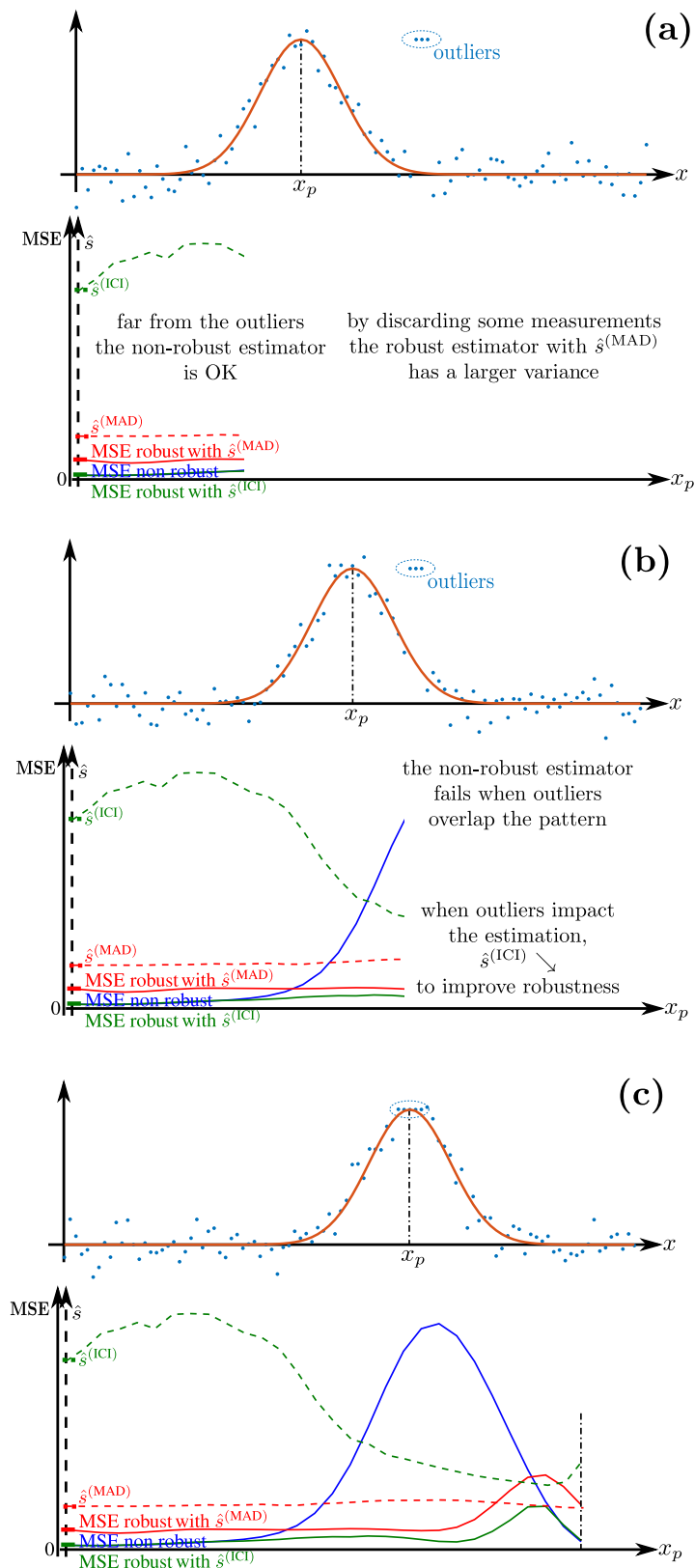


Figure 5.7 – Estimation of the position of a pattern by a robust approach using the MAD and the proposed ICI rule. Evolution of  $\hat{s}$  and MSE are respectively in dash and solid lines.

### A bias/variance tradeoff

The robust weighting of the residuals implies a bias/variance tradeoff:

- outliers data should be penalized to reduce the bias they induce on the estimation,
- part of inliers data are also penalized, which increases the estimation variance.

⇒ The penalization strength of the residuals should be chosen with care:

- usual approaches are based on a robust estimation of the residuals standard deviation which does not account for the real impact of outliers in the estimation,
- we propose a criterion based on the intersection of confidence intervals to automatically set the level that distinguishes between inliers and outliers.
  - Starting from a conservative guess of the penalization strength of the residuals using a classical method, the penalization is progressively relaxed until the estimation variance is similar to the estimation bias.
  - We show on numerical experiments that the proposed criterion takes intrinsically into account the actual impact of outliers on the estimation thus achieving a better bias/variance tradeoff than the usual MAD estimator.

## 5.4 Application to lensless microscopy videos

In this section, the performance of the proposed robust estimation scheme is evaluated on two holographic microscopy videos recorded in different conditions. The goal is to accurately characterize the spherical opaque objects imaged in the presence of several outliers. Since the objects to be characterized are spherical and opaque, we model their diffraction patterns with Thompson's model (Tyler and Thompson, 1976). This physical model, valid when the transversal distance  $z_p$  between the object and the sensor is such that  $z_p \gg \frac{4\pi r_p^2}{\lambda}$  (this condition is satisfied in the following experiments), describes the diffraction pattern of an opaque sphere located at  $(x_p, y_p, z_p)$ , with a radius  $r_p$ , by (Tyler and Thompson (1976), see also Section 1.3.2.2.1 for more background on diffraction models):

$$m_p(x, y) = \frac{\pi r_p^2}{\lambda z_p} J_{1c} \left( \frac{2\pi r_p \rho_p}{\lambda z_p} \right) \sin \left( \frac{\pi \rho_p^2}{\lambda z_p} \right), \quad (5.10)$$

where  $\rho_p = \sqrt{(x - x_p)^2 + (y - y_p)^2}$  is the transversal distance to the center of the sphere and  $J_{1c}(u) = J_1(u)/u$  is the cardinal Bessel function of first order. A vector of parameters  $\theta = \{x_p, y_p, z_p, r_p\}$  fully characterizes the diffraction pattern of a spherical object.



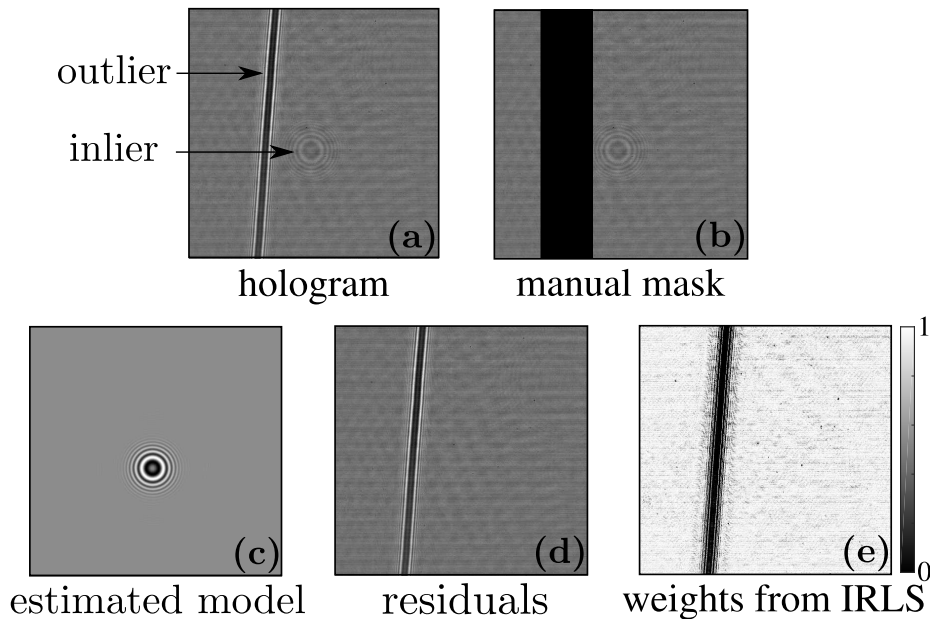


Figure 5.8 – Calibrated circular object near an outlier. (a) example of a time frame; (b) hand-drawn binary mask roughly discarding the outlier; (c) estimated hologram model from the robust minimization problem (5.3); (d) residuals (subtraction between (a) and (c)); (e) resulting IRLS weights at the final iteration.

## 5.4.1 Holographic video of an object of constant size

### 5.4.1.1 Dataset and algorithm description

We consider a 200 frames video of a slightly moving particle located near an unwanted object. The object of interest is a circular chromium deposit on a glass plate, with a calibrated radius of  $50\ \mu\text{m}$  (OPTIMASK<sup>TM</sup>, diameter  $\pm 1\ \mu\text{m}$ , roundness error  $\pm 0.25\ \mu\text{m}$ ). This object is manually moved with a subpixel shift between each image (by slightly translating the microscope stage). The unwanted object is a human hair fixed near the circular object. This series of images is presented in Figure 5.1, series #1. It shows that the outlier produces diffraction fringes mixing with the diffraction rings of the inlier object. The time sequence was recorded and previously analyzed by Verrier and Fournier (2015), using the non-robust least squares estimators (5.1). Our goal is to compare radius estimates from the non-robust (5.1) and robust (5.2) least squares optimization problems. Note that the optical magnification of the setup was calibrated with care in Verrier and Fournier (2015). The results presented hereafter are corrected for this value so that the radius estimates of the object can be directly compared with the expected value of  $50\ \mu\text{m}$ .

Since the outlier remains static throughout the video, it is possible to roughly remove outlier pixels by applying a static binary weighting mask  $w(a, b) = 0$  if pixel  $(a, b)$  is in the masked region,  $w(a, b) = 1$  otherwise. Figure 5.8,(a-b) shows a frame from the video and the manual removal of the outlier by masking. Due to the mask  $w$ , part of the signal due to the particle of interest (diffraction rings) is not accounted for.

Moreover, since the radius  $r_p$  of the particle remains constant during acquisition, it is possible to jointly estimate this parameter in several consecutive frames. This

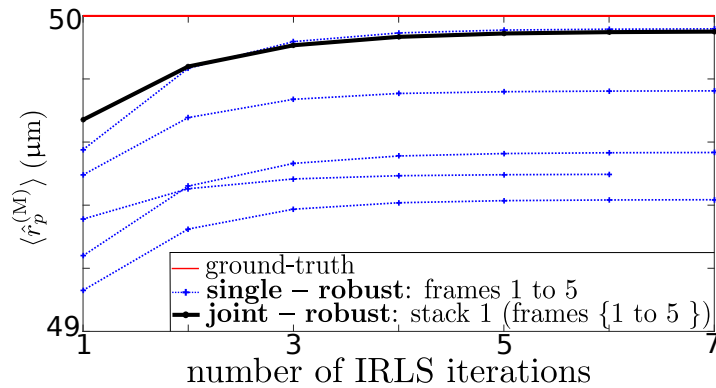


Figure 5.9 – Estimated radius as a function of the number of IRLS iterations.

digital super-resolution approach has already been successfully applied in holographic microscopy (Verrier and Fournier, 2015) considering the non-robust least squares estimator (5.1). We propose to combine this digital super-resolution approach with a robust estimation scheme (minimization problem (5.3)) considering 40 stacks of 5 successive frames.

#### 5.4.1.2 Results analysis

Figure 5.8(c) is an example of an estimated hologram model, and (d) gives the resulting residuals after subtracting the estimated model to the hologram (a). Figure 5.8(d) gives the weights obtained from the residuals (d) used in the last IRLS iteration. The weights are close to a segmentation of the pixels impacted by the unwanted object. The diffraction rings characterizing the particle of interest are well preserved (weights close to 1).

Figure 5.9 shows the evolution of the estimated radius during the IRLS iterations for the first 5 frames of the video. This shows that the algorithm converges in a few iterations and that the joint estimate of the radius carried out by super-resolution is very close to the ground-truth (radius of  $50 \mu\text{m}$  given by the manufacturer).

Figure 5.10 presents the estimated radius  $\hat{r}_p$  for the considered time series. The estimation is performed (i) on each frame independently, and (ii) jointly on stacks of 5 frames (digital super-resolution). Table 5.3 completes this study by listing the mean estimated radius  $\langle \hat{r}_p^{(M)} \rangle$ , the corresponding standard deviation  $\sigma$  and the CRLB  $\delta$  obtained for each method tested. The manual removal of the outliers by a binary mask appears to reduce the estimation bias. The bias is further reduced when a robust weighting of residuals by IRLS is applied since it preferentially eliminates the outliers while retaining the signal of interest. As a result, the estimation using a robust approach leads to a very small increase in CLRb which is negligible compared to the reduction of the bias. The combination of a robust estimation method with a super-resolution scheme (**joint – robust**) exploiting the information redundancy between different frames significantly reduce the estimation standard deviation. In agreement with statistical results (Robinson and Milanfar, 2006), we observe a decrease in the standard deviation by a factor at least equal to  $\sqrt{5}$ . This joint robust estimation approach enables accurate (i.e., low bias and low standard deviation) estimates of the radius of the holographic objects and thus improves the overall performance of a conventional least squares estimation process.

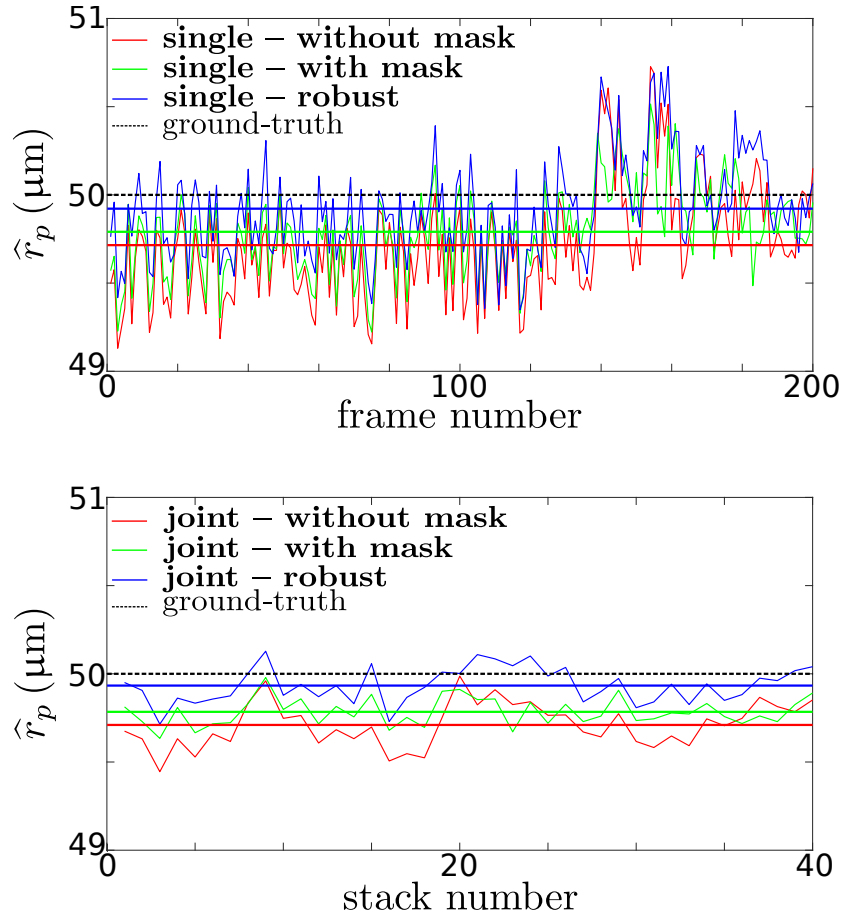


Figure 5.10 – Estimated radius  $\hat{r}_p$  for the time series. Top: the estimation is performed independently on each frame. Bottom: the estimation is performed jointly on stacks of 5 images (digital super-resolution). For each case, the results are obtained with non-robust least squares estimation (**without mask**), with a non-robust least squares estimation combined with a rough manually removal of the outliers by a binary mask (**with mask**), and with a robust least squares estimation (**robust**). The horizontal straight lines represent the mean estimate over the image series.

Table 5.3 – Mean estimated radius, standard deviation  $\sigma$  and CRLB  $\delta$  for the different methods tested (see caption of Figure 5.10).

Method:	$\langle \hat{r}_p^{(M)} \rangle$ ( $\mu\text{m}$ )	$\sigma$ ( $\mu\text{m}$ )	$\delta$ ( $\mu\text{m}$ )
<i>Single frame</i>			
<b>single – without mask</b>	49.71	0.31	0.014
<b>single – with mask</b>	49.78	0.25	0.016
<b>single – robust</b>	49.91	0.26	0.015
<i>Stack of 5 frames (super-resolution)</i>			
<b>joint – without mask</b>	49.71	0.13	$0.014 / \sqrt{5}$
<b>joint – with mask</b>	49.78	0.08	$0.016 / \sqrt{5}$
<b>joint – robust</b>	49.93	0.09	$0.015 / \sqrt{5}$

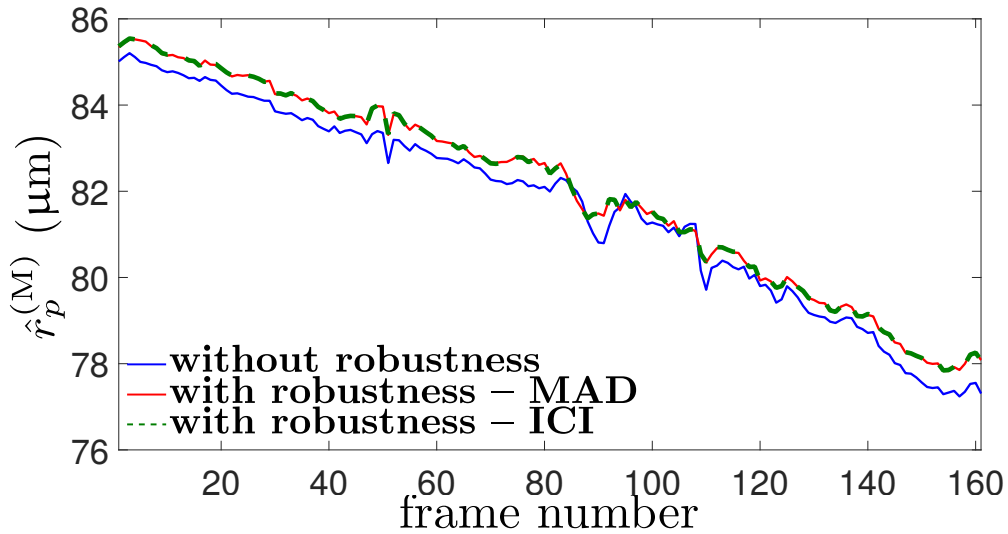


Figure 5.11 – Estimated radius over time of the evaporating droplet with the different methods tested.

## 5.4.2 Holographic video of evaporating droplets

### 5.4.2.1 Dataset and algorithm description

We use a 160 frames video of an evaporating diethyl ether droplet dispersed in a homogeneous and nearly isotropic turbulence that is tracked over time. This series of images is presented in Figure 5.1, series #3. As the particle evaporates, it produces a plume of vapor that diffuses around it. The vapor plume creates outliers since its signal mixes with the signal produced by the particle of interest. Other evaporating particles and dust particles passing close to the particle of interest also act as outliers. This time sequence was recorded and previously analyzed by Marié et al. (2017), using the standard least squares estimator (5.1). Based on their study and their previous works (Seifi et al., 2013; Marié et al., 2014), the authors show that the evaporation rate of this type of droplets is proportional to its area, in agreement to the theory.

### 5.4.2.2 Results analysis

Figure 5.12(a) shows the evolution of the tuning parameter  $s$  obtained with a MAD estimator and with the proposed ICI rule as well as the IRLS weights for two different frames. Figure 5.12(c) illustrates the evolution of confidence intervals for increasing values of  $s$ . Figure 5.12(d) shows the weights obtained at the end of the IRLS procedure for  $\hat{s}^{(\text{MAD})}$  (first row) and  $\hat{s}^{(\text{ICI})}$  (second row). On frame 60,  $\hat{s}^{(\text{ICI})}$  is significantly larger than  $\hat{s}^{(\text{MAD})}$ , leading to larger weights, while on frame 97  $\hat{s}^{(\text{MAD})} = \hat{s}^{(\text{ICI})}$  and the weights are identical. The ICI rule leads to a larger value of  $s$  than MAD but without notably modifying the estimation of the radius  $r_p$  (see Figure 5.11). This is the case when outliers do not disturb significantly the estimate like in frame 60 (see Figure 5.12, left column) since the particle of interest is isolated and the plume of vapor is rather small. In contrast,  $\hat{s}^{(\text{MAD})}$  and  $\hat{s}^{(\text{ICI})}$  are very close when the particle of interest is strongly disturbed by outliers. This is illustrated by frame 97 (see Figure 5.12, right column)

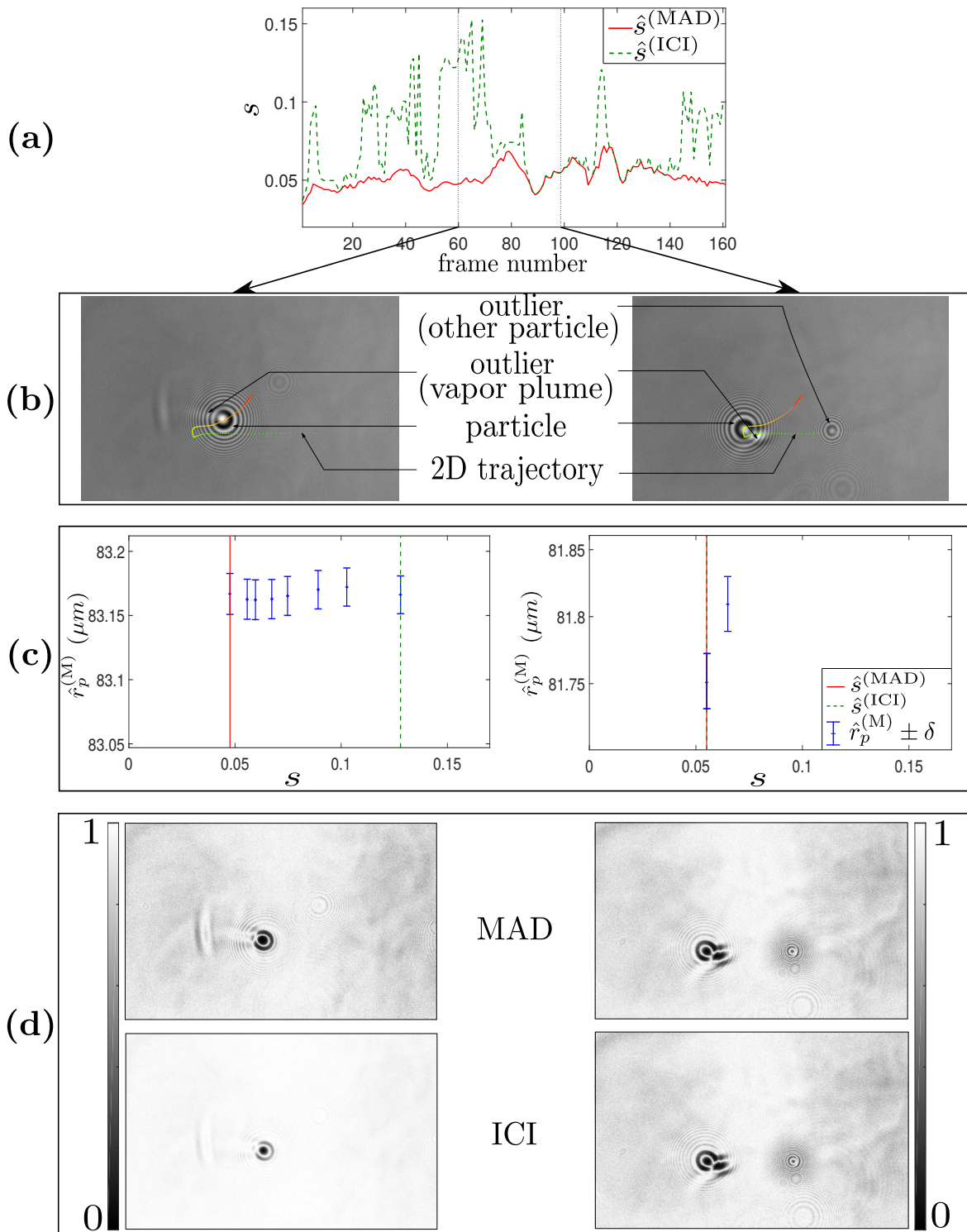


Figure 5.12 – Robust detection and tracking of an evaporating droplet. (a) evolution of  $\hat{s}^{(MAD)}$  and  $\hat{s}^{(ICI)}$ ; (b), (c) and (d) respectively give the holograms, confidence interval diagrams, and robust weighting maps for two video frames. For the example given in the left part of the figure, the intersection of confidence intervals is never empty since the current estimator reaches more than 99% of efficiency (compared to a non-robust approach), given the current weighting map. Thus, there is no significant variance reduction to expect by increasing further the value of  $s$ .

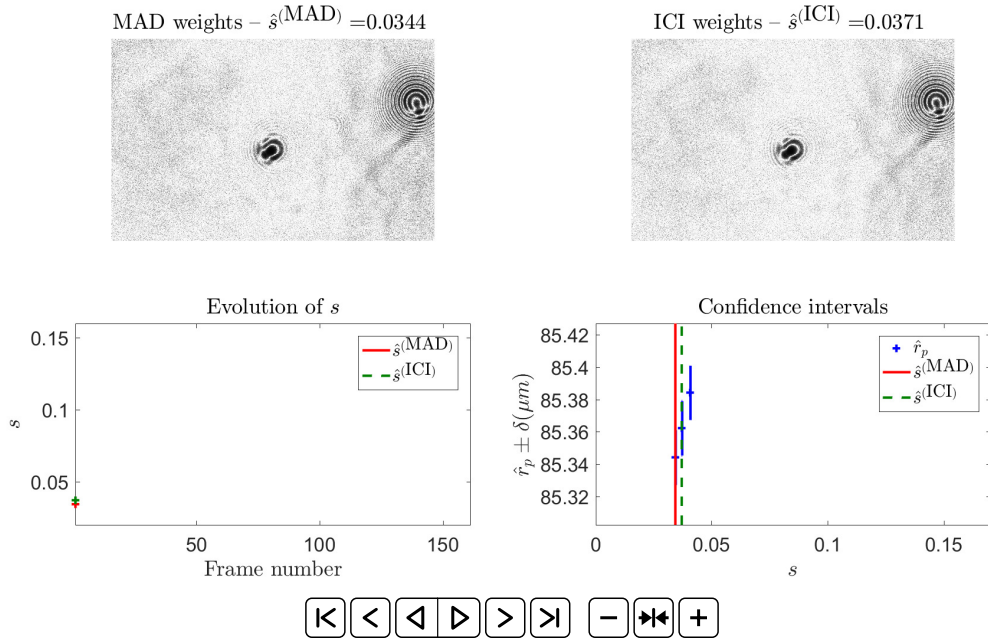


Figure 5.13 – Robust detection and tracking of an evaporating droplet: evolution of  $\hat{s}^{(MAD)}$  and  $\hat{s}^{(ICI)}$  over time, and the corresponding robust weighting maps. This video is visible in the PDF with ADOBE ACROBAT READER™.

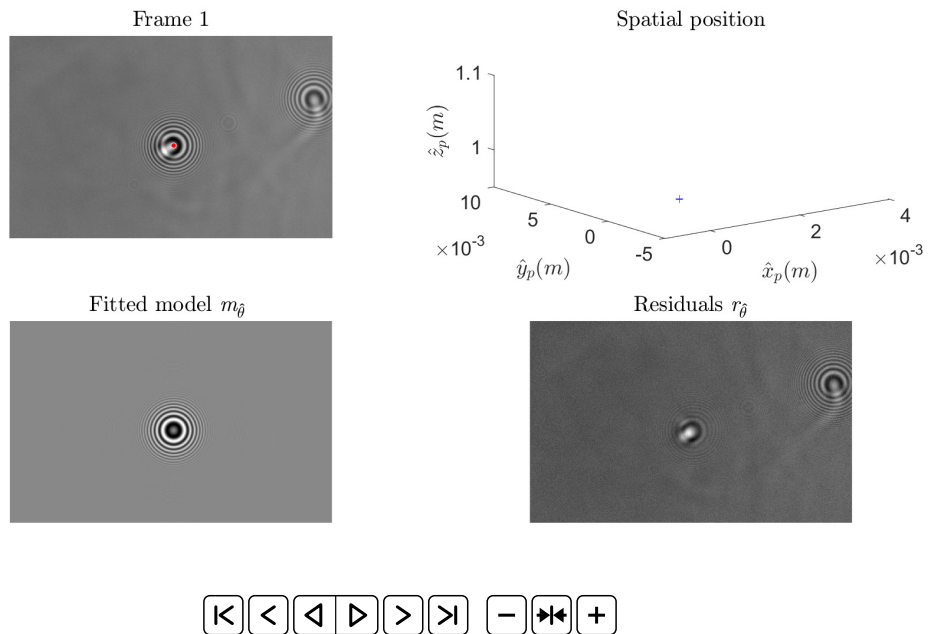


Figure 5.14 – Robust detection and tracking of an evaporating droplet: hologram, fitted model, residuals and estimated spatial 3-D location of the droplet. This video is visible in the PDF with ADOBE ACROBAT READER™.



where another evaporating particle is close to the particle of interest and disturbs its signal. These observations underline the fact that the MAD estimator only accounts for the presence of outliers strongly deviating from the model but does not account for their spatial localization and hence, their actual impact on the estimate. Figures 5.13 and 5.14 are videos showing the IRLS weighting maps obtained from the MAD and ICI criteria. The estimated model of the droplet and its estimated 3-D location over time are also presented.

Finally, Figure 5.11 shows the evolution of the estimated radius over time with the three methods of estimation tested. The robust estimation scheme leads to an average increase of  $0.4\ \mu\text{m}$  in the estimated radius. We also observed that it reduces the estimation standard deviation. These experimental results are explained by the fact that the moving outliers (vapor plume plus other particles) cause a nonstationary disturbance of the signal of interest over time. The robust approach considering a MAD or ICI rule to set the parameter  $s$  lead to close results in this application. This is due to the fact that the weighting matrix obtained with  $\hat{s}^{(\text{MAD})}$  already guarantees a high level of efficiency (around 90% of the maximum efficiency obtained without reweighting).



### Application on holographic microscopy videos

We show that the robust estimation procedure and the proposed criterion for setting the tuning parameter  $s$  can be useful for object characterization in holographic microscopy videos:

- the estimation bias is reduced thanks to the robustness,
- the variance is controlled thanks to the proposed ICI criterion taking into account the effective impact of the outliers on the estimation,
- the combination of a robust estimation procedure using our ICI criterion with a digital super-resolution estimation leads to accurate characterization of microscopic objects, thus improving the overall performance of the conventional least squares estimation process.

## 5.5 Conclusion

We have shown that the use of a robust approach to estimate the 3-D position and size of objects in holographic microscopy videos reduces the estimation bias caused by unwanted objects. We proposed a simple method to estimate the scale parameter that discriminates inliers and outliers in the robust estimation scheme. This method is based on a confidence interval intersection rule and achieves a better bias / variance tradeoff than the usual MAD rule. Finally, we have shown that the combination of the proposed robust approach with a joint estimation scheme also reduces the standard deviation of the estimation and consequently improves the overall performance of the method. In the following chapters, we illustrate that multi-spectral diversity is a complementary means of deriving accurate estimations both for astronomy and microscopy applications thanks to the introduced information redundancy.

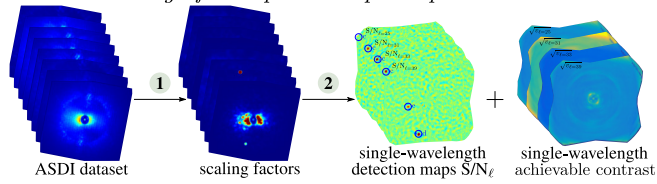
# Part IV Multi-spectral processing

## ASTRONOMY APPLICATIONS

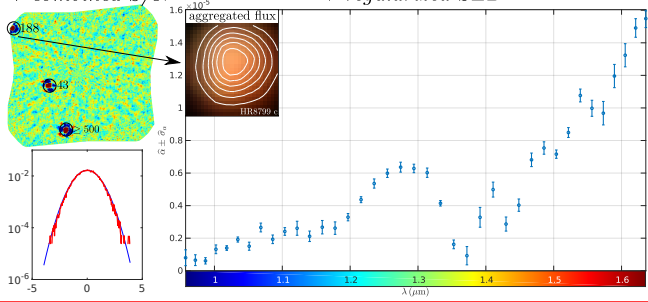
### Chapter 6

#### PACO-ASDI: detection & characterization algorithm

→ local learning of the spatio-temporo-spectral correlations



→ combined S/N → regularized SED



to be sub. to Astronomy & Astrophysics (2019)

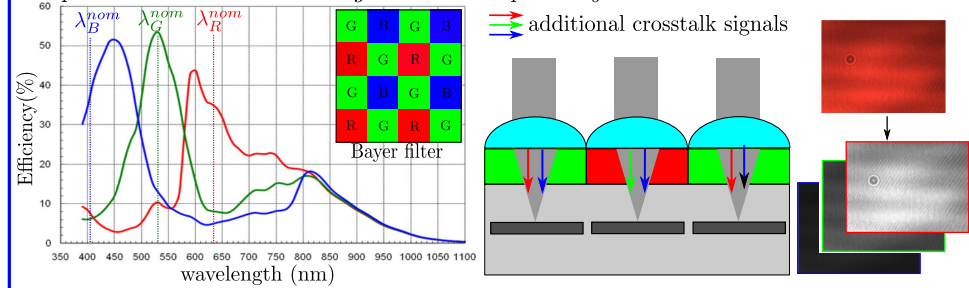
SPIE Astro. (2018)

## MICROSCOPY APPLICATIONS

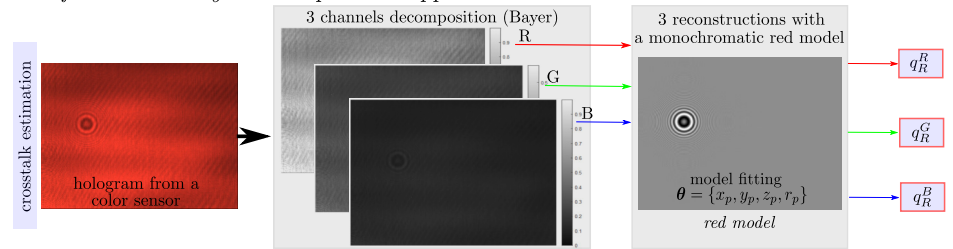
### Chapter 7

#### self-calibration for lensless color microscopy

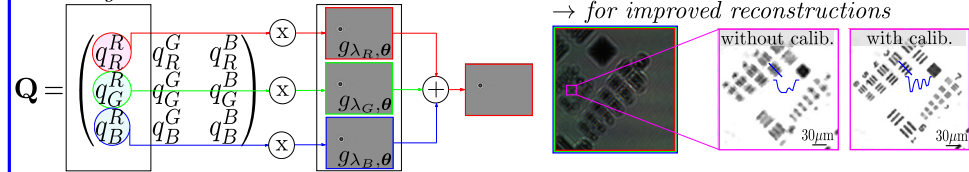
→ spectral crosstalk + wavelengths known imprecisely



→ self-calibration by inverse problem approach



→ taking into account calibration



Applied Optics (2017)

SPIE Photonics (2018)

## Part IV

# Multi-spectral processing



# Exoplanet detection and characterization with integral field spectrographs

---

**Abstract**

*Angular and spectral differential imaging (ASDI) combines observations at different times and several wavelengths to separate the residual signal from the host star and the signal of interest corresponding to off-axis sources. Successful detection is only possible with accurate modeling of those two components, in particular of the background due to stellar leakages of the host star masked out by the coronagraph. Beyond the detection of point-like sources in the field of view, it is also essential to characterize the detection in terms of statistical significance, astrometry and to estimate the spectral energy distribution (SED). We extend the PACO (see Chapter 2) and robust PACO (see Chapter 4) algorithms to capture the spectral and temporal fluctuations of the background spatial correlations. From this statistical modeling, we build a detection algorithm and a SED estimation method: PACO-ASDI. The modeling of spectral correlations proves useful both to reduce detection artifacts and to obtain accurate statistical guarantees (detection thresholds and SED confidence intervals).*

---

## 6.1 Introduction

As discussed in Section 1.2.2.2.3, several observation strategies can be used for direct imaging, such as ADI, SDI, and ASDI. We recall that ADI produces 3-D datasets (2-D + time) in which the speckles are quasi-static, while the signature of the companions describes an apparent motion along a circular trajectory around the host star. Spectral differential imaging (SDI) consists of recording images in different spectral channels using an integral field spectrograph (IFS). Reduced 3-D datasets (2-D + spectral) are obtained by mapping raw observations of the IFS cameras into a multi-spectral cube (Pavlov et al., 2008). In the reduced datasets, the stellar speckles due to diffraction are very similar from one wavelength to the other, up to a chromatic scaling (Perrin et al., 2003). After compensating for this scaling, speckles are aligned and can be combined in order to cancel and thus reveal the presence of off-axis sources whose positions are achromatic. A natural extension is then to use simultaneously these two complementary modes of observation: angular differential imaging and spectral differential imaging.

This hybrid observation mode called angular and spectral differential imaging (ASDI) produces 4-D datasets (2-D + time + spectral) and combines the properties of both ADI and SDI. Using ASDI datasets such as the ones obtained with the VLT/SPHERE-IFS or GEMINI/GPI instruments brings a spectral diversity compared to simple ADI. The discrimination between the signal from off-axis sources and the background signal due to stellar leakages is thus improved. In addition, ASDI datasets allow both the detection and the characterization of the exoplanets (Beuzit et al., 2019). The characterization is performed by fitting orbit models, exoplanet formation models, and by estimating the astrometry and photometry (Vigan et al., 2010). Physical information such as age, effective temperature, composition or surface gravity can be derived for the detected exoplanets (Müller et al., 2018; Cheetham et al., 2019; Mawet et al., 2019; Claudi et al., 2019).

Whatever the observation mode, the recorded images should be combined by a processing method to cancel as much as possible the stellar leakages (speckles) which largely dominate the exoplanet signal. Current state-of-the-art detection algorithms applied in direct imaging can be split into two families: algorithms specifically designed to work in SDI mode, and algorithms initially designed to work in ADI mode which were later adapted to also work in ASDI mode.

There are few methods specific to SDI. They are mainly based on physical modeling of the stellar PSF. The Planet eXtractor (PeX) algorithm (Thiébaud et al., 2016; Devaney and Thiébaud, 2017) derives a model of the chromatic dependence of the speckles based on diffraction theory. The Multispectral Exoplanet Detection Using Simultaneous Aberration Estimation (MEDUSAE) method (Ygouf, 2012; Cantalloube, 2016; Cantalloube et al., 2018) uses an analytic model of the coronagraphic PSF and performs speckle modeling by an inverse problem approach that estimates phase aberrations from the measurements. It also includes an object restoration step via a deconvolution procedure combined with suitable regularization penalties.

There is a much larger variety of ADI processing methods. The main ones are described in Section 2.2. Generally, they are adapted to work in ASDI mode by taking into account the specific motion of sources in this type of datasets (see the following paragraph).

Algorithms able to process ASDI datasets are generally subject to different limitations. Most of them are not fully-unsupervised so that the tuning of several hyperparameters is often mandatory to reach the best performance of the methods. Such tuning is very time consuming and should ideally be repeated for each dataset since it depends on the dataset properties (considered spectral bands, number of temporal and spectral frames, quality of the observations, amount of parallactic rotation, etc.). For both SDI and ASDI processing, the recorded images at wavelength  $\lambda$  are scaled by a factor  $\lambda_{\text{ref}}/\lambda$ , where  $\lambda_{\text{ref}}$  is a reference wavelength, so that the on-axis PSF and the speckle field are approximately aligned throughout the ASDI stack (reduced chromatic variations). Due to the difference between the scaling factor applied respectively to the shortest and the longest wavelengths, only a central area of the field of view is covered by all rescaled images. Some source detection techniques process only that area common to all wavelengths. This leads to a drastic reduction of the field of view (typically 25% to 50%), which limits the ability to detect sources. In addition, as for ADI algorithms, ASDI processing methods are subject to the self-subtraction phenomenon. By com-



binning information (either by image subtraction as in the TLOCI type methods, or by modes subtraction as in the PCA type methods) at different times and/or wavelengths to attenuate the speckle background, the signal of the exoplanets is also attenuated. Consequently, the photometry is not intrinsically preserved so that resorting to a calibration step via Monte-Carlo injections is mandatory to compensate for the exoplanet self-subtraction. Finally, the main limitation of existing approaches is the lack of control of the probability of false alarm on the detection maps and contrast curves (see Section 6.6 for a discussion). It is common for state-of-the-art methods to produce detection maps with many more false alarms than theoretically expected.

Based on an analysis of the limitations of existing algorithms for ASDI data processing and of the needs of astronomers that use planet finder instruments, the following desirable specifications for an exoplanet detection algorithm may be listed:

- unsupervised source detection with statistical guarantees (i.e., control of the probability of false alarm),
- characterization of the sources detected: subpixel astrometry and unbiased estimation of the spectral energy distribution (SED), with reliable confidence intervals,
- ability to process the whole field of view covered by the instrument without artifacts,
- computation of a map reporting the contrast required for a source to be detected at a given detection threshold.

In this chapter, we attempt to address these different points by deriving an algorithm from a data-driven statistical modeling of ASDI observations. The proposed algorithm, named PACO-ASDI, is an extension of our ADI exoplanet detection method PACO introduced in Chapter 2. The main methodological adaptations are the following:

- modeling of local covariances based both on temporal and spectral information (see Section 6.2),
- adaptation to the time-specific and wavelength-specific magnitude of the background fluctuations (see Section 6.2),
- an approach to combine detection maps at different wavelengths that accounts for spectral correlations (see Section 6.3.2),
- estimation of the SED of sources including an unsupervised spectral smoothing (see Section 6.4.2).

Figure 6.1 gives the general scheme of PACO-ASDI to which we will refer throughout this Chapter. It illustrates the four main steps of the algorithm:

- *learning of a model of the background* that accounts for the patch spatial covariance (step ①, detailed in Section 6.2),
- *single-wavelength detection*, by application of detection theory to our statistical model of the background (step ②, detailed in Section 6.3.1),

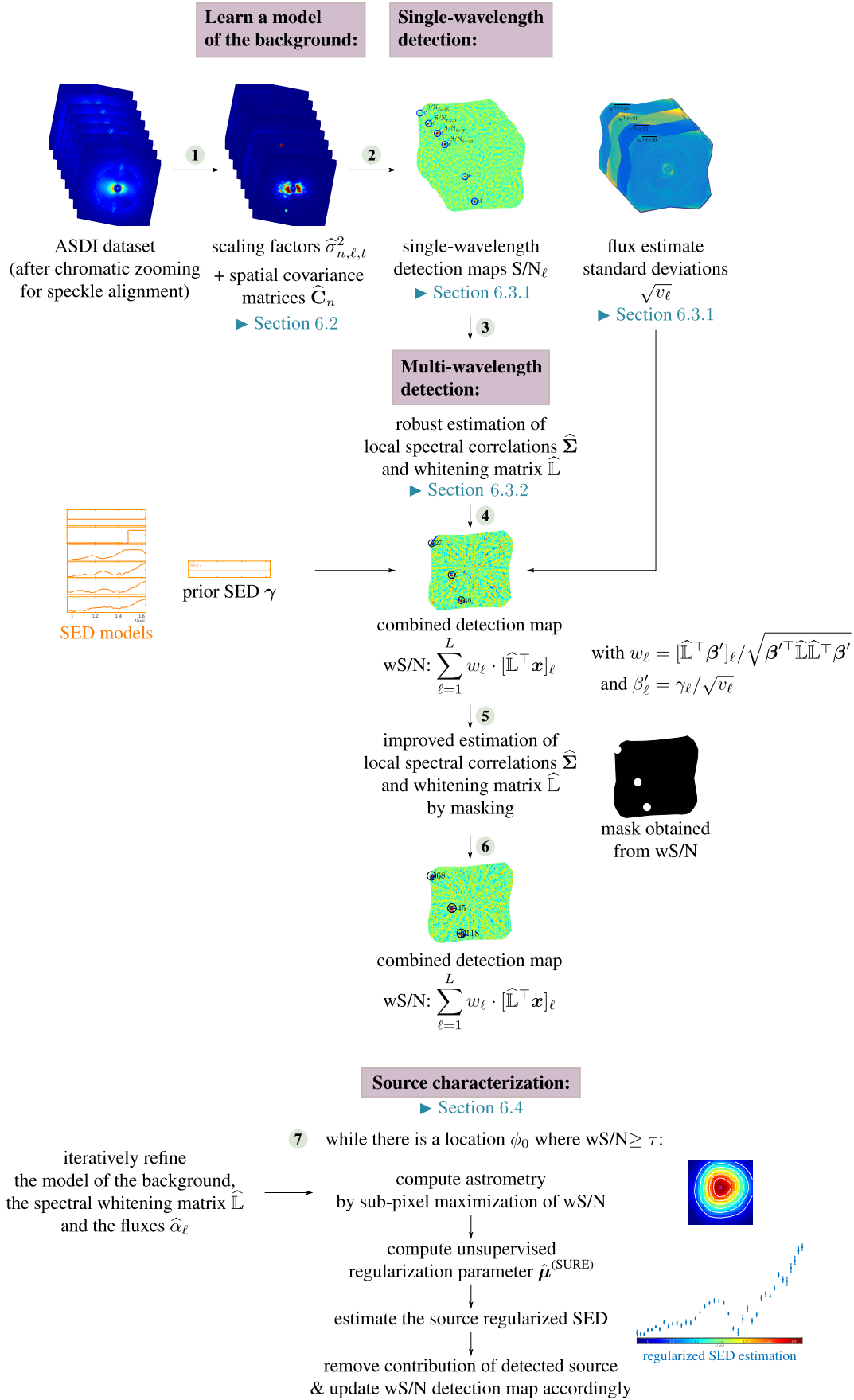


Figure 6.1 – Scheme of the PACO-ASDI algorithm.

- *multi-wavelength detection*, by combining the single-wavelength detection maps; this is achieved by learning the spectral correlations between single-wavelength detection maps (steps ③ to ⑥) and introducing a (coarse) prior information on the SED of the source (detailed in Section 6.3.2),
- once a source has been detected, its astrometry and photometry are *characterized* (step ⑦, described in Section 6.4), by iteratively refining the source parameters (angular location, SED and total flux) and the statistical model of the background (spatial and spectral correlations).

Statistical modeling of the spatial, temporal, and spectral fluctuations of ASDI datasets is a guiding thread throughout this chapter for grounding the detection and estimation method and to obtain reliable indications on the probability of false alarm and on the astrometric and photometric confidence intervals. Those statistical guarantees are essential to the astronomers to automate the analysis of ASDI datasets, for the scientific exploitation of the results, but also to characterize the performance of the instrument (detection limits and photometric accuracy depending on the observation strategy, the observation conditions and the performance of the adaptive optics + coronagraph).

This chapter is organized as follows. We describe in Section 6.2 our statistical modeling of the background fluctuations for ASDI datasets. In Section 6.3, we detail how to obtain single wavelength and combined detection maps at a controlled probability of false alarm. Section 6.4 details our unsupervised and regularized SED estimation procedure applied to the detected sources. Section 6.5 discusses the implementation details of the proposed algorithm. In Section 6.6, we illustrate on VLT/SPHERE-IFS datasets the performance of the proposed PACO-ASDI algorithm in terms of detection maps, achievable contrast, and SED estimation. This chapter is based on the journal paper submission [Flasseur et al. \(2020a\)](#) and on our conference paper [Flasseur et al. \(2018c\)](#).

## 6.2 Statistical modeling of background fluctuations

After speckle alignment by spectral zooming, background structures (i.e., speckles due to stellar leakages) are approximately constant (up to a multiplication by a chromatic factor accounting for the star SED) through time and the wavelengths. A closer observation reveals some temporal and spectral fluctuations. These fluctuations are spatially structured. It is essential to model these fluctuations in order to discriminate between an insignificant change of the background and the apparition of a point source. We describe in this section a statistical model of the background fluctuations. The detection and source characterization algorithm PACO-ASDI is grounded on this model.

### 6.2.1 Local multivariate Gaussian model

As discussed in Chapter 2, our modeling of the spatial covariances in ADI datasets with PACO algorithm led to two conclusions: (i) to account for the nonstationarity of the background, local modeling is necessary; and (ii) given the limited number of

samples available at any given location, a tradeoff must be found between the size of the covariance matrices and the estimation variance.

To extend the modeling from ADI datasets to the 4-D spatio-temporo-spectral datasets of ASDI, we keep a local Gaussian modeling: parameters of the Gaussians are estimated by analyzing patches extracted at a given location. For the  $n$ -th pixel of the field of view (identified by its 2-D angular location  $\theta_n$ ), we extract  $T \cdot L$  patches (where  $T$  is the number of temporal frames and  $L$  is the number of spectral channels), each made of  $K$  pixels. As discussed in Section 2.4.1, the patch size is constant for a given instrument. We fix it with the same empirical rule than the one derived in the PACO algorithm: it should be chosen so that twice the FWHM of the off-axis PSF is encompassed by the patches. Those patches  $\mathbf{r}_{n,\ell,t}$  are all centered on the same sky location  $\theta_n$  but correspond to different frames and spectral channels leading to the local collection  $\{\mathbf{r}_{n,\ell,t}\}_{\ell=1..L, t=1..T}$ , where  $\ell$  indicates the spectral channel and  $t$  the frame index. If this collection contains no off-axis point source, we model each patch  $\mathbf{r}_{n,\ell,t}$  as a random realization of the  $K$ -dimensional Gaussian  $\mathcal{N}(\mathbf{m}_{n,\ell}, \sigma_{n,\ell,t}^2 \mathbf{C}_n)$ . The mean patch  $\mathbf{m}_{n,\ell}$  is the same for all  $t$  but is chromatic. The  $K \times K$  covariance matrix is modeled as a product of two factors: a time and wavelength-dependent scaling  $\sigma_{n,\ell,t}^2$  and a spatial covariance matrix  $\mathbf{C}_n$  that are constant for a given patch collection extracted around pixel  $n$ . This modeling follows the two guidelines: (i) local adaptivity to account for background nonstationarities, in particular, the model is specific to a given spatial location and captures different fluctuation magnitudes for different wavelengths or different temporal frames; and (ii) a limitation of the number of parameters that have to be estimated from the collection of patches by neglecting temporal and spectral correlations. Several variants of this modeling have been evaluated in experiments, not reported here, that led to worse detection performances. Appendix C gives a view of the main alternative strategies considered. The effectiveness of introducing a temporal scaling factor in ADI was illustrated in Chapter 4. Neglecting the spectral correlations of the background may seem a crude approximation. There are indeed some strong correlations, but these correlations are difficult to capture at the scale of patches given our limited number of samples. In Section 6.3.2, we describe how to account for spectral correlations at a later stage of the algorithm, with satisfying results.

### 6.2.2 Local learning of the parameters

Since a different multivariate Gaussian model is defined for each angular location  $\theta_n$ , the estimation of the parameters  $\mathbf{m}_{n,\ell}$ ,  $\sigma_{n,\ell,t}^2$  and  $\mathbf{C}_n$  can be performed independently on each collection  $\{\mathbf{r}_{n,\ell,t}\}_{\ell=1..L, t=1..T}$  of 2-D patches centered on a given location  $\theta_n$ . Under our assumptions of negligible temporal and spectral correlations, the neg-log-likelihood  $\mathcal{L}_n$  of the collection can be written:

$$\begin{aligned} \mathcal{L}_n = & -\log p\left(\{\mathbf{r}_{n,\ell,t}\}_{\ell=1..L, t=1..T} \mid \{\mathbf{m}_{n,\ell}\}_{\ell=1..L}, \{\sigma_{n,\ell,t}^2\}_{\ell=1..L, t=1..T}, \mathbf{C}_n\right) = \frac{LTK}{2} \log 2\pi \\ & + \sum_{\substack{\ell=1..L \\ t=1..T}} \frac{1}{2} \log \det(\sigma_{n,\ell,t}^2 \mathbf{C}_n) + \sum_{\substack{\ell=1..L \\ t=1..T}} \frac{1}{2} \left(\mathbf{r}_{n,\ell,t} - \mathbf{m}_{n,\ell}\right)^\top \left(\sigma_{n,\ell,t}^2 \mathbf{C}_n\right)^{-1} \left(\mathbf{r}_{n,\ell,t} - \mathbf{m}_{n,\ell}\right). \quad (6.1) \end{aligned}$$

In the following, we derive the maximum likelihood estimator of the Gaussian parameters. The expression of this estimator is obtained by minimizing the neg-log-likelihood

$\mathcal{L}_n$  defined in Equation (6.1). The first-order optimality condition  $\nabla \mathcal{L}_n = \mathbf{0}$  leads to equations defining each parameter.

- The condition  $\left. \frac{\partial \mathcal{L}_n}{\partial \mathbf{m}_{n,\ell}} \right|_{\mathbf{m}_{n,\ell} = \widehat{\mathbf{m}}_{n,\ell}} = 0$  gives:

$$\mathbf{C}_n^{-1} \sum_{t=1..T} \frac{1}{\sigma_{n,\ell,t}^2} (\widehat{\mathbf{m}}_{n,\ell} - \mathbf{r}_{n,\ell,t}) = \mathbf{0}.$$

Since  $\mathbf{C}_n^{-1}$  is necessarily non-singular, we obtain the expression of the wavelength-specific average patch:

$$\widehat{\mathbf{m}}_{n,\ell} = \frac{1}{\sum_{t=1..T} 1/\sigma_{n,\ell,t}^2} \cdot \sum_{t=1..T} \frac{1}{\sigma_{n,\ell,t}^2} \mathbf{r}_{n,\ell,t}, \quad (6.2)$$

which corresponds to a weighted average of the spatial patches, computed over time indexes 1 to  $T$ , with weights  $1/\sigma_{n,\ell,t}^2$  that reduce the impact of frames and spectral channels displaying a large variance  $\sigma_{n,\ell,t}^2$ .

- The condition  $\left. \frac{\partial \mathcal{L}_n}{\partial \sigma_{n,\ell,t}^2} \right|_{\sigma_{n,\ell,t}^2 = \widehat{\sigma}_{n,\ell,t}^2} = 0$  leads to:

$$\frac{K}{2\widehat{\sigma}_{n,\ell,t}^2} - \frac{1}{2\widehat{\sigma}_{n,\ell,t}^4} \bar{\mathbf{r}}_{n,\ell,t}^\top \mathbf{C}_n^{-1} \bar{\mathbf{r}}_{n,\ell,t} = 0,$$

with  $\bar{\mathbf{r}}_{n,\ell,t} = \mathbf{r}_{n,\ell,t} - \mathbf{m}_{n,\ell}$  the residual patches. This gives:

$$\widehat{\sigma}_{n,\ell,t}^2 = \frac{1}{K} \bar{\mathbf{r}}_{n,\ell,t}^\top \mathbf{C}_n^{-1} \bar{\mathbf{r}}_{n,\ell,t}. \quad (6.3)$$

The time and wavelength-specific scaling factors  $\sigma_{n,\ell,t}$  are thus obtained by computing the variance of each spatially whitened patch.

- Finally, the condition  $\nabla_{\mathbf{C}_n} \mathcal{L} |_{\mathbf{C}_n = \widehat{\mathbf{S}}_n} = \mathbf{0}$  gives:

$$\frac{TL}{2} \widehat{\mathbf{S}}_k^{-1} - \widehat{\mathbf{S}}_k^{-1} \left( \sum_{\substack{\ell=1..L \\ t=1..T}} \frac{1}{2\sigma_{n,\ell,t}^2} \bar{\mathbf{r}}_{n,\ell,t} \bar{\mathbf{r}}_{n,\ell,t}^\top \right) \widehat{\mathbf{S}}_k^{-1} = \mathbf{0},$$

leading to:

$$\widehat{\mathbf{S}}_k = \frac{1}{TL} \sum_{\substack{\ell=1..L \\ t=1..T}} \frac{1}{\sigma_{n,\ell,t}^2} \bar{\mathbf{r}}_{n,\ell,t} \bar{\mathbf{r}}_{n,\ell,t}^\top, \quad (6.4)$$

which is the sample covariance matrix of the spatial patches, each rescaled by the corresponding time and wavelength-specific factor.

In summary, the maximum likelihood estimates for the Gaussian parameters are the solutions to the following system of non-linear equations:

$$\begin{cases} \widehat{\mathbf{m}}_{n,\ell} = \frac{1}{\sum_{t=1..T} 1/\widehat{\sigma}_{n,\ell,t}^2} \cdot \sum_{t=1..T} \frac{1}{\widehat{\sigma}_{n,\ell,t}^2} \mathbf{r}_{n,\ell,t} \\ \widehat{\sigma}_{n,\ell,t}^2 = \frac{1}{K} (\mathbf{r}_{n,\ell,t} - \widehat{\mathbf{m}}_{n,\ell})^\top \widehat{\mathbf{S}}_n^{-1} (\mathbf{r}_{n,\ell,t} - \widehat{\mathbf{m}}_{n,\ell}) \\ \widehat{\mathbf{S}}_n = \frac{1}{TL} \sum_{\substack{\ell=1..L \\ t=1..T}} \frac{1}{\widehat{\sigma}_{n,\ell,t}^2} (\mathbf{r}_{n,\ell,t} - \widehat{\mathbf{m}}_{n,\ell}) (\mathbf{r}_{n,\ell,t} - \widehat{\mathbf{m}}_{n,\ell})^\top, \end{cases} \quad (6.5)$$

---

**Algorithm 6.1:** Local background statistics estimation

---

**Input:**  $\{\mathbf{r}_{n,1,1}, \dots, \mathbf{r}_{n,L,T}\}$  (stack of  $LT$  patches, each patch has  $K$  pixels)  
**Output:**  $\{\widehat{\mathbf{m}}_{n,\ell}\}_{\ell=1..L}$  (mean patches)  
**Output:**  $\widehat{\mathbf{C}}_n$  ( $K \times K$  spatial covariance)  
**Output:**  $\{\widehat{\sigma}_{n,1,1}, \dots, \widehat{\sigma}_{n,L,T}\}$  (scaling factors)

---

$\widehat{\mathbf{C}}_n \leftarrow \mathbf{I}$  (initialization at identity matrix)

$\forall \ell, \forall t, \widehat{\sigma}_{n,\ell,t}^{(\text{old})} \leftarrow 1$

**for**  $\ell \leftarrow 1$  **to**  $L$  **do**

$\widehat{\mathbf{m}}_{n,\ell} \leftarrow \frac{1}{T} \sum_{t=1}^T \mathbf{r}_{n,\ell,t}$  (sample mean)

**do**

$\widehat{\mathbf{C}}_n \leftarrow \frac{K}{\text{tr}(\widehat{\mathbf{C}}_n)} \widehat{\mathbf{C}}_n$  (normalization)

    ▷ **Step 1:** Estimate scaling parameters

**for**  $\ell \leftarrow 1$  **to**  $L$  **do**

**for**  $t \leftarrow 1$  **to**  $T$  **do**

$\widehat{\sigma}_{n,\ell,t}^2 \leftarrow \frac{1}{K} (\mathbf{r}_{n,\ell,t} - \widehat{\mathbf{m}}_{n,\ell})^\top \widehat{\mathbf{C}}_n^{-1} (\mathbf{r}_{n,\ell,t} - \widehat{\mathbf{m}}_{n,\ell})$

    ▷ **Step 2:** Update the mean patches

**for**  $\ell \leftarrow 1$  **to**  $L$  **do**

$s \leftarrow \sum_{t=1}^T 1/\widehat{\sigma}_{n,\ell,t}^2$  (normalization factor)

$\widehat{\mathbf{m}}_{n,\ell} \leftarrow \frac{1}{s} \sum_{t=1}^T \frac{1}{\widehat{\sigma}_{n,\ell,t}^2} \mathbf{r}_{n,\ell,t}$  (weighted mean)

    ▷ **Step 3:** Update the spatial covariance

$\widehat{\mathbf{S}}_n \leftarrow \sum_{\substack{\ell=1..L \\ t=1..T}} \frac{1/(TL)}{\widehat{\sigma}_{n,\ell,t}^2} (\mathbf{r}_{n,\ell,t} - \widehat{\mathbf{m}}_{n,\ell}) (\mathbf{r}_{n,\ell,t} - \widehat{\mathbf{m}}_{n,\ell})^\top$

$\tilde{P} \leftarrow \left( \sum_{\ell,t} 1/\widehat{\sigma}_{n,\ell,t}^2 \right)^2 / \left( \sum_{\ell,t} 1/\widehat{\sigma}_{n,\ell,t}^4 \right)$  (equivalent number of patches)

$\widehat{\mathbf{C}}_n \leftarrow \text{Alg2}(\widehat{\mathbf{S}}_n, \tilde{P})$  (shrinkage estimator)

**while**  $\max_{\ell,t} |\widehat{\sigma}_{n,\ell,t} - \widehat{\sigma}_{n,\ell,t}^{(\text{old})}| \geq \epsilon;$

---

**Algorithm 6.2:** Shrinkage covariance estimator

---

**Input:**  $\widehat{\mathbf{S}}_n$  ( $K \times K$  sample covariance matrix)

**Input:**  $\tilde{P}$  (equivalent number of patches)

**Output:**  $\widehat{\mathbf{C}}_n$  (covariance matrix estimate)

---

$\widehat{\rho} \leftarrow \frac{\text{tr}(\widehat{\mathbf{S}}_n^2) + \text{tr}^2(\widehat{\mathbf{S}}_n) - 2 \sum_{i=1}^K [\widehat{\mathbf{S}}_n]_{ii}^2}{(\tilde{P}+1) \left( \text{tr}(\widehat{\mathbf{S}}_n^2) - \sum_{i=1}^K [\widehat{\mathbf{S}}_n]_{ii}^2 \right)}$  (shrinkage factor)

**for**  $i \leftarrow 1$  **to**  $K$  **do**

$[\widehat{\mathbf{C}}_n]_{i,i} \leftarrow [\widehat{\mathbf{S}}_n]_{i,i}$  (copy diagonal)

**for**  $j \leftarrow i + 1$  **to**  $K$  **do**

$[\widehat{\mathbf{C}}_n]_{i,j} \leftarrow (1 - \widehat{\rho}) [\widehat{\mathbf{S}}_n]_{i,j}$  (shrink off-diagonal)

$[\widehat{\mathbf{C}}_n]_{j,i} \leftarrow (1 - \widehat{\rho}) [\widehat{\mathbf{S}}_n]_{j,i}$  (shrink off-diagonal)

---



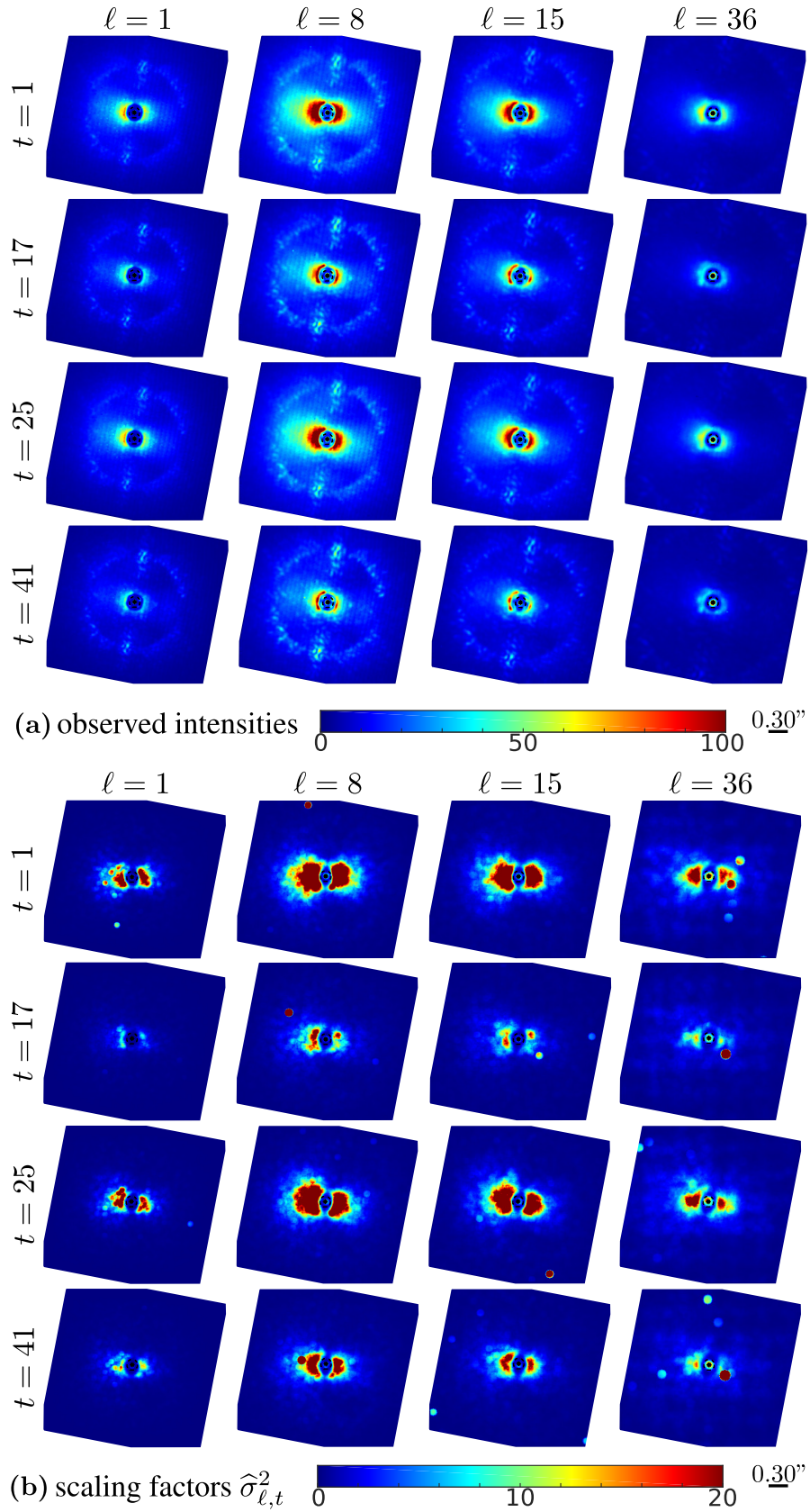


Figure 6.2 – Accounting for temporal and spectral fluctuations with time and wavelength-specific scaling factors: (a) observed intensities, for some selected frames (4 wavelengths  $\times$  4 exposures); (b) corresponding spatial distribution of scaling factors.

where the maximum likelihood estimate of the covariance  $\hat{\mathbf{S}}_n$  is not directly used as an estimate of the covariance  $\hat{\mathbf{C}}_n$ , but is replaced by an estimator with a smaller risk, as described in the following paragraphs. We solve the system (6.5) by the method of fixed-point iteration, i.e., by alternatively updating each unknown until convergence. This leads to Algorithm 6.1, where we chose the arbitrary normalization  $\text{tr}(\hat{\mathbf{C}}_n) = K$  for matrix  $\hat{\mathbf{C}}_n$  (some form of normalization is necessary to remove the scaling degeneracy in the product  $\hat{\sigma}_{n,\ell,t}^2 \hat{\mathbf{C}}_n$ ).

For locations  $\theta_n$  outside of the central region of the field of view, some patches  $\mathbf{r}_{n,\ell,t}$  fall outside of the measured area for the largest wavelengths. In that case, the sum for the computation of  $\mathbf{S}_n$  in the system (6.5) and in Algorithm 6.1 is restricted to the wavelengths  $\ell$  for which the patch is measured and the normalization factor  $1/TL$  is corrected to match the actual number of terms in the sum. Given the severe reduction in the number of patches actually used close to the borders of the field of view, it is important to regularize the sample covariance to reduce the estimation variance and to prevent obtaining singular or ill-conditioned matrices. As in Chapters 2, 3, and 4 we use a shrinkage estimator, implemented according to Algorithm 6.2. Because of the weighting by factors  $1/\hat{\sigma}_{n,\ell,t}^2$ , some patches have more importance than others and an equivalent number of patches  $\tilde{P}$  is used in the shrinkage formula, step 3 of Algorithm 6.1, see also Section 4.3.1. The rationale behind this equivalent number of patches comes from the variance reduction when performing the weighted mean<sup>1</sup>.

Figure 6.2(a) depicts the observed intensities in some frames of an ASDI dataset. Fluctuations can be noted both through time and through the wavelengths. In Figure 6.2(b), maps of the time and wavelength-specific scaling factors  $\hat{\sigma}_{n,\ell,t}^2$  are displayed for 16 pairs  $(\ell, t)$ . At a given location  $n$ , large values of this scaling factor compared to other frames  $t$  or other wavelengths  $\ell$  indicate that the corresponding patches have a moderate or negligible weight when estimating the mean background and the spatial covariance matrix. In the source detection and characterization steps described in the following sections, patches with comparatively larger scaling factors  $\hat{\sigma}_{n,\ell,t}^2$  also play a minor role. The method is thus robust to the presence of outliers in the data, see Chapter 4. A close inspection of the maps in Figure 6.2(b) reveals the presence of outliers: when an outlier affects a patch, the whole patch is discarded, outliers are thus visible as a disk-shaped area of large  $\hat{\sigma}_{n,\ell,t}^2$  values (corresponding to all spatial locations  $n$  that contain the outlier, i.e., the disk shape of our patches).

The convergence of Algorithm 6.1 is illustrated in Figure 6.3. Three different locations in the field of view, depicted by a red dot in the insert, are selected: a small angular separation in Figure 6.3(a), an intermediate separation in (b) and a large separation in (c).

---

1. The equivalent number of patches  $\tilde{P}$  corresponds to the number of samples if all weights are equal and is smaller when some weights differ. Let us assume that  $\{r_t\}_{t=1..T}$  be a collection of  $T$  independent and identically distributed random variables. The weighted mean  $\hat{m} = \sum_{t=1}^T w'_t r_t$ , where  $w'_t \geq 0$  are normalized weights ( $w'_t = w_t / \sum_{t=1}^T w_t$ ), is an unbiased estimator of  $\mathbb{E}[r]$  with a variance  $\text{Var}[\hat{m}] = \sum_{t=1}^T \text{Var}[w'_t r_t]$  (by independence of the  $r_t$ ), which leads to  $\text{Var}[\hat{m}] = \text{Var}[r]/\tilde{P}$ , with  $\tilde{P} = 1 / \sum_{t=1}^T w_t'^2 = (\sum_{t=1}^T w_t)^2 / (\sum_{t=1}^T w_t^2)$  the effective number of samples. If all weights are equal,  $\tilde{P} = T$ : the effective number of samples is equal to the total number of samples. If all weights but one are zero,  $\tilde{P} = 1$ . In our case, the weights  $w_t$  correspond to  $1/\hat{\sigma}_{n,\ell,t}^2$ , which leads to the formula to compute  $\tilde{P}$  in Algorithm 6.1, step 3. In practice, the samples  $\{r_t\}_{t=1..T}$  are not identically distributed (their variances differ), but  $\tilde{P}$  still indicates if the mean is reliable.

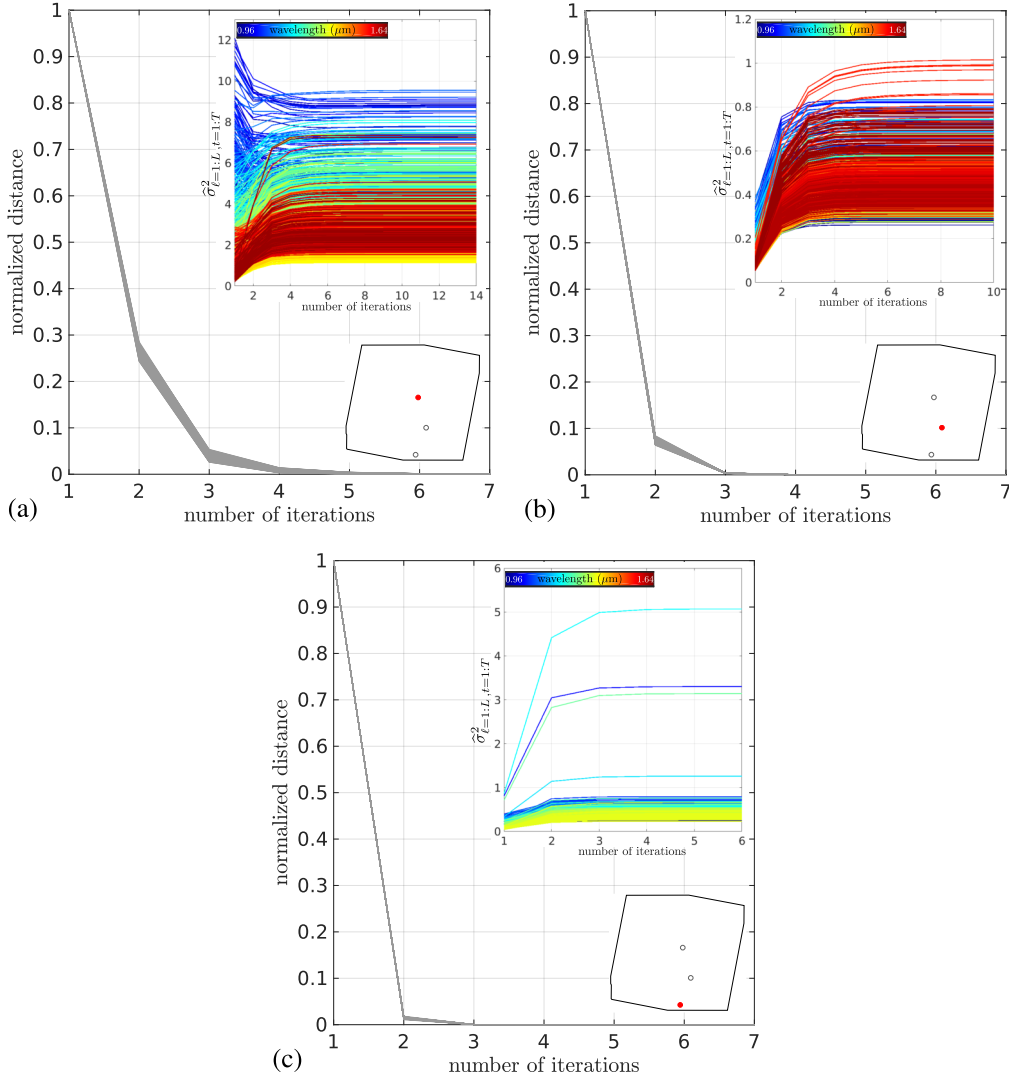


Figure 6.3 – Convergence of the scaling factors, starting from many random initializations. In the inserts, the location in the field of view is indicated as well as the evolution of the weights until the convergence criterion is reached.

ration in (c). In each case, 1,000 different random draws were used as an initialization. The graphs report the normalized distance to the solution found with a constant initialization after a large number of iterations. Convergence to the same solution is observed experimentally in all cases. An insert also gives the evolution of each scaling factor  $\hat{\sigma}_{n,\ell,t}^2$  with the iterations, until the convergence criterion is reached. A satisfactory convergence is reached in about 10 iterations. At large angular separations, as in (c), only the shortest wavelengths are available after the speckles are aligned by spectral zooming. The convergence is even faster in this case.

Figure 6.4 evaluates the statistical accuracy of our modeling of the background on HR 8799 ASDI dataset (see Table 6.2 for the observation logs). The left column gives the values and empirical distributions of the collection of centered patches  $\{\mathbf{r}_{n,\ell,t} - \mathbf{m}_{n,\ell}\}_{\ell=1:L, t=1:T}$ , at a location  $n$  near the coronagraph (rows (a) and (b)), at a location farther from the coronagraph (rows (c) and (d)), and for all patches from the

field of view (row (e)). Since only the modeling of the background is considered here, all patches around and at the location of the three known point-like sources were excluded. Simply removing an average background per wavelength is not satisfactory: values are not distributed according to a Gaussian distribution, there are numerous large deviations. The central column of Figure 6.4 gives the intensity values and the empirical distributions when only a spatial whitening is applied, using the same spatial covariance matrix for all frames and all wavelengths. The distribution of whitened intensities is closer to a Gaussian distribution. The right column considers the case of whitening by a covariance matrix scaled by the time and wavelength-specific factors  $\hat{\sigma}_{n,\ell,t}$ . The empirical distributions follow more closely a standard Gaussian, yet the match is not perfect close to the coronagraph. Accounting for the spectral or temporal correlations would probably further improve the statistical modeling of the background. Such modeling, however, seems difficult to carry out given the limited number of samples and is left to further studies. It is shown in the following sections that the proposed modeling already provides consistent results.



### PACO-ASDI's statistical modeling of the background

We extend the (robust) modeling of ADI datasets described in Chapters 2 and 4 to the 4-D spatio-temporo-spectral datasets of ASDI.

⇒ Each background patch centered on pixel  $n$  is modeled as a random realization of the  $K$ -dimensional Gaussian  $\mathcal{N}(\mathbf{m}_{n,\ell}, \sigma_{n,\ell,t}^2 \mathbf{C}_n)$ :

- the mean patch  $\mathbf{m}_{n,\ell}$  is the same for all  $t$  but is chromatic (i.e., specific to each wavelength),
- the spatial covariance matrix  $\mathbf{C}_n$  is common to the collection of patches extracted at pixel  $n$ ,
- parameters  $\sigma_{n,\ell,t}^2$  are time and wavelength-dependent scaling factors distinguishing inliers and outliers and accounting for different variances at each wavelength.

Within this statistical framework, the empirical intensity distributions of background patches matches a standard Gaussian, in a first approximation. In areas close to the coronagraph, this match is not perfect.

While accounting for the spectral correlations of the data would probably improve our statistical modeling, we defer the consideration of these correlations to a latter stage of the algorithm (where a sufficient number of samples can be identified to appropriately estimate the spectral correlations).

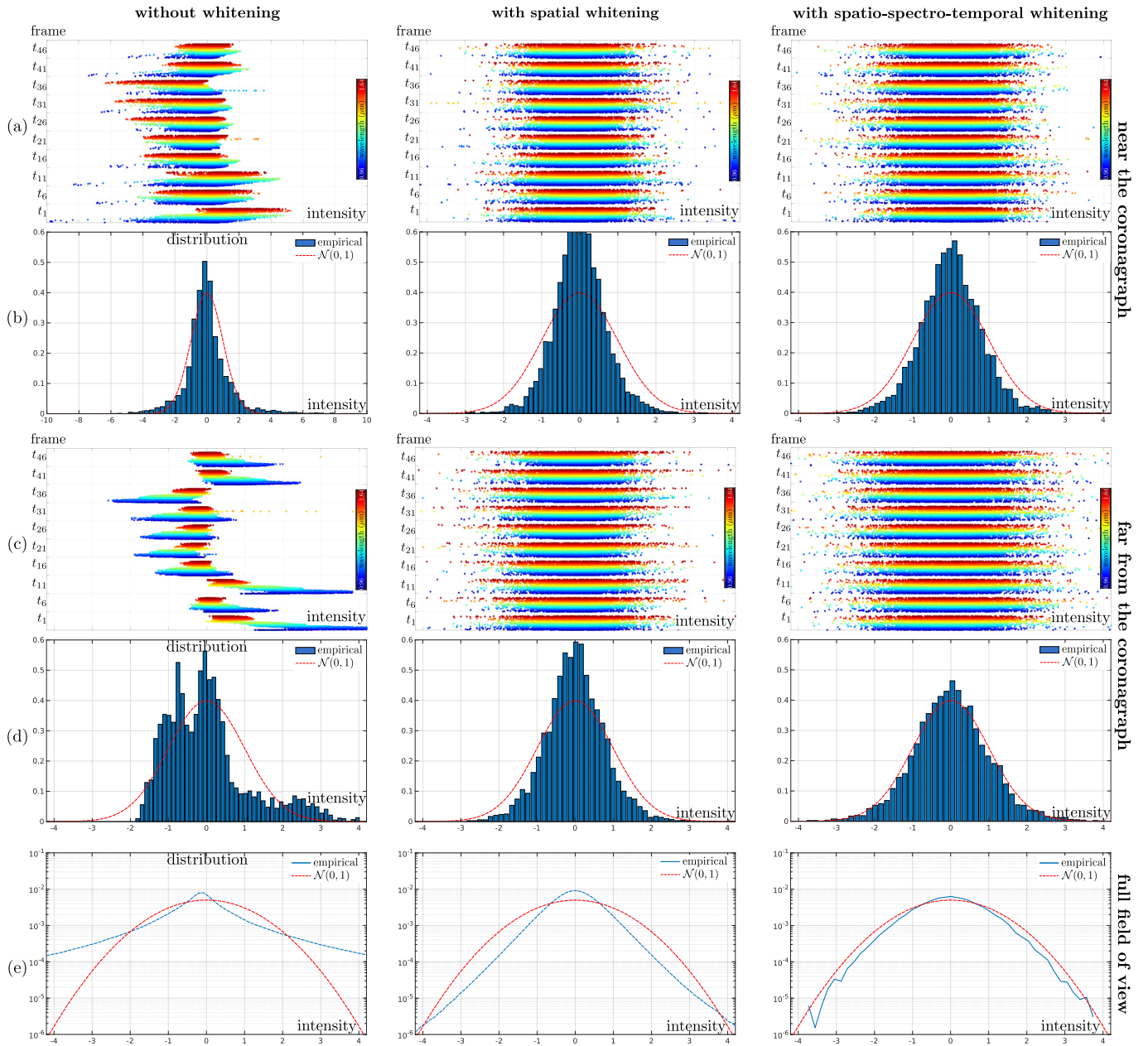


Figure 6.4 – Distribution of the centered patches: (left) without whitening; (center) after spatial whitening; (right) after spatial whitening and correction by the wavelength and time-specific scaling factors. Rows (a) and (b) correspond to a location selected at a small angular separation; rows (c) and (d) correspond to a location at a larger angular separation; row (e) gives the empirical distribution computed over the whole field of view. Patches represented in this figure contain no point-source. The rainbow false colors stand for the different wavelengths.



## 6.3 Detection maps

The statistical model of the background in ASDI datasets introduced in the previous section is essential to derive the detection and characterization method. Backgrounds at all wavelengths are combined to estimate the parameters of this model. We first describe how this multi-wavelength background model can be applied to produce a detection map at a single wavelength. We then discuss the combination of detection maps at several wavelengths.

### 6.3.1 Detection at a single wavelength

Let  $\phi_0$  be the hypothetical location of a point source in some reference frame. If a point source is present at that location, with a flux  $\alpha_\ell$  in the  $\ell$ -th band of the spectrum, then the signal of that source corresponds, at time  $t$  and in the  $n$ -th patch, to  $\alpha_\ell \mathbf{h}_{n,\ell}(\phi_{\ell,t})$ , with  $\mathbf{h}_{n,\ell}(\phi_{\ell,t})$  the zoomed-in off-axis PSF centered at the subpixel location  $\phi_{\ell,t}$  of the source at the  $\ell$ -th wavelength and  $t$ -th frame. Given the scarcity of sources in the field of view, it is safe to suppose that, within a small patch of a few tens of pixels, only a single source may be present. Detecting a point source at location  $\phi_0$  then amounts to deciding for one of two hypotheses:

$$\left\{ \begin{array}{l} \mathcal{H}_0 : \{\mathbf{r}_{[\phi_{\ell,t}],\ell,t}\}_{t=1:T} = \{\mathbf{f}_{[\phi_{\ell,t}],\ell,t}\}_{t=1:T} \\ \text{(background only)} \\ \mathcal{H}_1 : \{\mathbf{r}_{[\phi_{\ell,t}],\ell,t}\}_{t=1:T} = \alpha_\ell \{\mathbf{h}_{[\phi_{\ell,t}],\ell}(\phi_{\ell,t})\}_{t=1:T} + \{\mathbf{f}_{[\phi_{\ell,t}],\ell,t}\}_{t=1:T}, \\ \text{(background+source)} \end{array} \right. , \quad (6.6)$$

where  $\mathbf{f}$  is the notation for patches that contain pure background. The collection of patches considered in this hypothesis test corresponds to all patches that would contain the source if it was present: patches centered at pixel locations  $[\phi_{\ell,t}]$  that match the location of the source at time  $t$  and wavelength  $\ell$  due to the rotation of the field of view and the zoom applied to align the speckles at all wavelengths, see Figure 6.5. Under hypothesis  $\mathcal{H}_0$ , the collection of patches corresponds to pure background: no source is present at location  $\phi_0$ . Under hypothesis  $\mathcal{H}_1$ , the patches result from the superimposition of an off-axis PSF and of the background.

Under our statistical model of the background given in Equation (6.1), the likelihood of each hypothesis can be compared for a given flux  $\alpha_\ell$ :

$$2 \log \frac{\text{p}(\{\mathbf{r}_{[\phi_{\ell,t}],\ell,t}\} | \mathcal{H}_1, \alpha_\ell)}{\text{p}(\{\mathbf{r}_{[\phi_{\ell,t}],\ell,t}\} | \mathcal{H}_0)} = \alpha_\ell \sum_{t=1}^T \mathbf{u}_{[\phi_{\ell,t}],\ell,t}^\top \widehat{\mathbf{C}}_{[\phi_{\ell,t}]}^{-1} \mathbf{h}_{[\phi_{\ell,t}],\ell}(\phi_{\ell,t}) \quad (6.7)$$

with

$$\mathbf{u}_{n,\ell,t} = \frac{1}{\widehat{\sigma}_{n,\ell,t}^2} \left( \mathbf{r}_{n,\ell,t} - \widehat{\mathbf{m}}_{n,\ell} - \alpha_\ell \mathbf{h}_{n,\ell}(\phi_{\ell,t}) \right). \quad (6.8)$$

Since the flux  $\alpha_\ell$  is generally not known beforehand, it has to be estimated from the



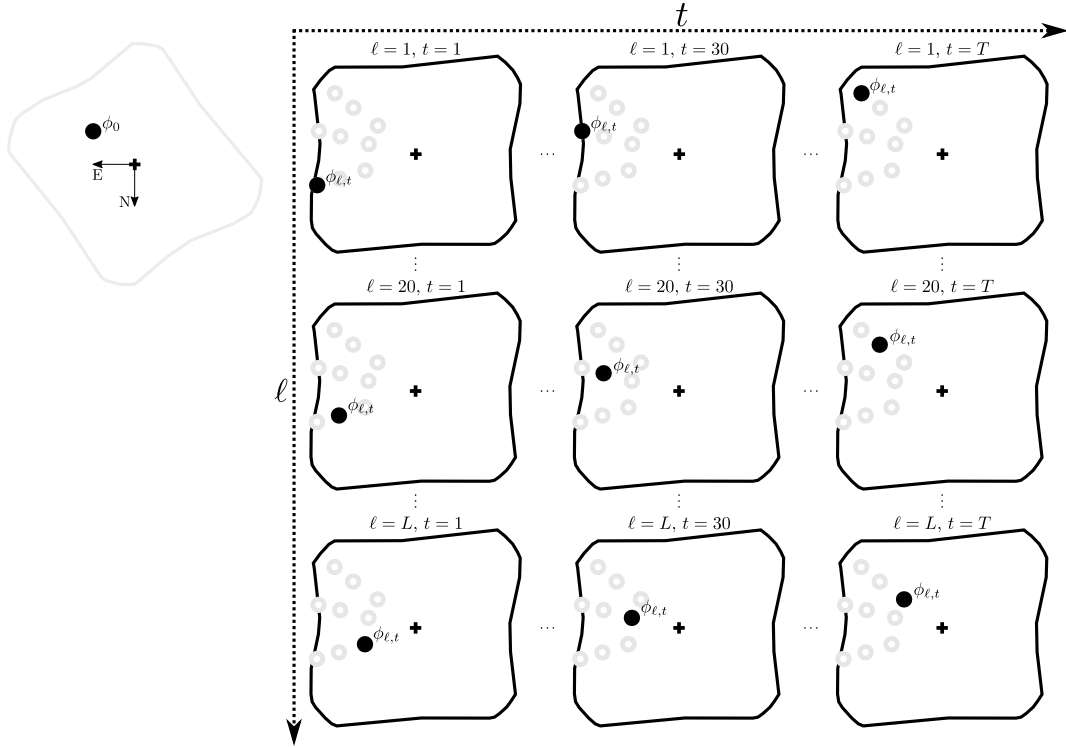


Figure 6.5 – Evolution of the 2-D location  $\phi_{\ell,t}$  of a source in a speckle-aligned ASDI dataset:  $\phi_0$  defines the 2-D angular location of a point source in a reference frame; the apparent location of the point source in the  $t$ -th observation and the  $\ell$ -th spectral band is indicated by a black disk; the apparent locations of a point source at other observation times and spectral bands are indicated by gray circles. The location  $\phi_{\ell,t}$  describes a radial motion with the wavelength and a rotation about the optical axis over time.

data. The maximum likelihood estimator, under our model of the background, is:

$$\hat{\alpha}_\ell = \frac{\sum_{t=1}^T b_{\ell,t} / \hat{\sigma}_{[\phi_{\ell,t}],\ell,t}^2}{\sum_{t=1}^T a_{\ell,t} / \hat{\sigma}_{[\phi_{\ell,t}],\ell,t}^2}, \quad (6.9)$$

with

$$a_{\ell,t} = \mathbf{h}_{[\phi_{\ell,t}],\ell}(\phi_{\ell,t})^\top \hat{\mathbf{C}}_{[\phi_{\ell,t}]}^{-1} \mathbf{h}_{[\phi_{\ell,t}],\ell}(\phi_{\ell,t}) \quad (6.10)$$

and

$$b_{\ell,t} = \mathbf{h}_{[\phi_{\ell,t}],\ell}(\phi_{\ell,t})^\top \hat{\mathbf{C}}_{[\phi_\ell]}^{-1} (\mathbf{r}_{[\phi_\ell],\ell,t} - \hat{\mathbf{m}}_{[\phi_{\ell,t}],\ell}). \quad (6.11)$$

Substituting  $\alpha_\ell$  with its estimate  $\hat{\alpha}_\ell$  in Equation (6.7) leads to the generalized likelihood ratio test:

$$\text{GLRT}_\ell : \frac{\left( \sum_{t=1}^T b_{\ell,t} / \hat{\sigma}_{[\phi_{\ell,t}],\ell,t}^2 \right)^2}{\sum_{t=1}^T a_{\ell,t} / \hat{\sigma}_{[\phi_{\ell,t}],\ell,t}^2} \underset{\mathcal{H}_0}{\overset{\mathcal{H}_1}{\gtrless}} \eta. \quad (6.12)$$

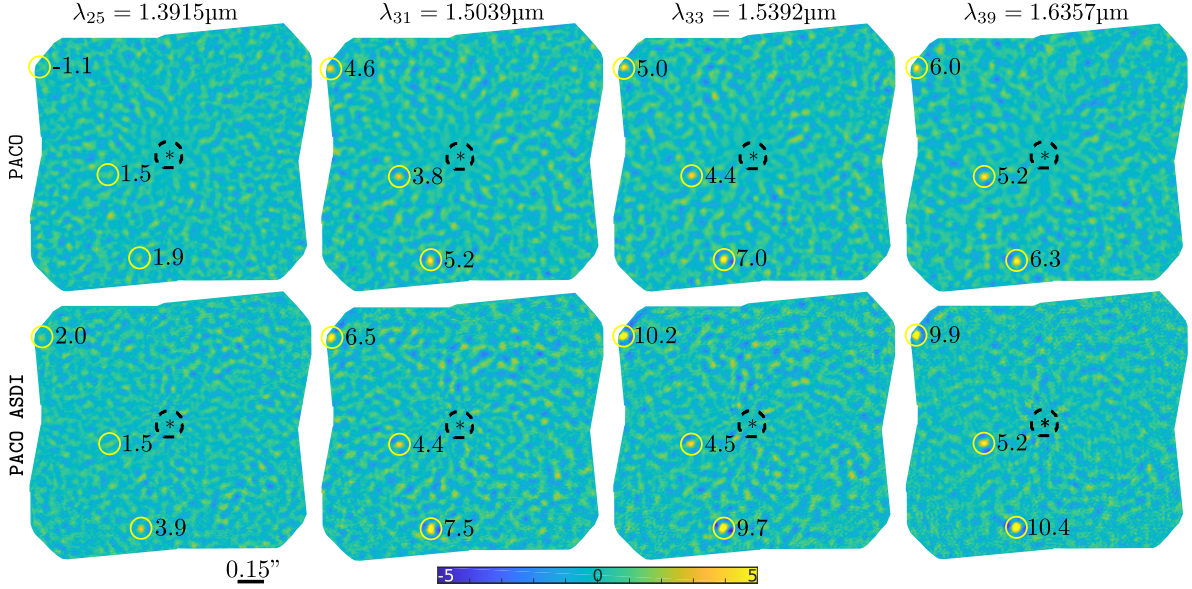


Figure 6.6 – PACO vs PACO-ASDI: impact of learning background structures at a single wavelength (PACO, first row) or jointly from all the wavelengths (PACO-ASDI, second row). Single-wavelength detection maps  $S/N_\ell$  are shown for PACO-ASDI. The differences between the two rows are related to the estimation of the covariance matrices  $\mathbf{C}$  and of the scaling parameters  $\sigma$ . The combination of those maps leads to a single detection map, not shown here, with improved sensitivity (see text and Figure 6.11).

Only positive flux estimates are physically meaningful for point sources. The test can then be improved by discarding locations leading to negative flux estimates  $\hat{\alpha}_\ell$  (see also Chapter 2):

$$S/N_\ell : \frac{\sum_{t=1}^T b_{\ell,t} / \hat{\sigma}_{[\phi_{\ell,t}],\ell,t}^2}{\sqrt{\sum_{t=1}^T a_{\ell,t} / \hat{\sigma}_{[\phi_{\ell,t}],\ell,t}^2}} \underset{\mathcal{H}_0}{\overset{\mathcal{H}_1}{\geq}} \tau, \quad (6.13)$$

which matches  $GLRT_\ell$  when  $\tau = \sqrt{\eta}$  and  $\hat{\alpha}_\ell \geq 0$ . As noted by Mugnier et al. (2009), the ratio in (6.13) corresponds to a signal-to-noise ratio. It is obtained by linearly transforming the data and accounts for the local, time and wavelength-specific covariance of the background. The variance of the estimator  $\hat{\alpha}_\ell$ , hereafter noted  $v_\ell$ , is:

$$\underbrace{\text{Var}[\hat{\alpha}_\ell]}_{v_\ell} = \left( \sum_{t=1}^T a_{\ell,t} / \hat{\sigma}_{[\phi_{\ell,t}],\ell,t}^2 \right)^{-1}. \quad (6.14)$$

The  $S/N_\ell$  therefore corresponds to the ratio  $\hat{\alpha}_\ell / \sqrt{v_\ell}$ , i.e., the signal-to-noise ratio of the flux estimate, and is distributed as a standard normal variate under  $\mathcal{H}_0$  (Mugnier et al., 2009).

Figure 6.6 compares the detection maps  $S/N_\ell$  computed with Equation (6.13) and detection maps obtained by PACO on ADI subsets (i.e., by processing the data one

wavelength at a time, as defined in Chapter 2). The major difference between the two approaches is that PACO-ASDI combines information from all wavelengths to learn the background model, more specifically its covariance. Therefore, a more accurate model is obtained and point-sources are better discriminated against the background: the signal-to-noise ratio of the sources is improved at all wavelengths while the fluctuations in the absence of sources are comparable.

Beyond the improvement of the detection map at a given wavelength, PACO-ASDI also benefits from combining detection maps at different wavelengths to better detect sources, as described in the next section.

## 6.3.2 Combining multiple detection maps

### 6.3.2.1 Combination assuming spectral independence

The detection of point sources can be largely improved by combining information from different wavelengths. The most straightforward approach consists of the extension of the hypothesis test in Equation (6.6) in order to include the patches at all times and all wavelengths (all locations depicted in Figure 6.5 rather than a single row). Under the assumption that spectral channels are independent, the likelihood can be factored as a product over all channels and fluxes  $\alpha_\ell$  can be separately estimated. Deciding for the presence of a source at location  $\phi_0$  based on the generalized likelihood ratio amounts to:

$$\text{GLRT} : \sum_{\ell=1}^L \frac{\left( \sum_{t=1}^T b_{\ell,t} / \hat{\sigma}_{[\phi_{\ell,t}],\ell,t}^2 \right)^2}{\sum_{t=1}^T a_{\ell,t} / \hat{\sigma}_{[\phi_{\ell,t}],\ell,t}^2} = \sum_{\ell=1}^L \frac{\hat{\alpha}_\ell^2}{v_\ell} \underset{\mathcal{H}_0}{\overset{\mathcal{H}_1}{\geq}} \eta. \quad (6.15)$$

To account for the non-negativity of source fluxes, the test can be slightly modified:

$$\text{GLRT}^+ : \sum_{\ell=1}^L \frac{[\hat{\alpha}_\ell]_+^2}{v_\ell} \underset{\mathcal{H}_0}{\overset{\mathcal{H}_1}{\geq}} \eta, \quad (6.16)$$

where  $[x]_+ = \max(x, 0)$  is the positive part of  $x$ .

The  $\text{GLRT}^+$  is defined as the sum  $\sum_{\ell=1}^L \frac{[\hat{\alpha}_\ell]_+^2}{v_\ell} = \sum_{\ell=1}^L s_\ell$  with  $s_\ell = [\hat{\alpha}_\ell]_+^2 / v_\ell$ . In the absence of source and under the simplifying assumption of an absence of spectral correlation of the backgrounds (i.e., under  $\mathcal{H}_0$  and within our Gaussian model with statistically independent channels – a hypothesis that will be rejected in the following paragraphs –) the terms  $s_\ell$  are independent and identically distributed. Due to the thresholding of negative values, the distribution of each  $s_\ell$  corresponds to a mixture of a  $\chi^2$  random variable and a Dirac mass at 0:

$$p(s_\ell | \mathcal{H}_0) = \frac{1}{2} \delta_0(s_\ell) + \frac{1}{2} \chi_1^2(s_\ell), \quad (6.17)$$

where the Dirac mass  $\delta_0$  centered in 0 accounts for the probability 1/2 that  $S/N_\ell$  be negative and the Chi-square distribution with one degree of freedom  $\chi_1^2$  corresponds to

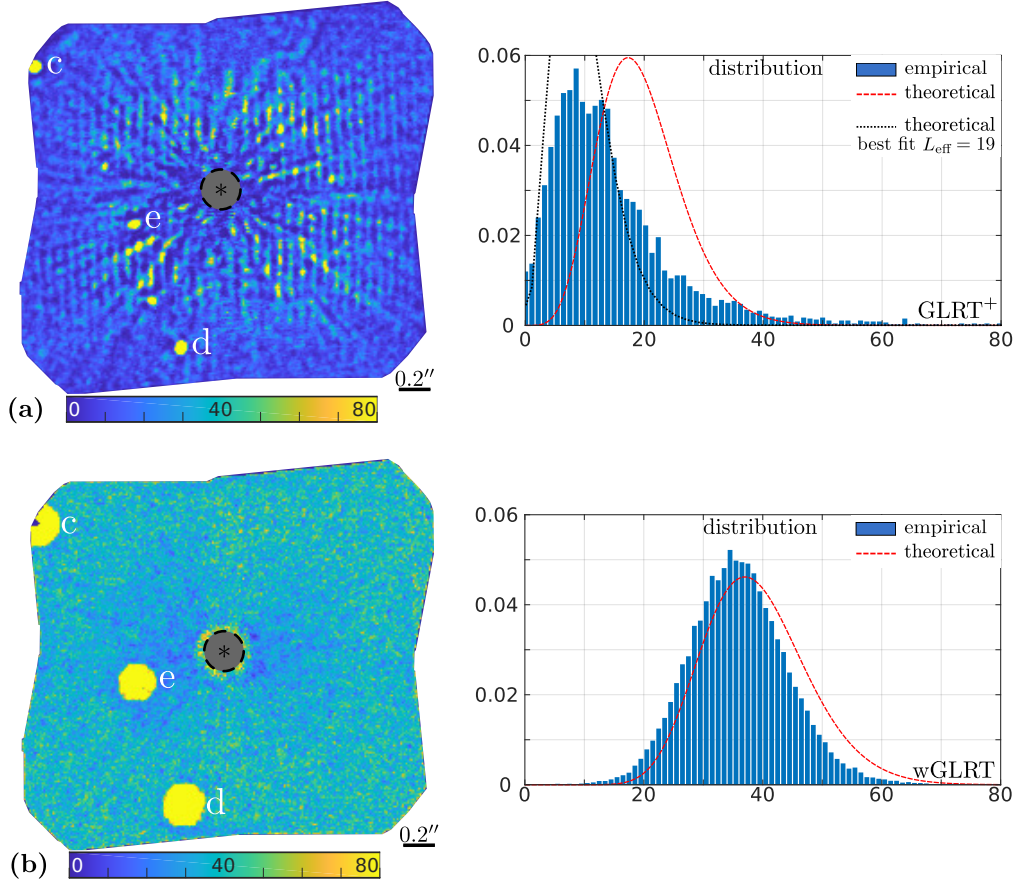


Figure 6.7 – Combined detection maps computed on HR 8799 ASDI dataset: (a)  $\text{GLRT}^+$  criterion and its distribution in the absence of sources; (b)  $\text{wGLRT}$  criterion, including a spectral whitening operation, and its distribution. The three sources are excluded for the computation of the empirical distributions. The blue histograms represent empirical distributions, and the red curves are the corresponding theoretical distributions. The black curve represents the best fit of the theoretical  $\text{GLRT}^+$  distribution (see Equation (6.18)) to the empirical distribution. It is obtained for an effective number of wavelengths equal to 19.

the distribution of the square of a standard Gaussian variable. By independence of the  $s_\ell$ , the distribution of their sum, i.e.,  $\text{GLRT}^+$ , is given by the convolution product:

$$\begin{aligned}
 p(\text{GLRT}^+ | \mathcal{H}_0) &= \underbrace{\left( p(s_1 | \mathcal{H}_0) * \dots * p(s_L | \mathcal{H}_0) \right)}_{L \text{ times}}(\text{GLRT}^+) \\
 &= \frac{1}{2^L} \delta_0(\text{GLRT}^+) + \sum_{\ell=0}^{L-1} \frac{L!}{2^L \ell! (L-\ell)!} \chi_{L-\ell}^2(\text{GLRT}^+), \quad (6.18)
 \end{aligned}$$

by application of the binomial expansion and the property  $\chi_a^2 * \chi_b^2 = \chi_{a+b}^2$  (the sum of two independent  $\chi^2$  random variables with respective degrees of freedom  $a$  and  $b$  is a  $\chi^2$ -distributed random variable with  $a + b$  degrees of freedom).

Figure 6.7(a) displays the  $\text{GLRT}^+$  obtained with Equation (6.16) on an ASDI dataset of HR 8799 obtained with SPHERE-IFS. Three point-sources can be detected in this

dataset, at the locations marked c, d and e. To perform an automated detection, it is necessary to set a threshold corresponding to a fixed probability of false alarm. The empirical distribution of  $\text{GLRT}^+$  values, excluding the 3 regions that contain the point-sources, is shown at the right of the detection map of Figure 6.7(a). This empirical distribution is compared to the theoretical distribution of  $\text{GLRT}^+$  under  $\mathcal{H}_0$ , drawn in dashed line. A strong mismatch is observed. Due to this discrepancy, it is not possible to derive a detection threshold from the model of Equation (6.18). The empirical distribution is shifted to left as if the number of wavelengths was smaller than  $L$ . An effective number of wavelengths could be derived by fitting the parameter  $L$  in Equation (6.18) to the empirical distribution, see Figure 6.7(a). This effective number of wavelengths accounts for the correlations of S/N values between adjacent wavelengths, but the resulting fit with the empirical distribution is quite bad. To limit the number of false alarms, the detection threshold is typically set in order to reach probabilities as low as  $10^{-7}$ . A miss-modeling of the right tail of the distribution may have a large impact on the value of the threshold. Rather than estimating an effective number of wavelengths to adjust the model (6.18), we model the distribution of the  $S/N_\ell$  values.

### 6.3.2.2 Accounting for spectral correlations

Signal-to-noise ratio values  $S/N_\ell$  defined in Equation (6.13) are Gaussian distributed. However, they are not independent of one another because the background patches, in a given frame, are very similar for adjacent wavelengths. Before combining detection maps, it is necessary to learn the spectral correlations between the maps  $S/N_\ell$ . With this strategy, the spectral correlations of the data are not directly accounted for within the statistical model of the data but deferred until a latter stage of the algorithm (during the combination of the  $S/N_\ell$  maps). We justify this choice by the difficulty that we have encountered in our tests to accurately model the spatio-temporo-spectral fluctuations of the background from a finite set of samples, see Appendix C.

The vector  $\mathbf{x}$  of  $S/N_\ell$  values is a sufficient statistic for the fluxes  $\hat{\alpha}_\ell$  of a point source. The detection of a point source can thus be defined directly on the vector  $\mathbf{x}$ :

$$\begin{cases} \mathcal{H}_0 : \mathbf{x} &= \boldsymbol{\epsilon} & \text{(no source)} \\ \mathcal{H}_1 : \mathbf{x} &= \boldsymbol{\epsilon} + \boldsymbol{\beta}, & \text{(a point source is present)} \end{cases} \quad (6.19)$$

where  $\boldsymbol{\beta} \in \mathbb{R}^L$  is the vector of expected S/N values at each of the  $L$  wavelengths:  $\beta_\ell = \alpha_\ell / \sqrt{v_\ell}$ , and  $\boldsymbol{\epsilon}$  is a random vector accounting for the fluctuations of  $S/N_\ell$  values. According to our model of spectral correlations,  $\boldsymbol{\epsilon}$  follows the Gaussian distribution  $\mathcal{N}(\mathbf{0}, \boldsymbol{\Sigma})$ . Replacing the unknown vector  $\boldsymbol{\beta}$  by its maximum likelihood estimate  $\hat{\boldsymbol{\beta}} = \mathbf{x}$  leads to the following GLR test:

$$\text{wGLRT} : \quad \|\hat{\mathbb{L}}^\top \mathbf{x}\|_2^2 \underset{\mathcal{H}_0}{\overset{\mathcal{H}_1}{\gtrless}} \eta, \quad (6.20)$$

where  $\hat{\mathbb{L}}$  is the  $L \times L$  whitening matrix obtained by Cholesky factorization, i.e., such that  $\hat{\mathbb{L}}\hat{\mathbb{L}}^\top = \hat{\boldsymbol{\Sigma}}^{-1}$ . Matrix  $\hat{\mathbb{L}}$  is such that  $\hat{\mathbb{L}}^\top \mathbf{x}$  be distributed according to  $\mathcal{N}(\mathbf{0}, \mathbf{I})$  under  $\mathcal{H}_0$ : it whitens vectors of  $S/N_\ell$  values. In Section 6.3.2.4, we discuss two strategies to estimate the matrix  $\hat{\mathbb{L}}$ .

In the absence of spectral correlations ( $\Sigma = \mathbf{I}$ ),  $\mathbb{L} = \mathbf{I}$  and the wGLRT equals the GLRT defined in Equation (6.15). Under  $\mathcal{H}_0$ , the wGLRT follows a  $\chi^2$  distribution with  $L$  degrees of freedom.

Figure 6.7(b) displays the wGLRT detection map and, by masking out the 3 sources, the distribution of wGLRT under  $\mathcal{H}_0$ . The comparison with  $\text{GLRT}^+$  shows that the spectral whitening reduces artifacts in the absence of sources (periodic structures observed in Figure 6.7(a) are no longer visible in Figure 6.7(b)). The empirical distribution of wGLRT is much closer to the expected distribution, however, the match is not perfect, which motivates considering another approach for combining detection maps.



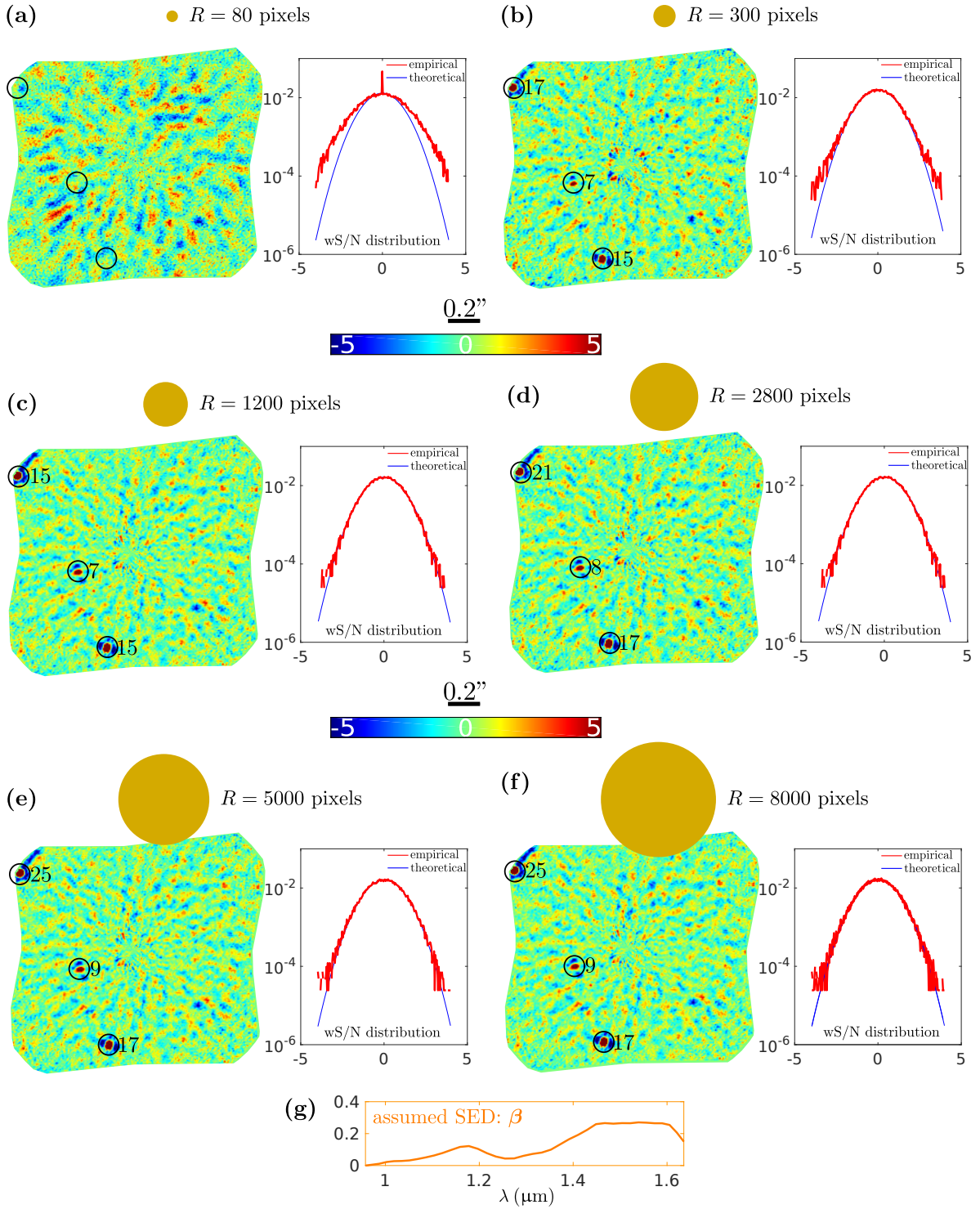


Figure 6.8 – Influence of the size  $R$  (given in pixels and displayed as a disk at the scale of the field of view) of the region over which the spectral covariances  $\hat{\Sigma}$  are estimated. The  $S/N_\ell$  maps are combined assuming the SED shown in (g), for whitening matrices  $\hat{\mathbb{L}}$  obtained from each estimate of the spectral covariance. From (a) to (f), combined maps wS/N and the empirical distribution of wS/N under  $\mathcal{H}_0$  are shown side by side.

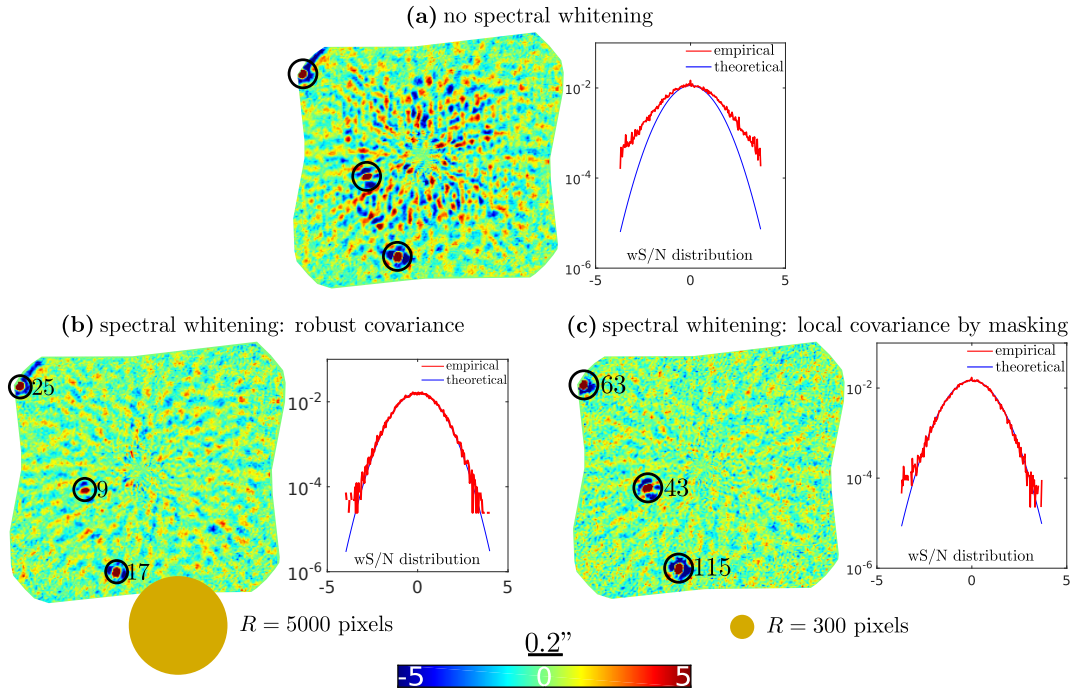


Figure 6.9 – Comparison of three spectral whitening strategies: (a) no whitening; (b) spectral whitening based on a robust estimate of the covariance computed over a large area ( $R = 5000$  pixels, shown at the bottom); (c) spectral whitening based on a local estimate of the covariance computed over a smaller area ( $R = 300$  pixels, shown at the bottom) by masking out regions of high wS/N given by the method (b).

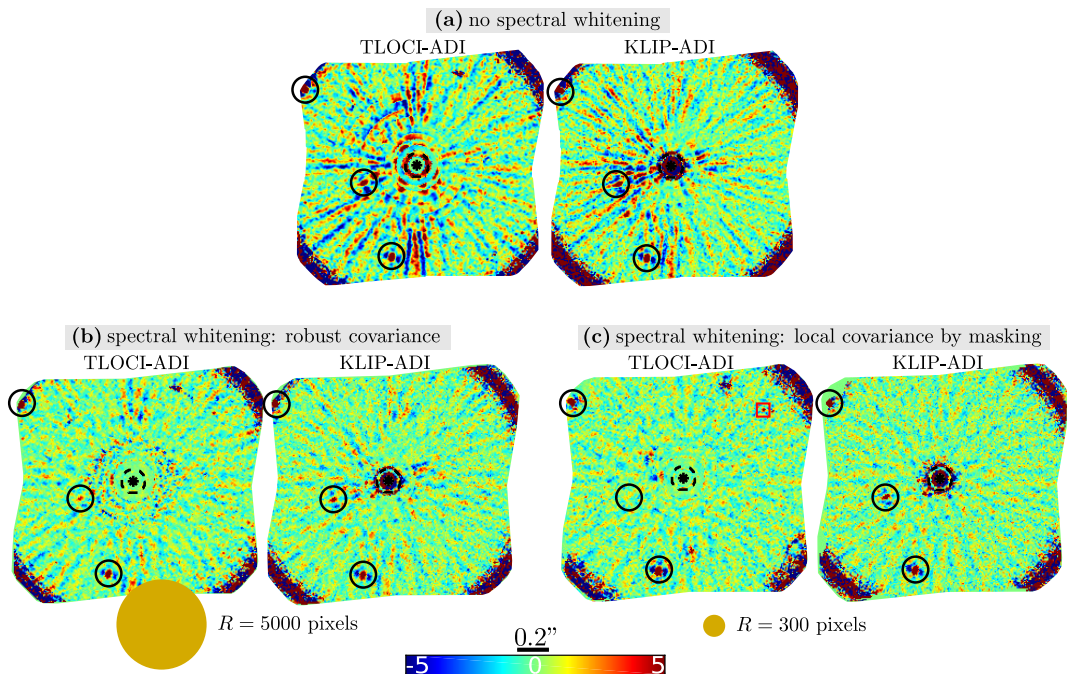


Figure 6.10 – Combination of S/N maps with our spectral whitening strategy: (a) simple spectral averaging of TLOCI and KLIP S/N maps, (b-c) combination with spectral whitening and the SED shown in Figure 6.8(g).

### 6.3.2.3 Improving the detection based on a prior spectrum model

If a coarse model of the SED of the point source under study is available prior to the detection, this model can be used to improve the detection performance by giving more weight to spectral bands where larger values are expected. Let  $\boldsymbol{\gamma}$  be the SED of a point source. Given that SED, the hypothesis test (6.19) takes the simplified form:

$$\left\{ \begin{array}{ll} \mathcal{H}_0 : & \mathbf{x} = \boldsymbol{\epsilon} \\ \text{(no source)} & \\ \mathcal{H}_1 : & \mathbf{x} = \boldsymbol{\epsilon} + \alpha^{\text{int}} \cdot \underbrace{\begin{pmatrix} | \\ \gamma_\ell / \sqrt{v_\ell} \\ | \end{pmatrix}}_{\boldsymbol{\beta}'}, \\ \text{(a point source is present)} & \end{array} \right. \quad (6.21)$$

where  $\alpha^{\text{int}}$  is the spectrally integrated flux, i.e., the flux such that  $\alpha_\ell = \alpha^{\text{int}} \gamma_\ell$ , for all  $\ell$ . In contrast to the hypothesis test (6.19), this new test requires estimating a single scalar parameter:  $\alpha^{\text{int}}$ . The maximum likelihood estimator for the integrated flux  $\alpha^{\text{int}}$  is:

$$\hat{\alpha}^{\text{int}} = \frac{\mathbf{x}^\top \hat{\mathbb{L}} \hat{\mathbb{L}}^\top \boldsymbol{\beta}'}{\boldsymbol{\beta}'^\top \hat{\mathbb{L}} \hat{\mathbb{L}}^\top \boldsymbol{\beta}'}, \quad (6.22)$$

where  $\boldsymbol{\beta}'$  is the vector of  $\mathbb{R}^L$  whose  $\ell$ -th element is equal to  $\gamma_\ell / \sqrt{v_\ell}$  (the expected  $S/N_\ell$  value if  $\alpha_\ell$  was equal to  $\gamma_\ell$ , i.e.  $\alpha^{\text{int}} = 1$ ). The variance of the estimator  $\hat{\alpha}^{\text{int}}$  is  $(\boldsymbol{\beta}'^\top \hat{\mathbb{L}} \hat{\mathbb{L}}^\top \boldsymbol{\beta}')^{-1}$ . By substituting  $\alpha^{\text{int}}$  with its estimate  $\hat{\alpha}^{\text{int}}$ , another GLRT is obtained:

$$2 \log \frac{p(\mathbf{x} | \mathcal{H}_1, \hat{\alpha}^{\text{int}})}{p(\mathbf{x} | \mathcal{H}_0)} = \frac{(\mathbf{x}^\top \hat{\mathbb{L}} \hat{\mathbb{L}}^\top \boldsymbol{\beta}')^2}{\boldsymbol{\beta}'^\top \hat{\mathbb{L}} \hat{\mathbb{L}}^\top \boldsymbol{\beta}'}. \quad (6.23)$$

Since only positive integrated fluxes  $\alpha^{\text{int}}$  make sense, vectors  $\mathbf{x}$  such that  $\mathbf{x}^\top \hat{\mathbb{L}} \hat{\mathbb{L}}^\top \boldsymbol{\beta}' < 0$  can be discarded. The square root of the GLRT then leads to the test:

$$\text{wS/N} : \frac{\mathbf{x}^\top \hat{\mathbb{L}} \hat{\mathbb{L}}^\top \boldsymbol{\beta}'}{\sqrt{\boldsymbol{\beta}'^\top \hat{\mathbb{L}} \hat{\mathbb{L}}^\top \boldsymbol{\beta}'}} = \sum_{\ell=1}^L w_\ell \cdot \left[ \hat{\mathbb{L}}^\top \mathbf{x} \right]_\ell \underset{\mathcal{H}_0}{\gtrsim} \underset{\mathcal{H}_1}{\tau}, \quad (6.24)$$

which takes the form of a linear combination of the whitened vector of  $S/N_\ell$  values, with weights  $w_\ell$  defined by  $w_\ell = [\hat{\mathbb{L}}^\top \boldsymbol{\beta}']_\ell / \sqrt{\boldsymbol{\beta}'^\top \hat{\mathbb{L}} \hat{\mathbb{L}}^\top \boldsymbol{\beta}'}$ . Like in our previous derivation of  $S/N_\ell$ , wS/N can be interpreted as a signal-to-noise ratio:  $\text{wS/N} = \hat{\alpha}^{\text{int}} / \sqrt{\text{Var}[\hat{\alpha}^{\text{int}}]}$ .

### 6.3.2.4 Robust estimation of the spectral correlations

In the two previous sections, we discuss how modeling the covariance between the detection maps  $S/N_\ell$  at each wavelength could be used to combine the spectral information. In this section, we discuss how to learn the spectral correlation between the maps  $S/N_\ell$ .



When estimating covariance matrices  $\Sigma$ , we face two difficulties: (i) the estimation cannot be performed in the presence of sources (since the spectral correlations would then also depend on the SED of the source and on the values of  $v_\ell$ ), and (ii) the estimation must be local in order to capture the nonstationarities of those correlations.

Since there might be a point source within the region, it is necessary to use a robust estimator  $\hat{\Sigma}$  of the spectral covariance (otherwise, spectral whitening would suppress the source). There are several robust estimators for the covariance, see for example the review in [Hubert et al. \(2008\)](#). The minimum covariance determinant (MCD) method identifies a subset of observations of a fixed size whose covariance matrix has the lowest determinant. To identify this subset quickly, we use the algorithm FAST-MCD introduced in [Rousseeuw and Driessen \(1999\)](#). The region over which an estimate  $\hat{\Sigma}$  is computed must be large enough to guarantee that the area of large  $S/N_\ell$  values corresponding to a point source be considered as an outlier.

Figure 6.8(a)-(f) displays the combined detection maps wS/N obtained on HR 8799 when assuming the SED plotted in (g). The size of the region over which the robust estimation of  $\Sigma$  is performed is given both in terms of pixels and by a disk at the same scale as the detection map. If the spectral covariances are learned in a region that is too small, as in Figure 6.8(a), the detection map is flattened even at the location of the sources. By increasing the size of the region, the robust estimator of the spectral covariance correctly captures the correlations in the absence of sources. However, when the region gets too large, the whitening operation slightly lacks locality.

It can be observed in Figure 6.8 that the empirical distribution in the absence of source correctly matches the expected standard Gaussian model. From a detection map like Figure 6.8(e), it is then possible to detect point sources by thresholding at  $\tau = 5$ , and a binary mask can be obtained in order to mask the point sources. In a second step, the spectral covariance matrices  $\Sigma$  can be re-estimated on much smaller windows by excluding all pixels that fall in the binary mask. Figure 6.9 compares the detection map obtained (a) without spectral whitening, (b) with spectral whitening performed after estimating the spectral covariances over a large area with a robust estimator, and (c) with spectral whitening performed on small areas by computing the sample covariance after discarding of the pixels around the point sources. This last strategy can be applied to small areas ( $R = 300$  pixels), and thus, better eliminate spurious structures in the background. However, it requires a two-step processing: first the computation of the whitened detection map (b) with the robust covariance estimator, then the formation of the exclusion map, the re-estimation of the covariance matrices and the re-computation of a new detection map.

### 6.3.2.5 Optimality of the detection criterion wS/N

Interestingly, wS/N corresponds to the optimal linear combination of the  $S/N_\ell$  values, in the sense that the probability of detection is maximized for all false alarm rates.

The general form of a test based on a linear combination of (whitened)  $S/N_\ell$  values takes the form:

$$\text{wS/N} : \sum_{\ell=1}^L w_\ell \cdot \left[ \hat{\mathbb{L}}^\top \mathbf{x} \right]_\ell \underset{\mathcal{H}_0}{\overset{\mathcal{H}_1}{\gtrless}} \tau, \quad (6.25)$$

where  $w_\ell$  are weights whose value is to be determined.

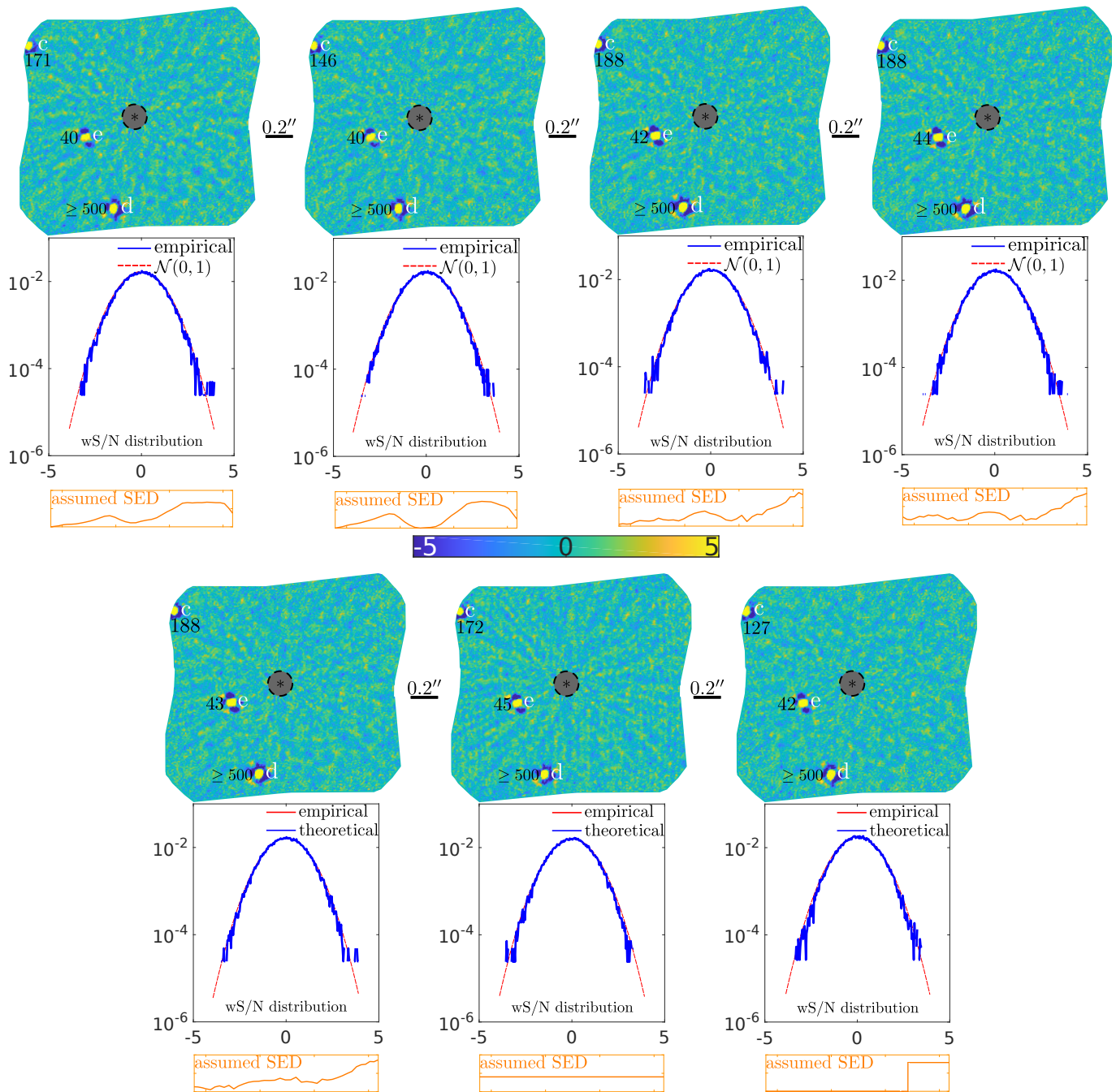


Figure 6.11 – Combined detection map with SED priors: in the absence of sources the empirical distribution matches very closely a Gaussian distribution (red parabola in the log-scale representations).

Under hypothesis  $\mathcal{H}_1$ , the value of wS/N is to be maximized, while the variance of wS/N under  $\mathcal{H}_0$  remains equal to one, so that under  $\mathcal{H}_0$  wS/N is a standard Gaussian variate and a detection threshold can be straightforwardly set.

Since the vector  $\widehat{\mathbb{L}}^\top \mathbf{x}$  follows  $\mathcal{N}(\mathbf{0}, \mathbf{I})$  under  $\mathcal{H}_0$ , the variance of wS/N under  $\mathcal{H}_0$  equals  $\sum_{\ell=1}^L w_\ell^2$ . The constraint that wS/N has unit variance leads to the condition  $\sum_{\ell=1}^L w_\ell^2 = \|\mathbf{w}\|_2^2 = 1$ .

Under  $\mathcal{H}_1$ , the expected value of wS/N is:

$$\mathbb{E}_{\mathcal{H}_1}[\text{wS/N}] = \sum_{\ell=1}^L w_\ell \cdot \left[ \widehat{\mathbb{L}}^\top \mathbb{E}_{\mathcal{H}_1}[\mathbf{x}] \right]_\ell, \quad (6.26)$$

where  $[\mathbb{E}_{\mathcal{H}_1}[\mathbf{x}]]_\ell = \alpha^{\text{int}} \beta'_\ell$ . Equation (6.26) is a scalar product between the vector of weights  $w_\ell$  and the whitened expected S/N $_\ell$  values. Given the normalization constraint  $\|\mathbf{w}\| = 1$ , Equation (6.26) is maximized for a vector of weights that has unit Euclidean norm and is collinear to  $\widehat{\mathbb{L}}^\top \mathbb{E}_{\mathcal{H}_1}[\mathbf{x}]$ . This leads to the following definition of optimal weights:

$$\mathbf{w} = \frac{\widehat{\mathbb{L}}^\top \boldsymbol{\beta}'}{\|\widehat{\mathbb{L}}^\top \boldsymbol{\beta}'\|}, \quad (6.27)$$

which corresponds to the values of the weights obtained in Equation (6.24).

### 6.3.2.6 Combination of S/N maps with spectral whitening

Our approach to combine detection maps computed at different wavelengths is general and can also be applied to the output of other algorithms, as illustrated in Figure 6.10. We process the signal-to-noise ratio maps produced by TLOCI and KLIP algorithms. In (a), we show the combined signal-to-noise ratio obtained by simple averaging, in (b) and (c) we apply a spectral whitening and the prior SED of Figure 6.8(g) according to the definition of wS/N (we have set  $v_\ell = 1$  for both TLOCI and KLIP). In (b), the whitening matrix  $\widehat{\mathbb{L}}$  is computed from the robust covariance estimator applied on a large area, in (c) the two-step approach with masking of the point sources in the second step is applied. The detection maps are clearly improved by our spectral whitening scheme. Compared to PACO-ASDI, the combined detection maps display a lower value for the 3 sources of the field of view as well as some border artifacts, which indicates that modeling the nonstationary spatial covariance also plays an important role in PACO-ASDI.

### 6.3.2.7 Comparison between wGLRT and wS/N

In order to select a detection criterion between wGLRT and wS/N, several aspects must be considered: (i) does the criterion follow the expected distribution under  $\mathcal{H}_0$ , i.e., can detection thresholds be set for prescribed false alarm rates? (ii) how large is the gain obtained when the SED of the source is available? (iii) how does wS/N degrade if the assumed SED differs from the true SED?

Under  $\mathcal{H}_0$ , wGLRT is expected to follow a  $\chi^2$  distribution with  $L$  degrees of freedom, while wS/N is expected to follow a standard Gaussian distribution. The analysis of



Figure 6.7(b) led to the conclusion that the fit with a  $\chi^2$  distribution with  $L$  degrees of freedom was not accurate. Figure 6.11 illustrates the empirical distribution of wS/N for several prior SEDs. For all the SED considered, the empirical distribution is in very good fit with a centered standard Gaussian. A possible explanation for this better fit of wS/N with the theoretical distribution under  $\mathcal{H}_0$  is that the weights  $w_\ell$  give more importance to spectral channels of good quality (i.e., with a low variance  $v_\ell$ ) and that these channels follow more closely our Gaussian model. The good fit of wS/N under  $\mathcal{H}_0$  with the expected distribution makes it possible to reliably set detection thresholds for a prescribed false alarm rate.

In order to assess the gain in detection performance brought by the prior knowledge of the SED of the source, we compare the contrasts achievable at a  $5\sigma$  false alarm rate. We derive the theoretical contrast values based on our statistical modeling even if, in practice, a deviation is observed between the theoretical distribution and the empirical distribution of wGLRT. Under  $\mathcal{H}_0$ , wGLRT is expected to follow a  $\chi^2$  distribution with  $L$  degrees of freedom. The probability of false alarm is thus:  $\text{PFA} = \text{P}(\chi_L^2 > \eta)$ . The probability of detection of a source of flux  $\alpha^{\text{int}}\boldsymbol{\gamma}$ ,  $\text{PD} = \text{P}(\text{wGLRT} > \eta | \mathcal{H}_1)$ , corresponds to the probability that a noncentral  $\chi^2$  distribution with  $L$  degrees of freedom and noncentrality parameter  $(\alpha^{\text{int}})^2 \boldsymbol{\beta}'^\top \widehat{\mathbf{L}} \widehat{\mathbf{L}}^\top \boldsymbol{\beta}'$  exceeds the detection threshold  $\eta$ . This probability corresponds to  $\text{Q}_{L/2}(\alpha^{\text{int}} (\boldsymbol{\beta}'^\top \widehat{\mathbf{L}} \widehat{\mathbf{L}}^\top \boldsymbol{\beta}')^{1/2}, \sqrt{\eta})$ , where  $\text{Q}_M(a, b)$  is Marcum Q-function (Simon, 2007). Hence, the theoretical  $5\sigma$  contrast reached by wGLRT can be computed by first solving the equation  $\frac{1}{\Gamma(L/2)} \gamma(L/2, \eta/2) = \Phi(5)$  for  $\eta$  (where  $\gamma$  is here the lower incomplete gamma function and  $\Phi$  is the cumulative distribution function of the standard normal distribution), and then solving  $\text{Q}_{L/2}(\alpha^{\text{int}} (\boldsymbol{\beta}'^\top \widehat{\mathbf{L}} \widehat{\mathbf{L}}^\top \boldsymbol{\beta}')^{1/2}, \sqrt{\eta}) = 1/2$  for  $\alpha^{\text{int}}$ . For example, when  $L = 39$  (as is the case of SPHERE-IFS), we find  $\eta \approx 100$  and  $\alpha^{\text{int}} \approx 7.87 (\boldsymbol{\beta}'^\top \widehat{\mathbf{L}} \widehat{\mathbf{L}}^\top \boldsymbol{\beta}')^{-1/2}$ .









Since the expectation  $\mathbb{E}[\text{wS/N} | \mathcal{H}_1]$  is equal to  $\alpha^{\text{int}} (\boldsymbol{\beta}'^\top \widehat{\mathbf{L}} \widehat{\mathbf{L}}^\top \boldsymbol{\beta}')^{1/2}$ , the  $5\sigma$  contrast reached by wS/N is readily obtained:  $\alpha^{\text{int}} = 5 (\boldsymbol{\beta}'^\top \widehat{\mathbf{L}} \widehat{\mathbf{L}}^\top \boldsymbol{\beta}')^{-1/2}$ . Including the prior knowledge of the source SED, therefore, improves the contrast by a factor 1.57 (wS/N reaches a theoretical contrast that is 1.57 times better than wGLRT).

Rather than expressing the contrast in terms of the value of the integrated flux  $\alpha^{\text{int}}$  required in order to achieve the detection, it can also be expressed as the flux of the source, at a given wavelength, so that the detection using jointly all wavelengths is possible. This wavelength-specific contrast corresponds to the values  $\alpha_\ell = \alpha^{\text{int}} \gamma_\ell$ . For example, the achievable contrast using only a single detection map  $\text{S/N}_\ell$  is  $5\sqrt{v_\ell}$ . When the multi-wavelength criterion wS/N is applied, if  $\widehat{\mathbf{L}} = \mathbf{I}$  and if the prior actually matches the true SED of the source, then the achievable contrast corresponds to a flux  $5\gamma_\ell / \sqrt{\sum_\ell \gamma_\ell^2 / v_\ell}$  in the  $\ell$ -th channel. Therefore, with respect to the single-wavelength map, the contrast is improved by a factor:

$$\sqrt{1 + \sum_{\ell' \neq \ell} \frac{(\gamma_{\ell'} / \gamma_\ell)^2}{v_{\ell'} / v_\ell}}. \quad (6.28)$$

This factor is strictly greater than one (i.e., the contrast is strictly improved) provided that there is at least one wavelength  $\ell'$ , different from  $\ell$ , such that the SED is non zero ( $\gamma_{\ell'} \neq 0$ ) and the variance is finite ( $v_{\ell'} < \infty$ ). Obviously, if these two conditions are not met, either the source emits no light at the additional wavelengths or no meaningful

Table 6.1 – Degradation of the achievable contrast when the prior SED differs from the true SED (contrast ratio with respect to a detection with the true SED, closer to 1 is better).

true SED:				
prior SED:				
	1.07 ± 0.02	1.11 ± 0.03	1.005 ± 0.001	1.48 ± 0.14
		1.015 ± 0.004	1.04 ± 0.01	1.22 ± 0.06
			1.08 ± 0.02	1.12 ± 0.03
				1.4 ± 0.1

measurement is available so that the performance cannot be improved compared to when using a single wavelength detection map. In all other cases, there is a gain, i.e., the combined detection map leads to a better sensitivity than even the detection map  $S/N_\ell$  at the wavelength providing the best contrast. In particular, if the SED is flat ( $\forall \ell, \gamma_\ell = 1/L$ ) and the variances  $v_\ell$  are all equal, the contrast is improved by a factor  $\sqrt{L}$ , which is to be expected when combining  $L$  measurements of identical statistical weight. This factor should, however, be considered as an upper bound that cannot be reached in practice for several reasons: (i) the whitening matrix  $\hat{\mathbb{L}}$  differs from the identity because of the correlations between channels, the effective number of (independent) channels is, in fact, smaller than  $L$ , (ii) the estimation of matrix  $\hat{\mathbb{L}}$  is performed in two steps and relies, in the second step, on a thresholding strategy that requires a detection to prevent the attenuation of point-like sources, (iii) neither the SED nor the variance are constant with respect to the wavelength, (iv) the true SED of the source may differ from the prior SED used in  $wS/N$ .

Finally, the impact of a mismatch between the assumed SED in  $wS/N$  and the true SED of the source needs to be assessed. This impact can be evaluated by comparing the contrast that is reached when the actual SED is used with respect to the contrast when an incorrect prior SED is used in  $wS/N$ . Let  $\gamma_\star$  be the true SED and  $\beta'_\star$  the vector such that  $\beta'_{\star\ell} = \gamma_{\star\ell}/\sqrt{v_\ell}$  for all  $\ell$ . The achievable contrast under the true SED prior is  $5(\beta'^\top_\star \hat{\mathbb{L}} \hat{\mathbb{L}}^\top \beta'_\star)^{-1/2}$ . Under the incorrect prior  $\gamma$ ,  $wS/N$  is distributed, under  $\mathcal{H}_1$ , according to the Gaussian  $\mathcal{N}(\alpha^{\text{int}}(\beta'^\top_\star \hat{\mathbb{L}} \hat{\mathbb{L}}^\top \beta')(\beta'^\top_\star \hat{\mathbb{L}} \hat{\mathbb{L}}^\top \beta')^{-1/2}, 1)$ . The contrast that is achieved is thus equal to  $5(\beta'^\top_\star \hat{\mathbb{L}} \hat{\mathbb{L}}^\top \beta')^{1/2}/(\beta'^\top_\star \hat{\mathbb{L}} \hat{\mathbb{L}}^\top \beta')$ . With respect to the ideal case where the true SED  $\gamma_\star$  is used as a prior, the achievable contrast is degraded by a factor:

$$\frac{\sqrt{\beta'^\top \hat{\mathbb{L}} \hat{\mathbb{L}}^\top \beta'} \sqrt{\beta'^\top_\star \hat{\mathbb{L}} \hat{\mathbb{L}}^\top \beta'_\star}}{\beta'^\top_\star \hat{\mathbb{L}} \hat{\mathbb{L}}^\top \beta'}, \quad (6.29)$$

which corresponds to the inverse of the normalized correlation between the whitened true SED and the whitened assumed SED.

Table 6.1 reports the factors by which the achievable contrast is degraded when the prior SED differs from the true SED. Due to the symmetry in Equation (6.29), the role of the prior SED and the true SED can be interchanged. These factors have been computed for 1,681 whitening filters computed on a SPHERE-IFS dataset around HR 8799. The mean factor and its standard deviation are reported in the table. When

the true SED and the prior SED are very close (third true SED and first prior, in the table) the contrast degradation is negligible (the factor is not significantly greater than 1). Even when the SED differs significantly (last true SED and first or last prior), the contrast degradation remains modest (at most a factor 1.48 in this case) and smaller than that observed when replacing wS/N by wGLRT (a factor 1.57 was predicted in the previous paragraph).

These comparisons between wGLRT and wS/N lead to a clear conclusion: wS/N is to be preferred since (i) its distribution under  $\mathcal{H}_0$  is more accurately modeled (so that detection thresholds can be automatically set to reach prescribed false alarm rates), (ii) the detection performance is higher when the SED of the source is known in advance, (iii) even if the prior SED used in wS/N differs significantly from the true SED of the source, the detection performance of wS/N is higher than that of wGLRT.

### Exoplanet detection with PACO-ASDI

Based on the PACO-ASDI statistical modeling of the background fluctuations, the final detection maps of PACO-ASDI are obtained in a two steps approach:

1. As described in Chapter 2 for ADI datasets, we derive for ASDI datasets the maximum likelihood estimator of the exoplanet flux at each wavelength, a detection test, and subsequent statistical guarantees:

⇒ The detection test can be interpreted as a signal-to-noise ratio ( $S/N_\ell$ ) for each spectral channel  $\ell$  and follows, in the absence of exoplanet, a centered and reduced Gaussian distribution.

2. The detection can be improved by combining information from different wavelengths. However, we show that the strong spectral correlations of the  $S/N_\ell$  values prevent the setting of a detection threshold at a controlled probability of false alarm on the combined detection quantities.

⇒ The spectral correlations of the  $S/N_\ell$  are learned before combination.

The resulting combined detection criterion (wS/N) also includes a weighting strategy of the  $S/N_\ell$  values based on photometric confidence and (eventually) a SED prior on the exoplanets to be detected. wS/N maps have the following properties:

- they can be thresholded at a controlled probability of false alarm,
- they demonstrate superior detection sensitivity compared to individual  $S/N_\ell$  maps,
- the optional SED prior (if known) further improves the detection performance.

## 6.4 Source characterization

So far, we introduced two modelings of the data: (i) the background model introduced in Section 6.2, accounting for spatial covariances as well as wavelength-specific and time-specific scaling factors, and (ii) the model of the spectral covariances of vectors  $\mathbf{x}$  of  $S/N_\ell$  values. The second model, based on the intermediate detection maps  $S/N_\ell$ , includes both the patch covariances (through the computation of  $S/N_\ell$  values) and the spectral covariances. Rather than performing the astrometric and photometric characterizations of a detected point source based on the neg-log-likelihood  $\mathcal{L}_n$  introduced in Equation (6.1), which does not account for spectral correlations, we define the neg-log-likelihood  $\mathcal{C}$  on the vectors of  $S/N_\ell$  values:

$$\mathcal{C}(\phi_0, \boldsymbol{\alpha}) = -\log p(\mathbf{x} | \phi_0, \boldsymbol{\alpha}, \{v_\ell\}_{\ell=1..L}, \mathbb{L}) = \frac{1}{2} \left\| \mathbb{L}^\top \begin{pmatrix} x_\ell - \frac{\alpha_\ell}{\sqrt{v_\ell}} \\ \vdots \end{pmatrix} \right\|_2^2 + \text{const.}, \quad (6.30)$$

where the vector  $\mathbf{x}$  of  $S/N_\ell$  values is extracted at the integer location  $\lfloor \phi_0 \rfloor$  of the field of view, and variance values  $v_\ell$  depend on the level of background fluctuations in the patches extracted from spectral channel  $\ell$ . The constant term depends only on  $L$  and on the determinant of the whitening matrix  $\mathbb{L}$ .

Similarly to PACO algorithm (see Chapter 2), when characterizing a point source found in the detection map, the background statistics are re-estimated jointly with the determination of the subpixel location and flux of the source. This prevents any bias that may occur due to self-subtraction (computation of the mean patches  $\widehat{\mathbf{m}}_{n,\ell}$  without accounting for the presence of the source). An alternating estimation strategy is carried out by iteratively applying the following steps, see also Figure 6.1:

- Algorithm 6.1 is applied to the residual patches  $\{\mathbf{r}_{\lfloor \phi_{\ell,t} \rfloor, \ell, t} - \alpha_\ell \mathbf{h}_{\lfloor \phi_{\ell,t} \rfloor, \ell}(\phi_{\ell,t})\}_{\ell,t}$ , with  $\boldsymbol{\alpha}$  initially set to  $\mathbf{0}$ , to learn the local background statistics,
- $S/N_\ell$  values  $x_\ell$  and variances  $v_\ell$  are computed for each wavelength,
- the spectral covariance  $\boldsymbol{\Sigma}$  under  $\mathcal{H}_0$  is estimated based on the vectors of values  $x_\ell - \alpha_\ell/\sqrt{v_\ell}$  in a local area centered at  $\lfloor \phi_0 \rfloor$ ; the whitening matrix  $\mathbb{L}$  is then derived by Cholesky factorization of the inverse of  $\boldsymbol{\Sigma}$ ,
- the subpixel location  $\phi_0$  and the flux values  $\alpha_\ell$  are estimated, then all the steps are repeated to improve the background modeling and progressively separate source and background.

The last step, corresponding to the astrometric and photometric estimations, is detailed in the following two subsections.

### 6.4.1 Astrometric estimation

The estimation of the location  $\phi_0$ , with subpixel accuracy, can be performed by maximizing one of the combined-wavelengths detection criteria. In practice, we maximize  $wS/N$  over a refined grid of locations  $\phi_0$  with the current flux estimates as a prior

SED:  $\boldsymbol{\gamma} = \boldsymbol{\alpha}/(\sum_{\ell} \alpha_{\ell})$ . By definition of the GLR, this corresponds to jointly maximizing  $\mathcal{C}(\phi_0, \mathbf{0}) - \mathcal{C}(\phi_0, \boldsymbol{\alpha}^{\text{int}}\boldsymbol{\gamma})$  with respect to the location  $\phi_0$  and the integrated source flux  $\boldsymbol{\alpha}$ .

### 6.4.2 Estimation of the spectral energy distribution

At a given source location  $\phi_0$ , estimating the vector of source fluxes  $\boldsymbol{\alpha}$  by minimizing  $\mathcal{C}$  leads to the following maximum likelihood estimates, for each wavelength:

$$\hat{\alpha}_{\ell} = x_{\ell}\sqrt{v_{\ell}}, \quad (6.31)$$

i.e., the same flux estimates as obtained when computing the  $S/N_{\ell}$  values channel by channel with Equation (6.9). It can be noted that accounting for the spectral correlations does not lead to a different estimator, because  $\hat{\mathbf{L}}$  is non-singular. The estimator covariance, on the other hand, reflects that flux variations are correlated:

$$[\text{Cov}[\hat{\boldsymbol{\alpha}}]]_{i,j} = \sqrt{v_i v_j} [\boldsymbol{\Sigma}]_{i,j}. \quad (6.32)$$

When using instruments with many contiguous spectral bands, a spectral smoothness can also be enforced by favoring fluxes with small variations from one spectral band to the other, as captured by the following regularization term:

$$\mathcal{R}(\boldsymbol{\alpha}) = \frac{1}{2} \|\mathbf{D}\boldsymbol{\alpha}\|_2^2, \quad (6.33)$$

with  $\mathbf{D}$  the matrix of the finite differences.

If a large library of spectra is available, an a priori covariance  $\boldsymbol{\Gamma}$  of the spectrum can be learned, providing a richer modeling than the simple smoothness prior. In the definition of  $\mathcal{R}$ , the matrix  $\mathbf{D}$  is then replaced by  $\mathbf{D} = \boldsymbol{\Gamma}^{-1/2}$ , i.e.,  $\mathcal{R}(\boldsymbol{\alpha}) = -\log p(\boldsymbol{\alpha}) + \text{const} = \frac{1}{2}(\boldsymbol{\alpha} - \bar{\boldsymbol{\alpha}})^{\top} \boldsymbol{\Gamma}^{-1}(\boldsymbol{\alpha} - \bar{\boldsymbol{\alpha}}) = \frac{1}{2} \|\boldsymbol{\Gamma}^{-1/2}(\boldsymbol{\alpha} - \bar{\boldsymbol{\alpha}})\|_2^2$ , where the prior distribution  $p(\boldsymbol{\alpha})$  is a multivariate Gaussian with mean vector  $\bar{\boldsymbol{\alpha}}$  and covariance matrix  $\boldsymbol{\Gamma}$ , see for example Tarantola (2005).

When a regularization term is considered, the estimation of the fluxes  $\boldsymbol{\alpha}$  corresponds to a maximum a posteriori (MAP):

$$\hat{\boldsymbol{\alpha}}^{(\text{MAP})} = \arg \min_{\boldsymbol{\alpha}} \mathcal{C}(\phi_0, \boldsymbol{\alpha}) + \mu \mathcal{R}(\boldsymbol{\alpha}), \quad (6.34)$$

where  $\mu$  is a hyperparameter that controls the amount of smoothing introduced by the regularization term. Since both  $\mathcal{C}$  and  $\mathcal{R}$  are quadratic in  $\boldsymbol{\alpha}$ , the MAP estimate can be obtained in closed form and corresponds to the following linear transform of the vector  $\boldsymbol{x}$  of  $S/N_{\ell}$  values:

$$\hat{\boldsymbol{\alpha}}^{(\text{MAP})} = \underbrace{(\mathbf{V}\hat{\boldsymbol{\Sigma}}^{-1}\mathbf{V} + \mu\mathbf{D}^{\top}\mathbf{D})^{-1}}_{\mathbf{M}(\mu)} \mathbf{V}\hat{\mathbf{L}}\hat{\mathbf{S}}, \quad (6.35)$$

where  $\hat{\mathbf{S}} = \hat{\mathbf{L}}^{\top}\boldsymbol{x}$  is the whitened vector of spectral  $S/N_{\ell}$  values (with  $\hat{\mathbf{L}}\hat{\mathbf{L}}^{\top} = \hat{\boldsymbol{\Sigma}}^{-1}$ ),  $\mathbf{V}$  is a diagonal matrix with diagonal entry  $[\mathbf{V}]_{\ell,\ell} = 1/\sqrt{v_{\ell}}$  and  $\mathbf{M}(\mu)$  is the matrix defining the linear estimator  $\hat{\boldsymbol{\alpha}}^{(\text{MAP})}$ , parameterized by the smoothing parameter  $\mu$ .

Setting the value of the hyperparameter  $\mu$  requires some adaptation to both the SED smoothness and the integrated flux. In order to obtain a detection and characterization method that is fully unsupervised, we investigated several strategies to select automatically the value of  $\mu$ . In the following, we report the different regularization schemes explored.

### 6.4.2.1 Unsupervised setting of the smoothing parameter $\mu$ for SED estimation

We chose to investigate three well-known regularization strategies: (i) the generalized maximum likelihood also known as the evidence method (GML, Wahba et al. (1985); MacKay (1992)), (ii) the generalized cross-validation (GCV, Craven and Wahba (1978); Golub et al. (1979)), and (iii) the Stein's unbiased risk estimator (SURE, Stein (1981)).

The GML estimator first marginalizes the joint distribution  $p(\widehat{\mathbf{S}}, \boldsymbol{\alpha} | \mu, \phi_0)$  with respect to the unknown spectrum  $\boldsymbol{\alpha}$ , then maximizes the so-called generalized likelihood  $p(\widehat{\mathbf{S}} | \mu, \phi_0)$  with respect to  $\mu$ . The resulting optimal parameter  $\widehat{\mu}^{(\text{GML})}$  is given by (see Appendix B for a sketch of proof):

$$\widehat{\mu}^{(\text{GML})} = \arg \min_{\mu} \log \det \mathbf{\Lambda}(\mu) + \widehat{\mathbf{S}}^{\top} \mathbf{\Lambda}^{-1}(\mu) \widehat{\mathbf{S}}, \quad (6.36)$$

where  $\mathbf{\Lambda}(\mu)$  is expressed as:

$$\mathbf{\Lambda}(\mu) = \left( \mathbf{I} - \underbrace{\widehat{\mathbf{L}}^{\top} \mathbf{V} \mathbf{M}(\mu)}_{\mathbf{\Lambda}(\mu)} \right)^{-1}. \quad (6.37)$$

The GCV estimator approximates the error obtained by a leave-one-out validation strategy and is agnostic of the noise variance. The resulting optimal parameter  $\widehat{\mu}^{(\text{GCV})}$  is then (Craven and Wahba, 1978):

$$\widehat{\mu}^{(\text{GCV})} = \arg \min_{\mu} L \frac{\|(\mathbf{I} - \mathbf{A}(\mu)) \widehat{\mathbf{S}}\|_2^2}{\text{tr}^2(\mathbf{I} - \mathbf{A}(\mu))}. \quad (6.38)$$

Since the vector  $\widehat{\mathbf{S}}$  of whitened  $S/N_{\ell}$  values is distributed according to a centered Gaussian distribution, the unbiased risk<sup>2</sup> estimate provided by SURE is then (Thompson et al., 1991):

$$\widehat{\text{risk}} = \frac{1}{L} \|(\mathbf{I} - \mathbf{A}(\mu)) \widehat{\mathbf{S}}\|_2^2 + \frac{2}{L} \text{tr}(\mathbf{A}(\mu)) - 1. \quad (6.39)$$

Therefore, the parameter  $\widehat{\mu}^{(\text{SURE})}$  that minimizes the risk estimate is given by:

$$\widehat{\mu}^{(\text{SURE})} = \arg \min_{\mu} \|(\mathbf{I} - \mathbf{A}(\mu)) \widehat{\mathbf{S}}\|_2^2 + 2 \text{tr}(\mathbf{A}(\mu)). \quad (6.40)$$

Estimating  $\widehat{\mu}^{(\text{GML})}$ ,  $\widehat{\mu}^{(\text{GCV})}$  or  $\widehat{\mu}^{(\text{SURE})}$  from Equations (6.36), (6.38) and (6.40) requires solving a mono-dimensional minimization problem, which can be performed, for instance, by a golden section search (Brent, 2013). Whatever the chosen strategy, once  $\widehat{\mu}$  is obtained, the vector of fluxes is computed by:

$$\widehat{\boldsymbol{\alpha}}^{(\text{MAP})} = \mathbf{M}(\widehat{\mu}) \widehat{\mathbf{S}}. \quad (6.41)$$

The expected gain when regularizing the SEDs by one of the above strategies is a reduction of the MSE ( $\text{MSE} = \langle \|\widehat{\boldsymbol{\alpha}} - \boldsymbol{\alpha}\|^2 \rangle$ ) of the estimation, in particular when the

2. The risk is defined by:  $\text{risk} = \mathbb{E} [\|\widehat{\boldsymbol{\alpha}} - \boldsymbol{\alpha}\|^2]$ .



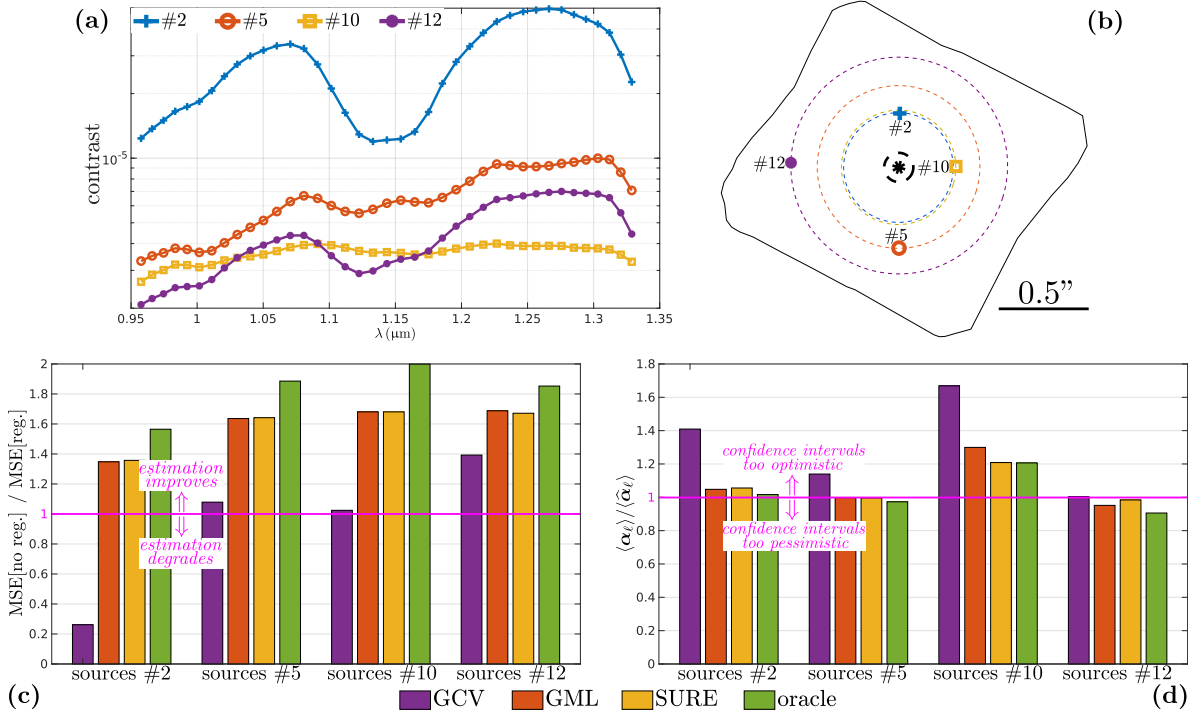


Figure 6.12 – Comparison of the GCV, GML, and SURE regularization strategies on 30 Monte-Carlo injections / SED estimations for sources #2, #5, #10, and #12. (a) ground truth spectra; (b) ground truth angular separations; (c) gain in terms of MSE reduction comparing with the absence of spectral regularization (values higher than one indicates a decrease of the MSE); (d) comparison between the empirical  $1\sigma$  confidence intervals predicted by PACO-ASDI and the empirical ones (values higher than one indicate that predicted confidence intervals are smaller than the empirical ones so that the algorithm estimation is too optimistic).

source contrast is very weak. In the following, we numerically compare these three types of regularization. For this purpose, we perform 30 Monte-Carlo injections and SED estimations on four sources (#2, #5, #10, #12) on a dataset of HD 172555 free from known faint point sources, see Section 6.6.3 for more details about the dataset and the considered injections. For each of the four sources, the injections and SED estimations are done on a circular annulus at a fixed angular separation, see Figure 6.12(a) and (b). Figure 6.12(c) and (d) compare the GCV, GML, and SURE regularization strategies in terms of MSE and agreement between the estimates and empirical  $1\sigma$  confidence intervals. The performance is also given when the regularization hyperparameter  $\mu$  is set in an *oracle* mode, i.e., by selecting  $\mu$  that minimizes the MSE between the SED estimate and the SED ground truth. These experiments illustrate that the GML and SURE approaches lead to very similar results with a slight improvement brought by SURE with respect to GML. In comparison, the GCV leads to significantly worst results. This can be explained by the fact the GCV is generally used when the noise variance is unknown. Regularizing the SED estimation with GML or SURE is beneficial since it reduces the MSE. As expected, the gain brought by the regularization is larger when the contrast of the source is weak and for sources located near the host star, i.e.,

when the estimated SED is very noisy. For example, the MSE is reduced by about 37% for the source #2 (brightest one of the four considered) while it is reduced up to 67% for the source #10 which is the faintest one. In addition, the results obtained with the unsupervised setting of the hyperparameter  $\mu$  by GML or SURE are not very far from the optimal results achieved by the oracle. Finally, as shown by Figure 6.12 (c) and (d), the estimated confidence intervals are in good match with the empirical ones (a factor between 0.94 and 1.21 is observed in our experiments) when the regularization is performed with the SURE approach. More detailed results can be found in Appendix B. In particular, we investigate the influence on the estimate SEDs of the size of the area on which the spectral covariance matrix  $\hat{\Sigma}$  is computed.

In conclusion, estimating  $\mu$  with SURE leads to the best overall performance in our simulations, with a slight improvement over GML and a clear gain with respect to GCV. Thus, based on this study, the hyperparameter  $\mu$  is estimated in an unsupervised fashion with the SURE approach in the following.

### Exoplanet characterization with PACO-ASDI

The SEDs of detected exoplanets from ASDI datasets can be estimated in a similar way to the photometry estimation described in Chapter 2 for ADI datasets: the background statistics, the exoplanet astrometry and photometry are estimated jointly to prevent photometric bias. The proposed procedure differs on two points:

- We account for the spectral correlations of the  $S/N_\ell$  values.
- A spectral smoothness is enforced by favoring fluxes with small variations from one spectral channel to the next. The amount of smoothing is estimated in a data-driven fashion based on the SURE approach.

This framework allows to obtain:

- estimates of the SED of the detected exoplanets that have an optimal bias/variance tradeoff,
- reliable confidence intervals,
- a low risk (close to the minimal achievable one with our estimator) thanks to the automatic spectral regularization.

## 6.5 Implementation details of PACO-ASDI

The same implementation considerations than the ones derived in Section 2.4 for PACO can be considered with PACO-ASDI:

- *optimal patch size* – We apply the empirical rule derived in Section 2.4.1: we chose the patch size as twice the off-axis PSF FWHM. The relevance of this criterion is illustrated by Figure 6.13(a). Two GLRT<sup>+</sup> maps on a dataset around HR 8799 are obtained by PACO-ASDI using two different patch sizes:  $K = 49$  pixels which corresponds to the patch size derived for the SPHERE-IRDIS data in K1-K2 spectral band (i.e,  $\lambda \in [2.11 \mu\text{m}; 2.25 \mu\text{m}]$ ), and  $K = 113$  pixels which corresponds to the patch size derived for the considered SPHERE-IFS data in Y-H spectral band (i.e,  $\lambda \in [0.96 \mu\text{m}; 1.64 \mu\text{m}]$ ). While the mean level of the background structures is not significantly different in the two examples, we observe that the source throughput is lower when the patch size is not adapted to the spatial spread of the off-axis PSF. Note that since each spectral channel at wavelength  $\lambda$  of the raw ASDI data is zoomed before processing by the factor  $\lambda_{\text{ref}}/\lambda$  to spectrally co-align the speckles, the signature of the sources takes the form of the off-axis PSF at the wavelength  $\lambda_{\text{ref}}$  on the different spectral channels. In all the experiments of this Chapter, we fixed  $\lambda_{\text{ref}}$  at  $\lambda_L$ , i.e. at the largest wavelength.
- *taking into account missing data* – We apply the trick described in Section 2.4.2. Aberrant data arising on the borders of the field of view and the missing data due to the different zooming factors applied to each spectral channel of ASDI data are taken into account by binary masks. Denoting  $R \times C$  the spatial size of the raw ASDI data frames (before spectral zooming), the PACO-ASDI results are of size  $\lfloor \sqrt{2}R \rfloor \times \lfloor \sqrt{2}C \rfloor$ . As for PACO, it is theoretically enough that an exoplanet (with a sufficient level of contrast) be seen in the field of view at a single wavelength or a single time in the zoomed data to be possibly detected. Consequently, PACO-ASDI outputs should be adapted by considering in the summation only terms at wavelength(s)  $\ell$  and time(s)  $t$  for which the expected location  $\phi_{\ell,t}$  of the exoplanet lies in the masks defining the valid field of view. Figure 6.13(b) illustrates this principle and emphasizes that only a central area of the field of view ( $\simeq 34\%$  of the whole field of view) is covered by all rescaled images for SPHERE-IFS data in Y-H spectral band. We show in Section 6.6.2.1 that taking into account both the aberrant and missing data is important to detect sources that are not located in this central area.
- *fast and approximate version of PACO-ASDI for large surveys* – We derive a **fast** PACO-ASDI algorithm as described in Section 2.4.4 for **fast** PACO. The acceleration relies on the pre-computation of terms that appear multiple times in the sums of Equations (6.10) and (6.11) when considering all possible source locations. Computations of the background statistics are thus recycled. The S/N map and other outputs are obtained in a second step by interpolating the pre-computed terms. For the reasons discussed in Section 2.4.4, the fast version has a computational burden reduced by a factor at least equal to the number  $TL$  of temporal and spectral frames. For example, the application of this fast algorithm requires approximately 15 minutes to process (until S/N $_{\ell}$  combination) a dataset

made of  $T = 56$  temporal frames and  $L = 39$  spectral channels of size  $496 \times 496$  (after chromatic zooming). The computation time required for the  $S/N_\ell$  combination including the robust estimation of the spectral correlations depends only on the number of spectral channels and takes approximately 15 more minutes for  $L = 39$  spectral channels. In comparison, the non-fast and complete algorithm requires approximately 500 hours to process a similar dataset using a basic parallelization done in MATLAB<sup>TM</sup> on 24 cores (processor INTEL<sup>TM</sup> Xeon E5-46170 at 2.90 GHz and  $K = 113$  pixels per patch). Since this time is prohibitive, we use only the **fast** PACO-ASDI framework to produce the detection results defined in Section 6.3. The use of the non-fast PACO-ASDI is reserved to the characterization step that extracts unbiased astrometry and photometry information on small areas around detected sources, as described in Section 6.4.

- *sampling of possible exoplanet locations* – As described in Section 2.4.5 for PACO, the direct model of PACO-ASDI does not impose any finite precision for the source position  $\phi_{\ell,t}$  in each frame, so detection maps and other quantities defined in Section 6.3 can be computed at a resolution small enough to avoid the possible negative bias due to the finite sampling of the data. The ratio  $\mathbb{E}(S/N(\mathcal{G}_s(\phi_0) | \phi_0))/\mathbb{E}(S/N(\phi_0 | \phi_0))$  defined in Equation (2.40) informing about the fraction of S/N lost due to the sampling grid  $\mathcal{G}_s$  under consideration (where  $s$  is the number of nodes per pixel), can be adapted to the quantities  $S/N_\ell$  produced by PACO-ASDI with the ratio  $\mathbb{E}(S/N_\ell(\mathcal{G}_s(\phi_0) | \phi_0))/\mathbb{E}(S/N_\ell(\phi_0 | \phi_0))$  where:

$$\mathbb{E}(S/N_\ell(\phi | \phi_0)) = \alpha_\ell \frac{\sum_{t=1}^T \mathbf{h}_{[\phi_{\ell,t}]}(\phi_{\ell,t})^\top \cdot \hat{\mathbf{C}}_{[\phi_{\ell,t}]}^{-1} \cdot \mathbf{h}_{[\phi_{\ell,t}]}(\mathcal{F}_{\ell,t}(\phi_0))}{\sqrt{\sum_{t=1}^T \mathbf{h}_{[\phi_{\ell,t}]}(\phi_{\ell,t})^\top \cdot \hat{\mathbf{C}}_{[\phi_{\ell,t}]}^{-1} \cdot \mathbf{h}_{[\phi_{\ell,t}]}(\phi_{\ell,t})}}. \quad (6.42)$$

Figure 6.13(c) gives examples of  $S/N_\ell$  maps at  $\lambda_{39} = 1.64 \mu\text{m}$  computed with  $s = 1$  and  $s = 4$ . It emphasizes that the choice  $s = 4$  (oversampling of the data with 4 nodes per pixel) leads to a negative bias on  $S/N_\ell$  lower than 1%.

- *unsupervised detection and characterization* – Like PACO, the PACO-ASDI algorithm is totally unsupervised, no tuning parameter is necessary. The regularization of the covariance matrices is based on automatic shrinkage, the patch size  $K$  is constant for a given instrument, the size  $R$  of the areas used to compute robustly the spectral correlations of  $S/N_\ell$  values is fixed since it depends only on the spatial spread of the source signature which is almost constant for a given instrument, the detection threshold  $\tau$  is set according to a prescribed false alarm rate, and the regularization of the estimated SEDs is performed automatically with SURE.

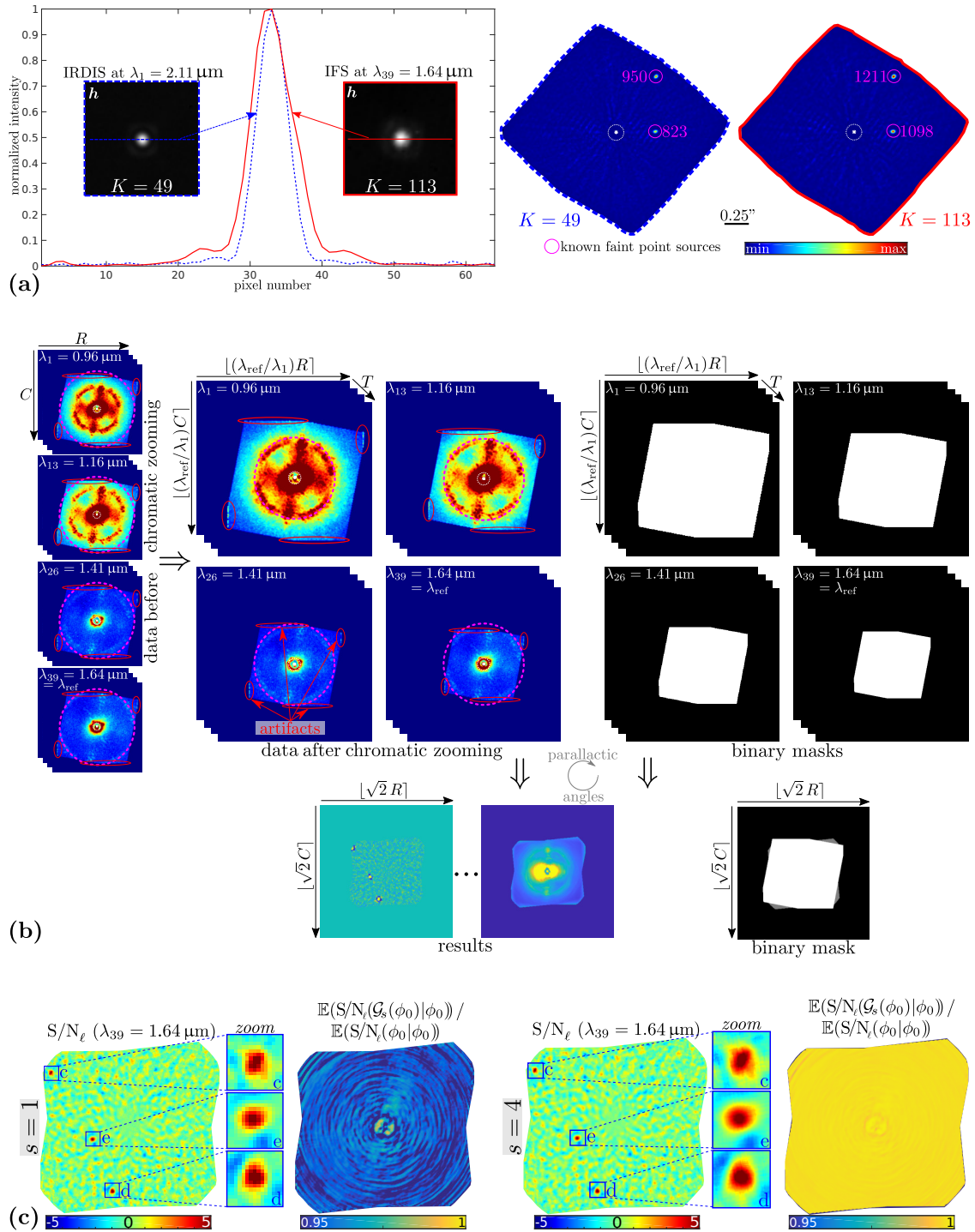


Figure 6.13 – Implementation details of PACO-ASDI. (a) *optimal patch size* – two different patch-size adapted to two off-axis PSF (left) and the resulting GLRT<sup>+</sup> maps (right). (b) *missing data* – the raw data are spectrally zoomed to co-align the speckles; aberrant data (circled in red) that are on the borders of the field of view are discarded by binary masks; the resulting total field of view accounts for the parallax rotation. Magenta dashed circles indicate speckles around the correction limit of the coronagraph which are not aligned before chromatic zooming. (c) *sampling* –  $S/N_\ell$  at  $\lambda_{39} = 1.64 \mu\text{m}$  and sampling ratio  $\mathbb{E}(S/N(\mathcal{G}_s(\phi_0)|\phi_0))/\mathbb{E}(S/N(\phi_0|\phi_0))$  for two values of the sampling factor:  $s = 1$  (1 node per pixel), and  $s = 4$  (oversampling, 4 nodes per pixel).

Table 6.2 – Observation logs of the considered ASDI datasets.  $\Delta_{\text{par}}$  is for the total amount of rotation of the field of view and the seeing value was reported at the beginning of the observations. (\*): The recorded dataset around HD 172555 was made of 62 temporal frames but we selected  $T = 31$  frames by discarding one of them over two, preserving the amount of the parallactic rotation  $\Delta_{\text{par}}$  to slightly increase the difficulty of the SED estimation task.

Target	ESO ID	Obs. date	$T$	$\Delta_{\text{par}}$	Seeing
HR 8799	095.C-0298	2015-07-04	46	16.4°	1.43
$\beta$ Pictoris	097.C-0865	2016-09-16	116	38.5°	0.45
HD 131399	095.C-0389	2015-06-12	49	37.2°	1.30
HD 172555	095.C-0192	2015-07-11	31*	12.9°	1.20

## 6.6 Performance evaluation with on-sky data

In this section, we assess the performance of the proposed PACO-ASDI algorithm both in terms of source detection and SED estimation.

### 6.6.1 Datasets and algorithms description

The PACO-ASDI results are compared to two standard algorithms: TLOCI and KLIP (see Section 2.2 for a description). These two algorithms are currently used for the exploitation of the SPHERE science data (Lagrange et al., 2019a; Mesa et al., 2019a; Gratton et al., 2019; Gibbs et al., 2019; Maire et al., 2019). In the following, they are applied both in ADI and ASDI mode. In ADI mode, each spectral channel is processed independently. A combined detection map is obtained by a simple summation of the detection maps from the different spectral channels. The SED estimation is obtained by a photometry estimation per wavelength. The reason we considered the ADI mode is that it is a common practice to process independently each spectral channel of an ASDI series. We used the SpeCal (Galicher et al., 2018) implementation of TLOCI-A(S)DI and KLIP-A(S)DI algorithms of the SPHERE data center (Delorme et al., 2017). There are several variants of this implementation, especially for the KLIP-ASDI method. However, these custom routines are not necessarily public and the corresponding description of the implementation is not always published too. We have performed some tests with these alternative implementations that are not reported in this document. In spite of the peculiarities of these alternative routines, we reached the same general conclusions. Comparative results from state-of-the-art algorithms are kindly provided by Maud Langlois.

For the comparisons, we selected four datasets from the SPHERE-IFS instrument obtained in various conditions of observation leading to different degrees of difficulty for the detection and estimation tasks. Three of these datasets are dedicated to the evaluation of the detection performance on fields reported in the literature to contain point sources. The fourth one is used for the evaluation of the SED recovery performance. We numerically injected fake point sources at low fluxes to perform this evaluation. The four datasets considered were recorded around the following reference targets:

- HR 8799 (HIP 114189) which is a A5V type star located in the Pegasus constellation. It hosts four confirmed exoplanets, only three of them (HR 8799 c, d and e)



are within the SPHERE-IFS field of view (the last one, HR 8799 b, is visible with the larger field of SPHERE-IRDIS). All of them were discovered (Marois et al., 2008), confirmed (Marois et al., 2010) and widely studied (Bowler et al., 2010; Currie et al., 2011; Marley et al., 2012) by direct imaging. In the following, this dataset is used as a baseline to compare the overall performance of the detection algorithms on sources at a standard level of contrast (between  $10^{-6}$  and  $10^{-5}$ ) in the considered spectral band.

- $\beta$  Pictoris (HIP 27321) which is a A6V type star located in the Pictor constellation. It hosts two known exoplanets ( $\beta$  Pictoris b and c) as well as a protoplanetary disk made of gas and dust (too sparse to be visible within the field of view of the SPHERE-IFS imager).  $\beta$  Pictoris b was discovered (Lagrange et al., 2009) and confirmed (Lagrange et al., 2010) by direct imaging.  $\beta$  Pictoris c was discovered very recently by the radial velocities method (Lagrange et al., 2019b). In the following, we do not consider the presence of  $\beta$  Pictoris c any more<sup>3</sup>. New datasets around this star are currently under analysis to complete the orbit of  $\beta$  Pictoris b and to refine its photometry (Lagrange et al., 2019a). In the following, we use a dataset at a challenging epoch since the angular separation of the exoplanet is smaller than 0.15 arcsec, which corresponds to 9 pixels after the coronagraph mask.
- HD 131399 (HIP 72940) which is a A1V type star located in the Centaurus constellation. It forms a triple system with two other stars (HD 131399 B and C) located about 349 AU from the brightest star HD 131399 A (De Zeeuw et al., 1999; Dommangeat and Nys, 2002; Pecaute and Mamajek, 2013). This system also hosts a faint point source (HD 131399 Ab) discovered by direct imaging (Wagner et al., 2016), at first supposed to be a bounded exoplanet. However, further joint analysis of GEMINI/GPI and VLT/SPHERE datasets to refine the astrometry and the SED estimation of the candidate companion led to the conclusion that HD 131399 Ab is more likely to be a background brown dwarf (Nielsen et al., 2017). In the following, this dataset is used to compare the behavior of detection algorithms in the case of a faint point source falling close to the limit of the instrument's field of view.
- HD 172555 (HIP 92024) which is a A5V type star located in the Pavo constellation (Schütz et al., 2005; Lisse et al., 2009). The analysis of directly imaged (A)(S)DI series was conducted in several surveys but, to the best of our knowledge, no point source was ever detected (Nielsen et al., 2008; Nielsen and Close, 2010). We use this dataset to conduct the SED estimation of numerically injected fake point sources.

Table 6.2 summarizes the main observation parameters of these datasets.

---

3.  $\beta$  Pictoris c has a very small angular separation with its host star (0.10-0.15 arcsec at its maximal elongation). For comparison, the limit of the classical coronagraphs of SPHERE-IRDIS masking the host star and its close environment is 0.125 arcsec. Besides,  $\beta$  Pictoris c has a very low contrast given its separation (about  $1 \times 10^{-4}$  in the H Johnson's band). For these two reasons, it could be detected by direct imaging when it is at its maximal elongation only, given the current instrumental and processing capabilities, see Lagrange et al. (2019b).

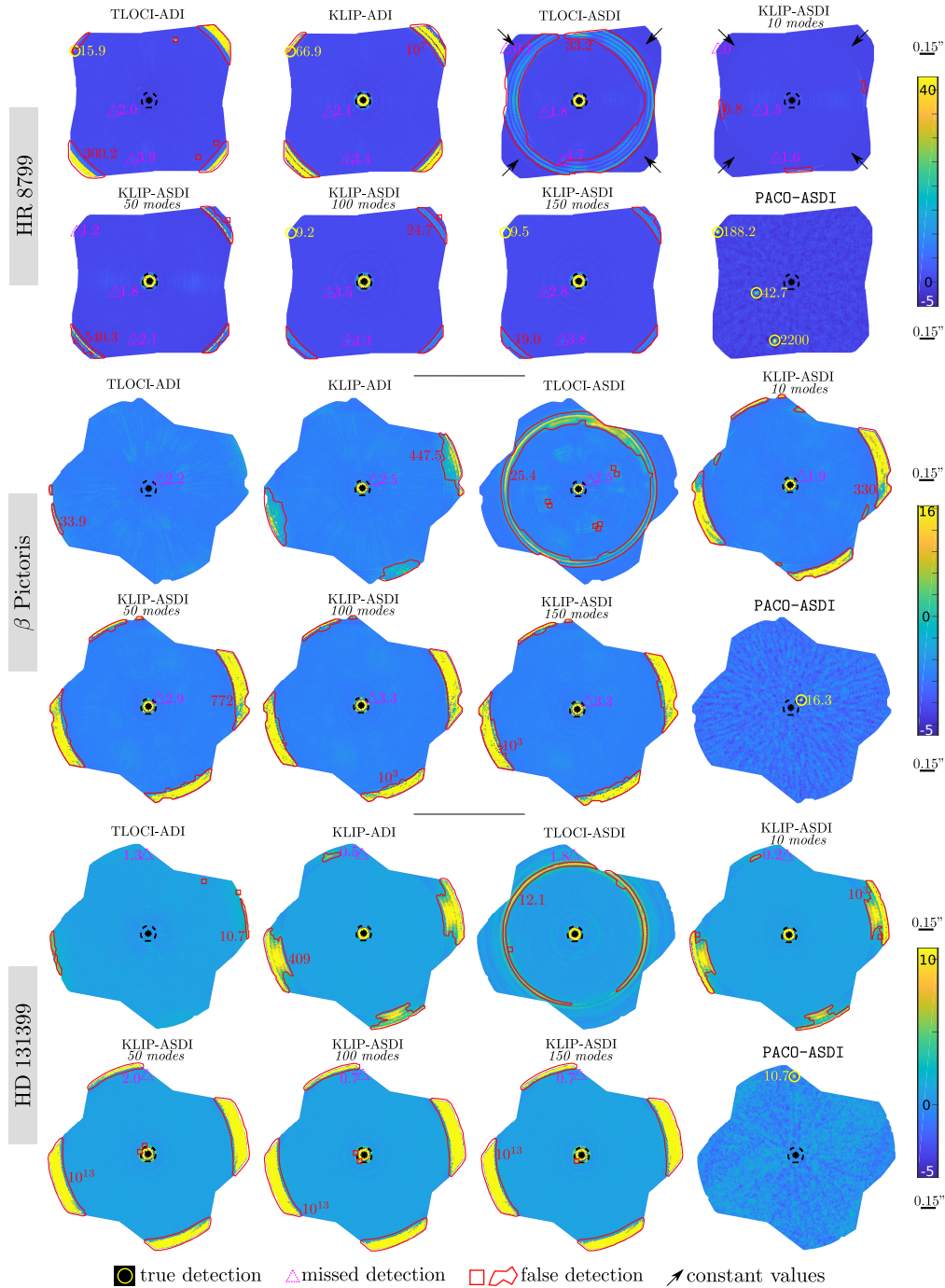


Figure 6.14 – Detection maps (wS/N for PACO-ASDI and combined-S/N for the other algorithms) around HR 8799,  $\beta$  Pictoris and HD 131399 obtained with TLOCI-ADI, KLIP-ADI (50 modes), TLOCI-ASDI, KLIP-ASDI (10, 50, 100 and 150 modes) and the proposed PACO-ASDI algorithm. The color bars are common for all methods and are set between -5 and the highest true detection peak provided by PACO-ASDI (excepted for HR 8799 for which the color bar is set between -5 and 42.7 corresponding to the wS/N value of HR 8799 e with PACO-ASDI). The detection threshold is set at  $\tau = 5$  and the values above this threshold are classified as true detections (yellow circles) and false detections (red squares and polygons). Missed detections are indicated by pink triangles. The value of the largest false alarm is also indicated in red on each map. Black arrows point at areas with constant values.

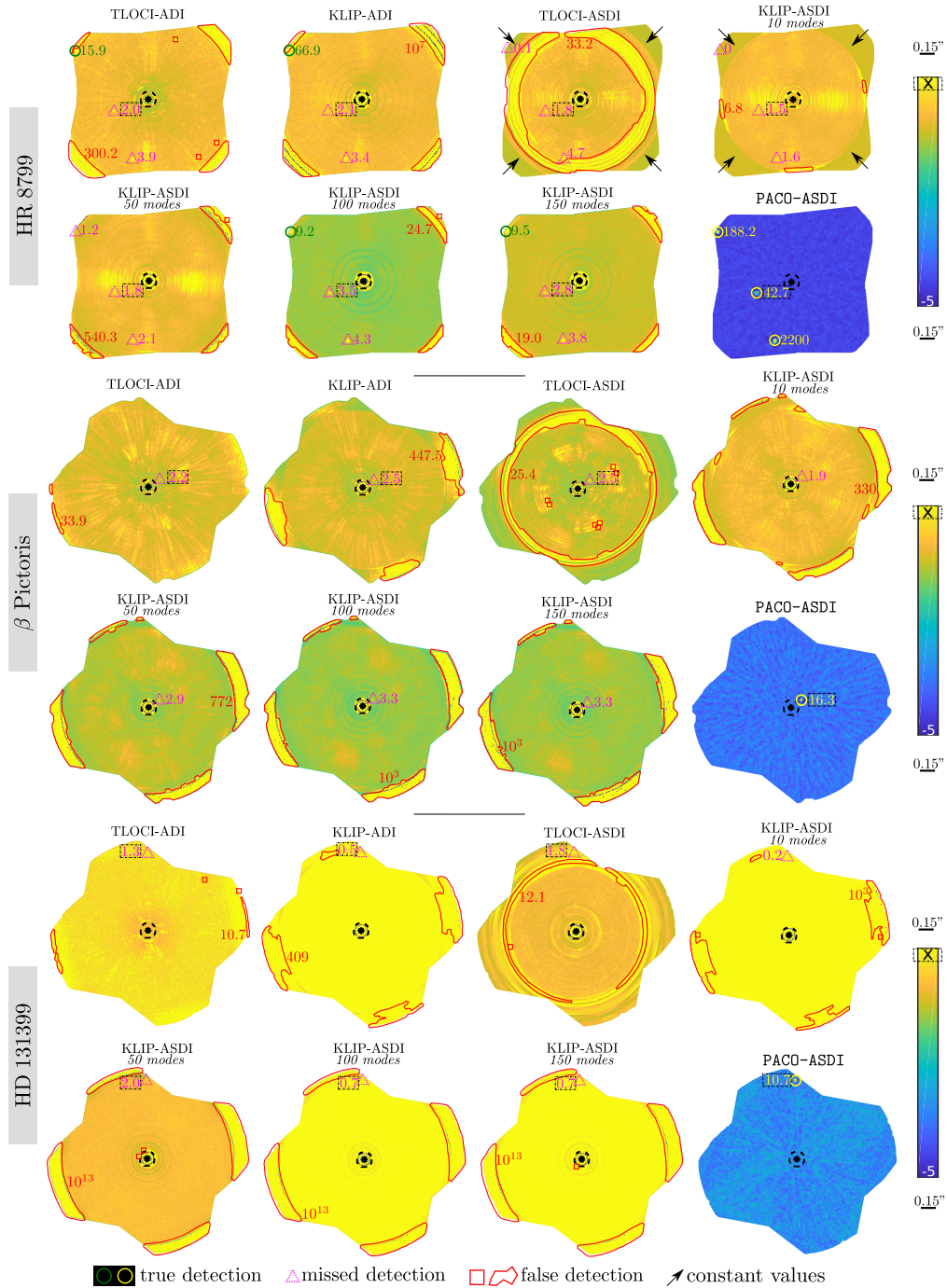


Figure 6.15 – Same caption than Figure 6.14. The color bars are adapted to each method and are set between -5 and the detection peak associated with one of the real sources to be detected (respectively HR 8799 e which is the closest to the host star,  $\beta$  Pictoris b, and HD 131399 Ab).

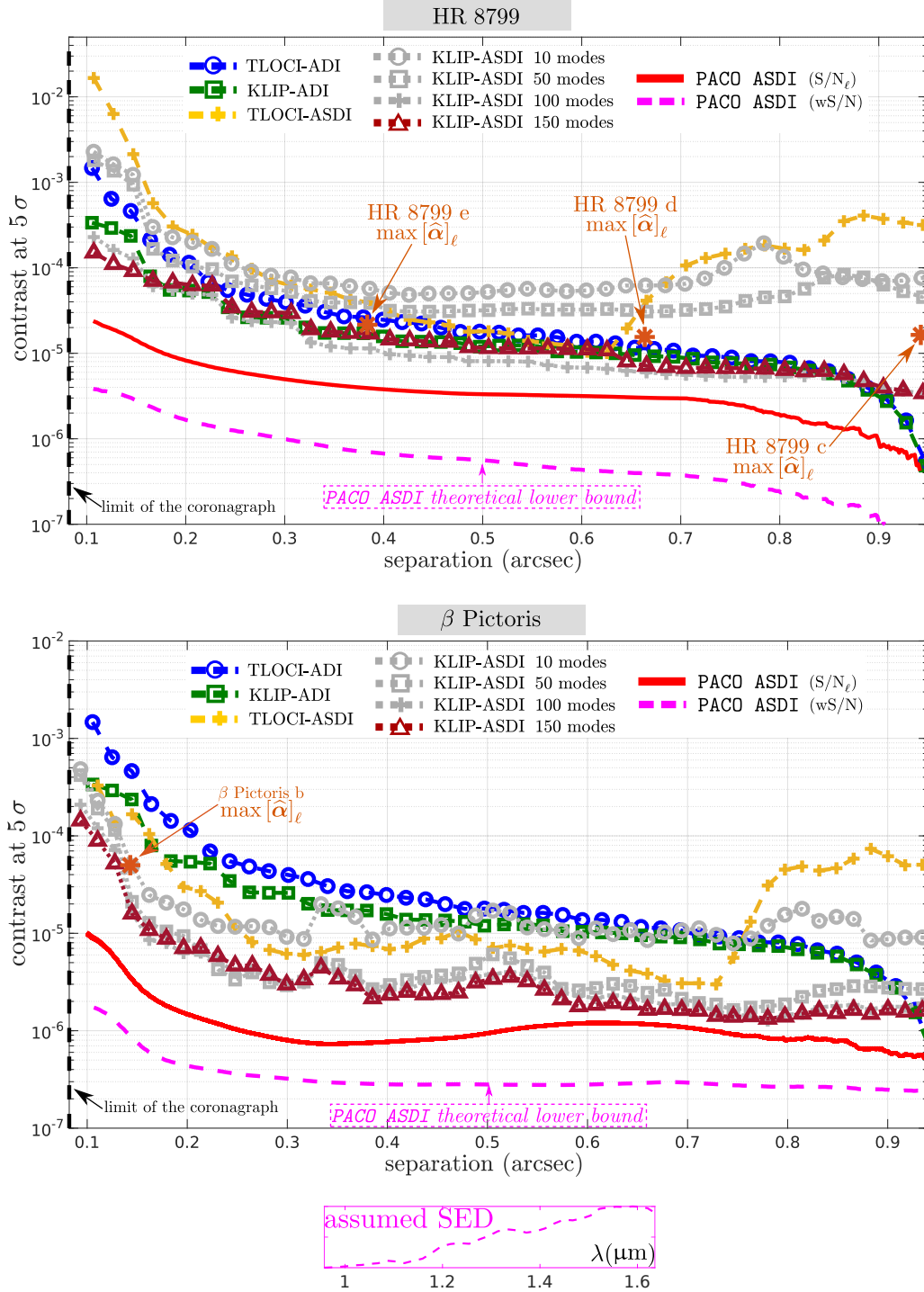


Figure 6.16 – Achievable  $5\sigma$  contrast curves on HR 8799 and  $\beta$  Pictoris obtained with TLOCI-ADI, KLIP-ADI, TLOCI-ASDI, KLIP-ASDI, and PACO-ASDI. All curves correspond to the mean contrast along spectral channels. For PACO-ASDI, the solid red line is for the spectral mean  $S/N_\ell$  estimated contrast while the dashed pink line is for the combined  $wS/N$  contrast estimated assuming the SED given at the bottom as prior. Contrast curves as provided by KLIP and TLOCI do not correspond to a  $5\sigma$  false alarm rate contrarily to the contrast curves of PACO-ASDI. The achievable contrasts are thus significantly over-optimistic for KLIP and TLOCI, see discussion in the text (Section 6.6.2.2).



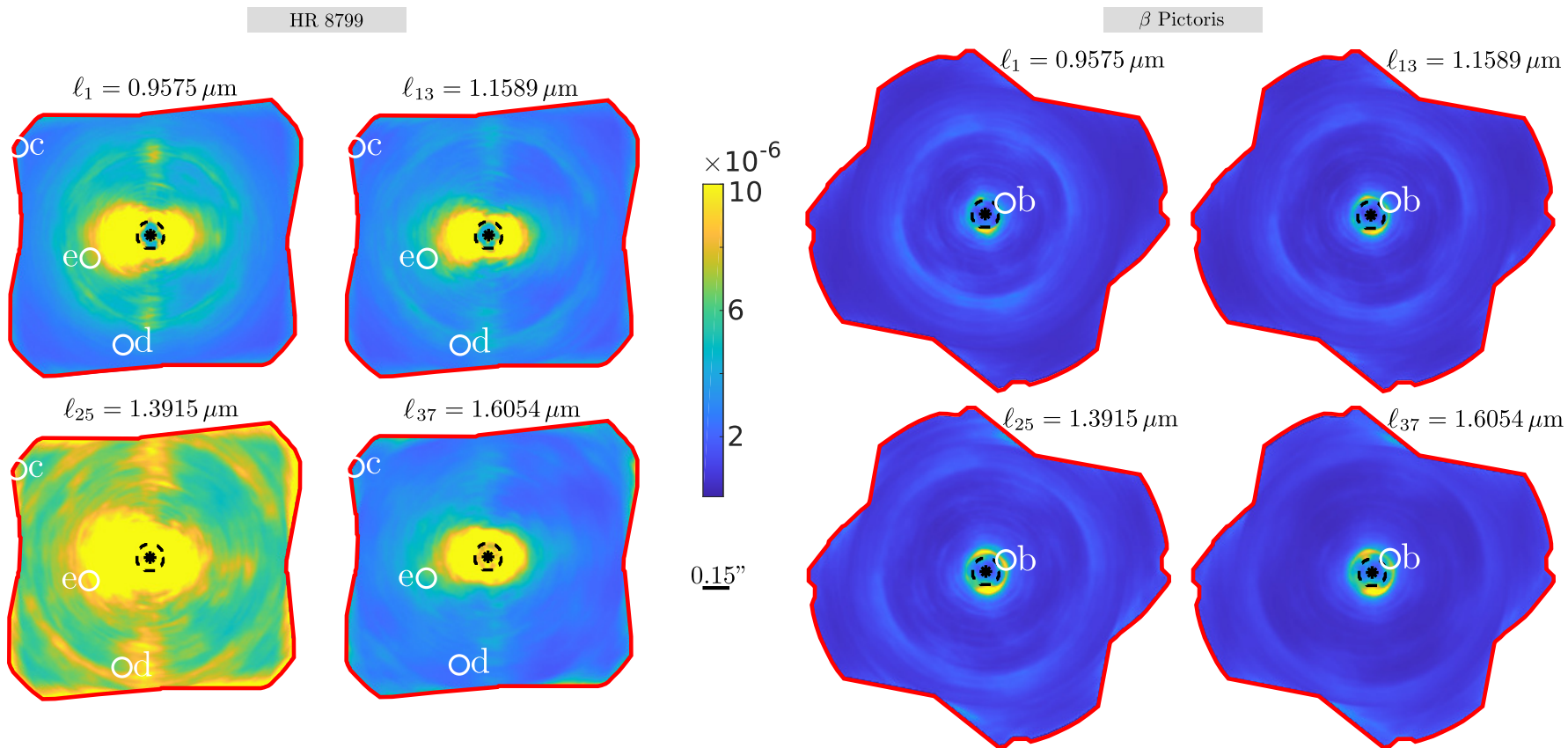


Figure 6.17 – Examples of 2-D  $S/N_\ell$  contrast maps estimated by PACO-ASDI for four spectral channels:  $\lambda_1 = 0.96 \mu\text{m}$ ,  $\lambda_{13} = 1.16 \mu\text{m}$ ,  $\lambda_{25} = 1.39 \mu\text{m}$ , and  $\lambda_{37} = 1.61 \mu\text{m}$  on HR 8799 and  $\beta$  Pictoris. The superimposed white circles represent the locations of the known exoplanets (HR 8799 c, d, e, and  $\beta$  Pictoris b).

## 6.6.2 Detection performance

### 6.6.2.1 Detection results

In the following, the detection is done using wS/N map with PACO-ASDI since it offers interesting properties in terms of detection sensitivity and controlled false alarm rate when thresholding at  $5\sigma$  (see Section 6.3.2.3). In our comparison to the state-of-the-art algorithms, we use the final signal-to-noise map (denoted *combined S/N*) provided by the different pipelines. The combined S/N map is generally obtained with a simple weighted mean of the signal-to-noise ratio computed in each channel. This combination is generally followed by a post-processing step via so-called *unsharp filtering* (high pass filtering) to improve the visual quality of the combined S/N map by attenuating some spurious background artifacts. In PACO-ASDI, the spatial whitening and spectral whitening operations can be seen as data-driven and locally-adaptive filters. No additional filtering is required to enhance the detection maps produced by PACO or PACO-ASDI.

Figures 6.14 and 6.15 show the combined detection maps around HR 8799,  $\beta$  Pictoris, and HD 131399 obtained with TLOCI-ADI, KLIP-ADI, TLOCI-ASDI, KLIP-ASDI, and PACO-ASDI for two sets of color bars. The detection is performed by thresholding the maps at  $\tau = 5$  (corresponding to a PFA =  $2.87 \times 10^{-7}$ ), as classically done in direct imaging. Several observations can be made:

State-of-the-art algorithms lead to strong background structures due to a miss-modeling of the spatial and spectral correlations. In addition, the detection seems very difficult in the regions close to the borders of the instrument’s field of view due to strong artifacts, in particular with TLOCI-ADI and KLIP-ADI, possibly due to a miss-modeling of the aberrant data occurring on the borders. For example, distinguishing the signature of the exoplanet HR 8799 c (top-left corner of the field of view) from the artifacts seems almost impossible with TLOCI-ADI and KLIP-ADI. In ASDI mode, the quality of the detection maps is generally not significantly better in these areas due to artifacts (in particular with TLOCI-ASDI) or regions with zeros or constant values obtained with KLIP-ASDI (indicated by arrows in the figures), possibly caused by the absence of explicit modelization of areas with missing data for the longest wavelengths. All these sources of artifacts cause a severe limitation of the workable field of view in which an exoplanet can be actually detected. The unusable portion of the field of view increases with the parallactic rotation and with the ratio  $\lambda_{\max}/\lambda_{\min}$ . It reaches more than 20% for TLOCI-ASDI on the  $\beta$  Pictoris and HR 8799 datasets. PACO-ASDI provides stationary detection maps on the whole field of view (including at the vicinity of the host star and close to the borders of the field of view) so that a unique detection threshold can be set. The stationarity is explained both by the local statistical modeling of spatio-spectral correlations of the background and the explicit consideration of the missing and/or aberrant data which are flagged as outliers.

Regarding the detection accuracy of the algorithms, only PACO-ASDI ensures a statistically-grounded control of the PFA in the sense that no false alarm is generally observed at the  $5\sigma$  threshold. Unlike PACO-ASDI, all other algorithms considered lead to several false detections in the field of view (many more than expected at  $5\sigma$ ). In practice, astronomers are familiar with the “false alarms issue” and generally try to differentiate candidate companions from the false alarms by visual inspection of the



data and of the reduction results, a very time-consuming task.

Regarding the detection sensitivity of the tested algorithms, only PACO-ASDI leads to detection peaks significantly higher than the conventional detection threshold ( $\tau = 5$ ) for all the known point sources, even when they are close to the host star (as  $\beta$  Pictoris b) or close to the borders of the field of view (as HD 131399 Ab). For example, for HR 8799, only one source can be unambiguously detected at  $5\sigma$  with state-of-the-art algorithms. The other sources can be distinguished by visual inspection of the detection maps but require to lower the detection confidence at about 3.5 for the exoplanet HR 8799 e and at 4.3 for the exoplanet HR 8799 d. The best results with existing methods are obtained with KLIP-ADI, leading to the detection of HR 8799 c (top-left corner of the field of view) at a combined signal-to-noise ratio equal to 66.9. On the same dataset, the three known exoplanets are detected with PACO-ASDI and the wS/N reaches 188.2 for HR 8799 c. For  $\beta$  Pictoris and HD 131399, only PACO-ASDI can detect the known sources without any false alarm in the field of view. Lowering the detection threshold with TLOCI-A(S)DI and KLIP-A(S)DI leads to several false alarms in the field of view thus preventing their automatic detection. Moreover, our experiments tend to show that in certain cases it is not so easy to distinguish true detections from false alarms via visual inspection: on the considered  $\beta$  Pictoris dataset processed with TLOCI-A(S)DI and KLIP-A(S)DI algorithms, it seems difficult to us to visually discriminate  $\beta$  Pictoris b (combined S/N  $\in [1.9; 3.3]$ ) and HD 131399 Ab (combined S/N  $\in [0.2; 2.0]$ ) from false alarms since the shape of the detection peaks (blobs spatially correlated on a few pixels) are very similar.

### 6.6.2.2 Achievable contrast

In this section, we compare the minimal contrast required to achieve a detection with PACO-ASDI to the contrasts of TLOCI and KLIP. As is done in the literature, we derive the so-called  $5\sigma$  *contrast curves* representing the minimum contrast of a source to still be detected with a probability of detection PD = 0.5 when the detection threshold is set to obtain a probability of false alarm PFA =  $2.87 \times 10^{-7}$ . This achievable contrast can be computed for the single-wavelength detection maps. As detailed in Section 6.3.2.3, the  $5\sigma$  contrast in channel  $\ell$  is  $5\sqrt{v_\ell}$  (the minimum contrast  $\alpha_\ell$  of the source in the spectral channel  $\ell$  so that  $P(S/N_\ell > \tau) = 0.5$ ). As detailed in Section 6.3.2.3, the combination of the  $S/N_\ell$  maps improves the achievable contrast. When the combined detection map wS/N is used, the achievable contrast in spectral channel  $\ell$  is  $5(\beta_\star^\top \hat{\mathbb{L}} \hat{\mathbb{L}}^\top \beta'_\star)^{-1/2}$  if the prior SED perfectly matches the source SED.

Figure 6.16 gives the achievable  $5\sigma$  contrast curves obtained with TLOCI-ADI, KLIP-ADI, TLOCI-ASDI, KLIP-ASDI, and PACO-ASDI on HR 8799 and  $\beta$  Pictoris. For PACO-ASDI, both the  $S/N_\ell$  contrast and the combined wS/N contrast are represented.

- Considering the  $S/N_\ell$  contrast curves of PACO-ASDI, a clear gain is observed at small angular separations ( $\leq 0.7$  arcsec) comparatively to the state-of-the-art algorithms. At larger separations, this gain is maintained except for KLIP-ASDI which can reach better contrasts. However, as already observed and discussed in Section 2.5.3.2 on ADI series, contrast curves produced by state-of-the-art algorithms are often overly optimistic both in terms of PD and PFA. These previous observations also verify here in ASDI mode: all detection maps of state-of-the-

arts algorithms present many more false alarms than what would be expected at  $5\sigma$ . According to Figure 6.16, far from the  $\beta$  Pictoris star, the best achievable contrast is reached when using KLIP-ASDI with 150 modes and PACO-ASDI that approximately converge towards the same detection limit. However, Figures 6.14 and 6.15 show that KLIP-ASDI produces several false alarms in the field of view and a lower signal-to-noise ratio for the exoplanet  $\beta$  Pictoris b compared to PACO-ASDI. With KLIP-ASDI, the largest value of a false alarm is significantly higher than 5, while it should be very unlikely to have a background value larger than 4.0. This illustrates that the  $5\sigma$  contrast of state-of-the-art algorithms does not correspond to the expected level of PFA and can thus only be used to perform relative comparisons.

- Considering the wS/N contrast curves of PACO-ASDI, obtained when single-wavelength detection maps are combined, a gain slightly less than one order of magnitude is expected due to the combination, according to Figure 6.16. As discussed in Section 6.3.2.3, the combined (wS/N) contrast is only a theoretical lower bound that can not be exactly reach because at the detection stage the  $S/N_\ell$  values are underestimated, the background statistics being estimated in the presence of the source, like with PACO. When comparing the  $S/N_\ell$  values of the point sources in the single-detection maps of HR 8799 shown in Figure 6.6 (values in the range 1.5 to 5.2) to the values in the combined detection maps of Figures 6.14, 6.15 (wS/N = 42.7), the improvement is in relatively good agreement with the contrast curves of Figure 6.16. From our experience, values of the contrast achieved for single-wavelength detections are typically reached in practice with  $S/N_\ell$  and can thus be used as a safe value of the achievable contrast.

As detailed in Chapter 2 for PACO, the PACO-ASDI contrast can be computed at every point of the field of view. Figure 6.17 gives examples of 2-D contrast maps obtained with PACO-ASDI for some selected spectral channels. They show that the detection is more favorable on certain spectral channels than others. For example, the achievable contrast on spectral channel  $\ell_{25} = 1.39 \mu\text{m}$  is about twice worst than the one obtained on spectral channel  $\ell_{13} = 1.16 \mu\text{m}$  for the HR 8799 dataset. This can be explained by the presence of large spectral variations of the intensity fluctuations and/or additional noise probably caused by the pre-reduction pipeline (see our discussion in Section 6.1) and/or the low atmospheric transmission. Interestingly, these maps indicate that the achievable contrast varies significantly along an annulus of fixed angular separation. It is particularly the case near the host star since the residual central halo is not isotropic. Thus, the 2-D contrast information can be useful to derive an accurate estimation of the achievable contrast given the 2-D angular location of a detected source.

### 6.6.3 SED estimation performance

In this section, we evaluate the performance of the SED estimation of point sources. We first use numerical injections of fake point sources for the quantitative characterization of PACO-ASDI. For this purpose, we use a dataset around HD 172555 (see Section 6.6.1) with no detectable source. Figure 6.18 gives the wS/N map obtained with PACO-ASDI and the combined signal-to-noise ratio maps obtained with other algo-

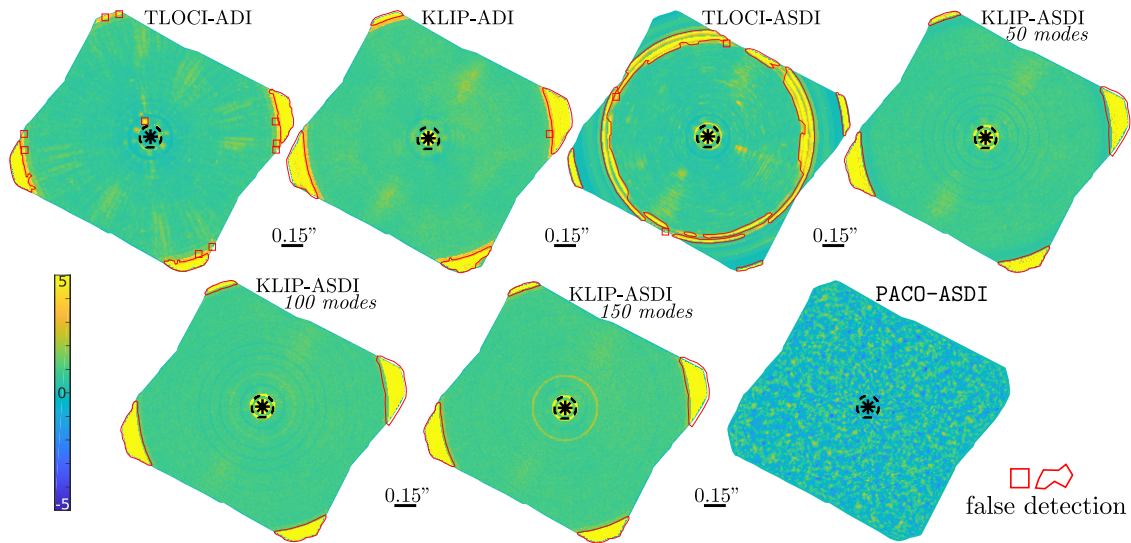


Figure 6.18 – Detection maps (wS/N for PACO-ASDI and combined-S/N for the other algorithms) around HD 172555 in the absence of fake point sources.

Table 6.3 – Angular separation, minimum, maximum, and mean contrast of the 12 fake point sources injected in the fourth dataset around HD 172555. The four sources (#2, #5, #10, and #12) on which we perform additional Monte-Carlo estimations are emphasized in bold font.

ID	separation	min[ $\alpha_\ell$ ]	max[ $\alpha_\ell$ ]	mean[ $\alpha_\ell$ ]
#1	0.220"	$2.3 \times 10^{-5}$	$8.0 \times 10^{-5}$	$5.0 \times 10^{-5}$
<b>#2</b>	<b>0.306"</b>	<b><math>1.2 \times 10^{-5}</math></b>	<b><math>5.0 \times 10^{-5}</math></b>	<b><math>2.8 \times 10^{-5}</math></b>
#3	0.264"	$1.3 \times 10^{-5}$	$2.0 \times 10^{-5}$	$1.8 \times 10^{-5}$
#4	0.399"	$6.2 \times 10^{-8}$	$3.0 \times 10^{-5}$	$1.1 \times 10^{-5}$
<b>#5</b>	<b>0.454"</b>	<b><math>3.3 \times 10^{-6}</math></b>	<b><math>1.0 \times 10^{-5}</math></b>	<b><math>6.6 \times 10^{-6}</math></b>
#6	0.682"	$1.9 \times 10^{-7}$	$9.0 \times 10^{-5}$	$3.3 \times 10^{-5}$
#7	0.166"	$1.8 \times 10^{-6}$	$6.6 \times 10^{-6}$	$3.8 \times 10^{-6}$
#8	0.187"	$3.6 \times 10^{-6}$	$1.5 \times 10^{-5}$	$8.5 \times 10^{-6}$
#9	0.219"	$4.1 \times 10^{-9}$	$2.0 \times 10^{-6}$	$7.5 \times 10^{-7}$
<b>#10</b>	<b>0.318"</b>	<b><math>2.6 \times 10^{-6}</math></b>	<b><math>4.0 \times 10^{-6}</math></b>	<b><math>3.6 \times 10^{-6}</math></b>
#11	0.504"	$3.3 \times 10^{-7}$	$1.0 \times 10^{-6}$	$6.6 \times 10^{-7}$
<b>#12</b>	<b>0.618"</b>	<b><math>2.1 \times 10^{-6}</math></b>	<b><math>7.0 \times 10^{-6}</math></b>	<b><math>4.4 \times 10^{-6}</math></b>

rithms on this dataset, before injecting the fake point sources. While state-of-the-art algorithms reveal several areas above the detection threshold at  $\tau = 5$ , experts did not identify consistent detection peaks by closer inspection. In addition, PACO-ASDI does not identify any significant detection peak at  $5\sigma$ . We inject 12 fake point sources in the field of view with a variety of mean contrast and true SED. Table 6.3 gives astrometric and photometric information about fake point sources. Sources #1 to #6 have a mean contrast lower or equal to  $5 \times 10^{-5}$  while sources #7 to #12 have a mean contrast lower or equal to  $8.5 \times 10^{-6}$ . Figure 6.19 presents the wS/N maps obtained with PACO-ASDI around HD 172555 with fake point sources #1 to #6 (left) and #7 to #12

(right) simultaneously injected. Figure 6.20 gives contrast curves at  $5\sigma$  obtained on the considered dataset with PACO-ASDI comparatively to TLOCI-ADI. Contrast curves indicate that sources #1 to #6, #8, #10, and #12 can be detected at  $5\sigma$  by PACO-ASDI while the sources #7, #9 and #11 are too faint to be detected from the  $S/N_\ell$  maps at the considered angular separations.

Figure 6.21 shows the SED estimation for the 9 detectable fake sources obtained by PACO-ASDI, TLOCI-ADI, and TLOCI-ASDI. These results show that the SED estimations provided by PACO-ASDI are in good agreement with the ground truth since no systematic photometric bias can be observed. We note only one significant discrepancy between the estimated SED by PACO-ASDI and the ground truth occurring for source #8 between  $1.07 \mu\text{m}$  and  $1.22 \mu\text{m}$ . This discrepancy can be explained both by the very faint source contrast in this spectral band (lower than  $5 \times 10^{-6}$ ), the proximity with the host star (angular separation equals to  $0.187 \text{ arcsec}$ ), and the presence of a “dark” speckle near the injection leading to a negative estimated source flux (thresholded at 0) at the corresponding wavelengths. The predicted SED confidence intervals also seem coherent with the empirical standard deviation of estimation. The SED estimates obtained by PACO-ASDI are qualitatively much better than those obtained with TLOCI. To complete this statistical study, we consider 3 sources from the 12 previous ones (sources #5, #10, and #12) for which we perform 30 Monte-Carlo injections / SED estimations over a circular annulus (i.e., at constant angular separations). Figure 6.22 gives the 30 estimated SEDs obtained with TLOCI-ADI, KLIP-ADI, TLOCI-ASDI, and PACO-ASDI and the mean estimations. The confidence intervals provided by the different algorithms can be compared to the empirical  $1\sigma$  confidence intervals. Table 6.4 complements this figure with statistical results in terms of photometric bias, agreement between the predicted and the empirical confidence intervals, and root mean square error (RMSE). These results show that PACO-ASDI is photometrically unbiased in the sense that the photometric bias is negligible (about  $\pm 1\%$  of the mean contrast of the sources) without resorting to Monte-Carlo methods to estimate and compensate the potential source self-subtraction phenomenon, as is common practice with most of the state-of-the-art algorithms. In comparison, this relative photometric bias reaches in most of the cases 4% of the mean contrast of the sources with other methods (excepted for source #12 with TLOCI-ADI). The results of state-of-the-art methods are generally not better in ASDI than in ADI mode. This could be explained by the stronger source self-subtraction that occurs when several spectral channels are processed jointly. This observation illustrates why experts tend to apply preferentially ADI reduction algorithms even on ASDI datasets by processing each spectral channel independently. The empirical confidence intervals are also smaller with PACO-ASDI. The RMSE of the estimated SEDs is reduced by a factor at least two by PACO-ASDI with respect to other algorithms (on average, by a factor 3.6 for the three sources analyzed in Table 6.4). Moreover, the confidence intervals provided by the method are in good match with the observed standard deviations of the Monte-Carlo simulation: the ratio between the predicted standard deviation and the empirical standard deviation is between 0.94 and 1.21 for PACO-ASDI, which is closer to one than for other methods (i.e., PACO-ASDI confidence intervals are more reliable).

We also illustrate astrometric and SED estimations on the real point sources in the first three datasets. Table 6.5 presents the estimated astrometry, and Figure 6.23

gives the estimated SEDs with PACO-ASDI of the exoplanets HR 8799 c-d-e,  $\beta$  Pictoris b and the background source HD 131399 Ab. The datasets are processed in a totally unsupervised fashion as described in Section 2.4.6 for ADI datasets. A joint refinement of the astrometry and photometry estimations of the source with the highest wS/N is performed. Its estimated flux contribution is then subtracted to the data and the wS/N map is updated using a conventional CLEAN approach (see Figure 6.23 for residual wS/N examples). This procedure is repeated until no source at a significant level of signal-to-noise ratio is detected in the wS/N map. These results are not corrected for the SED of the host star. The estimated SEDs are quite smooth and coherent between one spectral channel to the other with reliable confidence intervals. The spectrum extraction is especially challenging for HD 131399 Ab since it is located near the borders of the SPHERE-IFS field of view (see Figures 6.14 and 6.15), and the observing conditions of the considered dataset were not particularly good (seeing about 1.30, see Table 6.2). Nielsen et al. (2017) use photometric and astrometric estimations from VLT/SPHERE and GEMINI/GPI to show that HD 131399 Ab is more likely a background brown dwarf. This result was a revision of the previous status of HD 131399 Ab firstly considered as an exoplanet just after its discovery and confirmation on the basis of (noisy) extracted astrometry and photometry (Wagner et al., 2016). The difficulty to ascertain that HD 131399 Ab was an exoplanet based on the first observations illustrates the importance of algorithms that can provide reliable astrometric and spectrum estimations. We expect PACO-ASDI to help refining the estimated orbit and the spectral characterization of future candidate companions.



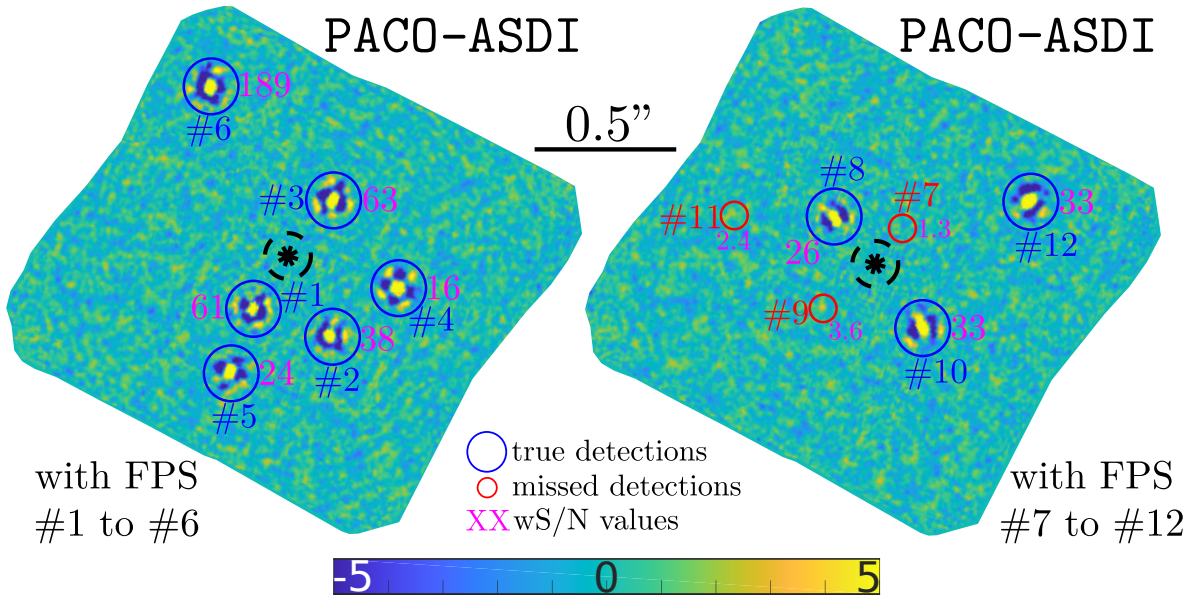


Figure 6.19 – wS/N maps obtained with PACO-ASDI around HD 172555 with injected fake point sources #1 to #6 (left) and #7 to #12 (right).

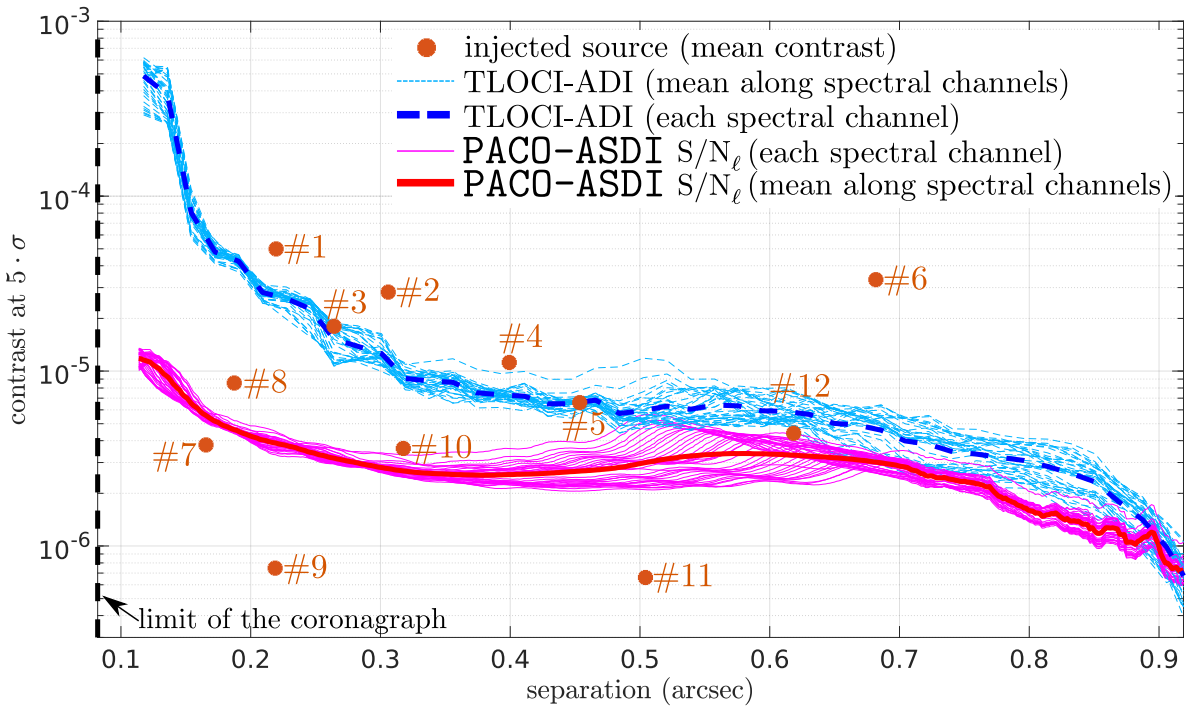


Figure 6.20 – Contrast curves at  $5\sigma$  obtained with PACO-ASDI comparatively to TLOCI-ADI. The mean contrast of the fake faint point sources #1 to #12 is marked by orange points.



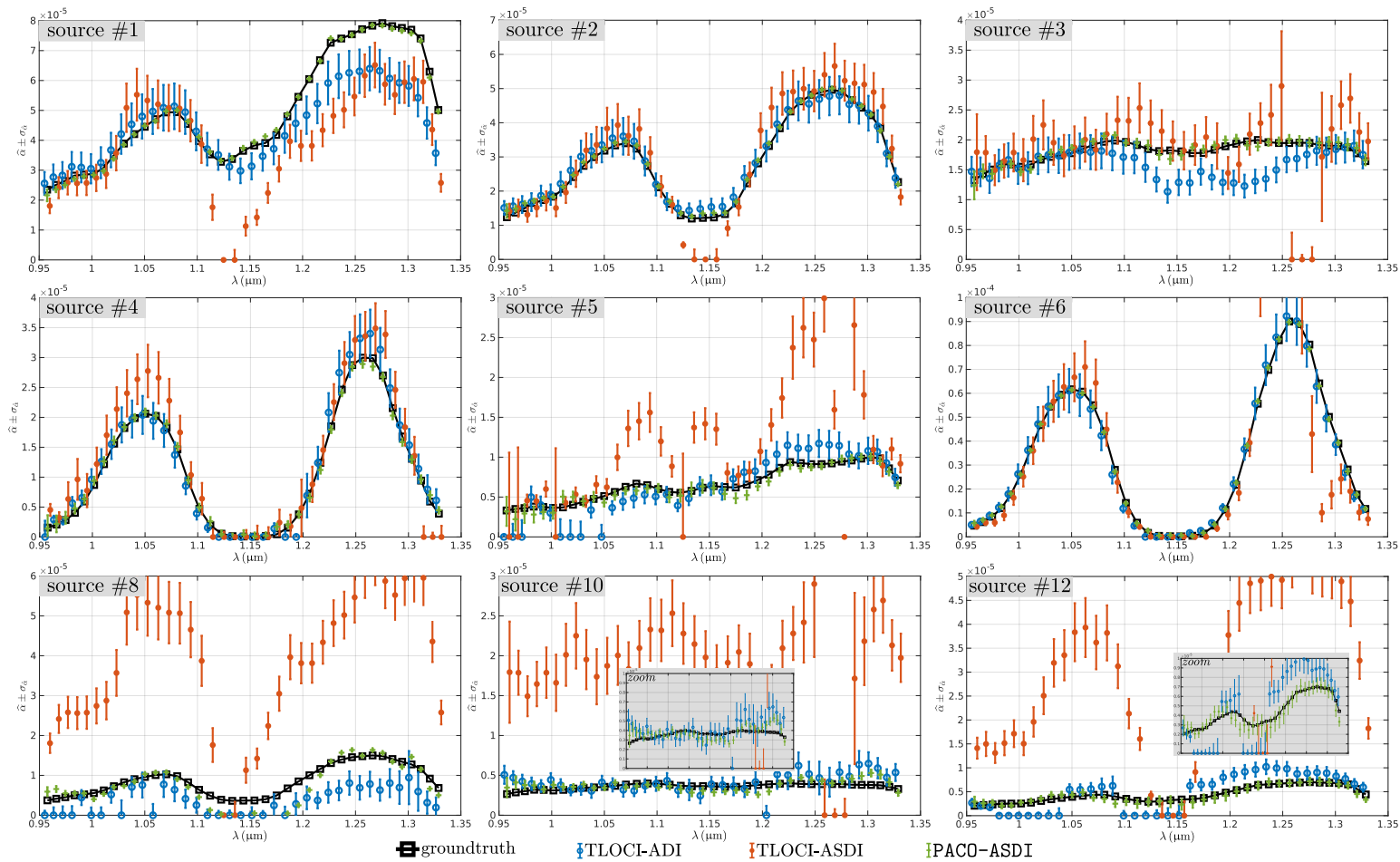


Figure 6.21 – Estimated SED of the detectable fake faint point sources (#1 to #6 plus #8, #10, and #12) obtained with PACO-ASDI (green), TLOCI-ADI (blue), and TLOCI-ASDI (orange). The SED ground truths of the different fake faint point sources are marked by black lines. The given  $1\sigma$  confidence intervals are those predicted by the considered algorithms. A zoom around the ground truth is added for sources #10 and #12.

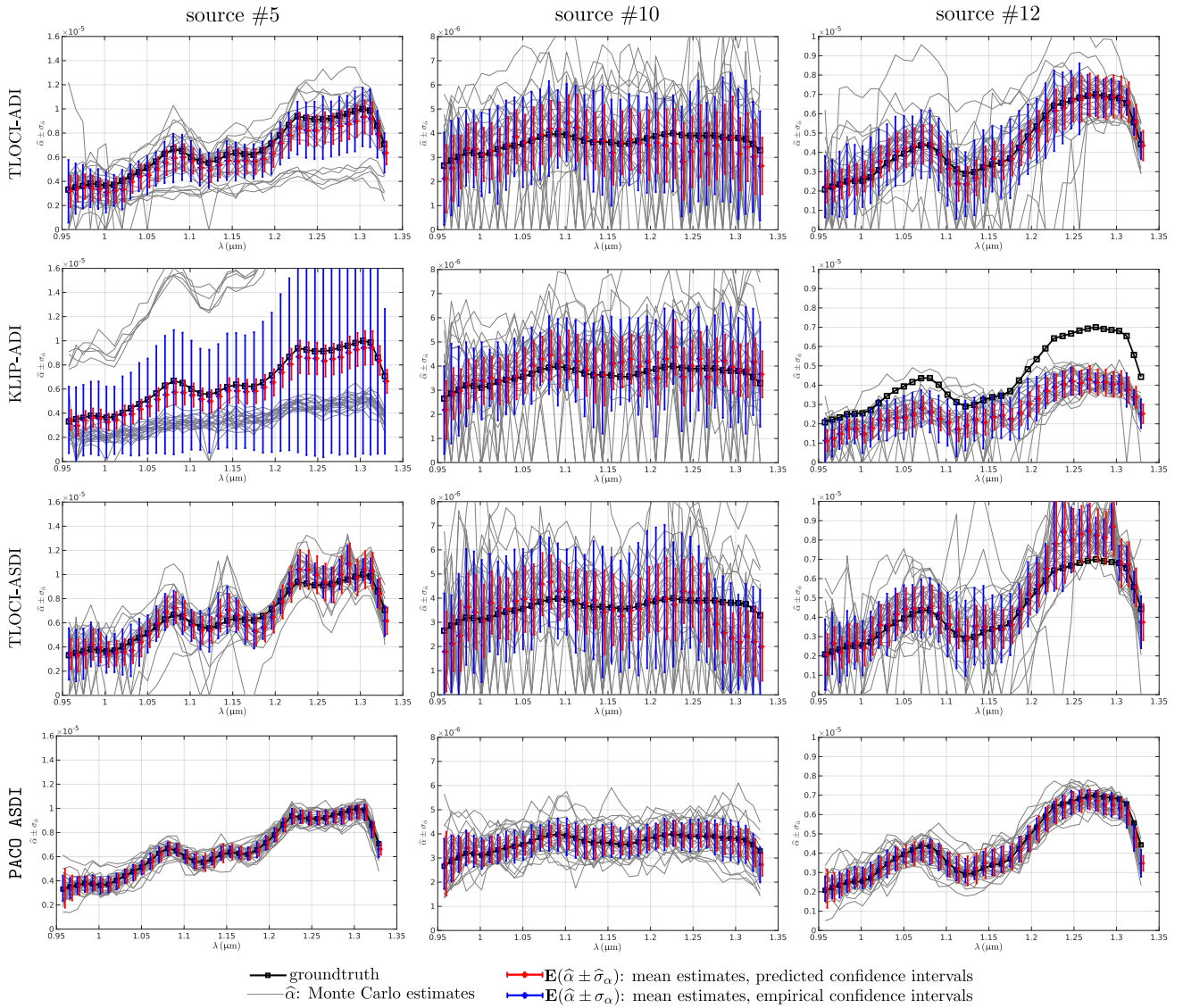


Figure 6.22 – Monte-Carlo estimated SED for fake point sources #5, #10, and #12 obtained with TLOCI-ADI, KLIP-ADI (5 PCA modes), TLOCI-ASDI, and PAC0-ASDI. For each of the 3 considered sources, the 30 Monte-Carlo SED estimations are given in gray line. Red and blue lines compare the  $1\sigma$  predicted confidence intervals to the empirical ones centered on the mean estimated SED over the 30 Monte-Carlo estimations. The SED ground truth of the considered sources is in black.

Table 6.4 – Monte-Carlo validation of SED estimation methods. Best results are highlighted in blue while the worst results are in red.

	TLOCI-ADI	KLIP-ADI	TLOCI-ASDI	PACO-ASDI
<i>Source #5: <math>\langle \alpha_\ell \rangle_\ell = 6.6 \times 10^{-6}</math></i>				
<b>bias:</b> $\left\langle \frac{\langle \hat{\alpha}_\ell - \alpha_\ell \rangle}{\langle \alpha_\ell \rangle_\ell} \right\rangle_\ell$	<b>-9.2%</b>	-7.4%	+1.3%	<b>-0.7%</b>
<b>predicted std:</b> $\langle \hat{\sigma}_{\alpha_\ell} \rangle_\ell$	$1.1 \times 10^{-6}$	$1.0 \times 10^{-6}$	$1.3 \times 10^{-6}$	$6.2 \times 10^{-7}$
<b>empirical std:</b> $\langle \sigma_{\alpha_\ell} \rangle_\ell$	$1.8 \times 10^{-6}$	$5.4 \times 10^{-6}$	$1.5 \times 10^{-6}$	$6.0 \times 10^{-7}$
<b>ratio</b> $\langle \sigma_{\alpha_\ell} \rangle_\ell / \langle \hat{\sigma}_{\alpha_\ell} \rangle_\ell$	1.65	<b>5.24</b>	1.13	<b>0.97</b>
<b>RMSE:</b> $\sqrt{\langle \ \hat{\alpha} - \alpha\ ^2 \rangle}$	$1.9 \times 10^{-6}$	<b><math>5.7 \times 10^{-6}</math></b>	$1.6 \times 10^{-6}$	<b><math>6.1 \times 10^{-7}</math></b>
<i>Source #10: <math>\langle \alpha_\ell \rangle_\ell = 3.6 \times 10^{-6}</math></i>				
<b>bias:</b> $\left\langle \frac{\langle \hat{\alpha}_\ell - \alpha_\ell \rangle}{\langle \alpha_\ell \rangle_\ell} \right\rangle_\ell$	-4.2%	<b>+5.8%</b>	-4.7%	<b>-0.1%</b>
<b>predicted std:</b> $\langle \hat{\sigma}_{\alpha_\ell} \rangle_\ell$	$1.3 \times 10^{-6}$	$1.0 \times 10^{-6}$	$1.3 \times 10^{-6}$	$5.5 \times 10^{-7}$
<b>empirical std:</b> $\langle \sigma_{\alpha_\ell} \rangle_\ell$	$2.0 \times 10^{-6}$	$1.9 \times 10^{-6}$	$2.3 \times 10^{-6}$	$6.7 \times 10^{-7}$
<b>ratio</b> $\langle \sigma_{\alpha_\ell} \rangle_\ell / \langle \hat{\sigma}_{\alpha_\ell} \rangle_\ell$	1.54	<b>1.90</b>	1.78	<b>1.21</b>
<b>RMSE:</b> $\sqrt{\langle \ \hat{\alpha} - \alpha\ ^2 \rangle}$	$2.0 \times 10^{-6}$	$1.9 \times 10^{-6}$	<b><math>2.4 \times 10^{-6}</math></b>	<b><math>6.9 \times 10^{-7}</math></b>
<i>Source #12: <math>\langle \alpha_\ell \rangle_\ell = 4.4 \times 10^{-6}</math></i>				
<b>bias:</b> $\left\langle \frac{\langle \hat{\alpha}_\ell - \alpha_\ell \rangle}{\langle \alpha_\ell \rangle_\ell} \right\rangle_\ell$	<b>-0.3%</b>	<b>-38.5%</b>	+10.0%	+1.1%
<b>predicted std:</b> $\langle \hat{\sigma}_{\alpha_\ell} \rangle_\ell$	$9.4 \times 10^{-7}$	$6.0 \times 10^{-7}$	$1.1 \times 10^{-7}$	$6.0 \times 10^{-7}$
<b>empirical std:</b> $\langle \sigma_{\alpha_\ell} \rangle_\ell$	$1.5 \times 10^{-6}$	$9.2 \times 10^{-7}$	$1.5 \times 10^{-6}$	$5.7 \times 10^{-7}$
<b>ratio</b> $\langle \sigma_{\alpha_\ell} \rangle_\ell / \langle \hat{\sigma}_{\alpha_\ell} \rangle_\ell$	<b>1.66</b>	1.53	1.29	<b>0.94</b>
<b>RMSE:</b> $\sqrt{\langle \ \hat{\alpha} - \alpha\ ^2 \rangle}$	$1.6 \times 10^{-6}$	<b><math>2.0 \times 10^{-6}</math></b>	$1.7 \times 10^{-6}$	<b><math>6.2 \times 10^{-7}</math></b>

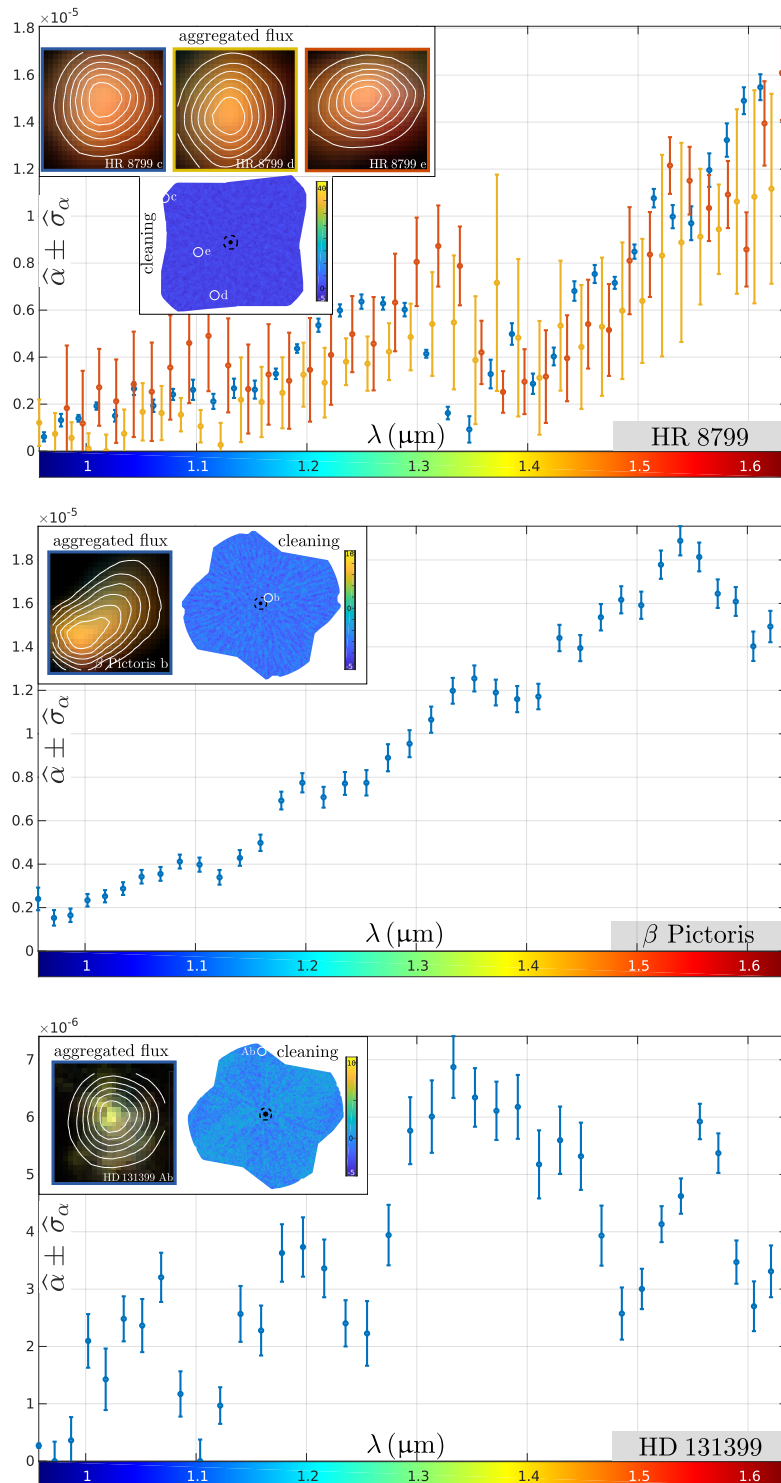


Figure 6.23 – Estimated SED using PACO-ASDI of the known real faint point sources of the considered datasets (top: HR 8799 c-d-e, middle:  $\beta$  Pictoris b, bottom: HD 131399 Ab). The inserts (whose frame color is related to the color of the corresponding SED curve) show a residual wS/N map after “cleaning” the contribution of the SED of the detected source. Synthetic subpixel views (4 nodes per pixels) show with false colors the aggregated flux of the detected sources along the different spectral channels (blue for  $\lambda_1 = 0.96\mu\text{m}$  and red for  $\lambda_{39} = 1.64\mu\text{m}$ ).

Table 6.5 – Estimated astrometry (separation and true-north aligned angle) of the real faint point sources known in the used datasets with PACO-ASDI. The confidence intervals are given at  $1\sigma$ .

source	est. sep. (arcsec)	est. angle ( $^{\circ}$ )
HR 8799 c	$0.9425 \pm 0.0031$	$328.31 \pm 0.19$
HR 8799 d	$0.6636 \pm 0.0065$	$218.94 \pm 0.51$
HR 8799 e	$0.3834 \pm 0.0068$	$274.80 \pm 1.09$
$\beta$ Pictoris b	$0.1423 \pm 0.0063$	$216.25 \pm 1.70$
HD 131399 Ab	$0.8412 \pm 0.0065$	$194.74 \pm 0.59$

### PACO-ASDI main characteristics

Based on the analysis of several ASDI datasets, PACO-ASDI shows several appealing characteristics:

- It produces stationary and statistically grounded detection maps on the whole field of view offered by the IFS. These maps can be directly interpreted in terms of probability of false alarm and probability of detection.
- It demonstrates better detection sensitivity than other state-of-the-art methods.
- It produces statistically-grounded 2-D contrast maps.
- It provides unbiased and automatically regularized SED estimation with reliable confidence intervals.

## 6.7 Conclusion on PACO-ASDI's capabilities

ASDI observations provide very rich data for the detection and characterization of point sources such as exoplanets. Despite the large instrumental efforts in the design of coronagraphic imaging, the separation of the signal of interest (off-axis sources) from the background signal of the on-axis star has to be performed under adverse conditions: strong temporal and spectral fluctuations, presence of spatially-structured evolutions and contamination by outliers.

We have shown in this chapter that data-driven statistical modeling paved the way to reliable source detection and source characterization methods. PACO-ASDI, the data processing algorithm introduced in this chapter, produces detection maps with improved sensitivity compared to existing methods. An important practical feature is the control of the probability of false alarm: detection maps can be reliably thresholded. Using the conventional  $5\sigma$  threshold generally produces no false alarm in an IFS field. This contrasts with detection maps obtained with other methods for which many false alarms are observed, in particular at very small angular separations and close to the borders of the field of view. Full exploitation of the field of view seems to be a feature of PACO-ASDI that is shared by few other methods.

The elaborate statistical model of PACO-ASDI, accounting for spatial, spectral, and temporal fluctuations is also used to characterize the astrometry and photometry of the detected point sources. By refining the model of the background jointly with the estimation of the source SED and flux, the bias due to source self-subtraction is prevented. The SED is estimated using an unsupervised spectral regularization. Our numerical experiments show reduced estimation errors compared to standard methods.

Beyond the direct analysis of ASDI datasets, as PACO presented in Chapter 2, PACO-ASDI also provides information on the achievable contrast as well as on the photometric and astrometric accuracies that are reached for given instrumental and observational conditions. The impact of different observation scenarios (spectral coverage, parallactic rotation) can then be assessed using a data-driven model whose prediction accuracy has been validated on real data.







# Improved characterization of microscopic objects with multi-spectral holography

---

**Abstract**

*The main advantages of holographic microscopy are related to its simplicity, compactness, low sensitivity of the setup to vibrations and the possibility to accurately characterize objects. The cost-effectiveness of the method can be further increased using low-end laser diodes as coherent sources and CMOS color sensors equipped with a Bayer filter array. However, the central wavelength delivered by this type of laser is generally known only with limited precision and can evolve because of its dependence on temperature and power supply voltage. Besides, Bayer-type filters of conventional color sensors are not very selective, resulting in spectral mixing of signals from each color channel (crosstalk phenomenon). Ignoring this phenomenon leads to significant errors in holographic reconstructions. We propose a maximum likelihood estimation method to calibrate the setup (central wavelength of the laser sources and spectral mixing due to the Bayer filters) using spherical objects naturally present in the field of view, or added as calibration objects. This calibration method provides accurate estimates of the wavelengths and the crosstalk, with an uncertainty comparable to that of a high-resolution spectrometer. We show on experimental holograms that the self-calibration of the setup leads to an improvement of the subsequent reconstructions.*

*This chapter, devoted to calibration algorithms for color holography, corresponds chronologically to the first subject studied in this thesis.*

---

## 7.1 Introduction

As discussed in Section 1.3.2, holographic microscopy is an established method to characterize microscopic objects spread in a volume. The combination of this technique with multiple sources of illumination (at different wavelengths) brings a diversity of information useful to derive quantitative physical properties, i.e., to characterize the samples of interest with an improved resolution and accuracy. Figure 7.1 illustrates

some current trends related to multi-spectral holography imaging applied in diverse application fields. Among them, we can cite the imaging of human tissues for pathology diagnosis (see Figure 7.1(a)) or the analysis with a holographic cytometer of samples put into a fluid flow (see Figure 7.1(b)). Multi-spectral holographic microscopy can also turn into a *tomographic mode* in which the samples are illuminated over time by several coherent light sources under various angles of view giving access to the 3-D time-evolving structures of the microscopic samples (see Figure 7.1(c)). In all these applications, specific care is given to the design of setups ever more compact (see first column of Figure 7.1). Their simplicity is generally counter-balanced by elaborate processing of the recorded holograms. The cost-effectiveness of the setups can be further improved by using consumer materials which are initially not designed to be used for microscopy applications. For example, Rawat et al. (2017); Javidi et al. (2018) demonstrate the possibility to conduct malaria disease diagnostic with an on-chip printed shearing holographic microscope made of a mobile-phone's CMOS camera and a DVD player's laser diode.

Whatever the application and the reconstruction strategy of the recorded holograms, the quality of the reconstructions is potentially limited by additional sources of error due to the imprecise knowledge of the setup parameters specific to multi-spectral holography, in particular, those related to the sources and sensor. This is especially the case in a cost-effective perspective in which conventional lasers are replaced by laser diodes and the CMOS color sensor is equipped with a Bayer filter array to record the color information in one shot with a single photodetector layer. In this chapter, we aim to illustrate, estimate, and account for these limitations in the hologram reconstruction methods. More specifically, we attempt to perform a *self-calibration* of the setup, i.e. to estimate the source and sensor parameters directly from the recorded holograms with no additional (expensive) element or calibration process required. Our approach is based on the analysis of diffraction patterns that encode, in the form of signal modulation, information about the setup parameters.

For this purpose, we consider the lensless color holographic setup presented in Figure 1.15 of Section 1.3.2.2.2. The three laser diodes are switched on simultaneously, and the camera is a CMOS color sensor. Figure 7.2 reminds the configuration of this setup and summarizes the main notations used throughout this chapter.

Section 7.2 addresses the possible sources of errors due to the incorrect calibration of the color setup. Based on Section 1.3.2.2, Section 7.3 briefly recalls the general principle of object reconstruction with a parameter-based inverse problem approach adapted to color holograms. Section 7.4 describes a simple, fast, and accurate method to perform the *self-calibration* of a color holographic setup; i.e. estimating the central wavelength of the sources and characterizing the signal mixing taking place on Bayer-type color sensors from the recorded holograms themselves. Section 7.5 describes how to account for the self-calibration of the setup during the reconstruction step. We show that the accuracy of both parameter-based and image-based reconstructions are improved when the setup is correctly calibrated. Finally, Section 7.6 concludes this chapter. This chapter is based on the journal paper Flasseur et al. (2017b) and the conference paper Flasseur et al. (2018d). The starting point for this work was a study of color holography conducted by Corinne Fournier and Nicolas Verrier.

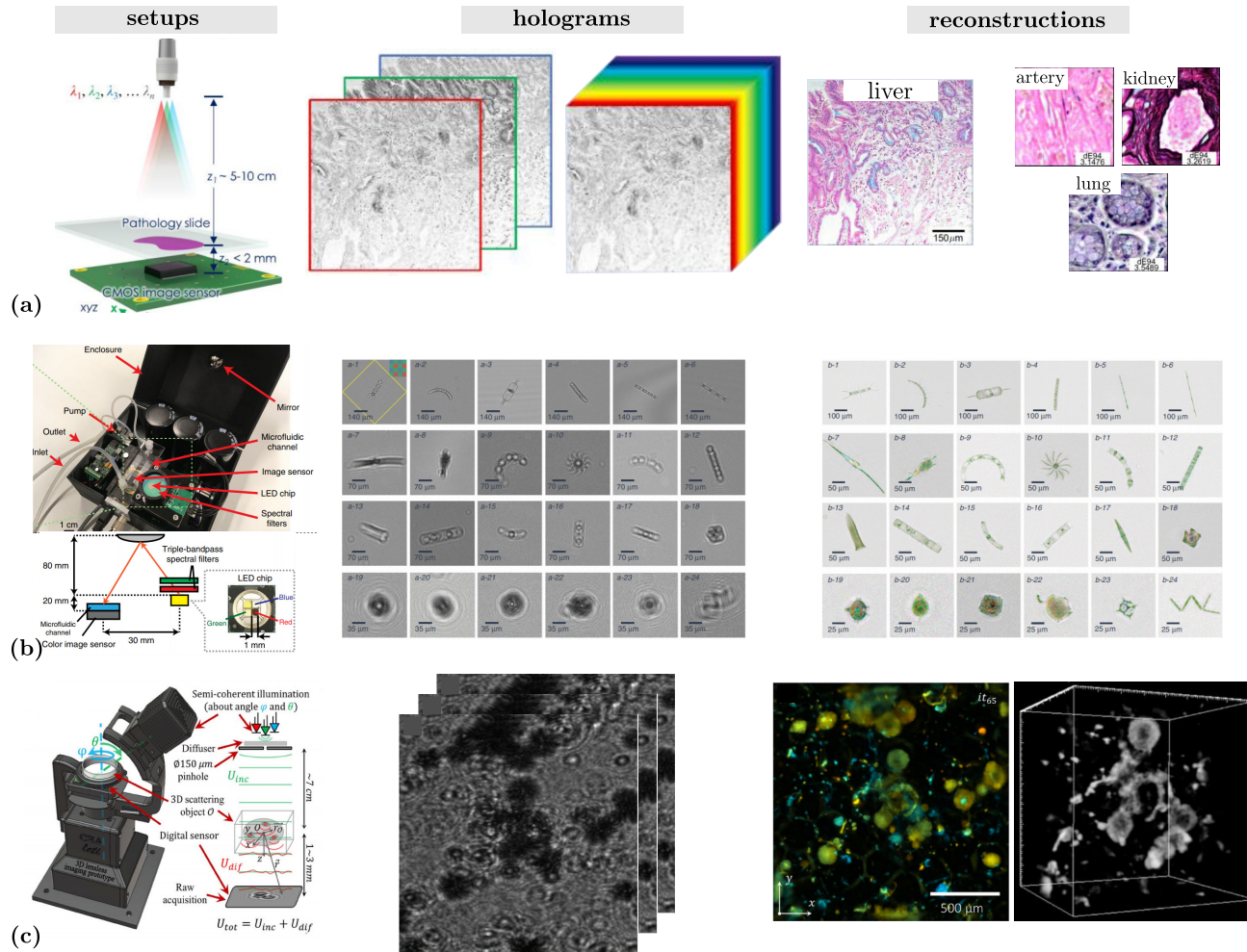


Figure 7.1 – Examples of applications of multi-spectral holography. (a) pathology slides are imaged by a lensless holographic microscope for clinical diagnoses, adapted from Zhang et al. (2019); (b) flowing water samples are imaged by a holographic microscope, phase-contrast color images are reconstructed, adapted from Göröcs et al. (2018); (c) growing cells are imaged over time by a lensless tomographic microscopy, 3-D + time views of the samples are reconstructed, adapted from Berdeu et al. (2018a,b).

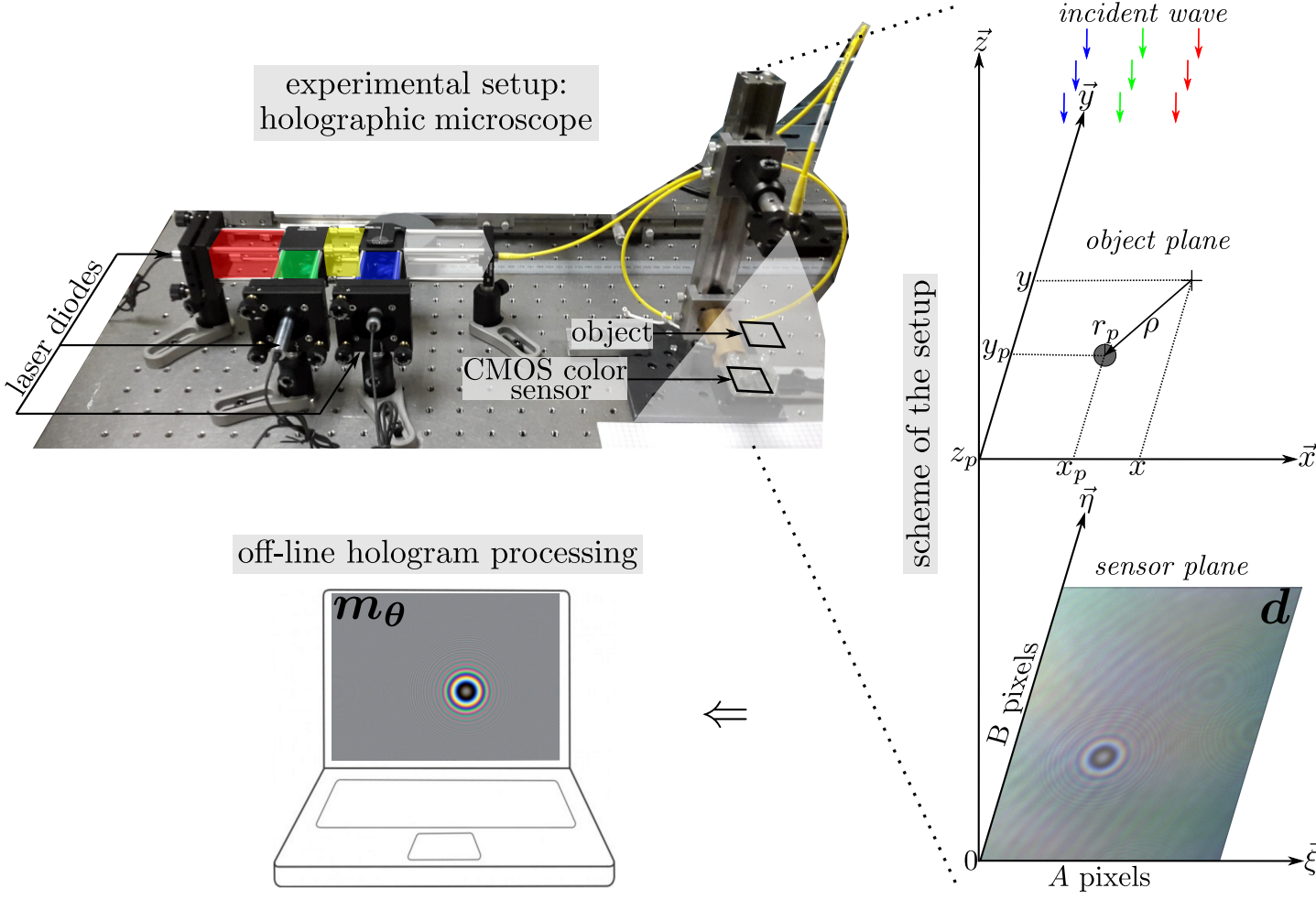


Figure 7.2 – Illustration of the considered color holographic setup. It is made of three laser diodes; one red (THORLABS™, CPS635R, 1.5 mW), one green (THORLABS™, CPS532, 4.5 mW) and one blue (THORLABS™, CPS405, 4.5 mW); and a 12-bit CMOS color sensor (BASLER™, daA2500-14uc) with  $A \times B = 1944 \times 2592$  pixels with a  $2.2 \mu\text{m}$  pitch. The right part gives a schematic representation of the setup presented in the left part.



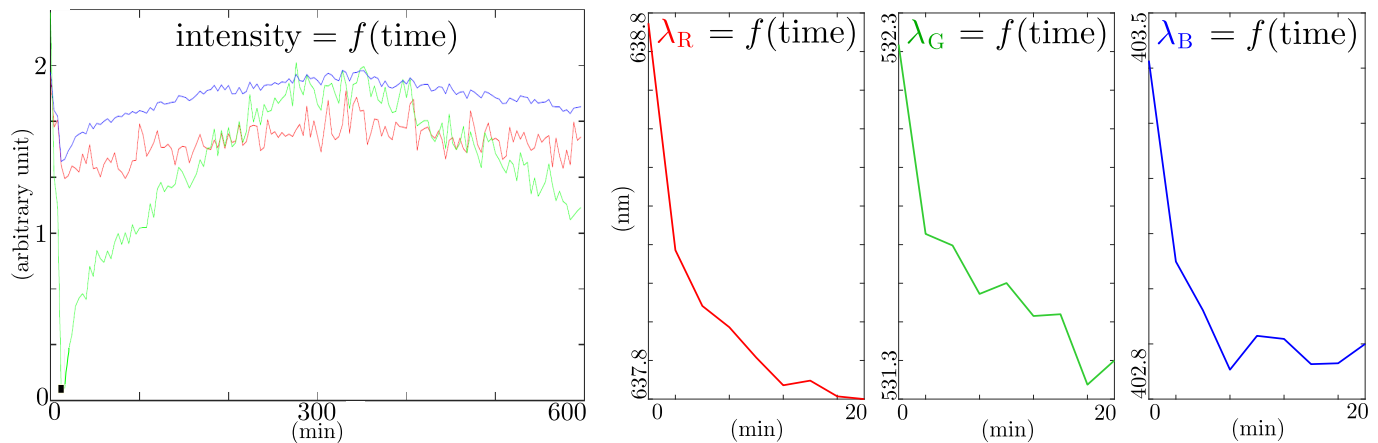


Figure 7.3 – Illustration of the laser diodes instability. Left: evolution of the mean intensity received on our camera over time. Right: evolution of the central wavelengths delivered by our laser diodes over time.

Table 7.1 – Ranges of wavelengths of the laser diodes used, as provided by the manufacturer. The central wavelength can evolve between  $\lambda^{\min}$  and  $\lambda^{\max}$ .  $\lambda^{\text{nom}}$  is the expected nominal value at 20°C.

	$\lambda^{\min}$ (nm)	$\lambda^{\text{nom}}$ (nm)	$\lambda^{\max}$ (nm)	temp. (°C)	power (mW)
<b>red source</b>	630	635	645	-10 / 50	1.0 / 1.4
<b>green source</b>	531	532	533	10 / 40	4.0 / 5.0
<b>blue source</b>	400	405	410	-10 / 40	4.0 / 5.0

## 7.2 Calibration issues of holographic color microscopy

To ensure the compactness and cost-effectiveness of the setup, the sources used are often laser diodes. For the same reason, the color sensor is often a single-channel color sensor equipped with a Bayer filter. In this section, we describe the possible sources of error during the reconstruction step in holographic color microscopy if no calibration procedure is applied. It can be noted that the consequences of the lack of calibration are similar when the reconstruction is performed with a conventional approach (light backpropagation simulation) or with an inverse problem approach (see Section 1.3.2.2).

### 7.2.1 Calibration issues related to the wavelengths of the sources

To perform reconstruction from color holograms, accurate knowledge of the wavelengths of the laser sources is mandatory. Indeed, whatever the reconstruction approach; the propagation kernel used in the classical reconstruction approach and the model describing the image formation both depend on the wavelength. In monochromatic holography,

an error on the wavelength leads to an error on the depth of the reconstruction. In color holography, errors on the wavelengths lead to a non-unique focus plane.

The present study is also justified by the development and the massive use of inexpensive laser sources, which represent a good compromise between cost and performance, compared to the high-end lasers commonly used in lensless microscopy. Unfortunately, cost-effective lasers do not always deliver light at a wavelength that matches the nominal value announced by the manufacturer (Garcia-Sucerquia, 2016). Wavelengths can also evolve during the experiment due to the heating of the lasers or fluctuations of the power level (unless they are stabilized by control loops). This phenomenon is illustrated in Figure 7.3 representing the evolution of the mean intensity (average of pixel values) received on our camera over time as well as the evolution of the central wavelengths delivered by our laser diodes measured with a high-resolution spectrometer (OCEANOPTICS™, QE65000). Table 7.1 gives the ranges of wavelengths provided by the manufacturer for the three laser diodes that we use, for the temperature and power operating ranges given by the manufacturer. The measured evolution of the central wavelength of the laser diodes is in agreement with the values given by the manufacturer.

In the following, the row vector  $\boldsymbol{\lambda} = (\lambda_R, \lambda_G, \lambda_B)$  designates the set of the wavelengths of the three sources. The optional exponent indicates the set of wavelengths considered, e.g.,  $\boldsymbol{\lambda}^{\text{nom}} = (\lambda_R^{\text{nom}}, \lambda_G^{\text{nom}}, \lambda_B^{\text{nom}})$ .

Conventionally, when estimating the object depth  $z_p$  (i.e., the distance from the object to the sensor), the source wavelength  $\lambda$  is kept fixed. However, under Fresnel assumption, Fresnel free-space propagator  $h(x, y)$  depends on the product  $\lambda z_p$ :  $h(x, y) \propto \exp[j\pi(x^2 + y^2)/(\lambda z_p)]$ , see Goodman (2005). As a result, the imprecision  $\Delta_{z_p}$  on the estimated value  $z_p$  is related to the imprecision  $\Delta_\lambda$  on the wavelength  $\lambda$  of the source through:

$$\frac{\Delta_\lambda}{\lambda} = \frac{\Delta_{z_p}}{z_p}. \quad (7.1)$$

According to Equation (7.1) and the uncertainties on the wavelengths listed in Table 7.1, the maximum bias  $\Delta_{z_p}^{\text{max}}$  on the estimated parameter  $z_p$  can reach 1 mm for an object located 7 cm from the sensor plane. This error appears to be prohibitive for the optical metrology applications that we consider (in particular, for 3-D measurements in fluids mechanics). In the case of a discrepancy between the real wavelengths  $\boldsymbol{\lambda}^{\text{real}} = (\lambda_R^{\text{real}}, \lambda_G^{\text{real}}, \lambda_B^{\text{real}})$  and the wavelengths considered in the diffraction model, independent reconstructions of the holograms recorded in each color channel lead to three different depths for a given object  $p$ . These three independently estimated distances  $\{z_R^{\text{est}}, z_G^{\text{est}}, z_B^{\text{est}}\}$  differ from the actual distance of the object  $z_p$  according to the following system of equations:

$$\begin{cases} \lambda_R^{\text{nom}} z_R^{\text{est}} &= \lambda_R^{\text{real}} z_p, \\ \lambda_G^{\text{nom}} z_G^{\text{est}} &= \lambda_G^{\text{real}} z_p, \\ \lambda_B^{\text{nom}} z_B^{\text{est}} &= \lambda_B^{\text{real}} z_p. \end{cases} \quad (7.2)$$

Rather than using the nominal values given by the manufacturer, these wavelengths should be calibrated, either using a spectrometer during a calibration step or a self-calibration approach, as described in Section 7.4.2.

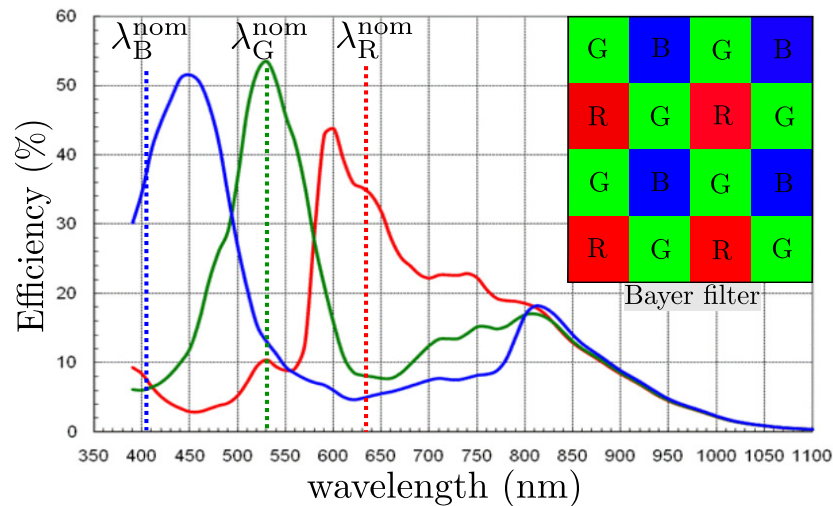


Figure 7.4 – Spectral responses of Bayer filters of our color CMOS camera. The nominal wavelengths ( $\lambda_R^{\text{nom}}$ ,  $\lambda_G^{\text{nom}}$ ,  $\lambda_B^{\text{nom}}$ ) provided by the manufacturer of our laser diodes are also indicated.

## 7.2.2 Calibration issues related to the CMOS color sensor

In a cost-effective perspective, color sensors using CMOS technology and a Bayer filter are a preferred choice. In this part, we describe the different crosstalk phenomena which occur on this type of sensors as well as their possible consequences during the holographic reconstruction.

The term *crosstalk* refers to the undesirable effects that occur when a signal transmitted on a channel modifies or impacts signals transmitted on the other channels. This global phenomenon leads to a reduction in sensitivity, poor separation of colors, and degradation of spatial and frequency resolution. The main crosstalk phenomena appearing on color sensors are *spectral*, *optical*, and *electronic* (Li et al., 2002; Getman et al., 2007; Blockstein and Yadid-Pecht, 2010). In the following sections, we give a brief description of each of them, focusing on how to quantify and reduce them.

### 7.2.2.1 Spectral crosstalk

CMOS sensors classically used in color holographic microscopy generally do not capture a trichromatic information at each photodetector (Hubel et al., 2004; Tankam et al., 2010). Photodetector sites are rather covered by a matrix of chromatic filters called a *Bayer color filter array* (Bayer, 1976), which filters the incident light by transmitting only one of the three primary components at each pixel. This so-called *mosaicking* step is mandatory to record color images with this type of sensor since the photodetectors used are sensitive to incident wave intensity over a wide spectral range. Spectral crosstalk is due to the Bayer filter covering the photodetector layer of the CMOS color sensors: their spectral responses are not ideal bandpass (Göröcs et al., 2010). Figure 7.4 shows the spectral responses as a function of the wavelength for the filters of our CMOS color sensor. A significant overlap between the different spectral responses can be noted. As a consequence, a signal mixing occurs on the different sensor channels of our color CMOS camera. Figure 7.5 illustrates this signal mixing by showing that a

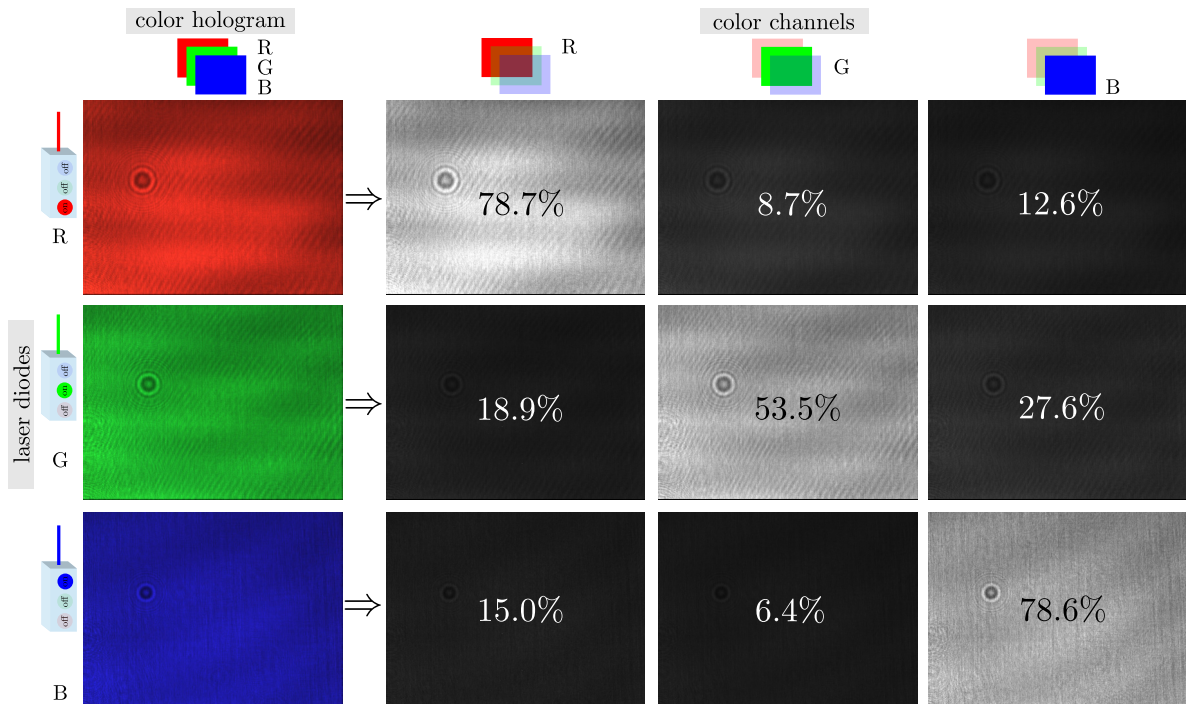


Figure 7.5 – Recorded intensity on each of the three planes of our color CMOS camera under (quasi) monochromatic illuminations provided by our three laser diodes. The imaged object is a circular chromium deposit. The superimposed values corresponds to the mean intensities measured on each channel of the camera under monochromatic illumination.

non-zero signal is received on the different channels of the color sensor when a hologram is generated by a (quasi) monochromatic illumination.

Yamaguchi et al. (2002) have presented one of the first use of digital sensors equipped with a Bayer filter for a color holography application. The spectral crosstalk was mentioned in the sensor spectral responses, but its characterization was not addressed. A simple average of the light intensity received on each channel during a monochromatic exposure does not provide a sufficiently accurate estimate of the spectral crosstalk. For example, some time-varying fringes can be observed on the background of the holograms recorded with cost-effective cameras, see Figure 7.5. These fringes may be produced by a parallelism defect of the fine glass slides that protect the detector and/or by inhomogeneities of the optical index near these slides due to the heating of the sensor. This phenomenon makes it difficult to characterize the spectral crosstalk since the number of dark fringes does not remain constant during the recording, whereas the spectral crosstalk phenomenon remains constant. Actually, we show in Section 7.4.2.2 that accurate estimations of the crosstalk contributions present a significant discrepancy with mean intensities measured on each channel of the camera under monochromatic illumination (see Figure 7.5). As a consequence, the gold standard method for quantitatively studying the spectral crosstalk phenomenon remains the measurement of the spectral responses of the Bayer filters. For example, Ozcan’s group at UCLA has recently proposed to use a setup composed of a broadband laser source coupled to an acousto-optical

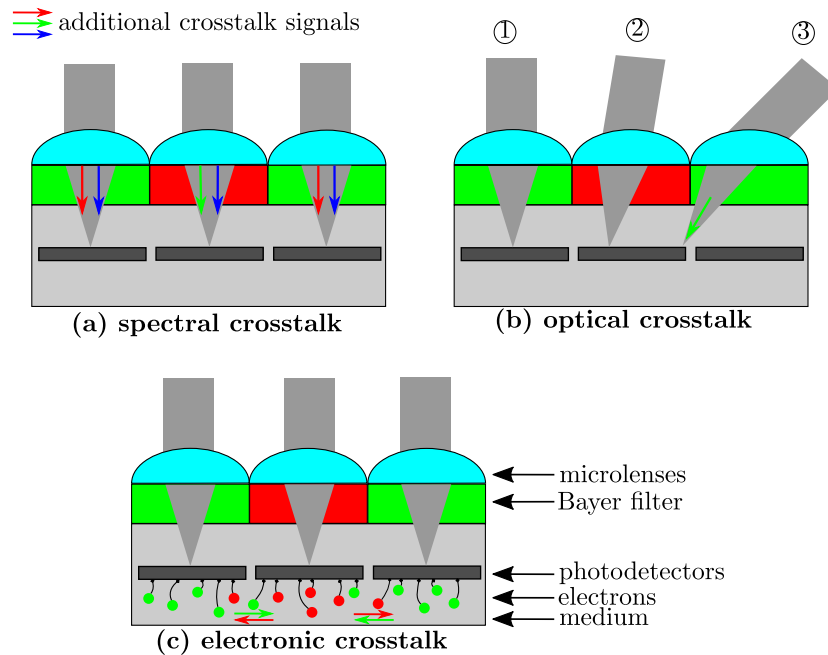


Figure 7.6 – Illustration of the different types of crosstalk occurring on a color CMOS sensor: (a) spectral crosstalk; (b) optical crosstalk; (c) electronic crosstalk.

filter that can be adjusted in wavelength around a fine bandwidth to accurately measure the spectral response of the filters (Wu et al., 2016).

To reduce the influence of spectral crosstalk, it is possible to use more selective pigments to stain Bayer filters such as those developed by MICRON TECHNOLOGIES™, Aptina. It is also possible to reduce the visual degradation induced by spectral crosstalk with additional numerical processing and/or with a configuration of the color filter array different from that proposed by Bayer (Hirakawa and Wolfe, 2007; Anzagira and Fossum, 2015). However, in digital holography, the low-pass filtering induced by demosaicking attenuates the high frequencies and blurs the reconstruction, which makes this solution unsatisfactory. Note that, it has been recently proposed to replace the traditional color filter array by a plasmonic color filter directly lithographed close to the photodetectors (Chen and Cumming, 2010; Yokogawa et al., 2012; Yu et al., 2015). This method has the advantage of simultaneously reducing the spectral and optical crosstalk while increasing the transmission of the filters. This method is not yet applicable in a low-cost scheme, though.

Rather than trying to reduce this phenomenon, we show in Sections 7.4 and 7.5 a method to model and estimate the signal mixing induced by this crosstalk phenomenon and to take it into account in the hologram processing algorithms for applications in color holographic microscopy.

### 7.2.2.2 Optical crosstalk

Optical crosstalk occurs when the incident angle becomes too large for the microlenses array to focus light on the photodetector immediately below. In this case, a portion of the signal of interest may be lost in the gap that separates two adjacent pho-



photodetectors or, worse, may impact a neighboring photodetector. Figure 7.6 illustrates this phenomenon. No optical crosstalk occurs at null or weak incidence angles (cases (b)① and (b)②). At higher incidence angles (case (b)③), optical crosstalk can occur.

Since it is difficult to study this effect without taking into account the influence of other crosstalk phenomena, its importance is mainly determined by numerical simulations (Agranov et al., 2001). Since the incidence angle of the light beams striking the pixels located at the edge of the sensor is naturally higher than for pixels in the central part of the sensor, it is possible to optimize the placement of the microlenses with respect to the Bayer filters (by slightly shifting their center), to favor the convergence of the rays on the photodetectors of interest and thus reduce the optical crosstalk (Agranov et al., 2003). It is also possible to apply surface treatments (e.g., anti-reflective) to the surface of photodetectors (Furumiya et al., 2001).

In holographic microscopy, local optical crosstalk can be disregarded since the laser is collimated and thus the incidence angles of the light on the sensor are small (less than  $2^\circ$ ).

### 7.2.2.3 Electronic crosstalk

Electronic crosstalk is due to an interaction between signals received at two neighboring photodetectors. Some electrons created as a result of the detection of light in the depletion zone are diffused to adjacent photodetectors. This results in an additional error in the signal of interest, as illustrated in Figure 7.6 (case (c)).

This phenomenon is commonly quantified by the use of an S-cube system to illuminate a single pixel (at normal incidence) and thus measure the proportion of signal leaking to the neighboring pixels due to the electronic crosstalk effect (Blockstein and Yadid-Pecht, 2010).

Since the advent of CMOS sensors, many improvements and optimizations of the architecture have been made by foundries to limit the effects of electronic crosstalk. It can be considerably reduced by adding an insulating cage around neighboring photodetectors which acts as a waveguide (Furumiya et al., 2001; Hsu et al., 2004; Estribeau and Magnan, 2005; Koo et al., 2007). This technique also reduces the optical crosstalk (Hsu et al., 2004). It is also possible to increase the depth of the substrate (Furumiya et al., 2001).

While this effect is generally negligible compared to spectral crosstalk for wavelengths lower than 650 nm (Estribeau and Magnan, 2005), its possible effects are also taken into account in the overall crosstalk estimation scheme presented in Section 7.4.

### 7.2.2.4 Summary of crosstalk effects


Table 7.2 summarizes the causes and the conventional means of estimating and correcting the various crosstalk phenomena.

Section 7.4 demonstrates that inaccuracy on wavelengths of cost-effective laser diodes, as well as the crosstalk phenomena, can significantly degrade the performance of the holographic reconstruction. We detail in Section 7.4 a simple, fast and cost-effective experimental method to reduce the uncertainty on the wavelength of the sources and to characterize the crosstalk phenomenon.



Table 7.2 – Main characteristics of spectral, optical and electronic crosstalk phenomena.

	spectral	optical	electronic
<b>cause</b>	Bayer filters	microlenses	electrons leakage
<b>classical method of quantification</b>	Bayer filters responses	numerical simulations	S-cube system
<b>classical methods of reduction</b>	filters improvement, processing	microlenses position, photodetector treatment	waveguide, deep substrate

 **Low-cost color holographic setup: the need for calibration**

- The diversity of information brought by a color holographic setup can improve the accuracy of the hologram reconstructions thanks to the modulation of the recorded signal on different color channels.
- However, from a cost-effective perspective, the camera is generally a CMOS sensor equipped with a Bayer filter array, and the sources are generally low-end laser diodes. These two elements are subject to several limitations:
  - the central wavelength of laser diodes is known inaccurately due to their temperature and power supply dependence,
  - a signal mixing (crosstalk phenomenon) occurs on the different channels of the CMOS sensor due to Bayer filters.
- These limitations are the cause of errors during the reconstruction step limiting the performance of holographic microscopy for optical metrology applications if these effects are not estimated and taken into account.

⇒ An accurate and cost-effective calibration of the setup is needed.

### 7.3 Reconstruction using a parameter-based inverse problem approach

As detailed in Section 1.3.2.2, based on an adequate image formation model, parameter-based inverse problem approaches provide accurate reconstructions that are “optimal” in a signal processing point of view, under an additive white Gaussian noise hypothesis. They have been successfully used for optical metrology applications (Lee et al., 2007; Soulez et al., 2007a; Seifi et al., 2013; Verrier et al., 2016) and appear to be the best methods to calibrate a monochromatic holographic setup (Verrier et al., 2014). We propose to use such an approach to reconstruct a spherical opaque object naturally present in the field of view or added as calibration object and thus obtain an accurate (i.e., low bias and standard deviation) self-calibration of the setup. The proposed method can be considered cost-effective as it only requires a spherical object in addition to the holographic color microscope. Hereafter, we give some basics and

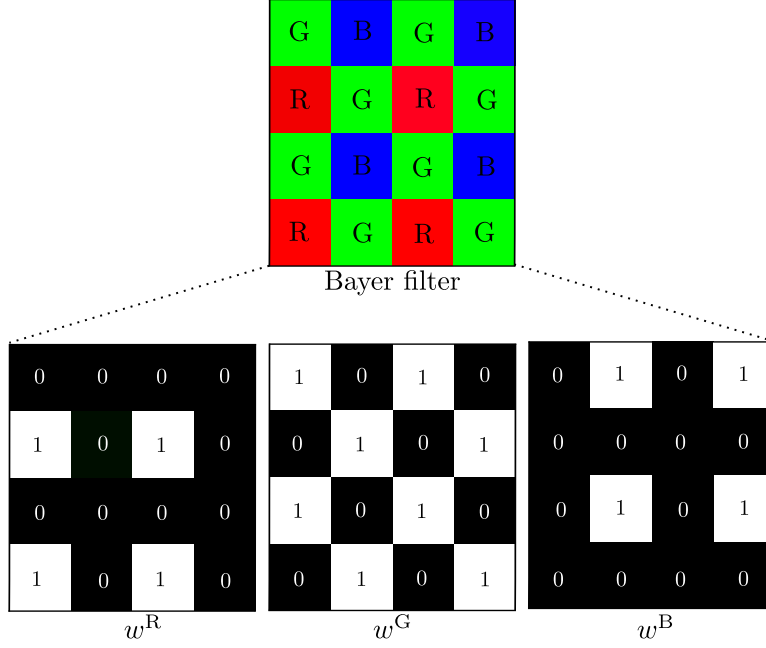


Figure 7.7 – Illustration of the Bayer filters and associated weighting matrices  $w^c$  for each color channel.

mathematical formulation of the parameter-based reconstruction method presented in Section 1.3.2.2, which is here adapted to the reconstruction of color holograms.

We consider an opaque sphere characterized by the parameter vector  $\boldsymbol{\theta} = \{x_p, y_p, z_p, r_p\}$  in which  $\{x_p, y_p\}$  represent the longitudinal coordinates in the object plane,  $z_p$  is the depth coordinate, and  $r_p$  is the radius of the object, see Figure 7.2.

The intensity diffracted by the object and recorded at the  $\{x, y\}$  position in the sensor plane on channel  $c$  ( $c \in \{R, G, B\}$ ) is:

$$m_{\boldsymbol{\theta}}^c(x, y) = m_0^c - \alpha_{\lambda(c)}^c \cdot g_{\lambda(c), \boldsymbol{\theta}}(x, y), \quad (7.3)$$

in which  $m_0^c$  is an offset representing the intensity of the illumination wave,  $\alpha_{\lambda(c)}^c$  is the amplitude factor of the interference pattern and  $g_{\lambda(c), \boldsymbol{\theta}}$  represents the analytical model of the diffraction pattern for the object characterized by the parameters set  $\boldsymbol{\theta}$  and illuminated by a plane wave at wavelength  $\lambda(c)$ .

Since the opaque sphere is illuminated by a collimated coherent source and  $z_p$  is chosen so that  $z_p \gg \frac{4\pi r_p^2}{\min_c \lambda(c)}$ ,  $g_{\lambda(c), \boldsymbol{\theta}}$  can be described by a simplified Thompson's model (Tyler and Thompson (1976)), see Section 1.3.2.2) in which the second order interference terms are neglected:

$$g_{\lambda, \boldsymbol{\theta}}(x, y) = \frac{\pi r_p^2}{\lambda z_p} J_{1c} \left( \frac{2\pi r_p \rho_p}{\lambda z_p} \right) \sin \left( \frac{\pi \rho_p^2}{\lambda z_p} \right), \quad (7.4)$$

where  $\rho_p = \sqrt{(x - x_p)^2 + (y - y_p)^2}$  is the transversal distance to the center of the sphere and  $J_{1c} = J_1(u)/u$  is the cardinal Bessel function of the first order.

Therefore, the color hologram model  $\mathbf{m}_{\boldsymbol{\theta}}(x, y)$  at position  $(x, y)$  on the sensor plane is the vector given in Equation (7.5) in which each component is associated with one of the three sensor channels  $c \in \{R, G, B\}$ :

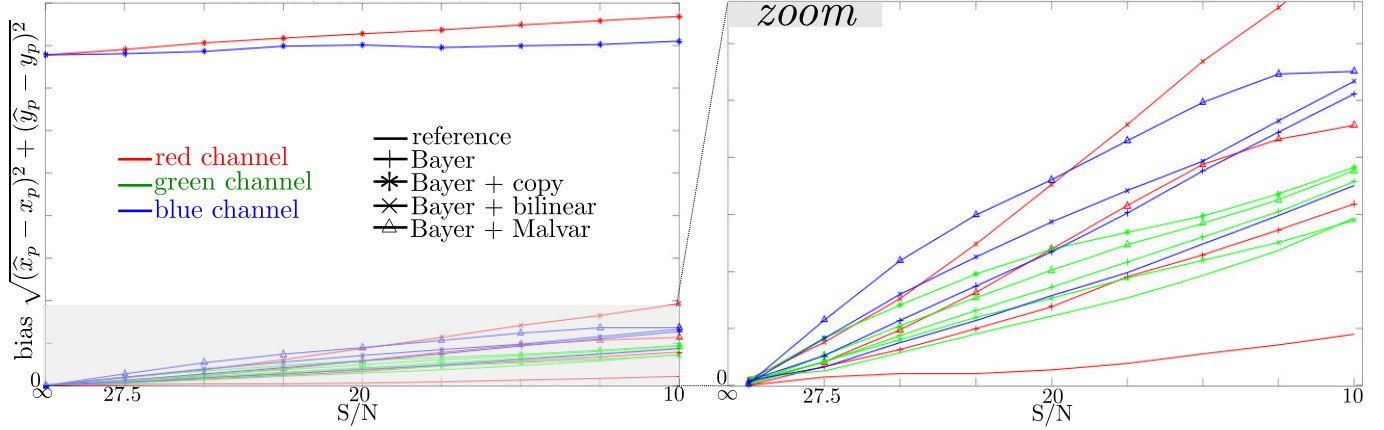


Figure 7.8 – Illustration of the effect of demosaicking on simulations of color holograms recorded with a CMOS camera covered by a Bayer filter array. The simulated object is a bead of  $r_p = 20 \mu\text{m}$  radius centered on the field of view, and located at  $z_p = 0.01 \text{ m}$  from the sensor plane. The bias on the estimation of the 2-D location of a spherical and opaque bead is given for different levels of S/N. Reference: the simulated holograms are formed of three full channels (no Bayer filters, i.e. no missing data) as it would be recorded by a full-frame trichromatic color sensor. Bayer: no demosaicking is applied on the simulated holograms, missing data are taken into account via the weights matrix  $\mathbf{w}^c$ . Bayer + copy, Bayer + bilinear, Bayer + Malvar: the simulated color holograms are demosaicked with neighbor pixel copy, bilinear or Malvar (Malvar et al., 2004) interpolations, respectively. The Malvar method is based on a bilinear interpolation and accounts for the presence of edges in the images.

$$\mathbf{m}_\theta(x, y) = \begin{pmatrix} m_\theta^R(x, y) \\ m_\theta^G(x, y) \\ m_\theta^B(x, y) \end{pmatrix}. \quad (7.5)$$

The inverse approach consists of finding the best set of parameters  $\theta$  from the recorded color hologram  $\mathbf{d}$ , i.e., the set  $\theta$  that minimizes, in the least-squares sense, the distance to the data:

$$\mathcal{E}(\theta) = \sum_{c \in \{R, G, B\}} \sum_{a=1}^A \sum_{b=1}^B w^c(a, b) \cdot (d^c(a, b) - m_\theta^c(a, b))^2, \quad (7.6)$$

in which  $w^c$  is a binary weighting matrix of size  $A \times B$  describing the Bayer mask ( $w^c$  is equal to zero for 75% of the red and blue channels and for 50% of the green channel as shown in Figure 7.7) and possibly any defective pixel on channel  $c$ . More generally,  $w^c(a, b)$  stands for the inverse of the noise variance at pixel  $(a, b)$  on channel  $c$  (Fournier et al., 2014), as also discussed in Section 5.2.1. The estimation process is performed jointly on the three channels. Figure 7.8 illustrates the importance of taking into account missing data with the  $\mathbf{w}^c$  matrices for accurate estimation of object properties from color holograms recorded by a sensor equipped a Bayer filter array. It emphasizes that a demosaicking of each color channel of the hologram (i.e., replacement

of missing data by interpolated values from neighboring data) leads to larger bias than the absence of a demosaicking step, whatever the interpolation technique used. It can be explained by the low-pass filtering (i.e., blurring of the hologram fringes) induced by the demosaicking step. This figure also illustrates that the choice of the interpolation method can severely impact the quality of the demosaicking. For example, the method consisting of replicating the nearest data of missing pixels (denoted “Bayer + copy” in Figure 7.8) is generally the worst of the tested strategies (see upper curves in left part of Figure 7.8).

## 7.4 Self-calibration of a color microscope

The self-calibration process described hereafter has several advantages. First of all, it can be considered as a cost-effective method as it only requires a spherical and calibrated opaque object. It is also simple to implement and fast. The overall process takes less than 4 minutes to obtain an estimate of the wavelengths and 5 minutes to obtain an estimate of the crosstalk phenomenon (MATLAB™ code launched on 1 core, processor INTEL™ i7-4800MQ at 2.70 GHz) which seems reasonable in comparison with experimental measurement of these parameters with high-end devices.

To study the proposed calibration method, we used a chrome deposited opaque object behaving as an opaque sphere. Its radius is 15 μm (OPTIMASK™, diameter ± 1 μm, roundness error ± 0.25 μm). It should be noted that, in practice, any spherical opaque object can be used.

### 7.4.1 Estimation of the wavelength of the sources

From Equation (7.2), it is clear that it is impossible to jointly estimate the three wavelengths values as well as the  $z_p$  parameter (three equations for four unknown). It is thus necessary to select one of the wavelengths as a reference that will not be estimated. In practice, the laser source with the smallest uncertainty is chosen. As a result, in the following it is assumed that  $\lambda_G^{\text{real}}$  is equal to  $\lambda_G^{\text{nom}}$ , since the green laser wavelength used has the smallest manufacturer uncertainty ( $\pm 1$  nm, see Table 7.1). We briefly discuss in Section 7.4.1.3, how this problem could be circumvented to estimate also the reference wavelength with a more expensive setup.

#### 7.4.1.1 Wavelength calibration in color holography with a parameter-based inverse approach

**Step ①:** *Acquisition of three monochromatic holograms at the wavelengths  $\lambda^{\text{real}}$ .*

**Step ②:** *Independent reconstruction of each hologram using the inverse parameter-based approach with nominal wavelength values  $\lambda^{\text{nom}}$ . At the end of this step, estimated parameters  $\{x_{\{R,G,B\}}^{\text{est}}, y_{\{R,G,B\}}^{\text{est}}, z_{\{R,G,B\}}^{\text{est}}, r_{\{R,G,B\}}^{\text{est}}\}$  are obtained.*

**Step ③:** *Coarse estimation of the wavelengths of the sources.* It can be deduced from the hypothesis that  $\lambda_G^{\text{real}}$  equals  $\lambda_G^{\text{nom}}$  that  $z_G^{\text{est}}$  and  $r_G^{\text{est}}$  are respectively the best estimation of  $z_p$  and  $r_p$  in the current step. From Equations (7.1) and (7.2), a first estimated wavelength of the red and blue sources is given by:

$$\begin{cases} \lambda_R^{\text{est}1} &= \lambda_R^{\text{nom}} + \Delta_{\lambda_R} \approx \lambda_R^{\text{nom}} + \lambda_R^{\text{nom}} \cdot \frac{z_G^{\text{est}} - z_R^{\text{est}}}{z_G^{\text{est}}} \\ \lambda_B^{\text{est}1} &= \lambda_B^{\text{nom}} + \Delta_{\lambda_B} \approx \lambda_B^{\text{nom}} + \lambda_B^{\text{nom}} \cdot \frac{z_G^{\text{est}} - z_B^{\text{est}}}{z_G^{\text{est}}} \end{cases} \quad (7.7)$$

**Step ④**: *Refinement of the red and blue wavelengths.* This estimation is carried out using an inverse problem approach in which the parameters  $z_p$  and  $r_p$  are jointly estimated. The transversal coordinates  $(x_p, y_p)$  and the red and blue wavelengths are also estimated. The estimation process is initialized to the most accurate parameter values available at this step:  $\{x_{\{R,G,B\}}^{\text{est}}, y_{\{R,G,B\}}^{\text{est}}, z_G^{\text{est}}, r_G^{\text{est}}\}$  and  $(\lambda_R^{\text{est}1}, \lambda_G^{\text{nom}}, \lambda_B^{\text{est}1})$ . At the end of this step, a second estimated wavelength  $(\lambda_R^{\text{est}2}, \lambda_G^{\text{nom}}, \lambda_B^{\text{est}2})$  of the sources is obtained.

It is important to note that **Step ③** is a first estimate to be refined in **Step ④**. By initializing **Step ④** to estimated parameters closer to the real parameters than those available in **Step ②**, the computation time of **Step ④** is reduced. It also reduces the risk of converging to a local minimum of the cost function given in Equation (7.6).

#### 7.4.1.2 Experimental results and discussion

This method is applied to a set of 65 experimental holograms ( $z_p \simeq 7$  cm,  $r_p = 15$   $\mu\text{m}$  transversely shifted by a few pixels from each other). The obtained results are compared with measured wavelengths using a high-resolution spectrometer (OCEANOPTICS<sup>TM</sup>, QE65000). Before running our experiments, we have calibrated it with care by measuring the spectral rays of a mercury lamp (PHILIPS<sup>TM</sup>, 93136E). Second-order polynomial interpolation is also applied to reduce measurement inaccuracy of the spectrometer from 0.8 nm to 0.3 nm on the central wavelength of the laser. Table 7.3 lists the mean value and standard deviation of estimated wavelengths  $\{\lambda_R^{\text{est}2}, \lambda_B^{\text{est}2}\}$  (line 1 and 3) as well as the measured wavelengths (line 2). Line 1 gives the estimates if the green wavelength is set at its nominal value  $\lambda_G^{\text{nom}}$  (no use of the spectrometer) and line 3 gives the estimates if the green wavelength is set at the wavelength  $\lambda_G^{\text{mes}}$  measured using the spectrometer.

Table 7.3 – Estimated and measured wavelengths of the sources.

	$\lambda_R$ (nm)	$\lambda_G$ (nm)	$\lambda_B$ (nm)
<b>estimation</b> ( $\lambda_G^{\text{ref}} = \lambda_G^{\text{nom}}$ )	$638.3 \pm 0.2$	532 ( <i>ref.</i> )	$403.3 \pm 0.2$
<b>high-resolution spectrometer</b>	$637.8 \pm 0.3$	$531.4 \pm 0.3$	$402.9 \pm 0.3$
<b>estimation</b> ( $\lambda_G^{\text{ref}} = \lambda_G^{\text{mes}}$ )	$637.6 \pm 0.2$	531.4 ( <i>ref.</i> )	$402.8 \pm 0.2$

Within our experimental framework, it appears that the hypothesis assimilating the real green wavelength to its nominal value results in an overestimation of 0.6 nm. By considering the Equation (7.1) and a unique  $z$  for the three wavelengths, this bias generates a theoretical overestimation of 0.7 nm for the red wavelength as well as a theoretical overestimation of 0.5 nm for the blue wavelength. This is in agreement with the measured wavelengths of the sources obtained experimentally.

This method is constrained by the hypothesis that one of the three nominal wavelengths can be considered correct. The uncertainty on the estimated wavelengths (for

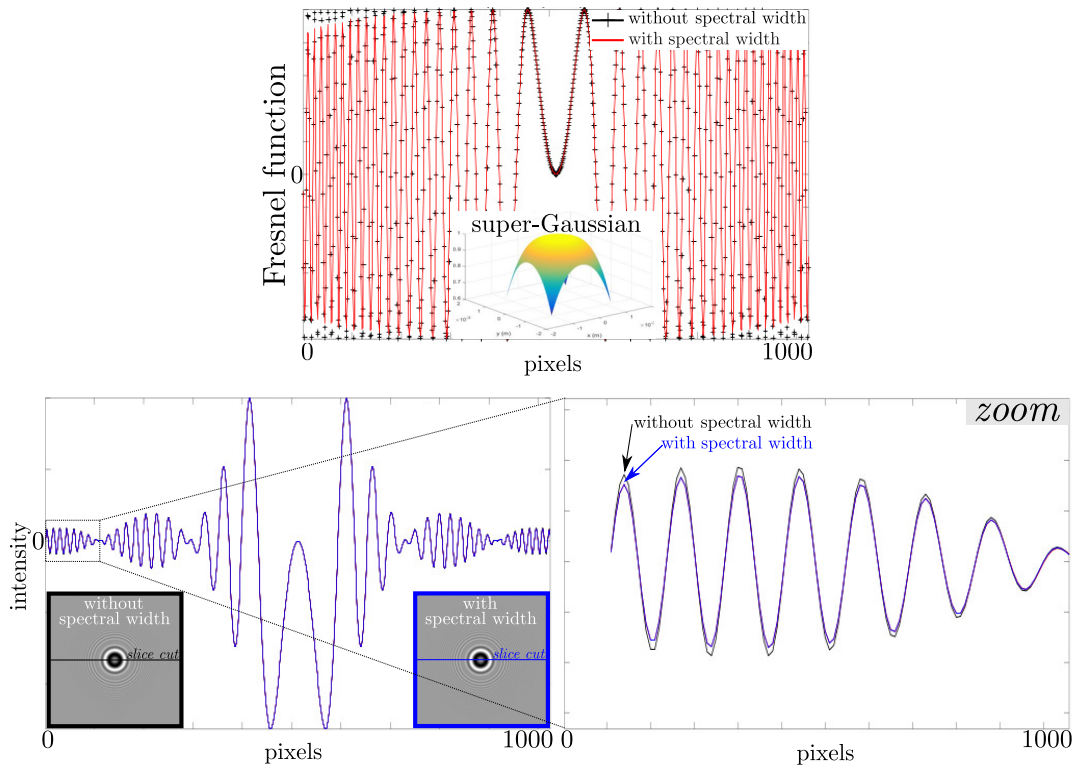


Figure 7.9 – Illustration of the effect of the spectral width of a laser source at  $\lambda^{\text{nom}} = 435 \text{ nm}$  of  $0.4 \text{ nm}$  FWHM. Top: impact illustrated on the Fresnel propagation kernel. Bottom: resulting impact on a hologram simulation.

the two other sources) increases with the manufacturer uncertainty range for the wavelength chosen as reference. In this experiment, this hypothesis generates an uncertainty of  $\pm 1 \text{ nm}$  on the wavelength value of this source. This leads to an uncertainty of  $\pm 1.2 \text{ nm}$  on the estimated red wavelength  $\lambda_{\text{R}}^{\text{est}2}$  and uncertainty of  $\pm 0.8 \text{ nm}$  on the estimated blue wavelength  $\lambda_{\text{B}}^{\text{est}2}$ . Thus, using this estimation procedure reduces the uncertainty on the range of wavelength from  $15 \text{ nm}$  (manufacturer value) to  $1.2 \times 2 = 2.4 \text{ nm}$  for the red source. Similarly, the uncertainty on the range of wavelength has been reduced from  $10 \text{ nm}$  (manufacturer value) to  $0.8 \times 2 = 1.6 \text{ nm}$  for the blue source. It is thus shown in Table 7.3 line 3, that using the value measured with an high-resolution spectrometer for  $\lambda_{\text{G}}^{\text{real}}$  leads to a very accurate estimation of the other two wavelengths.

Moreover, beyond the relative precision of the estimation, it should also be noted that the deviations between the different estimated wavelengths are equal to the deviations between the different measured wavelengths. This point again emphasizes the interest of this method to improve the quality of the reconstructions. The limit of the method is reached when the uncertainties on the range of wavelength associated with each source provided by the manufacturer are similar. In that case, there is no gain in applying this method for absolute wavelength estimation. It is still beneficiary to refine the wavelengths in order to obtain the same focus distance at each wavelength when performing a joint multi-spectral reconstruction.

The proposed method is limited to estimating the central wavelength of the sources, while in practice laser diodes deliver a quasi-monochromatic light, only. In our setup,



according to the datasheets of our laser diodes, a temperature variation may also result in a slight change in the shape of the laser emission spectrum. In the literature, the effects of the spectral width of the light source on the hologram formation have been studied. It is shown that a non-monochromatic source generates an apodization of the propagation impulse response by a super-Gaussian function depending on the spectral width of the source (Nicolas et al., 2006, 2007). Thus, it could be possible to estimate this effect as an additional parameter in our hologram formation model (7.4). However, it appears that the spectral width of the sources is less crucial than their central wavelength. Indeed, Figure 7.9 gives an example of hologram simulations taking into account or not the typical FWHM of the spectral responses of our laser diodes which is about 0.4 nm. It shows that only the amplitude of the diffraction pattern is (slightly) impacted by the apodization induced by the width of the spectral responses of our lasers while the localization of the interference fringes is preserved. Indeed, not taking into account the spectral width in the image formation model (Equations (7.3) and (7.4)) results only in a small impact on the minimization of (7.6): the model mismatch is small given the signal-to-noise ratio of the holograms.

#### 7.4.1.3 Estimation of the reference wavelength

As discussed in the previous section, our wavelength calibration procedure requires a prior on one wavelength value, which is kept fixed and not estimated. In this section, we briefly describe how the reference wavelength could be estimated jointly with the others using a more expensive setup (with an accurate translation stage).

The setting of a reference wavelength is due to the impossibility to jointly estimate the three wavelengths as well as the  $z_p$  parameter from Equation (7.2) with a single color hologram. The system underdetermination can be alleviated by recording several color holograms obtained with the same object at different known defocus. For example, the recording of two holograms resulting from the illumination of a spherical object at  $z_p$  and  $z_p + z_{\text{shift}}$ , where  $z_{\text{shift}}$  is a known axial displacement of the object between the two acquisitions, leads to the following systems of equations:

$$\left\{ \begin{array}{l} \lambda_{\text{R}}^{\text{nom}} z_{\text{R}}^{\text{est}} = \lambda_{\text{R}}^{\text{real}} z_p, \\ \lambda_{\text{G}}^{\text{nom}} z_{\text{G}}^{\text{est}} = \lambda_{\text{G}}^{\text{real}} z_p, \\ \lambda_{\text{B}}^{\text{nom}} z_{\text{B}}^{\text{est}} = \lambda_{\text{B}}^{\text{real}} z_p, \end{array} \right. \quad \text{and} \quad \left\{ \begin{array}{l} \lambda_{\text{R}}^{\text{nom}} z'_{\text{R}}^{\text{est}} = \lambda_{\text{R}}^{\text{real}} (z_p + z_{\text{shift}}), \\ \lambda_{\text{G}}^{\text{nom}} z'_{\text{G}}^{\text{est}} = \lambda_{\text{G}}^{\text{real}} (z_p + z_{\text{shift}}), \\ \lambda_{\text{B}}^{\text{nom}} z'_{\text{B}}^{\text{est}} = \lambda_{\text{B}}^{\text{real}} (z_p + z_{\text{shift}}), \end{array} \right. \quad (7.8)$$

which is no longer underdetermined (six equations for four unknown parameters  $\{z_p, \lambda_{\text{R}}^{\text{real}}, \lambda_{\text{G}}^{\text{real}}, \lambda_{\text{B}}^{\text{real}}\}$  to be estimated).

For the same object parameters as the ones used in Section 7.4.1.2 (i.e.  $z_p \simeq 7$  cm,  $r_p = 15$   $\mu\text{m}$ ), our numerical Monte-Carlo hologram simulations (with an additive white Gaussian noise at  $S/N = 5$ ) lead to a mean bias of about 0.1 nm on the three estimated wavelengths when  $z_{\text{shift}}$  is perfectly known. When  $z_{\text{shift}}$  is known within 5  $\mu\text{m}$ , the mean bias on the three estimated wavelengths is up to 0.2 nm, which stays below the systematic error due to the hypothesis of a reference wavelength, see Section 7.4.1.2. However, these simulations emphasize that the axial shift  $z_{\text{shift}}$  of the object should be known with relatively good precision to achieve a low estimation bias on the wavelengths. In practice, such precision on the object displacement may be obtained only with a precision translation stage, which was not part of our cost-effective setup.

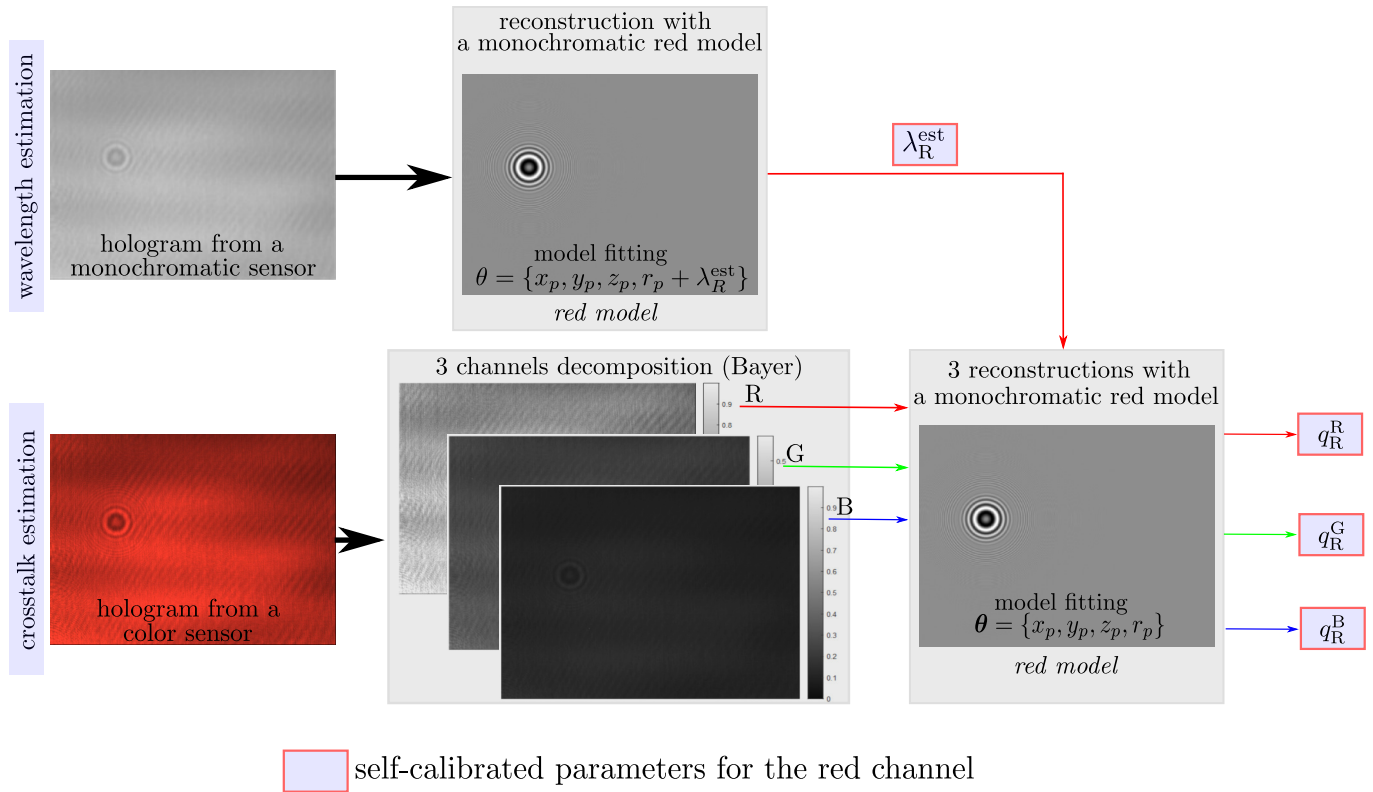


Figure 7.10 – Parameter-based estimation principle of channel mixing coefficients induced by crosstalk phenomenon.

## 7.4.2 Calibration of the crosstalk phenomenon affecting the sensor

As detailed in Section 7.2, the optical crosstalk which is spatially dependent can be neglected in holographic microscopy. In the following, we do not attempt to separate the contribution of the spectral crosstalk and the electronic crosstalk, but rather obtain an estimate of the overall crosstalk that can be included in the hologram formation model to improve the quality of the holographic reconstructions.

As a result, the proposed self-calibration method consists in determining a unique set of coefficients modeling the mixture of the signals received on each channel due to both the spectral and the electronic crosstalks.

### 7.4.2.1 Principle of crosstalk estimation using the parameter-based inverse approach

Once the central wavelengths of the lasers are calibrated, it remains to estimate the crosstalk phenomenon. In this section, we propose a simple experimental method based on an inverse parameter-based approach to determine the mixing coefficients between the different color channels, for a trichromatic illumination (the calibrated ones resulting from the procedure described in Section 7.4.1). In the presence of crosstalk, Equation (7.3) modeling the intensity diffracted on channel  $c$  should be changed to take into

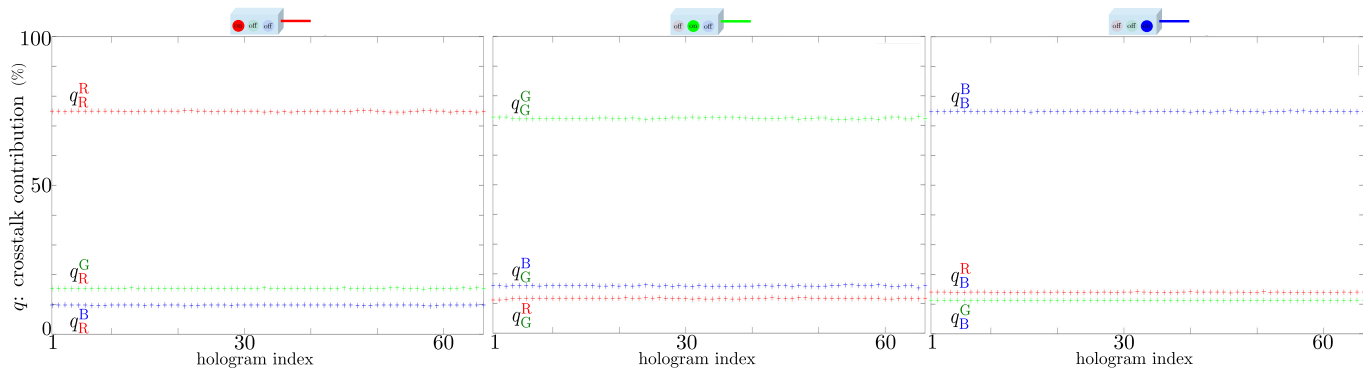


Figure 7.11 – Estimated crosstalk contributions  $q$  of the crosstalk matrix  $\mathbf{Q}_{\text{exp}_1}$  from 65 sets of three color holograms recorded by the color CMOS sensor #1. From left to right, crosstalk contributions induced by the red, green, and blue laser diodes.

account the mixture of signals coming from the different channels:

$$m_{\theta}^c(x, y) = m_0^{c*} - \sum_{\ell=1}^3 \alpha_{\lambda(\ell)}^c \cdot g_{\lambda(\ell), \theta}(x, y), \quad (7.9)$$

where  $\alpha_{\lambda(\ell)}^c$  represents the multiplicative factor between the holographic data recorded on channel  $c \in \{\text{R}, \text{G}, \text{B}\}$  and the model generated at the wavelength  $\lambda(\ell)$ ,  $m_0^{c*}$  is the offset that results from mixing offsets  $m_0^{\text{R}}$ ,  $m_0^{\text{G}}$  and  $m_0^{\text{B}}$ .

The signal ratio  $q_{\lambda(\ell)}^c$  produced by illumination at wavelength  $\lambda(\ell)$  and which is actually recorded on sensor channel  $c$  due to the spectral crosstalk effect can be estimated by:

$$q_{\lambda(\ell)}^c = \frac{\alpha_{\lambda(\ell)}^c}{\sum_{c \in \{\text{R}, \text{G}, \text{B}\}} \alpha_{\lambda(\ell)}^c} \Rightarrow \mathbf{Q} = \begin{pmatrix} q_{\text{R}}^{\text{R}} & q_{\text{R}}^{\text{G}} & q_{\text{R}}^{\text{B}} \\ q_{\text{G}}^{\text{R}} & q_{\text{G}}^{\text{G}} & q_{\text{G}}^{\text{B}} \\ q_{\text{B}}^{\text{R}} & q_{\text{B}}^{\text{G}} & q_{\text{B}}^{\text{B}} \end{pmatrix}. \quad (7.10)$$

Thus, the mixing matrix  $\mathbf{Q}$  characterizes the crosstalk effect. Its nine mixing coefficients  $q_{\lambda(\ell)}^c$  are obtained by recording the three color holograms produced by the illumination of an opaque disk at the three available wavelengths. For each of these three holograms, reconstructions have to be carried out for each of the three channels using a parametric model for each wavelength. The multiplicative factors  $\alpha_{\lambda(\ell)}^c$  correspond to the correlation coefficient between data recorded on channel  $c$  illuminated by wavelength  $\lambda(\ell)$  and the model at this same wavelength. The principle of the crosstalk calibration method is illustrated in Figure 7.10 for wavelength  $\lambda_{\text{R}}$ .

As detailed in Section 7.2, the crosstalk phenomenon cannot be accurately estimated by an average of the intensities received on each channel due to the nonuniform background varying over time. The proposed calibration method takes advantage of the modulation of the recorded signal induced by the holographic object to accurately estimate this phenomenon.

Table 7.4 – Estimated crosstalk mixing matrices  $\mathbf{Q}_{\text{exp}_1}$  and  $\mathbf{Q}_{\text{exp}_2}$  (in percent) for two different color CMOS sensor as well as manufacturer’s spectral crosstalk mixing matrix  $\mathbf{Q}_m$  (in percent), roughly deduced from the sensor datasheet (see Figure 7.4).

	red channel	green channel	blue channel
$\mathbf{Q}_{\text{exp}_1}$ : <i>Estimated crosstalk matrix on sensor #1</i>			
<b>red laser</b>	$74.9 \pm 0.1$	$15.4 \pm 0.1$	$9.7 \pm 0.1$
<b>green laser</b>	$11.7 \pm 0.1$	$72.4 \pm 0.2$	$15.9 \pm 0.2$
<b>blue laser</b>	$14.0 \pm 0.1$	$11.1 \pm 0.1$	$74.9 \pm 0.1$
$\mathbf{Q}_{\text{exp}_2}$ : <i>Estimated crosstalk matrix on sensor #2</i>			
<b>red laser</b>	$75.6 \pm 0.1$	$14.9 \pm 0.1$	$9.5 \pm 0.1$
<b>green laser</b>	$11.5 \pm 0.1$	$72.3 \pm 0.2$	$16.2 \pm 0.2$
<b>blue laser</b>	$13.9 \pm 0.1$	$11.2 \pm 0.1$	$75.0 \pm 0.2$
$\mathbf{Q}_m$ : <i>Manufacturer’s crosstalk matrix</i>			
<b>red laser</b>	74	16	10
<b>green laser</b>	12	70	18
<b>blue laser</b>	14	14	72

#### 7.4.2.2 Experimental results and discussion

Table 7.4 gives the estimated mean and standard deviation (related to the standard deviation of the estimated parameters  $\theta$ ) of the crosstalk mixing matrices  $\mathbf{Q}_{\text{exp}_1}$  and  $\mathbf{Q}_{\text{exp}_2}$  obtained from 2 batches of 65 sets of three color holograms recorded on two different color CMOS sensors (#1 and #2) of the same make at the respective wavelengths  $\{\lambda_R^{\text{real}}, \lambda_G^{\text{real}}, \lambda_B^{\text{real}}\}$ . Figure 7.11 presents each crosstalk estimation characterizing sensor #1. Table 7.4 also gives the  $\mathbf{Q}_m$  mixing matrix extracted from the sensor datasheet, see Figure 7.4.

Using this self-calibration scheme, it appears that the mixing coefficients estimated are close to those deduced from the manufacturer spectral responses of the Bayer filters. This indicates that the crosstalk effect of our camera is mainly due to the spectral crosstalk (the electronic crosstalk effect being negligible). Thus, it appears that for each channel, approximately 25% of the signal of interest is transferred to the two other channels due to the crosstalk effect. This observation suggests that it is important to take this phenomenon into account in the holographic model used during the reconstruction step. Note that, in practice, only one set of holograms is needed to obtain a spectral crosstalk estimation (whose standard deviation is given in Table 7.4). The application of this method to another camera of the same make leads to a similar crosstalk matrix. Minor variations can be attributed to the camera’s variability (e.g., homogeneity of the filters, local orientation of the microlenses, etc.).

In the following paragraph, it will be shown that it is beneficial to estimate more accurate mixing matrix than the ones of the datasheet of the sensor. Indeed, a significant discrepancy can be observed for the blue light intensity distribution on the different channels between the estimated values and the values derived from the manufacturer datasheets.

**Self-calibration of color holographic setups**

- We propose an experimental, simple and fast method to calibrate color holographic setups, i.e.:
  - estimate the central wavelength of the sources,
  - estimate the mixing contributions of the crosstalk phenomenon.
- The estimation method is based on the reconstruction of holograms of spherical absorbing objects (naturally present in the field of view or added as calibration object) using an inverse problem approach.
- We show on experimental holograms that this method leads to accurate estimations comparable to that obtained using a high-resolution spectrometer.

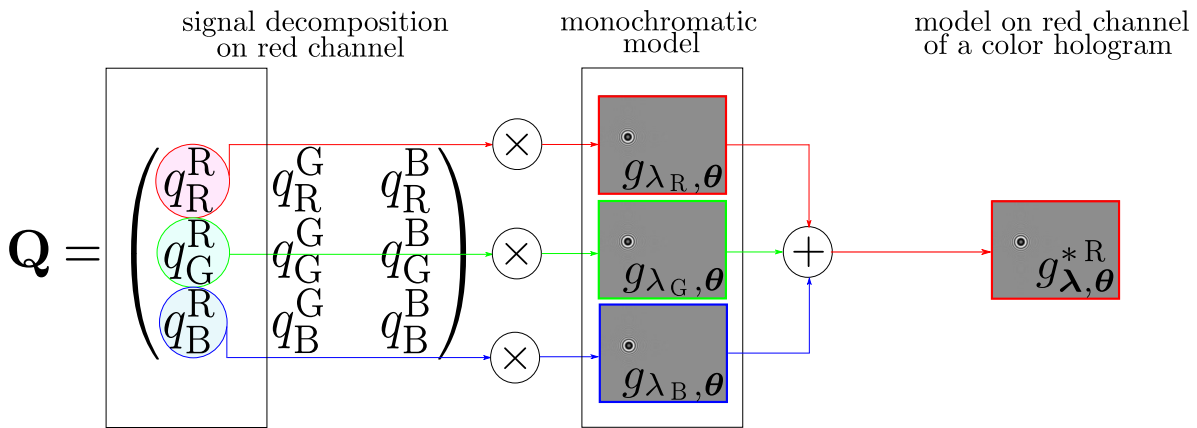


Figure 7.12 – Principle of crosstalk correction.

## 7.5 Improving object reconstruction with self-calibration

Once the central wavelength of the sources and the crosstalk phenomenon occurring on CMOS color sensors are both calibrated, they can be accounted for in the hologram formation model to improve the quality of the reconstructions whatever the strategy used. In the following, we explain how to account for the calibration in the reconstruction process and show that the proposed approach is beneficial.

### 7.5.1 Accounting for self-calibration in physics-based models

Accounting for the calibration of the sources is straightforward since the set of wavelengths  $\lambda$  is replaced by the estimated one  $\lambda^{\text{est}}$  in the hologram formation models. Accounting for the crosstalk phenomenon is also simple since the color hologram

Table 7.5 – Bias and standard deviation on estimated parameters  $z_p$  and  $r_p$  without crosstalk correction (1st line), with crosstalk correction using  $\mathbf{Q}_m$  (2nd line) and with crosstalk correction using  $\mathbf{Q}_{\text{exp}_1}$  (3rd line) for a centered object whose radius is  $r_p = 15 \mu\text{m}$  located at  $z_p = 7 \text{ cm}$  from the sensor plane.

	bias on $z_p$ (nm)	std. dev. on $z_p$ (nm)
<b>without correction</b>	52	316.3
<b>with crosstalk correction (<math>\mathbf{Q}_m</math>)</b>	15	315.5
<b>with crosstalk correction (<math>\mathbf{Q}_{\text{exp}_1}</math>)</b>	9.9	315.5
	bias on $r_p$ (nm)	std. dev. on $r_p$ (nm)
<b>without correction</b>	21	5.0
<b>with crosstalk correction (<math>\mathbf{Q}_m</math>)</b>	0.50	4.8
<b>with crosstalk correction (<math>\mathbf{Q}_{\text{exp}_1}</math>)</b>	0.28	4.8

models can be modified to account for the signal mixing on the different channels of the sensor. For that purpose, the vector  $\mathbf{g}$  containing the holographic models on the different channels  $c$  is replaced by  $\mathbf{g}^*$  according to:

$$\mathbf{g}^*(x, y) = \begin{pmatrix} g_{\lambda, \theta}^{*R}(x, y) \\ g_{\lambda, \theta}^{*G}(x, y) \\ g_{\lambda, \theta}^{*B}(x, y) \end{pmatrix} = \mathbf{Q}^\top \begin{pmatrix} g_{\lambda_R, \theta}(x, y) \\ g_{\lambda_G, \theta}(x, y) \\ g_{\lambda_B, \theta}(x, y) \end{pmatrix} = \mathbf{Q}^\top \mathbf{g}(x, y). \quad (7.11)$$

This equation thus expresses the mixture of signals from the different sources on each channel  $c$ . Rather than separating the signals received on each sensor channel (by unmixing), this method mixes the hologram formation model in the same way as the recorded data. Figure 7.12 illustrates this principle.

## 7.5.2 Self-calibration applied to the reconstruction of parametric objects

### 7.5.2.1 Reconstruction of parametric opaque objects

To study the benefits of the calibration procedure described in Section 7.4, we turn to simulations of color holograms impacted by the crosstalk phenomenon according to estimated crosstalk matrix  $\mathbf{Q}_{\text{exp}_1}$ , see Table 7.4. The object of interest is a spherical bead located in the center of the field of view. Simulations are carried out for different sets of parameters  $z_p$  ( $z_p \in [7 \text{ cm}; 12 \text{ cm}]$ ) and  $r_p$  ( $r_p \in [15 \mu\text{m}; 50 \mu\text{m}]$ ). For each pair of values  $\{z_p, r_p\}$ , 100 color holograms are generated (using the direct model (7.9)) with an additive white Gaussian noise at  $S/N = 2.5$ .

Figure 7.13 shows the reconstruction bias on the estimated parameters  $z_p$  and  $r_p$  when the crosstalk phenomenon is not taken into account in the reconstruction step and taken into account by replacing the model  $\mathbf{g}$  in Equation (7.3) by  $\mathbf{g}^*$  from Equation (7.11). When the crosstalk mixing is accounted for in the reconstruction step, we use both  $\mathbf{Q}_{\text{exp}_1}$  and  $\mathbf{Q}_m$  mixing matrices. Table 7.5 gives the corresponding results for one of the configurations illustrated in Figure 7.13. Table 7.5 shows that taking the crosstalk into account in the hologram formation model reduces the estimation bias



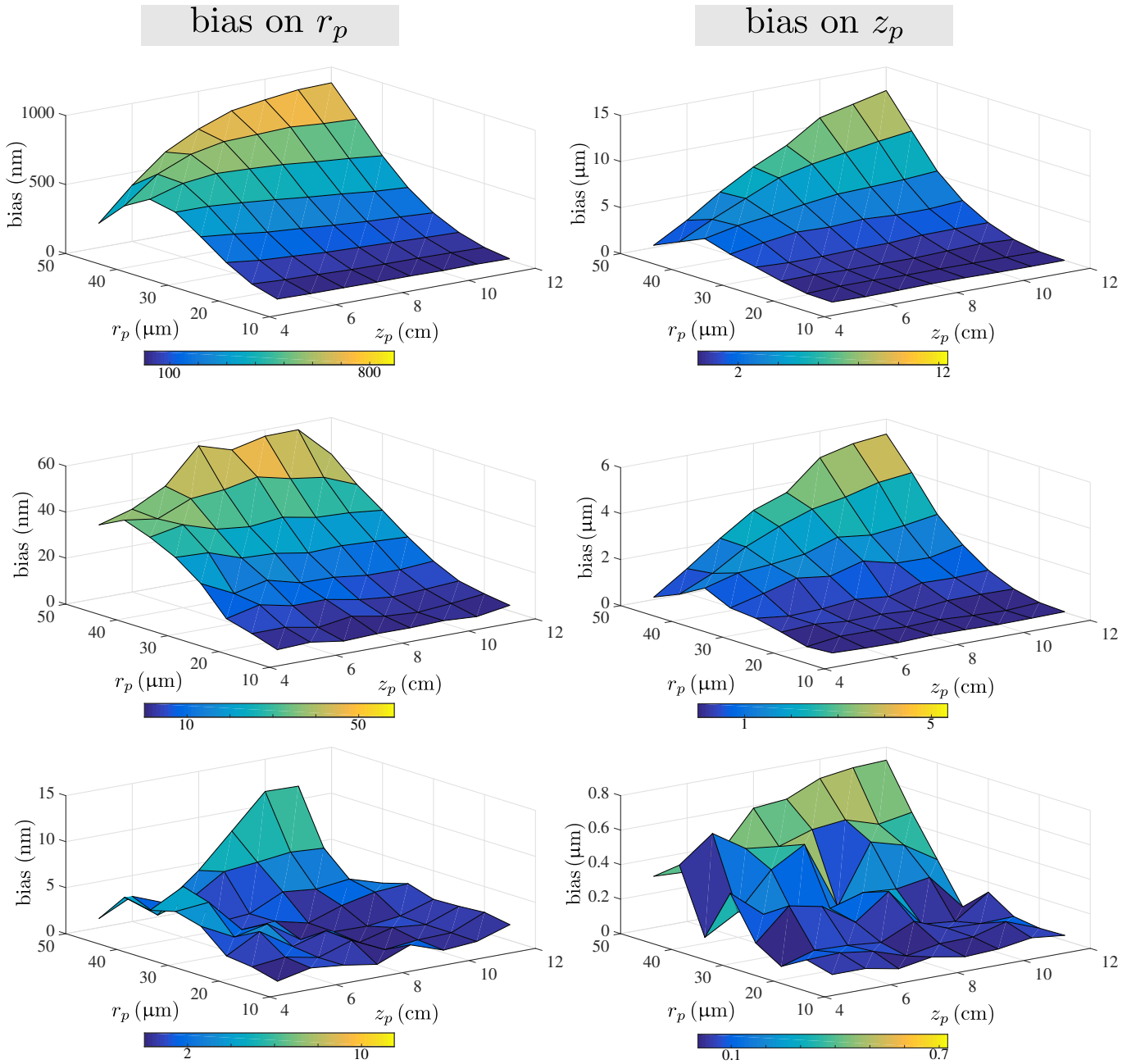


Figure 7.13 – Bias on estimated  $r_p$  (left) and  $z_p$  (right) without crosstalk correction (1st line), with crosstalk correction using  $\mathbf{Q}_m$  (2nd line) and with crosstalk correction using  $\mathbf{Q}_{\text{exp}_1}$  (3rd line) for a centered object whose radius is  $r_p \in [15 \mu\text{m}; 50 \mu\text{m}]$  located at  $z_p \in [7 \text{ cm}; 12 \text{ cm}]$  from the plane of the sensor.

by a factor between 3 (using  $\mathbf{Q}_m$ ) and 5 (using  $\mathbf{Q}_{\text{exp}_1}$ ) for the estimated  $z_p$  parameter and by a factor between 40 (using  $\mathbf{Q}_m$ ) and 70 (using  $\mathbf{Q}_{\text{exp}_1}$ ) for the estimated  $r_p$  parameter for an object whose radius is  $15 \mu\text{m}$  and located at  $7 \text{ cm}$  from the sensor plane. Correction by an approximate crosstalk matrix enables a significant reduction of the estimation bias. This bias is further reduced when the crosstalk matrix used in the

Table 7.6 – CRLBs on the 3-D location and radius of a bead.

	$\delta_x$ (nm)	$\delta_y$ (nm)	$\delta_z$ (nm)	$\delta_r$ (nm)
$\lambda_R$	0.56	0.49	31	0.37
$\lambda_G$	0.59	0.55	35	0.40
$\lambda_B$	0.70	0.63	41	0.46
$\lambda_{R,G,B}$	0.32	0.35	20	0.13
$\lambda_{R,G,B} + \text{Bayer}$	0.53	0.50	31	0.22
$\lambda_{R,G,B} + \text{Bayer} + \text{ct}$	0.70	0.80	40	0.30

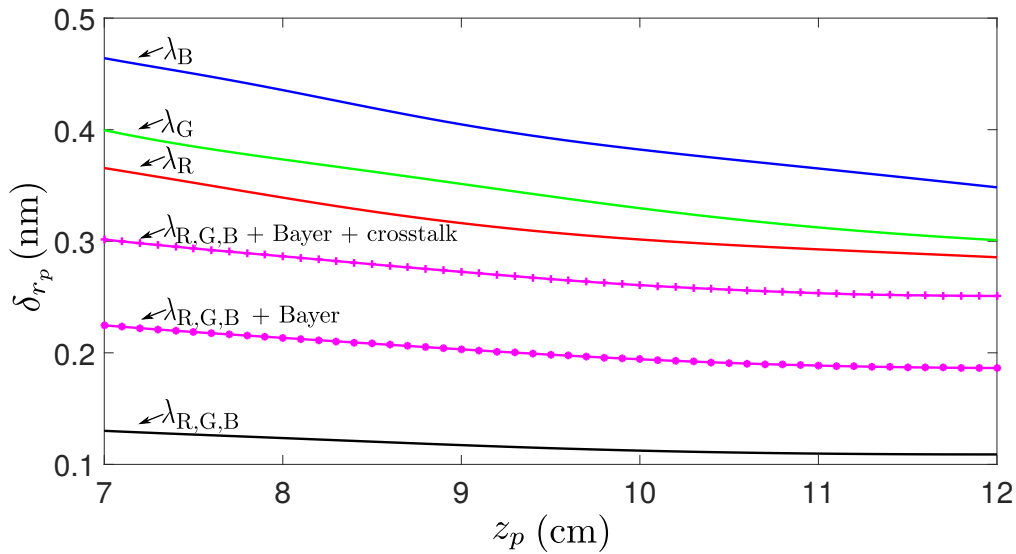


Figure 7.14 – CRLBs on bead radius for different distances between the sensor and object.

reconstruction step is closer to that generating the channels mixing. This justifies the use of an accurate estimation of spectral crosstalk. It should be noted that the empirical standard deviation is not reduced by taking the spectral crosstalk into account. Indeed, it is dependent on the S/N and the estimation method. Also, since a change of the  $z_p$  and  $r_p$  parameters causes a frequencies modification in the hologram signal, the crosstalk phenomenon can generate a more or less important frequency mixing according to the experimental parameters. As a result, the estimation of these parameters without crosstalk correction generates a bias depending on the importance of the frequency mixing (especially important when  $z_p$  and  $r_p$  increase simultaneously, as shown by Figure 7.13). This shows that reconstructions without accounting for crosstalk cannot be easily compensated for the bias since the bias is not constant.

### 7.5.2.2 Theoretical limits of precision

In this section, we discuss the theoretical limits of precision achievable on the estimated parameters  $\theta = \{x_p, y_p, z_p, r_p\}$  in a monochromatic or a color holography framework. The aim is to investigate whether the consideration of a mosaicked color hologram which can be impacted by the crosstalk phenomenon provides at least equal performance to

those obtained with a monochromatic hologram, in the case of a spherical object.

As discussed in Section 1.3.2.2, the best resolution on the estimated parameters can be statistically evaluated using the Cramér-Rao Lower Bounds (CRLBs). The variance of any unbiased estimator is bounded from below by the CRLBs, which are obtained from the diagonal of the inverse Fisher information matrix (Kendall et al., 1948). As a result, these limits represent the minimum estimation variance theoretically achievable when the noise is additive white and Gaussian. CRLBs constitute a theoretical tool useful for relative comparison between different experimental configurations. By describing the light intensity recorded on the sensor by the direct model (Equation (7.4)) and by performing a statistical analysis on the estimated parameters for a given noise variance, it is possible to obtain the theoretical standard deviation  $\delta_p$  for each estimated parameter  $p \in \boldsymbol{\theta}$ . This method, which was applied to digital holography in Fournier et al. (2010), is applied here to color holograms by taking into account the possible mixture of the color signals due to a crosstalk phenomenon. Equation (7.12), gives the Fisher information matrix  $\mathbf{I}^F$  depending on the model gradients, the amplitude factor of the model  $\alpha$  and the variance  $\sigma_b^2$  of the noise. Equation (7.13) gives the link between the CRLBs and the matrix  $\mathbf{I}^F$ . When signal mixing occurs due to crosstalk, the color model vector  $\mathbf{g}$  is replaced by  $\mathbf{g}^*$  according to Equation (7.11).

$$[\mathbf{I}^F(\boldsymbol{\theta})]_{i,j} = \frac{\alpha^2}{\sigma_b^2} \cdot \sum_{a=1}^A \sum_{b=1}^B \left( \frac{\partial \mathbf{g}_{\boldsymbol{\theta}}^*(a,b) \cdot \sqrt{\mathbf{w}(a,b)}}{\partial \theta(i)} \right) \left( \frac{\partial \mathbf{g}_{\boldsymbol{\theta}}^*(a,b) \cdot \sqrt{\mathbf{w}(a,b)}}{\partial \theta(j)} \right), \quad (7.12)$$

$$[\boldsymbol{\delta}]_i = \sqrt{[\mathbf{I}^F(\boldsymbol{\theta})^{-1}]_{i,i}}. \quad (7.13)$$

The theoretical limits of precision are obtained by considering a hologram model of a spherical opaque object whose radius is  $r_p = 15 \mu\text{m}$ , located at the distance  $z_p = 7 \text{ cm}$  with a S/N equal to 2.5. Table 7.6 gives the theoretical resolutions achievable for each parameter  $p \in \boldsymbol{\theta}$ . This study is performed in the following six cases:

- a monochromatic hologram obtained with only one source and recorded by a monochromatic sensor (cases 1 to 3, respectively denoted  $\lambda_R$ ,  $\lambda_G$  and  $\lambda_B$  in Table 7.6 and Figure 7.14),
- a trichromatic hologram artificially formed by the concatenation of three holograms recorded by a monochromatic sensor without mosaicking, as in Demoli et al. (2003); Zhao et al. (2008), (case 4 denoted  $\lambda_{R,G,B}$ ),
- a mosaicked color hologram recorded by a Bayer color sensor not affected by the crosstalk phenomenon (case 5 denoted  $\lambda_{R,G,B} + \text{Bayer}$ ),
- a mosaicked color hologram recorded by a Bayer color sensor affected by the crosstalk phenomenon defined by the mixing matrix  $\mathbf{Q}_{\text{exp1}}$  estimated from the experimental holograms (case 6 denoted  $\lambda_{R,G,B} + \text{Bayer} + \text{ct}$ ).

The mean results may vary slightly depending on the position of the bead in the sensor field. Figure 7.14 completes this study by showing the evolution of the achievable

precision limits for a distance between the sensor and the object varying from 7 to 12 cm in the same cases as those listed in Table 7.6.

It appears that color holograms that undergo mosaicking during the acquisition step suffer from an increase in CRLBs (and hence degradation in the reconstruction) compared to a color hologram artificially formed by the concatenation of three monochromatic holograms (obtained with the three available wavelengths in our experimental setup). This is explained by the fact that the mosaicking step results in a reduction by a factor of 3 in the number of pixels recorded, resulting in a loss of information. It also appears that holograms not tainted by a crosstalk phenomenon lead to finer resolutions than holograms tainted by this effect. This can be explained by the blurring of high frequencies due to the mixing of the color signals when spectral crosstalk occurs. This observation justifies why the spectral crosstalk phenomenon that occurs with most color sensors equipped with a Bayer filter influences optical metrology applications using an in-line holographic setup. Finally, we observed that it is possible to obtain a finer precision of the  $r_p$  parameter by considering a color hologram, due to additional information provided by wavelength diversity.

### 7.5.3 Self-calibration applied to the reconstruction of images in color holography

In this section, we illustrate the benefits of the self-calibration procedure described in Section 7.4 for the reconstruction of images from color holograms with an image-based inverse problem. For this purpose, we use a regularized inversion approach. Physical priors are thus introduced in the form of regularization terms (sparsity plus edge-preserving constraints) to better enforce problem conditioning. The approach used in this part was developed with Frédéric Jolivet during his PhD thesis at the Hubert Curien Laboratory (Jolivet, 2018). Hereafter, we give the key elements of the reconstruction algorithm. More details about the inverse problem and the regularization strategies can be found in Fournier et al. (2017); Jolivet et al. (2018).

#### 7.5.3.1 Color hologram reconstruction method

The recorded intensity of the hologram of a plane object located at distance  $z$  can be modeled by the 2-D convolution between the transmittance  $t$  of the plane object and a free-space propagator kernel  $\underline{h}_z^\lambda$  (e.g., the Fresnel propagator, see Goodman (2005)):

$$I^\lambda \propto |t * \underline{h}_z^\lambda|^2. \quad (7.14)$$

For opaque, sparse and small (i.e.,  $\frac{\pi r^2}{4\lambda z} \ll 1$ ) objects, the recorded intensity can be expressed as the linear approximation (Denis et al., 2009):

$$I^\lambda = m_0 - 2.\text{Re} \left( \underline{h}_z^\lambda \right) * \vartheta, \quad (7.15)$$

where  $\vartheta$  represents the opacity ( $\vartheta = 1 - t$ ),  $m_0$  is a constant to be estimated,  $z$  is the object to sensor distance and  $\text{Re} \left( \underline{h}_z^\lambda \right)$  is the real part of the Fresnel free-space propagator:

$$\text{Re} \left( \underline{h}_z^\lambda(x, y) \right) = \frac{1}{\lambda z} \sin \left( \frac{\pi(x^2 + y^2)}{\lambda z} \right). \quad (7.16)$$

In the following,  $\mathbf{H}_\lambda$  denotes the linear operator (i.e., an  $AB \times AB$  matrix) corresponding to the discrete convolution with the kernel  $\text{Re}\left(\frac{h_z^\lambda}{z}\right)$  and  $\boldsymbol{\vartheta}$  is the column vector representing the discretized object opacity. In this discretized space, the intensity  $\mathbf{d}^\lambda \in \mathbb{R}^{(AB \times 1)}$  of a hologram recorded at wavelength  $\lambda$  is given, up to the noise, by the affine relationship:

$$\mathbf{d}^\lambda \approx m_0 \mathbf{1} - \mathbf{H}_\lambda \boldsymbol{\vartheta}, \quad (7.17)$$

where  $\mathbf{1} \in \mathbb{R}^{(AB \times 1)}$  stands for a column vector full of ones. The maximum likelihood estimation of the constant  $m_0$  can be obtained in closed form (Denis et al., 2009), leading to the simplified linear model:

$$\bar{\mathbf{d}}^\lambda \approx \bar{\mathbf{H}}_\lambda \boldsymbol{\vartheta}, \quad (7.18)$$

where  $\bar{\mathbf{H}}_\lambda$  is a modified propagation operator ( $\bar{\mathbf{H}}_\lambda = -\mathbf{H}_\lambda + \mathbf{1} \frac{\mathbf{1}^T}{\mathbf{1}^T \mathbf{1}} \mathbf{H}_\lambda$ ) and the hologram  $\bar{\mathbf{d}}^\lambda$  is centered (i.e., its mean value is subtracted).

In the absence of spectral crosstalk (i.e., no signal mixing on the different channels of the CMOS color sensor), the joint reconstruction of the opacity  $\boldsymbol{\vartheta}$  from a color hologram  $\bar{\mathbf{d}}_{\text{RGB}}$  is obtained by solving the following minimization problem:

$$\hat{\boldsymbol{\vartheta}} \in \arg \min_{\mathbf{0} \leq \boldsymbol{\vartheta} \leq \mathbf{1}} \sum_{c \in \{\text{R,G,B}\}} \left\| \bar{\mathbf{H}}_{\lambda_c} \boldsymbol{\vartheta} - \bar{\mathbf{d}}_{\text{RGB}} \right\|_{\mathbf{w}^c}^2 + \tau_1 \|\boldsymbol{\vartheta}\|_1 + \tau_2 \mathcal{TV}_\epsilon(\boldsymbol{\vartheta}), \quad (7.19)$$

where  $\mathbf{w}^c$  is the weights taking into account the Bayer mask ( $\mathbf{w}^c$  is equal to 0 for 75% of the red and blue channels and for 50% of the green channel, see Figure 7.7).  $\mathcal{TV}_\epsilon(\boldsymbol{\vartheta})$  is a regularization term (so-called *total-variation*, see for example Rudin et al. (1992); Chambolle et al. (2010)) in the form of an edge-preserving function defined by:

$$\mathcal{TV}_\epsilon(\mathbf{u}) = \sum_{m=1}^{AB} \sqrt{(\mathbf{D}_m^{\text{horz}} \mathbf{u})^2 + (\mathbf{D}_m^{\text{vert}} \mathbf{u})^2 + \epsilon^2}, \quad (7.20)$$

where  $\epsilon > 0$ ,  $\mathbf{D}_m^{\text{horz}}$  and  $\mathbf{D}_m^{\text{vert}}$  stand for the finite differences operators along the horizontal and vertical directions:  $(\mathbf{D}_m^{\text{horz}} \mathbf{u}, \mathbf{D}_m^{\text{vert}} \mathbf{u})$  is the (discrete) spatial gradient at pixel  $m$ .

A finer image formation model is obtained by taking into account the color signal mixing on the different channels of the CMOS color sensor as illustrated by Figure 7.12:

$$\sum_{\ell \in \{\text{R,G,B}\}} q_\ell^c \bar{\mathbf{H}}_{\lambda(\ell)} \boldsymbol{\vartheta}. \quad (7.21)$$

Following the notations introduced in Equation (7.10), we can express the image formation model that accounts for the spectral crosstalk according to the mixing principle illustrated in Figure 7.10:

$$\hat{\boldsymbol{\vartheta}} \in \arg \min_{\mathbf{0} \leq \boldsymbol{\vartheta} \leq \mathbf{1}} \sum_{c \in \{\text{R,G,B}\}} \left\| \left( q_{\text{R}}^c \bar{\mathbf{H}}_{\lambda_{\text{R}}} + q_{\text{G}}^c \bar{\mathbf{H}}_{\lambda_{\text{G}}} + q_{\text{B}}^c \bar{\mathbf{H}}_{\lambda_{\text{B}}} \right) \boldsymbol{\vartheta} - \bar{\mathbf{d}}_{\text{RGB}} \right\|_{\mathbf{w}^c}^2 + \tau_1 \|\boldsymbol{\vartheta}\|_1 + \tau_2 \mathcal{TV}_\epsilon(\boldsymbol{\vartheta}), \quad (7.22)$$

where  $\tau_1$  and  $\tau_2$  are two parameters controlling the strength of the regularizations. This optimization problem is solved using a limited memory quasi-Newton algorithm with bound constraints (Thiébaud, 2002).

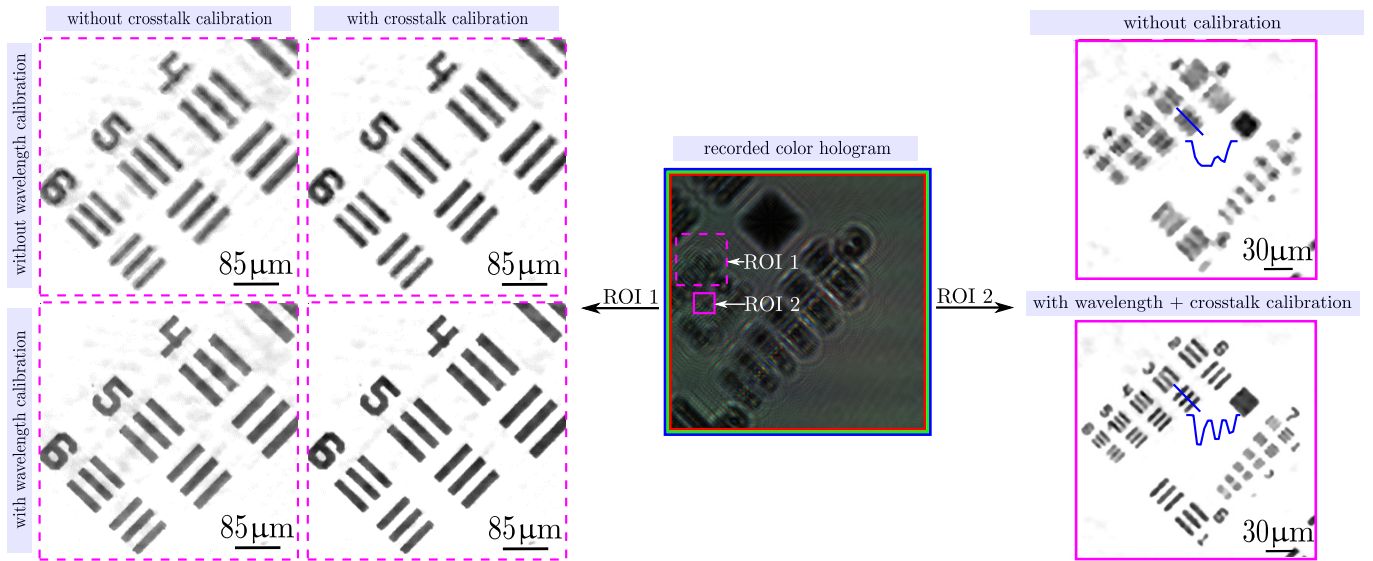


Figure 7.15 – Illustration of the regularized reconstruction of a color hologram from an opaque USAF target without or with a preliminary self-calibration of the holographic color microscope.

### 7.5.3.2 Reconstruction of non-parametric opaque objects

In Figure 7.15, we illustrate the reconstruction of non-parametric objects with the method described in the previous section combined with a self-calibration of the setup as described in Section 7.4. The reconstructions were performed by Frédéric Jolivet. The considered object is an opaque 1951-R1DS1P USAF THORLABS™ target. We compare the reconstruction of a color hologram without or with self-calibration of the setup. When no self-calibration is performed, the wavelengths of the sources are set at the typical values provided by the manufacturer (see Table 7.1) and the crosstalk matrix  $\mathbf{Q}$  is roughly estimated from the manufacturer datasheet (see  $\mathbf{Q}_m$  in Table 7.4). One observes that structures larger than  $20\ \mu\text{m}$  are well reconstructed by the inversion method thanks to the regularization terms enforcing sharp objects and smooth background. The reconstruction of finer structures (about  $5\ \mu\text{m}$ ) is significantly improved by performing beforehand the self-calibration of the setup, thereby illustrating its benefits for color hologram reconstructions.

**Improving reconstructions by self-calibration**

- The calibration of holographic color setups (i.e., wavelengths and crosstalk estimations) can be taken into account in the hologram reconstructions.
- We show that it improves the accuracy of the reconstructions of parametric objects and the resolution of the reconstructions of non-parametric objects.



## 7.6 Conclusion

In this chapter, we have illustrated two potential sources of errors in the reconstruction of a color hologram recorded by a cost-effective holographic color microscope (based on low-end laser diodes and a Bayer-type color sensor). They arise from (i) an inaccurate knowledge of the central wavelengths of the sources and (ii) a color signal mixing (crosstalk phenomenon) on Bayer-type CMOS color sensors. We have proposed a simple and fast experimental method based on the reconstruction of holograms of spherical objects (naturally present in the field of view or added as calibration object) using an inverse problem approach. This method leads to accurate estimations of the wavelengths of the sources and of the crosstalk mixing matrix comparable to that obtained using a high-resolution spectrometer. Including this self-calibration in the hologram reconstruction step improves the quality of the reconstructions. As discussed in Section 1.5, this chapter corresponds to the first study considered in the thesis. Thus, the methods discussed in this Chapter could be combined with a statistical modeling of the background as described in Chapter 3, and robust approaches as described in Chapter 5 to further improve the hologram reconstructions, see Section 8.3.



**Part V**  
**Conclusion**



# Conclusion, ongoing and future works

## 8.1 Summary of the main contributions

In this thesis, we have proposed several algorithms dedicated to object detection and characterization from faint signals in image series. In particular, the methods developed have been applied in two different applicative contexts: (i) the quest for exoplanets by direct imaging in astronomy, and (ii) the optical metrology of samples by holographic microscopy. The resulting algorithms follow three methodological angles in order to address common signal processing challenges:

### **First angle – Background fluctuations modeling**

The image series in high contrast astronomy and holographic microscopy present a spatially textured background that strongly dominates the patterns to be detected. We proposed to model locally the correlated and nonstationary background of the image series using patch-based statistical approaches. The model of the background leads to a detection method by application of the statistical detection theory. We described in Part II two algorithms dedicated to the detection of known patterns within the low S/N regime. The two proposed algorithms differ in the spatial extent of the patterns to be detected:

- In Chapter 2, we presented a totally unsupervised algorithm (PACO) dedicated to the detection and characterization of point-source-like exoplanets from ADI series. The underlying statistical model of the background fluctuations, although only approximate, achieves a good compromise between the computational burden and the fidelity to the data. It leads to an efficient algorithm that demonstrates better detection performance than state-of-the-art exoplanet hunter methods. Beyond the improved sensibility, a major feature of our algorithm is the ability to reliably control the false alarm rate and thus, to obtain a fully unsupervised method.
- In Chapter 3, we presented an extension (EXPACO) of the previous algorithm. EXPACO is dedicated to the detection of spatially extended patterns such as the diffraction patterns in holographic microscopy. Specific algorithmic developments were necessary to obtain a method that could be applied to experimental data in

a reasonable time. The evaluation of the performance of this approach on image series obtained with a holographic microscope shows an interesting detection capability compared to a standard maximum correlation approach.

### **Second angle – Robustness to outliers**

Image series in astronomy and in microscopy present several aberrant values in spite of the care taken during the image acquisition process. We proposed in this thesis to account for these aberrant values. In Part III, we described two robust algorithms dedicated to the detection and characterization of model patterns, in the presence of outliers:

- In Chapter 4, we presented the **robust PACO** algorithm; an extension of the PACO method introduced in Chapter 2. To improve the robustness of PACO, we adapted the statistical model of the background fluctuations by replacing our Gaussian model by a Gaussian scale mixture model. This led to spatially weighting each frame in a data-driven fashion, based on its relative degree of fluctuations. We have shown that the achievable contrast and the detection performance were particularly improved at small separations, where the stellar residuals dominate.
- In Chapter 5, we presented an algorithm dedicated to the detection and characterization of microscopic objects in the presence of numerous outliers. It is based on M-estimators, iterative residuals weighting, and on a new criterion to distinguish outliers from inliers. In contrast to existing strategies consisting in setting the threshold that distinguishes inliers from outliers and considering only the distribution of the data, our approach evaluates the impact on the estimation task and is therefore adaptive. We have shown on series of holograms that this approach achieves a bias/variance tradeoff improving the overall performance of the conventional least squares method and of standard robust estimators.

### **Third angle – Spectral diversity exploitation**

In astronomy as well as in microscopy, it is possible to record multi-spectral data in addition to the natural time extent of the image series. In this thesis, we proposed to account for the specificities of the multi-spectral data. Part IV described two algorithms dealing with the spectral diversity of the acquired datasets:

- In Chapter 6, we presented the **PACO-ASDI** algorithm dedicated to the detection and characterization of point-sources (like exoplanets) from ASDI series. Based on the PACO algorithm, PACO-ASDI also presents several methodological adaptations to deal with the specificities of ASDI observations such as the strong spectral correlations of the data. The underlying statistical model of the background fluctuations achieves a good compromise between the model complexity, the difficulty to estimate model parameters, and the relevance of the statistical model with respect to the data. We have shown that it leads to an efficient algorithm that demonstrates better detection and characterization performance than state-of-the-art exoplanet hunter methods.
- In Chapter 7, we have shown that an inaccurate knowledge of the experimental parameters related to the sources and sensor in color holography leads to an inaccurate characterization of the imaged microscopic objects. This issue is



critical since the induced errors can outweigh the theoretical gain brought by a joint multi-spectral processing. We described a new self-calibration method based on an inverse problem approach. We have shown on real holograms that the accuracy of the estimations and of the image reconstructions is improved by the proposed calibration approach.

Throughout the thesis, special care has been paid on developing algorithms that are totally unsupervised: weighting and/or regularization parameters are estimated in a data-driven fashion.

In the following Sections 8.2 and 8.3, we discuss some ongoing and possible future works, both from an applicative and methodological point of view. Beyond the particular examples that follow, the developed algorithms are general and could be applied to other application fields in which the detection/characterization of faint point-like or extended patterns from image series is encountered.

## 8.2 Ongoing and future works for astronomy

### 8.2.1 On the applicative side

In this section, we discuss some ongoing and possible future works related to the exploitation of the PACO-based algorithms for astronomy applications.

#### 8.2.1.1 Automatic processing pipeline

As discussed in Chapters 2, 4, and 6, the astronomers who use the exoplanet hunter algorithms are in need of automatic processing engines to conduct the analysis of large amounts of data. This point is all the more critical as the detection task is, to date, mostly performed by visual inspection of the results obtained by the different algorithms. Such a manual validation is still necessary due to the lack of control of the false alarm rate, see discussions in Sections 2.5.2, 4.4.1, and 6.6.2.

Throughout this thesis, we have paid particular care to derive totally unsupervised algorithms; weighting and/or regularization parameters are estimated in a data-driven fashion, see Sections 2.4.3 and 6.5. Based on these methodological developments, we developed an automatic processing pipeline whose schematic representation is given in Figure 8.1. It is inspired by the ANDROMEDA processing pipeline (Cantalloube et al., 2015; Cantalloube, 2016) aiming to provide a user-friendly interface for the analysis of ADI and ASDI datasets. The PACO pipeline is split into three main steps:

- a *reduction* step consisting in the reduction of the science data, mainly producing detection and achievable contrast results.
- a *detection* step analyzing the detection maps automatically to identify the detections of interest and the possible extended objects like protoplanetary disks. For each point-like detection, it also derives the expected shape of the pattern signing the presence of a source at the location of a given detection (see Equations (2.17), (4.9), and (6.10)). The normalized correlation coefficient between the observed and expected pattern is also computed.

- a *characterization* step deriving subpixel astrometry and an unbiased photometry estimation of the detected sources of interest. It also refines the additional quantities computed during the reduction step.

Each step can be run independently based on the results obtained and saved from the previous steps, see *input doors* and *output doors* in Figure 8.1.

One of the peculiarities of the PACO pipeline is related to the automatic generation of a Portable Document Format report summarizing the main results obtained from the processing of each dataset<sup>1</sup> for a quicker visualization of the key information. Appendix D shows selected excerpts from a PACO report generated automatically after processing a dataset of HD 95086.

The PACO pipeline takes the form of a console compiled application coded in MATLAB™, accompanied by a detailed technical user guide. It has been delivered to Maud Langlois for a testing phase on a large amount of data (more than 300 datasets) from the SHINE survey (Langlois et al., in prep.) of the SPHERE instrument. The pipeline is regularly updated with new functionalities coming from new methodological developments.

While it gives a first implementation of the PACO-type algorithms, this pipeline can be significantly improved on several points. The main issue is probably related to the choice of the programming language. We have chosen the MATLAB™ language for its simplicity and the large variety of precoded functions, including signal processing and numerical optimization routines. However, the PACO pipeline would benefit from being cleaned and coded in a more effective compiled language like C++. This task was the subject of a two months internship during spring 2018, and a preliminary architecture was obtained, but the code has significantly evolved since this date.

---

1. At the time we write, the generation of the automatic report is possible only for ADI datasets. We plan to extend this tool for ASDI datasets soon.

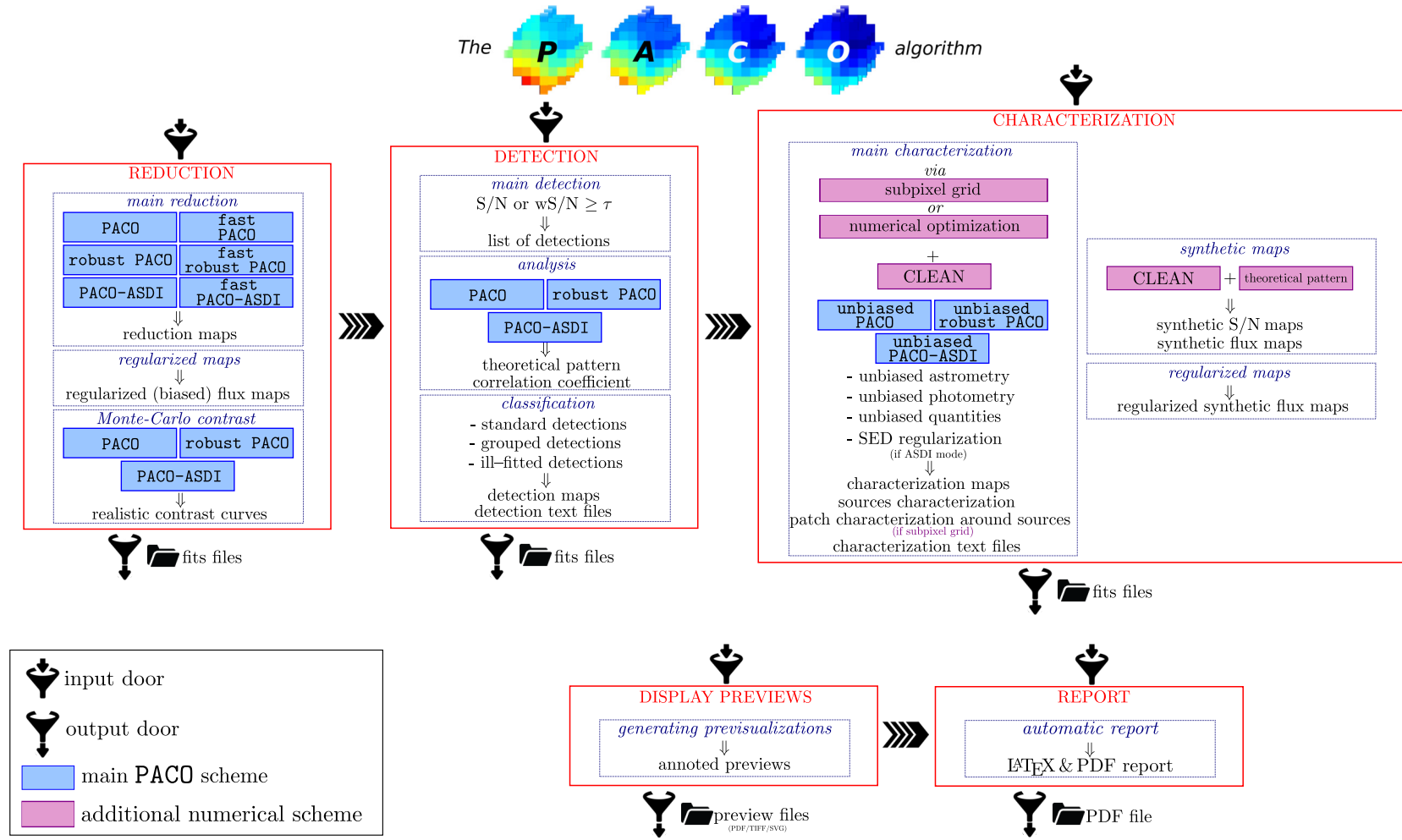


Figure 8.1 – Schematic representation of the PACO processing pipeline.

### 8.2.1.2 Exploitation of PACO for astronomy applications

In this section, we illustrate with two case studies the potential benefit of the PACO algorithm, in combination with other state-of-the-art algorithms, to conduct the analysis of ADI and ASDI datasets.

#### 8.2.1.2.1 Determination of mass limits

As discussed in Section 1.2.2.1, one of the main advantages of direct imaging is the possibility to derive a large panel of physical properties characterizing the detected sources. Besides, even if no source is detected in a dataset, the achievable contrast (i.e., the minimal exoplanet flux that is possible to detect at a given PFA) can be used to derive constraints on the presence of stellar companions. In other words, an upper bound on the mass of (potential) exoplanets can be inferred from the achievable contrast and exoplanet formation / evolution models. We illustrate hereafter an example of such a derivation on a dataset recorded by the VLT/SPHERE-IRDIS and IFS imagers around the HD 163296 star. HD 163296 is a Herbig Ae/Be star<sup>2</sup> hosting a protoplanetary disk with a ringed structure. The morphology of the disk (including inner and outer gaps) and its relatively old age could be in favor of the presence of (partially-formed) stellar companions like the exoplanets PDS 70 b and c in formation inside the accretion disk of the star PDS 70, see Section 1.2.2.2.4.

PACO was used<sup>3</sup> together with the KLIP algorithm to analyze recent datasets acquired at two different epochs, see Mesa et al. (2019b). For this star, the detection of faint point sources is particularly challenging since it is located very near the VLT latitude, thus preventing observations during the passage of the star at the meridian. This leads to a severe limitation of the field of view: the total amount of parallactic rotation over time is about only 1.3° for the IRDIS dataset. Figure 8.2(a) gives the GLRT<sup>+</sup> map obtained from the IRDIS dataset. The inner ring of the protoplanetary disk can be seen in the vicinity of the host star. Figure 8.2(b) presents the 5 $\sigma$  contrast curves obtained with PACO and KLIP-ADI for the considered IRDIS dataset as well as PACO-ASDI and KLIP-ASDI for the IFS dataset. It shows that PACO leads to a better achievable contrast than KLIP, especially on the IRDIS dataset at small angular separations. These contrast limits are converted in Figure 8.2(c-d) into limits on the mass of potential companions hosted by HD 163296. The conversion procedure is based on the AMES-COND (Allard et al., 2003) and AMES-DUSTY (Allard et al., 2001) evolutionary models. Besides, several works reported in the literature have proposed different exoplanet formation scenario to explain the observed morphology of the protoplanetary disk (Liu et al., 2018; Teague et al., 2018; Pinte et al., 2018; Guidi et al., 2018). The separations/masses of the hypothetic exoplanets predicted by these models are superimposed to the mass limit curves.

While no point source was discovered at the different (hypothetic) locations predicted by the evolutionary models, this study put strong constraints on the presence of potential companions orbiting HD 163696. First, the (potential) exoplanets may have a mass below 3-7 M<sub>J</sub> at projected separations between 30-80 AU based on the analysis of

---

2. A Herbig Ae/Be star is a star of the sequence preceding the main sequence.

3. I took part in the reduction of the considered datasets with PACO, see Mesa et al. (2019b).

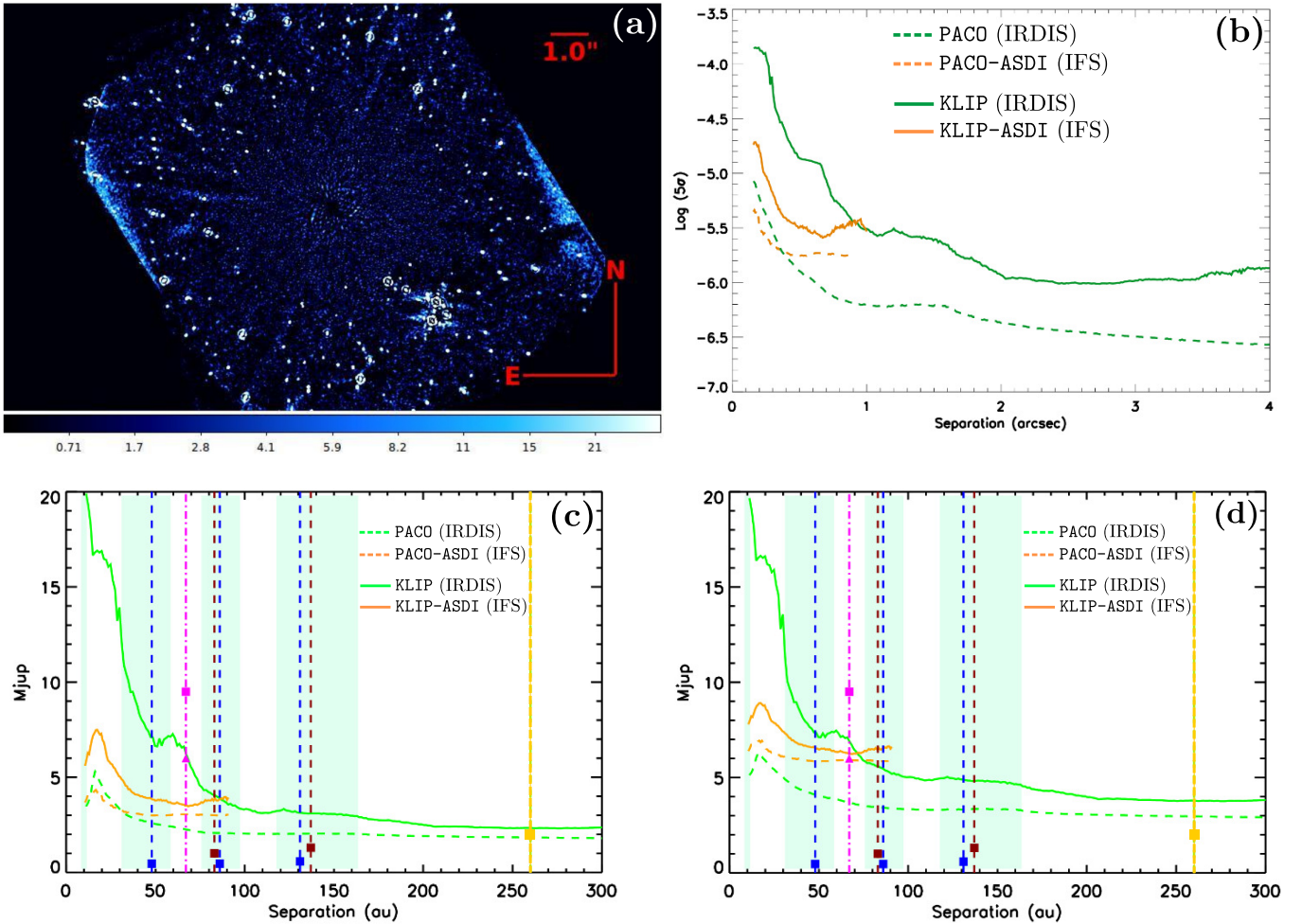


Figure 8.2 – Determining mass limits around HD 163296. (a) GLRT<sup>+</sup> map obtained with PACO on the considered IRDIS dataset; (b)  $5\sigma$  contrast curves obtained with PACO and KLIP-ADI for the considered IRDIS dataset as well as PACO-ASDI and KLIP-ASDI for the IFS dataset; (c-d) conversion of the  $5\sigma$  contrast curves into companion mass limits based on the AMES-COND (c) and AMES-DUSTY (d) evolutionary models. The light cyan areas represent the estimated positions of the disk gaps around the star (Isella et al., 2018). The dashed lines and markers represent the positions and masses of the exoplanets proposed by Liu et al. (2018) (dark blue), Teague et al. (2018) (brown), Pinte et al. (2018) (yellow), and Guidi et al. (2018) (pink). For the latter case, the exoplanet initially proposed by Guidi et al. (2018) is identified by a pink square and a revision of its mass (based on a revision of the mass of the star) is identified by a pink triangle. Adapted from Mesa et al. (2019b).

the considered IFS dataset, and below 2-4  $M_J$  at projected separations larger than 200 AU based on the analysis of the considered IRDIS dataset. Besides, this analysis seems to show (with some caveats) that the presence of multiple companions is more likely than that of a single companion (which was assumed up to now in direct imaging). Finally, 166 additional point sources have been identified at different locations of the field of view, see Figure 8.2(a). These detections are studied through astrometry comparisons for the sources already reported by other works, and through their photometry for the detections not reported in the literature. This study shows that 163 of these 166 detections are background sources (not gravitationally bounded to the host star, or with an estimated photometry not compatible with exoplanet physics-based models). It is not possible to conclude yet for the three remaining sources.

#### 8.2.1.2.2 Analyzing an IFS sequence around $\beta$ Pictoris

As discussed in Section 1.2.2.2.4, one of the recent breakthroughs obtained with the SPHERE instrument is the re-detection of the exoplanet  $\beta$  Pictoris b in the north-east part of its orbit in September 2018 (Lagrange et al., 2019a). Since its discovery (Lagrange et al., 2009, 2010) and until November 2016,  $\beta$  Pictoris b was systematically imaged in the southwestern part of its orbit, and was no longer detectable between November 2016 and September 2018 due to its too small angular separation with the host star ( $\beta$  Pictoris b was hidden by the coronagraph of the instrument during this period). The re-detection of  $\beta$  Pictoris b on an unexplored part of its orbit allows to refine and put tighter constraints on the estimation of its orbital parameters, see Lagrange et al. (2019a).

Datasets of this star are of particular interest since no other exoplanet has ever been imaged at such small separations to a star: for the smallest projected distance,  $\beta$  Pictoris b was about 0.125 arcsec to its star (i.e., at 10.2 pixels from the center of the IRDIS field of view). Lagrange et al. (2019a) also report the detection maps obtained with the KLIP algorithm on 12 ADI datasets recorded by the SPHERE-IRDIS imager between 2014 and 2018.

We have used PACO-ASDI to process a similar sequence of 14 ASDI datasets<sup>4</sup> of  $\beta$  Pictoris recorded by the SPHERE-IFS imager between December 2014 and March 2019. This short study aims to evaluate the ability of PACO-ASDI at detecting point-like sources at very small angular separations. Figure 8.3 gives the statistically grounded wS/N detection maps that we have obtained. It shows that the exoplanet  $\beta$  Pictoris b can be detected without ambiguity at all epochs, including the ones in which its projected separation is extremely limited. This study confirms that PACO-ASDI is capable to detect point-like sources orbiting at a large variety of angular separations. Ongoing tests of PACO-ASDI concern the estimation of the astrometry and photometry of  $\beta$  Pictoris b as well as the achievable contrast from these different ASDI datasets.

### 8.2.2 On the methodological side

In this section, we discuss some ongoing and possible future improvements/extensions of the PACO-based algorithms from a methodological point of view.

---

4. We thank Anne-Marie Lagrange and Maud Langlois who provided us the datasets.



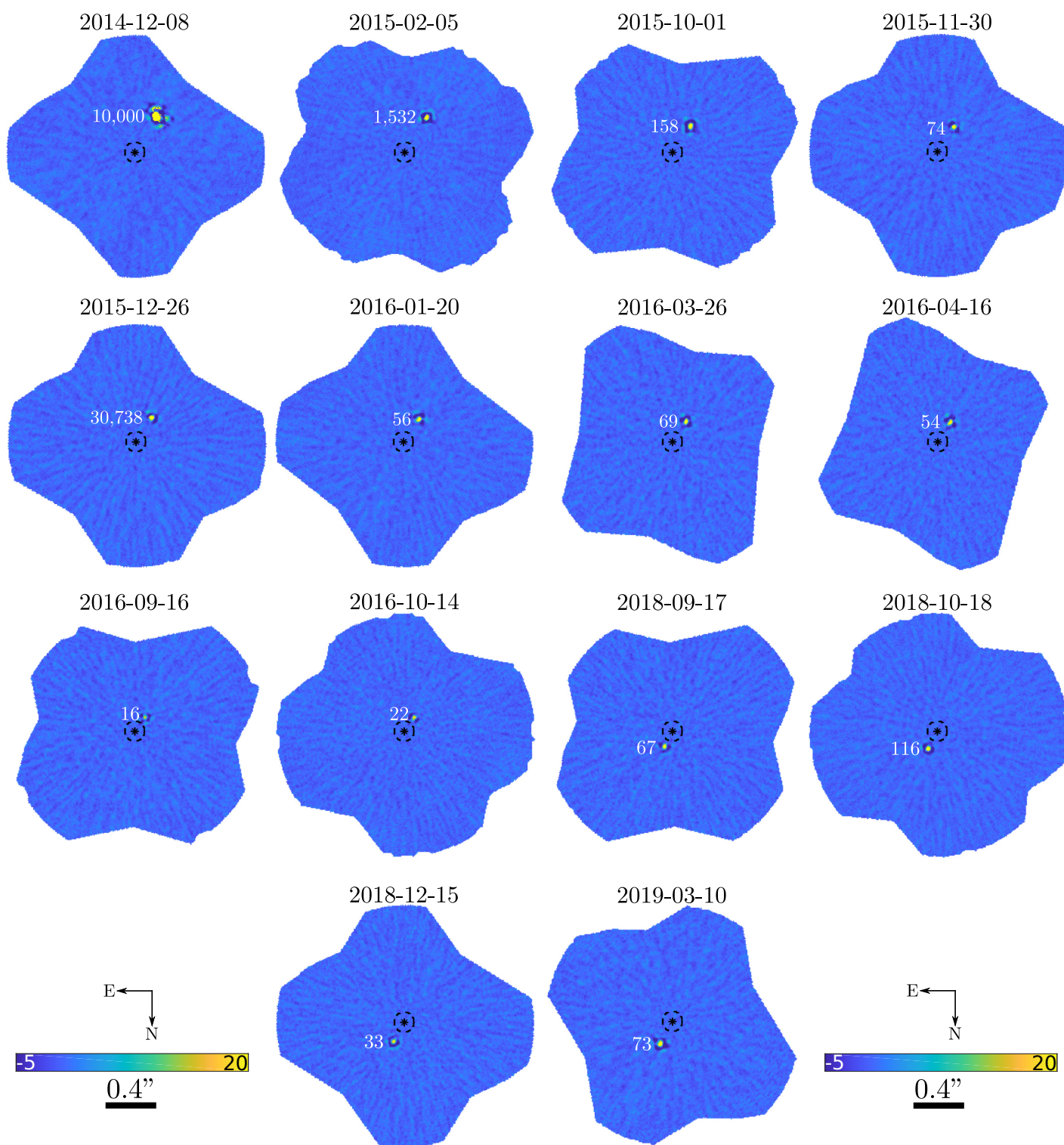


Figure 8.3 – wS/N detection maps obtained with PACO-ASDI on 14 ASDI datasets recorded between December 2014 and March 2019 by the SPHERE-IFS imager around  $\beta$  Pictoris.

### 8.2.2.1 Statistical model of the background

While PACO proves to produce satisfactory results on several datasets, its underlying statistical model of the background is only approximative, in particular for ASDI datasets, see discussion in Section 6.2. Since the performance of the method is directly related to the agreement between the statistical model and the actual distribution of the data, future works should first focus on this point, in our opinion.

In particular, as discussed in Section 6.2, the strong spectral correlations of ASDI datasets are not directly modeled but taken into account in a later stage of the algorithm (during the combination of the individual  $S/N_\ell$  maps from the different spectral channels). We have justified this choice by the difficulty that we have encountered in our tests to fully model the spatio-temporo-spectral fluctuations of the background from a finite set of samples, see Appendix C.

However, these tests do not include spectral or temporal weighting factors as the ones provided by a GSM model (since we investigated this methodological framework later in the thesis). Then, the numerous outliers arising in ASDI data were not correctly taken into account in our tests that led to reject a full modeling of spatio-temporo-spectral correlations. From our point of view, it would be interesting to investigate the combination of a spatio-spectral modeling of the background with temporo-spectral weights as in our GSM model (see Section 6.2.1).

### 8.2.2.2 Detection and reconstruction of extended objects

Since the first direct imaging of an exoplanet in formation inside a protoplanetary disk (Keppler et al., 2018; Müller et al., 2018), it is the golden age of the study of such extended objects through high contrast imaging. A *protoplanetary disk* (or *circumstellar disk*) is a rotating stellar disk made of gas and/or dust surrounding young stars. Exoplanets can form inside these disks by, for example, accretion effect of the matter. The morphological structure of the disks (e.g., multiple rings, presence of inner and/or outer gaps) are of primary interest since they are directly related to the formation process of (potential) exoplanets. When they are observed in ADI, SDI, or PDI<sup>5</sup>, they are generally detected by conventional processing of the datasets with state-of-the-art exoplanet hunter algorithms such as TLOCI or KLIP, see (Gratton et al., 2019; D’Orazi et al., 2019; Boccaletti et al., 2019) for recent case studies. However, the estimated structure of the disks is generally approximative due to the presence of high stellar leakages at the proximity of the disks in the final reduction maps obtained with these algorithms.

PACO is not designed to detect extended objects (it is based on the assumption of point-like objects, i.e., objects seen as an off-axis PSF). However, experiments tend to show that extended objects such as protoplanetary disks can also be detected with PACO as a succession of point-like sources, as illustrated in Figure 8.4<sup>6</sup>. The detection benefits from the statistical modeling of the background, making it easier to distinguish between the background and the disk structures. However, such detections are not optimal and suffer from several artifacts. In particular, the faintest parts and flat areas

---

5. Polarimetric differential imaging, see Section 1.2.2.2.3.

6. The name of the stars and the observation logs are voluntarily not reported since these results are not yet published.



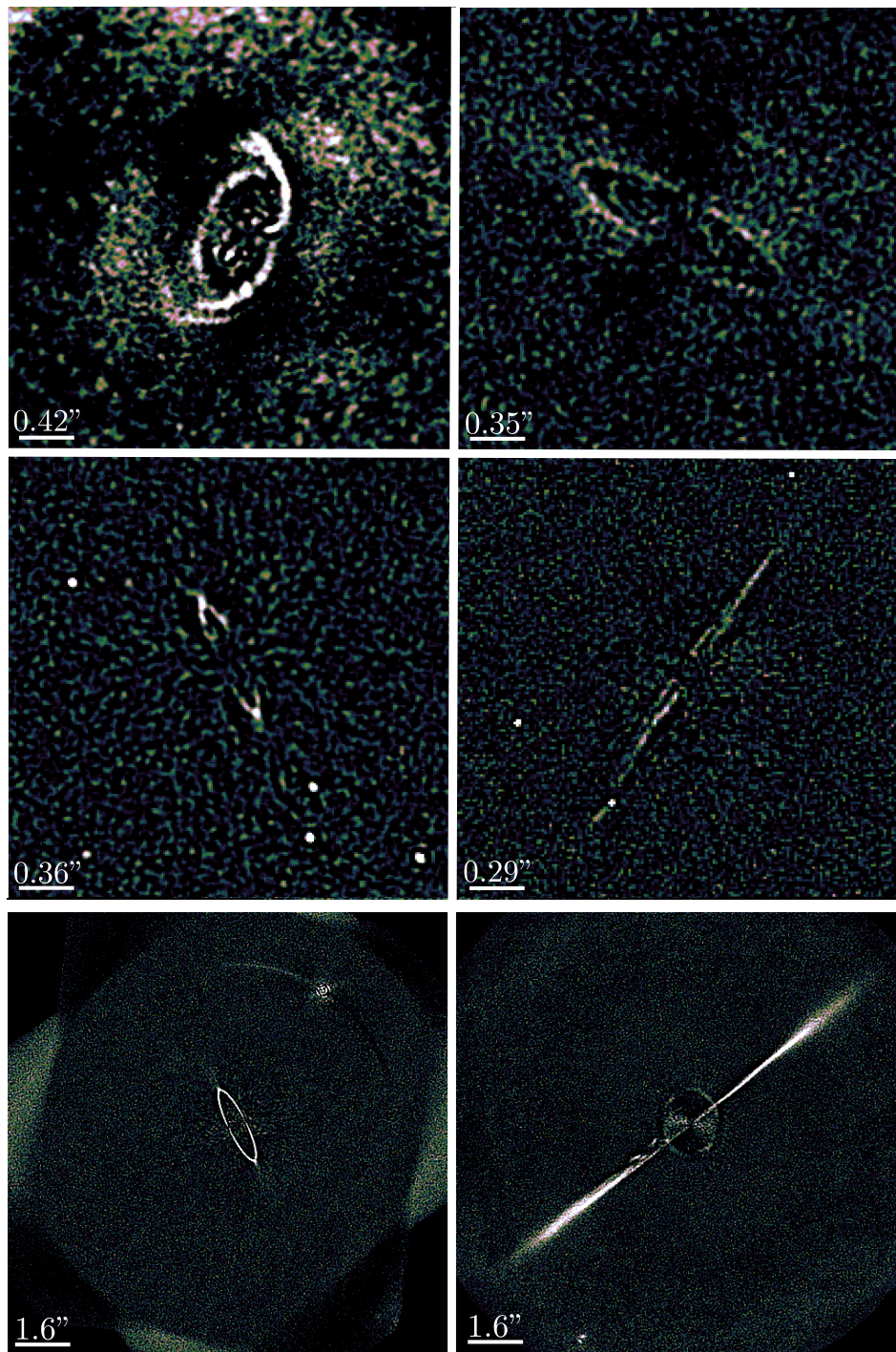


Figure 8.4 – Illustration of S/N maps obtained with PACO on ADI datasets recorded by the SPHERE-IRDIS imager around stars hosting a known protoplanetary disk. The processing was made by Maud Langlois with the first (suboptimal) version of the PACO pipeline (May 2018). The appearance of the disks (e.g., jets, ellipses, annulus) depends both on the morphology of the disk and the configuration of the stellar system during the observation (e.g., edge-on or face-on).

of the extended structures are not detected or appear with spatial discontinuities on the PACO's S/N maps.

It can sometimes be useful to produce flux maps at each point of the field of view. This is particularly the case when PACO is (wrongfully) applied to detect extended objects since images of the flux estimated at every location of the field of view are easier to interpret than S/N detection maps. However, a significant drawback of those flux images is that the estimation variance fluctuates largely within the field of view, especially near the host star, see Section 2.5.3.1 and Figure 8.5(a). To reduce the flux errors, we consider a simple shrinkage estimator (which also corresponds to a MAP estimator with a zero-mean white Gaussian prior):

$$\hat{\alpha}^{(\text{shrink})} = \kappa \hat{\alpha}, \quad (8.1)$$

where  $\kappa \in [0, 1]$  is the shrinkage coefficient.

The original flux estimator  $\hat{\alpha}$  defined in Equation (2.16) is distributed according to a Gaussian distribution with mean  $\bar{\alpha}$ <sup>7</sup> and variance  $\sigma_{\alpha}^2$ . The shrinkage estimator has an expectation  $\kappa \bar{\alpha}$  and variance  $\kappa^2 \sigma_{\alpha}^2$ . To adaptively reduce the flux variances, we consider selecting  $\kappa$  in order to minimize the expected square loss with respect to  $\bar{\alpha}$ :

$$\begin{aligned} \mathbb{E} [(\hat{\alpha}^{(\text{shrink})} - \bar{\alpha})^2] &= \mathbb{E} [(\hat{\alpha}^{(\text{shrink})})^2] - 2\bar{\alpha}\mathbb{E} [\hat{\alpha}^{(\text{shrink})}] + \bar{\alpha}^2 \\ &= \text{Var} [(\hat{\alpha}^{(\text{shrink})})^2] + \mathbb{E}^2 [\hat{\alpha}^{(\text{shrink})}] - 2\bar{\alpha}\mathbb{E} [\hat{\alpha}^{(\text{shrink})}] + \bar{\alpha}^2 \\ &= \kappa^2 \sigma_{\alpha}^2 + \kappa^2 \bar{\alpha}^2 - 2\kappa \bar{\alpha} + \bar{\alpha}^2 \\ &= \kappa^2 \sigma_{\alpha}^2 + \bar{\alpha}^2(\kappa - 1)^2. \end{aligned} \quad (8.2)$$

The value of  $\kappa$  that minimizes this expected square loss is:

$$\kappa = \frac{\bar{\alpha}^2}{\sigma_{\alpha}^2 + \bar{\alpha}^2} = \frac{\mathbb{E}[\text{S/N}]^2}{1 + \mathbb{E}[\text{S/N}]^2}. \quad (8.3)$$

Only a noisy S/N map is available, yet the formula (8.3) can be used by replacing  $\mathbb{E}[\text{S/N}]$  by the noisy S/N values (sub-optimal shrinkage).

When the S/N equals 5 (typical detection limit), the bias introduced on the flux is about 4%. This increases to 10% when the S/N equals 3, or more than 50% when  $\text{S/N} \leq 1$ . On the other hand, if the source detection S/N is equal to 10, less than 1% bias is produced by this shrinkage strategy. Figure 8.5(b) shows close-up views of the shrunk flux  $\hat{\alpha}^{(\text{shrink})}$  estimated near the host star for three datasets: we have injected 12 fake sources in the dataset ①, the dataset ② contains one known exoplanet near the host star, and dataset ③ contains a known protoplanetary disk. A comparison with flux maps before shrinkage is given in Figure 8.5(a). Figure 8.5(c) shows the resulting amount of shrinkage  $\kappa$  over the field of view. They emphasize that this simple strategy (slightly) improves the stationarity of the flux maps: the large fluctuations occurring near the host star are attenuated while the throughput of the objects of interest (point sources or disk) is preserved.

A more satisfactory solution could be to use the synthetic S/N and flux maps in which detected point-like sources are re-injected at an unbiased level of S/N and flux on

---

7. Note that  $\bar{\alpha}$  corresponds to the flux of the source only in oracle mode, i.e., when the statistics of the background are estimated in the absence of source.



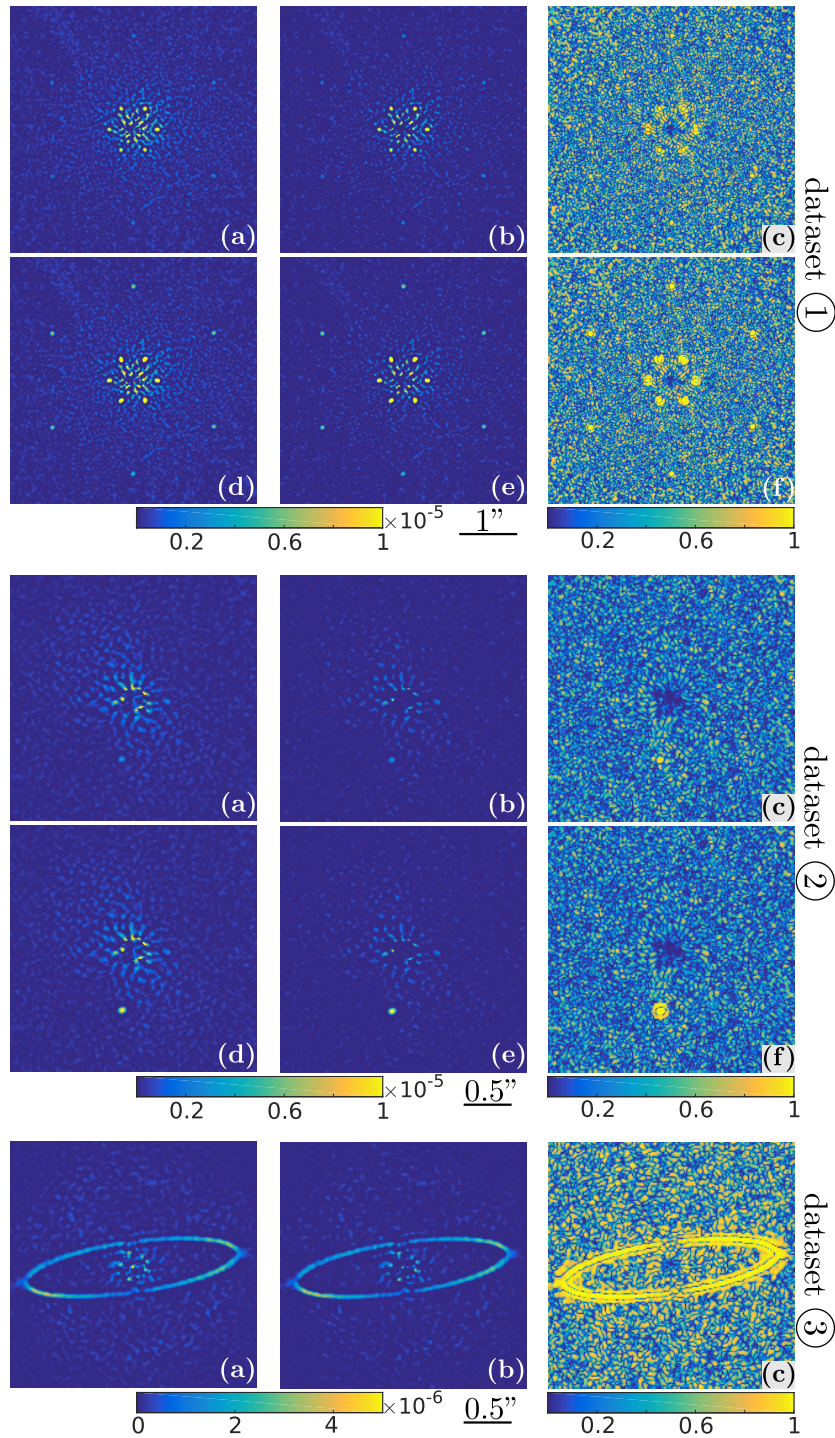


Figure 8.5 – Illustration of the shrinkage of the flux maps on three datasets. (a) flux maps; (b) shrunk flux maps; (c) shrinkage weights ( $\kappa$ ). (d), (e), and (f) correspond respectively to (a), (b), and (c) when flux and S/N maps used to compute the shrinkage weight are replaced by the synthetic flux and S/N maps obtained after subtraction/re-injection of the unbiased contributions of the point-like sources, see text.

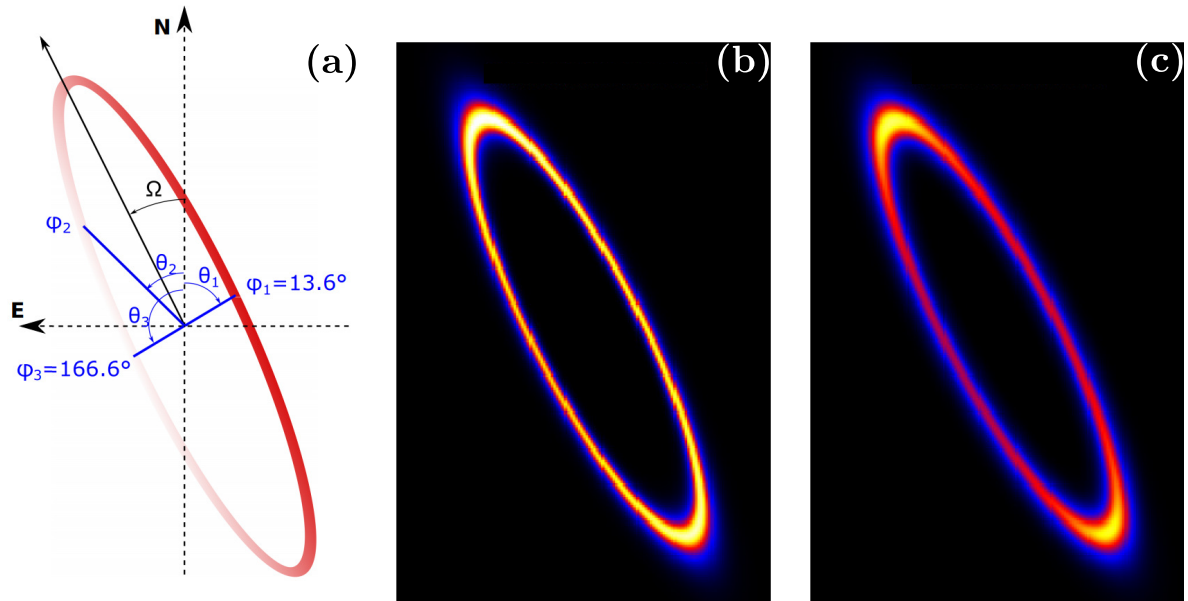


Figure 8.6 – Illustration of the parametric model of a protoplanetary disk. (a) schematic of the parametrized model; (b) physics-based intensity of the disk; (c) model of the observed intensity of the disk resulting from the convolution of (b) with the off-axis PSF. Adapted from Milli et al. (2017).

the residual S/N and flux maps obtained after subtraction of the contributions of the detected point-like sources in the data, see Appendix D. Boxes (d), (e), and (f) of Figure 8.5 give respectively the flux  $\hat{\alpha}$ , the shrunk flux  $\hat{\alpha}^{(\text{shrink})}$ , and the weight  $\kappa$  obtained over the field of view with this strategy. The attenuation of the large fluctuations of the flux is improved but the comparison is not completely fair since such a strategy creates a gap in the strength of the shrinkage between the background and the sources. Besides, this alternative strategy is limited to point-like sources and cannot work with extended objects such as disks since their contributions cannot be easily modeled and subtracted from the data in the current state of the PACO algorithm.

Since the solution discussed above is not very satisfactory, further methodological developments should be done in the aim to detect/reconstruct extended objects such as disks with PACO-based algorithms.

One of the possible solutions could be to combine the local statistical modeling of the background of PACO with a parametric model of the disks. There is a large literature addressing the physical modeling of gas/dust protoplanetary disks by few parameters, see for example Augereau et al. (1999); Stark et al. (2014); Milli et al. (2017). Figure 8.6 gives an example of a physics-based parametric model of the disk shown in the bottom left corner of Figure 8.4 and box ③ of Figure 8.5. From a signal processing point of view, the resulting algorithm could alternate between (i) the estimation of the background statistics, flux, and detection criterion of PACO, and (ii) the update of the parametric model of the disk and estimation of its flux. Such an approach could have several advantages. First, it could make it possible to disentangle the contribution of point-like sources from the contribution of extended objects, making easier the detection



of exoplanets embedded inside protoplanetary disks. Second, since the model is well constrained, such an approach could be adapted to detect accurately very faint disks such as the ones shown in the middle panels of Figure 8.4.

Another solution could be to combine the local statistical modeling of the background of PACO with an image-based reconstruction approach of the disk. Such an approach would benefit from the displacement of the disk (that follows a similar displacement than point-like sources and other background objects) in the A(S)DI sequences to disentangle their signature from the background of speckles. Additional regularization terms should be considered in the resulting inverse problem, such as sparsity constraints or an edge-preserving regularization, to constrain the solution.

### 8.2.2.3 Automatic adaptation of the detection threshold

In this section, we suggest that the detection threshold  $\tau$  conventionally fixed at  $\tau = 5$  in direct imaging (corresponding to  $\text{PFA} = 2.87 \times 10^{-7}$ ) could be adapted automatically to the content of the observed scene. Indeed, while this highly conservative threshold theoretically prevents numerous false alarms (for statistically grounded detection maps), it can also lead to numerous missed detections. This could be particularly problematic for datasets containing a lot of faint point-like sources. The presence of hundreds of point-like sources is not rare in direct imaging datasets as illustrated by Figure 8.7<sup>8</sup>. Most of the sources are generally sources or bright stars of the background which are imaged in the projected field of view. However, the target stars could also host (potential) exoplanets whose detection should not be missed because of a too conservative threshold.

There is a large signal processing literature related to this subject which was boosted, in particular, by the development of massive genomics tests in the middle of the 90s. By multiplying the number of tests (depending on distinct variables), there was a non-negligible probability to observe false positives which are normally rare.

In our context, we can rephrase this issue as: how to set the detection threshold to achieve a tradeoff between the false alarm rate (i.e., the proportion of false alarms in the peaks above the detection threshold), and the detection rate (i.e., the proportion of sources to be detected actually detected). One of the most successful approaches addressing the automatic control of the number of false *discoveries* (false alarms) is the *false discovery rate* (FDR) procedure of Benjamini and Hochberg (1995). Its mathematical formulation has a simple geometric interpretation. It consists of plotting in a graph the  $p$ -values<sup>9</sup> associated with each detection in increasing order (i.e., detections of highest confidence first). The tangent at the origin of the curves defined by the ordered  $p$ -values is then drawn. All detections whose  $p$ -values are above the tangent are assigned to the null hypothesis while the others are assigned to the alternative hypothesis, see Figure 8.8.

In the following, we illustrate that the adaptation of this type of approaches could also be suitable in our high-contrast imaging application.

8. The name of the stars and the observation logs are voluntarily not reported since these results are not yet published.

9. In statistical hypothesis testing, the  $p$ -value (for *probability*-value) is, for a given statistical model and under the null hypothesis ( $\mathcal{H}_0$ ), the probability of observing a deviation greater or equal to the deviation actually observed.

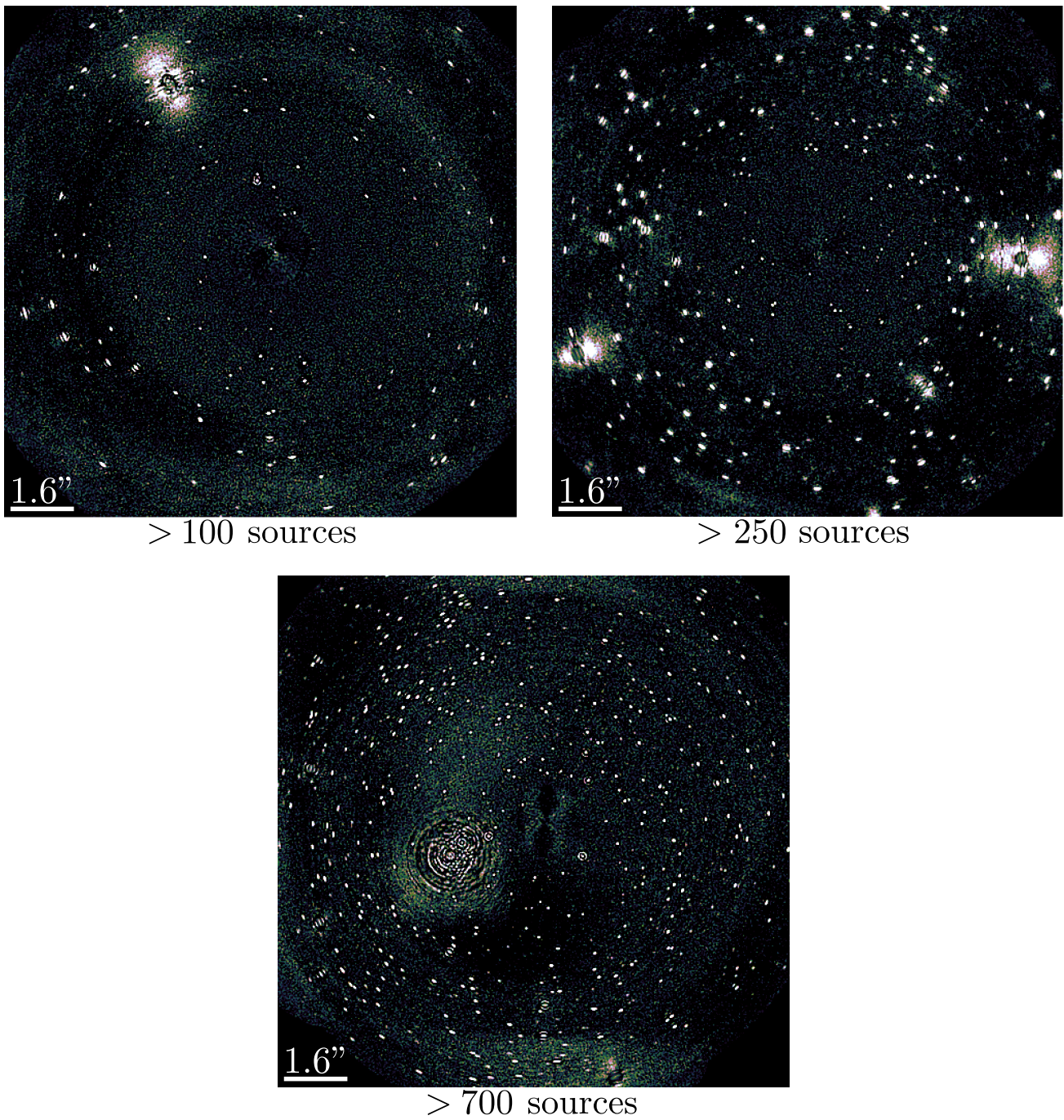


Figure 8.7 – Illustration of S/N maps obtained on three ADI datasets containing more than 100, 250, and 700 point-like sources. The processing was made by Maud Langlois with the first (suboptimal) version of the PACO pipeline (May 2018).

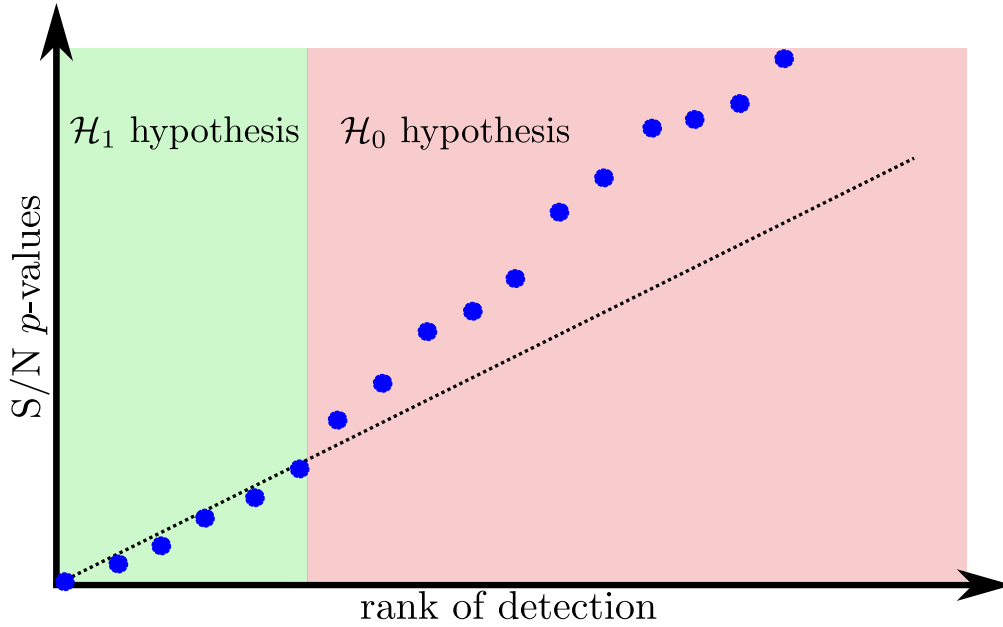


Figure 8.8 – Illustration of the control of the False Discovery Rate by the Benjamini-Hochberg procedure.

We have performed massive injections of point sources in an ADI dataset of HIP 72192 (see Table 2.3 for the observations logs) at five levels of contrasts (*level 1* for the faintest case, and *level 5* for the brightest case). We have varied the number of sources (3, 6, 60, 120, and 240), and we have processed the resulting datasets with PACO. Figures 8.9 and 8.10 give the S/N of the 300 first detections<sup>10</sup> converted into  $p$ -values, and represented in ascending order. Figure 8.11 summarizes these results and gives the resulting detection and false alarm rates for these different cases.

It shows that there is no gain to decrease the detection threshold when the sources are rare and bright since the detection rate will not be significantly improved while the false alarm rate will drastically increase. By opposition, when the datasets contain several faint sources, it could be beneficial to decrease the detection threshold to improve the detection rate without significant degradation of the false alarm rate. For example, the detection rate goes from about 5% to 55% when the detection threshold is set to 3.5 instead of 5 when 240 very faint sources (*level 1* of contrast) are in the field of view. In the same time, the increase of the false alarm rate is more limited since it goes from 0% to 10%.

10. Since the detection peaks of PACO are spatially correlated on several pixels, for each detection, the contribution of the source is estimated, subtracted to the data, and the S/N map is locally recomputed before looking for the next highest peak, see Section 2.4.6.

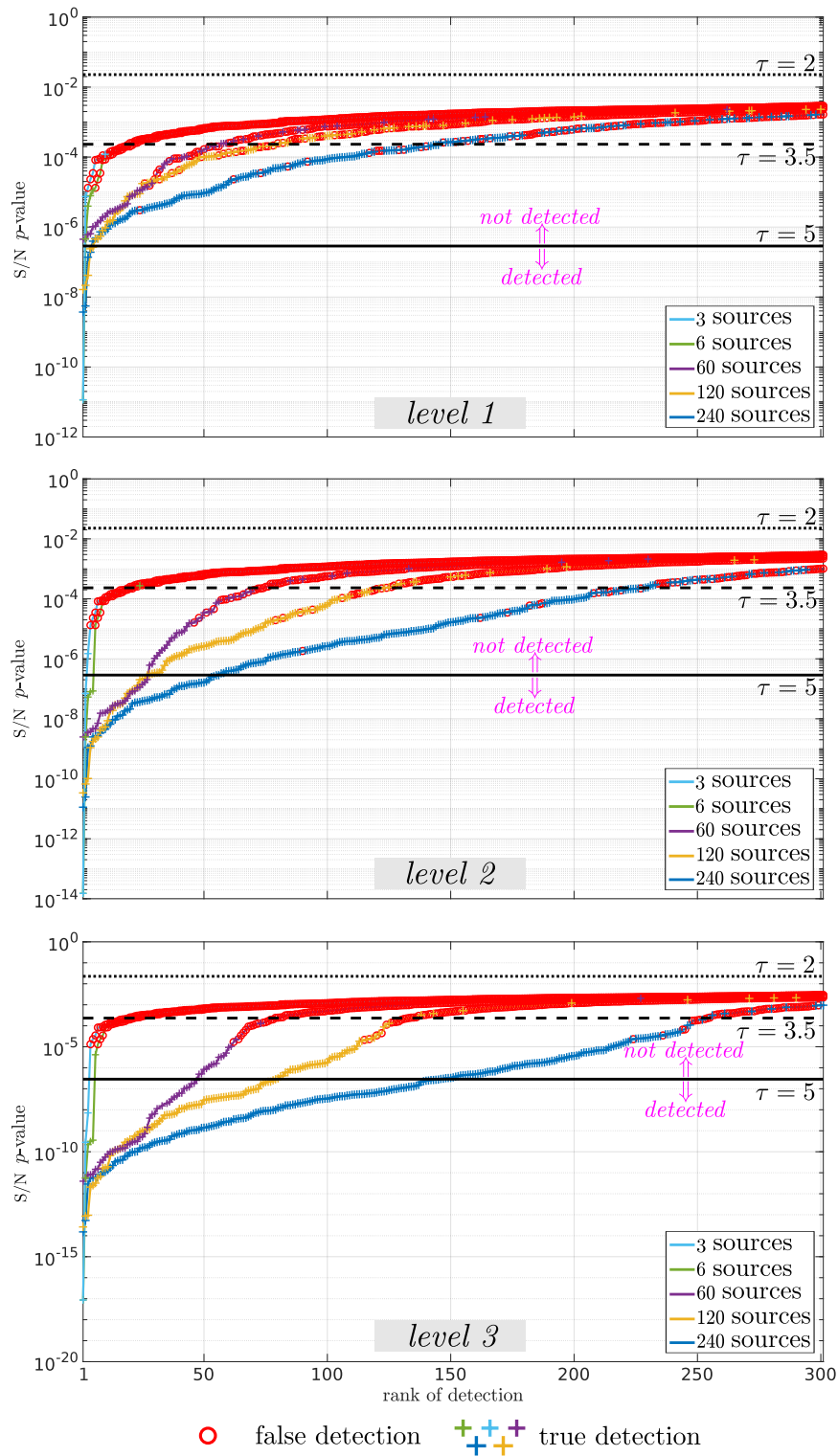


Figure 8.9 –  $p$ -values of the 300 first S/N detections ranked in increasing order for *levels 1, 2, and 3* of contrast of the injected sources. For each case, 3, 6, 60, 120, and 240 sources are injected in the field of view. Colored crosses indicate the true detections while red circles are for the false detections. The horizontal lines represent three detection thresholds:  $\tau \in \{2, 3.5, 5\}$ .



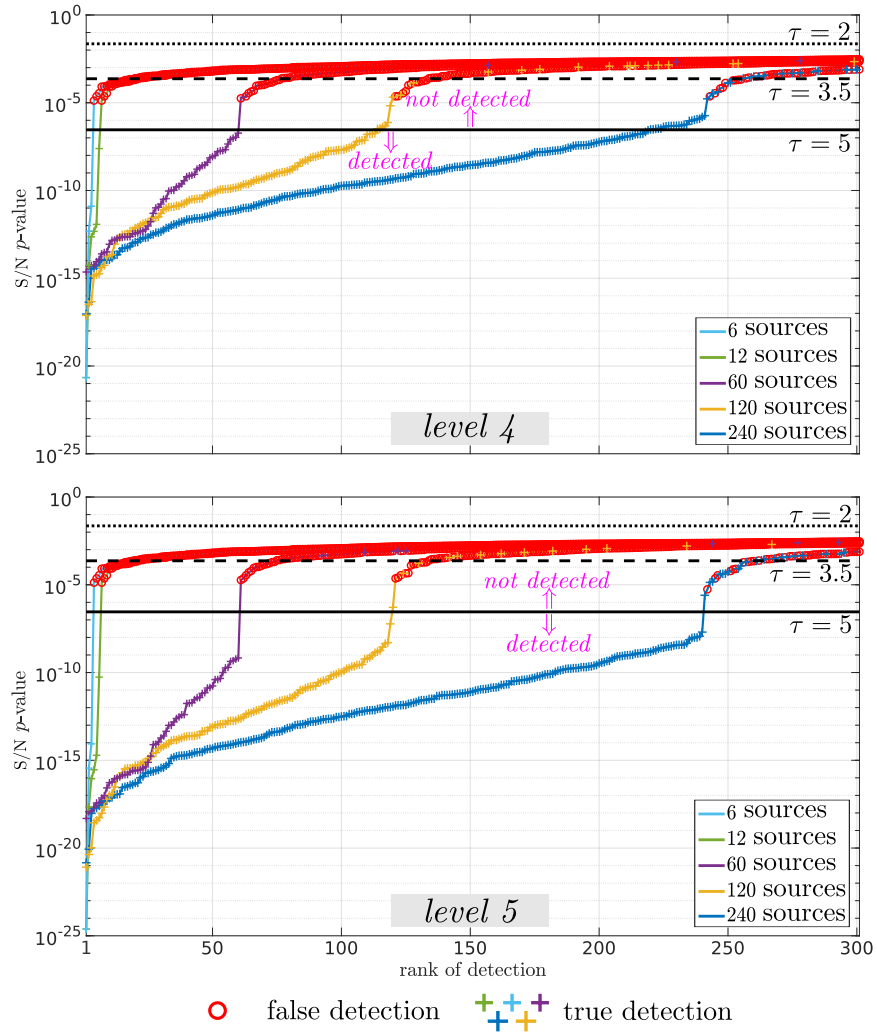


Figure 8.10 – Same representation than Figure 8.9 for *levels* of contrast 4 and 5.

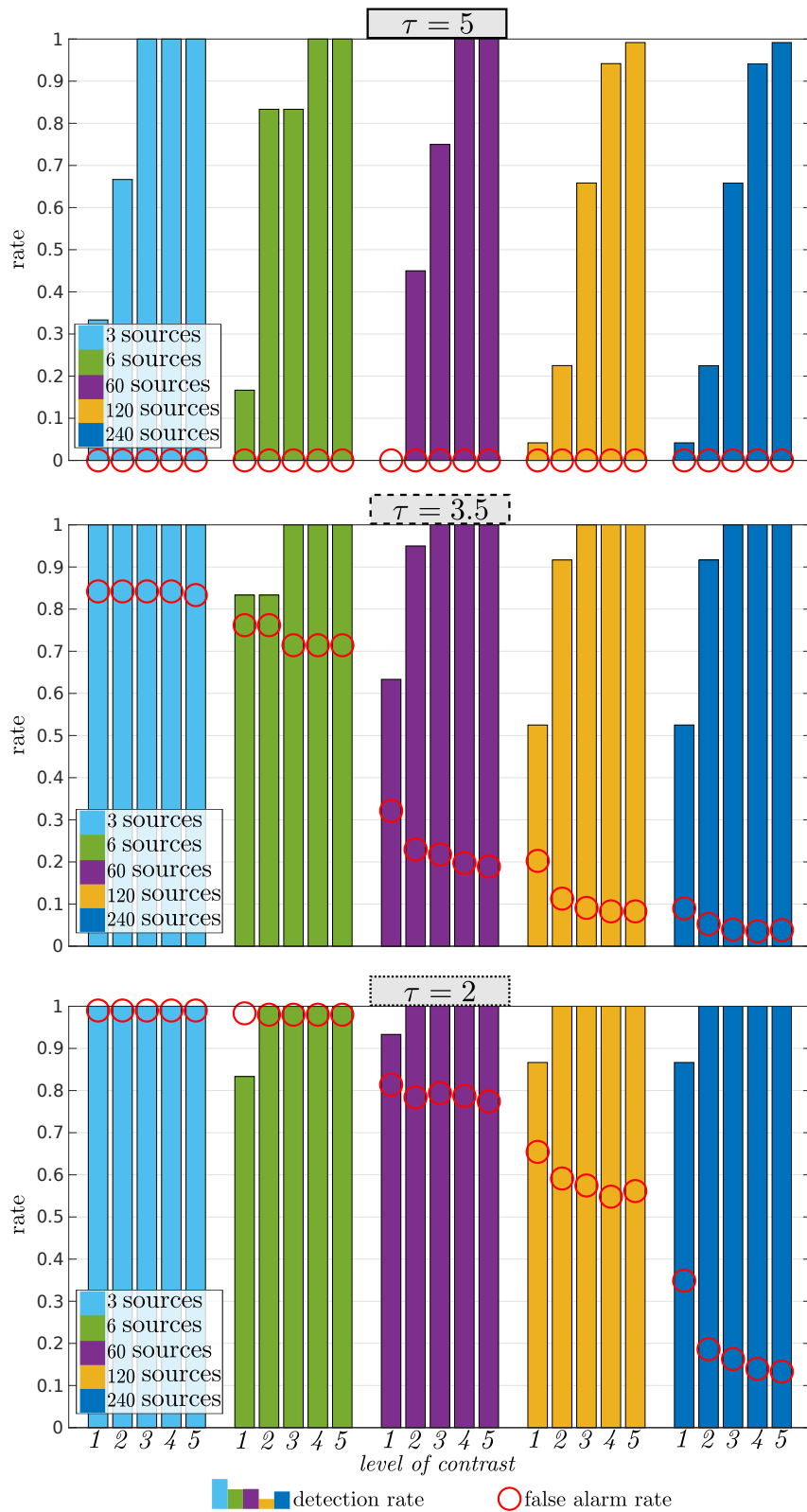


Figure 8.11 – Detection and false alarm rates for the different cases represented in Figures 8.9 and 8.10. Each graph corresponds to a different detection threshold ( $\tau \in \{2, 3.5, 5\}$ ) that are represented as horizontal black lines in Figures 8.9 and 8.10.



## 8.3 Ongoing and future works for microscopy

### 8.3.1 On the applicative side

During this thesis, we have developed several methods improving both the detection sensitivity and the characterization accuracy of microscopic objects spread in a volume.

Here, we suggest combining these different methodological approaches to benefit from the peculiarities of each one. One of the targeted applications could be the study of cells by fluid flow cytometry. With this technique, the samples are put into a fluid flow micro-channel so that each object is imaged several times and under several orientations. The nonstationary and fluctuating background of the recorded images could be modeled with a EXPACO-based method. This approach could be particularly useful to detect faint diffraction patterns when the refractive index of the samples is close to that of the medium (since the contrast is weak in this case, see Chapter 3). Multiple illuminations at different wavelengths and the robustness against unwanted objects could both improve the detection and the characterization performance. The processing could also benefit from the natural motion of the samples inside the micro-channel to further improve the estimation and/or to reconstruct the objects in 3-D.

### 8.3.2 On the methodological side

In this section, we discuss some ongoing and possible future improvements/extensions from a methodological point of view of the algorithms developed in this thesis for microscopy applications.

#### 8.3.2.1 Detection of extended patterns with a transform-based approach

Chapter 3 has illustrated the benefit of the local modeling of the background fluctuations arising in hologram series. In particular, we have shown that patches with holes lead to a good tradeoff between the size of the covariance matrices to estimate and the range of the correlations that are captured. However, the number of active pixels in a patch should not be too high due to the difficulty to estimate the covariances from a limited number of samples.

Based on this observation, we discuss here an alternative strategy to capture the relatively large scale correlations of this type of data with a limited number of samples. Instead of learning the correlations directly from the data, we suggest learning those correlations from linear transformations of the data. Such an approach is inspired by signal processing works showing that the covariance of the coefficients of transformations of the data (e.g., based on wavelets decomposition, or more generally, any multi-scaled oriented decomposition) can be learned to assess statistical properties of the noise and of the signal (Portilla et al., 2003; Chaux et al., 2007).

In our context, we suggest to convolve each of the  $T$  background images by  $S$  impulse responses from a bank filters. Each filter aims to produce a smoothed and spatially shifted version of each background image. From this procedure, it results  $T$  collections of  $S$  filtered background images. The mean  $\widehat{\mathbf{m}}_n$  (of size  $S \times 1$ ) and the covariance  $\widehat{\mathbf{C}}_n$  (of size  $S \times S$ ) are learned from the  $T$  collections of  $S$  filtered images at each pixel  $n$

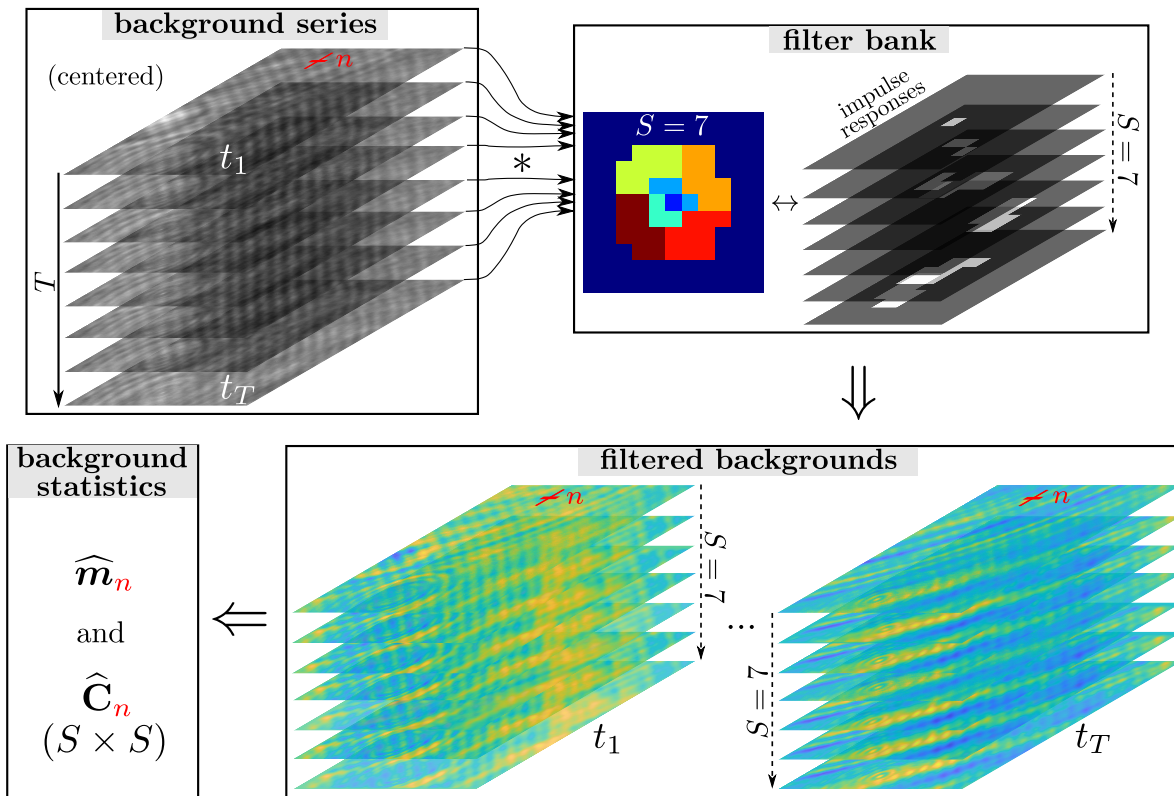


Figure 8.12 – Alternative version of the EXPACO algorithm. The statistics of the background are learned from linear transformations of the data.

of the field of view. Next, the detection of the (potential) holographic patterns follows the EXPACO approach described in Chapter 3. Figure 8.12 is a schematic representation of this procedure. In words, with this alternative version of EXPACO, the local learning of the background fluctuations by means of patches is replaced by the learning of the covariances of the vector of values formed by extracting values, at a pixel of interest, of linear transformed versions of the data.

Figure 8.13(b) shows examples of detection maps obtained with this approach for different numbers of filters  $S$  in the filter bank. The corresponding impulse responses are shown in Figure 8.13(a) (each of the  $S$  filters has a flat response color-coded with a different hue). For the experiments, we have considered the same time series of background images than in Section 3.5, and we have injected a synthetic holographic pattern (140 times fainter than the background) on a test image, see Section 3.5. The detection peak (circled in magenta) corresponding to the center location of the holographic pattern has the highest S/N value when the covariances of the background are captured with  $S \geq 7$  filters. Both the stationarity of the detection maps and the detection sensitivity degrade when  $S$  is larger than the number  $T$  of available samples (as in Section 3.5,  $T = 60$  here). Figure 8.13(c) compares an example of a detection map obtained with the alternative version of EXPACO and of the standard EXPACO. In the two cases, the dimension of the covariance matrices is almost the same:  $7 \times 7$  (corresponding to  $S = 7$  filters) for the alternative version of EXPACO, and  $9 \times 9$  (corresponding to  $K = 9$

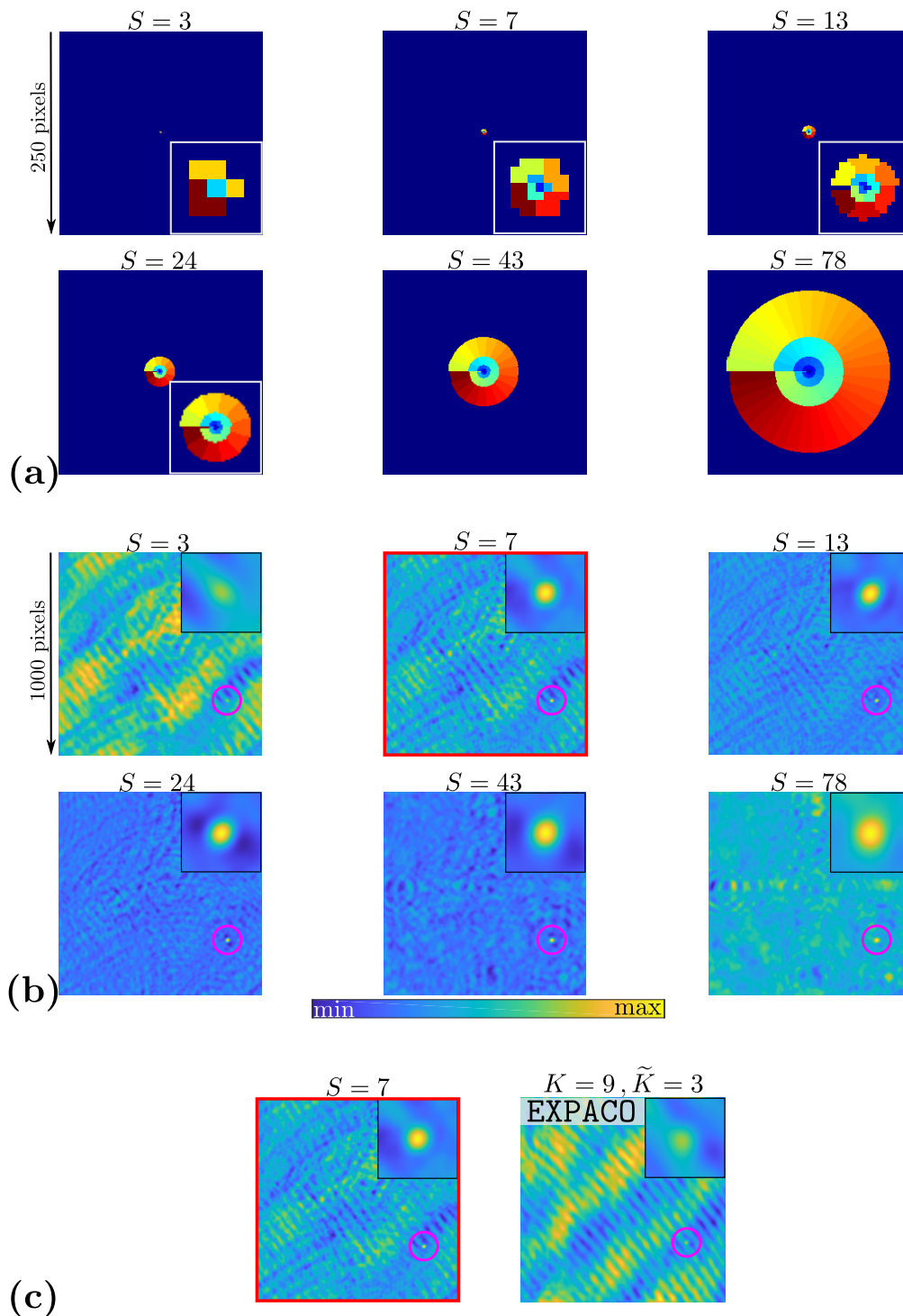


Figure 8.13 – Alternative version of the EXPACO algorithm. (a) view of the impulse responses of the filters for different numbers  $S$  of filters; (b) resulting detection maps; (c) comparison between detection maps obtained with the alternative version of EXPACO (left) and standard EXPACO (right). Zooms are shown when needed in the attached insets.

pixels in a patch) for **EXPACO**. It emphasizes that even with a limited size of covariance matrices, the alternative version of **EXPACO** achieves better detection performance than **EXPACO**. This may be due to its ability to capture longer-range correlations than **EXPACO** for a given size of the covariance matrices.

This preliminary study should be completed by analyzing, for example, the influence of the shape, size, and orientation of the impulse responses of the considered filters.

### **8.3.2.2 Image reconstructions accounting for the correlated background**

The local statistical modeling of the background fluctuations embedded in the **PACO** and **EXPACO** algorithms proved to be adapted to the nonstationarity of the typical images resulting from direct imaging and holographic microscopy observations. Here we suggest that the **PACO**-based modeling could also be used for object-based reconstructions in holographic microscopy, as similarly suggested in Section 8.2.2.2 for protoplanetary disks. As discussed in Section 8.2.2.2, regularization strategies and physical priors adapted to the imaged objects should also be considered to stabilize the inversion.







## Estimation of covariance matrices by shrinkage

In this Appendix, we derive the proofs of Equations (2.11), (2.12) and (2.14) considering the problem of the covariance matrix estimation from a few samples, in the general case of non-stationary Gaussian noise.

Let  $\mathbf{x} \in \mathbb{R}^p$  be a Gaussian random vector with  $\mathbb{E}[\mathbf{x}] = \mathbf{0}$  and  $\mathbb{E}[\mathbf{x}\mathbf{x}^\top] = \mathbf{\Sigma}$ . Given a collection of  $n$  samples  $\{\mathbf{x}_k\}_{k=1..n}$ , we try to estimate the covariance matrix  $\mathbf{\Sigma}$  by the convex combination:

$$\widehat{\mathbf{\Sigma}} = (1 - \widehat{\rho})\widehat{\mathbf{S}} + \widehat{\rho}\widehat{\mathbf{F}}, \quad (\text{A.1})$$

where  $\widehat{\mathbf{S}}$  is the sample covariance matrix:  $\widehat{\mathbf{S}} = \frac{1}{n} \sum_k \mathbf{x}_k \mathbf{x}_k^\top$ ,  $\widehat{\mathbf{F}}$  is the diagonal matrix defined by  $[\widehat{\mathbf{F}}]_{ii} = \frac{1}{n} \sum_k [\mathbf{x}_k]_i^2$  and  $\widehat{\rho}$  is a shrinkage parameter.  $\widehat{\mathbf{S}}$  is the maximum likelihood estimate of  $\mathbf{\Sigma}$ , a matrix with  $p(p+1)/2$  degrees of freedom while  $\widehat{\mathbf{F}}$  has only  $p$  non-zero values (it is a biased estimate of  $\mathbf{\Sigma}$ ). The parameter  $\widehat{\rho}$  tunes the tradeoff between the low-bias/high-variance estimate  $\widehat{\mathbf{S}}$  and the low-variance/high-bias estimate  $\widehat{\mathbf{F}}$ .

### A.1 The oracle estimator

The value  $\rho_{\text{O}}$  that minimizes the risk (i.e., the expectation of the squared Frobenius norm  $\|\widehat{\mathbf{\Sigma}} - \mathbf{\Sigma}\|_{\text{F}}^2$ ) is given in the general case by (see [Chen et al. \(2010\)](#), theorem 1, Equation (6)):

$$\rho_{\text{O}} = \frac{\mathbb{E} \left[ \text{tr} \left( (\mathbf{\Sigma} - \widehat{\mathbf{S}})(\widehat{\mathbf{F}} - \widehat{\mathbf{S}}) \right) \right]}{\mathbb{E} \left[ \|\widehat{\mathbf{S}} - \widehat{\mathbf{F}}\|_{\text{F}}^2 \right]} = \frac{\sum_{i,j} \text{Var}([\widehat{\mathbf{S}}]_{ij}) - \sum_{i,j} \text{Cov}([\widehat{\mathbf{S}}]_{ij}, [\widehat{\mathbf{F}}]_{ij})}{\mathbb{E} \left[ \|\widehat{\mathbf{S}} - \widehat{\mathbf{F}}\|_{\text{F}}^2 \right]} \quad (\text{A.2})$$

*Proof.* By definition of  $\widehat{\mathbf{\Sigma}}$ ,  $\|\widehat{\mathbf{\Sigma}} - \mathbf{\Sigma}\|_{\text{F}}^2$  can be expanded into  $\|(1 - \widehat{\rho})\widehat{\mathbf{S}} + \widehat{\rho}\widehat{\mathbf{F}} - \mathbf{\Sigma}\|_{\text{F}}^2 \equiv \text{tr} \left( [(1 - \widehat{\rho})\widehat{\mathbf{S}} + \widehat{\rho}\widehat{\mathbf{F}} - \mathbf{\Sigma}]^2 \right)$ . The expansion of this term gives a second degree polynomial in  $\widehat{\rho}$ :

$$\|\widehat{\mathbf{\Sigma}} - \mathbf{\Sigma}\|_{\text{F}}^2 = \widehat{\rho}^2 \|\widehat{\mathbf{F}} - \widehat{\mathbf{S}}\|_{\text{F}}^2 + \|\widehat{\mathbf{S}} - \widehat{\mathbf{F}}\|_{\text{F}}^2 + 2\widehat{\rho} \text{tr} \left( (\widehat{\mathbf{F}} - \widehat{\mathbf{S}})(\widehat{\mathbf{S}} - \mathbf{\Sigma}) \right). \quad (\text{A.3})$$

Hence, the condition  $\nabla_{\hat{\rho}} \left[ \mathbb{E} \left[ \|\hat{\Sigma} - \Sigma\|_{\text{F}}^2 \right] \right]_{\hat{\rho}=\rho_0} = 0$  leads straightforwardly to the left-most part of Equation (A.2). The last part of Equation (A.2) comes by expanding the numerator and using the fact that  $\hat{\mathbf{S}}$  is unbiased:  $\mathbb{E}[\hat{\mathbf{S}}] = \Sigma$ .  $\square$

Under our assumed form for estimators  $\hat{\mathbf{S}}$  and  $\hat{\mathbf{F}}$  and our Gaussian hypothesis,  $\rho_0$  is given by:

$$\rho_0 = \frac{\text{tr}(\Sigma^2) + \text{tr}^2(\Sigma) - 2 \sum_{i=1}^p [\Sigma]_{ii}^2}{(n+1) \text{tr}(\Sigma^2) + \text{tr}^2(\Sigma) - (n+2) \sum_{i=1}^p [\Sigma]_{ii}^2}. \quad (\text{A.4})$$

*Proof.* The numerator of Equation (A.2) can be expanded as:

$$\mathbb{E} \left[ \text{tr} \left( (\Sigma - \hat{\mathbf{S}})(\hat{\mathbf{F}} - \hat{\mathbf{S}}) \right) \right] = \mathbb{E} \left[ \text{tr} \left( \Sigma \hat{\mathbf{F}} \right) \right] - \mathbb{E} \left[ \text{tr} \left( \Sigma \hat{\mathbf{S}} \right) \right] - \mathbb{E} \left[ \text{tr} \left( \hat{\mathbf{S}} \hat{\mathbf{F}} \right) \right] + \mathbb{E} \left[ \text{tr} \left( \hat{\mathbf{S}}^2 \right) \right] \quad (\text{A.5})$$

$$= \sum_{i=1}^p [\Sigma]_{ii}^2 - \text{tr}(\Sigma^2) - \sum_{i=1}^p \mathbb{E} \left[ [\hat{\mathbf{S}}]_{ii}^2 \right] + \mathbb{E} \left[ \text{tr} \left( \hat{\mathbf{S}}^2 \right) \right]. \quad (\text{A.6})$$

The variance of the sample variance  $\text{Var} \left[ [\hat{\mathbf{S}}]_{ii}^2 \right]$  of Gaussian random variables is equal to  $2[\Sigma]_{ii}^2/n$ , and its expectation is  $[\Sigma]_{ii}^2$ , thus the expectation of the square of the sample variance  $\mathbb{E} \left[ [\hat{\mathbf{S}}]_{ii}^2 \right]$  is equal to  $2[\Sigma]_{ii}^2/n + [\Sigma]_{ii}^2 = \frac{n+2}{n} [\Sigma]_{ii}^2$ . The expectation  $\mathbb{E} \left[ \text{tr} \left( \hat{\mathbf{S}}^2 \right) \right]$  is given in [Chen et al. \(2010\)](#)  $\mathbb{E} \left[ \text{tr} \left( \hat{\mathbf{S}}^2 \right) \right] = \frac{n+1}{n} \text{tr}(\Sigma^2) + \frac{1}{n} \text{tr}^2(\Sigma)$ . The numerator then becomes:

$$\mathbb{E} \left[ \text{tr} \left( (\Sigma - \hat{\mathbf{S}})(\hat{\mathbf{F}} - \hat{\mathbf{S}}) \right) \right] = \sum_{i=1}^p [\Sigma]_{ii}^2 - \text{tr}(\Sigma^2) - \frac{n+2}{n} \sum_{i=1}^p [\Sigma]_{ii}^2 + \frac{n+1}{n} \text{tr}(\Sigma^2) + \frac{1}{n} \text{tr}^2(\Sigma) \quad (\text{A.7})$$

$$= \frac{1}{n} \text{tr}^2(\Sigma) + \frac{1}{n} \text{tr}(\Sigma^2) - \frac{2}{n} \sum_{i=1}^p [\Sigma]_{ii}^2. \quad (\text{A.8})$$

Next, the denominator can be expanded:

$$\mathbb{E} \left[ \|\hat{\mathbf{S}} - \hat{\mathbf{F}}\|_{\text{F}}^2 \right] = \mathbb{E} \left[ \text{tr} \left( (\hat{\mathbf{S}} - \hat{\mathbf{F}})^2 \right) \right] \quad (\text{A.9})$$

$$= \mathbb{E} \left[ \text{tr}(\hat{\mathbf{S}}^2) \right] - 2\mathbb{E} \left[ \text{tr}(\hat{\mathbf{S}}\hat{\mathbf{F}}) \right] + \mathbb{E} \left[ \text{tr}(\hat{\mathbf{F}}^2) \right] \quad (\text{A.10})$$

$$= \frac{n+1}{n} \text{tr}(\Sigma^2) + \frac{1}{n} \text{tr}^2(\Sigma) - 2\frac{n+2}{n} \sum_{i=1}^p [\Sigma]_{ii}^2 + \frac{n+2}{n} \sum_{i=1}^p [\Sigma]_{ii}^2 \quad (\text{A.11})$$

$$= \frac{n+1}{n} \text{tr}(\Sigma^2) + \frac{1}{n} \text{tr}^2(\Sigma) - \frac{n+2}{n} \sum_{i=1}^p [\Sigma]_{ii}^2 \quad (\text{A.12})$$

The optimal weight  $\rho_0$  is then given by (A.4).  $\square$

## A.2 The Oracle-Approximating Shrinkage (OAS) estimator

If we plug a previous estimate of  $\Sigma$  in Equation (A.4), an improved value of  $\rho_O$  is obtained. Re-iterating this process leads to the OAS estimator:

$$\hat{\rho} = \frac{\text{tr}(\hat{\mathbf{S}}^2) + \text{tr}^2(\hat{\mathbf{S}}) - 2 \sum_{i=1}^p [\hat{\mathbf{S}}]_{ii}^2}{(n+1)(\text{tr}(\hat{\mathbf{S}}^2) - \sum_{i=1}^p [\hat{\mathbf{S}}]_{ii}^2)}. \quad (\text{A.13})$$

*Proof.* Like in [Chen et al. \(2010\)](#), we define the recursion:

$$\begin{cases} \hat{\rho}_{j+1} &= \frac{\text{tr}(\hat{\Sigma}_j \hat{\mathbf{S}}) + \text{tr}^2(\hat{\Sigma}_j) - 2 \sum_{i=1}^p [\hat{\Sigma}_j]_{ii} [\hat{\mathbf{S}}]_{ii}}{(n+1) \text{tr}(\hat{\Sigma}_j \hat{\mathbf{S}}) + \text{tr}^2(\hat{\Sigma}_j) - (n+2) \sum_{i=1}^p [\hat{\Sigma}_j]_{ii} [\hat{\mathbf{S}}]_{ii}} \\ \hat{\Sigma}_{j+1} &= (1 - \hat{\rho}_{j+1}) \hat{\mathbf{S}} + \hat{\rho}_{j+1} \hat{\mathbf{F}} \end{cases} \quad (\text{A.14})$$

Replacing  $\hat{\Sigma}_j$  by its definition leads to:

$$\text{tr}(\hat{\Sigma}_j \hat{\mathbf{S}}) = (1 - \hat{\rho}_j) \text{tr}(\hat{\mathbf{S}}^2) + \hat{\rho}_j \text{tr}(\hat{\mathbf{F}} \hat{\mathbf{S}}), \quad (\text{A.15})$$

$$\text{tr}^2(\hat{\Sigma}_j) = \left[ (1 - \hat{\rho}_j) \text{tr}(\hat{\mathbf{S}}) + \hat{\rho}_j \text{tr}(\hat{\mathbf{F}}) \right]^2 = \text{tr}^2(\hat{\mathbf{S}}) \quad (\text{since } \text{tr}(\hat{\mathbf{F}}) = \text{tr}(\hat{\mathbf{S}})), \quad (\text{A.16})$$

$$[\hat{\Sigma}_j]_{ii} [\hat{\mathbf{S}}]_{ii} = [\hat{\mathbf{S}}]_{ii}^2 \quad \Rightarrow \quad \sum_i [\hat{\Sigma}_j]_{ii} [\hat{\mathbf{S}}]_{ii} = \text{tr}(\hat{\mathbf{F}} \hat{\mathbf{S}}) = \sum_i [\hat{\mathbf{S}}]_{ii}^2. \quad (\text{A.17})$$

The recursion over parameter  $\hat{\rho}_j$  is thus given by:

$$\hat{\rho}_{j+1} = \frac{(1 - \hat{\rho}_j) \text{tr}(\hat{\mathbf{S}}^2) + (\hat{\rho}_j - 2) \sum_{i=1}^p [\hat{\mathbf{S}}]_{ii}^2 + \text{tr}^2(\hat{\mathbf{S}})}{(n+1)(1 - \hat{\rho}_j) \text{tr}(\hat{\mathbf{S}}^2) + [(n+1)\hat{\rho}_j - (n+2)] \sum_{i=1}^p [\hat{\mathbf{S}}]_{ii}^2 + \text{tr}^2(\hat{\mathbf{S}})} \quad (\text{A.18})$$

$$= \frac{a \hat{\rho}_j + b}{c \hat{\rho}_j + d}, \quad (\text{A.19})$$

where  $a = \sum_{i=1}^p [\hat{\mathbf{S}}]_{ii}^2 - \text{tr}(\hat{\mathbf{S}}^2)$ ,  $b = \text{tr}(\hat{\mathbf{S}}^2) + \text{tr}^2(\hat{\mathbf{S}}) - 2 \sum_{i=1}^p [\hat{\mathbf{S}}]_{ii}^2$ ,  $c = (n+1) \left( \sum_{i=1}^p [\hat{\mathbf{S}}]_{ii}^2 - \text{tr}(\hat{\mathbf{S}}^2) \right)$

and  $d = (n+1) \text{tr}(\hat{\mathbf{S}}^2) - (n+2) \sum_{i=1}^p [\hat{\mathbf{S}}]_{ii}^2 + \text{tr}^2(\hat{\mathbf{S}})$  are 4 constants (independent of  $j$ ). If

the recursion converges, it converges to one of the fixed-points  $\hat{\rho} = 1$  or

$$\hat{\rho} = \frac{\text{tr}(\hat{\mathbf{S}}^2) + \text{tr}^2(\hat{\mathbf{S}}) - 2 \sum_{i=1}^p [\hat{\mathbf{S}}]_{ii}^2}{(n+1)(\text{tr}(\hat{\mathbf{S}}^2) - \sum_{i=1}^p [\hat{\mathbf{S}}]_{ii}^2)}, \quad (\text{A.20})$$

which is obtained after simplification of the roots of the equation in  $\hat{\rho}$ :  $\hat{\rho}(c \hat{\rho} + d) = a \hat{\rho} + b$ . This closed-form expression is an extension of the results given in [Chen et al. \(2010\)](#) to our estimator  $\hat{\mathbf{F}}$  with non-constant diagonal values.  $\square$

# Appendix B

## Unsupervised regularization of the estimated SEDs

In Section B.1 of this appendix, we derive a sketch of proof of Equations (6.36) and (6.37) considering the problem of the unsupervised regularization of the estimated SEDs of detected sources with the generalized maximum likelihood (GML) approach. In Section B.2, we complete the numerical experiments presented in Section 6.4.2.1 comparing the GML, GCV, and SURE regularization strategies.

### B.1 SED regularization with the GML approach

This section derives the expression of the GML estimation of the spectral smoothness  $\mu$ . The whitened vector  $\hat{\mathbf{S}}$  of the S/N $_{\ell}$  values extracted at a given location  $\phi_0$  of the field of view is assumed to be distributed according to a Gaussian distribution:  $\hat{\mathbf{S}} \sim \mathcal{N}(\hat{\mathbf{L}}^T \mathbf{V} \boldsymbol{\alpha}, \mathbf{I})$ , such that  $\hat{\mathbf{L}} \hat{\mathbf{L}}^T = \hat{\boldsymbol{\Sigma}}^{-1}$ . To estimate  $\mu^{(\text{GML})}$ , we need to derive the expression of the density  $p(\hat{\mathbf{S}}|\mu, \phi_0) = \int p(\hat{\mathbf{S}}, \boldsymbol{\alpha}|\mu, \phi_0) d\boldsymbol{\alpha} = \int p(\hat{\mathbf{S}}|\boldsymbol{\alpha}, \phi_0)p(\boldsymbol{\alpha}|\mu, \phi_0) d\boldsymbol{\alpha}$ . We have:

$$p(\hat{\mathbf{S}}|\boldsymbol{\alpha}, \phi_0) = (2\pi)^{-L/2} \exp \left[ -\frac{1}{2} (\hat{\mathbf{S}} - \hat{\mathbf{L}}^T \mathbf{V} \boldsymbol{\alpha})^T (\hat{\mathbf{S}} - \hat{\mathbf{L}}^T \mathbf{V} \boldsymbol{\alpha}) \right], \quad (\text{B.1})$$

and,

$$p(\boldsymbol{\alpha}|\mu, \phi_0) = (2\pi)^{-L/2} \left| \mu \mathbf{D}^T \mathbf{D} \right|_+^{1/2} \exp \left[ -\frac{\mu}{2} \boldsymbol{\alpha}^T \mathbf{D}^T \mathbf{D} \boldsymbol{\alpha} \right], \quad (\text{B.2})$$

with  $|\cdot|_+$  the product of all non-zero singular values (see Trouvé (2012)). The density  $p(\hat{\mathbf{S}}, \boldsymbol{\alpha}|\mu, \phi_0)$  is thus equal to:

$$p(\hat{\mathbf{S}}, \boldsymbol{\alpha}|\mu, \phi_0) = (2\pi)^{-L} |\boldsymbol{\mu}\mathbf{D}^\top\mathbf{D}|_+^{1/2} \exp \left[ -\frac{1}{2} (\hat{\mathbf{S}} - \hat{\mathbf{L}}^\top\mathbf{V}\boldsymbol{\alpha})^\top (\hat{\mathbf{S}} - \hat{\mathbf{L}}^\top\mathbf{V}\boldsymbol{\alpha}) - \frac{\mu}{2} \boldsymbol{\alpha}^\top\mathbf{D}^\top\mathbf{D}\boldsymbol{\alpha} \right] \quad (\text{B.3})$$

$$= (2\pi)^{-L} |\boldsymbol{\mu}\mathbf{D}^\top\mathbf{D}|_+^{1/2} \exp \left[ -\frac{1}{2} (\boldsymbol{\alpha} - \hat{\boldsymbol{\alpha}}^{(\text{reg})})^\top (\mathbf{V}\hat{\mathbf{L}}\hat{\mathbf{L}}^\top\mathbf{V} + \boldsymbol{\mu}\mathbf{D}^\top\mathbf{D}) (\boldsymbol{\alpha} - \hat{\boldsymbol{\alpha}}^{(\text{reg})}) - \frac{1}{2} \hat{\mathbf{S}}^\top \left( \mathbf{I} - \hat{\mathbf{L}}^\top\mathbf{V} (\mathbf{V}\hat{\mathbf{L}}\hat{\mathbf{L}}^\top\mathbf{V} + \boldsymbol{\mu}\mathbf{D}^\top\mathbf{D})^{-1} \mathbf{V}\hat{\mathbf{L}} \right) \hat{\mathbf{S}} \right] \quad (\text{B.4})$$

$$= (2\pi)^{-L/2} \frac{|\boldsymbol{\mu}\mathbf{D}^\top\mathbf{D}|_+^{1/2}}{|\mathbf{V}\hat{\mathbf{L}}\hat{\mathbf{L}}^\top\mathbf{V} + \boldsymbol{\mu}\mathbf{D}^\top\mathbf{D}|_+^{1/2}} \times \mathcal{G}(\boldsymbol{\alpha}; \mathbf{m} = \hat{\boldsymbol{\alpha}}^{(\text{reg})}, \boldsymbol{\Lambda}(\mu) = (\mathbf{V}\hat{\mathbf{L}}\hat{\mathbf{L}}^\top\mathbf{V} + \boldsymbol{\mu}\mathbf{D}^\top\mathbf{D})^{-1}) \times \exp \left[ -\frac{1}{2} \hat{\mathbf{S}}^\top \left( \mathbf{I} - \hat{\mathbf{L}}^\top\mathbf{V} (\mathbf{V}\hat{\mathbf{L}}\hat{\mathbf{L}}^\top\mathbf{V} + \boldsymbol{\mu}\mathbf{D}^\top\mathbf{D})^{-1} \mathbf{V}\hat{\mathbf{L}} \right) \hat{\mathbf{S}} \right], \quad (\text{B.5})$$

where  $\mathcal{G}(\cdot; \mathbf{m} = \cdot, \boldsymbol{\Lambda}(\mu) = \cdot)$  corresponds to the PDF of a Gaussian distribution of mean  $\mathbf{m}$  and covariance  $\boldsymbol{\Lambda}(\mu)$ .

By integrating with respect to  $\boldsymbol{\alpha}$ , this Gaussian PDF integrates to 1 and it remains the evidence (i.e., likelihood of  $\mu$ ):

$$p(\hat{\mathbf{S}}|\mu, \phi_0) = \mathcal{G} \left( \hat{\mathbf{S}}; \mathbf{m} = \mathbf{0}, \boldsymbol{\Lambda} = (\mathbf{I} - \hat{\mathbf{L}}^\top\mathbf{V}\mathbf{M}(\mu))^{-1} \right), \quad (\text{B.6})$$

with  $\mathbf{M}(\mu) = (\mathbf{V}\hat{\mathbf{L}}\hat{\mathbf{L}}^\top\mathbf{V} + \boldsymbol{\mu}\mathbf{D}^\top\mathbf{D})^{-1} \mathbf{V}\hat{\mathbf{L}} = (\mathbf{V}\hat{\boldsymbol{\Sigma}}^{-1}\mathbf{V} + \boldsymbol{\mu}\mathbf{D}^\top\mathbf{D})^{-1} \mathbf{V}\hat{\mathbf{L}}$ .

Hence, parameter  $\mu$  can be estimated by solving the 1-D optimization problem:

$$\hat{\mu}^{(\text{GML})} = \arg \min_{\mu} \log \det \boldsymbol{\Lambda}(\mu) + \hat{\mathbf{S}}^\top \boldsymbol{\Lambda}^{-1}(\mu) \hat{\mathbf{S}}, \quad (\text{B.7})$$

with  $\boldsymbol{\Lambda}(\mu)$  the covariance matrix defined in Equation (B.6), which corresponds to the Equations (6.36) and (6.37).

## B.2 SED regularization with the GML, GCV, and SURE approaches: additional numerical results

In this section, we detail and complete the results given in Section 6.4.2.1 comparing the GML, GCV, and SURE approaches for the unsupervised regularization of the estimated SEDs. Figures B.2, B.3, B.4, and B.5 give the estimated spectra of the 30 Monte-Carlo injections of sources #2, #5, #10, #12, respectively. The mean estimates, the empirical and the predicted (derived from the PACO-ASDI modeling) confidence intervals are also given. A comparison is also given with the results obtained when the regularization hyperparameter  $\mu$  is set in an *oracle* mode, i.e., by selecting  $\mu$  that minimizes the MSE between the SED estimate and the SED ground truth. For each tested

regularization strategy (GML, GCV, SURE, and oracle), we consider 5 sub-cases which are presented along the columns of Figures B.2, B.3, B.4, and B.5:

- *no spectral whitening*; the spectral whitening filter  $\widehat{\mathbf{L}}^\top = \mathbf{I}$ , such as the spectral covariances of the  $S/N_\ell$  values are not taken into account for the SED estimation in Equations (6.41) to (6.41).
- *spectral whitening covariance (not local)*; the spectral whitening filter  $\widehat{\mathbf{L}}$  is obtained from the Cholesky factorization of the covariance matrix  $\widehat{\mathbf{\Sigma}}$  which is computed from a large set (5,000 samples) of  $S/N_\ell$  vectors extracted around each pixel.
- *spectral whitening covariance (local)*; the spectral whitening filter  $\widehat{\mathbf{L}}$  is obtained from the Cholesky factorization of the covariance matrix  $\widehat{\mathbf{\Sigma}}$  which is computed from a small set (300 samples) of  $S/N_\ell$  vectors extracted locally around each pixel.
- *spectral whitening correlation (not local)*; the spectral whitening filter  $\widehat{\mathbf{L}}$  is obtained from the Cholesky factorization of the correlation matrix  $\widehat{\mathbf{\Sigma}}$  which is computed from a large set (5,000 samples) of  $S/N_\ell$  vectors extracted around each pixel.
- *spectral whitening correlation (local)*; the spectral whitening filter  $\widehat{\mathbf{L}}$  is obtained from the Cholesky factorization of the correlation matrix  $\widehat{\mathbf{\Sigma}}$  which is computed from a small set (300 samples) of  $S/N_\ell$  vectors extracted locally around each pixel.

Figures B.6 and B.7 complete this study by comparing the different strategies tested in terms of MSE and agreement between the estimated with the empirical  $1\sigma$  confidence intervals.

The same overall conclusions than in Section 6.4.2.1 can be made, i.e. GML and SURE approaches lead to very similar results while the GCV approach leads to significantly worse results. As expected, the gain brought by the regularization is larger when the contrast of the source is weak and for sources located near the host star, i.e., when the estimated SED is very noisy. A more complete discussion is carried out on these two points in Section 6.4.2.1.

Based on these detailed results, we also make additional observations. The gain in terms of MSE reduction is higher when the spectral whitening filter  $\widehat{\mathbf{L}}^\top$  is computed locally. This is because the covariance structure varies on moderate spatial scales (it is nonstationary). When the spectral whitening filter  $\widehat{\mathbf{L}}^\top$  is computed from a correlation matrix (i.e.,  $\widehat{\mathbf{\Sigma}}$  is a correlation matrix), the MSE reduction is slightly improved compared to that obtained with the whitening computed from the covariance matrix. However, as illustrated by Figure B.1, accounting only for the spectral correlations of the  $S/N_\ell$  values is not beneficial in the reduction step. Indeed, some spatial structures remain on the combined wS/N maps produced by PACO-ASDI when  $\widehat{\mathbf{\Sigma}}$  is a correlation matrix probably due to its reduced degrees of freedom. When the spectral whitening filter is computed from a covariance matrix, the predicted photometric standard-deviation



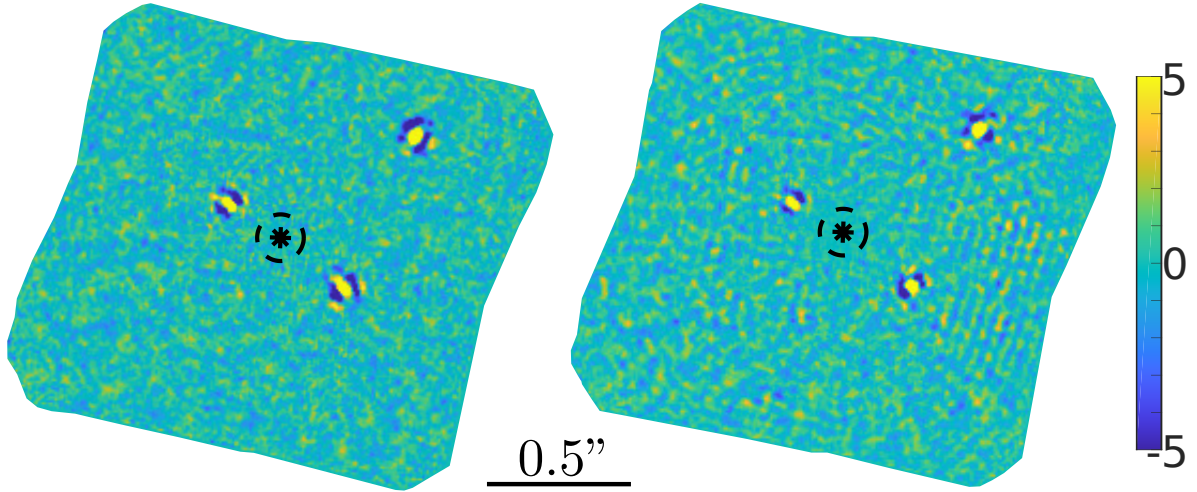


Figure B.1 – Combined wS/N maps from PACO-ASDI when the covariances (left) or the correlations of the  $S/N_\ell$  values are taken into account.

is in good agreement with the empirical photometric standard-deviation (ratio between 1.0 and 1.2).

Based on this study, we chose to regularize the estimated SEDs by the SURE approach. As detail in Section 6.4.2.1, we account for the spectral covariances of the  $S/N_\ell$  values during this process by deriving the whitening filter  $\hat{\mathbf{L}}^\top$  corresponding to a spectral covariance matrix computed from a reduced number of samples (about 300) extracted locally around each pixel of the field of view.

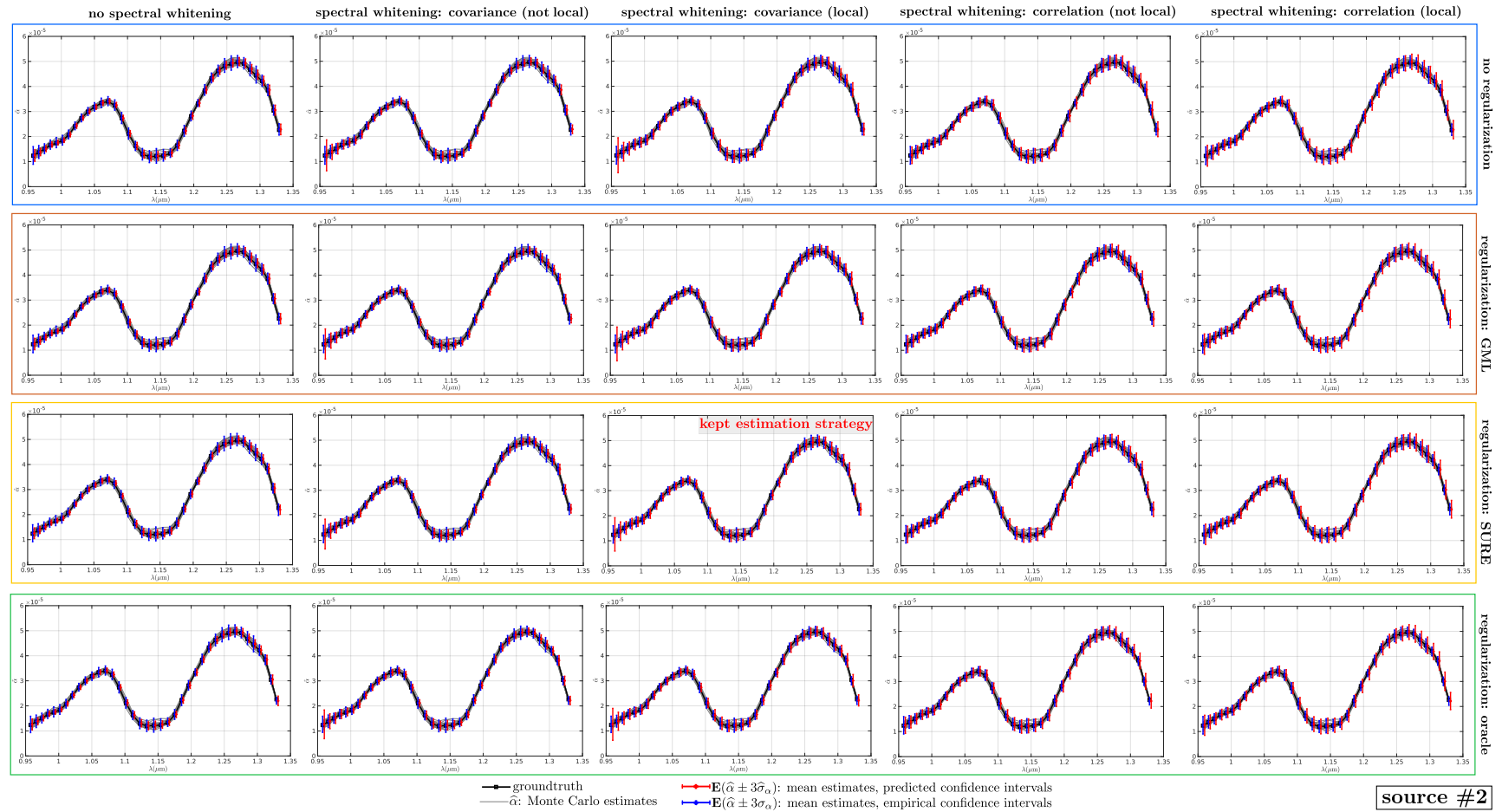


Figure B.2 – Monte-Carlo estimated spectra for the source #2 for different spectral regularization strategies (absence of regularization, regularizations GML, SURE, and oracle) and different spectral whitening strategies (no spectral whitening, non-local and local whitening) from the correlations and covariances matrices. For purpose of compactness, the detailed GCV results (which are significantly worst, see text) are not reported.

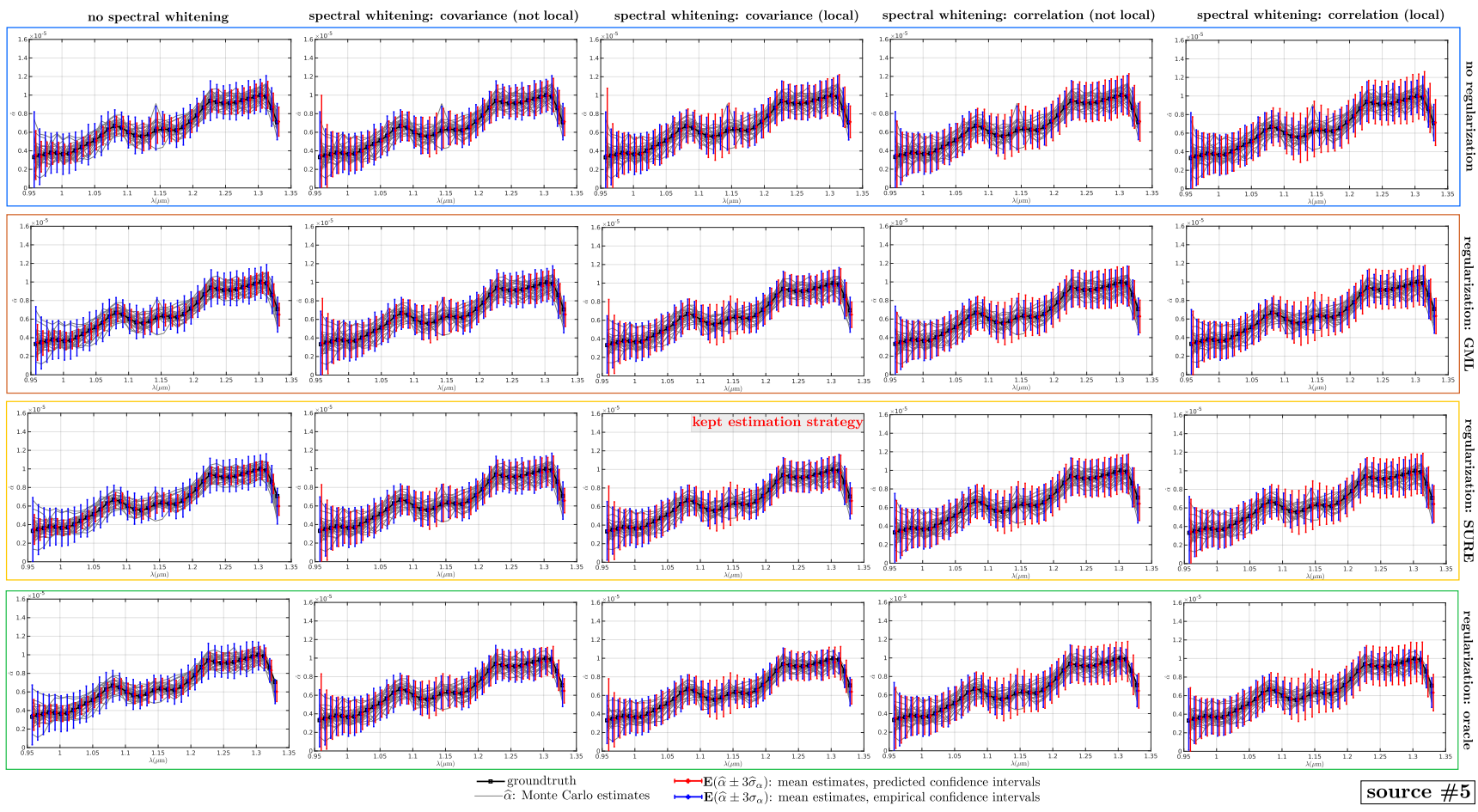


Figure B.3 – Same presentation than Figure B.2 for the source #5.

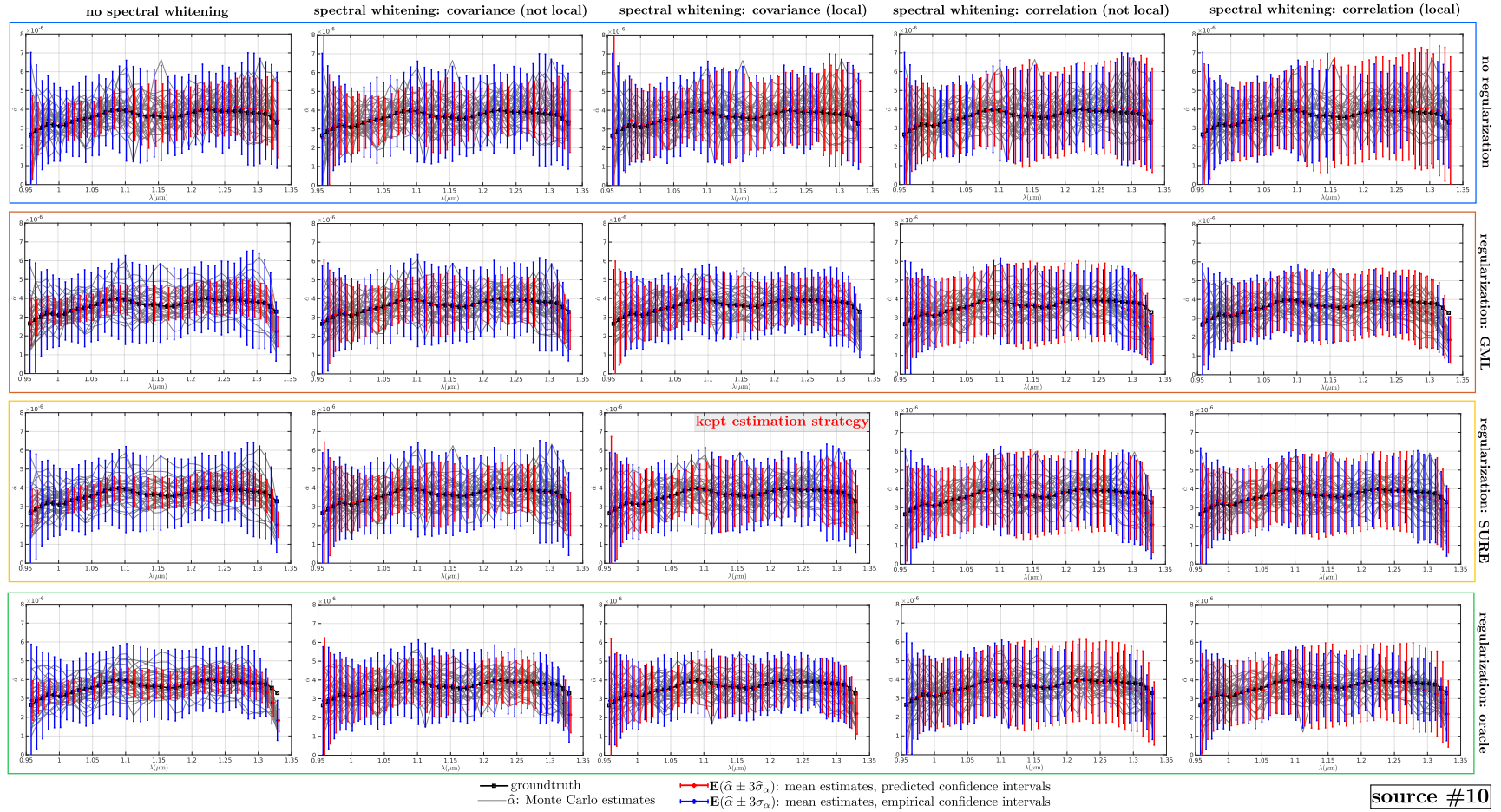


Figure B.4 – Same presentation than Figure B.2 for the source #10.



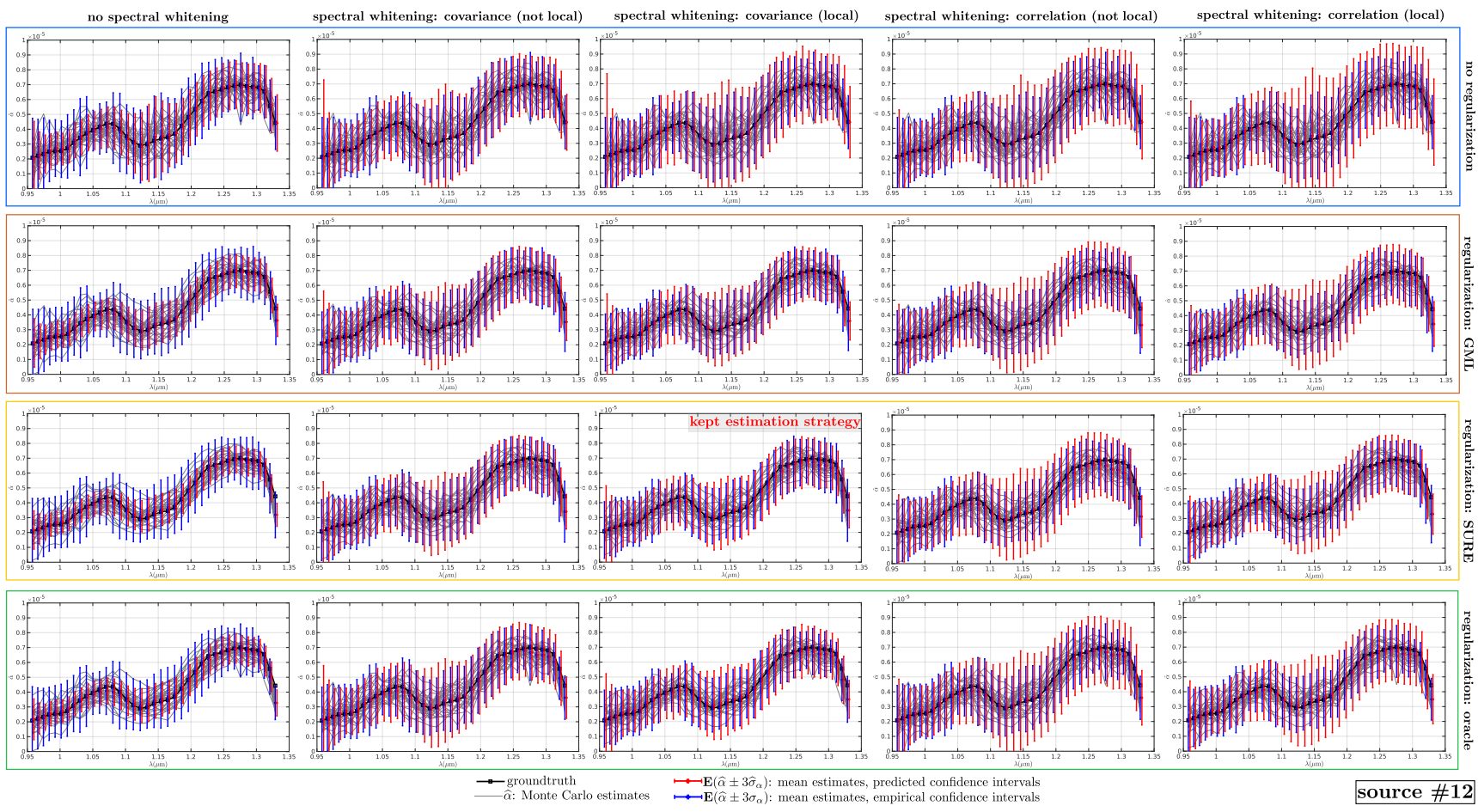


Figure B.5 – Same presentation than Figure B.2 for the source #12.

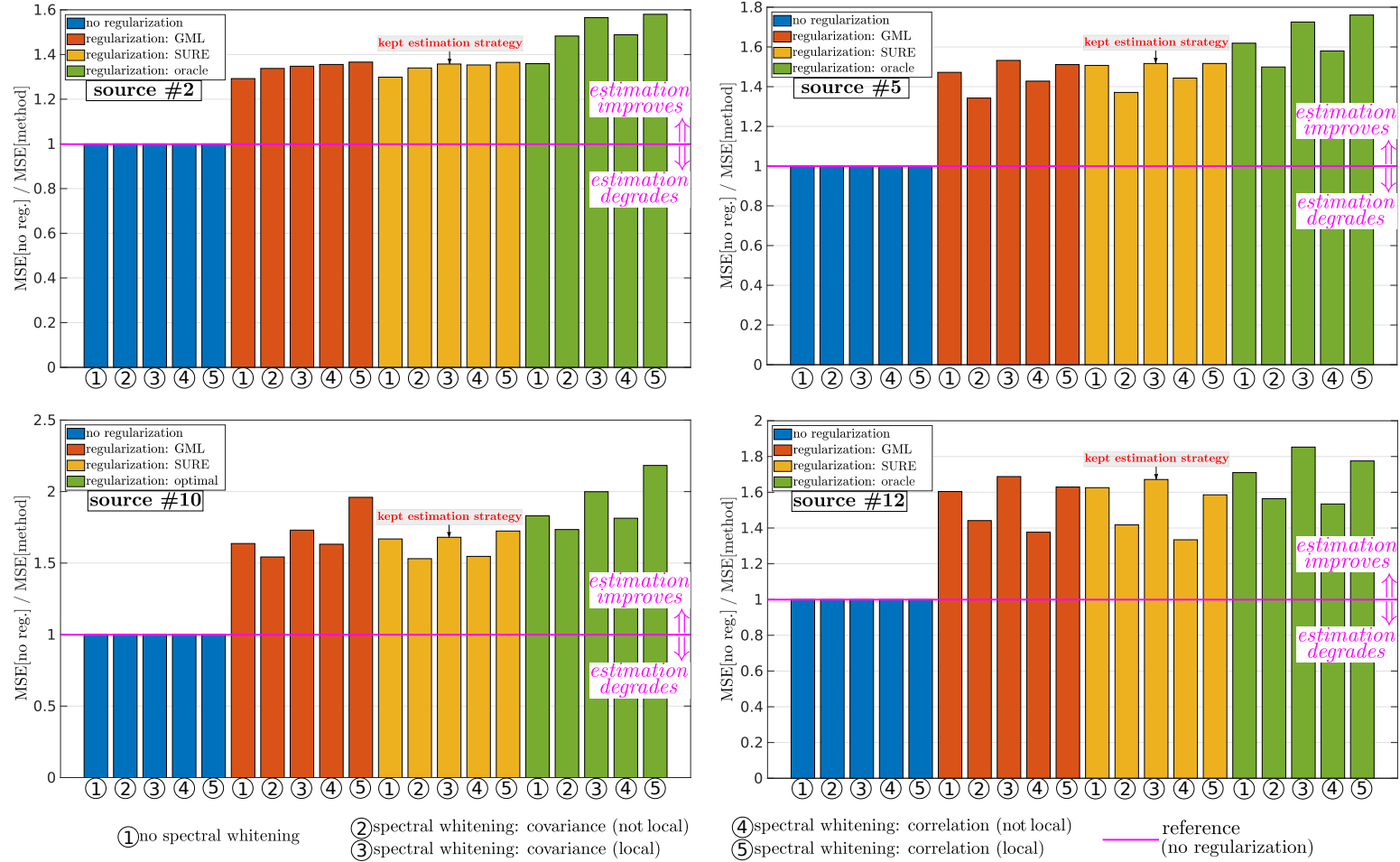


Figure B.6 – Comparison of the GCV, GML, and SURE regularization strategies on 30 Monte-Carlo injections / SED estimations for sources #2, #5, #10, and #12. The reported values are gain in terms of MSE reduction comparing with the absence of spectral regularization. Values higher than one indicate a decrease of the MSE.



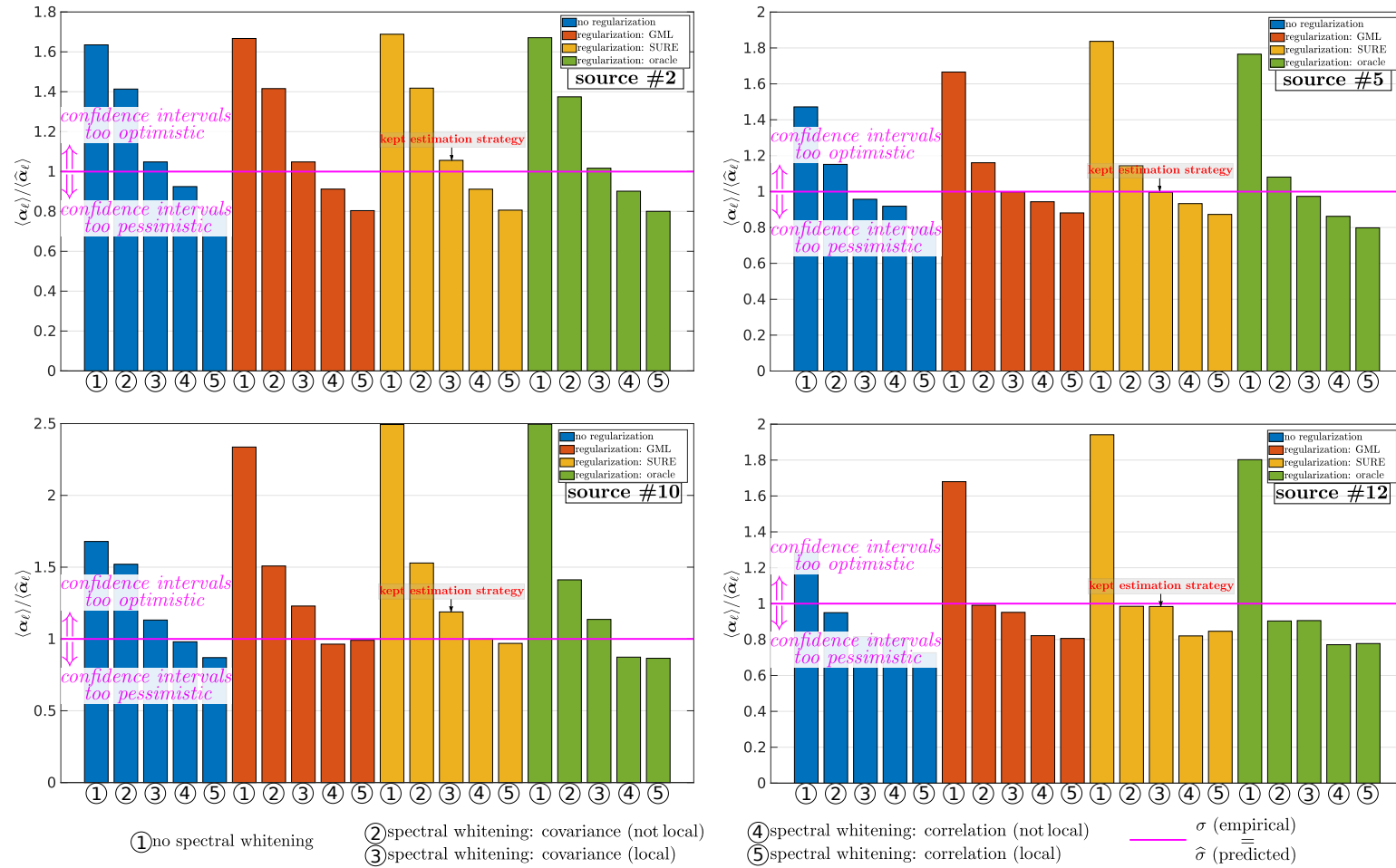


Figure B.7 – Comparison of the GCV, GML, and SURE regularization strategies on 30 Monte-Carlo injections / SED estimations for sources #2, #5, #10, and #12. The reported values are ratio between the  $1\sigma$  empirical and predicted (by the PACO-ASDI model) confidence intervals. Values higher than one indicate that predicted confidence intervals are smaller than the empirical ones so that the algorithm estimation is too optimistic.

# Modeling background fluctuations of ASDI datasets

In Section 6.2.1, we present the PACO-ASDI statistical modeling of the background. In the absence of source, we model each patch  $\mathbf{r}_{n,\ell,t}$  as a random realization of the  $K$ -dimensional Gaussian  $\mathcal{N}(\mathbf{m}_{n,\ell}, \sigma_{n,\ell,t}^2 \mathbf{C}_n)$ . At a given location, the mean patch  $\mathbf{m}_{n,\ell}$  is the same for all  $t$  but varies with the wavelength. The  $K \times K$  covariance matrix is modeled as a product of two factors: a time and wavelength-dependent scaling  $\sigma_{n,\ell,t}^2$  and a spatial covariance matrix  $\mathbf{C}_n$  that is constant for a given patch collection. Several variants of this modeling have been considered and tested, but they were not selected because they led to worse detection performances.

This appendix aims to give a quick summary of some alternative strategies that were considered. The mathematical development (such as estimators) are not reported here.

## C.1 Estimation of the means

We have compared temporal and spectral means. Besides, we have considered spectral means weighted by spectral factors common for the entire mean patches. We found that temporal means were better suited since the mean intensity varies more significantly along the spectral channels than temporal frames in ASDI datasets. While this result may seem surprising, the spectral variability may be due to the pre-reduction step producing the 4-D datasets used by detection algorithms (see Section 1.2.2.3). Typically, signals from the first and last channels of the IFS spectral band are generally badly interpolated, leading to a lower mean intensity. The use of additional spectral factors weighting each spectral mean was more satisfactory in this respect but did not completely solve the problem due to its poor ability to counterbalance short spatial range fluctuations (inside the typical patch size) of the mean intensity.

Figure C.1 compares the use of temporal means versus spectral means weighted by spectral scaling factors. The spectral means and the spectral scaling factors are estimated jointly by a truncated rank-one SVD of the collection of  $L$  spatio-temporal patches extracted at a given pixel  $n$  of the field of view. Figure C.1(a) gives examples of residual patches after mean subtraction for different times and wavelengths. It appears

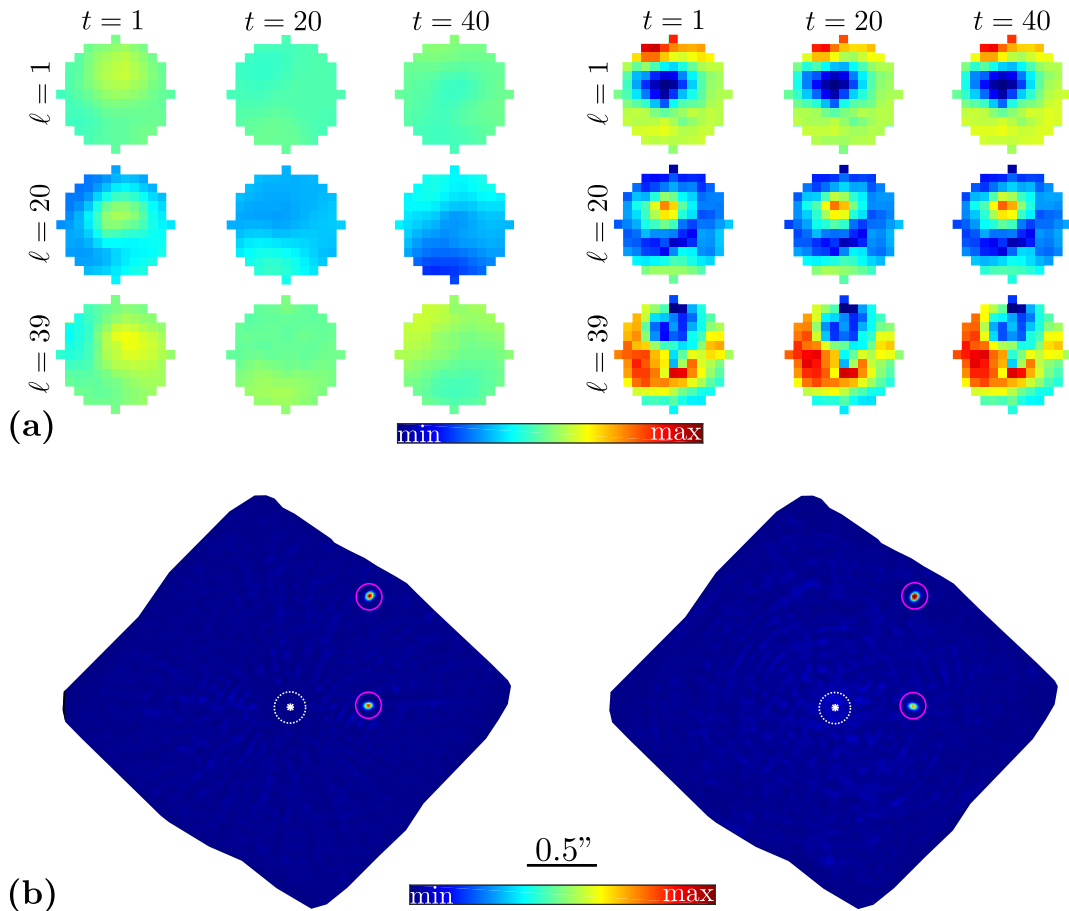


Figure C.1 – Comparison between the use of temporal and spectral means on the ASDI modeling of the background fluctuations. The dataset considered is centered on HR 8799. Only two exoplanets marked by magenta circles are expected to be detected since the third one falls outside of the field of view. (a) examples of residual patches after mean subtraction (left: temporal mean, right: spectral mean + spectral weights); (b) GLRT<sup>+</sup> maps (left: temporal mean, right: spectral mean + spectral weights).

that the mean residual intensity is lower when temporal means are used, as in our model described in Section 6.2.1. Finally, Figure C.1(b) illustrates GLRT<sup>+</sup> maps (the spectral correlations are not taken into account, see Equation (6.16)) computed by considering temporal or spectral means. While the mean level of the background structures is not significantly different in the two examples, we observe that the source throughput is lower (especially for the exoplanet closer to the host star) when a spectral mean is considered. For this reason, we defined our model of the background fluctuations based on a temporal mean per wavelength.

## C.2 Estimation of the scaling factors

We have tested several variants of the temporo-spectral GSM model (see Section 6.2.1). Among them, we considered weights that depend only on time or only on the spectral channel, but each of these two variants showed to be less adapted to our

problem. In particular, these two approaches failed to capture both the spectral and temporal outliers arising in ASDI datasets.

### C.3 Estimation of the covariances

As described in Section 6.2.1, instead of modeling the spectral correlations of ASDI datasets, we model and take into account the spectral correlations between  $S/N_\ell$  values. We have considered accounting for both the spatial and spectral correlations directly in our model of the background fluctuations. Hereafter, we briefly describe this resulting background modeling and discuss why we did not chose this approach.

Let  $\mathbf{f}_{n,t}^{\text{full}} = (-\mathbf{f}_{n,\ell_1,t} - \mathbf{f}_{n,\ell_2,t} - \dots - \mathbf{f}_{n,\ell_L,t})^\top$  be the vector obtained by concatenating the patches of background for all wavelengths, at a given pixel  $n$  of the field of view and at a given date  $t$ .

We suppose that  $\mathbf{f}_{n,t}^{\text{full}}$  is a realization of a Gaussian random vector of mean  $\mathbf{m}_n^{\text{full}} = (-\mathbf{m}_{n,\ell_1} - \mathbf{m}_{n,\ell_2} - \dots - \mathbf{m}_{n,\ell_L})^\top$  (i.e., a mean patch per wavelength) and of spatio-spectral covariance matrix  $\mathbf{C}_n^{\text{full}}$ . Since the dimension of the covariance matrix  $\mathbf{C}_n^{\text{full}}$  ( $K \cdot L$ ) is much greater than the number of available dates, we cannot estimate it directly (besides, it would be costly to manipulate).

Therefore, we assume that this matrix is structured and that it corresponds to a separable generative model:

$$\mathbf{C}_n^{\text{full}} = \mathbf{F}^{\text{full}} \mathbf{F}^{\text{full}\top}, \quad (\text{C.1})$$

with  $\mathbf{F}^{\text{full}}$  a linear and separable operator:

$$\mathbf{F}^{\text{full}} = \mathbf{F}_{\text{spectral}}^{\text{full}} \mathbf{F}_{\text{spatial}}^{\text{full}}, \quad (\text{C.2})$$

i.e., a random vector  $\mathbf{f}_{n,t}^{\text{full}}$  (multi-spectral collection of background patches) is obtained by the product  $\mathbf{F}^{\text{full}}\epsilon$  with  $\epsilon \sim \mathcal{N}(\mathbf{0}, \mathbf{I}_{K \cdot L})$  a white and Gaussian noise. Matrices  $\mathbf{F}_{\text{spectral}}^{\text{full}}$  and  $\mathbf{F}_{\text{spatial}}^{\text{full}}$  can be estimated alternatively by a fixed-point method.

Figure C.2 compares GLRT<sup>+</sup> maps obtained when spatial or spatio-spectral (under the separable model described above) are considered. It shows that some periodic background structures are attenuated when the spatio-spectral correlations of the data are accounted for. However, other artifacts appear and the source throughputs are weaker and noisier. Several elements may explain these observations. On the one hand, including a modeling of the spatio-spectral correlations gives a finer description of the observed background fluctuations of the ASDI data. In particular, the spectral correlations are accounted for. On the other hand, we face the difficulty to estimate these correlations accurately with the limited number of samples. Besides, another issue should be considered: these preliminary experiments do not include spectral or temporal weighting factors as the ones provided by a GSM model (since we investigated this methodological framework later in the thesis). Then, the numerous outliers arising in ASDI data are not taken into account. The resulting estimated parameters may be biased by this lack of modeling. From our point of view, it would be interesting to investigate the combination of a spatio-spectral modeling of the background with temporal plus spectral weights as in our GSM model (see Section 6.2.1). The different

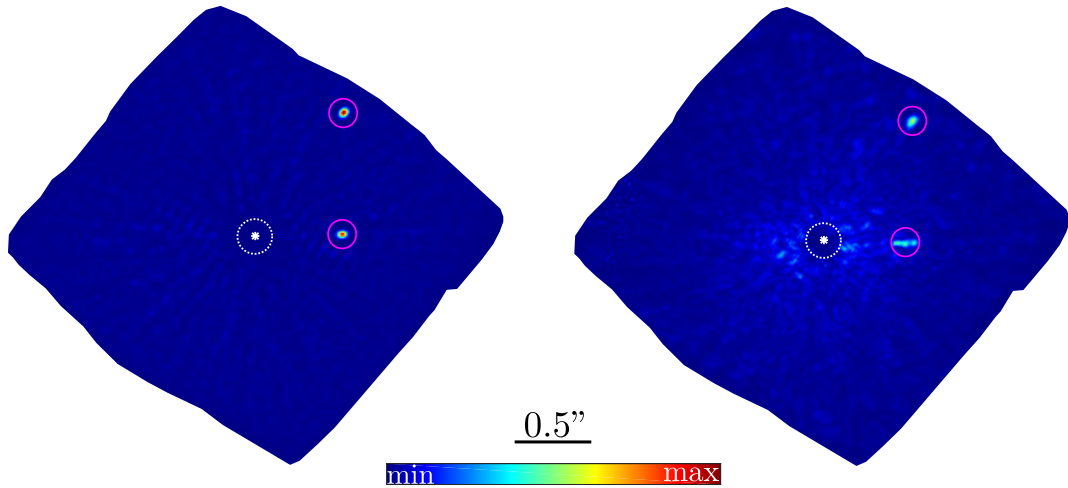


Figure C.2 – Comparison of  $\text{GLRT}^+$  maps obtained by modeling the spatial (left) and spatio-spectral (right) correlations of ASDI data. The dataset considered is centered on HR 8799. Only two exoplanets marked by magenta circles are expected to be detected since the third one falls outside of the field of view.

parameters (the temporal mean  $\mathbf{m}_{n,\ell}$ , the two terms of the spatio-spectral separable covariance  $\mathbf{C}_n^{\text{full}}$ , and the temporo-spectral weighting factors  $\sigma_{n,\ell,t}^2$ ) could be estimated alternatively by a fixed-point method.

## Example of an automatic report generated by PACO

In this appendix, we illustrate the automatic report generation of the PACO pipeline. The selected example summarizes the main results obtained from the processing of a dataset of HD 95086 hosting several point sources including one exoplanet (HD 95086 b) orbiting at about 0.62 arcsec from its host star, see Section 4.4. The following pages give excerpts of the resulting report and we refer to the page number indicated in the top right corners for the description. The information of the *reduction*, *detection*, and *characterization* steps are organized as follows:

- *reduction* step
  - Pages 1 and 2 give information about the processed dataset and the selected processing options.
  - Page 3 gives the S/N detection map, and page 4 is the (biased) flux map.
  - Pages 19 and 21 give the achievable  $5\sigma$  contrast.
  - Pages 22 and 24 give respectively the photometry and astrometry accuracy maps.
- *detection* step
  - Page 35 summarizes the main notation used throughout the following pages of the report.
  - Page 36 identifies the sources of interest; the typically very bright and/or spatially extended sources are flagged as of poor interest (as groups !G3 and !G4) since they are generally background stars. By default, these sources are not characterized during the *characterization* step to limit the computation time.
  - Page 40 gives a close-up view of the selected detections of interest.
  - For each detection, a table summarizing the main roughly estimated quantities is built. Page 43 is an example of such table for the source #1 appearing in page 36. These quantities should be refined by the characterization step.



- 
- Page 54 gives a view of the sources identified as of poor interest (typically too bright or spatially extended). The user can overrule the automatic classification of the pipeline by enforcing the characterization of such sources.
  - *characterization* step
    - Pages 88 and 89 summarize the main notation used throughout the following pages of the report.
    - Page 95 presents a view of the refined (subpixel and unbiased) quantities characterizing the source #1. The results are given on small patches around the source of interest, with four nodes per pixel in this example.
    - Page 109 gives a table summarizing the refined (subpixel and unbiased) quantities characterizing the source #1.
    - Page 116 gives a view of the trajectory of the characterized sources in the processed ADI dataset.
    - Page 118 shows the residual S/N map obtained after subtraction of the estimated contribution of the characterized sources in the ADI dataset (application of a *CLEAN* approach, see Section 2.4.6).
    - Finally, page 122 is a composite image in which the computed (expected) signature of the characterized sources are re-injected at an unbiased level of S/N on the residual S/N map. This purely qualitative map can be useful for a quick visualization of the results.

Automatically generated report by PACO, 20/05/2019.

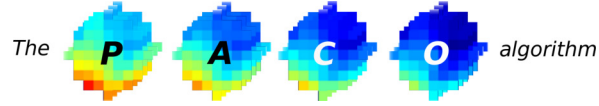


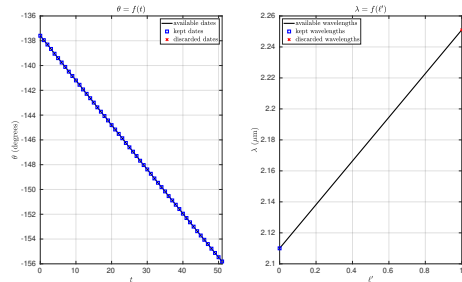
**Table of contents:**

1	GENERAL INFORMATION . . . . .	1
1.1	Dataset and algorithm information . . . . .	1
1.2	Links color chart . . . . .	1
2	ADI-REDUCTION . . . . .	3
2.1	ADI-reduction at $\lambda_{00} = 2.1100\mu\text{m}$ . . . . .	4
3	ADI-DETECTION . . . . .	36
3.1	ADI-detection at $\lambda_{00} = 2.1100\mu\text{m}$ . . . . .	37
4	ADI-CHARACTERIZATION . . . . .	89
4.1	ADI-characterization at $\lambda_{00} = 2.1100\mu\text{m}$ . . . . .	91

**1 GENERAL INFORMATION**

**1.1 Dataset and algorithm information**

Figure 1 summarizes information about the number of available dates ( $T_{\text{available}}$ ) & wavelengths ( $L_{\text{available}}$ ) and the number of used dates ( $T$ ) & wavelengths ( $L$ ). The used dates and wavelengths are specified by the user within the respective input fields `selected_frames` and `processed_channel_indexes` (all dates and wavelengths are used by default if they are not filled).



[preview file: ../HIP\\_53524\\_od20150505\\_0151326746\\_paco\\_outputs/5\\_info\\_paco/adi\\_results/HIP\\_53524\\_fast\\_paco1\\_dates\\_wavelengths\\_od20150505\\_0151326746\\_cd200519\\_143456.pdf](#)

Figure 1: Available vs kept dates and wavelengths.

Table 1 gives general information about the dataset and the used algorithm schemes.

Table 1: General information about the dataset and the processing algorithms.

Fields	Values
<b>CUBE NAME &amp; DATES</b>	
cube name	HIP 53524
observation date	2015/05/05
processing date	2019/05/20
report date	2019/05/20
<b>INSTRUMENT</b>	
instrument name	SPHERE/IRDIS
direction of rotation	positive
effective (corrected) pixel size in arcsec	0.012212
<b>DATASET</b>	
$R$ : number of rows in images	1024
$C$ : number of columns in images	1024
$R_{\text{expanded}}$ : number of rows in expanded images	1448
$C_{\text{expanded}}$ : number of columns in expanded images	1448
$T_{\text{available}}$ : number of available temporal frames	52
$T$ : number of kept temporal frames	52
$L_{\text{available}}$ : number of available wavelengths	2
$L$ : number of kept wavelengths	1
<b>USED PACO SCHEMES</b>	
ADI-reduction	fast-PACO1
ADI-reduction Monte-Carlo contrast	PACO1
ADI-detection	PACO1
ADI-characterization	alt-PACO1
ASDI-reduction	<i>was not processed</i>
ASDI-detection	<i>was not processed</i>
ASDI-characterization	<i>was not processed</i>

**1.2 Links color chart**

Table 2 gives the color chart of the links displayed below figures or tables according to their type. The links return to the corresponding files saved in the main results folder.

Table 2: Color chart for the links to source files, preview files and user files.

File types	Colors
source files	<span style="color: red;">.fits</span> or <span style="color: magenta;">.fits</span> (when several source files for the same item)
preview files	<span style="color: blue;">.pdf</span> or <span style="color: cyan;">.pdf</span> (when several preview files for the same item)
user files	<span style="color: green;">.txt</span> or <span style="color: lime;">.txt</span> (when several user files for the same item)

**Remark:**  $\triangle$  only the source files (in fits format) should be used for the final interpretation of the results since the preview files are compressed so that the detection blobs are usually distorted.

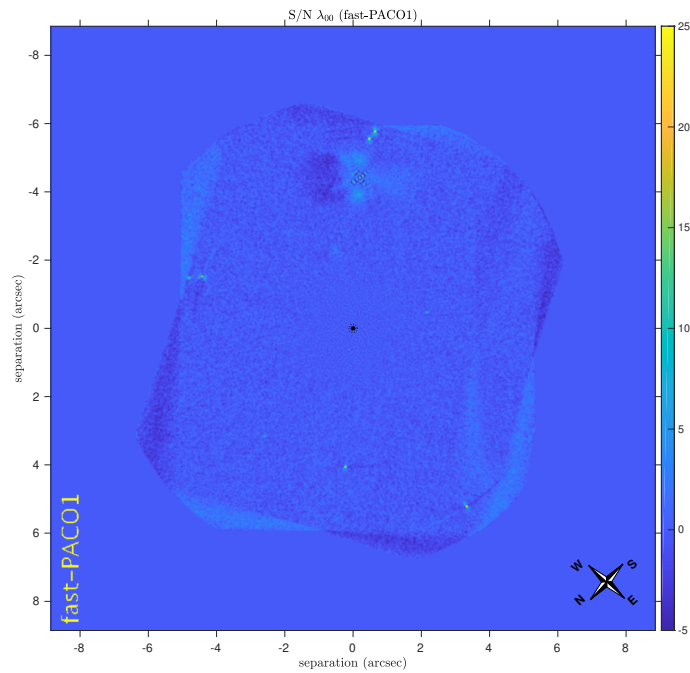
**2 ADI-REDUCTION**

The ADI-reduction step was performed with the **fast-PACO1** algorithm. We recall that the available algorithms for the ADI-reduction step were fast-PACO1, PACO1, fast-PACO1+Temp.Rob. and PACO1+Temp.Rob.. Monte Carlo contrast curve was computed with the **PACO1** algorithm. We recall that the available algorithms for the computation of a Monte Carlo contrast curve during the ADI-reduction step were PACO1 and PACO1+Temp.Rob..

## 2.1 ADI-reduction at $\lambda_{00} = 2.1100\mu\text{m}$

### 2.1.1 Signal-to-noise ratio

- Mathematical notation: SNR.
- Filename notation: snr.
- Description: signal-to-noise ratio.
- Properties: statistically-grounded (i.e can be thresholded at a controlled PFA). Suboptimal (i.e biased in presence of a source) during the ADI-reduction step.

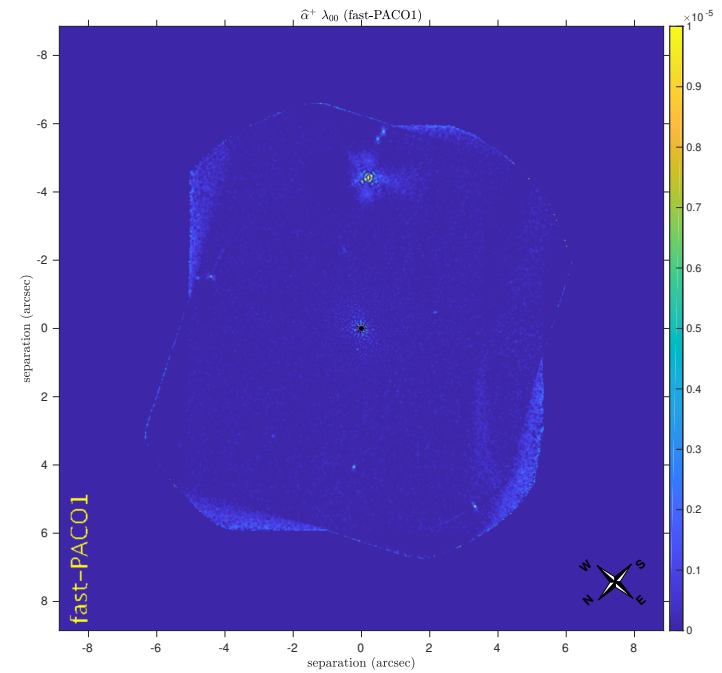


source file: [.../HIP\\_53524\\_od20150505\\_0151326746\\_paco\\_outputs/1\\_reduction\\_paco/adi\\_results/lam00/snr/HIP\\_53524\\_fast\\_paco1\\_snr\\_lam00\\_od20150505\\_0151326746\\_cd200519\\_143456.fits](http://.../HIP_53524_od20150505_0151326746_paco_outputs/1_reduction_paco/adi_results/lam00/snr/HIP_53524_fast_paco1_snr_lam00_od20150505_0151326746_cd200519_143456.fits)  
 preview file: [.../HIP\\_53524\\_od20150505\\_0151326746\\_paco\\_outputs/1\\_reduction\\_paco/adi\\_results/lam00/snr/HIP\\_53524\\_fast\\_paco1\\_snr\\_lam00\\_od20150505\\_0151326746\\_cd200519\\_143456\\_preview\\_compressed.pdf](http://.../HIP_53524_od20150505_0151326746_paco_outputs/1_reduction_paco/adi_results/lam00/snr/HIP_53524_fast_paco1_snr_lam00_od20150505_0151326746_cd200519_143456_preview_compressed.pdf)

Figure 2: SNR map at  $\lambda_{00} = 2.1100\mu\text{m}$  (default field of view alignment).

### 2.1.4 Constrained flux

- Mathematical notation:  $\alpha^+$ .
- Filename notation: alpha.
- Description: constrained (positive) flux.
- Properties: suboptimal (i.e biased in presence of a source) during the ADI-reduction step.

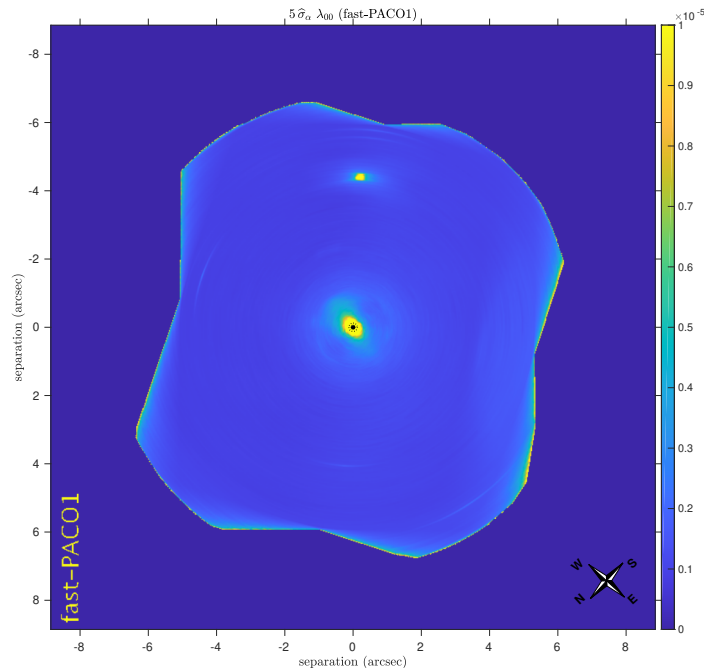


source file: [.../HIP\\_53524\\_od20150505\\_0151326746\\_paco\\_outputs/1\\_reduction\\_paco/adi\\_results/lam00/alpha/HIP\\_53524\\_fast\\_paco1\\_alpha\\_lam00\\_od20150505\\_0151326746\\_cd200519\\_143456.fits](http://.../HIP_53524_od20150505_0151326746_paco_outputs/1_reduction_paco/adi_results/lam00/alpha/HIP_53524_fast_paco1_alpha_lam00_od20150505_0151326746_cd200519_143456.fits)  
 preview file: [.../HIP\\_53524\\_od20150505\\_0151326746\\_paco\\_outputs/1\\_reduction\\_paco/adi\\_results/lam00/alpha/HIP\\_53524\\_fast\\_paco1\\_alpha\\_lam00\\_od20150505\\_0151326746\\_cd200519\\_143456\\_preview\\_compressed.pdf](http://.../HIP_53524_od20150505_0151326746_paco_outputs/1_reduction_paco/adi_results/lam00/alpha/HIP_53524_fast_paco1_alpha_lam00_od20150505_0151326746_cd200519_143456_preview_compressed.pdf)

Figure 8:  $\alpha^+$  map at  $\lambda_{00} = 2.1100\mu\text{m}$  (default field of view alignment).

### 2.1.9 Oracle contrast at $5\sigma_\alpha$

- **Mathematical notation:**  $5\sigma_\alpha$ .
- **Filename notation:** local\_5sigma\_oracle\_contrast.
- **Description:** oracle contrast at  $5\sigma_\alpha$ . Even if this value can be biased (very slightly overoptimist) due to potential source(s) disturbing the estimation of the background statistics, this quantity is a good approximation of the real achievable contrast. Moreover, is the temporal robustness is applied, the difference between this quantity and the real achievable contrast is very weak (even near the host star).
- **Properties:** statistically-grounded. Suboptimal (i.e biased in presence of a source) during the ADI-reduction step.

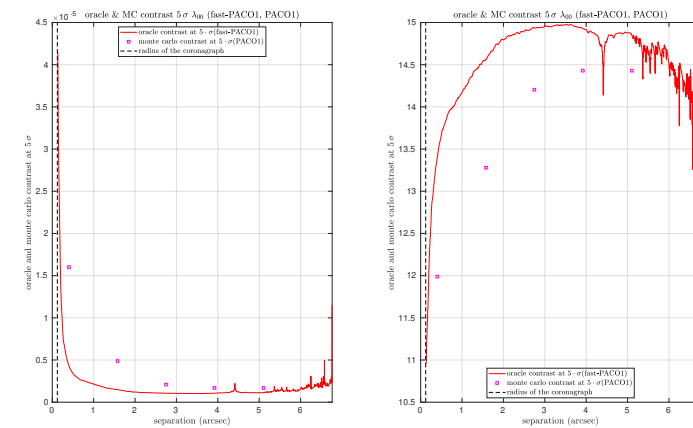


**source file:**  
`../../../../HIP_53524_od20150505_0151326746_paco_outputs/1_reduction_paco/adi_results/lam00/local_5sigma_oracle_contrast/HIP_53524_fast_paco1_local_5sigma_oracle_contrast_lam00_od20150505_0151326746_cd200519_143456.fits`  
**preview file:** `../../../../HIP_53524_od20150505_0151326746_paco_outputs/1_reduction_paco/adi_results/lam00/local_5sigma_oracle_contrast/HIP_53524_fast_paco1_local_5sigma_oracle_contrast_lam00_od20150505_0151326746_cd200519_143456_preview_compressed.pdf`

Figure 18:  $5\sigma_\alpha$  map at  $\lambda_{00} = 2.1100\mu\text{m}$  (default field of view alignment).

### 2.1.10 Oracle and Monte-Carlo contrast curves at $5\sigma_\alpha$

- **Mathematical notation:** curve- $5\sigma_\alpha$ -oracle and curve- $5\sigma_\alpha$ -monte-carlo.
- **Filename notation:** curve\_5sigma\_oracle\_contrast and curve\_5sigma\_monte\_carlo\_contrast.
- **Description:** oracle and Monte-Carlo contrast curves at  $5\sigma_\alpha$ . Even if the oracle contrast can be biased (slightly overoptimist) due to potential source(s) disturbing the estimation of the background statistics, the oracle contrast is a good approximation of the Monte-Carlo (really achievable) contrast. Moreover, is the temporal robustness is applied, the difference between the oracle and the Monte-Carlo contrast is further reduced (even near the host star). The Monte-Carlo contrast curve was also computed and it is superimposed to the oracle contrast curve.
- **Properties:** statistically-grounded. The temporal robustness scheme WAS NOT applied.

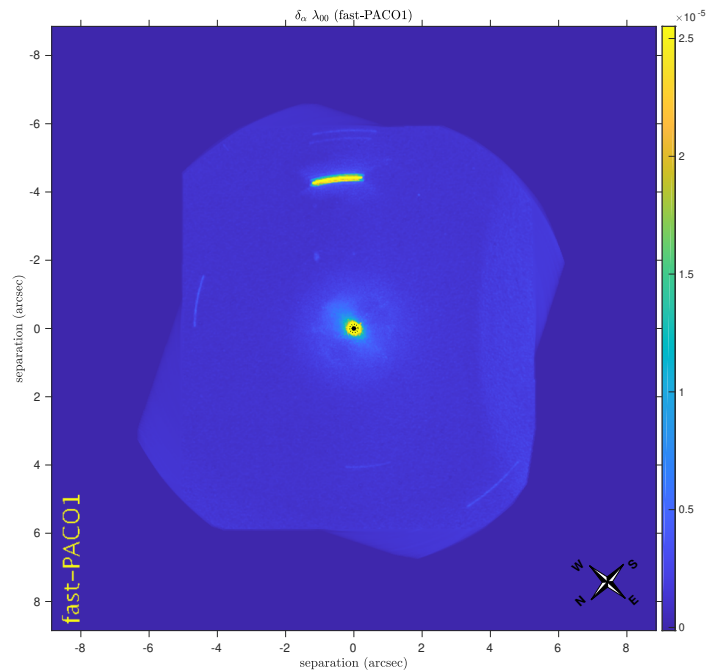


**source oracle file:**  
`../../../../HIP_53524_od20150505_0151326746_paco_outputs/1_reduction_paco/adi_results/lam00/curve_5sigma_oracle_contrast/HIP_53524_fast_paco1_curve_5sigma_oracle_contrast_lam00_od20150505_0151326746_cd200519_143456.fits`  
**source Monte-Carlo file:** `../../../../HIP_53524_od20150505_0151326746_paco_outputs/1_reduction_paco/adi_results/lam00/curve_5sigma_monte_carlo_contrast/HIP_53524_fast_paco1_curve_5sigma_monte_carlo_contrast_lam00_od20150505_0151326746_cd200519_143456.fits`  
**preview file:** `../../../../HIP_53524_od20150505_0151326746_paco_outputs/1_reduction_paco/adi_results/lam00/curve_5sigma_monte_carlo_contrast/HIP_53524_fast_paco1_curve_5sigma_monte_carlo_contrast_lam00_od20150505_0151326746_cd200519_143456_preview_compressed.pdf`

Figure 20: curve- $5\sigma_\alpha$ -oracle and curve- $5\sigma_\alpha$ -monte-carlo at  $\lambda_{00} = 2.1100\mu\text{m}$ .

### 2.1.11 Cramér-Rao lower bound on $\alpha$

- **Mathematical notation:**  $\delta_\alpha$ .
- **Filename notation:** crlb\_alpha.
- **Description:** Cramér-Rao lower bound (CRLB) on the flux giving a lower theoretical bound of the standard-deviation of estimation on the estimated flux. This quantity is expressed in contrast unit.
- **Properties:** statistically-grounded. Suboptimal (i.e biased in presence of a source) during the ADI-reduction step.

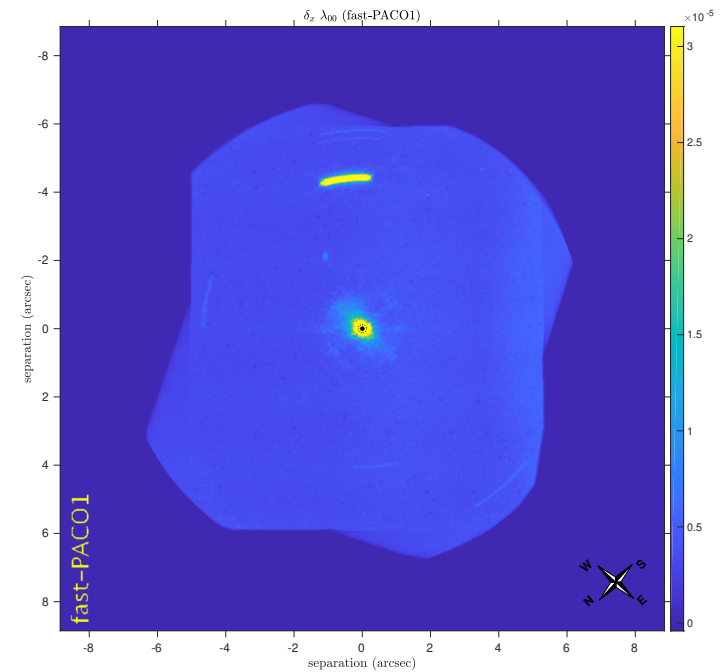


[source file: ../../HIP\\_53524\\_od20150505\\_0151326746\\_paco\\_outputs/1\\_reduction\\_paco/adi\\_results/lam00/crlb\\_alpha/HIP\\_53524\\_fast\\_paco1\\_crlb\\_alpha\\_lam00\\_od20150505\\_0151326746\\_cd200519\\_143456.fits](#)  
[preview file: ../../HIP\\_53524\\_od20150505\\_0151326746\\_paco\\_outputs/1\\_reduction\\_paco/adi\\_results/lam00/crlb\\_alpha/HIP\\_53524\\_fast\\_paco1\\_crlb\\_alpha\\_lam00\\_od20150505\\_0151326746\\_cd200519\\_143456\\_preview\\_compressed.pdf](#)

Figure 21:  $\delta_\alpha$  map at  $\lambda_0 = 2.1100\mu\text{m}$  (default field of view alignment).

### 2.1.12 Cramér-Rao lower bound on the $x$ -location

- **Mathematical notation:**  $\delta_x$ .
- **Filename notation:** crlb\_x.
- **Description:** Cramér-Rao lower bound (CRLB) on the  $x$ -location giving a lower theoretical bound of the standard-deviation of estimation on the estimated  $x$ -location.  $\delta_x$  depends on the source flux: the higher the source flux the lower the Cramér-Rao on the  $x$ -location is (i.e the lower the standard-deviation of estimation on the  $x$ -location is). Here, this quantity is expressed in pixel  $\times$  contrast, so that, at a given location,  $\delta_x$  should be divided by the expected contrast to fall into pixel unit.
- **Properties:** statistically-grounded. Suboptimal (i.e biased in presence of a source) during the ADI-reduction step.



[source file: ../../HIP\\_53524\\_od20150505\\_0151326746\\_paco\\_outputs/1\\_reduction\\_paco/adi\\_results/lam00/crlb\\_x/HIP\\_53524\\_fast\\_paco1\\_crlb\\_x\\_lam00\\_od20150505\\_0151326746\\_cd200519\\_143456.fits](#)  
[preview file: ../../HIP\\_53524\\_od20150505\\_0151326746\\_paco\\_outputs/1\\_reduction\\_paco/adi\\_results/lam00/crlb\\_x/HIP\\_53524\\_fast\\_paco1\\_crlb\\_x\\_lam00\\_od20150505\\_0151326746\\_cd200519\\_143456\\_preview\\_compressed.pdf](#)

Figure 23:  $\delta_x$  map at  $\lambda_0 = 2.1100\mu\text{m}$  (default field of view alignment).

### 3 ADI-DETECTION

The ADI-detection step was performed with the **PACO1** algorithm. We recall that the available algorithms for the ADI-detection step were PACO1 and PACO1+Temp.Rob.. The table 3 gives the *ad hoc* parameters used during the ADI-detection step. We recall that these parameters have NO influence on the PACO method. They just control *ad hoc* rules avoiding to characterize sources of poor interest (such as very bright sources). The input `detection_threshold` stands for the value  $\tau$  used to threshold the statistically grounded SNR map at a controlled probability of false alarms. The input `detection_borders_min_corr_coeff` controls the discarding rule of detections very close to the borders of the field of view (for which the number of temporal frames can be significantly lower than  $T$  due to the field of view rotation). A detection close to the borders of the field of view is kept if the normalized correlation coefficient  $c$  between the expected pattern of detection and the observed pattern is higher than the value pointed by the field `detection_borders_min_corr_coeff`. The input `detection_proximity_pixels` controls the size in pixels of the detected conglomerates (corresponding to very bright sources) for which the program proposes the user not to characterize them during the ADI-characterization step. The input `report_sigma_photo_astro_intervals` gives the degree of confidence on the astrometry and photometry. The astrometry is expressed as  $\{x, y\}$ -location-(aligned)  $\pm k\delta_{\{x,y\}}$  and the photometry by  $\alpha^+ \pm k\sigma_\alpha$  where  $\sigma_\alpha$  is the oracle standard-deviation on the flux and  $\delta_{\{x,y\}}$  are the CRLBs on the photometry.  $k$  is the factor indicated by the input `report_sigma_photo_astro_intervals` (it is generally common to use  $k = 1, 2$  or  $3$ ).

Table 3: *Ad hoc* parameters used during the ADI-detection step.

Inputs name	Values
<code>detection_threshold</code>	5
<code>detection_proximity_pixels</code>	10
<code>detection_borders_min_corr_coeff</code>	0.8
<code>report_sigma_photo_astro_intervals</code>	1

We recall that the ADI-detection procedure attributes flags to certain detections according to their degree of interest. The considered flags are:

- `flag_warning_high_density` set to 1 for spread detections (e.g very bright sources).
- `flag_warning_single_pixel` set to 1 when a detection is made of only one pixel above the detection threshold (can arise on the borders of the field of view is the instrument mask does not take into account correctly the aberrant data).
- `flag_warning_proximity_between_detections` set to 1 in case of multiple detections around the same object (e.g. near a bright source). In this case, they are grouped in a unique entity.
- `flag_warning_near_fov_borders` set to 1 in case of proximity with the initial field of view (as defined by the  $W_{bw\_expanded}$  binary mask).
- `flag_warning_near_extended_fov_borders` set to 1 in case of proximity with the field of view of interest taking into account the rotation along time (as defined by the  $W_{bw\_expanded\_rotation}$  binary mask).

In order to prepare the ADI-characterization step and avoid useless characterizations, the ADI-detection step classifies detections in 3 groups: "standard detections", "grouped detections" and "ill-fitted detections". We recall hereafter the *ad hoc* rules used for this classification:

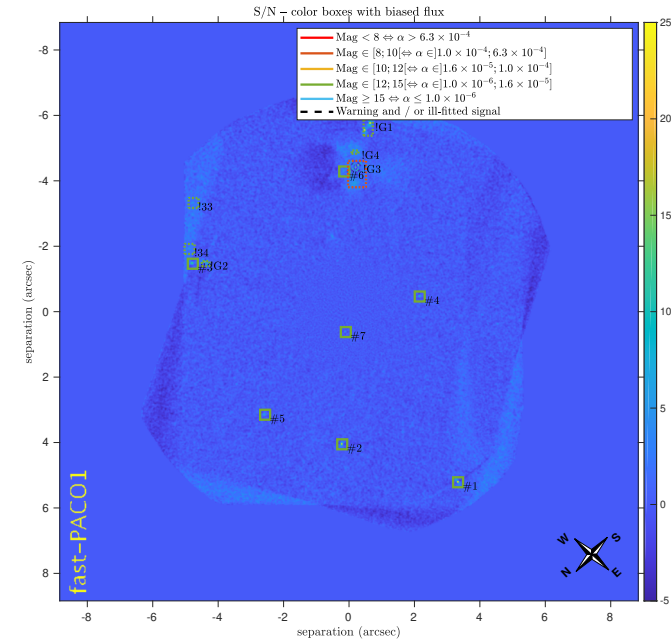
- *standard detections* (symbol "#xx"): (all flags set to 0) *or* (`flag_warning_near_fov_borders=1` & `pattern_correlation_coefficient`  $\geq$  `detection_borders_min_corr_coeff`) *or* (`flag_warning_near_extended_fov_borders=1` & `pattern_correlation_coefficient`  $\geq$  `detection_borders_min_corr_coeff`).
- *grouped detections* (symbol "!xx member of group !Gxx"): `flag_warning_proximity_between_detections=1`.
- *ill-fitted detections* (symbol "!xx"): any other combinations of flags.

By default, only the standard detections are characterized (`flag_characterization` set to 1), but the user can change the status of a detection or add manually additional sources (below the detection threshold) in the text `detection_file` to be characterized.

### 3.1 ADI-detection at $\lambda_{00} = 2.1100\mu\text{m}$

#### 3.1.1 Detection annotated signal-to-noise ratio

- **Mathematical notation:** detection-annoted-SNR.
- **Filename notation:** `detection_snr_full_map`.
- **Description:** signal-to-noise ratio from the ADI-reduction step annotated with the ADI-detection information. The color of the squares encodes for the (biased) estimate of the flux derived from the ADI-reduction step.
- **Properties:** statistically-grounded (i.e can be thresholded at a controlled PFA). Suboptimal (i.e biased in presence of a source) during the ADI-detection step.



source file: [./././HIP\\_53524\\_od20150505\\_0151326746\\_paco\\_outputs/1\\_reduction\\_paco/adi\\_results/lam00/snr/HIP\\_53524\\_fast\\_paco1\\_snr\\_lam00\\_od20150505\\_0151326746\\_cd200519\\_143456.fits](#)  
 preview file: [./././HIP\\_53524\\_od20150505\\_0151326746\\_paco\\_outputs/2\\_detection\\_paco/adi\\_results/lam00/detection\\_full\\_map/HIP\\_53524\\_fast\\_paco1\\_detection\\_snr\\_full\\_map\\_lam00\\_od20150505\\_0151326746\\_cd200519\\_143456.pdf](#)

Figure 33: detection-annoted-SNR map at  $\lambda_{00} = 2.1100\mu\text{m}$  (default field of view alignment).



### 3.1.3 Detection: zoom on standard detections

- **Mathematical notation:** zoomed-standard-detections-SNR.
- **Filename notation:** detection\_snr\_zoom\_detections.
- **Description:** zoom on the SNR of the ADI-reduction step around the detections classified as *standard* detections by the ADI-detection step. The color of the squares encodes for the (biased) estimate of the flux derived from the ADI-reduction step.
- **Properties:** statistically-grounded (i.e can be thresholded at a controlled PFA). Suboptimal (i.e biased in presence of a source) during the ADI-detection step.

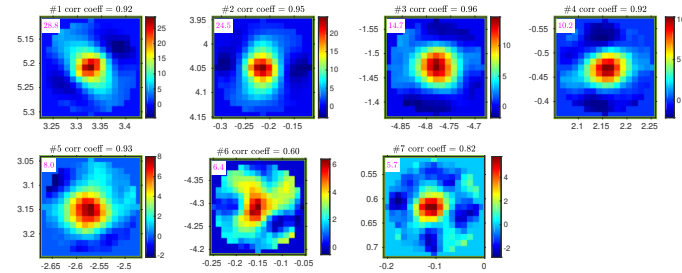


Figure 37: zoomed-standard-detections-SNR: detections #1, #2, #3, #4, #5, #6 and #7 at  $\lambda_0 = 2.1100\mu\text{m}$  (default field of view alignment).

```

preview file: ../../HIP_53524_od20150505_0151326746_paco_outputs/2_detection_paco/adi_results/lam00/detection_snr_zoom_detections/HIP_53524_fast_paco1_detection_snr_zoom_detections_index_1_to_7_lam00_od20150505_0151326746_cd200519_143456.pdf
source files for detection #1:
(source file: SNR patch)
../../HIP_53524_od20150505_0151326746_paco_outputs/2_detection_paco/adi_results/lam00/detection_snr_patch_and_expected_pattern/HIP_53524_fast_paco1_snr_patch_file_index_1_lam00_od20150505_0151326746_cd200519_143456.fits
(source file: expected pattern patch) ../../HIP_53524_od20150505_0151326746_paco_outputs/2_detection_paco/adi_results/lam00/detection_snr_patch_and_expected_pattern/HIP_53524_fast_paco1_expected_pattern_file_index_1_lam00_od20150505_0151326746_cd200519_143456.fits
source files for detection #2:
(source file: SNR patch)
../../HIP_53524_od20150505_0151326746_paco_outputs/2_detection_paco/adi_results/lam00/detection_snr_patch_and_expected_pattern/HIP_53524_fast_paco1_snr_patch_file_index_2_lam00_od20150505_0151326746_cd200519_143456.fits
(source file: expected pattern patch) ../../HIP_53524_od20150505_0151326746_paco_outputs/2_detection_paco/adi_results/lam00/detection_snr_patch_and_expected_pattern/HIP_53524_fast_paco1_expected_pattern_file_index_2_lam00_od20150505_0151326746_cd200519_143456.fits

```

Table 4: ADI-detection: information about the standard detection #1.

Fields	Notation	Ind.fits	Ind.txt	Values
<b>IDENTIFICATION</b>				
index	$i$	[1]	(1),[1]	#1
group	$g$	[2]	(2),[2]	-
flag_characterization	F-c	[3]	(3)	1
<b>ASTROMETRY (PIXELS)</b>				
x-location (pixels)	x-location (pix)	[4]	(4)	1151±0.38
y-location (pixels)	y-location (pix)	[5]	(5)	997±0.35
x-location_aligned (pixels)	x-loc.-aligned (pix)	[6]	(6)	593±0.38
y-location_aligned (pixels)	y-loc.-aligned (pix)	[7]	(7)	236±0.35
<b>ASTROMETRY (ARCSECONDS)</b>				
x-location (arcseconds)	x-location (as)	[8]	(8)	5.2084±0.0047
y-location (arcseconds)	y-location (as)	[9]	(9)	3.3278±0.0043
rho-location (arcseconds)	$\rho$ -location (as)	[10]	(10)	6.1808±0.0043
theta-location (degrees)	$\theta$ -location (deg)	[11]	(11)	327.42±0.04
x-location_aligned (arcseconds)	x-loc.-aligned (as)	[12]	(12)	-1.6059±0.0047
y-location_aligned (arcseconds)	y-loc.-aligned (as)	[13]	(13)	-5.9656±0.0043
rho-location_aligned (arcseconds)	$\rho$ -loc.-aligned (as)	[14]	(14)	6.1779±0.0043
theta-location_aligned (degrees)	$\theta$ -loc.-aligned (deg)	[15]	(15)	105.07±0.04
<b>DETECTION CONFIDENCE</b>				
snr	SNR	[16]	(16)	28.8
<b>PHOTOMETRY</b>				
alpha (contrast)	$\alpha^+$	[17]	(17)	$(1.34±0.05) \times 10^{-5}$
alpha (magnitude)	$\text{mag}(\alpha^+)$	[18]	(18)	$12.22 \geq 12.18 \geq 12.15$
<b>CLASSIFICATION DETAILS</b>				
pattern_correlation_coefficient	$c$	[19]	(19)	0.92
flag_warning_high_density	FW-hd	[20]	(20)	0
flag_warning_single_pixel	FW-sp	[21]	(21)	0
flag_warning_prox._between_detections	FW-pbd	[22]	(22)	0
flag_warning_near_extended_fov_borders	FW-nefb	[23]	(23)	0
flag_warning_near_fov_borders	FW-nfb	[24]	(24)	0
<b>ADDITIONAL RESULTS</b>				
glr	GLR	[25]	[3]	831
alpha_unc_std_dev	$\sigma_\alpha$	[26]	[4]	$4.65 \times 10^{-7}$
local_5sigma_oracle_contrast	$5\sigma_\alpha$	[27]	[5]	$2.32 \times 10^{-6}$
crlb_alpha	$\delta_\alpha$	[28]	[6]	$3.10 \times 10^{-6}$
{crlb_x,crlb_y} (arcseconds)	$\{\delta_x, \delta_y\}$	[29],[30]	[7],[8]	{0.0047,0.0043}
{crlb_rho,crlb_theta} (as,deg)	$\{\delta_\rho, \delta_\theta\}$	[31],[32]	[9],[10]	{0.0043,0.04}
e_ratio_max_sampling_error	$E(\cdot)$	[33]	[11]	-
denom	$\sum_{\ell=1}^T a_\ell$	[34]	[12]	$4.6 \times 10^{12}$

```

[source (detection) file]: ../../HIP_53524_od20150505_0151326746_paco_outputs/2_detection_paco/adi_results/lam00/detection_files/HIP_53524_fast_paco1_detection_file_index_1_lam00_od20150505_0151326746_cd200519_143456.fits.
[user (detection) file]: ../../HIP_53524_od20150505_0151326746_paco_outputs/2_detection_paco/adi_results/all_detection_main_files/HIP_53524_fast_paco1_detection_file_lam00_od20150505_0151326746_cd200519_143456.txt.
[user (detection) additional file]: ../../HIP_53524_od20150505_0151326746_paco_outputs/2_detection_paco/adi_results/all_detection_main_files/HIP_53524_fast_paco1_detection_file_additional_results_lam00_od20150505_0151326746_cd200519_143456.txt.

```



by the ADI-characterization step. We note that in case of an extended object such as a protoplanetary disk, only the regularization of the flux map produced by the ADI-reduction step has a real meaning since the production of a regularized synthetic flux map requires to clean the detection (which is not possible for an extended object). A synthetic regularized flux map is produced if `characterization_synthetic_regularized_flux_map` is set to 1.

Table 38: *Ad hoc* parameters used during the ADI-characterization step.

Inputs name	Values
<b>SCHEME 1: NUMERICAL OPTIMIZATION</b>	
<code>characterization_numerical_optimization</code>	0
<b>SCHEME 2: SUBPIXEL GRID</b>	
<code>characterization_subpixel_grid</code>	1
<code>characterization_subpixel_grid_subsampling_factor</code>	4
<code>characterization_subpixel_grid_subsampling_zoom_size</code>	4
<b>COMMON PARAMETERS</b>	
<code>characterization_iterations</code>	99
<code>report_sigma_photo_astro_intervals</code>	1
<b>CLEANING SCHEME</b>	
<code>cleaning</code>	2
<code>cleaning_update_only_patch</code>	0
<code>cleaning_authorized_additional_detections</code>	0
<code>cleaning_synthetic_snr_map</code>	1
<b>REGULARIZED FLUX MAP</b>	
<code>characterization_synthetic_regularized_flux_map</code>	1

The input `report_sigma_photo_astro_intervals` gives the degree of confidence on the astrometry and photometry. The astrometry is expressed as  $[x, y]$ -location-(aligned)  $\pm k\delta_{[x,y]}$  and the photometry by  $\alpha^+ \pm k\sigma_\alpha$  where  $\sigma_\alpha$  is the oracle standard-deviation on the flux and  $\delta_{[x,y]}$  are the CRLBs on the photometry.  $k$  is the factor indicated by the input `report_sigma_photo_astro_intervals` (it is generally common to use  $k = 1, 2$  or 3).

Each source having its `flag_characterization` set to 1 is characterized and is associated to an index (same index than in the ADI-detection step if it was seen during this step) plus to a symbol coding for its type:

- “#xx”: standard detection
- “!xx member of !Gxx”: grouped detection
- “!xx”: ill-fitted detection
- “\$xx”: detection below the detection threshold added manually by the user in the text detection file at the end of the ADI-detection step
- “\$xx member of \$Gxx”: grouped detection below the detection threshold added manually by the user in the text detection file at the end of the ADI-detection step
- “+xx”: detection not seen during the ADI-detection and revealed by the cleaning of another source (only if `cleaning_authorized_additional_detections` is explicitly set to 1).
- “+xx member of +Gxx”: grouped detection not seen during the ADI-detection and revealed by the cleaning of another source (only if `cleaning_authorized_additional_detections` is explicitly set to 1)

We recall that by default, only the standard detections pointed during ADI-detection step were characterized (`flag_characterization` set to 1), but the user can change the status of a detection or add manually additional sources (below the detection threshold) to be characterized.

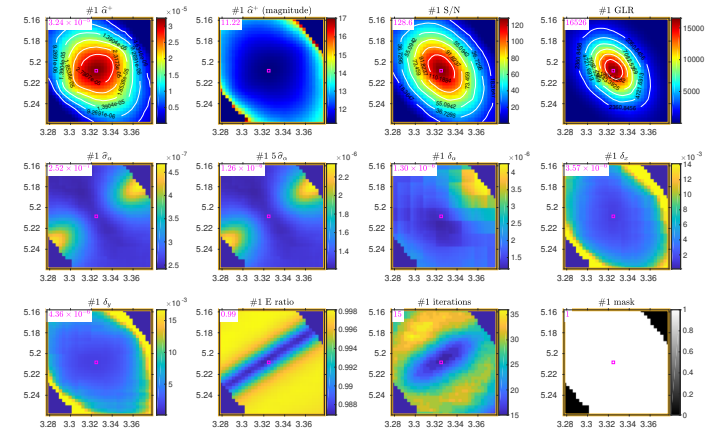


Figure 49: zoomed-characterizations: characterization #1 at  $\lambda_0 = 2.1100\mu\text{m}$  (default field of view alignment).

```
source file  $\alpha^+$  (magnitude) : ../HIP_53524_od20150505_0151326746_paco_outputs/3_characterization_paco/adi_results/lam00/characterization_patch_characterizations/alpha/HIP_53524_paco1_alt_characterization_alpha_patch_file_index_1_lam00_od20150505_0151326746_cd200519_143456.fits
source file  $\alpha^+$  (magnitude) : ../HIP_53524_od20150505_0151326746_paco_outputs/3_characterization_paco/adi_results/lam00/characterization_patch_characterizations/alpha/magnitude/HIP_53524_paco1_alt_characterization_alpha_magnitude_patch_file_index_1_lam00_od20150505_0151326746_cd200519_143456.fits
source file SNR: ../HIP_53524_od20150505_0151326746_paco_outputs/3_characterization_paco/adi_results/lam00/characterization_patch_characterizations/snr/HIP_53524_paco1_alt_characterization_snr_patch_file_index_1_lam00_od20150505_0151326746_cd200519_143456.fits
source file GLR: ../HIP_53524_od20150505_0151326746_paco_outputs/3_characterization_paco/adi_results/lam00/characterization_patch_characterizations/glr/HIP_53524_paco1_alt_characterization_glr_patch_file_index_1_lam00_od20150505_0151326746_cd200519_143456.fits
source file  $\sigma_\alpha$ : ../HIP_53524_od20150505_0151326746_paco_outputs/3_characterization_paco/adi_results/lam00/characterization_patch_characterizations/alpha_unc_std_dev/HIP_53524_paco1_alt_characterization_alpha_unc_std_dev_patch_file_index_1_lam00_od20150505_0151326746_cd200519_143456.fits
source file  $\delta_\alpha$ : ../HIP_53524_od20150505_0151326746_paco_outputs/3_characterization_paco/adi_results/lam00/characterization_patch_characterizations/local_5sigma_oracle_contrast/HIP_53524_paco1_alt_characterization_local_5sigma_oracle_contrast_patch_file_index_1_lam00_od20150505_0151326746_cd200519_143456.fits
source file  $\delta_\alpha$ : ../HIP_53524_od20150505_0151326746_paco_outputs/3_characterization_paco/adi_results/lam00/characterization_patch_characterizations/crlb_alpha/HIP_53524_paco1_alt_characterization_crlb_alpha_patch_file_index_1_lam00_od20150505_0151326746_cd200519_143456.fits
source file  $\delta_x$ : ../HIP_53524_od20150505_0151326746_paco_outputs/3_characterization_paco/adi_results/lam00/characterization_patch_characterizations/crlb_x/HIP_53524_paco1_alt_characterization_crlb_x_patch_file_index_1_lam00_od20150505_0151326746_cd200519_143456.fits
source file  $\delta_y$ : ../HIP_53524_od20150505_0151326746_paco_outputs/3_characterization_paco/adi_results/lam00/characterization_patch_characterizations/crlb_y/HIP_53524_paco1_alt_characterization_crlb_y_patch_file_index_1_lam00_od20150505_0151326746_cd200519_143456.fits
source file  $E[\text{SNR}(\vartheta_{e1}|\vartheta_0)]/E[\text{SNR}(\vartheta_0)]$ : ../HIP_53524_od20150505_0151326746_paco_outputs/3_characterization_paco/adi_results/lam00/characterization_patch_characterizations/e_ratio_max_sampling_error/HIP_53524_paco1_alt_characterization_e_ratio_max_sampling_error_patch_file_index_1_lam00_od20150505_0151326746_cd200519_143456.fits
source file iterations: ../HIP_53524_od20150505_0151326746_paco_outputs/3_characterization_paco/adi_results/lam00/characterization_patch_characterizations/iterations/HIP_53524_paco1_alt_characterization_iterations_patch_file_index_1_lam00_od20150505_0151326746_cd200519_143456.fits
source file mask: ../HIP_53524_od20150505_0151326746_paco_outputs/3_characterization_paco/adi_results/lam00/characterization_patch_characterizations/bv_mask_expand_rotation/HIP_53524_paco1_alt_characterization_bv_mask_expand_rotation_patch_file_index_1_lam00_od20150505_0151326746_cd200519_143456.fits
source file  $[x, y]$ -vectors (ancest): ../HIP_53524_od20150505_0151326746_paco_outputs/3_characterization_paco/adi_results/lam00/characterization_patch_characterizations/vectors_location/HIP_53524_paco1_alt_characterization_vectors_location_real_unit_patch_file_index_1_lam00_od20150505_0151326746_cd200519_143456.fits
preview file: ../HIP_53524_od20150505_0151326746_paco_outputs/3_characterization_paco/adi_results/lam00/characterization_zoom_characterizations/HIP_53524_paco1_alt_characterization_zoom_characterizations_index_1_lam00_od20150505_0151326746_cd200519_143456.pdf
```

Table 39: ADI-characterization: information about the characterization #1.

Fields	Notation	Ind.fits	Ind.txt	Values
<b>IDENTIFICATION</b>				
index	$i$	[1]	(1),[1]	#1
group	$g$	[2]	(2),[2]	-
flag_characterization	F-c	[3]	(3)	1
<b>ASTROMETRY (PIXELS)</b>				
x-location (pixels)	x-location (pix)	[4]	(4)	1151.00±0.11
y-location (pixels)	y-location (pix)	[5]	(5)	996.75±0.13
x-location_aligned (pixels)	x-loc.-aligned (pix)	[6]	(6)	593.15±0.11
y-location_aligned (pixels)	y-loc.-aligned (pix)	[7]	(7)	235.86±0.13
<b>ASTROMETRY (ARCSECONDS)</b>				
x-location (arcseconds)	x-location (as)	[8]	(8)	5.2084±0.0013
y-location (arcseconds)	y-location (as)	[9]	(9)	3.3247±0.0016
rho-location (arcseconds)	$\rho$ -location (as)	[10]	(10)	6.1791±0.0014
theta-location (degrees)	$\theta$ -location (deg)	[11]	(11)	327.45±0.01
x-location_aligned (arcseconds)	x-loc.-aligned (as)	[12]	(12)	-1.6041±0.0013
y-location_aligned (arcseconds)	y-loc.-aligned (as)	[13]	(13)	-5.9673±0.0016
rho-location_aligned (arcseconds)	$\rho$ -loc.-aligned (as)	[14]	(14)	6.1791±0.0014
theta-location_aligned (degrees)	$\theta$ -loc.-aligned (deg)	[15]	(15)	105.05±0.01
<b>DETECTION CONFIDENCE</b>				
snr	SNR	[16]	(16)	128.6
<b>PHOTOMETRY</b>				
alpha (contrast)	$\alpha^+$	[17]	(17)	$(3.24 \pm 0.02) \times 10^{-5}$
alpha (magnitude)	$\text{mag}(\alpha^+)$	[18]	(18)	$11.23 \geq 11.22 \geq 11.21$
<b>CLASSIFICATION DETAILS</b>				
pattern_correlation_coefficient	$c$	[19]	(19)	0.92
flag_warning_high_density	FW-hd	[20]	(20)	0
flag_warning_single_pixel	FW-sp	[21]	(21)	0
flag_warning_prox._between_detections	FW-pbd	[22]	(22)	0
flag_warning_near_extended_fov_borders	FW-nefb	[23]	(23)	0
flag_warning_near_fov_borders	FW-nfb	[24]	(24)	0
<b>ADDITIONAL RESULTS</b>				
glr	GLR	[25]	(3)	16526
alpha_unc_std_dev	$\sigma_\alpha$	[26]	(4)	$2.52 \times 10^{-7}$
local_5sigma_oracle_contrast	$5\sigma_\alpha$	[27]	(5)	$1.26 \times 10^{-6}$
crlb_alpha	$\delta_\alpha$	[28]	(6)	$1.30 \times 10^{-6}$
{crlb_x, crlb_y} (arcseconds)	$\{\delta_x, \delta_y\}$	[29],[30]	(7],[8)	{0.0013,0.0016}
{crlb_rho, crlb_theta} (as, deg)	$\{\delta_\rho, \delta_\theta\}$	[31],[32]	(9],[10)	{0.0014,0.01}
e_ratio_max_sampling_error	$E(\cdot)$	[33]	(11)	0.99
denom	$\sum_{\ell=1}^I a_\ell$	[34]	(12)	$4.5 \times 10^{12}$
characterization_iterations	$k$	[42]	-	15

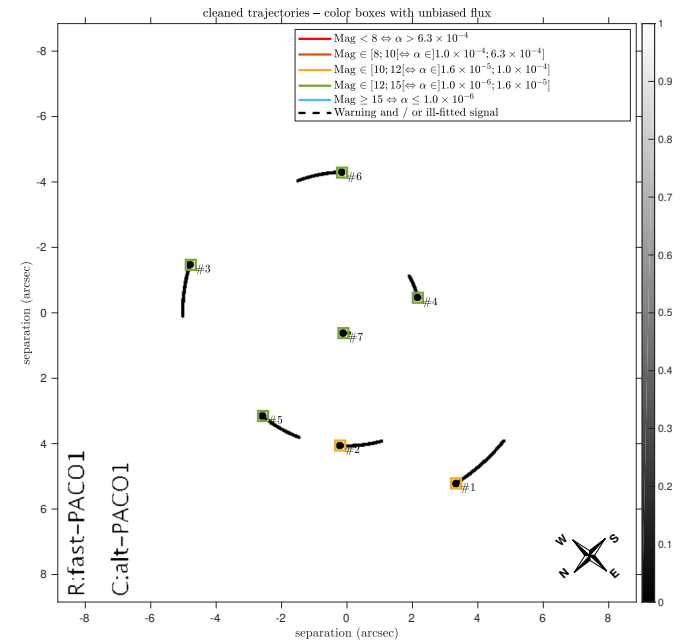
[fits detection file]: ../../HIP\_53524\_od20150505\_0151326746\_paco\_outputs/3\_characterization\_paco/adi\_results/lam00/characterization\_files/HIP\_53524\_paco1\_alt\_characterization\_file\_index\_1\_lam00\_od20150505\_0151326746\_cd200519\_143456.fits

[txt detection file]: ../../HIP\_53524\_od20150505\_0151326746\_paco\_outputs/3\_characterization\_paco/adi\_results/all\_characterization\_main\_files/HIP\_53524\_paco1\_alt\_characterization\_file\_lam00\_od20150505\_0151326746\_cd200519\_143456.txt

[txt detection file additional]: ../../HIP\_53524\_od20150505\_0151326746\_paco\_outputs/3\_characterization\_paco/adi\_results/all\_characterization\_main\_files/HIP\_53524\_paco1\_alt\_characterization\_file\_additional\_results\_lam00\_od20150505\_0151326746\_cd200519\_143456.txt

#### 4.1.4 Characterization cleaning: recomputed cleaned trajectories

- **Mathematical notation:** characterization\_cleaning\_recomputed\_trajectory.
- **Filename notation:** characterization\_cleaning\_recomputed\_trajectory.
- **Description:** trajectories on which the SNR is recomputed by the cleaning procedure after negative subtraction of each characterization. The color of the squares encodes for the (unbiased) estimate of the flux derived from the ADI-characterization step.
- **Properties:** depending on the cleaning level specified within the cleaning input, the recomputed trajectories can be more or less fine.

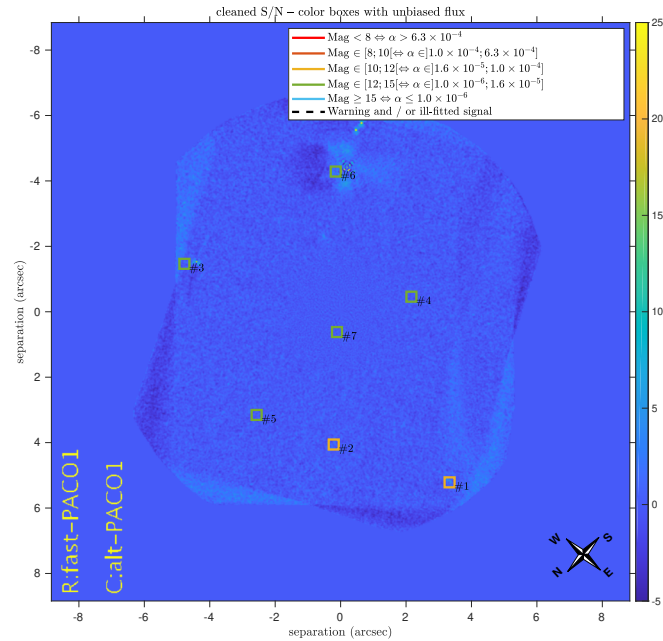


source file: ../../HIP\_53524\_od20150505\_0151326746\_paco\_outputs/3\_characterization\_paco/adi\_results/lam00/characterization\_cleaning/HIP\_53524\_paco1\_alt\_characterization\_cleaning\_recomputed\_trajectory\_full\_map\_lam00\_od20150505\_0151326746\_cd200519\_143456.fits  
 preview file: ../../HIP\_53524\_od20150505\_0151326746\_paco\_outputs/3\_characterization\_paco/adi\_results/lam00/characterization\_cleaning/HIP\_53524\_paco1\_alt\_characterization\_cleaning\_recomputed\_trajectory\_full\_map\_lam00\_od20150505\_0151326746\_cd200519\_143456.pdf

Figure 63: characterization\_cleaning\_recomputed\_trajectory map at  $\lambda_{00} = 2.1100\mu\text{m}$  (default field of view alignment).

#### 4.1.5 Characterization cleaning: SNR

- **Mathematical notation:** characterization–cleaning–SNR.
- **Filename notation:** characterization\_cleaning\_snr\_full\_map.
- **Description:** signal-to-noise ratio from the ADI–reduction step in which the contributions of the characterized sources have been removed by the cleaning procedure. The color of the squares encodes for the (unbiased) estimate of the flux derived from the ADI–characterization step.
- **Properties:** statistically-grounded. Depending on the cleaning level specified within the cleaning input, the recomputed trajectories can be more or less fine.



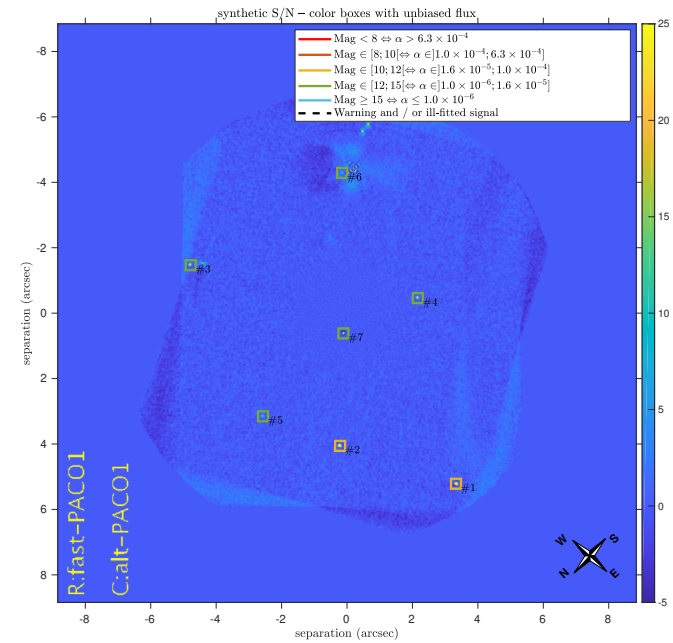
source file: [../../../../HIP\\_53524\\_od20150505\\_0151326746\\_paco\\_outputs/3\\_characterization\\_paco/adi\\_results/lam00/characterization\\_cleaning/HIP\\_53524\\_paco1\\_alt\\_characterization\\_cleaning\\_snr\\_full\\_map\\_lam00\\_od20150505\\_0151326746\\_cd200519\\_143456.fits](#)

preview file: [../../../../HIP\\_53524\\_od20150505\\_0151326746\\_paco\\_outputs/3\\_characterization\\_paco/adi\\_results/lam00/characterization\\_cleaning/HIP\\_53524\\_paco1\\_alt\\_characterization\\_cleaning\\_snr\\_full\\_map\\_lam00\\_od20150505\\_0151326746\\_cd200519\\_143456.pdf](#)

Figure 65: characterization–cleaning–SNR map at  $\lambda_{00} = 2.1100\mu\text{m}$  (default field of view alignment).

#### 4.1.7 Characterization: synthetic SNR

- **Mathematical notation:** characterization–synthetic–SNR.
- **Filename notation:** characterization\_synthetic\_snr\_full\_map.
- **Description:** cleaned signal-to-noise ratio from the cleaning procedure of the ADI–characterization step in which the contributions of the characterized sources have been reinjected with unbiased estimated photometry and astrometry. The color of the squares encodes for the (unbiased) estimate of the flux derived from the ADI–characterization step.
- **Properties:** statistically-grounded and unbiased.



source file: [../../../../HIP\\_53524\\_od20150505\\_0151326746\\_paco\\_outputs/3\\_characterization\\_paco/adi\\_results/lam00/characterization\\_synthetic\\_full\\_map/HIP\\_53524\\_paco1\\_alt\\_characterization\\_synthetic\\_snr\\_full\\_map\\_lam00\\_od20150505\\_0151326746\\_cd200519\\_143456.fits](#)

preview file: [../../../../HIP\\_53524\\_od20150505\\_0151326746\\_paco\\_outputs/3\\_characterization\\_paco/adi\\_results/lam00/characterization\\_synthetic\\_full\\_map/HIP\\_53524\\_paco1\\_alt\\_characterization\\_synthetic\\_snr\\_full\\_map\\_lam00\\_od20150505\\_0151326746\\_cd200519\\_143456.pdf](#)

Figure 69: characterization–synthetic–SNR map at  $\lambda_{00} = 2.1100\mu\text{m}$  (default field of view alignment).





# Bibliography

- Absil, O., Milli, J., Mawet, D., Lagrange, A.-M., Girard, J., Chauvin, G., Boccaletti, A., Delacroix, C., and Surdej, J. (2013). Searching for companions down to 2 au from  $\beta$  Pictoris using the L-band AGPM coronagraph on VLT/NaCo. *Astronomy & Astrophysics*, 559:L12.
- Adams, J. B., Smith, M. O., and Johnson, P. E. (1986). Spectral mixture modeling: A new analysis of rock and soil types at the Viking Lander 1 Site. *Journal of Geophysical Research: Solid Earth*, 91(B8):8098–8112.
- Agranov, G., Berezin, V., and Tsai, R. (2001). Crosstalk and sub-pixel distribution of sensitivity in color CMOS image sensor. In *IEEE Workshop on CCD and Advanced Image Sensors*.
- Agranov, G., Berezin, V., and Tsai, R. H. (2003). Crosstalk and microlens study in a color CMOS image sensor. *IEEE Transactions on Electron Devices*, 50(1):4–11.
- Aime, C., Soummer, R., Marois, C., Doyon, R., Nadeau, D., Racine, R., and Walker, G. (2003). Effects of quasi-static aberrations in faint companion searches. *European Astronomical Society Publications Series*, 8:233–243.
- Allard, F., Allard, N. F., Homeier, D., Kielkopf, J., McCaughrean, M. J., and Spiegelman, F. (2007). K – H<sub>2</sub> quasi-molecular absorption detected in the T-dwarf  $\epsilon$  Indi Ba. *Astronomy & Astrophysics*, 474(2):L21–L24.
- Allard, F., Guillot, T., Ludwig, H.-G., Hauschildt, P. H., Schweitzer, A., Alexander, D. R., and Ferguson, J. W. (2003). Model atmospheres and spectra: the role of dust. In *Symposium of the International Astronomical Union*, volume 211, pages 325–332.
- Allard, F., Hauschildt, P. H., Alexander, D. R., Tamanai, A., and Schweitzer, A. (2001). The limiting effects of dust in brown dwarf model atmospheres. *The Astrophysical Journal*, 556(1):357.
- Allier, C., Hervé, L., Mandula, O., Blandin, P., Usson, Y., Savatier, J., Monneret, S., and Morales, S. (2019). Quantitative phase imaging of adherent mammalian cells: a comparative study. *Biomedical Optics Express*, 10(6):2768–2783.

- Anzagira, L. and Fossum, E. R. (2015). Color filter array patterns for small-pixel image sensors with substantial cross talk. *Journal of the Optical Society of America A*, 32(1):28–34.
- Augereau, J., Lagrange, A., Mouillet, D., Papaloizou, J., and Grorod, P. (1999). On the HR 4796 A circumstellar disk. *Astronomy & Astrophysics*, 348:557–569.
- Babcock, H. W. (1953). The possibility of compensating astronomical seeing. *Publications of the Astronomical Society of the Pacific*, 65(386):229–236.
- Bacher, R., Meillier, C., Chatelain, F., and Michel, O. (2017). Robust control of varying weak hyperspectral target detection with sparse non-negative representation. *IEEE Transactions on Signal Processing*, 65(13):3538–3550.
- Bacon, R., Accardo, M., Adjali, L., Anwand, H., Bauer, S., Biswas, I., Blaizot, J., Boudon, D., Brau-Nogue, S., Brinchmann, J., et al. (2010). The MUSE second-generation VLT instrument. In *Ground-based and Airborne Instrumentation for Astronomy*, volume 7735. International Society for Optics and Photonics.
- Baraffe, I., Chabrier, G., Barman, T. S., Allard, F., and Hauschildt, P. H. (2003). Evolutionary models for cool brown dwarfs and extrasolar giant planets. The case of HD 209458. *Astronomy & Astrophysics*, 402(2):701–712.
- Baudino, J.-L., Bézard, B., Boccaletti, A., Bonnefoy, M., Lagrange, A.-M., and Galicher, R. (2015). Interpreting the photometry and spectroscopy of directly imaged planets: a new atmospheric model applied to  $\beta$  Pictoris b and SPHERE observations. *Astronomy & Astrophysics*, 582:A83.
- Bausson, S., Pascal, F., Forster, P., Ovarlez, J.-P., and Larzabal, P. (2007). First- and second-order moments of the normalized sample covariance matrix of spherically invariant random vectors. *IEEE Signal Processing Letters*, 14(6):425–428.
- Bayer, B. E. (1976). Color imaging array. *US Patent*, 3,971,065.
- Beaton, A. E. and Tukey, J. W. (1974). The fitting of power series, meaning polynomials, illustrated on band-spectroscopic data. *Technometrics*, 16(2):147–185.
- Benjamini, Y. and Hochberg, Y. (1995). Controlling the false discovery rate: a practical and powerful approach to multiple testing. *Journal of the Royal statistical society*, 57(1):289–300.
- Berdeu, A., Denis, L., Langlois, M., Soulez, F., and Thiébaud, É. (2020). PIC: a data reduction algorithm for integral field spectrographs. *accepted in Astronomy & Astrophysics*.
- Berdeu, A., Flasseur, O., Méès, L., Denis, L., Momey, F., Olivier, T., Grosjean, N., and Fournier, C. (2019). Reconstruction of in-line holograms: combining model-based and regularized inversion. *Optics Express*, 27(10):14951–14968.

- Berdeu, A., Laperrousaz, B., Bordy, T., Mandula, O., Morales, S., Gidrol, X., Picollet-D'hahan, N., and Allier, C. (2018a). Lens-free microscopy for 3D + time acquisitions of 3D cell culture. *Scientific reports*, 8(1):16135.
- Berdeu, A., Laperrousaz, B., Bordy, T., Morales, S., Gidrol, X., Picollet-D'hahan, N., and Allier, C. (2018b). 3D + time acquisitions of 3D cell culture by means of lens-free tomographic microscopy. volume 10499. International Society for Optics and Photonics.
- Beuzit, J.-L., Feldt, M., Dohlen, K., Mouillet, D., Puget, P., Wildi, F., Abe, L., Antichi, J., Baruffolo, A., Baudoz, P., et al. (2008). SPHERE: a planet finder instrument for the VLT. In *Ground-based and airborne instrumentation for astronomy*, volume 7014. International Society for Optics and Photonics.
- Beuzit, J.-L., Vigan, A., Mouillet, D., Dohlen, K., Gratton, R., Boccaletti, A., Sauvage, J.-F., Schmid, H., Langlois, M., Petit, C., et al. (2019). SPHERE: the exoplanet imager for the Very Large Telescope. *Astronomy & Astrophysics*, 631:A155.
- Bickel, P. J. (1975). One-step Huber estimates in the linear model. *Journal of the American Statistical Association*, 70(350):428–434.
- Biucas-Dias, J. M. and Leitao, J. M. N. (1996). Wall position and thickness estimation from sequences of echocardiographic images. *IEEE Transactions on Medical Imaging*, 15(1):25–38.
- Biucas-Dias, J. M., Plaza, A., Dobigeon, N., Parente, M., Du, Q., Gader, P., and Chanussot, J. (2012). Hyperspectral unmixing overview: Geometrical, statistical, and sparse regression-based approaches. *IEEE journal of selected topics in applied earth observations and remote sensing*, 5(2):354–379.
- Bishop, C. M. (2006). *Pattern recognition and machine learning*. Springer.
- Black, J. G. (2008). *Microbiology: principles and explorations*. John Wiley & Sons.
- Blockstein, L. and Yadid-Pecht, O. (2010). Crosstalk quantification, analysis, and trends in CMOS image sensors. *Applied Optics*, 49(24):4483–4488.
- Boccaletti, A., Thébault, P., Pawellek, N., Lagrange, A.-M., Galicher, R., Desidera, S., Milli, J., Kral, Q., Bonnefoy, M., Augereau, J.-C., et al. (2019). Two cold belts in the debris disk around the G-type star NZ Lupi. *Astronomy & Astrophysics*, 625:A21.
- Bonavita, M., Daemgen, S., Desidera, S., Jayawardhana, R., Janson, M., and Lafrenière, D. (2014). A new sub-stellar companion around the young star HD 284149. *The Astrophysical Journal Letters*, 791(2):L40.
- Bond, I. A., Udalski, A., Jaroszyński, M., Rattenbury, N., Paczyński, B., Soszyński, I., Wyrzykowski, L., Szymański, M., Kubiak, M., Szewczyk, O., et al. (2004). OGLE 2003-BLG-235/MOA 2003-BLG-53: a planetary microlensing event. *The Astrophysical Journal Letters*, 606(2):L155.

- Bowler, B. P., Liu, M. C., Dupuy, T. J., and Cushing, M. C. (2010). Near-infrared spectroscopy of the extrasolar planet HR 8799 b. *The Astrophysical Journal*, 723(1):850.
- Brady, D. J., Choi, K., Marks, D. L., Horisaki, R., and Lim, S. (2009). Compressive holography. *Optics Express*, 17(15):13040–13049.
- Brent, R. P. (2013). *Algorithms for minimization without derivatives*. Courier Corporation.
- Buades, A., Coll, B., and Morel, J.-M. (2005a). A non-local algorithm for image denoising. In *IEEE Computer Society Conference on Computer Vision and Pattern Recognition*, volume 2, pages 60–65. IEEE.
- Buades, A., Coll, B., and Morel, J.-M. (2005b). A review of image denoising algorithms, with a new one. *Multiscale Modeling & Simulation*, 4(2):490–530.
- Burrows, A., Marley, M., Hubbard, W., Lunine, J., Guillot, T., Saumon, D., Freedman, R., Sudarsky, D., and Sharp, C. (1997). A nongray theory of extrasolar giant planets and brown dwarfs. *The Astrophysical Journal*, 491(2):856.
- Cantalloube, F. (2016). *Détection et caractérisation d'exoplanètes dans des images à grand contraste par la résolution de problème inverse*. PhD thesis, Grenoble Alpes.
- Cantalloube, F., Mouillet, D., Mugnier, L., Milli, J., Absil, O., Gomez Gonzalez, C. A., Chauvin, G., Beuzit, J.-L., and Cornia, A. (2015). Direct exoplanet detection and characterization using the ANDROMEDA method: Performance on VLT/NaCo data. *Astronomy & Astrophysics*, 582:A89.
- Cantalloube, F., Ygouf, M., Mugnier, L., Mouillet, D., Herscovici-Schiller, O., and Brandner, W. (2018). Status of the MEDUSAE post-processing method to detect circumstellar objects in high-contrast multispectral images. *arXiv preprint arXiv:1812.04312*.
- Carillet, M., Bendjoya, P., Abe, L., Guerri, G., Boccaletti, A., Daban, J.-B., Dohlen, K., Ferrari, A., Robbe-Dubois, S., Douet, R., et al. (2011). Apodized lyot coronagraph for SPHERE/VLT. *Experimental Astronomy*, 30(1):39–58.
- Chabrier, G., Baraffe, I., Allard, F., and Hauschildt, P. (2000). Evolutionary models for very low-mass stars and brown dwarfs with dusty atmospheres. *The Astrophysical Journal*, 542(1):464.
- Chambolle, A., Caselles, V., Cremers, D., Novaga, M., and Pock, T. (2010). An introduction to total variation for image analysis. *Theoretical foundations and numerical methods for sparse recovery*, 9(263-340):227.
- Chang, C.-I. and Chiang, S.-S. (2002). Anomaly detection and classification for hyperspectral imagery. *IEEE transactions on geoscience and remote sensing*, 40(6):1314–1325.

- 
- Charbonneau, D., Brown, T. M., Latham, D. W., and Mayor, M. (1999). Detection of planetary transits across a sun-like star. *The Astrophysical Journal Letters*, 529(1):L45.
- Chatelain, F., Costard, A., and Michel, O. J. (2011). A bayesian marked point process for object detection. application to MUSE hyperspectral data. In *IEEE International Conference on Acoustics, Speech and Signal Processing*, pages 3628–3631. IEEE.
- Chauvin, G., Desidera, S., Lagrange, A.-M., Vigan, A., Gratton, R., Langlois, M., Bonnefoy, M., Beuzit, J.-L., Feldt, M., Mouillet, D., et al. (2017). Discovery of a warm, dusty giant planet around HIP 65426. *Astronomy & Astrophysics*, 605:L9.
- Chauvin, G., Lagrange, A.-M., Dumas, C., Zuckerman, B., Mouillet, D., Song, I., Beuzit, J.-L., and Lowrance, P. (2004). A giant planet candidate near a young brown dwarf-direct VLT/NaCo observations using IR wavefront sensing. *Astronomy & Astrophysics*, 425(2):L29–L32.
- Chaux, C., Pesquet, J.-C., and Duval, L. (2007). Noise covariance properties in dual-tree wavelet decompositions. *IEEE Transactions on Information Theory*, 53(12):4680–4700.
- Cheetham, A., Samland, M., Brems, S., Launhardt, R., Chauvin, G., Ségransan, D., Henning, T., Quirrenbach, A., Avenhaus, H., Cugno, G., et al. (2019). Spectral and orbital characterisation of the directly imaged giant planet HIP 65426 b. *Astronomy & Astrophysics*, 622:A80.
- Chen, C., Mahjoubfar, A., Tai, L.-C., Blaby, I., Huang, A., Niazi, K., and Jalali, B. (2016). Deep learning in label-free cell classification. *Scientific reports*, 6:21471.
- Chen, Q. and Cumming, D. R. (2010). High transmission and low color cross-talk plasmonic color filters using triangular-lattice hole arrays in aluminum films. *Optics Express*, 18(13):14056–14062.
- Chen, Y., Wiesel, A., Eldar, Y. C., and Hero, A. O. (2010). Shrinkage algorithms for MMSE covariance estimation. *IEEE Transactions on Signal Processing*, 58(10):5016–5029.
- Claudi, R., Maire, A.-L., Mesa, D., Cheetham, A., Fontanive, C., Gratton, R., Zurlo, A., Avenhaus, H., Bhowmik, T., Biller, B., et al. (2019). SPHERE dynamical and spectroscopic characterization of HD 142527 b. *Astronomy & Astrophysics*, 622:A96.
- Conte, E., De Maio, A., and Ricci, G. (2002). Recursive estimation of the covariance matrix of a compound-Gaussian process and its application to adaptive CFAR detection. *IEEE Transactions on Signal Processing*, 50(8):1908–1915.
- Conte, E., Lops, M., and Ricci, G. (1995). Asymptotically optimum radar detection in compound-Gaussian clutter. *IEEE Transactions on Aerospace and Electronic Systems*, 31(2):617–625.
- Cornia, A. (2010). *Traitement d’images différentielles à haut contraste pour la détection de planètes extrasolaires*. PhD thesis, Paris 7.
-

- Craven, P. and Wahba, G. (1978). Smoothing noisy data with spline functions. *Numerische mathematik*, 31(4):377–403.
- Currie, T., Burrows, A., Itoh, Y., Matsumura, S., Fukagawa, M., Apai, D., Madhusudhan, N., Hinz, P. M., Rodigas, T., Kasper, M., et al. (2011). A combined Subaru/VLT/MMT 1-5  $\mu\text{m}$  study of planets orbiting HR 8799: Implications for atmospheric properties, masses, and formation. *The Astrophysical Journal*, 729(2):128.
- Currie, T., Burrows, A., Madhusudhan, N., Fukagawa, M., Girard, J. H., Dawson, R., Murray-Clay, R., Kenyon, S., Kuchner, M., Matsumura, S., et al. (2013). A combined Very Large Telescope and Gemini study of the atmosphere of the directly imaged planet,  $\beta$  Pictoris b. *The Astrophysical Journal*, 776(1):15.
- Currie, T., Debes, J., Rodigas, T. J., Burrows, A., Itoh, Y., Fukagawa, M., Kenyon, S. J., Kuchner, M., and Matsumura, S. (2012a). Direct imaging confirmation and characterization of a dust-enshrouded candidate exoplanet orbiting Fomalhaut. *The Astrophysical Journal Letters*, 760(2):L32.
- Currie, T., Fukagawa, M., Thalmann, C., Matsumura, S., and Plavchan, P. (2012b). Direct detection and orbital analysis of the exoplanets HR 8799 bcd from archival 2005 Keck/NIRC2 data. *The Astrophysical Journal Letters*, 755(2):L34.
- Currie, T., Guyon, O., Tamura, M., Kudo, T., Jovanovic, N., Lozi, J., Schlieder, J. E., Brandt, T. D., Kuhn, J., Serabyn, E., et al. (2017). Subaru/SCEXAO first-light direct imaging of a young debris disk around HD 36546. *The Astrophysical Journal Letters*, 836(1):L15.
- Dainty, J. C. (2013). *Laser speckle and related phenomena*, volume 9. Springer science & business Media.
- Davies, R. and Kasper, M. (2012). Adaptive optics for astronomy. *Annual Review of Astronomy and Astrophysics*, 50:305–351.
- Davison, A. C. and Hinkley, D. V. (1997). *Bootstrap methods and their application*, volume 1. Cambridge university press.
- De Zeeuw, P., Hoogerwerf, R. v., de Bruijne, J. H., Brown, A., and Blaauw, A. (1999). A Hipparcos census of the nearby OB associations. *The Astronomical Journal*, 117(1):354.
- Delorme, P., Meunier, N., Albert, D., Lagadec, E., Le Coroller, H., Galicher, R., Mouillet, D., Boccaletti, A., Mesa, D., Meunier, J.-C., et al. (2017). The SPHERE data center: a reference for high contrast imaging processing. In *Proceedings of the Annual meeting of the French Society of Astronomy and Astrophysics*, pages 347–361.
- Demoli, N., Vukicevic, D., and Torzynski, M. (2003). Dynamic digital holographic interferometry with three wavelengths. *Optics Express*, 11(7):767–774.
- Denis, L., Lorenz, D., Thiébaud, É., Fournier, C., and Dennis, T. (2009). Inline hologram reconstruction with sparsity constraints. *Optics Letters*, 34(22):3475–3477.



- Dennis Jr, J. E. and Welsch, R. E. (1978). Techniques for nonlinear least squares and robust regression. *Communications in Statistics-Simulation and Computation*, 7(4):345–359.
- Devaney, N. and Thiébaud, É. (2017). PeX 1. multi-spectral expansion of residual speckles for planet detection. *Monthly Notices of the Royal Astronomical Society*, 472(3):3734–3748.
- Di, W., Zhang, L., Zhang, D., and Pan, Q. (2010). Studies on hyperspectral face recognition in visible spectrum with feature band selection. *IEEE Transactions on Systems, Man, and Cybernetics*, 40(6):1354–1361.
- Dolega, M. E., Allier, C., Kesavan, S. V., Gerbaud, S., Kermarrec, F., Marcoux, P., Dinten, J.-M., Gidrol, X., and Picollet-D’Hahan, N. (2013). Label-free analysis of prostate acini-like 3D structures by lensfree imaging. *Biosensors and Bioelectronics*, 49:176–183.
- Dommanget, J. and Nys, O. (2002). VizieR online data catalog: CCDM (Catalog of Components of Double & Multiple stars). *VizieR Online Data Catalog*, 1274.
- Dutter, R. and Huber, P. J. (1981). Numerical methods for the nonlinear robust regression problem. *Journal of Statistical Computation and Simulation*, 13(2):79–113.
- D’Orazi, V., Gratton, R., Desidera, S., Avenhaus, H., Mesa, D., Stolker, T., Giro, E., Benatti, S., Jang-Condell, H., Rigliaco, E., et al. (2019). Mapping of shadows cast on a protoplanetary disk by a close binary system. *Nature Astronomy*, 3(2):167.
- Eggenberger, A., Cornia, A., Mugnier, L., Mouillet, D., Chauvin, G., Boccaletti, A., and Rousset, G. (2010). Testing the ANDROMEDA method for exoplanet detection on VLT/NaCo data. In *In the Spirit of Lyot 2010*.
- Elad, M. and Aharon, M. (2006). Image denoising via sparse and redundant representations over learned dictionaries. *IEEE Transactions on Image processing*, 15(12):3736–3745.
- Estribeau, M. and Magnan, P. (2005). CMOS pixels crosstalk mapping and its influence on measurements accuracy for space applications. In *Remote Sensing*, page 597813. International Society for Optics and Photonics.
- Ferguson, T. S. (1962). Location and scale parameters in exponential families of distributions. *The Annals of mathematical statistics*, pages 986–1001.
- Fétick, R. J.-L., Jorda, L., Vernazza, P., Marsset, M., Drouard, A., Fusco, T., Carry, B., Marchis, F., Hanuš, J., Viikinkoski, M., et al. (2019). Closing the gap between earth-based and interplanetary mission observations: Vesta seen by VLT/SPHERE. *Astronomy & Astrophysics*, 623:A6.
- Fitzgerald, M. P. and Graham, J. R. (2006). Speckle statistics in adaptively corrected images. *The Astrophysical Journal*, 637(1):541.

- Flasseur, O., Denis, L., Fournier, C., and Thiébaud, É. (2017a). Robust object characterization from lensless microscopy videos. In *25th European Signal Processing Conference (EUSIPCO)*, pages 1445–1449. IEEE.
- Flasseur, O., Denis, L., Thiébaud, É., and Langlois, M. (2018a). Exoplanet detection in angular differential imaging by statistical learning of the nonstationary patch covariances – The PACO algorithm. *Astronomy & Astrophysics*, 618:A138.
- Flasseur, O., Denis, L., Thiébaud, É., and Langlois, M. (2018b). An unsupervised patch-based approach for exoplanet detection by direct imaging. In *25th IEEE International Conference on Image Processing (ICIP)*, pages 2735–2739.
- Flasseur, O., Denis, L., Thiébaud, É., and Langlois, M. (2020a). PACO ASDI: an algorithm for exoplanet detection and characterization in direct imaging with integral field spectrographs. *in revision for Astronomy & Astrophysics*.
- Flasseur, O., Denis, L., Thiébaud, É., and Langlois, M. (2020b). Robustness to bad frames in angular differential imaging: a local weighting approach. *Astronomy & Astrophysics*, 634:A2.
- Flasseur, O., Denis, L., Thiébaud, É., Olivier, T., and Fournier, C. (2019). ExPACO: detection of an extended pattern under nonstationary correlated noise by patch covariance modeling. In *27th European Signal Processing Conference (EUSIPCO)*, pages 1–5. IEEE.
- Flasseur, O., Denis, L., Thiébaud, É. M., and Langlois, M. (2018c). Exoplanet detection in angular and spectral differential imaging: local learning of background correlations for improved detections. In *SPIE Astronomical Telescopes and Instrumentation, Adaptive Optics Systems*, volume 10703. International Society for Optics and Photonics.
- Flasseur, O., Fournier, C., Verrier, N., Denis, L., Jolivet, F., Cazier, A., and Lépine, T. (2017b). Self-calibration for lensless color microscopy. *Applied Optics*, 56(13):189–199.
- Flasseur, O., Jolivet, F., Momey, F., Denis, L., and Fournier, C. (2018d). Improving color lensless microscopy reconstructions by self-calibration. In *SPIE Photonics Europe, Unconventional Optical Imaging*, volume 10677. International Society for Optics and Photonics.
- Fournier, C., Denis, L., and Fournel, T. (2010). On the single point resolution of on-axis digital holography. *Journal of the Optical Society of America A*, 27(8):1856–1862.
- Fournier, C., Denis, L., Seifi, M., and Fournel, T. (2014). *Digital hologram processing in on-axis holography, in multi-dimensional imaging*. John Wiley and Sons.
- Fournier, C., Jolivet, F., Denis, L., Verrier, N., Thiébaud, É., Allier, C., and Fournel, T. (2017). Pixel super-resolution in digital holography by regularized reconstruction. *Applied Optics*, 56(1):69–77.

- Fox, J. and Weisberg, S. (2018). *An R companion to applied regression*. Sage Publications.
- Frontera-Pons, J., Veganzones, M. A., Pascal, F., and Ovarlez, J.-P. (2015). Hyperspectral anomaly detectors using robust estimators. *IEEE Journal of Selected Topics in Applied Earth Observations and Remote Sensing*, 9(2):720–731.
- Frontera-Pons, J., Veganzones, M. A., Velasco-Forero, S., Pascal, F., Ovarlez, J. P., and Chanussot, J. (2014). Robust anomaly detection in hyperspectral imaging. In *IEEE Geoscience and Remote Sensing Symposium*, pages 4604–4607. IEEE.
- Fuchs, J.-J. (1999). An inverse problem approach to robust regression. In *IEEE International Conference on Acoustics, Speech, and Signal Processing*, volume 4, pages 1809–1812. IEEE.
- Furumiya, M., Ohkubo, H., Muramatsu, Y., Kurosawa, S., Okamoto, F., Fujimoto, Y., and Nakashiba, Y. (2001). High-sensitivity and no-crosstalk pixel technology for embedded CMOS image sensor. *IEEE transactions on Electron Devices*, 48(10):2221–2227.
- Gabor, D. (1948). A new microscopic principle. *Nature*, 161:777.
- Galicher, R., Boccaletti, A., Mesa, D., Delorme, P., Gratton, R., Langlois, M., Lagrange, A.-M., Maire, A.-L., Le Coroller, H., Chauvin, G., et al. (2018). Astrometric and photometric accuracies in high contrast imaging: The SPHERE speckle calibration tool (SpeCal). *Astronomy & Astrophysics*, 615:A92.
- Garcia-Sucerquia, J. (2016). Color digital lensless holographic microscopy: laser versus LED illumination. *Applied Optics*, 55(24):6649–6655.
- Garufi, A., Benisty, M., Stolker, T., Avenhaus, H., De Boer, J., Pohl, A., Quanz, S. P., Dominik, C., Ginski, C., Thalmann, C., et al. (2017). Three years of SPHERE: the latest view of the morphology and evolution of protoplanetary discs. *The Messenger*, 169:32–37.
- Getman, A., Uvarov, T., Han, Y., Kim, B., Ahn, J., and Lee, Y. (2007). Crosstalk, color tint and shading correction for small pixel size image sensor. In *International Image Sensor Workshop*, pages 166–169.
- Gibbs, A., Wagner, K., Apai, D., Moór, A., Currie, T., Bonnefoy, M., Langlois, M., and Lisse, C. (2019). VLT/SPHERE multiwavelength high-contrast imaging of the HD 115600 debris disk: New constraints on the dust geometry and the presence of young giant planets. *The Astronomical Journal*, 157(1):39.
- Gini, F. and Greco, M. (2002). Covariance matrix estimation for CFAR detection in correlated heavy tailed clutter. *Signal Processing*, 82(12):1847–1859.
- Gire, J. (2009). *Holographie numérique de micro-particules: apports de l’approche problème inverse et optimisation de l’algorithme de traitement*. PhD thesis, Université Jean Monnet.

- Gire, J., Denis, L., Fournier, C., Thiébaud, É., Soulez, F., and Ducottet, C. (2008). Digital holography of particles: benefits of the “inverse problem” approach. *Measurement Science and Technology*, 19(7):074005.
- Go, T., Yoon, G. Y., and Lee, S. J. (2019). Learning-based automatic sensing and size classification of microparticles using smartphone holographic microscopy. *Analyst*, 144(5):1751–1760.
- Goetz, A. F. (2009). Three decades of hyperspectral remote sensing of the Earth: A personal view. *Remote Sensing of Environment*, 113:5–16.
- Golub, G. H., Heath, M., and Wahba, G. (1979). Generalized cross-validation as a method for choosing a good ridge parameter. *Technometrics*, 21(2):215–223.
- Gomez Gonzalez, C. A., Absil, O., Absil, P.-A., Van Droogenbroeck, M., Mawet, D., and Surdej, J. (2016). Low-rank plus sparse decomposition for exoplanet detection in direct-imaging ADI sequences - The LLSG algorithm. *Astronomy & Astrophysics*, 589:A54.
- Gomez Gonzalez, C. A., Absil, O., and Van Droogenbroeck, M. (2018). Supervised detection of exoplanets in high-contrast imaging sequences. *Astronomy & Astrophysics*, 613:A71.
- Gomez Gonzalez, C. A., Wertz, O., Absil, O., Christiaens, V., Defrère, D., Mawet, D., Milli, J., Absil, P.-A., Van Droogenbroeck, M., Cantalloube, F., et al. (2017). VIP: Vortex Image Processing package for high-contrast direct imaging. *The Astronomical Journal*, 154(1):7.
- Goodman, J. W. (1976). Some fundamental properties of speckle. *Journal of the Optical Society of America A*, 66(11):1145–1150.
- Goodman, J. W. (2005). *Introduction to Fourier optics*. Roberts and Company Publishers.
- Goodman, J. W. and Lawrence, R. (1967). Digital image formation from electronically detected holograms. *Applied physics letters*, 11(3):77–79.
- Göröcs, Z., Orzó, L., Kiss, M., Tóth, V., and Tóké, S. (2010). In-line color digital holographic microscope for water quality measurements. In *Laser Applications in Life Sciences 2010*, page 737614. International Society for Optics and Photonics.
- Göröcs, Z., Tamamitsu, M., Bianco, V., Wolf, P., Roy, S., Shindo, K., Yanny, K., Wu, Y., Koydemir, H. C., Rivenson, Y., et al. (2018). A deep learning-enabled portable imaging flow cytometer for cost-effective, high-throughput, and label-free analysis of natural water samples. *Light: Science & Applications*, 7(1):66.
- Goudail, F., Laude, V., and Réfrégier, P. (1995). Influence of nonoverlapping noise on regularized linear filters for pattern recognition. *Optics Letters*, 20(21):2237–2239.
- Gouesbet, G. and Gréhan, G. (2011). *Generalized Lorenz-Mie theories*, volume 31. Springer.

- Gratton, R., Ligi, R., Sissa, E., Desidera, S., Mesa, D., Bonnefoy, M., Chauvin, G., Cheetham, A., Feldt, M., Lagrange, A.-M., et al. (2019). Blobs, spiral arms, and a possible planet around HD 169142. *Astronomy & Astrophysics*, 623:A140.
- Greenbaum, A., Luo, W., Su, T.-W., Göröcs, Z., Xue, L., Isikman, S. O., Coskun, A. F., Mudanyali, O., and Ozcan, A. (2012). Imaging without lenses: achievements and remaining challenges of wide-field on-chip microscopy. *Nature methods*, 9(9):889.
- Greenbaum, A. Z., Pueyo, L., Ruffio, J.-B., Wang, J. J., De Rosa, R. J., Aguilar, J., Rameau, J., Barman, T., Marois, C., Marley, M. S., et al. (2018). GPI spectra of HR 8799 c, d, and e from 1.5 to 2.4  $\mu\text{m}$  with KLIP forward modeling. *The Astronomical Journal*, 155(6):226.
- Grier, D. G., Yevick, A., and Hannel, M. (2017). Machine-learning approach to holographic particle characterization. US Patent App. 15/518,739.
- Guidi, G., Ruane, G., Williams, J., Mawet, D., Testi, L., Zurlo, A., Absil, O., Bottom, M., Choquet, É., Christiaens, V., et al. (2018). High-contrast imaging of HD 163296 with the Keck/NIRC2 L'-band vortex coronagraph. *Monthly Notices of the Royal Astronomical Society*, 479(2):1505–1513.
- Guyon, O., Pluzhnik, E., Kuchner, M., Collins, B., and Ridgway, S. (2006). Theoretical limits on extrasolar terrestrial planet detection with coronagraphs. *The Astrophysical Journal Supplement Series*, 167(1):81.
- Haffert, S., Bohn, A., de Boer, J., Snellen, I., Brinchmann, J., Girard, J., Keller, C., and Bacon, R. (2019). Two accreting protoplanets around the young star PDS 70. *Nature Astronomy*, 3(8):749–754.
- Hamaidi, L. K., Muma, M., and Zoubir, A. M. (2017). Robust distributed multi-speaker voice activity detection using stability selection for sparse non-negative feature extraction. In *25th European Signal Processing Conference*, pages 161–165. IEEE.
- Hannel, M. D., Abdulali, A., O'Brien, M., and Grier, D. G. (2018). Machine-learning techniques for fast and accurate feature localization in holograms of colloidal particles. *Optics Express*, 26(12):15221–15231.
- Hejna, M., Jorapur, A., Song, J., and Judson, R. (2017). High accuracy label-free classification of single-cell kinetic states from holographic cytometry of human melanoma cells. *Scientific reports*, 7(1):11943.
- Hervé, L., Cioni, O., Blandin, P., Navarro, F., Menneteau, M., Bordy, T., Morales, S., and Allier, C. (2018). Multispectral total-variation reconstruction applied to lens-free microscopy. *Biomedical Optics Express*, 9(11):5828–5836.
- Hill, R. W. and Holland, P. W. (1977). Two robust alternatives to least-squares regression. *Journal of the American Statistical Association*, 72(360a):828–833.
- Hirakawa, K. and Wolfe, P. J. (2007). Spatio-spectral color filter array design for enhanced image fidelity. In *IEEE International Conference on Image Processing*, volume 2, page 81. IEEE.

- Högbom, J. (1974). Aperture synthesis with a non-regular distribution of interferometer baselines. *Astronomy & Astrophysics Supplement Series*, 15:417.
- Holland, P. W. and Welsch, R. E. (1977). Robust regression using iteratively reweighted least-squares. *Communications in Statistics-theory and Methods*, 6(9):813–827.
- Hotelling, H. (1933). Analysis of a complex of statistical variables into principal components. *Journal of educational psychology*, 24(6):417.
- Houk, N. and Smith-Moore, M. (1988). *Michigan Catalogue of Two-dimensional Spectral Types for the HD Stars.*, volume 4.
- Howard, A. W., Johnson, J. A., Marcy, G. W., Fischer, D. A., Wright, J. T., Bernat, D., Henry, G. W., Peek, K. M., Isaacson, H., Apps, K., et al. (2010). The California planet survey I. four new giant exoplanets. *The Astrophysical Journal*, 721(2):1467.
- Hsu, T.-H., Fang, Y.-K., Lin, C., Chen, S., Lin, C., Yaung, D.-N., Wu, S.-G., Chien, H., Tseng, C., Lin, J., et al. (2004). Light guide for pixel crosstalk improvement in deep submicron CMOS image sensor. *IEEE electron device letters*, 25(1):22–24.
- Hubel, P. M., Liu, J., and Guttosch, R. J. (2004). Spatial frequency response of color image sensors: Bayer color filters and Foveon X3. In *Electronic Imaging 2004*, pages 402–407. International Society for Optics and Photonics.
- Huber, P. J. (2011). *Robust statistics*. Springer.
- Hubert, M., Rousseeuw, P. J., and Van Aelst, S. (2008). High-breakdown robust multivariate methods. *Statistical science*, pages 92–119.
- Isella, A., Huang, J., Andrews, S. M., Dullemond, C. P., Birnstiel, T., Zhang, S., Zhu, Z., Guzmán, V. V., Pérez, L. M., Bai, X.-N., et al. (2018). The disk substructures at high angular resolution project (DSHARP). a high-definition study of the HD 163296 planet-forming disk. *The Astrophysical Journal Letters*, 869(2):L49.
- Javidi, B., Markman, A., Rawat, S., O’Connor, T., Anand, A., and Andemariam, B. (2018). Sickle cell disease diagnosis based on spatio-temporal cell dynamics analysis using 3D printed shearing digital holographic microscopy. *Optics Express*, 26(10):13614–13627.
- Javidi, B. and Wang, J. (1992). Limitation of the classic definition of the correlation signal-to-noise ratio in optical pattern recognition with disjoint signal and scene noise. *Applied Optics*, 31(32):6826–6829.
- Jensen-Clem, R., Mawet, D., Gomez Gonzalez, C. A., Absil, O., Belikov, R., Currie, T., Kenworthy, M. A., Marois, C., Mazoyer, J., Ruane, G., et al. (2017). A new standard for assessing the performance of high contrast imaging systems. *The Astronomical Journal*, 155(1):19.
- Jolivet, F. (2018). *Approches “problèmes inverses” régularisées pour l’imagerie sans lentille et la microscopie holographique en ligne*. PhD thesis, Université Jean Monnet Saint-Etienne.



- Jolivet, F., Momey, F., Denis, L., Mèès, L., Faure, N., Grosjean, N., Pinston, F., Marié, J.-L., and Fournier, C. (2018). Regularized reconstruction of absorbing and phase objects from a single in-line hologram, application to fluid mechanics and microbiology. *Optics Express*, 26(7):8923–8940.
- Jolliffe, I. (2011). *Principal component analysis*. Springer.
- Jovanovic, N., Martinache, F., Guyon, O., Clergeon, C., Singh, G., Kudo, T., Garrel, V., Newman, K., Doughty, D., Lozi, J., et al. (2015). The Subaru coronagraphic extreme adaptive optics system: enabling high-contrast imaging on solar-system scales. *Publications of the Astronomical Society of the Pacific*, 127(955):890.
- Katkovnik, V., Egiazarian, K., and Astola, J. (2002). Adaptive window size image de-noising based on intersection of confidence intervals (ICI) rule. *Journal of Mathematical Imaging and Vision*, 16(3):223–235.
- Kay, S. M. (1998a). *Fundamentals of statistical signal processing: Detection theory, vol. 2*. Prentice Hall Upper Saddle River, NJ, USA.
- Kay, S. M. (1998b). *Fundamentals of statistical signal processing: Estimation theory, vol. 1*. Prentice Hall Upper Saddle River, NJ, USA.
- Kekatos, V. and Giannakis, G. B. (2011). From sparse signals to sparse residuals for robust sensing. *IEEE Transactions on Signal Processing*, 59(7):3355–3368.
- Kemper, B., Bauwens, A., Bettenworth, D., Götte, M., Greve, B., Kastl, L., Ketelhut, S., Lenz, P., Mues, S., Schneckeburger, J., et al. (2019). Label-free quantitative in vitro live cell imaging with digital holographic microscopy.
- Kendall, M. G., Stuart, A., and Ord, J. K. (1948). *The advanced theory of statistics*, volume 1. JSTOR.
- Keppler, M., Benisty, M., Müller, A., Henning, T., Van Boekel, R., Cantalloube, F., Ginski, C., Van Holstein, R., Maire, A.-L., Pohl, A., et al. (2018). Discovery of a planetary-mass companion within the gap of the transition disk around PDS 70. *Astronomy & Astrophysics*, 617:A44.
- Kesavan, S. V., Momey, F., Cioni, O., David-Watine, B., Dubrulle, N., Shorte, S., Sulpice, E., Freida, D., Chalmond, B., Dinten, J.-M., et al. (2014). High-throughput monitoring of major cell functions by means of lensfree video microscopy. *Scientific reports*, 4:5942.
- Keshava, N. and Mustard, J. F. (2002). Spectral unmixing. *IEEE signal processing magazine*, 19(1):44–57.
- Kim, M. S., Chen, Y., and Mehl, P. (2001). Hyperspectral reflectance and fluorescence imaging system for food quality and safety. *Transactions of the American Society of Agricultural and Biological Engineers*, 44(3):721.

- Kim, S.-J., Wang, C., Zhao, B., Im, H., Min, J., Choi, H. J., Tadros, J., Choi, N. R., Castro, C. M., Weissleder, R., et al. (2018). Deep transfer learning-based hologram classification for molecular diagnostics. *Scientific reports*, 8(1):17003.
- Koo, C.-H., Kim, H.-K., Paik, K.-H., Park, D.-C., Lee, K.-H., Park, Y.-K., Moon, C.-R., Lee, S.-H., Hwang, S.-H., Lee, D.-H., et al. (2007). Improvement of crosstalk on 5M CMOS image sensor with  $1.7 \times 1.7 \mu\text{m}^2$  pixels. In *Integrated Optoelectronic Devices*, page 647115. International Society for Optics and Photonics.
- Kreis, T. (2006). *Handbook of holographic interferometry: optical and digital methods*. John Wiley & Sons.
- Krishnatreya, B. J., Colen-Landy, A., Hasebe, P., Bell, B. A., Jones, J. R., Sunda-Meya, A., and Grier, D. G. (2014). Measuring Boltzmann’s constant through holographic video microscopy of a single colloidal sphere. *American Journal of Physics*, 82(1):23–31.
- Kuhn, J. R., Potter, D., and Parise, B. (2001). Imaging polarimetric observations of a new circumstellar disk system. *The Astrophysical Journal Letters*, 553(2):L189.
- Lafrenière, D., Marois, C., Doyon, R., Nadeau, D., and Artigau, E. (2007). A new algorithm for point-spread function subtraction in high-contrast imaging: a demonstration with angular differential imaging. *The Astrophysical Journal*, 660(1):770.
- Lagrange, A.-M., Boccaletti, A., Langlois, M., Chauvin, G., Gratton, R., Beust, H., Desidera, S., Milli, J., Bonnefoy, M., Cheetham, A., et al. (2019a). Post-conjunction detection of  $\beta$  Pictoris b with VLT/SPHERE. *Astronomy & Astrophysics*, 621:L8.
- Lagrange, A.-M., Bonnefoy, M., Chauvin, G., Apai, D., Ehrenreich, D., Boccaletti, A., Gratadour, D., Rouan, D., Mouillet, D., Lacour, S., et al. (2010). A giant planet imaged in the disk of the young star  $\beta$  Pictoris. *Science*, 329(5987):57–59.
- Lagrange, A.-M., Gratadour, D., Chauvin, G., Fusco, T., Ehrenreich, D., Mouillet, D., Rousset, G., Rouan, D., Allard, F., Gendron, É., et al. (2009). A probable giant planet imaged in the  $\beta$  Pictoris disk-VLT/NaCo deep L’-band imaging. *Astronomy & Astrophysics*, 493(2):L21–L25.
- Lagrange, A.-M., Meunier, N., Rubini, P., Keppler, M., Galland, F., Chapellier, E., Michel, E., Balona, L., Beust, L., Guillot, T., et al. (2019b). Evidence for an additional planet in the  $\beta$  Pictoris system. *Nature Astronomy*.
- Langlois, M., Pohl, A., Lagrange, A.-M., Maire, A.-L., Mesa, D., Boccaletti, A., Gratton, R., Denneulin, L., Klahr, H., Vigan, A., et al. (2018). First scattered light detection of a nearly edge-on transition disk around the T Tauri star RY Lupi. *Astronomy & Astrophysics*, 614:A88.
- Latham, D. W., Mazeh, T., Stefanik, R. P., Mayor, M., and Burki, G. (1989). The unseen companion of HD114762: a probable brown dwarf. *Nature*, 339(6219):38.
- Lebrun, M., Buades, A., and Morel, J.-M. (2013). A nonlocal bayesian image denoising algorithm. *SIAM Journal on Imaging Sciences*, 6(3):1665–1688.

- LeCun, Y., Bengio, Y., and Hinton, G. (2015). Deep learning. *Nature*, 521(7553):436.
- Ledoit, O. and Wolf, M. (2004). A well-conditioned estimator for large-dimensional covariance matrices. *Journal of multivariate analysis*, 88(2):365–411.
- Lee, S.-H., Roichman, Y., Yi, G.-R., Kim, S.-H., Yang, S.-M., Van Blaaderen, A., Van Oostrum, P., and Grier, D. G. (2007). Characterizing and tracking single colloidal particles with video holographic microscopy. *Optics Express*, 15(26):18275–18282.
- Leisenring, J. M., Skrutskie, M., Hinz, P. M., Skemer, A., Bailey, V., Eisner, J., Garnavich, P., Hoffmann, W., Jones, T., Kenworthy, M., et al. (2012). On-sky operations and performance of LMIRcam at the Large Binocular Telescope. In *Ground-based and Airborne Instrumentation for Astronomy*, volume 8446. International Society for Optics and Photonics.
- Leith, E. N. and Upatnieks, J. (1962). Reconstructed wavefronts and communication theory. *Journal of the Optical Society of America*, 52(10):1123–1130.
- Lenzen, R., Hartung, M., Brandner, W., Finger, G., Hubin, N. N., Lacombe, F., LAGRANGE, A.-M., Lehnert, M. D., Moorwood, A. F., and Mouillet, D. (2003). NAOS-CONICA first on-sky results in a variety of observing modes. In *Instrument Design and Performance for Optical/Infrared Ground-based Telescopes*, volume 4841, pages 944–952. International Society for Optics and Photonics.
- Levenberg, K. (1944). A method for the solution of certain non-linear problems in least squares. *Quarterly of applied mathematics*, 2(2):164–168.
- Li, Q., He, X., Wang, Y., Liu, H., Xu, D., and Guo, F. (2013). Review of spectral imaging technology in biomedical engineering: achievements and challenges. *Journal of biomedical optics*, 18(10):100901.
- Li, W., Ogunbona, P., Shi, Y., and Kharitonenko, I. (2002). Modelling of color cross-talk in CMOS image sensors. In *IEEE International Conference on Acoustics, Speech, and Signal Processing*, volume 4, page 3576. IEEE.
- Lilliefors, H. W. (1967). On the Kolmogorov-Smirnov test for normality with mean and variance unknown. *Journal of the American statistical Association*, 62(318):399–402.
- Lisse, C. M., Chen, C., Wyatt, M., Morlok, A., Song, I., Bryden, G., and Sheehan, P. (2009). Abundant circumstellar silica dust and SiO gas created by a giant hypervelocity collision in the 12 Myr HD 172555 system. *The Astrophysical Journal*, 701(2):2019.
- Liu, S.-F., Jin, S., Li, S., Isella, A., and Li, H. (2018). New constraints on turbulence and embedded planet mass in the HD 163296 disk from planet–disk hydrodynamic simulations. *The Astrophysical Journal*, 857(2):87.
- Liu, T., Wei, Z., Rivenson, Y., de Haan, K., Zhang, Y., Wu, Y., and Ozcan, A. (2019). Deep learning-based color holographic microscopy. *Journal of biophotonics*.

- Lyot, B. (1939). The study of the solar corona and prominences without eclipses. *Monthly Notices of the Royal Astronomical Society*, 99.
- Macintosh, B., Graham, J., Barman, T., De Rosa, R., Konopacky, Q., Marley, M., Marois, C., Nielsen, E., Pueyo, L., Rajan, A., et al. (2015). Discovery and spectroscopy of the young jovian planet 51 Eri b with the Gemini Planet Imager. *Science*, 350(6256):64–67.
- Macintosh, B., Graham, J. R., Ingraham, P., Konopacky, Q., Marois, C., Perrin, M., Poyneer, L., Bauman, B., Barman, T., Burrows, A. S., et al. (2014). First light of the Gemini Planet Imager. *Proceedings of the National Academy of Sciences*, 111(35):12661–12666.
- MacKay, D. J. (1992). Bayesian interpolation. *Neural computation*, 4(3):415–447.
- Mahalanobis, A., Kumar, B. V., and Casasent, D. (1987). Minimum average correlation energy filters. *Applied Optics*, 26(17):3633–3640.
- Maire, A., Rodet, L., Cantalloube, F., Galicher, R., Brandner, W., Messina, S., Lazzoni, C., Mesa, D., Melnick, D., Carson, J., et al. (2019). Hint of curvature in the orbital motion of the exoplanet 51 Eridani b using 3 years of VLT/SPHERE monitoring. *Astronomy & Astrophysics*, 624:A118.
- Maire, A.-L., Langlois, M., Dohlen, K., Lagrange, A.-M., Gratton, R., Chauvin, G., Desidera, S., Girard, J. H., Milli, J., Vigan, A., et al. (2016). SPHERE IRDIS and IFS astrometric strategy and calibration. In *Ground-based and Airborne Instrumentation for Astronomy*, volume 9908. International Society for Optics and Photonics.
- Malvar, H. S., He, L.-w., and Cutler, R. (2004). High-quality linear interpolation for demosaicing of bayer-patterned color images. In *IEEE International Conference on Acoustics, Speech, and Signal Processing*, volume 3, page 485. IEEE.
- Marié, J.-L., Grosjean, N., Méès, L., Seifi, M., Fournier, C., Barbier, B., and Lance, M. (2014). Lagrangian measurements of the fast evaporation of falling diethyl ether droplets using in-line digital holography and a high-speed camera. *Experiments in fluids*, 55(4):1708.
- Marié, J.-L., Tronchin, T., Grosjean, N., Méès, L., Öztürk, O. C., Fournier, C., Barbier, B., and Lance, M. (2017). Digital holographic measurement of the lagrangian evaporation rate of droplets dispersing in a homogeneous isotropic turbulence. *Experiments in Fluids*, 58(2):11.
- Marim, M. M., Atlan, M., Angelini, E., and Olivo-Marin, J.-C. (2010). Compressed sensing with off-axis frequency-shifting holography. *Optics Letters*, 35(6):871–873.
- Marley, M. S., Saumon, D., Cushing, M., Ackerman, A. S., Fortney, J. J., and Freedman, R. (2012). Masses, radii, and cloud properties of the HR 8799 planets. *The Astrophysical Journal*, 754(2):135.

- Marois, C., Correia, C., Galicher, R., Ingraham, P., Macintosh, B., Currie, T., and De Rosa, R. (2014). GPI PSF subtraction with TLOCI: the next evolution in exoplanet/disk high-contrast imaging. In *Adaptive Optics Systems*, volume 9148. International Society for Optics and Photonics.
- Marois, C., Correia, C., Véran, J.-P., and Currie, T. (2013). TLOCI: A fully loaded speckle killing machine. *Proceedings of the International Astronomical Union*, 8(S299):48–49.
- Marois, C., Doyon, R., Racine, R., and Nadeau, D. (2000). Differential imaging coronagraph for the detection of faint companions. In *Optical and IR Telescope Instrumentation and Detectors*, volume 4008, pages 788–796. International Society for Optics and Photonics.
- Marois, C., Lafrenière, D., Doyon, R., Macintosh, B., and Nadeau, D. (2006). Angular differential imaging: a powerful high-contrast imaging technique. *The Astrophysical Journal*, 641(1):556.
- Marois, C., Macintosh, B., Barman, T., Zuckerman, B., Song, I., Patience, J., Lafrenière, D., and Doyon, R. (2008). Direct imaging of multiple planets orbiting the star HR 8799. *Science*, 322(5906):1348–1352.
- Marois, C., Zuckerman, B., Konopacky, Q. M., Macintosh, B., and Barman, T. (2010). Images of a fourth planet orbiting HR 8799. *Nature*, 468(7327):1080.
- Marquardt, D. W. (1963). An algorithm for least-squares estimation of nonlinear parameters. *Journal of the society for Industrial and Applied Mathematics*, 11(2):431–441.
- Matteoli, S., Diani, M., and Theiler, J. (2014). An overview of background modeling for detection of targets and anomalies in hyperspectral remotely sensed imagery. *IEEE Journal of Selected Topics in Applied Earth Observations and Remote Sensing*, 7(6):2317–2336.
- Mawet, D., Hirsch, L., Lee, E. J., Ruffio, J.-B., Bottom, M., Fulton, B. J., Absil, O., Beichman, C., Bowler, B., Bryan, M., et al. (2019). Deep exploration of  $\epsilon$  Eridani with Keck MS-band Vortex coronagraphy and radial velocities: Mass and orbital parameters of the giant exoplanet. *The Astronomical Journal*, 157(1):33.
- Mawet, D., Milli, J., Wahhaj, Z., Pelat, D., Absil, O., Delacroix, C., Boccaletti, A., Kasper, M., Kenworthy, M., Marois, C., et al. (2014). Fundamental limitations of high contrast imaging set by small sample statistics. *The Astrophysical Journal*, 792(2):97.
- Mawet, D., Pueyo, L., Lawson, P., Mugnier, L., Traub, W., Boccaletti, A., Trauger, J. T., Gladysz, S., Serabyn, E., Milli, J., et al. (2012). Review of small-angle coronagraphic techniques in the wake of ground-based second-generation adaptive optics systems. In *Space Telescopes and Instrumentation: Optical, Infrared, and Millimeter Wave*, volume 8442. International Society for Optics and Photonics.

- Mayor, M. and Queloz, D. (1995). A Jupiter-mass companion to a solar-type star. *Nature*, 378(6555):355.
- Mbamalu, G. and El-Hawary, M. (1993). Load forecasting via suboptimal seasonal autoregressive models and iteratively reweighted least squares estimation. *IEEE Transactions on Power Systems*, 8(1):343–348.
- Meillier, C., Chatelain, F., Michel, O., and Ayasso, H. (2015). Nonparametric bayesian extraction of object configurations in massive data. *IEEE Transactions on Signal Processing*, 63(8):1911–1924.
- Meillier, C., Chatelain, F., Michel, O., Bacon, R., Piqueras, L., Bacher, R., and Ayasso, H. (2016). SELFI: an object-based, bayesian method for faint emission line source detection in MUSE deep field data cubes. *Astronomy & Astrophysics*, 588:A140.
- Mesa, D., Bonnefoy, M., Gratton, R., Van Der Plas, G., D’Orazi, V., Sissa, E., Zurlo, A., Rigliaco, E., Schmidt, T., Langlois, M., et al. (2019a). Exploring the R CrA environment with SPHERE - Discovery of a new stellar companion. *Astronomy & Astrophysics*, 624:A4.
- Mesa, D., Langlois, M., Garufi, A., Gratton, R., Desidera, S., D’Orazi, V., Flasseur, O., Barbieri, M., Benisty, M., Henning, T., et al. (2019b). Determining mass limits around HD 163296 through SPHERE direct imaging data. *Monthly Notices of the Royal Astronomical Society*.
- Middleton, C., Hannel, M. D., Hollingsworth, A. D., Pine, D. J., and Grier, D. G. (2019). Optimizing the synthesis of monodisperse colloidal spheres using holographic particle characterization. *Langmuir*.
- Milli, J., Kasper, M., Bourget, P., Pannetier, C., Mouillet, D., Sauvage, J.-F., Reyes, C., Fusco, T., Cantalloube, F., Tristram, K., et al. (2018). Low wind effect on VLT/SPHERE: impact, mitigation strategy, and results. In *Adaptive Optics Systems*, volume 10703. International Society for Optics and Photonics.
- Milli, J., Mawet, D., Mouillet, D., Kasper, M., and Girard, J. H. (2016). Adaptive optics in high-contrast imaging. In *Astronomy at High Angular Resolution*, pages 17–41. Springer.
- Milli, J., Vigan, A., Mouillet, D., Lagrange, A.-M., Augereau, J.-C., Pinte, C., Mawet, D., Schmid, H. M., Boccaletti, A., Matra, L., et al. (2017). Near-infrared scattered light properties of the HR 4796 a dust ring – A measured scattering phase function from 13.6° to 166.6°. *Astronomy & Astrophysics*, 599:A108.
- Morton, T. D., Bryson, S. T., Coughlin, J. L., Rowe, J. F., Ravichandran, G., Petigura, E. A., Haas, M. R., and Batalha, N. M. (2016). False positive probabilities for all Kepler objects of interest: 1284 newly validated planets and 428 likely false positives. *The Astrophysical Journal*, 822(2):86.
- Morzinski, K. M., Close, L. M., Males, J. R., Kopon, D., Hinz, P. M., Esposito, S., Riccardi, A., Puglisi, A., Pinna, E., Briguglio, R., et al. (2014). MagAO: Status



- and on-sky performance of the Magellan adaptive optics system. In *Adaptive Optics Systems*, volume 9148. International Society for Optics and Photonics.
- Mudanyali, O., Tseng, D., Oh, C., Isikman, S. O., Sencan, I., Bishara, W., Oztoprak, C., Seo, S., Khademhosseini, B., and Ozcan, A. (2010). Compact, light-weight and cost-effective microscope based on lensless incoherent holography for telemedicine applications. *Lab on a Chip*, 10(11):1417–1428.
- Mugnier, L. M., Cornia, A., Sauvage, J.-F., Rousset, G., Fusco, T., and Védrenne, N. (2009). Optimal method for exoplanet detection by angular differential imaging. *Journal of the Optical Society of America A*, 26(6):1326–1334.
- Müller, A., Keppler, M., Henning, T., Samland, M., Chauvin, G., Beust, H., Maire, A.-L., Molaverdikhani, K., van Boekel, R., Benisty, M., et al. (2018). Orbital and atmospheric characterization of the planet within the gap of the PDS 70 transition disk. *Astronomy & Astrophysics*, 617:L2.
- Muma, M., Cheng, Y., Roemer, F., Haardt, M., and Zoubir, A. M. (2012). Robust source number enumeration for R-dimensional arrays in case of brief sensor failures. In *IEEE International Conference on Acoustics, Speech and Signal Processing*, pages 3709–3712. IEEE.
- Muma, M. and Zoubir, A. M. (2016). Bounded influence propagation  $\tau$ -estimation: A new robust method for ARMA model estimation. *IEEE Transactions on Signal Processing*, 65(7):1712–1727.
- Murphy, D. B. (2002). *Fundamentals of light microscopy and electronic imaging*. John Wiley & Sons.
- Muterspaugh, M. W., Lane, B. F., Kulkarni, S., Konacki, M., Burke, B. F., Colavita, M., Shao, M., Hartkopf, W. I., Boss, A. P., and Williamson, M. (2010). The PHASES differential astrometry data archive. Candidate substellar companions to binary systems. *The Astronomical Journal*, 140(6):1657.
- Nicolas, F., Coëtmelec, S., Brunel, M., and Lebrun, D. (2006). Digital in-line holography with a sub-picosecond laser beam. *Optics communications*, 268(1):27–33.
- Nicolas, F., Coëtmelec, S., Brunel, M., and Lebrun, D. (2007). Suppression of the Moiré effect in sub-picosecond digital in-line holography. *Optics Express*, 15(3):887–895.
- Nielsen, E. L. and Close, L. M. (2010). A uniform analysis of 118 stars with high-contrast imaging: long-period extrasolar giant planets are rare around sun-like stars. *The Astrophysical Journal*, 717(2):878.
- Nielsen, E. L., Close, L. M., Biller, B. A., Masciadri, E., and Lenzen, R. (2008). Constraints on extrasolar planet populations from VLT NaCo/SDI and MMT SDI and direct adaptive optics imaging surveys: giant planets are rare at large separations. *The Astrophysical Journal*, 674(1):466.

- Nielsen, E. L., De Rosa, R. J., Rameau, J., Wang, J. J., Esposito, T. M., Millar-Blanchaer, M. A., Marois, C., Vigan, A., Ammons, S. M., Artigau, E., et al. (2017). Evidence that the directly imaged planet HD 131399 Ab is a background star. *The Astronomical Journal*, 154(6):218.
- Nilsson, R., Veicht, A., Godfrey, P. G., Rice, E., Aguilar, J., Pueyo, L., Roberts Jr, L., Oppenheimer, R., Brenner, D., Luszcz-Cook, S., et al. (2017). Project 1640 observations of brown dwarf GJ 758 b: Near-infrared spectrum and atmospheric modeling. *The Astrophysical Journal*, 838(1):64.
- Olivier, T., Flasseur, O., Méès, L., and Fournier, C. (2018). Optimizing phase object reconstruction using an in-line digital holographic microscope and a reconstruction based on a Lorenz-Mie model. In *SPIE Photonics Europe, Unconventional Optical Imaging*, volume 10677. International Society for Optics and Photonics.
- Oppenheimer, B. R., Beichman, C., Brenner, D., Burruss, R., Cady, E., Crepp, J., Hillenbrand, L., Hinkley, S., Ligon, E. R., Lockhart, T., et al. (2012). Project 1640: the world’s first ExAO coronagraphic hyperspectral imager for comparative planetary science. In *Adaptive Optics Systems*, volume 8447. International Society for Optics and Photonics.
- Oppenheimer, B. R. and Hinkley, S. (2009). High-contrast observations in optical and infrared astronomy. *Annual Review of Astronomy and Astrophysics*, 47:253–289.
- Pascal, F., Chitour, Y., Ovarlez, J.-P., Forster, P., and Larzabal, P. (2008). Covariance structure maximum-likelihood estimates in compound Gaussian noise: Existence and algorithm analysis. *IEEE Transactions on Signal Processing*, 56(1):34–48.
- Pati, Y. C., Rezaiifar, R., and Krishnaprasad, P. S. (1993). Orthogonal matching pursuit: Recursive function approximation with applications to wavelet decomposition. In *Conference on signals, systems and computers*, pages 40–44. IEEE.
- Paul, L. C. and Al Sumam, A. (2012). Face recognition using principal component analysis method. *International Journal of Advanced Research in Computer Engineering & Technology*, 1(9):135–139.
- Pavlov, A., Möller-Nilsson, O., Feldt, M., Henning, T., Beuzit, J.-L., and Mouillet, D. (2008). SPHERE data reduction and handling system: overview, project status, and development. In *Advanced Software and Control for Astronomy*, volume 7019, page 701939. International Society for Optics and Photonics.
- Pearson, K. (1901). On lines and planes of closest fit to systems of points in space. *The London, Edinburgh, and Dublin Philosophical Magazine and Journal of Science*, 2(11):559–572.
- Pecaut, M. J. and Mamajek, E. E. (2013). Intrinsic colors, temperatures, and bolometric corrections of pre-main-sequence stars. *The Astrophysical Journal Supplement Series*, 208(1):9.

- Perrin, M. D., Sivaramakrishnan, A., Makidon, R. B., Oppenheimer, B. R., and Graham, J. R. (2003). The structure of high strehl ratio point-spread functions. *The Astrophysical Journal*, 596(1):702.
- Perryman, M. (2018). *The exoplanet handbook*. Cambridge University Press.
- Philips, L. A., Ruffner, D. B., Cheong, F. C., Blusewicz, J. M., Kasimbeg, P., Waisi, B., McCutcheon, J. R., and Grier, D. G. (2017). Holographic characterization of contaminants in water: Differentiation of suspended particles in heterogeneous dispersions. *Water Research*, 122:431–439.
- Pinte, C., Price, D., Ménard, F., Duchêne, G., Dent, W., Hill, T., de Gregorio-Monsalvo, I., Hales, A., and Mentiplay, D. (2018). Kinematic evidence for an embedded protoplanet in a circumstellar disk. *The Astrophysical Journal Letters*, 860(1):L13.
- Pires, R. C., Costa, A. S., and Mili, L. (1999). Iteratively reweighted least-squares state estimation through givens rotations. *IEEE Transactions on Power Systems*, 14(4):1499–1507.
- Plaza, A., Benediktsson, J. A., Boardman, J. W., Brazile, J., Bruzzone, L., Camps-Valls, G., Chanussot, J., Fauvel, M., Gamba, P., Gualtieri, A., et al. (2009). Recent advances in techniques for hyperspectral image processing. *Remote sensing of environment*, 113:S110–S122.
- Poor, H. V. (2013). *An introduction to signal detection and estimation*. Springer Science & Business Media.
- Portilla, J., Strela, V., Wainwright, M. J., and Simoncelli, E. P. (2003). Image denoising using scale mixtures of Gaussians in the wavelet domain. *IEEE Trans Image Processing*, 12(11).
- Pueyo, L. (2016). Detection and characterization of exoplanets using projections on Karhunen–Loève eigenimages: forward modeling. *The Astrophysical Journal*, 824(2):117.
- Pueyo, L. (2018). Direct imaging as a detection technique for exoplanets. *Handbook of Exoplanets*, pages 705–765.
- Pueyo, L., Crepp, J. R., Vasisht, G., Brenner, D., Oppenheimer, B. R., Zimmerman, N., Hinkley, S., Parry, I., Beichman, C., Hillenbrand, L., et al. (2012). Application of a damped locally optimized combination of images method to the spectral characterization of faint companions using an integral field spectrograph. *The Astrophysical Journal Supplement Series*, 199(1):6.
- Pueyo, L. and Kasdin, N. J. (2007). Polychromatic compensation of propagated aberrations for high-contrast imaging. *The Astrophysical Journal*, 666(1):609.
- Racine, R., Walker, G. A., Nadeau, D., Doyon, R., and Marois, C. (1999). Speckle noise and the detection of faint companions. *Publications of the Astronomical Society of the Pacific*, 111(759):587.

- Rameau, J., Chauvin, G., Lagrange, A.-M., Boccaletti, A., Quanz, S. P., Bonnefoy, M., Girard, J., Delorme, P., Desidera, S., Klahr, H., et al. (2013a). Discovery of a probable 4-5 Jupiter-mass exoplanet to HD 95086 by direct imaging. *The Astrophysical Journal Letters*, 772(2):L15.
- Rameau, J., Chauvin, G., Lagrange, A.-M., Meshkat, T., Boccaletti, A., Quanz, S. P., Currie, T., Mawet, D., Girard, J., Bonnefoy, M., et al. (2013b). Confirmation of the planet around HD 95086 by direct imaging. *The Astrophysical Journal Letters*, 779(2):L26.
- Rameau, J., Chauvin, G., Lagrange, A.-M., Thébault, P., Milli, J., Girard, J., and Bonnefoy, M. (2012). High-contrast imaging of the close environment of HD 142527-VLT/NaCo adaptive optics thermal and angular differential imaging. *Astronomy & Astrophysics*, 546:A24.
- Rastogi, P. K. and Sharma, A. (2003). Systematic approach to image formation in digital holography. *Optical Engineering*, 42(5):1208–1215.
- Rawat, S., Komatsu, S., Markman, A., Anand, A., and Javidi, B. (2017). Compact and field-portable 3D printed shearing digital holographic microscope for automated cell identification. *Applied Optics*, 56(9):127–133.
- Réfrégier, P. (1990). Filter design for optical pattern recognition: multicriteria optimization approach. *Optics Letters*, 15(15):854–856.
- Réfrégier, P. and Goudail, F. (2013). *Statistical image processing techniques for noisy images: an application-oriented approach*. Springer Science & Business Media.
- Réfrégier, P., Goudail, F., and Chesnaud, C. (1999). Statistically independent region models applied to correlation and segmentation techniques. In *Euro-American Workshop Optoelectronic Information Processing: A Critical Review*, volume 10296. International Society for Optics and Photonics.
- Réfrégier, P., Goudail, F., and Gaidon, T. (1996). Optimal location of random targets in random background: random Markov fields modelization. *Optics communications*, 128(4-6):211–215.
- Ren, D., Dou, J., Zhang, X., and Zhu, Y. (2012). Speckle noise subtraction and suppression with adaptive optics coronagraphic imaging. *The Astrophysical Journal*, 753(2):99.
- Rizzuto, A., Ireland, M., and Robertson, J. G. (2011). Multidimensional Bayesian membership analysis of the Sco OB2 moving group. *Monthly Notices of the Royal Astronomical Society*, 416(4):3108–3117.
- Robinson, D. and Milanfar, P. (2006). Statistical performance analysis of super-resolution. *IEEE Transactions on Image Processing*, 15(6):1413–1428.
- Rodigas, T. J., Hinz, P. M., Leisenring, J., Vaitheeswaran, V., Skemer, A. J., Skrutskie, M., Su, K. Y., Bailey, V., Schneider, G., Close, L., et al. (2012). The gray needle: large

- grains in the HD 15115 debris disk from LBT/PISCES/Ks and LBTI/LMIRcam/L' adaptive optics imaging. *The Astrophysical Journal*, 752(1):57.
- Rodionova, O. Y., Houmøller, L. P., Pomerantsev, A. L., Geladi, P., Burger, J., Dorofeyev, V. L., and Arzamastsev, A. P. (2005). NIR spectrometry for counterfeit drug detection: a feasibility study. *Analytica Chimica Acta*, 549(1-2):151–158.
- Rostykus, M., Soulez, F., Unser, M., and Moser, C. (2018). Compact in-line lensfree digital holographic microscope. *Methods*, 136:17–23.
- Rousseeuw, P. J. and Driessen, K. V. (1999). A fast algorithm for the minimum covariance determinant estimator. *Technometrics*, 41(3):212–223.
- Rousseeuw, P. J. and Leroy, A. M. (2005). *Robust regression and outlier detection*, volume 589. John Wiley & Sons.
- Rousset, G., Fontanella, J., Kern, P., Gigan, P., and Rigaut, F. (1990). First diffraction-limited astronomical images with adaptive optics. *Astronomy & Astrophysics*, 230:29–32.
- Royer, H. (1974). An application of high-speed microholography: the metrology of fogs. *Nouvelle Revue d'Optique*, 5(2):87.
- Ruane, G., Mawet, D., Kastner, J., Meshkat, T., Bottom, M., Castella, B. F., Absil, O., Gomez Gonzalez, C., Huby, E., Zhu, Z., et al. (2017). Deep imaging search for planets forming in the TW Hya protoplanetary disk with the Keck/NIRC2 Vortex coronagraph. *The Astronomical Journal*, 154(2):73.
- Rudin, L. I., Osher, S., and Fatemi, E. (1992). Nonlinear total variation based noise removal algorithms. *Physica D: nonlinear phenomena*, 60(1-4):259–268.
- Ruffio, J.-B., Macintosh, B., Wang, J. J., Pueyo, L., Nielsen, E. L., De Rosa, R. J., Czekala, I., Marley, M. S., Arriaga, P., Bailey, V. P., et al. (2017). Improving and assessing planet sensitivity of the GPI exoplanet survey with a forward model matched filter. *The Astrophysical Journal*, 842(1):14.
- Ruffio, J.-B., Mawet, D., Czekala, I., Macintosh, B., De Rosa, R. J., Ruane, G., Bottom, M., Pueyo, L., Wang, J. J., Hirsch, L., et al. (2018). A bayesian framework for exoplanet direct detection and non-detection. *The Astronomical Journal*, 156(5):196.
- Santerne, A., Díaz, R., Moutou, C., Bouchy, F., Hébrard, G., Almenara, J.-M., Bonomo, A., Deleuil, M., and Santos, N. (2012). SOPHIE velocimetry of Kepler transit candidates-VII. A false-positive rate of 35% for Kepler close-in giant candidates. *Astronomy & Astrophysics*, 545:A76.
- Saumon, D. and Marley, M. S. (2008). The evolution of L and T dwarfs in color-magnitude diagrams. *The Astrophysical Journal*, 689(2):1327.
- Sauvage, J.-F., Fusco, T., Guesalaga, A., Wizinowitch, P., O'Neal, J., N'Diaye, M., Vigan, A., Grard, J., Lesur, G., Mouillet, D., et al. (2015). Low wind effect, the main limitation of the SPHERE instrument. In *Adaptive Optics for Extremely Large Telescopes*, volume 1.

- Schäck, T., Muma, M., Feng, M., Guan, C., and Zoubir, A. M. (2017). Robust nonlinear causality analysis of nonstationary multivariate physiological time series. *IEEE Transactions on Biomedical Engineering*, 65(6):1213–1225.
- Schmitt, J., Zinnecker, H., Cruddace, R., and Harnden Jr, F. (1993). ROSAT detections of X-ray emission from young B-type stars. *The Astrophysical Journal*, 402:L13–L16.
- Schnars, U. and Jüptner, W. P. (2002). Digital recording and numerical reconstruction of holograms. *Measurement science and technology*, 13(9):R85.
- Schneider, J., Dedieu, C., Le Sidaner, P., Savalle, R., and Zolotukhin, I. (2011). Defining and cataloging exoplanets: the exoplanet.eu database. *Astronomy & Astrophysics*, 532:A79.
- Schultz, R. A., Nielsen, T., Zavaleta, J. R., Ruch, R., Wyatt, R., and Garner, H. R. (2001). Hyperspectral imaging: a novel approach for microscopic analysis. *Cytometry*, 43(4):239–247.
- Schütz, O., Meeus, G., and Sterzik, M. (2005). Mid-IR observations of circumstellar disks-II. Vega-type stars and a post-main sequence object. *Astronomy & Astrophysics*, 431(1):175–182.
- Seifi, M., Fournier, C., Denis, L., Chareyron, D., and Marié, J.-L. (2012). Three-dimensional reconstruction of particle holograms: a fast and accurate multiscale approach. *Journal of the Optical Society of America A*, 29(9):1808–1817.
- Seifi, M., Fournier, C., Grosjean, N., Méès, L., Marié, J.-L., and Denis, L. (2013). Accurate 3D tracking and size measurement of evaporating droplets using in-line digital holography and “inverse problems” reconstruction approach. *Optics Express*, 21(23):27964–27980.
- Sentis, M. P., Onofri, F. R., and Lamadie, F. (2018). Bubbles, drops, and solid particles recognition from real or virtual photonic jets reconstructed by digital in-line holography. *Optics Letters*, 43(12):2945–2948.
- Shack, R. V. (1971). Production and use of a lecticular Hartmann screen. *Journal of the Optical Society of America*, 61:656–661.
- Sharif, W., Muma, M., and Zoubir, A. M. (2013). Robustness analysis of spatial time-frequency distributions based on the influence function. *IEEE Transactions on Signal Processing*, 61(8):1958–1971.
- Sigl, J. (2016). Nonlinear residual minimization by iteratively reweighted least squares. *Computational Optimization and Applications*, 64(3):755–792.
- Simon, M. K. (2007). *Probability distributions involving Gaussian random variables: A handbook for engineers and scientists*. Springer Science & Business Media.
- Sirovich, L. and Kirby, M. (1987). Low-dimensional procedure for the characterization of human faces. *Journal of the Optical Society of America A*, 4(3):519–524.



- Sivaramakrishnan, A., Koresko, C. D., Makidon, R. B., Berkefeld, T., and Kuchner, M. J. (2001). Ground-based coronagraphy with high-order adaptive optics. *The astrophysical journal*, 552(1):397.
- Smith, I., Ferrari, A., and Carillet, M. (2009). Detection of a moving source in speckle noise. application to exoplanet detection. *IEEE Transactions on Signal Processing*, 57(3):904–915.
- Soulez, F., Denis, L., Fournier, C., Thiébaud, É., and Goepfert, C. (2007a). Inverse-problem approach for particle digital holography: accurate location based on local optimization. *Journal of the Optical Society of America A*, 24(4):1164–1171.
- Soulez, F., Denis, L., Thiébaud, É., Fournier, C., and Goepfert, C. (2007b). Inverse problem approach in particle digital holography: out-of-field particle detection made possible. *Journal of the Optical Society of America A*, 24(12):3708–3716.
- Soummer, R., Pueyo, L., and Larkin, J. (2012). Detection and characterization of exoplanets and disks using projections on Karhunen-Loève eigenimages. *The Astrophysical Journal Letters*, 755(2):L28.
- Sparks, W. B. and Ford, H. C. (2002). Imaging spectroscopy for extrasolar planet detection. *The Astrophysical Journal*, 578(1):543.
- Stark, C. C., Schneider, G., Weinberger, A. J., Debes, J. H., Grady, C. A., Jang-Condell, H., and Kuchner, M. J. (2014). Revealing asymmetries in the HD 181327 debris disk: a recent massive collision or interstellar medium warping. *The Astrophysical Journal*, 789(1):58.
- Stein, C. M. (1981). Estimation of the mean of a multivariate normal distribution. *The annals of Statistics*, pages 1135–1151.
- Stephens, D. J. and Allan, V. J. (2003). Light microscopy techniques for live cell imaging. *Science*, 300(5616):82–86.
- Tankam, P., Picart, P., Mounier, D., Desse, J. M., and Li, J.-c. (2010). Method of digital holographic recording and reconstruction using a stacked color image sensor. *Applied Optics*, 49(3):320–328.
- Tarantola, A. (2005). *Inverse problem theory and methods for model parameter estimation*, volume 89. Siam.
- Teague, R., Bae, J., Bergin, E. A., Birnstiel, T., and Foreman-Mackey, D. (2018). A kinematical detection of two embedded jupiter-mass planets in HD 163296. *The Astrophysical Journal Letters*, 860(1):L12.
- Thalmann, C., Janson, M., Garufi, A., Boccaletti, A., Quanz, S. P., Sissa, E., Gratton, R., Salter, G., Benisty, M., Bonnefoy, M., et al. (2016). Resolving the planet-hosting inner regions of the LkCa 15 disk. *The Astrophysical journal letters*, 828(2).

- Thiébaud, É. (2002). Optimization issues in blind deconvolution algorithms. In *Astronomical Data Analysis*, volume 4847, pages 174–184. International Society for Optics and Photonics.
- Thiébaud, É., Devaney, N., Langlois, M., and Hanley, K. (2016). Exploiting physical constraints for multi-spectral exo-planet detection. In *SPIE Astronomical Telescopes+ Instrumentation*, page 99091. International Society for Optics and Photonics.
- Thiébaud, É. and Mugnier, L. (2005). Maximum a posteriori planet detection and characterization with a nulling interferometer. *Proceedings of the International Astronomical Union*, 1(C200):547–552.
- Thompson, A. M., Brown, J. C., Kay, J. W., and Titterton, D. M. (1991). A study of methods of choosing the smoothing parameter in image restoration by regularization. *IEEE Transactions on Pattern Analysis & Machine Intelligence*, (4):326–339.
- Traub, W. A. and Oppenheimer, B. R. (2010). Direct imaging of exoplanets. *Exoplanets*, pages 111–156.
- Trouvé, P. (2012). *Conception conjointe optique/traitement pour un imageur compact à capacité 3D*. PhD thesis, Ecole Centrale de Nantes (ECN).
- Turk, M. A. and Pentland, A. P. (1991). Face recognition using eigenfaces. In *Computer Society Conference on Computer Vision and Pattern Recognition*, pages 586–591. IEEE.
- Turon, F., Ahouzi, E., Campos, J., Chalasinska-Macukow, K., and Yzuel, M. (1994). Nonlinearity effects in the pure phase correlation method in multiobject scenes. *Applied Optics*, 33(11):2188–2191.
- Tyler, G. A. and Thompson, B. J. (1976). Fraunhofer holography applied to particle size analysis a reassessment. *Journal of Modern Optics*, 23(9):685–700.
- van Boekel, R., Henning, T., Menu, J., De Boer, J., Langlois, M., Müller, A., Avenhaus, H., Boccaletti, A., Schmid, H. M., Thalmann, C., et al. (2017). Three radial gaps in the disk of TW Hydrae imaged with SPHERE. *The Astrophysical Journal*, 837(2):132.
- Van Trees, H. L. (2004). *Detection, estimation, and modulation theory, part I: detection, estimation, and linear modulation theory*. John Wiley & Sons.
- Vandewiele, S., Strubbe, F., Schreuer, C., Neyts, K., and Beunis, F. (2017). Low coherence digital holography microscopy based on the Lorenz-Mie scattering model. *Optics Express*, 25(21):25853–25866.
- Vasile, G., Ovarlez, J.-P., Pascal, F., and Tison, C. (2009). Coherency matrix estimation of heterogeneous clutter in high-resolution polarimetric SAR images. *IEEE Transactions on Geoscience and Remote Sensing*, 48(4):1809–1826.
- Verrier, N. and Fournier, C. (2015). Digital holography super-resolution for accurate three-dimensional reconstruction of particle holograms. *Optics Letters*, 40(2):217–220.

- Verrier, N., Fournier, C., and Fournel, T. (2015). 3D tracking the brownian motion of colloidal particles using digital holographic microscopy and joint reconstruction. *Applied Optics*, 54(16):4996–5002.
- Verrier, N., Fournier, C., Méès, L., and Fournel, T. (2014). In-line particle holography with an astigmatic beam: setup self-calibration using an “inverse problems” approach. *Applied Optics*, 53(27):147–156.
- Verrier, N., Grosjean, N., Dib, E., Méès, L., Fournier, C., and Marié, J.-L. (2016). Improvement of the size estimation of 3D tracked droplets using digital in-line holography with joint estimation reconstruction. *Measurement Science and Technology*, 27(4):045001.
- Vigan, A., Langlois, M., Moutou, C., and Dohlen, K. (2008). Exoplanet characterization with long slit spectroscopy. *Astronomy & Astrophysics*, 489(3):1345–1354.
- Vigan, A., Moutou, C., Langlois, M., Allard, F., Boccaletti, A., Carbillet, M., Mouillet, D., and Smith, I. (2010). Photometric characterization of exoplanets using angular and spectral differential imaging. *Monthly Notices of the Royal Astronomical Society*, 407(1):71–82.
- Wagner, K., Apai, D., Kasper, M., Kratter, K., McClure, M., Robberto, M., and Beuzit, J.-L. (2016). Direct imaging discovery of a Jovian exoplanet within a triple-star system. *Science*, 353(6300):673–678.
- Wagner, K., Follete, K. B., Close, L. M., Apai, D., Gibbs, A., Keppler, M., Müller, A., Henning, T., Kasper, M., Wu, Y.-L., et al. (2018). Magellan adaptive optics imaging of PDS 70: Measuring the mass accretion rate of a young giant planet within a gapped disk. *The Astrophysical Journal Letters*, 863(1):L8.
- Wahba, G. et al. (1985). A comparison of GCV and GML for choosing the smoothing parameter in the generalized spline smoothing problem. *The Annals of Statistics*, 13(4):1378–1402.
- Wahhaj, Z., Cieza, L. A., Mawet, D., Yang, B., Canovas, H., de Boer, J., Casassus, S., Ménard, F., Schreiber, M. R., Liu, M. C., et al. (2015). Improving signal-to-noise in the direct imaging of exoplanets and circumstellar disks with MLOCI. *Astronomy & Astrophysics*, 581:A24.
- Wainwright, M. J. and Simoncelli, E. P. (2000). Scale mixtures of Gaussians and the statistics of natural images. In *Advances in neural information processing systems*, pages 855–861.
- Wang, C., Cheong, F. C., Ruffner, D. B., Zhong, X., Ward, M. D., and Grier, D. G. (2016). Holographic characterization of colloidal fractal aggregates. *Soft matter*, 12(42):8774–8780.
- Wang, J., Dogandzic, A., and Nehorai, A. (2006). Maximum likelihood estimation of compound-Gaussian clutter and target parameters. *IEEE Transactions on Signal Processing*, 54(10):3884–3898.

- Wolke, R. and Schwetlick, H. (1988). Iteratively reweighted least squares: algorithms, convergence analysis, and numerical comparisons. *SIAM journal on scientific and statistical computing*, 9(5):907–921.
- Wolszczan, A. and Frail, D. A. (1992). A planetary system around the millisecond pulsar PSR B1257+12. *Nature*, 355(6356):145.
- Wu, Y., Zhang, Y., Luo, W., and Ozcan, A. (2016). Demosaiced pixel super-resolution for multiplexed holographic color imaging. *Scientific Reports*, 6.
- Xu, H. and Wang, X.-j. (2007). Applications of multispectral/hyperspectral imaging technologies in military. *Infrared and Laser Engineering*, 36(1):13.
- Yamaguchi, I., Matsumura, T., and Kato, J.-I. (2002). Phase-shifting color digital holography. *Optics Letters*, 27(13):1108–1110.
- Yamaguchi, Y., Moriyama, T., Ishido, M., and Yamada, H. (2005). Four-component scattering model for polarimetric SAR image decomposition. *IEEE Transactions on Geoscience and Remote Sensing*, 43(8):1699–1706.
- Ygouf, M. (2012). *Nouvelle méthode de traitement d’images multispectrales fondée sur un modèle d’instrument pour la haut contraste: application à la détection d’exoplanètes*. PhD thesis, Grenoble.
- Yip, K. H., Nikolaou, N., Coronica, P., Tsiaras, A., Edwards, B., Changeat, Q., Morvan, M., Biller, B., Hinkley, S., Salmond, J., et al. (2019). Pushing the limits of exoplanet discovery via direct imaging with deep learning. *arXiv preprint arXiv:1904.06155*.
- Yohai, V. J. (1987). High breakdown-point and high efficiency robust estimates for regression. *The Annals of Statistics*, pages 642–656.
- Yokogawa, S., Burgos, S. P., and Atwater, H. A. (2012). Plasmonic color filters for CMOS image sensor applications. *Nano Letters*, 12(8):4349–4354.
- Yu, Y., Chen, Q., Wen, L., Hu, X., and Zhang, H.-F. (2015). Spatial optical crosstalk in CMOS image sensors integrated with plasmonic color filters. *Optics Express*, 23(17):21994–22003.
- Zhang, Y., Greenbaum, A., Luo, W., and Ozcan, A. (2015). Wide-field pathology imaging using on-chip microscopy. *Virchows Archiv*, 467(1):3–7.
- Zhang, Y., Liu, T., Huang, Y., Teng, D., Bian, Y., Wu, Y., Rivenson, Y., Feizi, A., and Ozcan, A. (2019). Accurate color imaging of pathology slides using holography and absorbance spectrum estimation of histochemical stains. *Journal of Biophotonics*, 12(3):e201800335.
- Zhao, J., Jiang, H., and Di, J. (2008). Recording and reconstruction of a color holographic image by using digital lensless fourier transform holography. *Optics Express*, 16(4):2514–2519.

- Zhao, Z.-Q., Zheng, P., Xu, S.-t., and Wu, X. (2019). Object detection with deep learning: A review. *IEEE transactions on neural networks and learning systems*.
- Zoran, D. and Weiss, Y. (2011). From learning models of natural image patches to whole image restoration. In *International Conference on Computer Vision*, pages 479–486. IEEE.
- Zoubir, A. M., Koivunen, V., Ollila, E., and Muma, M. (2018). *Robust statistics for signal processing*. Cambridge University Press.





# List of publications

Accepted publications are emphasized in black while submitted publications still in the peer-review process are marked in gray.

## Journal

[1] **O. Flasseur**, L. Denis, É. Thiébaud, and M. Langlois, “Robustness to bad frames in angular differential imaging: a local weighting approach”, *Astronomy & Astrophysics*, 634, A2, 2020.

⇒ DOI : <https://doi.org/10.1051/0004-6361/201935859>.

⇒ Cited in Chapter 4 as [Flasseur et al. \(2020b\)](#).

[2] **O. Flasseur**, L. Denis, É. Thiébaud, and M. Langlois, “Exoplanet detection in angular differential imaging by statistical learning of the nonstationary patch covariances – The PACO algorithm”, *Astronomy & Astrophysics*, 618, A138, 2018.

⇒ DOI : <https://doi.org/10.1051/0004-6361/201832745>.

⇒ Cited in Chapter 2 as [Flasseur et al. \(2018a\)](#).

[3] **O. Flasseur**, C. Fournier, N. Verrier, L. Denis, F. Jolivet, A. Cazier, and T. Lépine, “Self-calibration for lensless color microscopy”, *Applied Optics*, 56(13):F189–F199, 2017.

⇒ DOI : <https://doi.org/10.1364/AO.56.00F189>.

⇒ Cited in Chapter 7 as [Flasseur et al. \(2017b\)](#).

[4] A. Berdeu, **O. Flasseur**, L. Méès, L. Denis, F. Momey, T. Olivier, N. Grosjean, and C. Fournier, “Reconstruction of in-line holograms: combining model-based and regularized inversion”, *Optics Express* 27, 14951-14968, 2019.

⇒ DOI : <https://doi.org/10.1364/OE.27.014951>.

⇒ Cited in Chapter 1 as [Berdeu et al. \(2019\)](#).

(5) **O. Flasseur**, L. Denis, É. Thiébaud, and M. Langlois, “PACO ASDI: an algorithm for exoplanet detection and characterization in direct imaging with integral field spectrographs”, *in revision for Astronomy & Astrophysics*, 2020.

⇒ Cited in Chapter 6 as [Flasseur et al. \(2020a\)](#).

[6] D. Mesa, M. Langlois, A. Garufi, R. Gratton, S. Desidera, V. D’Orazi, **O. Flasseur**, M. Barbieri, M. Benisty, T. Henning, R. Ligi, E. Sissa, A. Vigan, A. Zurlo, A. Boccaletti, M. Bonnefoy, F. Cantalloube, G. Chauvin, A. Cheetham, V. De Caprio, P. Delorme, M. Feldt, T. Fusco, L. Gluck, J. Hagelberg, A.-M. Lagrange, C. Lazzoni, F. Madec, A.-L. Maire, F. Menard, M. Meyer, J. Ramos, E.L. Rickman, D. Rouan, and T. Schmidt, “Determining mass limits around HD 163296 through SPHERE direct imaging data”, *Monthly Notices of the Royal Astronomical Society*, 488, 37-46, 2019.

⇒ DOI : <https://doi.org/10.1093/mnras/stz1662>.

⇒ Cited in Chapter 8 as [Mesa et al. \(2019b\)](#).

[7] D. Mesa, M. Keppler, F. Cantalloube, L. Rodet, B. Charnay, R. Gratton, M. Langlois, A. Boccaletti, M. Bonnefoy, A. Vigan, **O. Flasseur**, J. Bae, M. Benisty, G. Chauvin, J. de Boer, S. Desidera, T. Henning, A.-M. Lagrange, M. Meyer, J. Milli, A. Müller, B. Pairet, A. Zurlo, S. Antonucci, J.-L. Baudino, S. Brown Sevilla, E. Cascone, A. Cheetham, R.U. Claudi, P. Delorme, V. D’Orazi, M. Feldt, J. Hagelberg, M. Janson, Q. Kral, E. Lagadec, C. Lazzoni, R. Ligi, A.-L. Maire, P. Martinez, F. Menard, N. Meunier, C. Perrot, S. Petrus, E.L. Rickman, S. Rochat, D. Rouan, M. Samland, J.-F. Sauvage, T. Schmidt, L. Weber, F. Wildi, “VLT/SPHERE exploration of the young multiplanetary system PDS70”, *Astronomy & Astrophysics*, 632, A25, 2019.

⇒ DOI : <https://doi.org/10.1051/0004-6361/201936764>.

### International Conferences

[8] **O. Flasseur**, L. Denis, É. Thiébaud, T. Olivier, and C. Fournier, “ExpACO: detection of an extended pattern under nonstationary correlated noise by patch covariance modeling”, *In European Signal Processing Conference (EUSIPCO)*, 1-5, 2019.

⇒ DOI : <https://doi.org/10.23919/EUSIPCO.2019.8903021>.

⇒ Cited in Chapter 3 as [Flasseur et al. \(2019\)](#).

[9] **O. Flasseur**, L. Denis, É. Thiébaud, and M. Langlois, “An unsupervised patch-based approach for exoplanet detection by direct imaging”, *In IEEE International Conference on Image Processing (ICIP)*, 2735-2739, 2018.

⇒ DOI : <https://doi.org/10.1109/ICIP.2018.8451431>.

⇒ Cited in Chapter 2 as [Flasseur et al. \(2018b\)](#).

[10] **O. Flasseur**, L. Denis, C. Fournier, and É. Thiébaud, “Robust object characterization from lensless microscopy videos”, *In European Signal Processing Conference (EUSIPCO)*, 1445-1449, 2017.

⇒ DOI : <https://doi.org/10.23919/EUSIPCO.2017.8081448>.

⇒ Cited in Chapter 5 as [Flasseur et al. \(2017a\)](#).

[11] **O. Flasseur**, L. Denis, É. Thiébaud, and M. Langlois, “Exoplanet detection in angular and spectral differential imaging: local learning of background

correlations for improved detection”, *In SPIE Astronomical telescopes + instrumentation, Adaptive Optics Systems VI*, 10703, 107032R, 2018.

⇒ DOI : <https://doi.org/10.1117/12.2313601>.

⇒ Cited in Chapter 6 as Flasseur et al. (2018c).

[12] **O. Flasseur**, F. Jolivet, F. Momey, L. Denis, and C. Fournier, “Improving color lensless microscopy reconstructions by self-calibration”, *In SPIE Photonics Europe, Unconventional Optical Imaging*, 10677, 106771A, 2018.

⇒ DOI : <https://doi.org/10.1117/12.2300005>.

⇒ Cited in Chapter 7 as Flasseur et al. (2018d).

[13] T. Olivier, **O. Flasseur**, L. Méès, and C. Fournier, “Optimizing phase object reconstruction using an in-line digital holographic microscope and a reconstruction based on a Lorenz Mie model”, *In SPIE Photonics Europe, Unconventional Optical Imaging*, 10677, 106772J, 2018.

⇒ DOI : <https://doi.org/10.1117/12.2311321>.

⇒ Cited in Chapter 1 as Olivier et al. (2018).

[14] A. Berdeu, **O. Flasseur**, C. Fournier, L. Méès, L. Denis, F. Momey, T. Olivier, N. Grosjean, “Reconstruction of in-line holograms combining model fitting and image-based regularized inversion”, *In Digital Holography and 3-D Imaging, Optical Society of America*, 2019.

⇒ DOI : <https://doi.org/10.1364/DH.2019.W2B.2>.

[15] C. Fournier, **O. Flasseur**, A. Berdeu, F. Momey, O. Thomas, and L. Denis, “Numerical reconstruction of holograms using inverse problems approaches”, *In Digital Holography and 3-D Imaging, Optical Society of America*, 2019.

⇒ DOI : <https://doi.org/10.1364/DH.2019.W2B.1>.

### National Conferences

[16] **O. Flasseur**, L. Denis, É. Thiébaud, and M. Langlois, “Détection d’exoplanètes par une modélisation statistique locale de la covariance spatio-temporelle du fond”, *In GretsI*, 2019.

[17] **O. Flasseur**, L. Denis, É. Thiébaud, and M. Langlois, “Détection d’exoplanètes basée sur une modélisation statistique locale des patches”, *In GretsI*, 2017.

### Other communications & workshops

[18] **O. Flasseur**, L. Denis, É. Thiébaud, M. Langlois, “Exoplanet detection in direct imaging by statistical learning of the non-stationary patch covariances – The PACO-based algorithms”, *In SPHERE annual workshop*, 2019.

[19] **O. Flasseur**, L. Denis, É. Thiébaud, and M. Langlois, “An unsupervised patch-based approach for exoplanet detection by direct imaging. The PACO

algorithm”, *In Inverse Problems Methods, Applications and Synergies workshop (IPMAS)*, 2019.

[20] **O. Flasseur**, L. Denis, É. Thiébaud, and M. Langlois, “Exoplanet detection in angular and spectral differential imaging by a local learning of background correlations”, *In Journées en Analyse et Traitement d’Images Astronomiques (JATIA)*, 2019.

[21] **O. Flasseur**, L. Denis, and C. Fournier, “Microscopie sans lentille : reconstruction par approche inverse robuste”, *In XIIèmes Journées de l’Imagerie Optique Non Conventiionnelle (JIONC) – GdR ISIS*, 2017.

[22] **O. Flasseur**, C. Fournier, N. Verrier, L. Denis, F. Jolivet, and A. Cazier, “Auto-étalonnage couleur pour la microscopie sans lentille”, *In IVème Rencontre d’Holographie Appliquée à la Métrologie des Fluides (HOLOPHI 4)*, 2016.

[23] A. Berdeu, **O. Flasseur**, L. Denis, F. Momey, L. Méès, N. Grosjean, and C. Fournier, “Joint reconstruction in in-line holography combining parametric and non-parametric inverse approaches: application to fluid mechanics”, *In Vème Rencontre d’Holographie Appliquée à la Métrologie des Fluides (HOLOPHI 5)*, 2018.

[24] F. Jolivet, **O. Flasseur**, F. Momey, L. Denis, and C. Fournier, “Auto-étalonnage d’un dispositif d’holographie couleur sans lentille et étude de performances”, *In Journée Co-Conception : Capteurs Hybrides et Algorithmes pour des Systèmes Innovants – GdR ISIS*, 2017.

[25] F. Momey, F. Jolivet, L. Denis, A. Berdeu, **O. Flasseur**, T. Olivier, and C. Fournier, “Méthodologie problèmes inverses pour la reconstruction d’hogrammes en ligne d’objets de phase et/ou absorbants”, *In Vème Rencontre d’Holographie Appliquée à la Métrologie des Fluides (HOLOPHI 5)*, 2018.

[26] F. Jolivet, C. Fournier, L. Denis, N. Verrier, **O. Flasseur**, F. Momey, and T. Fournel, “Reconstruction super-résolue d’hogrammes RVB”, *In IVème Rencontre d’Holographie Appliquée à la Métrologie des Fluides (HOLOPHI 4)*, 2016.

### **Seminars**

[27] **O. Flasseur**, L. Denis, É. Thiébaud, M. Langlois, “Exoplanet detection in direct imaging by statistical learning of the non-stationary patch covariances – The PACO-based algorithms”, *The European Southern Observatory*, Santiago, Chile, 2019.

[28] **O. Flasseur**, L. Denis, É. Thiébaud, M. Langlois, “Exoplanet detection in direct imaging by statistical learning of the non-stationary patch covariances – The PACO-based algorithms”, *Observatory of Geneva*, Geneva, Switzerland, 2019.

[29] **O. Flasseur**, L. Denis, É. Thiébaud, M. Langlois, “Exoplanet detection

in direct imaging by statistical learning of the non-stationary patch covariances – The PACO-based algorithms”, *Centre de Recherche Astrophysique de Lyon*, Saint-Genis-Laval, France, 2019.

**Informal communications**

[30] **O. Flasseur**, L. Denis, and C. Fournier, “Detection and characterization of faint signals in images: application in astronomy and lensless microscopy”, *Journée de la recherche de l’école doctorale EDSIS*, 2019.

⇒ 1<sup>er</sup> prix, concours basé sur une session posters suivie d’une présentation orale de 3 minutes, 91 participants.

[31] **O. Flasseur**, L. Denis, É. Thiébaud, M. Langlois, and C. Fournier, “Objects detection and characterization in images with weak signal-to-noise ratio: applications in microscopy and astronomy”, *In Gretsi Summer School on Signals, Images and Data Science*, 2018.







– *Abstract* –

Detecting and characterizing objects in images in the low signal-to-noise ratio regime is a critical issue in many areas such as astronomy or microscopy. In astronomy, the detection of exoplanets and their characterization by direct imaging from the Earth is a hot topic. A target star and its close environment (hosting potential exoplanets) are observed on short exposures. In microscopy, in-line holography is a cost-effective method for characterizing microscopic objects. Based on the recording of a hologram, it allows a digital focusing in any plane of the imaged 3-D volume. In these two fields, the object detection problem is made difficult by the low contrast between the objects and the nonstationary background of the recorded images.

In this thesis, we propose an unsupervised exoplanet detection and characterization algorithm based on the statistical modeling of background fluctuations. The method, based on a modeling of the statistical distribution of patches, captures their spatial covariances. It reaches a performance superior to state-of-the-art techniques on several datasets of the European high-contrast imager SPHERE operating at the Very Large Telescope. It produces statistically grounded and spatially-stationary detection maps in which detections can be performed at a constant probability of false alarm. It also produces photometrically unbiased spectral energy distributions of the detected sources. The use of a statistical model of the data leads to reliable photometric and astrometric accuracies. This methodological framework can be adapted to the detection of spatially-extended patterns in strong structured background, such as the diffraction patterns in holographic microscopy. We also propose robust approaches based on weighting strategies to reduce the influence of the numerous outliers present in real data. We show on holographic videos that the proposed weighting approach achieves a bias/variance tradeoff. In astronomy, the robustness improves the performance of our detection method in particular at close separations where the stellar residuals dominate. Our algorithms are adapted to benefit from the possible spectral diversity of the data, which improves the detection and characterization performance. All the algorithms developed are unsupervised: weighting and/or regularization parameters are estimated in a data-driven fashion. Beyond the applications in astronomy and microscopy, the signal processing methodologies introduced are general and could be applied to other detection and estimation problems.

– *Résumé* –

La détection et la caractérisation d'objets dans des images à faible rapport signal sur bruit est un problème courant dans de nombreux domaines tels que l'astronomie ou la microscopie. En astronomie, la détection des exoplanètes et leur caractérisation par imagerie directe depuis la Terre sont des sujets de recherche très actifs. Une étoile cible et son environnement proche (abritant potentiellement des exoplanètes) sont observés sur de courtes poses. En microscopie, l'holographie en ligne est une méthode de choix pour caractériser à faibles coûts les objets microscopiques. Basée sur l'enregistrement d'un hologramme, elle permet une mise au point numérique dans n'importe quel plan du volume 3-D imagé. Dans ces deux applications cibles, le problème est rendu difficile par le faible contraste entre les objets et le fond non stationnaire des images enregistrées.

Dans cette thèse, nous proposons un algorithme non-supervisé dédié à la détection et à la caractérisation d'exoplanètes par une modélisation statistique des fluctuations du fond. Cette méthode est basée sur une modélisation de la distribution statistique des données à une échelle locale de patches, capturant ainsi leur covariances spatiales. Testé sur plusieurs jeux de données de l'imageur haut-contraste SPHERE opérant au Très Grand Télescope Européen, cet algorithme atteint de meilleures performances que les méthodes de l'état de l'art. En particulier, les cartes de détection produites sont stationnaires et statistiquement fondées. La détection des exoplanètes peut ainsi être effectuée à probabilité de fausse alarme contrôlée. L'estimation de la distribution d'énergie spectrale des sources détectées est également non biaisée. L'utilisation d'un modèle statistique permet également de déduire des précisions photométriques et astrométriques fiables. Ce cadre méthodologique est ensuite adapté pour la détection de motifs spatialement étendus tels que les motifs de diffraction rencontrés en microscopie holographique qui sont également dominés par un fond non-stationnaire. Nous proposons aussi des approches robustes basées sur des stratégies de pondération afin de réduire l'influence des nombreuses valeurs aberrantes présentes sur les données réelles. Nous montrons sur des vidéos holographiques que les méthodes de pondération proposées permettent d'atteindre un compromis biais/variance. En astronomie, la robustesse améliore les performances de détection, en particulier à courtes séparations angulaires, où les fuites stellaires dominent. Les algorithmes développés sont également adaptés pour tirer parti de la diversité spectrale des données en plus de leur diversité temporelle, améliorant ainsi leurs performances de détection et de caractérisation. Tous les algorithmes développés sont totalement non-supervisés: les paramètres de pondération et/ou de régularisation sont estimés directement à partir des données. Au-delà des applications considérées en astronomie et en microscopie, les méthodes de traitement du signal introduites dans cette thèse sont générales et pourraient être appliquées à d'autres problèmes de détection et d'estimation.